NUMERICAL SIMULATIONS OF DISTURBANCE DEVELOPMENT IN ROTATING BOUNDARY-LAYERS

By

Christian Thomas

SUBMITTED IN PARTIAL FULFILLMENT OF THE
REQUIREMENTS FOR THE DEGREE OF
DOCTOR OF PHILOSOPHY
AT
CARDIFF UNIVERSITY
CARDIFF, UK
SEPTEMBER 2007

ProQuest LLC
789 East Eisenhower Parkway
P.O. Box 1346
Ann Arbor, MI 48106-1346

Declaration

This work has not previously been accepted in substance for any degree and is not concurrently submitted in candidature for any degree.

Signed.....C. Thomas.....(candidate) Date.....24/9/07.....

Statement 1

This thesis is being submitted in partial fulfillment of the requirements for the degree of PhD.

Signed.....C. Thomas.....(candidate) Date.....24/9/07.....

Statement 2

This thesis is the result of my own independent work/investigation, except where otherwise stated. Other sources are acknowledged by explicit references.

Signed.....C. Thomas.....(candidate) Date.....24/9/07.....

Statement 3

I hereby give consent for my thesis, if accepted, to be made available for photocopying and for interlibrary loan, and for the title and summary to be made available to outside organisations.

Signed.....C. Thomas.....(candidate) Date.....24/9/07.....

Table of Contents

Abstract

Recent theoretical studies by Lingwood (1995, 1997a,b) on the rotating-disk boundary-layer, have shown, using an analysis that deploys the usual 'parallel-flow' approximation, that there exists a region of absolute instability. However, by taking into account the radial variation of the mean flow, Davies & Carpenter (2003) have shown, using numerical simulations, that the absolute instability does not give rise to an unstable linear global mode. In fact convective behaviour is found to dominate the global response.

The aim of the current study is to further the studies of Davies & Carpenter (2003) to other rotating boundary-layers. Uniform suction and a uniform axial magnetic field are known to be stabilizing. However, by considering non-parallel effects, globally unstable behaviour is observed, albeit without the promotion of a fixed global frequency. An investigation is also carried out on the so called *BEK* family of rotating boundary-layers, which includes the Bödewadt, Ekman and von Kármán flows. All of these flows are absolutely unstable, when the parallel flow approximation is applied. However, by considering the genuine non-parallel flow, the numerical simulation results indicate that the kind of behaviour found for the von Kármán flow is carried over to other flows in the *BEK* family.

The numerical simulation results of the rotating-disk boundary-layer can be modeled using the linearized complex Ginzburg-Landau equation. By deriving expressions for the stability, convection velocity and diffusion/dispersion effects, in terms of the

numerical simulation results, the Green's solutions to the Ginzburg-Landau equation can be successfully matched to the parallel and non-parallel rotating-disk boundary-layer. The results suggest that the long-term behaviour depends on the precise balance of the varying frequency, varying growth rate, and diffusion/dispersion effects. It is then possible for an absolutely unstable disturbance to remain globally stable.

Acknowledgements

I would like to thank my friend and supervisor Dr. Christopher Davies, for his many suggestions and constant support during this research.

I should mention that the research in this thesis was carried out with the support of the Engineering and Physical Sciences Research Council.

I wish to thank Prof. Thomas Corke and the University of Notre Dame, for giving me the opportunity to present my findings, in the Autumn of 2006.

I wish to thank all of my friends (you know who you are), for all the past and future memories that we have and continue to share together.

Of course, I am grateful to my parents for their neverending *love*.

For my grandparents, I thank you.

To my brother, this time next year we will be millionaires.

And for Sarah, for your friendship. *Je vous aime.*

Cardiff, Wales — Christian Thomas

September 17th, 2007

Chapter 1

Stability

The study of spatially developing instabilities is concerned with understanding the local convective/absolute behaviour and the global properties. Such studies are widely documented and the interested reader is referred to Huerre & Monkewitz (1990), Monkewitz (1990), Huerre & Rossi (1998), Huerre (2000), Schmid & Henningson (2001) and Chomaz (2004) for excellent reviews of the subject. It is intended that this introduction will provide the reader with a brief account of instability definitions and methods (that have been developed by previous authors) for determining the nature of disturbances.

1.1 Parallel: convective and absolute instability

The concept of convective and absolute instability was originally introduced in Plasma Physics by Briggs (1964) and Bers (1975). Such notions have been successfully applied to understanding instabilities in shear flows. (Huerre & Monkewitz, 1990, contains a comprehensive list of references to such studies). In order to simplify the analysis, it is assumed that the basic flow of the problem in question is parallel, (spatially homogeneous), i.e. the basic flow is independent of the streamwise coordinate x. The

linear stability behaviour may then be characterized by the general dispersion relation

$$D(\alpha, \omega; R) = 0, \tag{1.1}$$

where α is the streamwise wavenumber, ω is the temporal frequency and R denotes the set of control parameters. Any solution of the dispersion relation (1.1), where α is real and ω is complex is known as a temporal mode $\omega(\alpha)$. Conversely, spatial branches $\alpha(\omega)$ are obtained when α is considered to be complex and ω real. However, in general both α and ω are considered to be complex.

One may introduce a differential operator D that acts in the physical space-time domain, (which corresponds to the dispersion relation (1.1)), so that fluctuations $\Psi(x,t)$ satisfy

$$D\left[-i\frac{\partial}{\partial x}, i\frac{\partial}{\partial t}; R\right]\Psi(x,t) = 0. \tag{1.2}$$

Here x is the streamwise direction and t denotes time. We are interested in the system response to an impulsive force at the origin of the $(x,t)-$plane. The response to impulsive forcing is given by the Green's function $G(x,t)$, which satisfies

$$D\left[-i\frac{\partial}{\partial x}, i\frac{\partial}{\partial t}; R\right]G(x,t) = \delta(x)\delta(t), \tag{1.3}$$

where δ denotes the Dirac delta function. The basic state is perturbed at $x = 0$, $t = 0$, and the system is then left to evolve.

1.1.1 Definitions of stability

The main objective of this section is to review the criteria that can be used to ascertain the type of stability/instability that evolves from a given disturbance.

The basic flow is linearly stable if

$$\lim_{t\to\infty} G(x,t) = 0 \text{ along all rays } x/t = \text{constant}, \tag{1.4}$$

and it is linearly unstable if

$$\lim_{t\to\infty} G(x,t) = \infty \text{ along at least one ray } x/t = \text{constant}. \tag{1.5}$$

For such unstable flows it is possible to distinguish between two types of impulse responses, namely convective and absolutely unstable behaviour. Convective instability takes place if

$$\lim_{t\to\infty} G(x,t) = 0 \text{ along the ray } x/t = 0, \tag{1.6}$$

and the response is referred to as absolute instability if

$$\lim_{t\to\infty} G(x,t) = \infty \text{ along the ray } x/t = 0. \tag{1.7}$$

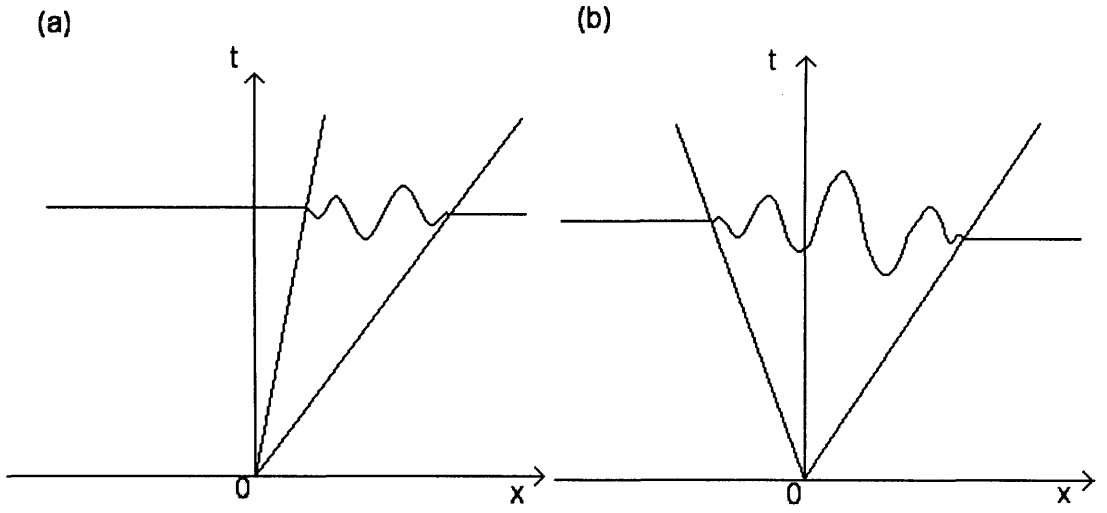

Figure 1.1: *(a): Convective instability - a disturbance grows at no fixed point in the flow, but does grow at moving points. (b): Absolute instability - disturbances grow in time at all fixed points.*

Figure 1.1 displays schematic sketches of convective and absolute instability in the form of an $(x,t)-$diagram. The wavepacket on the left demonstrates convective instability; both edges of the disturbance wavepacket are propagating away from the origin in the same direction. The second plot on the right displays absolute instability; the two edges of the disturbance wavepacket are propagating in opposite directions towards infinity.

1.1.2 The Green's function solution and Briggs' method

Equation (1.3) does not involve x or t dependent coefficients and the solution may be obtained by re-casting the problem in Fourier-space. The Green's function can be expressed as the double fourier integral

$$G(x,t) = \frac{1}{4\pi^2}\int_L\int_F \frac{\exp[i(\alpha x - \omega t)]}{D(\alpha,\omega)} d\alpha d\omega, \tag{1.8}$$

where L and F denote the inversion contours in the frequency and wavenumber planes, respectively. The F contour in the complex wavenumber plane initially lies upon the horizontal real axis. While the L contour in the complex frequency plane is a straight line located above all the singularities of the integrand, so as to satisfy causality, or to be precise, $G(x,t) = 0$ for all x when $t < 0$. Figures 1.2(a, b) illustrate the paths of integration.

The resulting Green's function assumes the form of a disturbance wavepacket in the $(x,t)-$plane. The response along each line x/t, within the disturbance wavepacket, is dominated by one complex wavenumber α_k, such that the group velocity satisfies $\partial\omega(\alpha_k)/\partial\alpha = x/t$.

The temporal growth rate $\omega_i(\alpha)$, attains its maximum value $\omega_{i,max} = \omega_{i,max}(\alpha_{max})$ when

$$\frac{\partial\omega_i}{\partial\alpha}(\alpha_{max}) = 0, \tag{1.9}$$

for α_{max} real, which has the corresponding group velocity $\partial\omega/\partial\alpha(\alpha_{max}) = x/t = U_{max}$. Using the earlier definitions (1.4) and (1.5) for linear stability, we obtain the simple criteria:

$$\begin{aligned} \omega_{i,max} &< 0 \qquad \text{linearly stable,} \\ \omega_{i,max} &> 0 \qquad \text{linearly unstable.} \end{aligned} \tag{1.10}$$

It is now necessary to establish criteria to differentiate between the different types of instability, namely convective and absolute instability. This can be achieved by

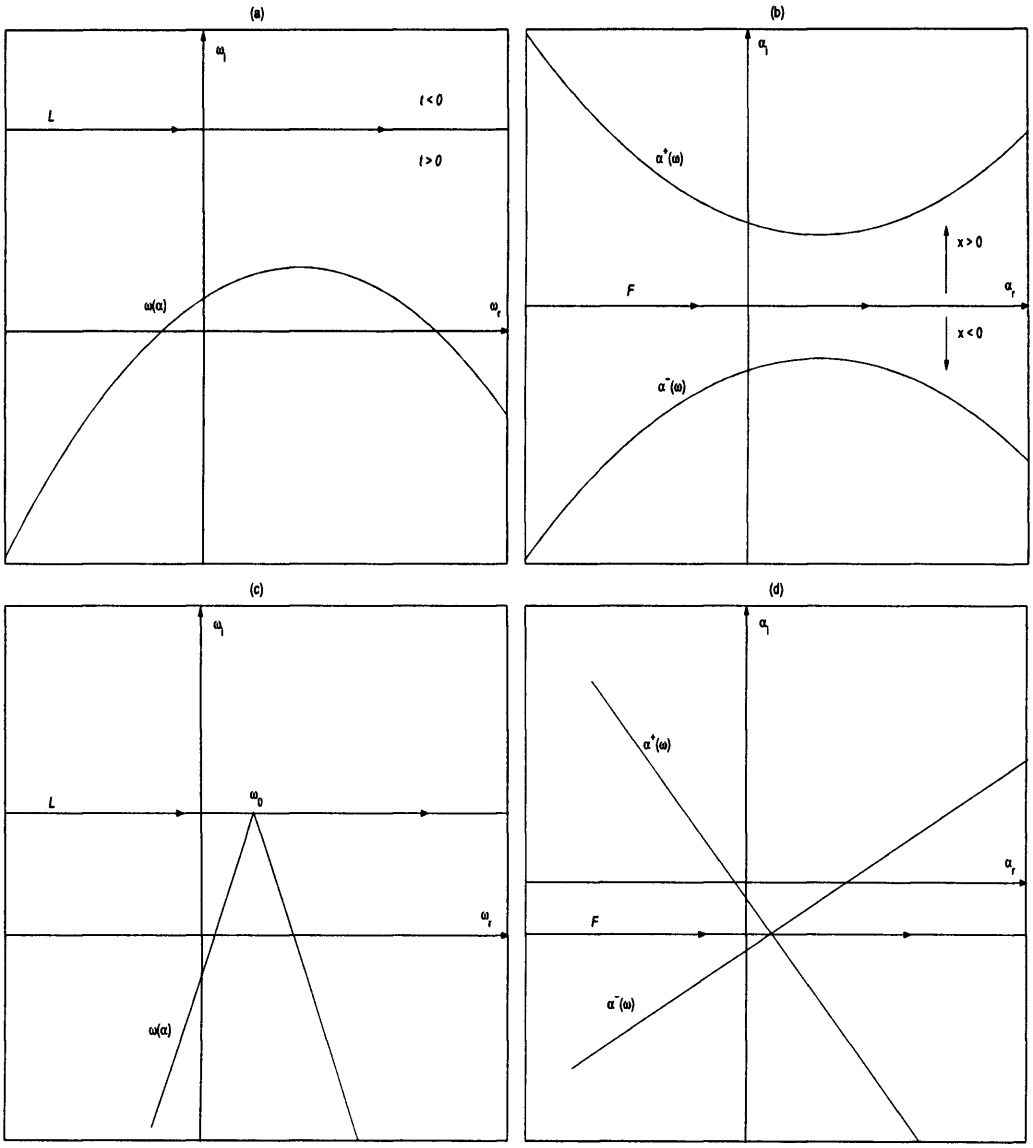

Figure 1.2: *Integration contour L in the complex frequency-plane, (a) and (c); integration contour F in the complex wavenumber-plane, (b) and (d). (a) and (b) display the initial contour positions, while (c) and (d) display the behaviour at the point of pinching.*

examining the long term behaviour of the wavenumber α_0 along the ray $x/t = 0$. By definition, the group velocity is zero for the complex wavenumber α_0,

$$\frac{\partial \omega}{\partial \alpha}(\alpha_0) = 0. \tag{1.11}$$

The corresponding frequency $\omega_0 = \omega(\alpha_0)$ is referred to as the complex absolute frequency. Subsequently, the absolute growth rate is defined as $\omega_{0,i} = \omega_i(\alpha_0)$. Whereas the earlier maximum growth rate $\omega_{i,max}$ is observed following the peak of the disturbance wavepacket, the absolute growth rate characterizes the temporal evolution at the location $x/t = 0$, as time tends to infinity. Hence, we obtain the following criteria on the type of instability,

$$\omega_{0,i} < 0 \qquad \text{convectively unstable,} \tag{1.12}$$

$$\omega_{0,i} > 0 \qquad \text{absolutely unstable.} \tag{1.13}$$

The absolute frequency ω_0 is generally an algebraic branch point of the spatial branch $\alpha(\omega)$ in the complex frequency plane, while the wavenumber α_0 is a saddle point of the temporal mode $\omega(\alpha)$ in the complex wavenumber plane. It should be noted that the maximum growth rate $\omega_{i,max}$ is an upper bound along any ray x/t, (Chomaz, Huerre & Redekopp, 1991). Thus, we have

$$\omega_{0,i} \leq \omega_{i,max}. \tag{1.14}$$

Definitions (1.11) and (1.13) are necessary conditions for absolute instability. However, they do not fully specify the onset of absolute instability (Briggs, 1964; Bers, 1975). The time-asymptotic behaviour of the double Fourier integral (1.8) may be evaluated using the so-called Briggs or Bers method. The Briggs/Bers method chooses the wavenumber integral to be

$$\bar{G}(x,\omega) = \frac{1}{2\pi} \int_F \frac{\exp(i\alpha x)}{D(\alpha,\omega;R)} d\alpha, \tag{1.15}$$

and a frequency inversion integral

$$G(x,t) = \frac{1}{2\pi}\int_L \bar{G}(x,\omega)\exp(-i\omega t)d\omega, \tag{1.16}$$

where the contours L and F are as described earlier, (refer to figure 1.2(a, b)). We then attempt to lower the original L contour below the real $\omega-$axis. If this is achieved, the exponent in the inversion integral (1.16) will ensure that the integrand tends to zero, as time tends to infinity. If this is not attainable, the highest singularity will govern the response. Since α is related to ω via the dispersion equation (1.1), any singularity appearing in the ω plane, will have an associated singularity within the α plane.

A temporal mode $\omega(\alpha)$ is assumed to exhibit a single branch point ω_0, with only two spatial branches α^+ and α^-. The two branches are located in separate halves of the α plane. Therefore, they reside on opposite sides of the F contour. The spatial branch above the real $\alpha-$axis governs the disturbance behaviour downstream of the source, $x > 0$. While the branch below the real $\alpha-$axis influences the dynamics of the disturbance upstream of the source, $x < 0$. As the L contour is lowered, the spatial branches α^+ and α^- tend towards one another. As the spatial branches move closer together, the original F contour must be deformed to ensure that both branches remain on opposite sides of F, so as to preserve causality. The successive deformations of the contours L and F will eventually stop, once the F contour becomes pinched between the two spatial branches α^+ and α^-. At the point of pinching, the zero group velocity condition (1.11) is satisfied. At the same time, the temporal mode $\omega(\alpha)$ forms a branch-point singularity in the complex $\omega-$plane. The branch-point can be detected by the formation of a cusp appearing at ω_0. The L contour cannot be deformed any further, since causality will be broken if the two spatial branches cross the F contour. If ω_0 is located beneath the real $\omega-$axis, the disturbance is convectively unstable or stable. Absolute instability is present if pinching occurs before ω_0 passes below the

real $\omega-$axis. Figure 1.2(c, d) displays schematic sketches of the contour deformation via the Briggs/Bers method.

The above methods have been successfully applied to the rotating-disk boundary-layer by Lingwood (1995, 1997a,b), amongst others. Further details on the studies by Lingwood and others are given in chapter 2.

1.2 Non-parallel effects: local and global instability concepts

To include non-parallel effects, it is necessary to look for solutions of the form

$$\Psi(x,t) = \phi(x)\exp(-i\omega_G t), \tag{1.17}$$

where $\phi_G(x)$ is the eigenfunction and ω_G is the corresponding frequency eigenvalue, i.e. $\omega_G = \omega_{G,r} + i\omega_{G,i}$. The solutions are found by carrying out the stability analysis globally, over the entire physical range of the streamwise coordinate x. The stability analysis is referred to as global, since x is considered to be an eigendirection, i.e. the x dependence on the eigenfunction is unknown.

We introduce a linear partial differential operator D, such that fluctuations $\Psi(x,t)$ satisfy

$$D\left[-i\frac{\partial}{\partial x}, \frac{\partial}{\partial t}; R, X\right]\Psi = 0, \tag{1.18}$$

where X is a slowly varying streamwise parameter.

For the parallel problem, modes of the form $\Psi(x,t) = A(x,t)\exp\{i(\alpha x - \omega t)\}$ are sought. However, for the present operator (1.18), it is more appropriate to assume modes of the form

$$\Psi(x,t)^{\pm} \sim A(X)^{\pm}\exp\left(i\left[\frac{1}{\epsilon}\int_0^X \alpha(X';\omega)dX' - \omega t\right]\right), \tag{1.19}$$

where $A(X)$ is an unknown complex amplitude, $\epsilon \ll 1$ incorporates slow streamwise variation effects, and ω and α again refer to the complex frequency and wavenumber.

The superscripts + and − refer to the respective downstream ($x > 0$) and upstream ($x < 0$) regions about the source $x = 0$.

The local dispersion relation, corresponding to equation (1.18) is given as

$$D[\alpha, \omega; R, X] = 0, \tag{1.20}$$

where the slowly varying streamwise variable X appears as a parameter. The zero group velocity condition (1.11), and convective/absolute instability definition (1.13), are again valid for the local dispersion relation (1.20).

We define a local absolute frequency as $\omega_0(X, R)$, with a corresponding wavenumber $\alpha_0(X, R)$, such that

$$\frac{\partial \omega}{\partial \alpha}(\alpha_0; X, R) = 0, \qquad \omega_0(X, R) = \omega(\alpha_0; X, R). \tag{1.21}$$

In a likewise manner, one may define a local maximum growth rate as $\omega_{i,max}(X, R)$ for a local complex frequency $\omega_{max}(X, R)$. The corresponding wavenumber $\alpha_{max}(X, R)$, is given by

$$\frac{\partial \omega_i}{\partial \alpha}(\alpha_{max}; X, R) = 0, \qquad \omega_{max}(X; R) = \omega(\alpha_{max}; X, R). \tag{1.22}$$

The type of instability displayed by any given disturbance may be divided into four separate groups, depending on the behaviour of the respective local maximum and local absolute growth rates $\omega_{i,max}(X, R)$ and $\omega_{0,i}(X, R)$. The sketches displayed in figure 1.3(a-d) illustrate the four distinct groups. Figure 1.3(a) depicts a flow that is locally stable everywhere, $\omega_{i,max}(X, R) < 0$ and $\omega_{0,i}(X, R) < 0$, for all X. A region of local convective instability is present in figure 1.3(b), since $\omega_{i,max}(X, R) > 0$, but $\omega_{0,i}(X, R) < 0$. The third group of flows are marginally absolutely unstable (refer to figure 1.3(c)), since the maximum absolute growth rate is still negative, but small. The final group of flows are locally absolutely unstable (refer to figure 1.3(d)), because the maximum absolute growth rate has crossed the real $X-$axis. The first three cases

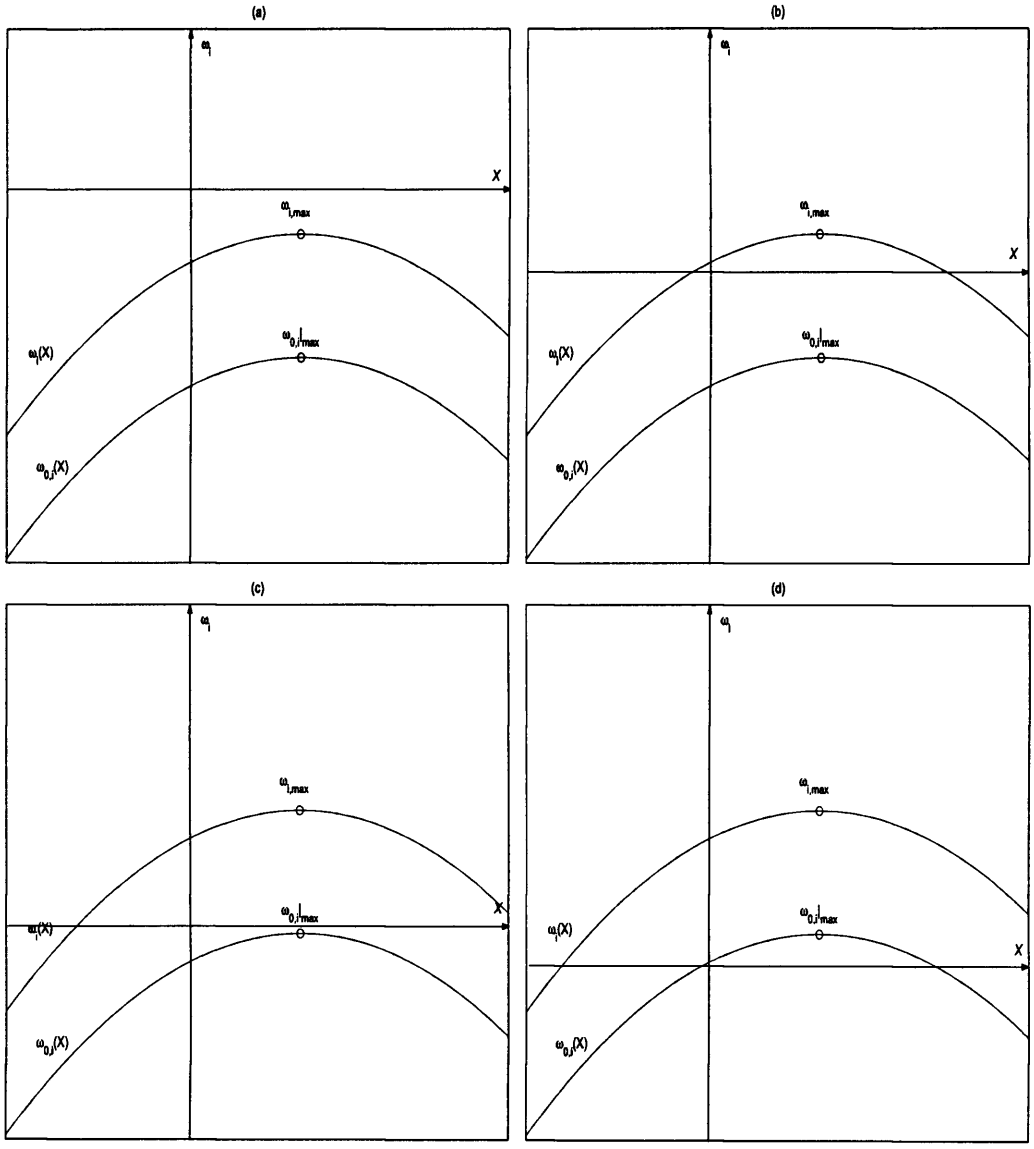

Figure 1.3: *Groups of spatially developing flows according to the characteristics of the local instability. (a) - stable; (b) - convectively unstable; (c) - marginally absolutely unstable; (d) - region of absolute instability.*

will always produce global stability or marginal global stability. While a finite region of absolute instability (refer to figure 1.3(d)), is a necessary condition for global instability to arise, Chomaz, Huerre & Redekopp (1991) and Monkewitz, Huerre & Chomaz (1993).

1.2.1 Definitions of global stability and instability

The definitions for global stability and instability may be presented in terms of the long-time behaviour of the Green's function *G(x,t)*, which is controlled by

$$D\left[-i\frac{\partial}{\partial x}, i\frac{\partial}{\partial t}; R, X\right] G(x,t) = \delta(x)\delta(t), \tag{1.23}$$

where δ is again the Dirac delta function. As emphasized by Huerre & Monkewitz (1990) and others, a flow is globally unstable when the long-time behaviour of the Green's function *G(x,t)* is dominated by a linear global response of the form (1.17). Therefore, we have the following definitions for global stability

$$\begin{aligned} \omega_{G,i} &< 0 \text{ globally stable,} \\ \omega_{G,i} &> 0 \text{ globally unstable.} \end{aligned} \tag{1.24}$$

Hence, for any flow to be globally stable, all eigenvalues $\omega_{G,i}$ must be negative.

1.2.2 The frequency-selection criterion

It was suggested by Pierrehumbert (1984) that the global mode ω_G is given by the frequency that corresponds to the location of the maximum absolute growth rate $\omega_{0,i}|_{max}$. While Koch (1985) proposed that the global mode should correspond to the local absolute frequency $\omega_{0,r}$, at the streamwise location separating the convective and absolutely unstable regions.

A global frequency selection criterion for ω_G was presented by Chomaz *et al.* (1991), and reviewed by Monkewitz *et al.* (1993), Huerre (2000), amongst others.

The global frequency is obtained by examining the long-time behaviour of equation (1.23). The time Fourier transform *G(x,t)* is written as

$$G(x,t) = \frac{1}{2\pi}\int_L G(x,\omega)\exp(-i\omega t)d\omega, \tag{1.25}$$

where the contour L is a straight line, parallel to the $\omega-$axis and above all singularities, (refer to figure 1.4(a)). While

$$G(x,\omega) \sim A^{\pm}(X)exp\left(\frac{i}{\epsilon}\int_0^X \alpha^{\pm}(X';\omega)dX'\right). \tag{1.26}$$

A contour M initially lies upon the real $X-$axis, and two branches $X^+(\omega)$ and $X^-(\omega)$ are located on either side of M, (refer to figure 1.4(b)). As the L contour is lowered, the M contour becomes pinched at some complex location X_s, between the two branches $X^+(\omega)$ and $X^-(\omega)$. The associated absolute frequency $\omega_0(X_s)$ is found at the branch-point in the complex frequency-plane, i.e. $\omega_0(X)$ forms a cusp with the L contour, (refer to figure 1.4(c, d)). Since the L contour cannot be lowered any further, the frequency $\omega_0(X_s)$ is expected to dominate the Green's function response. Once again the group velocity is zero and the pinching point X_s is located at a saddle point. Hence,

$$\frac{\partial\omega}{\partial\alpha}(\alpha_s;X_s) = \frac{\partial\omega}{\partial X}(\alpha_s;X_s) = 0, \tag{1.27}$$

where α_s is the complex wavenumber at the point of pinching. Due to the definition for the local absolute frequency (1.21), the global frequency ω_G is given by

$$\omega_G \sim \omega(\alpha_s;X_s). \tag{1.28}$$

As previously stated by Huerre & Monkewitz (1990), Chomaz *et al.* (1991), Le Dizes, Huerre, Chomaz & Monkewitz (1996) and others, the global growth rates $\omega_{G,i}$ are essentially less than the maximum local absolute growth rate $\omega_{0,i}|_{max}$ over all real X. Thus, we have

$$\omega_{G,i} \leq \omega_{0,i}|_{max}. \tag{1.29}$$

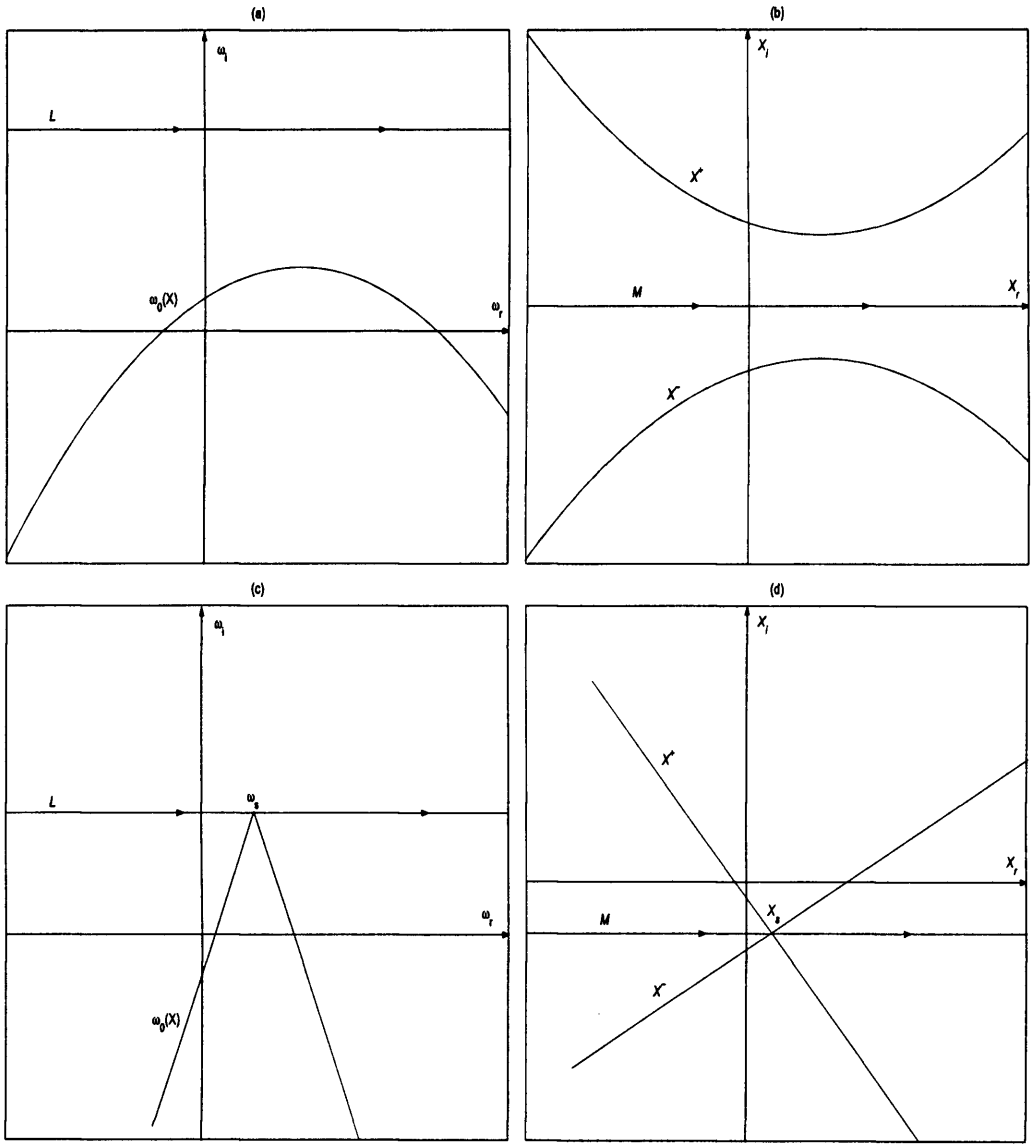

Figure 1.4: *Global frequency selection criterion. (a) and (b) refer to the L and M contours in their initial states. (c) and (d) refer to the L and M contours at the point of pinching.*

Hence, the existence of a region of local absolute instability is a necessary condition for global instability. However, such a condition is not sufficient as it stands. More importantly the pocket of absolute instability must reach a critical finite size before a self-sustained global-mode arises and prompts the onset of global instability.

Hammond & Redekopp (1997) have applied the above frequency selection methods to a two-dimensional wake-shear layer. In their investigation, the extrema of the $\omega_{0,r}$ and $\omega_{0,i}$ were found at different streamwise locations. Thus, the saddle point X_s (which satisfies equation (1.27)) does not lie on the real $X-$axis. The Cauchy-Riemann equations were called upon to calculate the approximate location of the saddle point, since the derivatives of ω_0 were only known along the real $X-$axis. Of the three methods (Pierrehumbert, 1984; Koch, 1985; Chomaz *et al.*, 1991), the Chomaz *et al.* (1991) frequency selection criterion was found to give the most accurate results.

1.3 Final remarks

The above definitions and methods will be called upon later in the thesis (chapter 7: The global stability of the rotating-disk) and applied to the rotating-disk boundary-layer, in the hope of finding the global frequency ω_G and the corresponding location of the saddle point X_s.

For a greater description of local and global stability characteristics, the interested reader is referred to Huerre & Monkewitz (1990), Monkewitz (1990), Chomaz *et al.* (1991), Monkewitz *et al.* (1993), Huerre & Rossi (1998), Huerre (2000), Schmid & Henningson (2001) and Chomaz (2004).

Chapter 2

Three dimensional boundary-layers

There are several three-dimensional flows that are of practical interest for studying instabilities and transition to turbulence. Examples are

1. Swept-wings,
2. Rotating-disks,
3. Rotating-cones,
4. Rotating-spheres.

2.1 The swept-wing

The study of swept-wings dates back to the 1950s and is one of the principal reasons for investigating other three-dimensional boundary-layers. Gray (1952) was one of the first to investigate the transition process over a swept-wing. The instability that was found to arise over a swept-wing is known as the crossflow instability, which is due to a point of inflection in the crossflow velocity component. There is a maximum velocity located along the crossflow velocity profile, while the velocity is zero at the body surface and boundary-layer edge. A schematic sketch of the velocity profile is

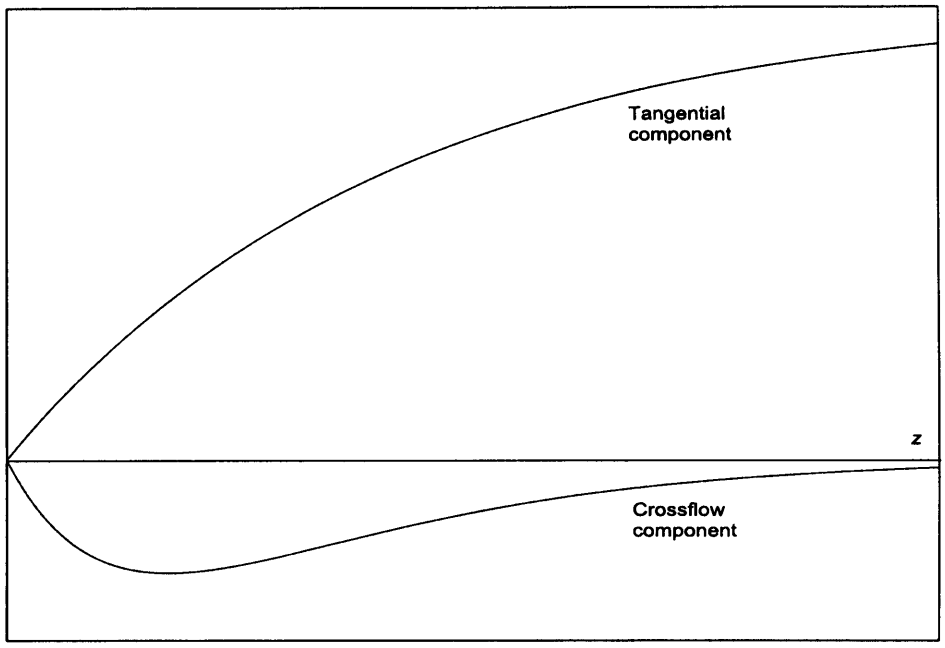

Figure 2.1: *Schematic sketches of the crossflow and tangential velocity profiles over a swept-wing.*

displayed in figure 2.1. Thus, to understand the transition process over a swept-wing, a greater understanding of the crossflow instability is required.

2.2 The rotating-disk

A model problem which is known to exhibit the crossflow instability, is the rotating-disk boundary-layer. The problem is modeled as an infinite planar disk rotating at a constant angular velocity, about the normal axis, which passes through the centre of the disk. The fluid above the disk is stationary and is infinite in extent. Cylindrical polar coordinates are employed, i.e. radial, azimuthal and normal directions. Figure 2.2 displays a schematic drawing of the rotating-disk with streamlines. The velocity

components u_r, u_θ, u_z refer to the radial, azimuthal and normal directions.

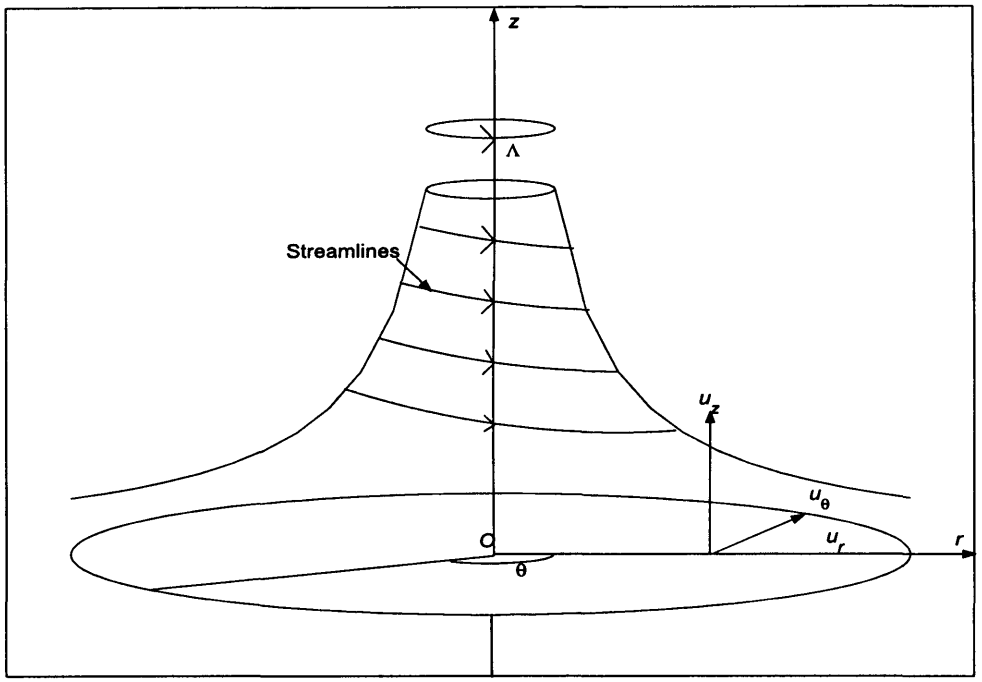

Figure 2.2: *Rotating-disk in still fluid and coordinate system.*

The Navier-Stokes equations in cylindrical polar co-ordinates are given as

$$\text{Momentum: } \frac{\partial \underline{u}}{\partial t} + (\underline{u}.\nabla)\underline{u} + 2\Lambda \wedge \underline{u} = -\frac{1}{\rho}\nabla p + \nu \nabla^2 \underline{u},$$

$$\text{Continuity: } \nabla.\underline{u} = 0, \tag{2.1}$$

where Λ is the angular velocity of the disk, $\underline{u} = \{u_r, u_\theta, u_z\}$, t is time, ρ is the fluid density, p is the fluid pressure and ν is the kinematic viscosity. The third term on the left hand side of the momentum equation is due to the Coriolis[1] force.

[1]The term Coriolis comes from the engineering professor, at the *École* Polytechnique in Paris, *Gustave-Gaspard de Coriolis (1792 - 1843).*

The rotating-disk is said to act as a centrifugal fan, where fluid is thrown radially outwards and is replaced by a normal flow directed towards the centre of the disk.

In 1921 *Theodore von Kármán* found an exact solution to the cylindrical Navier-Stokes equations (2.1), using what are now referred to as the von Kármán variables. On substituting the von Kármán variables into the cylindrical Navier-Stokes equations (2.1), a system of ordinary differential equations (ODE) is obtained. Of the ODE to be solved (equations (4.6) - (4.9), (5.9) - (5.12), (6.14) - (6.17) in chapters 4, 5 and 6), one of the equations can be removed by simple integration. The remaining ODE are dependent on the normal direction z and can be solved numerically. Th. von Kármán (1921) solved the system of ODE and resulting velocity profiles by numerical methods. Later Cochran (1934) obtained a more accurate solution to the problem. Today, high-powered computers are available. Thus, the system of ODE can be solved in a matter of seconds, allowing faster and easier investigation of the rotating-disk boundary-layer. The author has addressed the problem using the programming language *Matlab* and the interested reader is referred to the appendices for a detailed account of the program code. The velocity profiles are plotted in later chapters. The laminar radial velocity profile is inflectional. Therefore, the rotating-disk is susceptible to the same crossflow instability present within the swept-wing boundary-layer.

Batchelor (1951) pointed out that the rotating-disk or von Kármán flow is one particular example of a family of rotating-flows. As already mentioned, the von Kármán flow arises for a rotating-disk beneath a stationary fluid. Other limiting cases are the Ekman (1905) and Bödewadt (1940) flows. The Bödewadt flow arises for a rotating fluid above a stationary-disk, while the Ekman flow occurs when the fluid and disk rotate with approximately equal velocity. In between the Bödewadt, Ekman and von Kármán flows, lies an infinite number of rotating boundary-layers. Due to these particular examples, the system of rotating flows shall be known as the *BEK* family and will be discussed in greater detail in chapter 6.

It was also shown by Batchelor (1951) that the von Kármán solution can be extended to flows with a uniform normal flow, i.e. mass suction and injection. The effect of introducing a uniform normal flow will be discussed in chapter 4.

The crossflow instability or Type-1 mode was originally discovered by Gregory, Stuart & Walker (1955) in the rotating-disk boundary-layer, in their experimental and theoretical investigation. The mean velocity profile displays a point of inflection. This results in an inviscid neutral disturbance with zero frequency, which has an unstable counterpart, (Stuart in Gregory *et al.*, 1955). The stationary disturbances appear as co-rotating vortices, known as crossflow vortices. Such vortices can also be found on rotating-cones and swept-wings.

In the experiment by Gregory *et al.* (1955), a china-clay technique was used. A stationary vortex pattern was observed and there was approximately 30 vortices located on the disk surface, spiralling outwards at an angle of about 14 degrees, (i.e. the normals of the vortices make an angle of about 14 degrees with the outward drawn radius). The vortices were first observed for a Reynolds number of about $Re = 430$, while transition to turbulence arose for $Re \approx 530$.

Stuart's inviscid theoretical study predicted vortices with a similar wave angle to that observed experimentally. However, the number of stationary vortices was approximately four times greater. The discrepancy in vortices between experiment and theory can be attributed to the fact that viscous effects were ignored in the theoretical study.

In a similar experimental study, Fedorov, Plavnik, Prokhorov & Zhukhovitskii (1976), observed 27-30 vortices for Reynolds numbers $Re \geq 387$. However, for a Reynolds number $Re = 245$, 14-16 vortices were found to propagate at an angle of about 20 degrees. While transition to turbulence was found for $Re = 515$.

Faller & Kaylor (1966) conducted a numerical study, concerning the stability of

the Ekman boundary-layer. They observed the inviscid crossflow instability or Type-1 mode and a viscous Type-2 mode, which is attributed to the Coriolis force and curvature effects. The Type-2 mode was also observed in the rotating-disk boundary-layer (Malik, 1986). Malik (1986) found the critical Reynolds number for stationary modes Type-1 and Type-2, to occur for $Re_1 = 285.36$ and $Re_2 = 440.88$[1], respectively.

Malik, Wilkinson & Orszag (1981) conducted a theoretical and experimental investigation of the rotating-disk boundary-layer. The Type-1 stationary wave was found for a critical Reynolds number $Re_1 = 287$ at an angle of 11.2 degrees. A weakly unstable, propagating Type-2 mode was also located for a critical Reynolds number of approximately $Re_2 = 49$. Malik *et al.* (1981) found transition to turbulence to take place for $513 \leq Re \leq 526$.

An experimental study of the transitional flow over a rotating-disk was conducted by Wilkinson & Malik (1983). The experimental apparatus consisted of a hot-wire probe, which maps out the instability of the disk in terms of both spatial coordinates and velocity fluctuations. Experiments on a clean-disk and for a disk with a single isolated roughness were considered. Transition to turbulence was found for $543 < Re < 556$ for the clean disk, and $521 < Re < 530$ for the rough disk. Stationary, secondary vortices were also observed prior to turbulent breakdown. It was suggested that this is possibly the final stage of the transition process (Wilkinson & Malik, 1983).

One of the first investigations conducted on travelling disturbances (i.e. non-zero frequency) on the rotating-disk was carried out by Balakumar & Malik (1990). The Type-1 mode was found to have a minimum for a frequency $\omega = -2.9$ and Reynolds number $Re_1 = 283.6$, while the Type-2 mode was found to have a minimum for $\omega = 7.9$ and $Re_2 = 64.46$. For travelling waves, the Type-2 mode almost always occurs before the Type-1 mode.

[1]Here the subscripts 1 and 2 refer to the respective Type-1 and Type-2 modes.

Mack (1985) discovered a third mode, which is now known as the Type-3 mode. The Type-3 mode propagates energy towards the disk centre, but is spatially damped and this is why the mode was not discovered in previous stability studies.

Faller (1991) carried out a detailed numerical study on the *BEK* system for a range of parameters. For the von Kármán flow, the critical Reynolds number for the travelling Type-2 mode was found to be $Re = 69$, with a wavelength $L = 22$ at an angle of -19^o.

Further theoretical and experimental studies of interest are given by Kobayashi, Kohama & Takamadate (1980), Kohama (1984), Hall (1986), Bassom & Gajjar (1988), Spalart (1991), Malik & Balakumar (1992), Hall, Balalumar & Papageurgiu (1992), and Turkyilmazoglu & Gajjar (1997).

The rotating-disk flow has been studied by many investigators, using theoretical, experimental and analytical studies. By such methods, three modes have been discovered; an inviscid crossflow instability, a viscous instability due to the Coriolis forces and an inwardly propagating, spatially damped mode. Hence, one would assume that studies on the rotating-disk boundary-layer had been exhausted. This impression was to be dispelled by the findings of Lingwood (1995, 1996, 1997a,b).

2.2.1 Absolute instability

Lingwood (1995) showed that for a given set of parameters the rotating-disk boundary-layer is absolutely unstable. Such a revelation came as a complete surprise to other researchers. In order to search for an absolute instability a spatio-temporal method must be considered, by which we mean, both wavenumber and frequency are considered to be complex.

An inviscid stability analysis and viscous analysis (with Coriolis forces and curvature effects) were considered. The parallel flow approximation was assumed, where the mean flow is simplified by taking it to be homogeneous along the radial direction.

In both studies, a region of absolute instability was discovered. Outside this region the flow was found to be stable or convectively unstable. The theoretical critical Reynolds number for absolute instability was found to occur for $Re = 510$, later adjusted to $Re = 507.3$ (Lingwood, 1997a,b). Lingwood noted that this is very close to the point of transition to turbulence, where she took the average experimentally observed value to be $Re = 513 \pm 3\%$. Lingwood suggested that the absolute instability may be a cause for transition to turbulence. The fact that absolute instability appears in an inviscid analysis indicates that absolute instability is not caused by Coriolis forces, curvature effects or viscosity. Thus, it is possible that absolute instability may be possible on a swept-wing, where Coriolis effects are not present.

The absolutely unstable behaviour was identified by Lingwood using what is known as the Briggs/Bers method (Briggs, 1964; Bers, 1975). Absolute instability is identified by singularities in the dispersion relationship, which arise when waves propagating in opposite directions coalesce. These points are known as pinch-points. (For further details on the Briggs method, refer to chapter 1). The absolute instability was shown to result from the coalescence of the Type-1 and Type-3 modes, for a complex frequency with non-zero real part and more importantly a positive imaginary part, indicating temporal growth.

The Type-1 and Type-2 modes have also been shown to coalesce, Lingwood (1995) and Cooper & Carpenter (1997a), resulting in an algebraically growing disturbance, rather than an absolute instability.

Lingwood (1996) conducted an experimental investigation that aimed to corroborate her theoretical findings. In her experiment, the flow was impulsively excited at a point r_e, well inboard of the critical value for absolute instability r_c. Lingwood proposed that the global response to such an excitation, be as shown in figure 2.3. Initially the wavepacket propagates radially outwards in a convective manner. However, the trailing edge eventually asymptotes towards a constant vertical line at r_g,

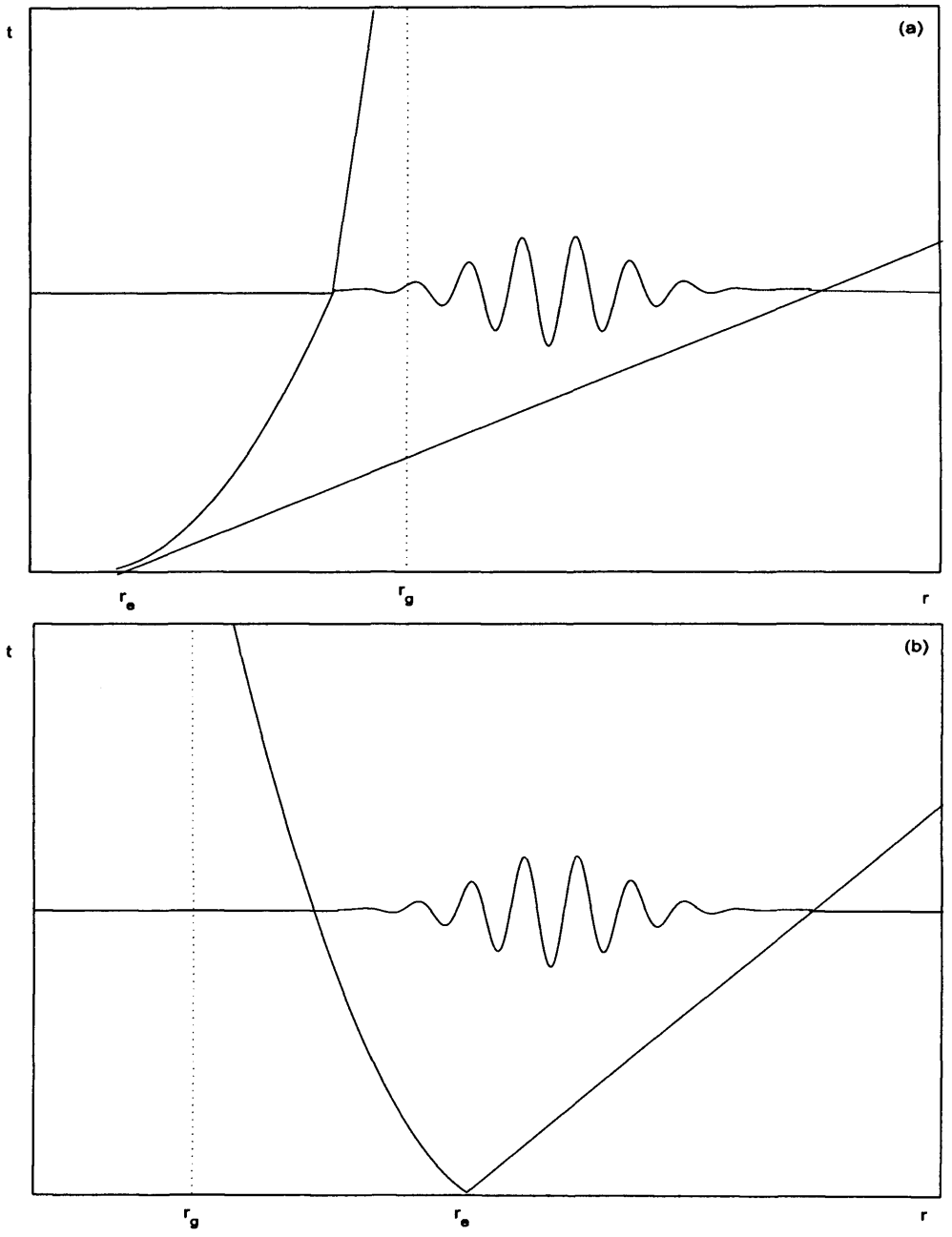

Figure 2.3: Typical wavepacket evolution for the rotating-disk boundary layer according to Lingwood's conjecture. Impulsive excitation (a) at $r_e < r_c < r_g$ (based on figure 1c of Lingwood 1996); and (b) at $r_e > r_g > r_c$.

which is in the region of r_c. Lingwood suggested that transition to turbulence may have been caused by the flow becoming absolutely unstable, where the average value for transition was found to be about 513. However, her results gave no evidence for the existence of a linear amplified global mode, of the form

$$A \sim \exp(-i\omega_G), \tag{2.2}$$

where $\omega_G = \omega_{G,r} + i\omega_{G,i}$ is the complex global frequency, for $\omega_{G,i} > 0$.

Lingwood (1997a,b) applied the above methods to rotating-disk flows with a uniform normal flow and to the *BEK* family of rotating flows. It can be shown that all of these flows are absolutely unstable, when the parallel flow approximation has been employed. The details and conclusions of her studies will be discussed in chapters 4 and 6.

The discovery of an absolute instability in the rotating-disk boundary-layer, led Lingwood (1997c) to investigate the possibility of such behaviour occurring in the swept-wing boundary-layer. The flow was found to be absolutely unstable in the chordwise direction, with a critical Reynolds number of approximately $Re_c = 681$. However, this did not prevent disturbances convecting in the streamwise direction. Thus, it was concluded that the laminar-turbulent transition process may still be a convective process.

2.2.2 The global behaviour - Davies & Carpenter (2003)

Using the velocity-vorticity formulation of Davies & Carpenter (2001), Davies & Carpenter (2003) were able to produce numerical simulation results for both parallel[1] (homogeneous) and non-parallel (inhomogeneous) mean flows. For the approximate parallel mean flow, the results of the numerical simulations agree with the theory of Lingwood (1995). For a disturbance excited within the theoretical absolutely unstable

[1]The so called parallel flow approximation assumes that the mean flow is independent of radius.

region, the simulations exhibit analogous behaviour. Also, behaviour consistent with convective instability was observed when the flow parameters were located within the theoretical convectively unstable region.

However, the non-parallel mean flow numerical simulations produce quite different behaviour. The outcome of their study is illustrated in figure 2.4. Figure 2.4(a) displays the wavepacket evolution for a disturbance impulsively excited within the convectively unstable region. The behaviour is quite similar to the sketch drawn by Lingwood (1996), figure 2.3(a). However, as the trailing edge approaches the absolutely unstable region it shows no indication of tending towards a vertical line in the vicinity of the critical Reynolds number. In fact, it appears that the trailing edge is propagating radially outwards in a convective manner. Figure 2.4(b) displays the wavepacket evolution for a disturbance excited within the absolutely unstable region. Initially, the trailing edge of the disturbance wavepacket propagates radially inwards, in a manner consistent with absolute instability and temporal growth. Nonetheless, such behaviour does not persist for long; it appears that as the trailing edge nears the region of critical absolute instability, it reverses direction and propagates radially outwards.

Davies & Carpenter (2003) found that the absolute instability did not give rise to any sustained unstable linear global mode (2.2). Instead convective behaviour was found to dominate the disturbance response for all Reynolds numbers considered, even those well within the region of absolute instability.

A recent experimental investigation by Othman & Corke (2006) supports the study of Davies & Carpenter (2003). In their experiment, they were able to study disturbances with a much smaller amplitude than those in the experiments of Lingwood (1996). By considering the initial disturbance (excited at the same location as that in Lingwood, 1996) to be small, the trailing edge of the disturbance wavepacket was found to travel radially outwards with a finite velocity at all radial locations,

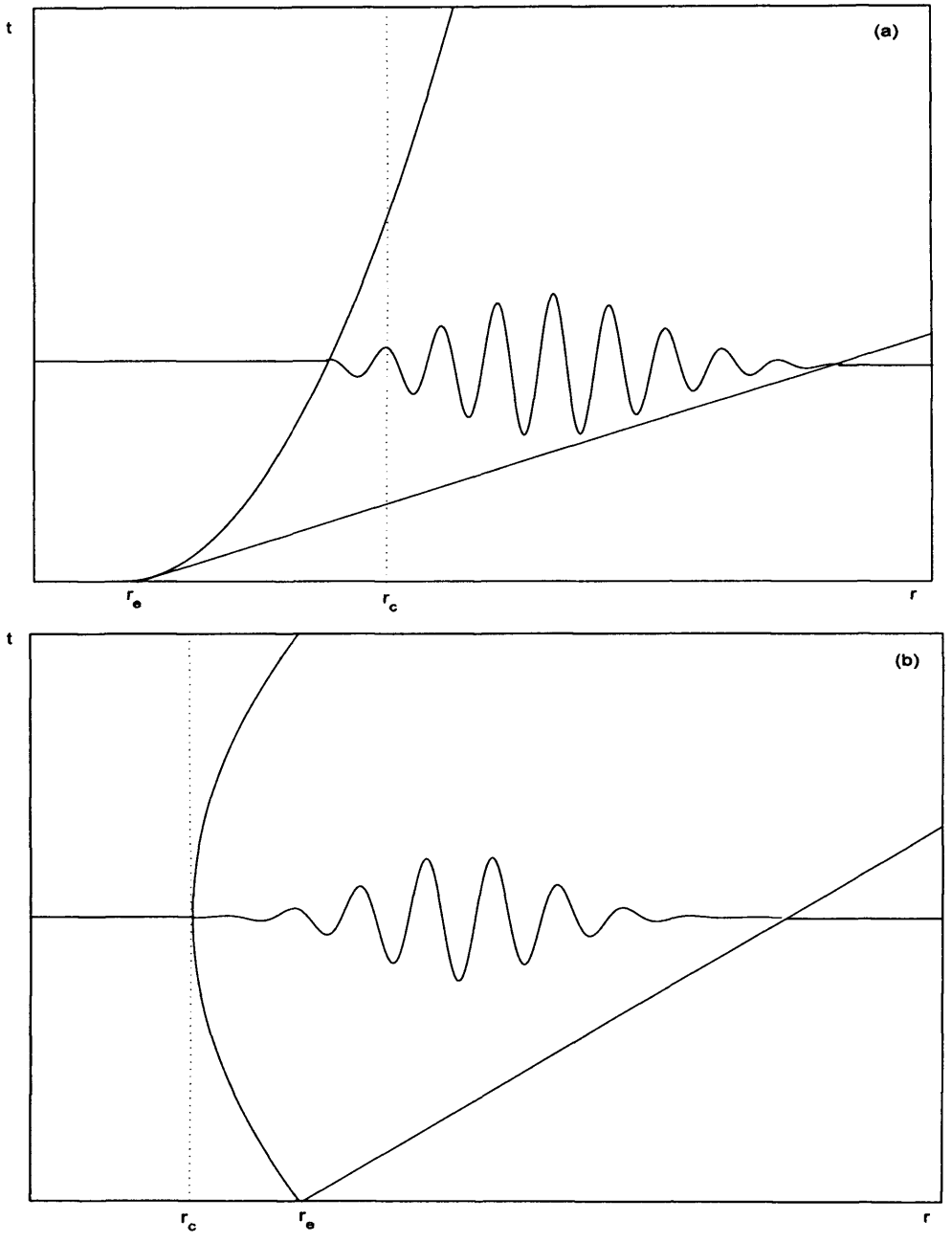

Figure 2.4: *Sketch of a typical wavepacket evolution for the rotating-disk boundary-layer as revealed by Davies and Carpenter (2003) and the results on rotating-disk flow with normal injection. (a): impulse excitation for* $r_e < r_c$*, (b): Impulse excitation for* $r_e > r_c$.

including those within the absolutely unstable region. Hence, their experiments are in good agreement with the linearized numerical simulations of Davies & Carpenter (2003).

By considering larger initial disturbance amplitudes, behaviour comparable with the Lingwood experiments was found. However, there was again no evidence of a dominant global temporal frequency (2.2).

2.2.3 Further studies on the rotating-disk and absolute instability

Jasmine (2003) and Jasmine & Gajjar (2005a,b,c) continued the study on the absolute instability over a rotating-disk by considering boundary-layers with a uniform magnetic field and temperature-dependent viscosity. The presence of a magnetic field in rotating boundary-layers has many industrial applications, such as electromagnetic stirring of liquid metals. Temperature-dependent viscosity problems also have a number of industrial applications, and in order to predict accurate behaviour it is important to consider viscous variations due to changes in temperature.

For the flow with a uniform axial magnetic field, increasing the magnetic field was found to be stabilizing. For a magnetic field parameter $m = 0.2$ ($m = 0$ for von Kármán flow), the critical Reynolds number for absolute instability was given as approximately $Re_c = 695.97$, which is almost 40% greater than the critical Reynolds number for the von Kármán flow. Further details of the rotating-disk with a magnetic field will be given in chapter 5.

It was found that for a rotating-disk with a temperature-dependent viscosity, the flow becomes increasingly unstable for small positive increases in viscous variation. For a small viscous variation parameter $\epsilon = 0.03$ ($\epsilon = 0$ for von Kármán flow), the critical Reynolds number for absolute instability was given as approximately $Re_c = 275.1$, which is nearly half of the critical Reynolds number for the von Kármán

flow.

Pier (2003) has shown - using parallel flow calculations - that the experimentally observed sharp transition from a laminar to turbulent state, coincides with the onset of secondary instabilities of the primary absolute instability.

Using the result (found by Lingwood, 1995) that the rotating-disk boundary-layer is absolutely unstable in the inviscid limit, Healey (2004) was able to (using large-Reynolds-number asymptotic expansions) find the non-parallel correction terms on the upper branch of the absolutely unstable neutral curve. His study revealed that the non-parallel effects are destabilizing. Healey's results also revealed that Lingwood's family of saddle points were distinct from a second family of saddle points. Lingwood's saddle points were only located along the upper branch of the neutral curve for absolute instability and below some finite Reynolds number. While the second family of saddle points was found to dominate for large Reynolds numbers. However, Lingwood's family of saddle points on the lower branch of the absolutely unstable neutral curve were found to be the pinch-points. The wavelengths along the lower neutral curve increase with increasing Reynolds number. This prompted Healey (2005, 2006a,b) to consider a long-wave inviscid theory to study the convective and absolute instabilities of the rotating-disk.

Healey (2005, 2006a) was able to locate a new convective instability in the normal direction to the disk. While the usual convective instabilities in the downstream direction are characterized by spatial modes with complex numbers, the new convective instability in the normal direction is characterized by exponentially diverging eigenfunctions, which are obtained by shifting sections of the branch-cuts in the complex wavenumber plane.

Using the inviscid long-wave theory, Healey (2006b) was able to study the lower branch of the absolutely unstable neutral curve. His study revealed that in the long-wave limit, the absolute instability is characterized by a wall-jet motion in the radial

direction, which is superimposed with a small azimuthal crossflow component. The absolute instability is formed by the coalescence of eight saddle-points. The pinch-point for absolute instability was found to asymptote towards the imaginary axis of the complex wavenumber plane as wavelengths increased. Eventually, this led to modes crossing the imaginary axis.

For further details of Healey's investigations the interested reader is referred to the above papers for further study.

2.2.4 Stability theory

For the rotating-disk boundary-layer, the instantaneous non-dimensional radial, azimuthal and normal velocities u_r, u_θ, u_z, and pressure p are given as

$$u_r(r,\theta,z,t) = \frac{r}{Re}F(z) + \bar{u}_r(r,\theta,z,t), \tag{2.3}$$

$$u_\theta(r,\theta,z,t) = \frac{r}{Re}G(z) + \bar{u}_\theta(r,\theta,z,t), \tag{2.4}$$

$$u_z(r,\theta,z,t) = \frac{1}{Re}H(z) + \bar{u}_z(r,\theta,z,t), \tag{2.5}$$

$$p(r,\theta,z,t) = \frac{1}{Re^2}P(z) + \bar{p}(r,\theta,z,t), \tag{2.6}$$

where r, θ, z refer to the radial, azimuthal and normal coordinates. The undisturbed mean flow in the radial, azimuthal and normal directions are denoted by F, G, H and are solved in chapters 4, 5 and 6; refer to equations (4.6) - (4.9), (5.9) - (5.12) and (6.14) - (6.17). Here P is the mean pressure and $Re = r_a^*\Lambda^*\delta^*/\nu^* = r_a^*/\delta^* = r_a$ is the Reynolds number for some radial position r_a^*. Here $\delta^* = (\nu^*/\Lambda^*)^{\frac{1}{2}}$ is the constant boundary-layer thickness, ν^* is the kinematic viscosity and Λ^* is the angular velocity of the rotating-disk. (Here $*$ denotes dimensional quantities). The terms $\bar{u}_r, \bar{u}_\theta, \bar{u}_z, \bar{p}$ refer to the velocity and pressure perturbations, which are defined as

$$(\bar{u}_r, \bar{u}_\theta, \bar{u}_z, \bar{p}) = (f(z), g(z), h(z), \pi(z))\exp[i(\alpha r + \beta Re\theta - \omega t)], \tag{2.7}$$

where α, β, ω refer to the radial wavenumber, azimuthal wavenumber and frequency, respectively. On substituting (2.3) - (2.6) into the cylindrical Navier-Stokes equations (2.1), the following system of equations can be obtained

$$i(\alpha F + \beta G - \omega)f + F'h + i\alpha\pi = \frac{1}{Re}[f'' - \lambda^2 f - Ff + 2(G+1)g - Hf'], \quad (2.8)$$

$$i(\alpha F + \beta G - \omega)g + G'h + i\beta\pi = \frac{1}{Re}[g'' - \lambda^2 g - Fg - 2(G+1)f - Hg'], \quad (2.9)$$

$$i(\alpha F + \beta G - \omega)h + \pi' = \frac{1}{Re}[h'' - \lambda^2 h - Hh' - H'h], \quad (2.10)$$

$$\left\{i\alpha + \frac{1}{Re}\right\}f + i\beta g + h' = 0, \quad (2.11)$$

where $\lambda^2 = \alpha^2 + \beta^2$. On eliminating π and ignoring terms of order R^{-2} and smaller, we obtain

$$[i(D^2 - \lambda^2)(D^2 - \bar{\lambda}^2) + Re(\alpha F + \beta G - \omega)(D^2 - \bar{\lambda}^2) - Re(\bar{\alpha}F'' + \beta G'')$$
$$-iHD(D^2 - \bar{\lambda}^2) - iH'(D^2 - \bar{\lambda}^2) - iFD^2]h + [2(G+1)D + 2G']\eta = 0, \quad (2.12)$$

and

$$[2(G+1)D - iRe(\alpha G' - \beta F')]h + [i(D^2 - \lambda^2) + Re(\alpha F + \beta G - \omega) - iHD - iF]\eta = 0, \quad (2.13)$$

where $\bar{\lambda}^2 = \alpha\bar{\alpha} + \beta^2$, $\bar{\alpha} = \alpha - i/Re$, $\eta = \alpha g - \beta f$ and $D = d/dz$. The parallel flow approximation has been assumed, where the radial dependence of the mean flow has been ignored. Therefore, we have assumed that $r = Re$. Previous investigators have called upon the above system of equations to conduct studies on the rotating-disk boundary-layer (e.g. Malik *et al.*, 1981; Malik, 1986; Lingwood, 1995, to name a few).

The sixth-order system is solved subject to the boundary conditions

$$h(0) = h'(0) = \eta(0) = 0, \quad (2.14)$$

and

$$h(\infty) = h'(\infty) = \eta(\infty) = 0. \quad (2.15)$$

If the Coriolis force and curvature effects are neglected, equations (2.12) - (2.13) reduce to the fourth-order Orr-Sommerfeld equation

$$[i(D^2 - \lambda^2)^2 + Re(\alpha F + \beta G - \omega)(D^2 - \lambda^2) - Re(\alpha F'' + \beta G'')]h = 0. \qquad (2.16)$$

If viscous terms are now neglected and $\beta = 0$, the above fourth-order equation reduces to the Rayleigh equation

$$(F - c)(h'' - \alpha^2 h) - F''h = 0, \qquad (2.17)$$

where $c = \omega/\alpha$ is the group velocity.

A method for solving the above sixth-order system (2.12) - (2.13) is given in the appendices, along with several results validating the code.

2.3 The rotating-cone and the rotating-sphere

The rotating-cone and rotating-sphere have been studied extensively, since they too exhibit the crossflow instability. Garrett & Peake (2002, 2004, 2007) have shown that there exists a region of absolute instability within the rotating-sphere and the rotating-cone. The interested reader is referred to the above papers and Banks (1965, 1976), Kobayashi (1981), Kobayashi & Izumi (1983), Kobayashi (1994), Kobayashi, Kohama & Kurosawa (1983), Kohama & Kobayashi (1983), Kohama (2000), Okamoto, Yagita & Kamijima (1976), Taniguchi, Kobayashi & Fukunishi (1998), Manohar (1967), Howarth (1951), Tien & Campbell (1963) and Reed & Saric (1989) for further details.

2.4 Remainder of thesis

The remainder of the thesis is as follows; chapter 3 briefly describes the velocity-vorticity formulation (in cartesian co-ordinates) and numerical methods (developed

by Davies & Carpenter, 2001, 2003) used throughout the numerical simulation investigations. The effects of mass transfer on the rotating-disk boundary-layer are considered in chapter 4 and the effects of introducing a uniform axial magnetic field to an electrically conducting fluid above a rotating-disk are discussed in chapter 5. The family of rotating boundary-layers - so-called *BEK* family - are investigated in chapter 6, where particular flows of interest are the Bödewadt, Ekman and von Kármán boundary-layers. The global stability of the rotating-disk boundary-layer is discussed in chapter 7 and comparisons are made with the two-dimensional linearized Ginzburg-Landau equation in chapter 8. Finally, the results are summarized and suggestions are made for future studies in chapter 9.

Chapter 3

Formulation and numerical methods

3.1 Introduction

The velocity-vorticity formulation and numerical methods are discussed in depth by Davies & Carpenter (2001), but for ease of reading the methods are reviewed in the present chapter.

The remainder of the chapter is as follows; the velocity-vorticity formulation for the three-dimensional problem in cartesian co-ordinates is discussed; the primary and secondary variables are defined and calculated; integral operators are given to replace first and second-order derivatives; and finally the radial and temporal discretization is discussed.

3.2 Velocity-vorticity formulation

3.2.1 Vorticity

The vorticity of a fluid is given by

$$\underline{\omega} = \nabla \wedge \underline{u}, \tag{3.1}$$

where $\underline{u}$ is the velocity of the fluid. Therefore, for a two-dimensional flow $\underline{u} = [u_x(x,y,t), u_y(x,y,t), 0]$, the vorticity $\underline{\omega} = (0,0,\omega)$ for

$$\omega = \frac{\partial u_y}{\partial x} - \frac{\partial u_x}{\partial y}. \tag{3.2}$$

While for a three-dimensional flow in cylindrical coordinates

$$\underline{u} = [u_r(r,\theta,z,t), u_\theta(r,\theta,z,t), u_z(r,\theta,z,t)],$$

the vorticity is given by

$$\underline{\omega} = \left[\frac{1}{r}\left\{\frac{\partial u_z}{\partial \theta} - \frac{\partial (r u_\theta)}{\partial z}\right\}, \frac{\partial u_r}{\partial z} - \frac{\partial u_z}{\partial r}, \frac{1}{r}\left\{\frac{\partial (r u_\theta)}{\partial r} - \frac{\partial u_r}{\partial \theta}\right\}\right], \tag{3.3}$$

where r, θ and z refer to the radial, azimuthal and normal directions.

3.2.2 The vorticity equation

The Euler equation is given as

$$\text{Momentum: } \frac{\partial \underline{u}}{\partial t} + (\underline{u}.\nabla)\underline{u} = -\frac{1}{\rho}\nabla P + \underline{g}, \tag{3.4}$$

$$\text{Continuity: } \nabla.\underline{u} = 0, \tag{3.5}$$

where $\underline{u}$ is the velocity of the fluid, $\underline{g}$ is the direction of the gravitational acceleration, P is the fluid pressure and ρ is the fluid density.

By introducing the identity

$$(\underline{A}.\nabla)\underline{A} = (\nabla \wedge \underline{A}) \wedge \underline{A} + \nabla\left(\frac{1}{2}\underline{A}^2\right), \tag{3.6}$$

equation (3.4) may be re-cast in the form

$$\frac{\partial \underline{u}}{\partial t} + \underline{\omega} \wedge \underline{u} = -\nabla B, \tag{3.7}$$

where B is a combination of the pressure and other external forces. On taking the curl of (3.7), we obtain

$$\frac{\partial \underline{\omega}}{\partial t} + \nabla \wedge (\underline{\omega} \wedge \underline{u}) = 0. \tag{3.8}$$

In turn this may be given as

$$\frac{\partial \underline{\omega}}{\partial t} + (\underline{u}.\nabla)\underline{\omega} = (\underline{\omega}.\nabla)\underline{u}, \tag{3.9}$$

or

$$\frac{D\underline{\omega}}{Dt} = (\underline{\omega}.\nabla)\underline{u}, \tag{3.10}$$

which is known as the vorticity equation.

The reader will notice that the pressure term has been eliminated from the vorticity equation. Indeed, equation (3.10) only depends on the velocity $\underline{u}$ and vorticity $\underline{\omega}$, which as we know are related by equation (3.1).

A similar approach can be applied to the viscous Navier-Stokes equations

$$\text{Momentum: } \frac{d\underline{u}}{dt} + (\underline{u}.\nabla)\underline{u} = -\frac{1}{\rho}\nabla P + \nu\nabla^2\underline{u}, \tag{3.11}$$

$$\text{Continuity: } \nabla.\underline{u} = 0, \tag{3.12}$$

which after some manipulation gives the vorticity equation with viscous effects

$$\frac{D\underline{\omega}}{Dt} = (\underline{\omega}.\nabla)\underline{u} + \nu\nabla^2\underline{\omega}, \tag{3.13}$$

where ν is the kinematic viscosity.

3.2.3 Formulation

The advantages of a velocity-vorticity formulation over a Navier-Stokes formulation have been reviewed by Fasel (1980), Speziale (1987) and Gatski (1991). As mentioned above, the main advantage of the velocity-vorticity method is that the pressure term has been removed, leaving only the velocity and vorticity fields.

Several investigators have conducted studies using the velocity-vorticity approach. In particular, Davies & Carpenter (2001) have described and developed a velocity-vorticity formulation, which has applications to many boundary-layer problems. The system of equations used in their formulation comprises of the vorticity equation

(3.13) and a Poisson equation (obtained by taking the curl of equation (3.1)), which replaces the usual continuity equation (3.12). The Poisson equation is given by

$$\nabla^2 \underline{u} = -\nabla \wedge \underline{\omega}. \tag{3.14}$$

Governing equations

For a three-dimensional cartesian system, there are six unknown perturbation variables, which are given as

$$\underline{u} = (u_x, u_y, u_z),$$

$$\underline{\omega} = (\omega_x, \omega_y, \omega_z).$$

Davies & Carpenter (2001) divide the unknown components into primary variables $\{\omega_x, \omega_y, u_z\}$ and secondary variables $\{u_x, u_y, \omega_z\}$. Here x, y, z refer to the streamwise, spanwise and normal directions. The primary variables are determined by three equations, which consist of two vorticity equations for the ω_x and ω_y components and a third equation, which is obtained by taking the wall-normal component of equation (3.14). The system of equations are

$$\frac{\partial \omega_x}{\partial t} + \frac{\partial N_z}{\partial y} - \frac{\partial N_y}{\partial z} = \frac{1}{Re}\nabla^2 \omega_x, \tag{3.15}$$

$$\frac{\partial \omega_y}{\partial t} + \frac{\partial N_x}{\partial z} - \frac{\partial N_z}{\partial x} = \frac{1}{Re}\nabla^2 \omega_y, \tag{3.16}$$

$$\nabla^2 u_z = \frac{\partial \omega_x}{\partial y} - \frac{\partial \omega_y}{\partial x}. \tag{3.17}$$

The convection term $\mathbf{N} = (N_x, N_y, N_z)$, may be either linear or non-linear. For a linear study, $\mathbf{N}$ is given by

$$\mathbf{N} = \mathbf{\Omega} \wedge \underline{u} + \underline{\omega} \wedge \mathbf{U}, \tag{3.18}$$

where $\mathbf{U}$ and $\mathbf{\Omega} = \nabla \times \mathbf{U}$ are the undisturbed velocity and vorticity fields.

The remaining secondary variables, which are required to calculate the term $\mathbf{N}$ are given in terms of the primary variables, by the following integral definitions

$$u_x = -\int_z^\infty \left(\omega_y + \frac{\partial u_z}{\partial x}\right) dz, \tag{3.19}$$

$$u_y = \int_z^\infty \left(\omega_x - \frac{\partial u_z}{\partial y}\right) dz, \tag{3.20}$$

$$\omega_z = \int_z^\infty \left(\frac{\partial \omega_x}{\partial x} + \frac{\partial \omega_y}{\partial y}\right) dz. \tag{3.21}$$

The first two integral definitions are obtained by integrating the appropriate terms in the definition (3.1). The third definition is given by integrating the solenoidal condition

$$\nabla . \underline{\omega} = 0. \tag{3.22}$$

The so-called secondary variables are given in terms of the primary variables only. Therefore, they can be removed from the vorticity equations. Hence, we have a system of three governing equations for the three unknown primary variables.

Integral constraints

For the Navier-Stokes equations, the boundary conditions on the velocity components at a flat rigid wall are given by the no-slip condition

$$u_x = u_y = u_z = 0, \qquad \text{at} \qquad z = 0. \tag{3.23}$$

However, for the velocity-vorticity formulation, Davies & Carpenter (2001) have introduced integral constraints on the vorticity terms ω_x and ω_y. These constraints are obtained from the secondary definitions (3.19) and (3.20), and are given as

$$\int_0^\infty \omega_x dz = \int_0^\infty \frac{\partial u_z}{\partial y} dz, \tag{3.24}$$

$$\int_0^\infty \omega_y dz = -\int_0^\infty \frac{\partial u_z}{\partial x} dz. \tag{3.25}$$

These two expressions are equivalent to the no-slip conditions for u_x and u_y and are used as constraints on the primary variables ω_x, ω_y.

Davies & Carpenter (2003) have successfully applied the above velocity-vorticity formulation to the rotating-disk boundary-layer. For further details of their study, refer to chapter 2.

3.3 Numerical method

3.3.1 Primary, secondary variables and integral constraints

Primary variables

The perturbation terms $(\omega_x, \omega_y, u_z)$ are chosen to be our primary variables, which are expanded in terms of odd Chebyshev polynomials

$$g(x,y,z,t) = \left\{ \sum_{k=1}^{N} g_k(x,t) T_{2k-1}(\xi) \right\} e^{i\beta y}, \tag{3.26}$$

where T_k is the kth Chebyshev polynomial of the first kind and $\xi \epsilon (0,1]$ is the mapped wall normal coordinate, defined as

$$\xi = \frac{L}{z+L}, \tag{3.27}$$

where L is a stretching factor. The Chebyshev expansion (3.26) has been restricted to an individual spanwise mode number β. Derivatives with respect to the physical coordinate z are related to derivatives with respect to the computational coordinate ξ by

$$\frac{\partial g}{\partial z} = -\frac{\xi^2}{L}\frac{\partial g}{\partial \xi}. \tag{3.28}$$

It is assumed that disturbances decay exponentially as $z \to \infty$. Therefore, the primary variables vanish as $\xi \to 0$. If our primary variable g is of the form $g \sim e^{-sz}$ as $z \to \infty$ for $s > 0$, then all derivatives disappear as $z \to \infty$.

Secondary variables

The so called secondary variables (u_x, u_y, ω_z) are defined in terms of even Chebyshev polynomials

$$f(x,y,z,t) = \left\{ \frac{1}{2} f_0(r,t) + \sum_{k=1}^{N} f_k(x,t) T_{2k}(\xi) \right\} e^{i\beta y}, \tag{3.29}$$

where

$$f_0(r,t) = -2 \sum_{k=1}^{N} f_k(x,t)(-1)^k. \tag{3.30}$$

This ensures that the secondary variables disappear as $z \to \infty$.

The secondary variables are defined in terms of the primary variables (equations (3.19) - (3.21)). They are of the general form

$$f = \int_z^\infty g \, dz, \tag{3.31}$$

where f is the secondary variable and g is a combination of primary variables. After applying the coordinate mapping transformation (3.27) (which maps the semi-infinite domain $[0, \infty)$ to the finite interval $(0, \xi]$), we obtain the expression

$$f = L \int_0^\xi \frac{g}{\xi^2} d\xi. \tag{3.32}$$

By letting

$$g = \sum_{k=1}^{\infty} g_k T_{2k-1}(\xi), \qquad h = \frac{g}{\xi^2} = \sum_{k=1}^{\infty} h_k T_{2k-1}(\xi), \tag{3.33}$$

and using

$$\xi^2 T_{2k-1} = \frac{1}{4}(T_{2k+1} + 2T_{2k-1} + T_{2k-3}), \tag{3.34}$$

the following expression may be obtained

$$g_k = \frac{1}{4}(h_{k-1} + 2h_k + h_{k+1}). \tag{3.35}$$

Since

$$\int_0^\xi h \, d\xi = \frac{1}{4} \sum_{k=1}^{\infty} \frac{1}{k}(h_k - h_{k+1})(T_{2k}(\xi) - T_{2k}(0)), \tag{3.36}$$

we may let

$$f = \sum_{k=1}^{\infty} f_k(T_{2k}(\xi) - T_{2k}(0)), \tag{3.37}$$

for

$$f_k = \frac{L}{4k}(h_k - h_{k+1}). \tag{3.38}$$

Thus, after some manipulation we can obtain

$$(k+1)f_{k+1} + 2kf_k + (k-1)f_{k-1} = \frac{L}{4}(h_{k-1} + 2h_k + h_{k+1} - (h_k + 2h_{k+1} + h_{k+2})). \tag{3.39}$$

Now from the above expression (3.35), relating the coefficients of g and h, we may obtain the following relation between the original f and g coefficients

$$(k+1)f_{k+1} + 2kf_k + (k-1)f_{k-1} = L(g_k - g_{k+1}). \tag{3.40}$$

This is the tri-diagonal relationship that is used for calculating the secondary variable Chebyshev coefficients (3.19) - (3.21). On combining the secondary variable definitions (3.19) - (3.21) with equation (3.40), the following tri-diagonal relations are obtained

$$\begin{aligned}
(k+1)u_{x,k+1} + 2ku_{x,k} + (k-1)u_{x,k-1} &= -L\left\{\omega_{y,k} - \omega_{y,k+1} + \frac{\partial}{\partial x}(u_{z,k} - u_{z,k+1})\right\} \\
(k+1)u_{y,k+1} + 2ku_{y,k} + (k-1)u_{y,k-1} &= L\left\{\omega_{x,k} - \omega_{x,k+1} - \frac{\partial}{\partial y}(u_{z,k} - u_{z,k+1})\right\} \\
(k+1)\omega_{z,k+1} + 2k\omega_{z,k} + (k-1)\omega_{z,k-1} &= L\left\{\frac{\partial}{\partial x}(\omega_{x,k} - \omega_{x,k+1}) + \frac{\partial}{\partial y}(\omega_{y,k} - \omega_{y,k+1})\right\}.
\end{aligned}$$

The secondary variables are only required for calculating the convective term **N** (equation (3.18)) in the vorticity equations, which is treated explicitly, using a predictor-corrector method, in the time marching procedure.

Integral constraints

The integral constraints (3.24) - (3.25) are of the general form

$$f|_{z=0} = \int_0^{\infty} g \, dz, \tag{3.41}$$

which may be re-cast in the form

$$f|_{z=0} = \sum_{k=1}^{N} p_k g_k. \tag{3.42}$$

Here p_k are fixed constants, which may be calculated by a similar method as that given for the secondary variables. We will now describe the method for calculating the unknown coefficients p_k.

The relation (3.40) can be given as

$$A\underline{\tilde{f}} = LB\underline{g}, \tag{3.43}$$

where L is the stretching parameter, $\underline{\tilde{f}}$ and $\underline{g}$ are $(N-1)$ and N vectors,

$$\underline{\tilde{f}}^T = \begin{pmatrix} f_1 & 2f_2 & \cdots & kf_k & \cdots & (N-1)f_{N-1} \end{pmatrix}, \tag{3.44}$$

$$\underline{g}^T = \begin{pmatrix} g_1 & g_2 & \cdots & g_k & \cdots & g_N \end{pmatrix}, \tag{3.45}$$

and A and B are sparse $(N-1)\times(N-1)$ and $(N-1)\times N$ matrices,

$$A = \begin{pmatrix} 2 & 1 & & & & \\ 1 & 2 & 1 & & & \\ & \ddots & \ddots & \ddots & & \\ & & \ddots & \ddots & \ddots & \\ & & & 1 & 2 & 1 \\ & & & & 1 & 2 \end{pmatrix}, \tag{3.46}$$

$$B = \begin{pmatrix} 1 & -1 & & & & & \\ & 1 & -1 & & & & \\ & & \ddots & \ddots & & & \\ & & & \ddots & \ddots & & \\ & & & & 1 & -1 & \\ & & & & & 1 & -1 \end{pmatrix}. \tag{3.47}$$

Here the superscript T refers to the transpose of a matrix or vector.

Now

$$\begin{aligned} f|_{z=0} &= \sum_{k=1}^{N-1} f_k(T_{2k}(\xi) - T_{2k}(0))\Big|_{z=0}, \\ &= \sum_{k=1}^{N-1} f_k(1-(-1)^k), \\ &= \sum_{k=1}^{N-1} 2f_k \mathrm{mod}(k,2), \\ &= 2\underline{r}^T\underline{\tilde{f}}, \end{aligned} \tag{3.48}$$

where

$$\underline{r}^T = \begin{pmatrix} 1 & 0 & 1/3 & 0 & 1/5 & \cdots & 1/(N-1) \end{pmatrix}. \tag{3.49}$$

Hence,

$$\begin{aligned} f|_{z=0} &= 2L\underline{r}^T A^{-1} B\underline{g}, \\ &= \underline{p}^T\underline{g}, \end{aligned} \tag{3.50}$$

where

$$\underline{p} = 2LB^T(A^{-1})^T\underline{r}, \tag{3.51}$$

is the vector of coefficients p_k, as defined in equation (3.42).

The third boundary condition is of the general form

$$v = 0. \tag{3.52}$$

This condition is far easier to discretize than the previous integral constraints, and is given as

$$\sum_{k=1}^{N} q_k v_k = 0, \tag{3.53}$$

where $q_k = T_{2k-1}(1) = 1$.

3.3.2 Chebyshev integral operators

As we are investigating the velocity-vorticity problem, there will only be first and second order derivatives (with respect to z) present in the governing equations (3.15) - (3.17). In order to remove these z-derivative operators, the equations are integrated twice with respect to the mapped variable ξ. Thus, the following ξ-integral operators are obtained

$$\mathbf{I}f(\xi) = \int^{\xi}\int^{\xi'} f(\xi'')d\xi' d\xi'', \tag{3.54}$$

$$\mathbf{J}f(\xi) = \frac{1}{L}\left(2\int^{\xi}\int^{\xi'} \xi'' f(\xi'')d\xi' d\xi'' - \int^{\xi} \xi'^2 f(\xi')d\xi'\right), \tag{3.55}$$

$$\mathbf{K}f(\xi) = \frac{1}{L^2}\left(\xi^4 f(\xi) - 6\int^{\xi} \xi'^3 f(\xi')d\xi' + 6\int^{\xi}\int^{\xi'} \xi''^2 f(\xi'')d\xi' d\xi''\right). \tag{3.56}$$

The integral operators are those given in Davies & Carpenter (2001); page 141. The integral operator $\mathbf{I}$ replaces the zeroth order z-derivatives; $\mathbf{J}$ replaces the first order z-derivatives; and $\mathbf{K}$ replaces the second order z-derivatives. The terms $\frac{1}{L}$ and $\frac{1}{L^2}$ in equation (3.55) and (3.56), arise, due to the coordinate transformation (3.27).

The integral operators can be represented as tri-diagonal, penta-diagonal or band-width four matrices, when they are applied to the appropriate Chebyshev series. When the integral $\mathbf{I}$ is applied to a series of odd Chebyshev polynomials, we obtain the following tri-diagonal matrix

$$\mathbf{I}\sum_{k=1}^{N} f_k T_{2k-1} = aT_0 + bT_1 + \sum_{k=2}^{N+1}\frac{1}{8}\left(\frac{f_{k-1}}{(2k-1)(k-1)} - \frac{f_k}{k(k-1)} + \frac{f_{k+1}}{k(2k-1)}\right)T_{2k-1}, \tag{3.57}$$

where a and b are arbitrary integral constants that arise due to the double indefinite integral. Similarly, we may obtain a matrix with a bandwidth of four, when $\mathbf{J}$ acts on a series of even Chebyshev polynomials, and a penta-diagonal matrix when $\mathbf{K}$ acts

on a series of odd Chebyshev polynomials

$$\mathbf{J}\sum_{k=1}^{N} f_k T_{2k} = aT_0 + bT_1 + \sum_{k=2}^{N+1} \frac{1}{8L(2k-1)}\left(\left[\frac{1}{(k-1)} - 1\right] f_{k-2} - \left[1 + \frac{1}{k}\right] f_{k-1} + \left[1 - \frac{1}{(k-1)}\right] f_k + \left[1 + \frac{1}{k}\right] f_{k+1}\right) T_{2k-1}, \quad (3.58)$$

$$\mathbf{K}\sum_{k=1}^{N} f_k T_{2k-1} = aT_0 + bT_1 + \sum_{k=2}^{N+1} \frac{1}{16L^2}\left(\left[1 - \frac{6}{(2k-1)} + \frac{3}{(k-1)(2k-1)}\right] f_{k-2} + \left[1 - \frac{12}{(2k-1)} + \frac{3}{k(k-1)(2k-1)}\right] f_{k-1} + \left[6 - \frac{3}{k(k-1)}\right] f_k + \left[4 + \frac{12}{(2k-1)} - \frac{3}{k(k-1)(2k-1)}\right] f_{k+1} + \left[1 + \frac{6}{(2k-1)} + \frac{3}{k(2k-1)}\right] f_{k+2}\right) T_{2k-1}. \quad (3.59)$$

On substituting the odd Chebyshev series (3.26) for the primary variables into the given integrated governing equations and then matching the coefficients of T_{2k-1} for $k = 1, 2, ..., N$, we obtain a system of $m(N-1)$ partial differential equations, for mN unknown primary variables. (Here m is the number of governing equations or primary variables: $m = 3$ for the rotating-disk boundary-layer formulation). The remaining m equations are given by the boundary conditions, which replace the m equations that would have been obtained from the coefficients of the lowest order polynomial T_1. This gives a system of mN partial differential equations for the mN unknown primary variables.

3.3.3 Radial and temporal discretization and a predictor-corrector method

Radial discretization

Radial derivatives are discretized using a compact, fourth-order, centered, finite-difference method, which are of the general form

$$\alpha\left(\frac{\partial f^l}{\partial r}\right)_{k,j-1} + \left(\frac{\partial f^l}{\partial r}\right)_{k,j} + \alpha\left(\frac{\partial f^l}{\partial r}\right)_{k,j+1} = \frac{2(\alpha+2)}{3}\left(\frac{f^l_{k,j+1} - f^l_{k,j-1}}{2\Delta r}\right) + \frac{4\alpha - 1}{3}\left(\frac{f^l_{k,j+2} - f^l_{k,j-2}}{4\Delta r}\right), \tag{3.60}$$

and

$$\beta\left(\frac{\partial^2 f^l}{\partial r^2}\right)_{k,j-1} + \left(\frac{\partial^2 f^l}{\partial r^2}\right)_{k,j} + \beta\left(\frac{\partial^2 f^l}{\partial r^2}\right)_{k,j+1} = \frac{4(1-\beta)}{3}\left(\frac{f^l_{k,j+1} - 2f^l_{k,j} + f^l_{k,j-1}}{(\Delta r)^2}\right) + \frac{10\beta - 1}{3}\left(\frac{f^l_{k,j+2} - 2f^l_{k,j} + f^l_{k,j-2}}{4(\Delta r)^2}\right). \tag{3.61}$$

Here α and β may be chosen freely and

$$f^l_{k,j} = f_k|_{r=j\Delta r, t=l\Delta t}, \tag{3.62}$$

where Δr and Δt are the radial and temporal increments. As in the study by Davies & Carpenter (2001), α and β are given the respective values 1/4 and 1/10, which removes the last terms on the right-hand-side of equations (3.60) and (3.61).

Time discretization and the predictor-corrector method

We define

$$f^l = f|_{t=l\Delta t}, \tag{3.63}$$

which allows the three-point backward difference scheme to be given as

$$\frac{\partial f}{\partial t} = \frac{1}{2\Delta t}\left(3f^l - 4f^{l-1} + f^{l-2}\right). \tag{3.64}$$

The time-stepping is carried out using a predictor-corrector method for the convective terms in the governing equations (3.15) - (3.17). The viscous terms in (3.15) - (3.16) are treated implicitly, as is the Poisson equation (3.17). The remaining Coriolis force terms, (which appear in the governing equations for the rotating-disk boundary-layer; refer to chapter 4, equations (3.15) - (3.16)) can be treated either implicitly or by applying the predictor-corrector method. (The predictor-corrector method has been used here for the Coriolis force terms). In chapter 5, which is concerned with the rotating-disk and a uniform magnetic field, the terms which arise because of the Lorentz force are treated using the predictor-corrector method.

The predictor step is given as

$$\begin{aligned}(N^l)^p &= 2N^{l-1} - N^{l-2} \\ &= 2(\mathbf{\Omega} \wedge u^{l-1} + \omega^{l-1} \wedge \mathbf{U}) - (\mathbf{\Omega} \wedge u^{l-2} + \omega^{l-2} \wedge \mathbf{U}),\end{aligned} \tag{3.65}$$

for a corrector stage

$$\begin{aligned}(N^l)^c &= N((u^l)^p, (\omega^l)^p) \\ &= \mathbf{\Omega} \wedge (u^l)^p + (\omega^l)^p \wedge \mathbf{U}),\end{aligned} \tag{3.66}$$

where $(u^l)^p$ and $(\omega^l)^p$ are the predicted disturbance velocity and viscosity fields, respectively. Here $\mathbf{U}$ and $\mathbf{\Omega}$ are the undisturbed velocity and vorticity fields.

The finite-difference discretization methods described above can be used to replace the temporal and radial derivatives, to give a fully discretized version of the governing equations (3.15) - (3.17). The mN equations consist of m subsets of N equations, where the first equation in each subset N is the appropriate boundary condition, while the remaining $N-1$ equations are given by the integrated governing equations. The fully integrated governing equations are now ready to be solved.

The interested reader is referred to Davies & Carpenter (2001) for further details of the numerical methods used here, and other alternative methods for solving the given system of equations.

3.4 Final remarks

The above numerical methods have been successfully applied by Davies & Carpenter (2003) to the rotating-disk boundary-layer for parallel and non-parallel mean flows. Using the same methods we will now study several other rotating flows;

1. rotating-disk with mass transfer;
2. rotating-disk with a magnetic field;
3. Ekman and Bödewadt flows - so called *BEK* family.

Essentially the same numerical methods have also been applied to the two-dimensional boundary-layer over a flat plate; Davies & Carpenter (1997a,b).

Chapter 4

The rotating-disk boundary-layer with mass transfer

4.1 Introduction

There are many methods and appliances used in fluid mechanics and industry to reduce unstable behaviour or delay the onset of transition from a laminar to turbulent state. One stabilizing method is to introduce a uniform normal flow of suction. Suction has the effect of stabilizing a boundary-layer flow, and in some cases only a small level of suction is required to greatly increase the critical point of instability. Blowing or injection has the opposite effect and is known to be destabilizing.

It was first noted by Batchelor (1951) that the ordinary differential equations found using the von Kármán (1921) similarity variables, can be extended to rotating-disk flows with a uniform normal flow at the disk surface, (i.e. uniform suction and injection). Hall, Malik & Poll (1984) have theoretically shown that suction has a stabilizing effect on the leading edge of the swept-wing. Uniform suction was found to extend the laminar flow region, by reducing the magnitude of the crossflow velocity and by decreasing the thickness of the boundary-layer. Thus, the crossflow velocity profile is stabilized. Therefore, it should be possible to apply suction to the rotating-disk boundary-layer and achieve significant delays in instabilities and

transition to turbulence. However, it was shown by Stuart (1954) that there is no significant change in the shape of the mean velocity profiles with uniform suction. Thus, it might have been anticipated that suction would not significantly increase the region of laminar flow. Nonetheless, an experiment on the effects of suction on the rotating-disk by Gregory & Walker (1960), showed that the critical Reynolds number for instability and turbulence increased greatly with increasing uniform suction. The experiment consisted of a microphone probe and a hotfilm anemometer with suction distributed through either a woven wire cloth or a slitted surface. They found the critical Reynolds numbers to be dependent on the angular velocity of the disk, because of roughnesses on the disk surface. For the flow with a slitted surface, the effects were less dependent on the angular velocity and the Reynolds number, since the onset of turbulence was found to increase to approximately $Re = 632$ for the suction parameter $\mathbf{a} = 0.4$. Here $\mathbf{a}$ is a negative constant for injection and a positive constant for suction. For suction slots, it was found that 75% more suction was required to achieve a given level of stability than that was predicted by stability theory (Dhanak, 1992; Lingwood, 1997a). Possible reasons for this were the deficiencies of the experimental apparatus available at the time, such as surface roughness of the rotating-disk and non-uniformity of suction. In the experiment (where suction was distributed through slots) by Gregory & Walker (1960), the maximum stabilization occurred for a relatively low suction rate. While for larger suction rates the onset of transition decreased and then increased again for greater values of the suction parameter $\mathbf{a}$. It was suggested that due to the reduction in the mean flow radial velocity profiles for higher rates of suction, turbulent contamination was allowed to spread inwards from the outer edge of the disk. This effect was called 'self-contamination' (Gregory & Walker, 1960).

Since Gregory & Walker (1960) were unable to extend the laminar flow region to values corresponding to flight conditions on a swept-wing, they concluded that the

rotating-disk boundary-layer is not a satisfactory tool for investigating the effects of suction on the crossflow instability, nor the testing of suction surfaces.

The effects of mass transfer at the surface of the rotating-disk on heat transfer and on the flow field about the disk were investigated in detail by Sparrow & Gregg (1960). Solutions to their governing equations were obtained over a wide range of suction and injection velocities. They obtained results for the velocity, temperature, mass-fraction distributions and the heat-transfer, mass-transfer and torque requirements. Sparrow & Gregg (1960) also showed that fluid injection sharply decreases the heat transfer at the surface. Thus, injection is useful in cooling turbine blades and high-speed aero-vehicles.

A number of researchers have used asymptotic methods to find solutions to the flows with suction/injection. By such methods Ockendon (1972) found an approximate solution to the problem where the suction parameter **a** is small. In Kuiken (1971) a study was conducted on the effects of normal blowing/injection through the rotating-disk. It was found that for strong blowing, the flow is almost completely inviscid. Kuiken (1971) also compares results of an asymptotic analysis with numerical integrations of the full equations and they are found to agree.

Dhanak (1992) studied the effects of suction on the stationary convectively unstable Types-1 and -2 modes in the rotating disk boundary-layer. Linear stability theory was employed. The Type-1 mode is the inviscid crossflow instability and was originally discovered by Gray (1952) in his experimental study on the flow over a swept wing. Gregory *et al.* (1955) conducted an experimental investigation on the von Kármán flow and gave evidence for the presence of the crossflow instability within the rotating-disk boundary-layer. The Type-2 mode is essentially viscous and is destabilized by the Coriolis forces present within the rotating-disk boundary-layer. It was first discovered by Faller & Kaylor (1966) within the Ekman layer; Malik (1986) gave evidence for its presence within the von Kármán flow. Other than the Type-1 and

-2 modes, there also exists a third Type-3 mode that was first discovered by Mack (1985). The Type-3 mode is spatially damped and propagates radially inward. We will see later that the Type-1 and -3 eigen-modes coalesce to produce absolute instability; Lingwood (1995, 1996, 1997a). In Dhanak (1992) uniform suction was shown to increase the critical Reynolds number associated with the Types-1 and -2 modes. The convectively unstable region of the parameter space was reduced. On the other hand, injection was found to lower the critical Reynolds number and to enlarge the convectively unstable region of the parameter space.

Bassom & Seddougui (1992) studied the effects of suction/injection on nonlinear disturbances. They found that suction lowers the threshold disturbance amplitude (disturbances smaller than this decay, while those larger grow without limit), while injection increases the threshold disturbance amplitude. Thus, they suggested that an experiment with suction would require smaller forcing, for non-linear growth to take hold, than the zero normal flow case, whereas injection would require a larger forcing for sub-critical stationary instability to occur. In the earlier experiment by Gregory & Walker (1960) the methods used to induce suction may have introduced severe roughness effects to the disk surface. Thus, it is likely that the surface roughness was causing instability and turbulence to occur earlier than what is theoretically possible. Therefore, future experimental investigators should be careful in limiting the surface roughness introduced through the uniformly distributed suction.

Wilson & Schryer (1978) numerically determined the viscous flow between two coaxial infinite disks, one stationary and the other rotating. The flow belongs to the two parameter family described by Batchelor (1951). The family represents a flow which is in rigid-body rotation, over each of the two planes, at a finite distance apart. Wilson & Schryer (1978) also investigated the effects of applying uniform suction through the disk. Initially, the two disks and fluid core are stationary. The angular velocity of the rotating-disk and amount of uniform suction is then gradually

increased, to various constant values. For large Reynolds numbers the flow tends towards a state of equilibrium, in which thin boundary-layers exist near both disks and an interior core of fluid rotates with an approximately constant angular velocity. It was found that for zero suction the core rotation rate was about 0.3131 times that of the rotating-disk. Fluid near the disk is thrown centrifugally outwards. As the suction parameter **a** is increased, the core rotation rate increases and the centrifugal outflow decreases. For $\mathbf{a} > 1.3494$, the core rotation rate is greater than the disk rotation rate and the radial flow near the rotating-disk is directed inwards. This final case is similar to the Bödewadt flow, where a block of fluid rotates with constant angular velocity above a stationary disk. The radial flow is also directed towards the centre of the disk for the Bödewadt flow.

4.1.1 Absolute instability

Lingwood (1997a) extended her work on the rotating-disk boundary-layer for absolute instability by studying flows with a constant normal flow through the disk wall. Uniform suction across the disk surface was found to delay the onset of absolute instability, while uniform injection promotes the onset of absolute instability. For the given injection/suction parameter **a**, it was found that for $\mathbf{a} = -1$ ($\mathbf{a} < 0$ corresponds to uniform injection) the critical Reynolds number for absolute instability is approximately 202, less than half that observed for the case with zero normal flow. Whereas for $\mathbf{a} = 1$ ($\mathbf{a} > 0$ corresponds to uniform suction) the critical Reynolds number is approximately 1861, almost four times that observed for the case with zero normal flow. For the case $\mathbf{a} = 0.4$, absolute instability was found to arise for $Re \approx 803$. The Reynolds number for the onset of turbulence observed by Gregory & Walker (1960) for this suction rate is about 80 percent of this Reynolds number. However, Lingwood proposed that the absolute instability may still be responsible

for the onset of transition, if the limitations of the apparatus reduced the effectiveness of suction in stabilizing the flow. The effects on the stationary and travelling Types-1 and -2 modes were again investigated. The Type-1 stationary and travelling modes were found to be strongly stabilized and destabilized by suction and injection, respectively. The stationary Type-2 mode was also stabilized and destabilized by the respective suction and injection flows, while there was little effect on the travelling Type-2 mode.

In the present chapter the effect of injection and suction on the global mode behaviour corresponding to the absolute instability of the rotating-disk boundary-layer is investigated. The simulations are produced using the new velocity-vorticity formulation by Davies & Carpenter (2001). As discussed in chapter 2, Davies & Carpenter (2003) have investigated the global mode behaviour corresponding to the absolute instability of the rotating-disk boundary-layer. Thus, the present chapter may be considered, amongst other things, as providing further justification for their conclusions.

For the cases of injection and suction considered, the parallel flow simulations produce behaviour that is in agreement with the theory of Lingwood (1997a). If the flow parameters lie within the theoretical absolutely unstable region, the simulations always exhibit equivalent behaviour. Likewise for convective instability. However, the non-parallel simulations produce quite different behaviour. The mean flows with injection produce similar behaviour to that observed in Davies & Carpenter (2003) for the case of zero normal flow. Initially disturbances within the absolutely unstable region exhibit temporal growth and upstream propagation. However, this does not persist and the study suggests that convective behaviour will eventually dominate at all Reynolds numbers investigated, in a similar way to that found in Davies & Carpenter (2003). On the other hand a mean flow with uniform suction is found

to be destabilized by non-parallel flow effects. Disturbances excited within the absolutely unstable region appear to exhibit an increasing temporal growth and radial inward propagation. The study suggests that for cases with sufficiently strong suction, temporal growth and globally unstable behaviour will eventually dominate the flow. On comparing the temporal growth rates for each flow, the study suggests that the growth rates increase with increasing suction. The present investigation was recently discussed by Davies & Thomas (2005).

The remainder of this chapter is outlined as follows; in section 4.2 the mean flow equations and the velocity-vorticity formulation (in cylindrical co-ordinates) by Davies & Carpenter (2001) are discussed. The next section contains results for four cases of uniform axial flow, and their growth rates are compared. The cases investigated are for the normal flow parameter $\mathbf{a} = \pm 1$ and $\mathbf{a} = \pm 0.5$. Where positive $\mathbf{a}$ corresponds to suction and negative $\mathbf{a}$ corresponds to injection. Finally conclusions are given in section 4.5.

4.2 Rotating-disk theory

4.2.1 The mean flow

The disk is taken to be infinite in diameter, rotating at a constant angular velocity Λ^* about the vertical axis that passes through the centre of the disk. Cylindrical polar co-ordinates are used where r^* is the radial distance from the vertical axis of rotation, θ^* is the azimuthal angle and z^* is the normal component. The domain above the disk is taken to be infinite, $z^* > 0$. The momentum and continuity equations in cylindrical polar coordinates are given as

$$\frac{\partial U_r^*}{\partial t^*} + (\mathbf{U}^*.\nabla)U_r^* - \frac{U_\theta^{*2}}{r^*} - 2\Lambda^* U_\theta^* = -\frac{1}{\rho^*}\frac{\partial P^*}{\partial r^*} + \nu^*\left(\nabla^2 U_r^* - \frac{U_r^*}{r^{2*}} - \frac{2}{r^{2*}}\frac{\partial U_\theta^*}{\partial \theta^*}\right), \quad (4.1)$$

$$\frac{\partial U_\theta^*}{\partial t^*} + (\mathbf{U}^*.\nabla)U_\theta^* + \frac{U_\theta^* U_r^*}{r^*} + 2\Lambda^* U_r^* = -\frac{1}{r^*\rho^*}\frac{\partial P^*}{\partial \theta^*} + \nu^*\left(\nabla^2 U_\theta^* - \frac{U_\theta^*}{r^{2*}} + \frac{2}{r^{2*}}\frac{\partial U_r^*}{\partial \theta^*}\right), \quad (4.2)$$

$$\frac{\partial U_z^*}{\partial t^*} + (\mathbf{U}^*.\nabla)U_z^* = -\frac{1}{\rho^*}\frac{\partial P^*}{\partial z^*} + \nu^*\nabla^2 U_z^*, \tag{4.3}$$

$$\frac{1}{r^*}\frac{\partial (r^* U_r^*)}{\partial r^*} + \frac{1}{r^*}\frac{\partial U_\theta^*}{\partial \theta^*} + \frac{\partial U_z^*}{\partial z^*} = 0, \tag{4.4}$$

where $\mathbf{U}^* = (U_r^*,\ U_\theta^*,\ U_z^*)$, which refers to the mean radial, azimuthal and normal velocities, respectively. Here P^* denotes the mean pressure and ρ^* the fluid density. (Here $*$ denotes dimensional quantities).

The mean velocity profiles are found using the von Kármán (1921) exact similarity solution to the Navier-Stokes equations. The dimensionless similarity variables are defined as

$$(U_r^*, U_\theta^*, U_z^*, P^*) = (r^*\Lambda^* F(z), r^*\Lambda^* G(z), \delta^*\Lambda^* H(z), \rho^*\nu^*\Lambda^* P(z)), \tag{4.5}$$

where F, G, H are the non-dimensional radial, azimuthal and normal mean flow velocities, and P is the non-dimensional pressure. Here ν^* is the kinematic viscosity and $z = z^*/\delta^*$ is the non-dimensional normal direction, where $\delta^* = (\nu^*/\Lambda^*)^{\frac{1}{2}}$ is the constant boundary-layer thickness, providing the non-dimensionalization of distances. On substituting equation (4.5) into the Navier-Stokes equations (4.1) - (4.4), the following non-dimensional mean flow equations are obtained

$$F^2 + F'H - (G+1)^2 = F'', \tag{4.6}$$

$$2F(G+1) + G'H = G'', \tag{4.7}$$

$$P' + H'H = H'', \tag{4.8}$$

$$2F + H' = 0, \tag{4.9}$$

where the prime denotes differentiation with respect to the normal component z. Equations (4.6) - (4.9) are solved subject to the boundary conditions

$$F(0) = G(0) = P(0) = 0, \qquad H(0) = \frac{H_0^*}{\nu^*\Lambda^*} = -\mathbf{a}, \tag{4.10}$$

$$F(z \to \infty) = 0, \qquad G(z \to \infty) = -1, \tag{4.11}$$

where **a** is a positive constant for suction through the disk and is negative for injection, and H_0^* is the constant dimensional velocity at the disk surface.

We can take the non-dimensional undisturbed flow to be

$$\mathbf{U}(r,z) = \left(\frac{r}{Re}F(z), \frac{r}{Re}G(z), \frac{1}{Re}H(z)\right), \tag{4.12}$$

where Re, the Reynolds number is defined as

$$Re = r_a^*\Lambda^*\delta^*/\nu^* = r_a^*/\delta^* = r_a, \tag{4.13}$$

for some radial position r_a^*. The non-dimensionalized velocity, pressure and time scales are $r_a^*\Lambda^*$, $\rho^* r_a^{*2}\Lambda^{*2}$ and $\delta^*/(\Lambda^* r_a^*)$, respectively. Also, the non-dimensionalized rotation rate is equal to $1/Re$. Therefore, when working in a frame of reference that rotates with the disk,

$$\Lambda = \frac{1}{Re} = \frac{1}{r_a}, \tag{4.14}$$

which is required for the Coriolis terms included in the velocity transport equations, which are to be discussed later in the chapter.

4.2.2 Solving the mean flow equations

The ordinary differential equations (4.6) - (4.11) were solved using the programming language Matlab, which evaluates the numerical solution using collocation methods. (Refer to the appendix for a detailed account of the code used). The collocation points were selected using

$$\xi(j) = \cos\frac{(j-1)\pi}{2N}, \tag{4.15}$$

for $j = 1, 2, 3...N$ and N = 48, for a co-ordinate transformation

$$\xi = \frac{L}{z+L}, \tag{4.16}$$

which maps the semi-infinite physical domain $z\epsilon[0,\infty)$ onto the finite computational domain $\xi\epsilon(0,1]$. The parameter L is a stretching factor and is chosen to take the value 4 for the present thesis. Equation (4.15) ensures that the majority of collocation points are selected near the disk surface, which is where most of the variations in the mean flow profiles occur. The physical limit $z \to \infty$ corresponds to the limit $\xi \to 0$ in the computational domain.

Figure 4.1 displays plots of the mean velocity profiles for the rotating-disk flow for **a** = -1, 0 and 1. In all three cases the radial velocity profile is inflectional. Values for F', G' at $z = 0$ and H as $z \to \infty$ are given to eight decimal places in table 1 for varying **a**. On comparing with previous results (Dhanak, 1992; Lingwood, 1997a), the tabulated results agree. Further, it can be shown that $H(z \to \infty) + \mathbf{a} \to 0$ as $\mathbf{a} \to \infty$, and $|H(z \to \infty) + \mathbf{a}| \to \infty$ as $\mathbf{a} \to -\infty$.

a	$F'(0)$	$G'(0)$	$H(\infty)$
-1.0	0.48948122	-0.30217350	-0.76070553
-1.0	**0.48948**	**-0.30217**	**-0.76071**
-0.5	0.51456629	-0.43643199	-0.80720514
-0.5	**0.51457**	**-0.43643**	**-0.80721**
0.0	0.51023262	-0.61592206	-0.88447339
0.0	*0.5102326*	*-0.6159220*	*-0.8844705*
0.0	**0.51023**	**-0.61592**	**-0.88447**
0.5	0.46688002	-0.85519306	-1.02129449
0.5	*0.4668800*	*-0.8551930*	*-1.021294*
0.5	**0.46688**	**-0.85519**	**-1.0213**
1.0	0.38956627	-1.17522077	-1.26055309
1.0	*0.3895662*	*-1.175221*	*-1.260553*
1.0	**0.38957**	**-1.1752**	**-1.2606**

Table 4.1: *Values of F', G' at $z = 0$ and H at infinity for various values of* **a**. *Results: roman - present thesis; italics - Dhanak (1992); bold - Lingwood (1997a).*

It can be seen from figure 4.1 and table 4.1 that when injection is applied to the

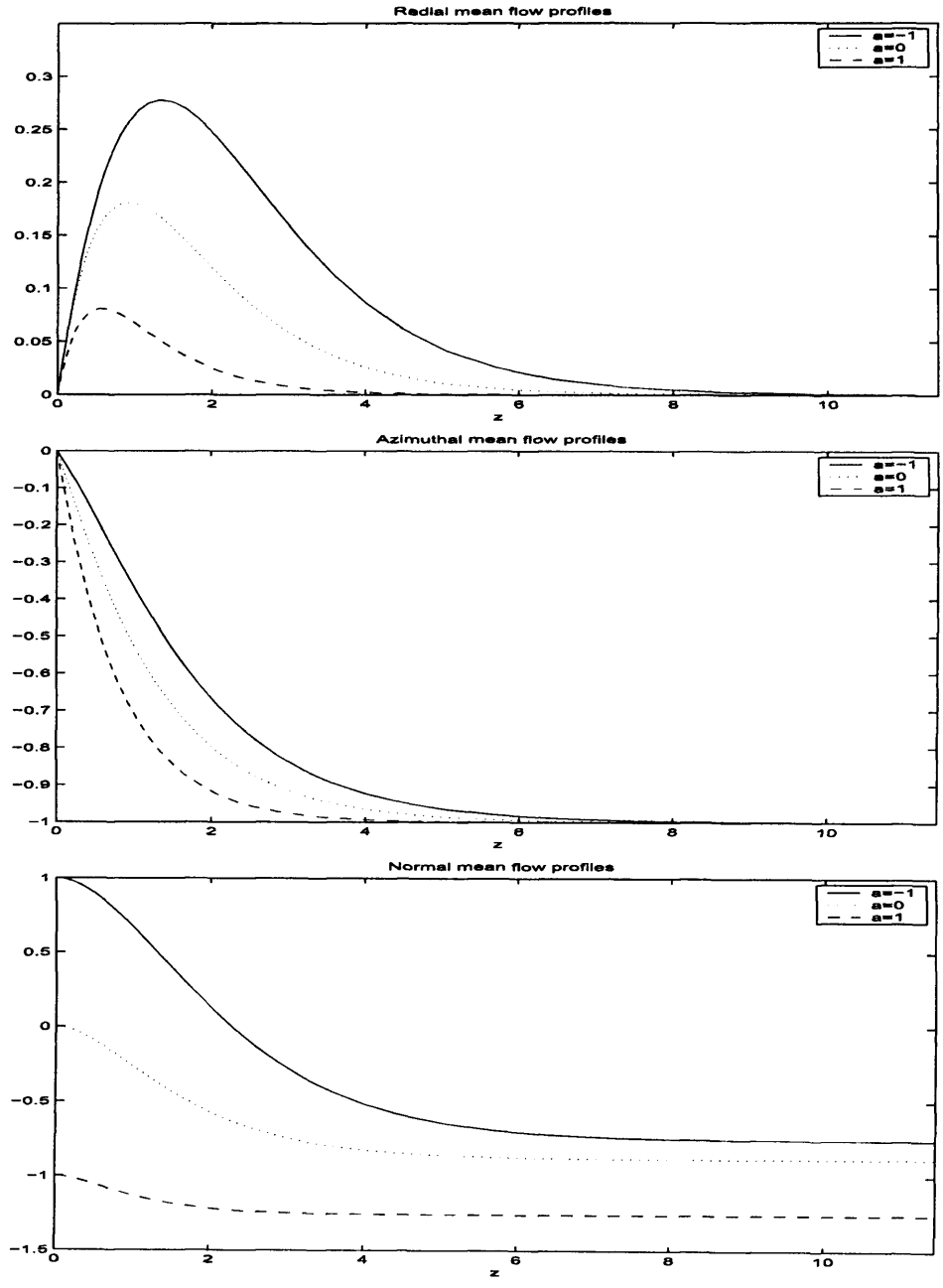

Figure 4.1: *The mean flow velocity profiles for the radial (F), azimuthal (G) and normal (H) components for the von Kármán flow over a rotating-disk with* **a** *= 0, (dotted lines),* **a** *= 1, (solid lines) and* **a** *= -1, (dashed lines).*

rotating-disk the maximum magnitude of the radial velocity profile increases. Thus, the three-dimensionality of the boundary-layer is enhanced, while the magnitude of the normal flow at infinity decreases. The opposite is true for suction; the maximum magnitude of the radial velocity profile decreases, but the magnitude of the normal flow at infinity increases.

4.2.3 Velocity-vorticity formulation

A detailed account of the velocity formulation is given in Davies & Carpenter (2001). Thus, we only give a brief outline here.

For the rotating-disk, the total velocity and vorticity fields are given as

$$\underline{U} = \mathbf{U} + \underline{u}, \qquad \underline{\Omega} = \mathbf{\Omega} + \underline{\omega}, \tag{4.17}$$

where $\mathbf{U}$ and $\mathbf{\Omega}$ are the undisturbed velocity and vorticity fields, while the velocity and vorticity perturbation variables may be represented as

$$\underline{u} = (u_r, u_\theta, u_z), \qquad \underline{\omega} = (\omega_r, \omega_\theta, \omega_z), \tag{4.18}$$

where the subscripts r, θ and z refer to the radial, azimuthal and normal directions, respectively. Then on taking the primary variables to be the components $\{\omega_r, \omega_\theta, u_z\}$, the Navier-Stokes equations are fully equivalent to the following set of governing equations for the perturbation variables,

$$\frac{\partial \omega_r}{\partial t} + \frac{1}{r}\frac{\partial N_z}{\partial \theta} - \frac{\partial N_\theta}{\partial z} - 2\Lambda\left(\omega_\theta + \frac{\partial u_z}{\partial r}\right) = \frac{1}{Re}\left(\left(\nabla^2 - \frac{1}{r^2}\right)\omega_r - \frac{2}{r^2}\frac{\partial \omega_\theta}{\partial \theta}\right), \tag{4.19}$$

$$\frac{\partial \omega_\theta}{\partial t} + \frac{\partial N_r}{\partial z} - \frac{\partial N_z}{\partial r} + 2\Lambda\left(\omega_r - \frac{1}{r}\frac{\partial u_z}{\partial \theta}\right) = \frac{1}{Re}\left(\left(\nabla^2 - \frac{1}{r^2}\right)\omega_\theta + \frac{2}{r^2}\frac{\partial \omega_r}{\partial \theta}\right), \tag{4.20}$$

$$\nabla^2 u_z = \frac{1}{r}\left(\frac{\partial \omega_r}{\partial \theta} - \frac{\partial (r\omega_\theta)}{\partial r}\right), \tag{4.21}$$

where

$$\nabla^2 f = \frac{\partial^2 f}{\partial r^2} + \frac{1}{r}\frac{\partial f}{\partial r} - \frac{n^2}{r^2} f + \frac{\partial^2 f}{\partial z^2},$$

and

$$\mathbf{N} = (N_r, N_\theta, N_z) = \mathbf{\Omega} \times \underline{u} + \underline{\omega} \times \mathbf{U} + \underline{\omega} \times \underline{u}. \tag{4.22}$$

For the linearized case, where the $\underline{\omega} \times \underline{u}$ has been dropped

$$N_r : \frac{1}{Re}(-2Gu_\theta + H\omega_\theta - rG\omega_z), \tag{4.23}$$

$$N_\theta : \frac{1}{Re}(rG'u_z + 2Gu_r - H\omega_r + rF\omega_z), \tag{4.24}$$

$$N_z : \frac{r}{Re}(-G'u_\theta - F'u_r + G\omega_r - F\omega_\theta), \tag{4.25}$$

$$\frac{\partial N_z}{\partial r} : \frac{1}{Re}\left(-G'u_\theta - rG'\frac{\partial u_\theta}{\partial r} - rF''u_z + F'inu_\theta + G\omega_r + rG\frac{\partial \omega_r}{\partial r} - F\omega_\theta - rF\frac{\partial \omega_\theta}{\partial r}\right). \tag{4.26}$$

Here $\mathbf{U}$ is the non-dimensional undisturbed base flow (4.12) and the factor Λ represents the non-dimensional angular velocity (4.14). The last terms on the left hand side of (4.19) and (4.20) are the Coriolis terms, which arise for rotating systems. (The most well known application of the Coriolis force is for the atmospheric flow of air across the Earth). The convective quantity $\mathbf{N}$ defined in equation (4.22) can only be evaluated if the remaining components $\{u_r, u_\theta, \omega_z\}$ are known. These so called secondary variables are defined in terms of the primary variables as follows

$$u_r = -\int_z^\infty \left(\omega_\theta + \frac{\partial u_z}{\partial r}\right) dz, \tag{4.27}$$

$$u_\theta = \int_z^\infty \left(\omega_r - \frac{1}{r}\frac{\partial u_z}{\partial \theta}\right) dz, \tag{4.28}$$

$$\omega_z = \frac{1}{r}\int_z^\infty \left(\frac{\partial (r\omega_r)}{\partial r} + \frac{\partial \omega_\theta}{\partial \theta}\right) dz. \tag{4.29}$$

4.2.4 Linearization and integral constraints

For the linearized simulations, the non-linear term $\underline{\omega} \times \underline{u}$ in the convective equation (4.22) is ignored. (This is because the governing equations have been linearized, since we are only interested in disturbances with small amplitudes). This linearization

then allows the problem to become separable with respect to the azimuthal direction. Thus, modes of the following form can be considered

$$\underline{u} = (\hat{u}_r, \hat{u}_\theta, \hat{u}_z)e^{in\theta}, \qquad \underline{\omega} = (\hat{\omega}_r, \hat{\omega}_\theta, \hat{\omega}_z)e^{in\theta}, \tag{4.30}$$

where $\hat{u}_r$, etc. are functions only of r, z and t, and $n = \beta Re$ is the azimuthal mode number. Here β is the azimuthal wavenumber used by Malik (1986); Lingwood (1995, 1997a), among others. Due to the circumferential periodicity of the disk, the azimuthal mode number n can only take integer values.

For parallel flows it is necessary to ignore variations in the Reynolds number with radius. This so called parallel-flow approximation involves replacing the radial variable r, which appears in the linearized governing equations with the Reynolds number Re. For non-parallel flows, the radius r is unchanged, i.e. it is not approximated by such methods.

The linearization also allows the governing equations (4.19) - (4.21) to admit solutions of the form

$$f \sim \exp\{i(\alpha r - \omega Ret)\}, \tag{4.31}$$

where α and ω are the spatial wavenumber and local temporal frequency, respectively. Here ωRe is the non-dimensional global frequency, that is used throughout the current study. Further details of the global non-dimensionalization are available in Davies, Thomas & Carpenter (2007) and are discussed in chapter 7.

We introduce a non-dimensional vertical wall displacement $\eta = \eta(r, \theta, t)$, which is used to generate disturbances at the disk surface. The linearization permits the no-slip conditions and the wall-normal zero-displacement conditions to become

$$u_r = -\frac{r}{Re}F'(0)\eta, \tag{4.32}$$

$$u_\theta = -\frac{r}{Re}G'(0)\eta, \tag{4.33}$$

$$u_z = \frac{\partial \eta}{\partial t}. \tag{4.34}$$

On substituting equations (4.32) and (4.33) into the definitions (4.27) and (4.28) for the secondary variables u_r, u_θ, we obtain the following integral constraints on the primary variables, which replace the no-slip conditions (4.32) and (4.33)

$$\int_0^\infty \omega_\theta dz = \frac{r}{Re} F'(0)\eta - \int_0^\infty \frac{\partial u_z}{\partial r} dz, \tag{4.35}$$

$$\int_0^\infty \omega_r dz = -\frac{r}{Re} G'(0)\eta + \int_0^\infty \frac{inu_z}{r} dz. \tag{4.36}$$

Equation (4.34) acts as the third constraint on the primary variables. Also, the assumed azimuthal mode structure has been used to replace partial derivatives with respect to θ by the factor in, where n is as before.

The numerical methods adopted for discretization of the governing equations are discussed in detail in Davies & Carpenter (2001) and briefly mentioned in Davies & Carpenter (2003); refer to chapter 3. A finite-difference scheme is used for discretization in the radial direction, a Chebyshev spectral scheme is used in the wall-normal direction and a Fourier spectral scheme is implemented in the azimuthal direction.

As outlined in Davies & Carpenter (2003), great care had to be taken when dealing with the radial inflow and outflow boundaries. Davies & Carpenter (2001) describe a number of methods for dealing with these boundary conditions. In the following study, all primary variable perturbation quantities were set equal to zero at the radial inflow boundary. For the radial outflow boundary, we always ensured that it was located well ahead of any disturbance of sufficiently large magnitude, to ensure that spurious effects were not introduced. Since we are primarily investigating absolute instability and the possibility of a global instability, the introduction of spurious effects had to be carefully assessed. Thus, it was important to ensure that the computational radial domain was sufficiently large, so as to avoid such effects.

In order to ensure that the results (that follow) are accurately justified, the simulations were repeated a number of times for varying computational radial domains.

In all cases investigated, the results corresponding to different radial domains were in agreement. Further details are given in the appendices.

4.3 Results

In all simulations, we considered the development of disturbances that were excited by an impulsive wall motion. The wall displacement η is taken to be of the form

$$\eta(r, \theta\, z) = a(r - r_e)b(t)e^{in\theta}, \tag{4.37}$$

with the temporal impulse given by

$$b(t) = (1 - e^{-\sigma t^2})e^{-\sigma t^2}, \tag{4.38}$$

where the parameter σ fixes the duration of the impulse, which is chosen large enough, so that a wide range of temporal frequencies are initially excited.

The cases of uniform normal flow through the disk wall, considered, were for $\mathbf{a} = 0$, ± 0.5 and ± 1. (Note: **a** negative corresponds to injection and **a** positive corresponds to suction). As mentioned in Davies & Carpenter (2003), numerical simulations can be performed using the parallel-flow approximation (spatially homogeneous) or with the genuine non-parallel mean flow (spatially inhomogeneous). Table 4.2 gives the critical values for the onset of absolute instability for various values of **a**, using the parallel flow approximation. Here Re_c is the Reynolds number, β_c is the azimuthal wavenumber, n_c is the integer-valued azimuthal mode number (for Lingwood's results, n_c has been rounded to the nearest integer), α_c is the complex radial wavenumber and ω_c and $\omega_c Re_c$ are the complex temporal frequencies for critical absolute instability. (The values given in italics refer to those found by Lingwood, 1997a, and correspond to table III in her paper). These critical values were used to verify the results for the parallel flow simulations. The values in bold correspond to the results found from the numerical simulations.

The Reynolds number and azimuthal mode number, in the numerical simulations, were prescribed to the nearest integer, so as to avoid excessive parametric studies. Nonetheless, the numerical simulation results are consistent with those given by Lingwood (1997a). The reader may have some doubts to the accuracy of the simulation results, but as we will discuss in the appendices, the temporal frequency and radial wavenumber do not vary significantly over small variations in the Reynolds number and the azimuthal mode number.

Davies & Carpenter (2003) studied the frequencies and growth rates for the case with zero normal flow, by considering the complex-valued quantity

$$\omega = \frac{i}{A}\frac{\partial A}{\partial t}, \tag{4.39}$$

where A is taken to be a measure of the disturbance amplitude at all radial locations and points in time. The azimuthal vorticity $\omega_{\theta,w}$ was chosen for A. If the complex quantity ω, does not vary too rapidly in either the radial direction or time, its real and imaginary parts may be interpreted as being, the local temporal frequency and local temporal growth rate, respectively. Here we have assumed that there is only one significant mode of disturbance, at all specified radial locations and points in time. If there were several different discrete modes, which were superimposed, it would not be possible to identify the temporal frequency and growth rate, from the real and imaginary parts of complex ω.

Similarly, the spatial wavenumbers are calculated using the complex-valued expression

$$\alpha = -\frac{i}{A}\frac{\partial A}{\partial x}. \tag{4.40}$$

Here A is again taken to be a measure of the disturbance amplitude at all radial locations and points in time. The azimuthal vorticity $\omega_{\theta,w}$ was chosen for A.

A central difference scheme was used to calculate the derivative on the right hand side of equation (4.39) and further details may be found in the appendices. (Note:

other difference schemes were also implemented and used to calculate the frequencies/growth rates, i.e. three-point backward difference. The results obtained by these other methods were always identical, to a certain number of decimal places, to those calculated using the central difference scheme).

The complex temporal frequencies (given in table 4.2) were calculated at the radial location of excitation $r = r_e$. The temporal frequency at this position, was constant at all points in time, after the initial transient phase. (The initial transient phase was caused by the initial excitation of several frequencies. Eventually, all but one mode dissipates, leaving the one dominant mode to be observed). The temporal frequency at all other radial locations was found to converge to the frequency at $r = r_e$. Similar behaviour was found for the temporal growth rates. Eventually all growth rates, at all radial positions, approached a constant value. For the critical absolute frequency ω_c (in table 4.2), the temporal growth rates were found to asymptote to approximately zero. Such behaviour is consistent with critical absolute instability. To three decimal places, the temporal frequencies ω_c are identical to those given by Lingwood (1997a).

The complex radial wavenumbers α_c took longer to converge (than the temporal frequencies). However, the radial wavenumbers α_c were found to be consistent with the results of Lingwood (1997a), to within two decimal places in most cases.

The critical azimuthal mode number n_c has been rounded to the nearest integer value, which is required to satisfy the circumferential periodicity of the problem. To ensure that the azimuthal mode number n_c is the same for all simulations, the azimuthal wavenumber β must be changed accordingly. For example: if $n = 50$, then for $Re = 300$ and $Re = 400$, $\beta = 0.16\dot{6}$ and $\beta = 0.125$, respectively. From table 4.2 it may be noted that as the parameter **a** is increased from -1 to 1, the azimuthal mode number $n_c = \beta_c Re_c$ increases. The frequency $\omega_c Re_c$ also increases with increasing **a**.

Further validation checks are given in the appendices, for the critical stationary and travelling convective disturbances. The reader will notice that these are also in

a	Re_c	β_c	n_c	ω_c	α_c	$\omega_c\ Re_c$
-1.0	*201.54*	*0.1424*	*29*	*-0.03622*	*0.1735 - i0.1166*	*-7.300*
-1.0	**202**		**29**	**-0.03587**	**0.1767 - i0.1131**	**-7.245**
-0.5	*309.71*	*0.1398*	*43*	*-0.03550*	*0.1903 - i0.1197*	*-10.995*
-0.5	**310**		**43**	**-0.03530**	**0.1919 - i0.1157**	**-10.943**
0.0	*507.30*	*0.1348*	*68*	*-0.03485*	*0.2173 - i0.1216*	*-17.679*
0.0	**508**		**68**	**-0.03435**	**0.2192 - i0.1153**	**-17.451**
0.5	*911.54*	*0.1235*	*113*	*-0.03261*	*0.2637 - i0.1228*	*-29.725*
0.5	**912**		**113**	**-0.03256**	**0.2634 - i0.1173**	**-29.695**
1.0	*1860.82*	*0.1044*	*194*	*-0.02796*	*0.3420 - i0.1300*	*-52.029*
1.0	**1861**		**194**	**-0.02786**	**0.3380 - i0.1198**	**-51.847**

Table 4.2: *Critical values for the onset of absolute instability as found by Lingwood (1997a) - italics. (Table corresponds to table III in Lingwood (1997a)). The values in bold correspond to the values found here.*

excellent agreement with the values given by previous authors.

4.3.1 The von Kármán flow, a = 0

The case **a** = 0, which corresponds to the rotating-disk without either suction or injection has already been investigated in detail by Davies & Carpenter (2003). The critical Reynolds number for absolute instability is $Re = 507.3$ for an azimuthal mode number $n = 68$; Lingwood (1997a). The interested reader should refer to the above papers for further results and conclusions on the global mode behaviour corresponding to the absolute instability of the rotating-disk boundary-layer (or refer back to chapter 2 for an account of this paper).

In the subsequent sections, the results of simulations for four separate levels of uniform normal flow through the disk wall, are discussed.

4.3.2 Injection

Uniform injection is known to be strongly destabilizing, and promotes the onset of the transition process. So one would assume that a boundary-layer flow with injection should be avoided. However, uniform injection is useful in cooling turbine blades and the surfaces of high speed aircraft, Sparrow & Gregg (1960). Therefore, it is important that such models are investigated, so that we may understand what problems (by problems we mean instabilities, turbulence) could arise and how best to deal with them.

The case a = -1

The first case considered is when the parameter **a** = -1. This corresponds to a boundary-layer flow that is strongly destabilized. It was shown by Lingwood (1997a) that such a mean flow first becomes absolutely unstable for a Reynolds number $Re \approx 202$ for an azimuthal mode number $n = 29$. The critical Reynolds number here is approximately 40 percent of that Reynolds number corresponding to the case with zero normal flow.

Figure 4.2 shows time histories for four successive radial locations, for a disturbance with an azimuthal mode number $n = 29$ for an impulsively excited disturbance in a non-parallel flow, centered at $r_e = 202$. The azimuthal component of the vorticity $\omega_{\theta,w}$ at the wall is plotted for a fixed value of θ, along with the corresponding envelopes $\pm|\omega_{\theta,w}|$ obtained from the complex-valued amplitude. Here $T = 2\pi Re$ corresponds to one rotation of the disk. For the time histories at the radii $r = r_e$ - 25 and $r = r_e = 202$, the disturbance decays, whereas the plots at $r = r_e + 25$ and $r = r_e + 50$ display a period of growth followed by a relatively weak decay. It is evident that the perturbations exhibit strong spatial growth along the radial direction, when account is taken of the the different scales used for the axis.

Figure 4.3(a) and 4.3(b) display the spatio-temporal development plots for the

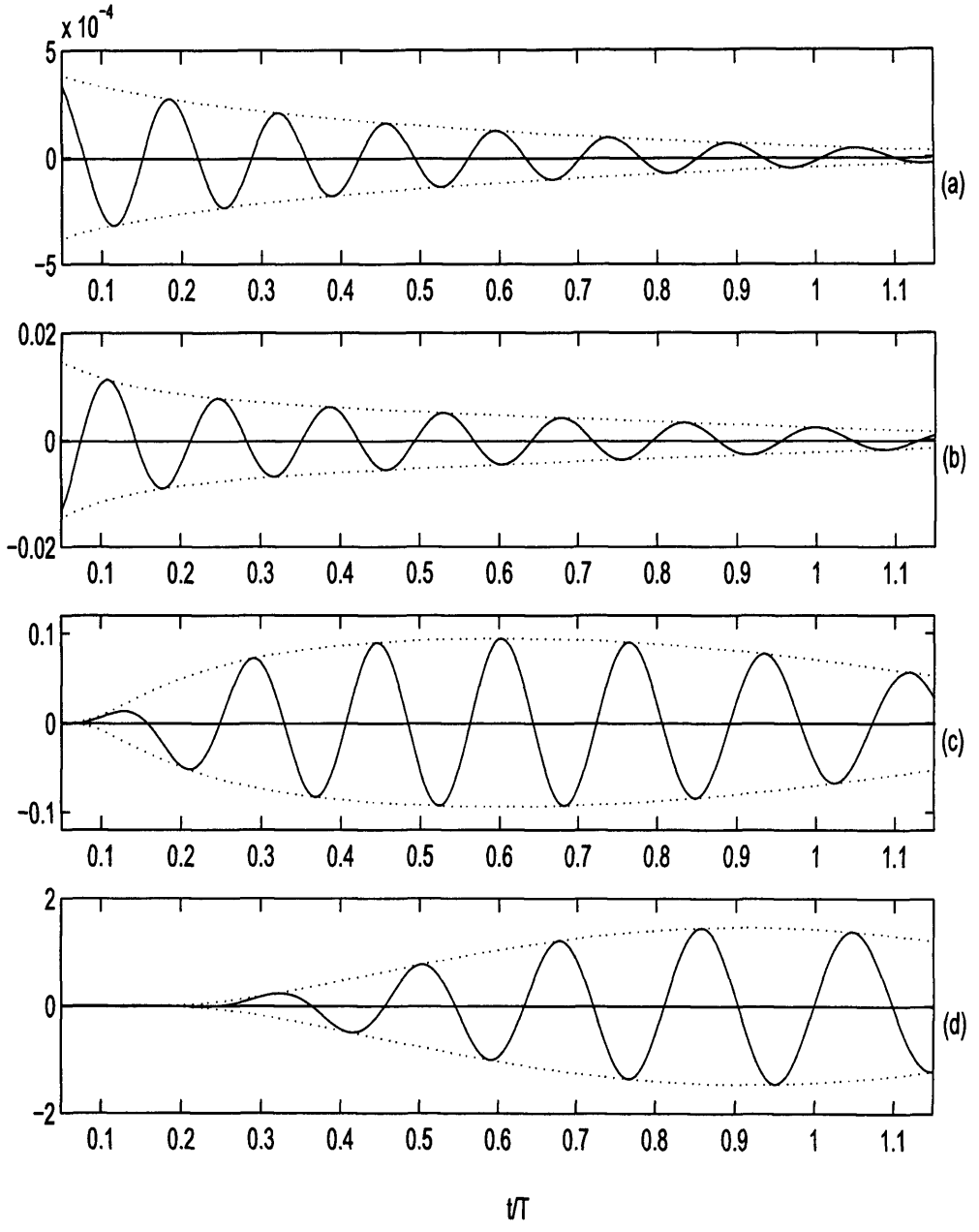

Figure 4.2: *Time histories for $\omega_{\theta,w}$ (solid lines) with corresponding envelopes $\pm|\omega_{\theta,w}|$ (dotted lines), for an impulsively excited disturbance in a non-parallel flow with injection* a *= -1. The azimuthal mode number n = 29 and the disturbance was excited at r_e = 202. The temporal development is plotted for four different radial positions, (a) : r_e-25, (b) : r_e, (c) : r_e+25, (d) : r_e+50.*

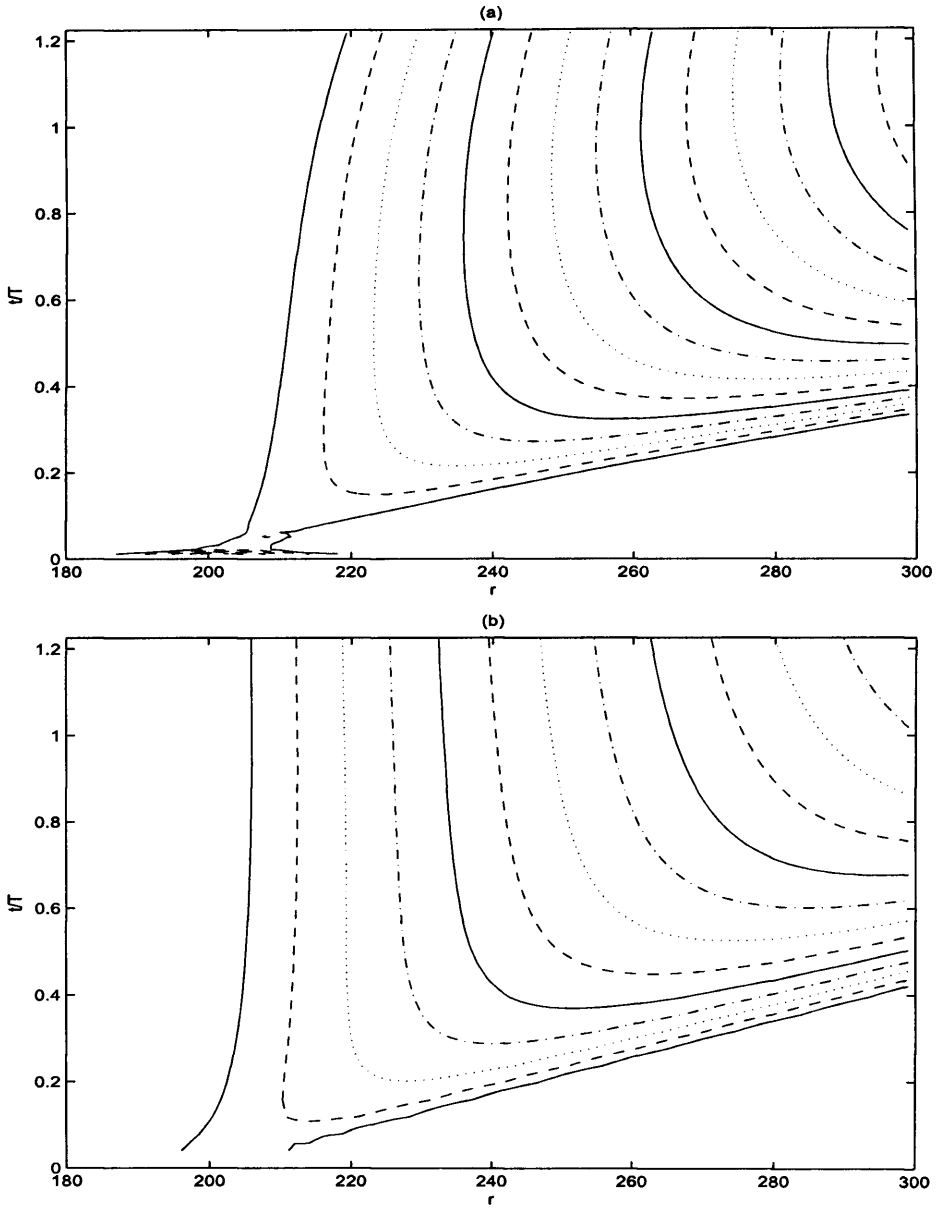

Figure 4.3: *Spatio-temporal development of* $|\omega_{\theta,w}|$ *for an impulsively excited disturbance with injection* $\mathbf{a} = -1$, *and an azimuthal mode number* $n = 29$. *The disturbance was excited at* $r_e = 202$. *(a) - non-parallel flow, (b) - parallel flow with* $Re = 202$. *(Contours are drawn using a logarithmic scale, with levels separated by factors of two).*

above disturbance in the non-parallel flow and the corresponding parallel flow, where the Reynolds number $Re = 202$. The development is plotted using contours of the azimuthal perturbation vorticity at the wall $|\omega_{\theta,w}|$. The leading and trailing edges of the wavepacket are easily identified. In both cases, the leading edge propagates radially outwards with approximately the same non-zero velocity. However, the trailing edges are distinctively different, and it is this that is most interesting. The trailing edge for the parallel flow is propagating with a diminishing velocity. Hence, critical absolute instability is indicated, i.e. the trailing edge is not propagating outwards or inwards. However, the non-parallel trailing edge propagates radially outwards with an increasing, positive velocity. Thus, the disturbance behaves much like a convective instability.

The local temporal frequencies and growth rates (calculated using (4.39)) for the parallel simulation are displayed in figure 4.4. Plots are given for $r_e = 202$, and three additional positions that are taken radially inwards and outwards from r_e. The temporal frequency found at the centre of excitation r_e, for the parallel flow with $Re = 202$ and $n = 29$ is in excellent agreement with that found by Lingwood (1997a). The temporal frequency is (to three decimal places) exactly the same as that found by Lingwood; refer to table 4.2. The frequency at the three other locations, asymptotes to the constant frequency found at $r_e = 202$. It may be concluded that after a certain time period, the temporal frequency at all radial positions, settles to this one frequency. Such behaviour is to be expected for the approximate parallel flow since all radial positions are equivalent. The temporal growth rates also display similar behaviour. As time progresses the growth rates asymptote towards a constant value. In this case the constant is approximately zero, which indicates that the disturbance is exhibiting critical absolute instability.

The corresponding temporal frequencies and growth rates for the non-parallel

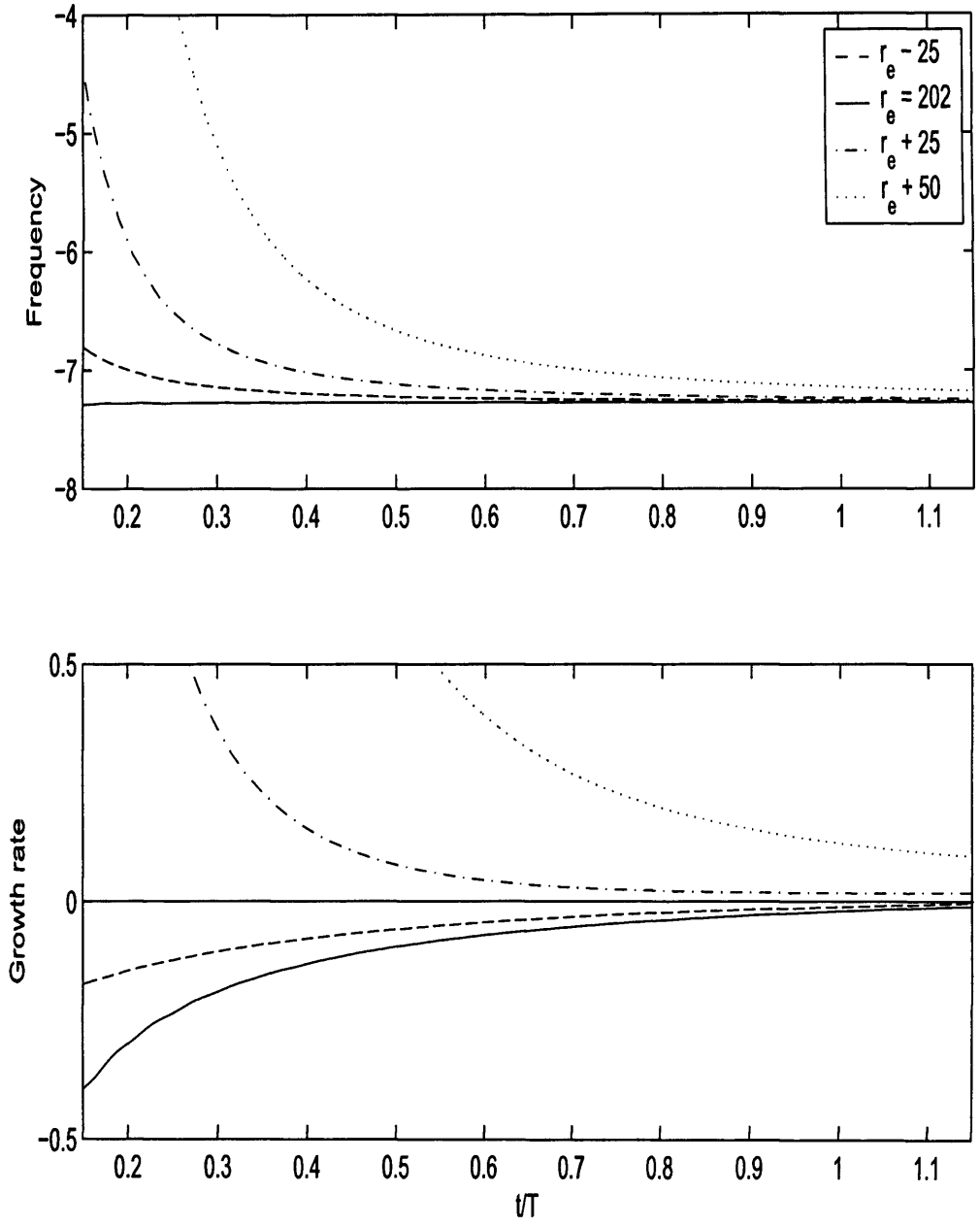

Figure 4.4: *Local temporal frequencies $\omega_r Re$ and temporal growth rates $\omega_i Re$ for a disturbance with $n = 29$ developing in a parallel flow with injection* $\mathbf{a} = -1$ *and* $Re = 202$. *The impulsive excitation was centred at $r_e = 202$. The temporal development is plotted for four different radial positions, r_e - 25, r_e, r_e + 25 and r_e + 50.*

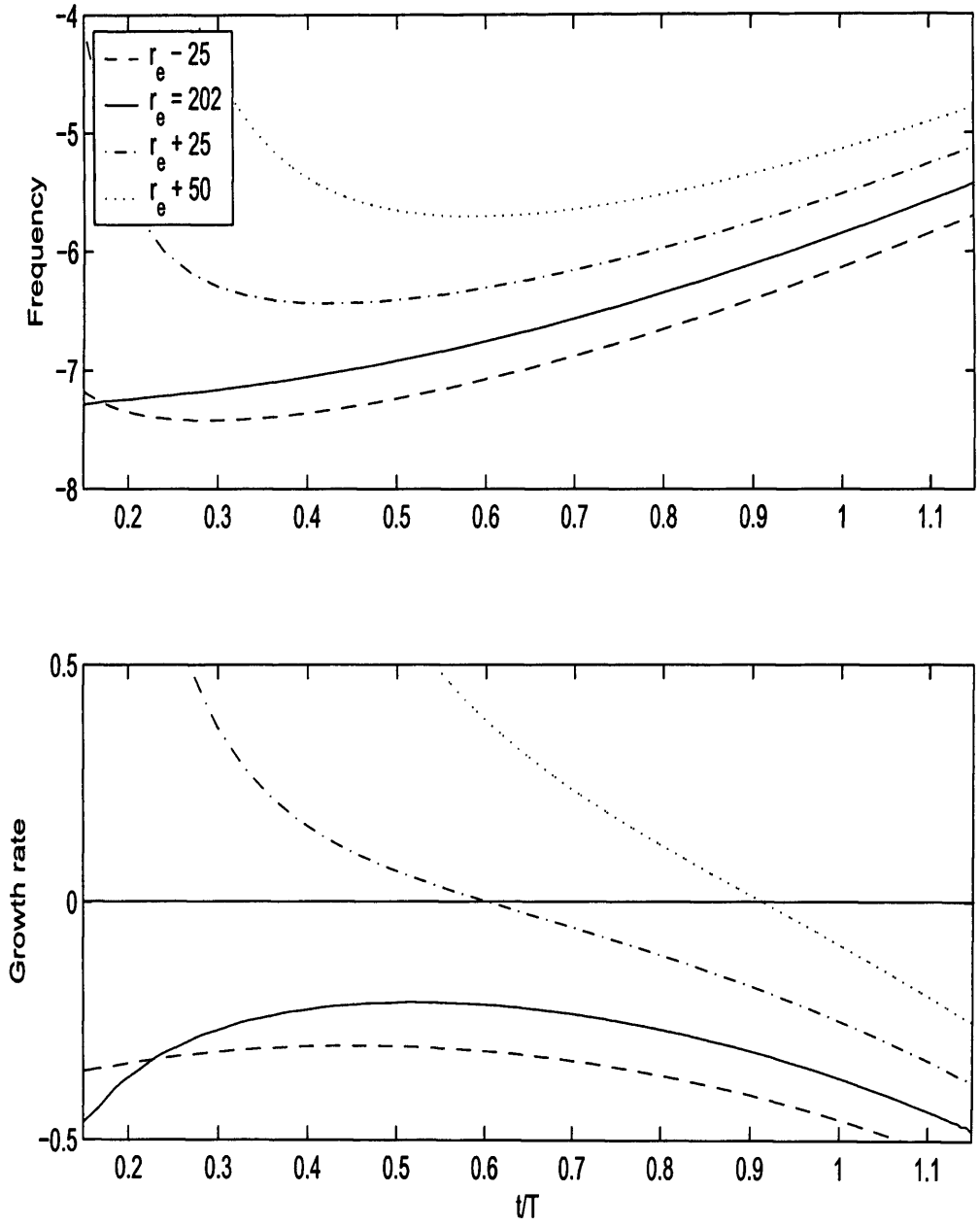

Figure 4.5: *Local temporal frequencies $\omega_r Re$ and temporal growth rates $\omega_i Re$ for a disturbance with $n = 29$ developing in a non-parallel flow with injection* $\mathbf{a} = -1$. *The impulsive excitation was centred at $r_e = 202$. The temporal development is plotted for four different radial positions, r_e - 25, r_e, r_e + 25 and r_e + 50.*

numerical simulation are plotted in figure 4.5. The reader should notice that the behaviour is qualitatively the same as that observed in Davies & Carpenter (2003). The local frequencies initially evolve in the same manner as in the parallel case. However, after this initial period, the frequency at each selected radial position, increases, and there is no indication that they will eventually asymptote towards a constant. For all the selected radial positions, the temporal growth rates are eventually negative and decreasing. Thus, temporal decay sets in at all selected radial positions.

The development of the temporal frequencies and growth rates can be understood by making comparisons with the Green's solutions to the Ginzburg-Landau equation. The initial behaviour is found to depend on a $1/t^2$ term, while the long-term development depends on the variations in the complex frequency. For further details the reader is referred to chapter 8.

Therefore, the results suggest that the global behaviour may well be convective and that the behaviour is comparable with that observed by Davies & Carpenter (2003) for the von Kármán flow with zero suction/injection. However, it may be that non-parallel effects alter the region of absolute instability and that the critical point is raised.

A simulation was carried out using non-parallel effects, for an impulsively excited disturbance centered at $r_e = 252$ with an azimuthal mode number $n = 29$. According to Lingwood (1997a) this is well within the bounds of absolute instability. The time histories plotted in figure 4.6 clearly indicate that the disturbance is more unstable than the earlier simulation, (as expected). For the radial positions $r = r_e - 25, r_e$, there is an initial weak growth followed by a small decay. The disturbance at the radial position $r = r_e + 25$ undergoes an initial period of growth, but for larger times t/T, the growth appears to be decreasing, while for $r = r_e + 50$ the disturbance exhibits continuous growth for the time period shown.

The temporal frequencies and growth rates for this simulation are plotted in figure

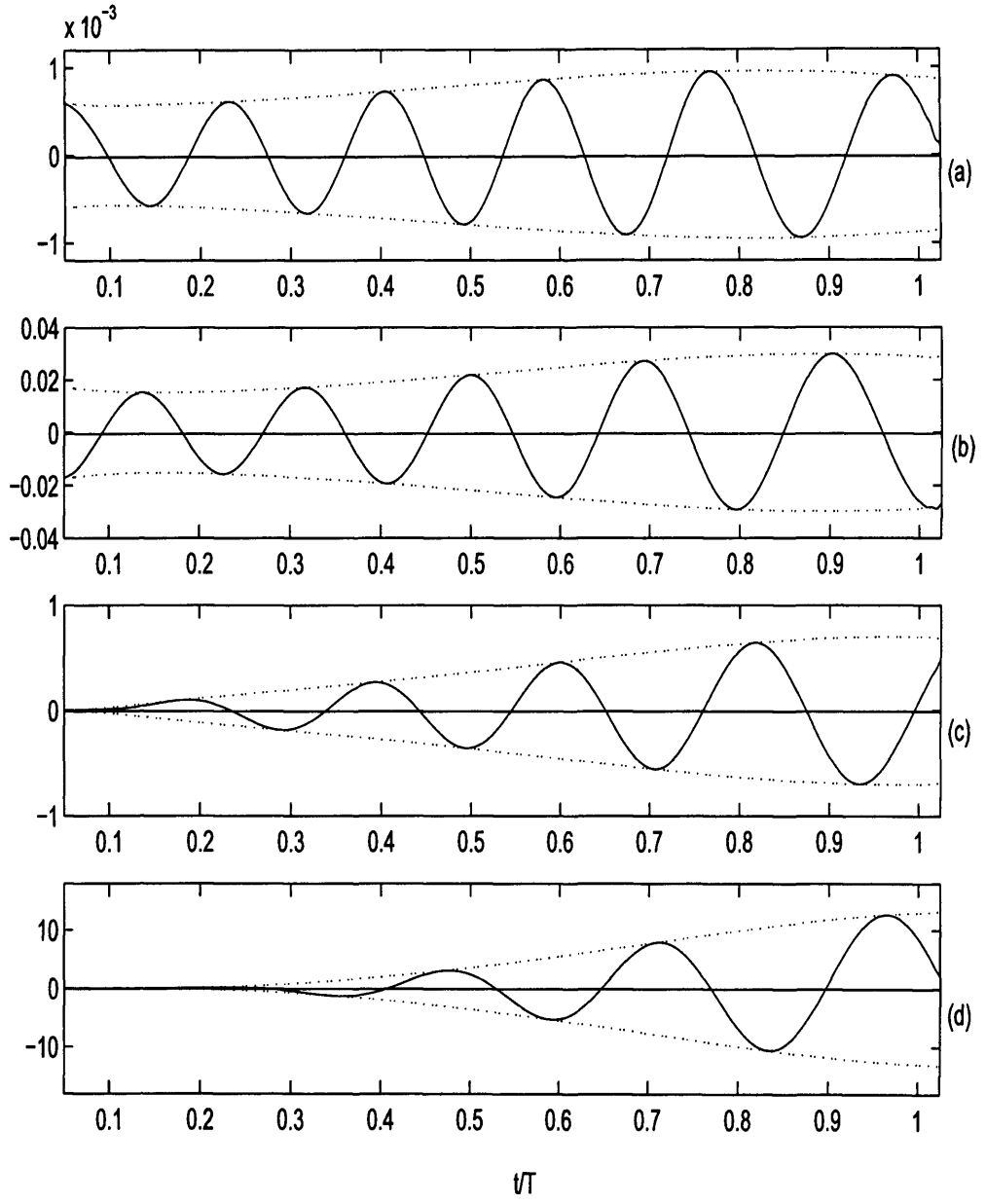

Figure 4.6: *Time histories for $\omega_{\theta,w}$ (solid lines) with corresponding envelopes $\pm|\omega_{\theta,w}|$ (dotted lines), for an impulsively excited disturbance in a non-parallel flow with injection* **a** *= -1. The azimuthal mode number is n = 29 and the disturbance was excited at r_e = 252. The temporal development is plotted for four different radial positions, (a): r_e-25, (b): r_e, (c): r_e+25, (d): r_e+50.*

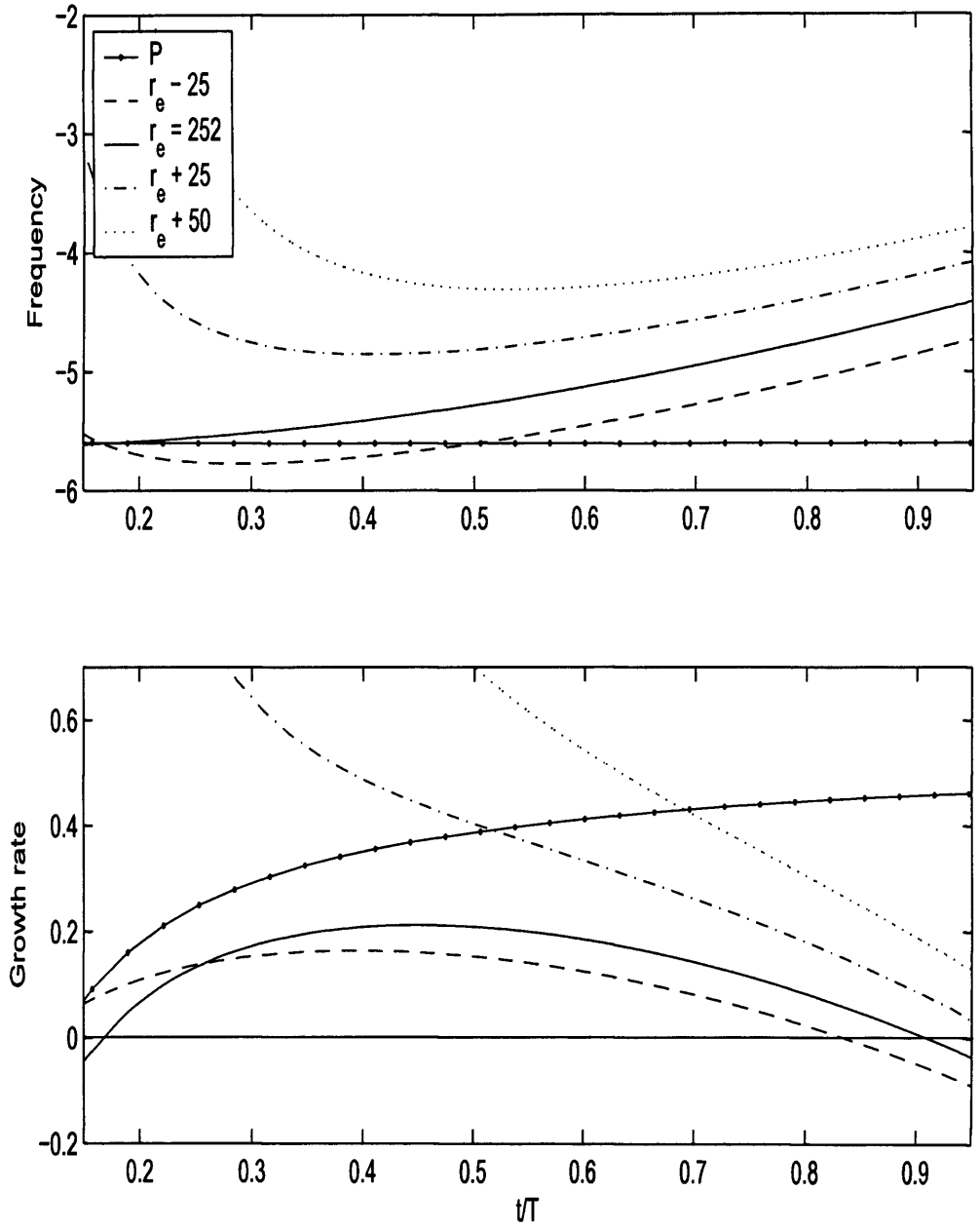

Figure 4.7: *Local temporal frequencies $\omega_r Re$ and temporal growth rates $\omega_i Re$ for a disturbance with $n = 29$ developing in a non-parallel flow with injection* $\mathbf{a} = -1$. *The impulsive excitation was centred at $r_e = 252$. The temporal development is plotted for four different radial positions, r_e - 25, r_e, r_e + 25 and r_e + 50. The lines labeled with a P show the development at the point of impulsive excitation of a similar disturbance in a parallel flow with $Re = 252$.*

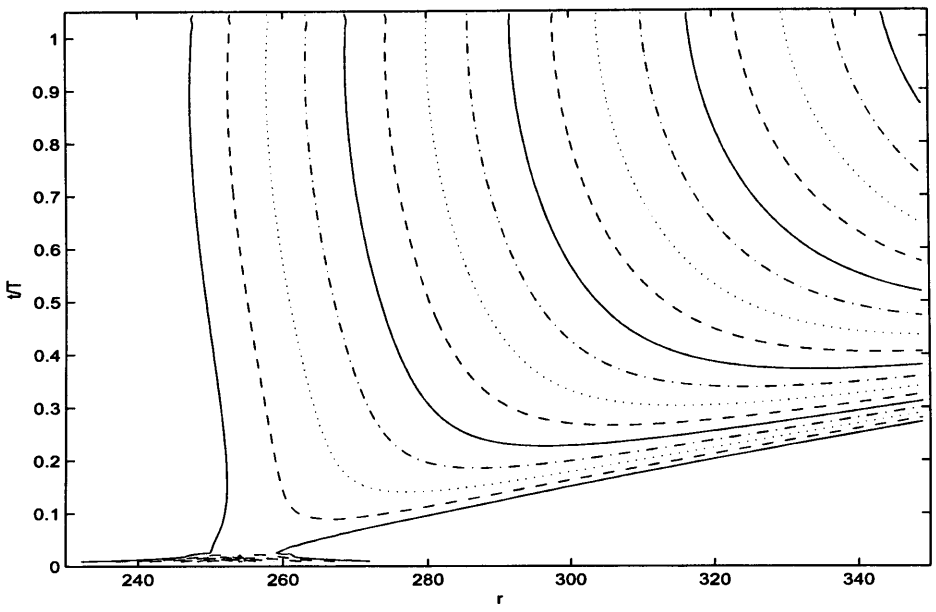

Figure 4.8: *Spatio-temporal development of* $|\omega_{\theta,w}|$ *for an impulsively excited disturbance in a non-parallel flow with injection* $\mathbf{a} = -1$. *The azimuthal mode number is* $n = 29$ *and the disturbance was excited at* $r_e = 252$.

4.7. The solid curves represent results for the corresponding parallel flow simulation with $Re = 252$. For the non-parallel flow the temporal development is again plotted for four equally spaced radial locations. The local frequencies behave in the same manner as the previous case; their magnitudes decrease as time increases. The growth rates also exhibit similar behaviour to that seen previously; they decrease and it appears that given time all radial positions considered will have a negative growth rate. Thus, temporal decay will be observed. The spatio-temporal evolution of the wavepacket disturbance for this simulation is plotted in figure 4.8. Initially the trailing edge propagates radially inwards. Thus, the disturbance exhibits behaviour in accordance with absolute instability. However, as time increases the trailing edge slows down and appears to be reversing direction. Therefore, the wavepacket disturbance is behaving

more like a convective instability. Again this is similar behaviour to that observed in Davies & Carpenter (2003) for the case with zero suction/injection.

Longer simulations which may have confirmed the above ideas were extremely difficult to carry out. As outlined by Davies & Carpenter (2003), convergence problems were encountered with the iteration scheme used to solve the discretized governing equations. This was due to the large variety of disturbance magnitudes that developed within the computational domain. Since non-linearity was not present, the maximum amplitude of the disturbance was allowed to grow exponentially without limit. It would have been very difficult to increase the time duration, even by only half a time period. However, the fact remains that in both situations so far considered, the growth rates always decrease and so it is reasonable to conjecture that temporal decay will eventually be observed for all radial locations. Therefore, the behaviour is consistent with that first observed by Davies & Carpenter (2003). The long-term global behaviour is consistent with convective instability, and is not consistent with a linear amplified global mode of the form

$$A \sim e^{-\omega_G t}, \tag{4.41}$$

where ω_G is a complex frequency, for which $\omega_G|_i > 0$, i.e there is no unstable fixed global frequency.

The trailing edge of the disturbance wavepackets reverse direction and propagate radially outwards in the manner proposed by figure 4(b) of Davies & Carpenter (2003), or displayed in figure 2.4(b) of the present thesis.

In order to be more sure that the above ideas are accurately justified, and not just a consequence of simulations taking place near the boundary of the absolutely unstable region, a numerical simulation was conducted where the disturbance was excited at $r_e = 302$ for an azimuthal mode number $n = 29$. This radial location is approximately 50 percent greater than the critical value for absolute instability in

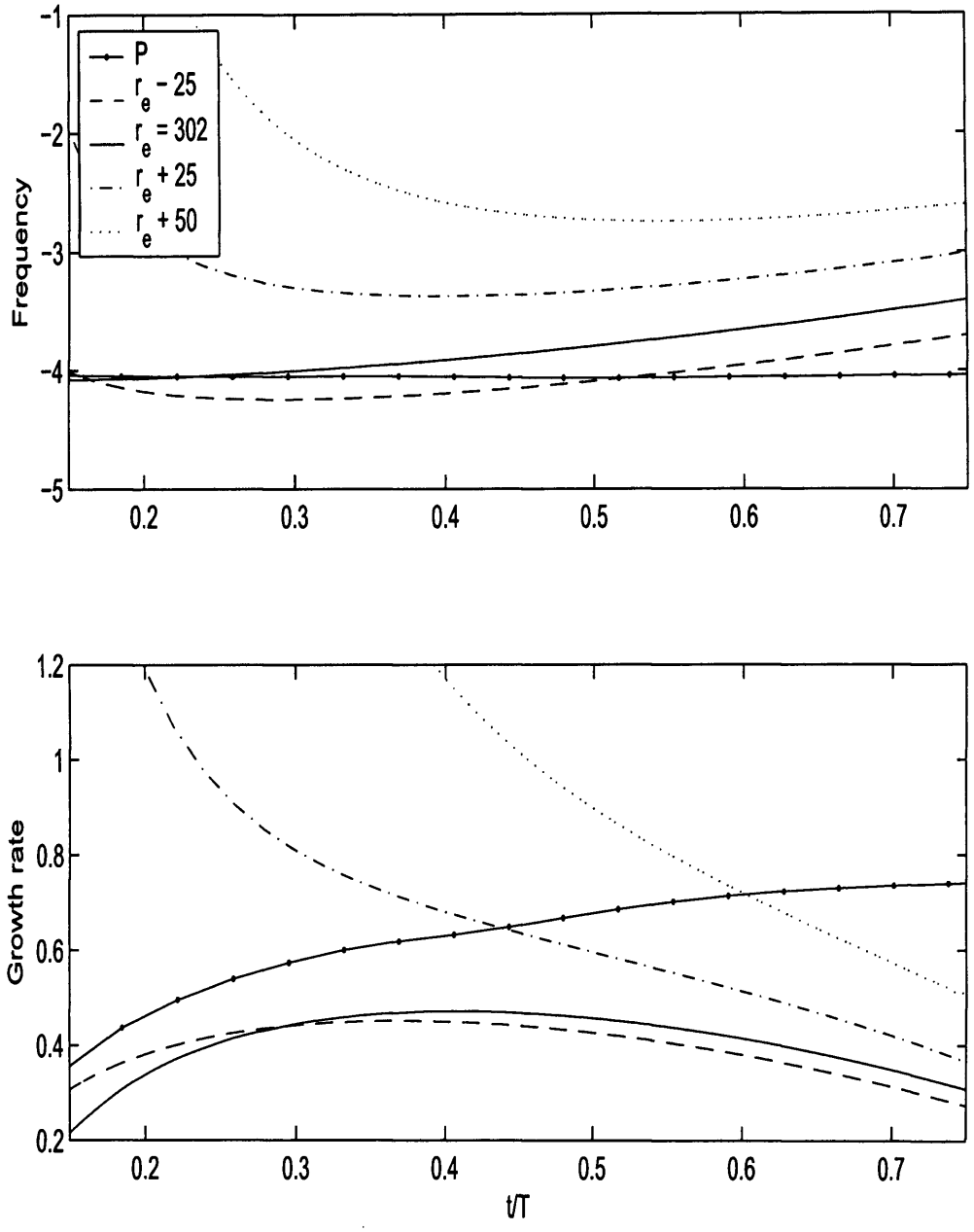

Figure 4.9: *Local temporal frequencies $\omega_r Re$ and temporal growth rates $\omega_i Re$ for a disturbance with $n = 29$ developing in a non-parallel flow with injection* $\mathbf{a} = -1$. *The impulsive excitation was centred at $r_e = 302$. The temporal development is plotted for four different radial positions, r_e - 25, r_e, r_e + 25 and r_e + 50. The lines labeled with a P show the development at the point of impulsive excitation of a similar disturbance in a parallel flow with $Re = 302$.*

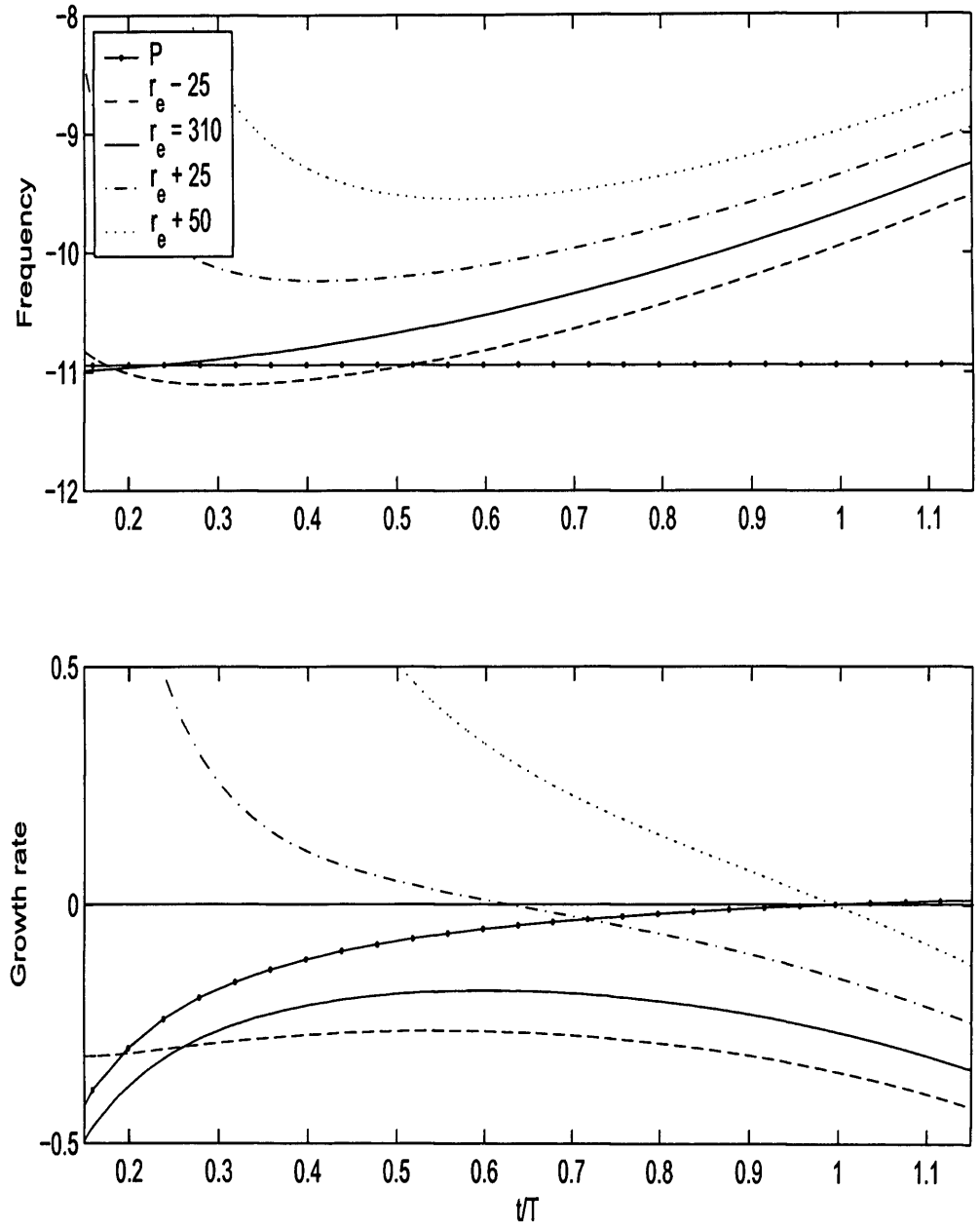

Figure 4.10: *Local temporal frequencies $\omega_r Re$ and temporal growth rates $\omega_i Re$ for a disturbance with $n = 43$ developing in a non-parallel flow with injection* $\mathbf{a} = -0.5$. *The impulsive excitation was centred at $r_e = 310$. The temporal development is plotted for four different radial positions, r_e - 25, r_e, r_e + 25 and r_e + 50. The lines labeled with a P show the development at the point of impulsive excitation of a similar disturbance in a parallel flow with $Re = 310$.*

the parallel flow. The frequencies and growth rates are plotted in figure 4.9 and once again it is clear that the growth rates are decreasing at all radial locations. Thus, we assume temporal decay will eventually set in.

The case a = -0.5

We now consider the mean flow with $\mathbf{a} = -0.5$. This problem is not as unstable as the previous problem (i.e. mean flow with **a** = -1), but it is less stable than the von Kármán flow. Lingwood (1997a) found that absolute instability sets in at approximately $Re = 310$ for $\mathbf{a} = -0.5$. Which is approximately 60 percent of the Reynolds number corresponding to the case with zero normal flow.

A numerical simulation is carried out for an impulsively excited disturbance centered at $r_e = 310$ with an azimuthal mode number $n = 43$. These are the approximate critical values for absolute instability. The temporal frequencies and growth rates are plotted in figure 4.10. The frequency for the parallel flow simulation (labeled P) is in good agreement with that found by Lingwood (1997a). The non-parallel frequencies behave as before; they decrease in magnitude as time increases. The temporal growth rates also behave in an identical manner to earlier cases. At all selected radial locations, the growth rates decrease and there is a tendency for all the selected radial points (r_e - 25, r_e, r_e + 25 and r_e + 50) to eventually display temporal decay.

A second disturbance was excited at $r_e = 360$ with $n = 43$. Figure 4.11 compares the temporal evolution of the disturbance in the parallel flow (solid line) with the corresponding non-parallel flow (dotted line). The Reynolds number is taken to be Re = 360 for the parallel case. Initially the two plots are quite close together. However, as time increases the growth in the non-parallel case is substantially less and there is also a clear increase in the temporal frequency. Thus, the non-parallel flow effects are stabilizing. The corresponding frequencies and growth rates are plotted in figure 4.12 and as we may now have anticipated, the frequencies increase, while the growth

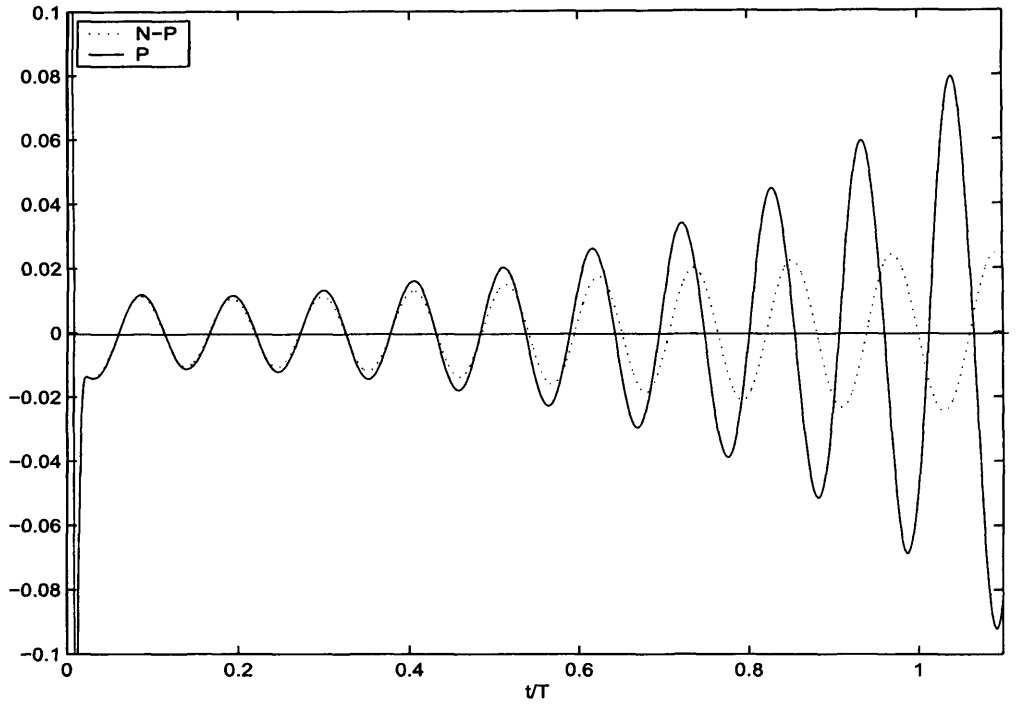

Figure 4.11: *Comparison of the variation of* $|\omega_{\theta,w}|$ *for a disturbance with* $n = 43$ *evolving in non-parallel and parallel flow with injection* $\mathbf{a} = -0.5$. *The temporal development is shown for the radius* $r_e = 360$ *where the impulsive excitation was centred. Dotted line: The non-parallel flow labeled N-P; solid line: parallel flow labeled P with* $Re = 360$.

rates decrease. Thus, the global behaviour found for the flow with a normal injection constant $\mathbf{a} = -0.5$, is similar to that found for the earlier case $\mathbf{a} = -1$ and the von Kármán flow studied by Davies & Carpenter (2003), i.e. convective.

Although only the injection cases $\mathbf{a} = -1, -0.5$ have been so far investigated, it seems likely that all injection flows or at the very least the flows between $\mathbf{a} = -1$ and $\mathbf{a} = 0$ would behave in the manner found above and by Davies & Carpenter (2003). For a disturbance excited in the theoretical absolutely unstable region there is an initial

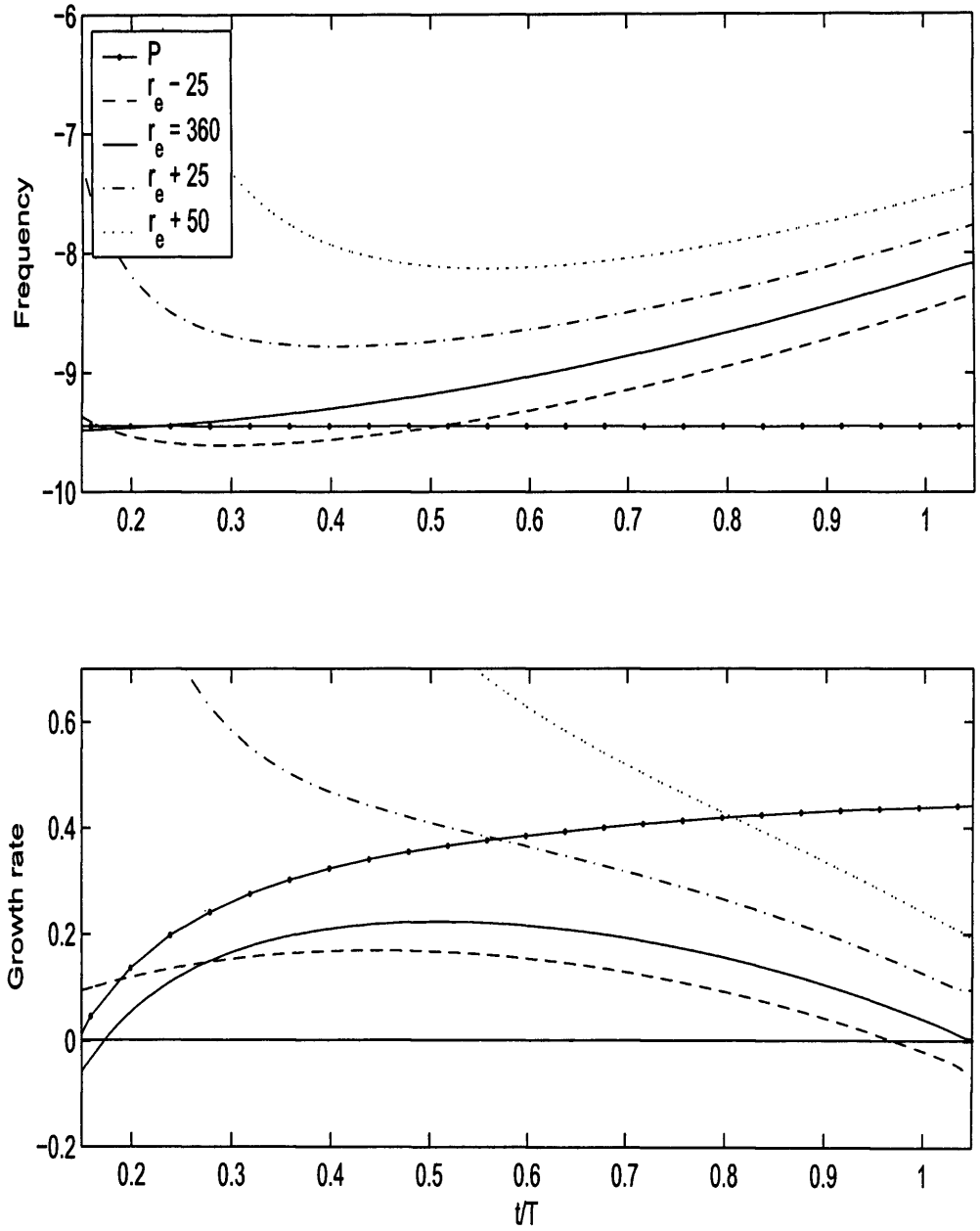

Figure 4.12: *Local temporal frequencies $\omega_r Re$ and temporal growth rates $\omega_i Re$ for a disturbance with $n = 43$ developing in a non-parallel flow with injection* $\mathbf{a} = -0.5$. *The impulsive excitation was centred at $r_e = 360$. The temporal development is plotted for four different radial positions, r_e - 25, r_e, r_e + 25 and r_e + 50. The lines labeled with a P show the development at the point of impulsive excitation of a similar disturbance in a parallel flow with $Re = 360$.*

period of temporal growth. However, for a larger time interval, convective behaviour dominates. Thus, the absolute instability does not produce a linear amplified global mode.

4.3.3 Suction

The case a = 0.5

Lingwood (1997a) has shown that for a suction parameter value **a** = 0.5, the critical Reynolds number for absolute instability is almost double that of the case where **a** = 0; refer to table 4.2. For **a** = 0.5, absolute instability occurs for Reynolds numbers greater than $Re = 912$.

A disturbance was impulsively excited at the location $r_e = 912$ with an azimuthal mode number $n = 113$, for a non-parallel flow. Such a disturbance arises at the boundary of the absolutely unstable region. Figure 4.13 displays time histories for four equally spaced radial locations, using $\omega_{\theta,w}$, the azimuthal component of the vorticity at the wall and the corresponding wavepacket envelopes $\pm|\omega_{\theta,w}|$. For $r_e \leq 912$ the disturbance initially decays, but then appears to asymptote to a constant amplitude. The radial location $r_e + 25$ experiences a steady increase in amplitude. Thus, temporal growth is present. The position $r_e + 50$ also exhibits an amplitude increase, but this is far more pronounced. This behaviour is quite different to that observed in figure 4.2 (critical absolute instability for **a** = -1) where temporal decay was eventually found at all selected radial locations.

The spatio-temporal development of the above disturbance is displayed in figure 4.15(a). The equivalent parallel disturbance with $Re = 912$ is plotted in figure 4.14. As with all previous cases the leading edges propagate radially outwards with a non-zero velocity. The parallel disturbance clearly exhibits critical absolute instability, since the trailing edge is parallel to the vertical axis and is travelling with a velocity that is approximately zero. The trailing edge of the non-parallel disturbance is also

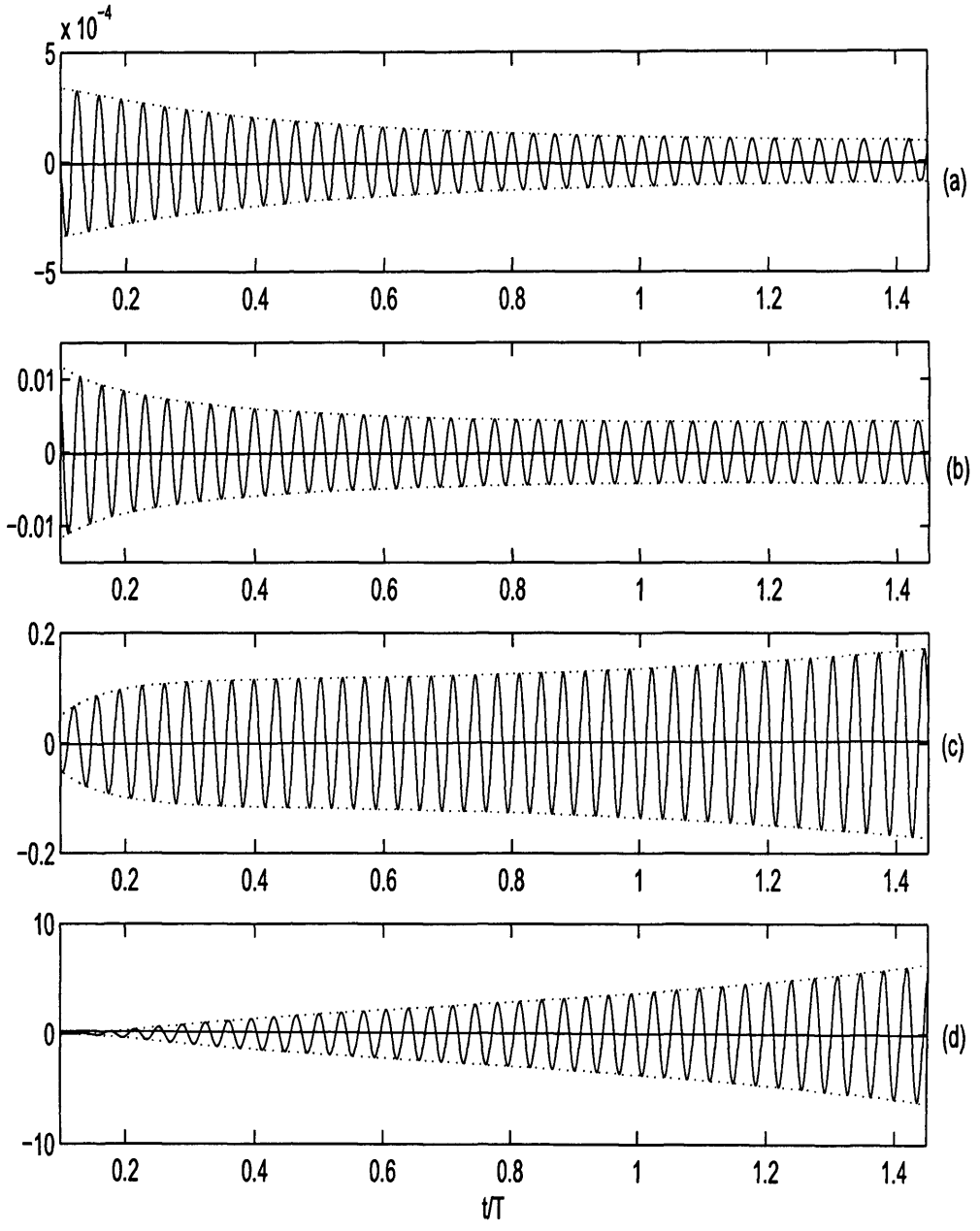

Figure 4.13: *Time histories for $\omega_{\theta,w}$ (solid lines) with corresponding envelopes $\pm|\omega_{\theta,w}|$ (dotted lines), for an impulsively excited disturbance in a non-parallel flow with suction* $\mathbf{a}$ *= 0.5. The azimuthal mode number is n = 113 and the disturbance was excited at r_e = 912. The temporal development is plotted for four different radial positions, (a) : r_e-25, (b) : r_e, (c) : r_e+25, (d) : r_e+50.*

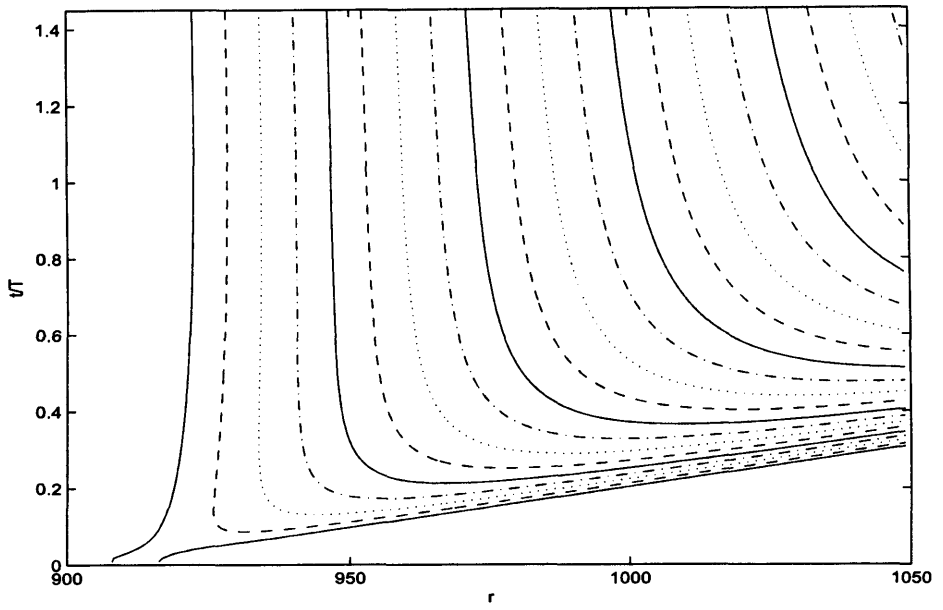

Figure 4.14: *Spatio-temporal development of* $|\omega_{\theta,w}|$ *for an impulsively excited disturbance in a parallel flow with suction* $\mathbf{a} = 0.5$. *The azimuthal mode number is* $n = 113$ *and the disturbance was excited at* $r_e = 912$. *The Reynolds number* $Re = 912$.

propagating with what at first glance, appears to be a near zero velocity. In fact when a smaller radial range is considered, (refer to figure 4.15(b)), the trailing edge can be seen to propagate radially inwards with a small velocity. This behaviour is quite different to what has been seen before for the injection flows, where the trailing edge was always found to reverse direction and propagate radially outwards. Thus, the long term behaviour does not appear to be like that found by Davies & Carpenter (2003) for the von Kármán flow or the earlier injection mean flows.

The temporal frequencies and growth rates for the above disturbance are plotted in figure 4.16. The parallel frequency, corresponding to the solid line labeled P, is comparable with that found by Lingwood (1997a); refer to table 4.2. The non-parallel frequencies behave in the manner that we have become accustomed too; the

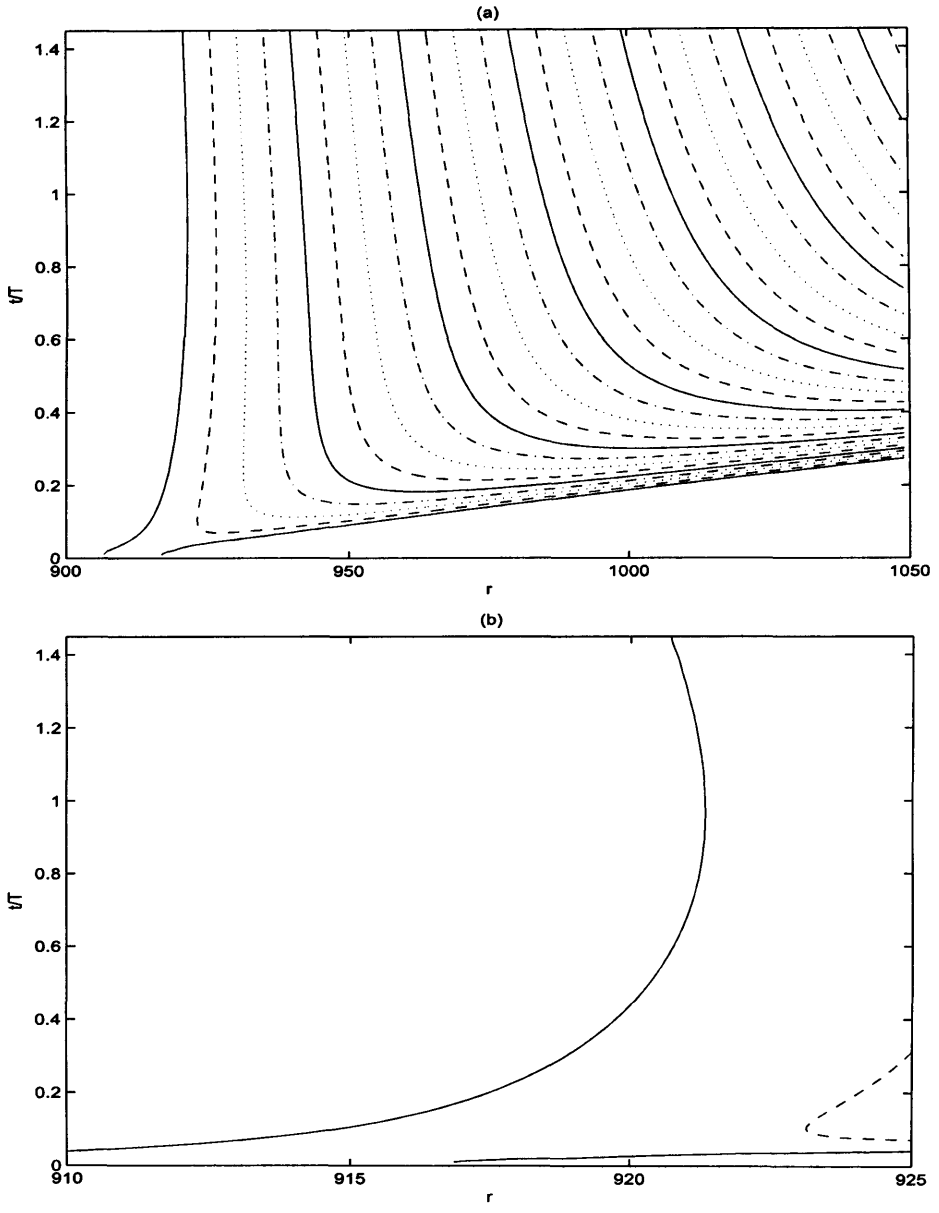

Figure 4.15: *Spatio-temporal development of* $|\omega_{\theta,w}|$ *for an impulsively excited disturbance in a non-parallel flow with suction* $\mathbf{a} = 0.5$. *The azimuthal mode number is* $n = 113$ *and the disturbance was excited at* $r_e = 912$. *(a) - full radial range, (b) - reduced radial range.*

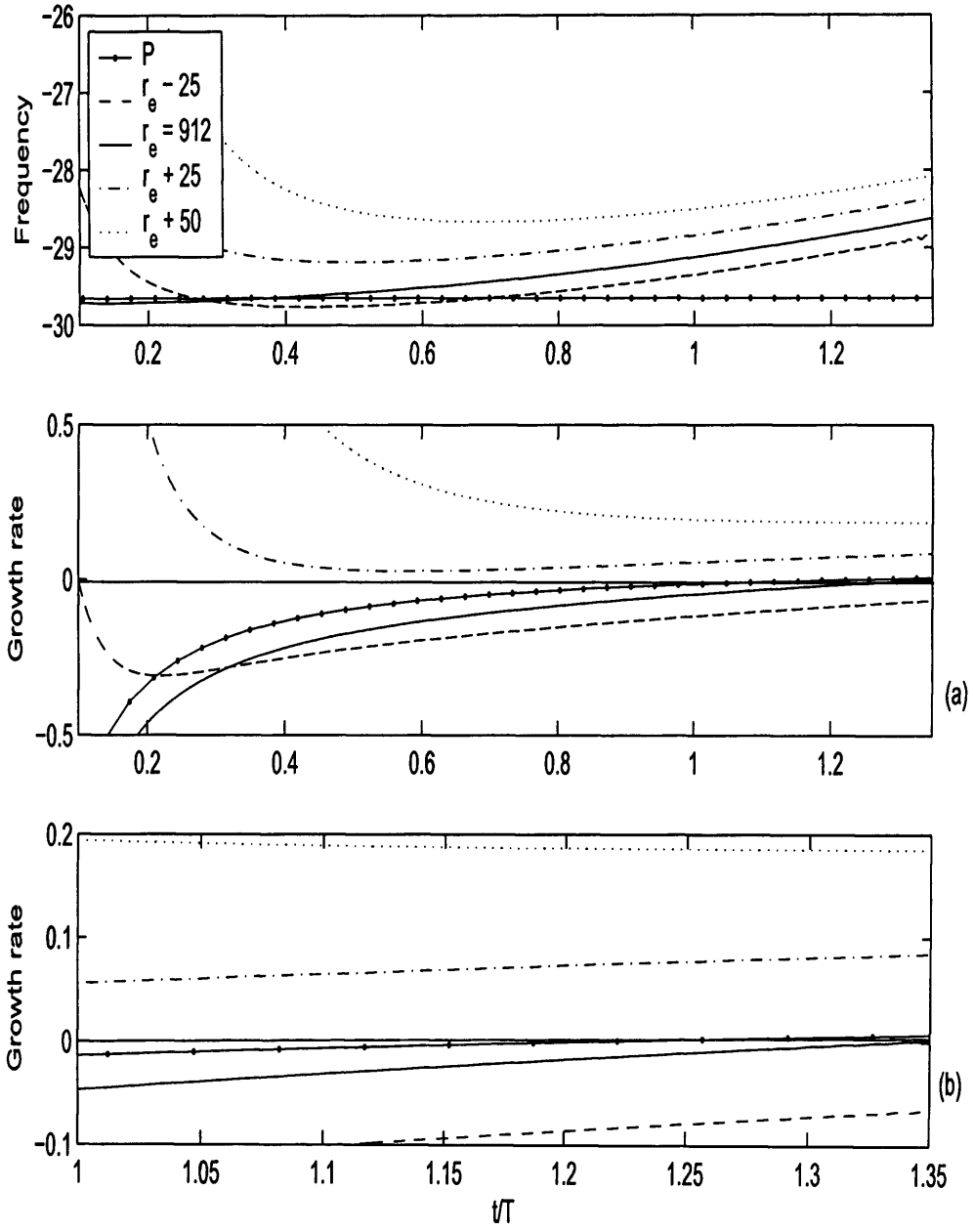

Figure 4.16: *Local temporal frequencies $\omega_r Re$ and temporal growth rates $\omega_i Re$ for a disturbance with $n = 113$ developing in a non-parallel flow with suction* **a** $= 0.5$, *centred at $r_e = 912$. The temporal development is plotted for four different radial positions, r_e - 25, r_e, r_e + 25 and r_e + 50. The solid lines labeled with a P show the development in a parallel flow with $Re = 912$. The temporal growth rates are displayed over a full time range (a), and for a reduced time range, (b).*

magnitude decreases for increasing time. The temporal growth rates are displayed over a full time range (a), and for a reduced time range (b). The parallel growth rate asymptotes to zero, which is indicative of the critical absolutely unstable behaviour. However, the non-parallel growth rates behave very differently from what we have seen previously. At all selected radial locations the growth rates steadily increase and appear to be asymptoting towards a positive constant. Therefore, temporal growth is observed for all selected radial locations, $r \geq r_e$. Thus, behaviour consistent with global instability is observed, although there appears to be no definite global frequency.

Could it be that the flow with suction $\mathbf{a} = 0.5$ displays characteristics consistent with global instability, and not the convective behaviour we have seen previously. The above results most definitely point towards such an interpretation. Of course there is the possibility that convergence problems caused errors, but this is very unlikely, since the author was most careful and conducted many simulations for the above disturbance, for varying radial ranges, different discretization (i.e. vary the radial increment Δr, and temporal increment Δt), and for very large iteration values, and each time the same results were found. There is also the possibility that the flow with suction $\mathbf{a} = 0.5$ will take a longer time to show any sign of exhibiting the convective behaviour that we have seen previously for flows with injection. In other words the growth rates may stop increasing and eventually start to decrease towards negative numbers, leading to temporal decay. (Due to convergence problems, simulations could not be run far enough to see if this is the case). However, from what we have seen of the growth rates for the above disturbance this does not seem to be the case. The growth rate at the radial position $r_e + 25$ initially decreases but then reverses at some point and then steadily increases. On comparing with other disturbances at the theoretical critical point of absolute instability for flows with injection and zero normal flow, (figures 4.5 and 4.10) there is no tendency for the growth rate at $r_e +$

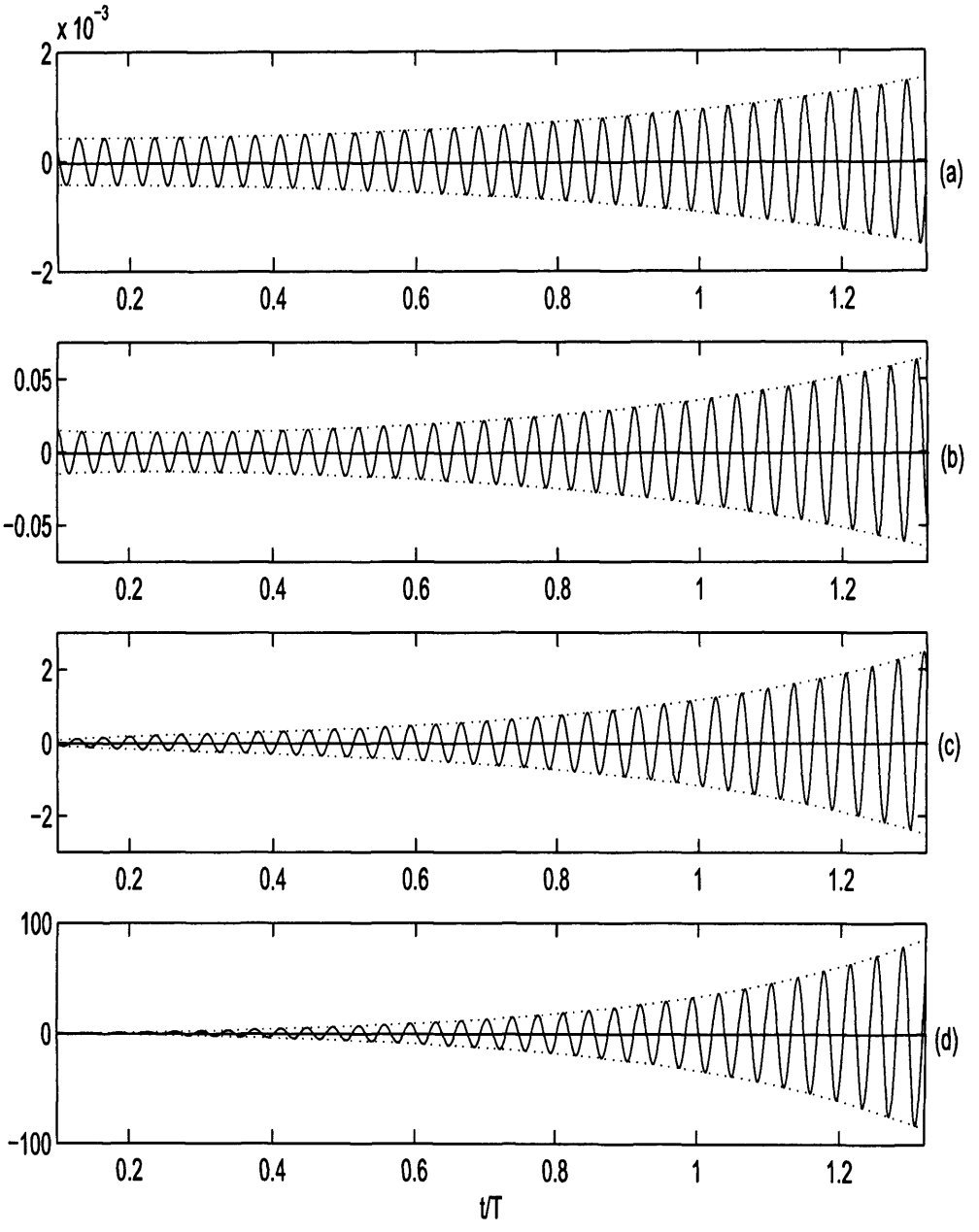

Figure 4.17: *Time histories for $\omega_{\theta,w}$ (solid lines) with corresponding envelopes $\pm|\omega_{\theta,w}|$ (dotted lines), for an impulsively excited disturbance in a non-parallel flow with suction* **a** *= 0.5. The azimuthal mode number is n = 113 and the disturbance was excited at r_e = 962. The temporal development is plotted for four different radial positions, (a) : r_e-25, (b) : r_e, (c) : r_e+25, (d) : r_e+50.*

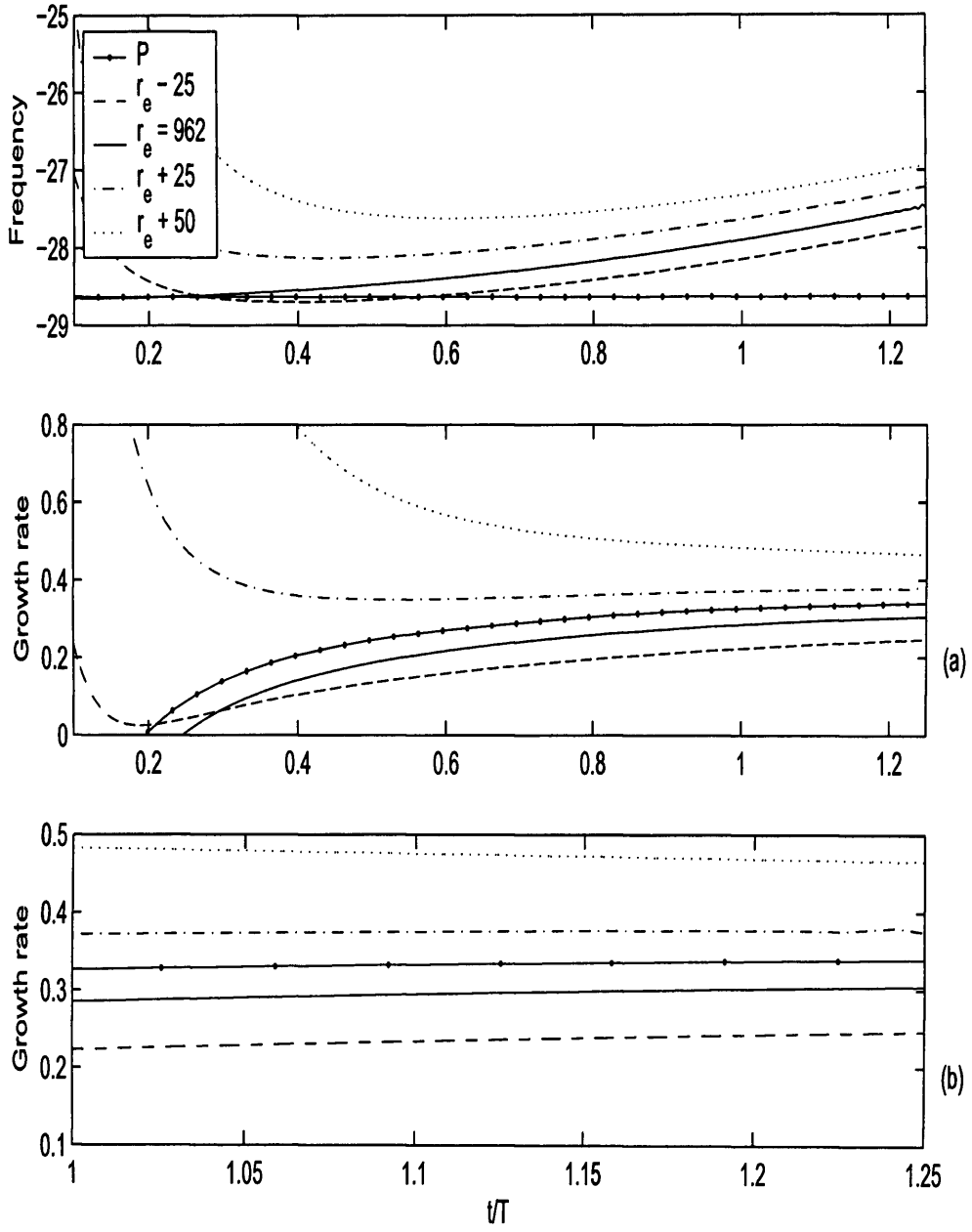

Figure 4.18: *Local temporal frequencies $\omega_r Re$ and temporal growth rates $\omega_i Re$ for a disturbance with $n = 113$ developing in a non-parallel flow with suction* $\mathbf{a} = 0.5$, *centred at $r = 962$. The temporal development is plotted for four different radial positions, r - 25, r, r + 25 and r + 50. The solid lines labeled with a P show the development in a parallel flow with $Re = 962$. The temporal growth rates are displayed over a full time range (a), and for a reduced time range, (b).*

25 to increase.

Although what we are seeing may be an attribute of mean flows with suction, it might also be due to the fact that the disturbance has occurred near the critical region of absolute instability and that disturbances well within this region show completely different behaviour. However, this is highly unlikely, since the flow should experience greater temporal growth for locations well within the theoretical absolutely unstable domain.

To confirm whether or not disturbances experience greater growth at larger radial locations, we also conducted a second simulation for $n = 113$ and $r_e = 962$. This point is well inside the theoretical region of absolute instability. The time histories are plotted in figure 4.17. At all the radial locations considered, the disturbance increases at a steady rate, even for the location radially inwards of the origin of the source. The corresponding temporal frequencies and growth rates are plotted in figure 4.18. Again, the growth rates at all selected radial positions are plotted for a full time range and a reduced time range. The growth rates are increasing and appear to be asymptoting towards a positive constant. Thus, temporal growth is experienced at all radial locations.

A non-parallel numerical simulation was carried out for a disturbance situated in the theoretical region of convective instability. The azimuthal mode number was taken to be $n = 113$, which corresponds to the first mode number to become absolutely unstable. The impulsive excitation was carried out for $r_e = 712$. Such a position is well inboard of the theoretical region of absolute instability. The spatio-temporal development for the above situation is plotted in figure 4.19(a). Figure 4.19(b) displays the spatio-temporal development for a disturbance excited within the theoretical convective region for the rotating-disk with $\mathbf{a}$ = -0.5, i.e. injection. The disturbance was excited at the radial location $r_e = 240$. The contrasting behaviour between the two wavepackets is quite apparent. The trailing edge of the disturbance wavepacket for

$\mathbf{a} = 0.5$ can be seen to be propagating with a diminishing velocity, while the trailing edge of the disturbance wavepacket for $\mathbf{a} = -0.5$ is propagating with what appears to be an increasing velocity.

Figure 4.20 displays the trailing edge velocities (C_t) of the spatio-temporal plots in figure 4.19, as functions of time. Initially, both velocity profiles decrease at a rapid rate. However, the velocity corresponding to the $\mathbf{a} = -0.5$ problem (figure 4.20(b)), eventually reverses direction and increases. Hence, the disturbance propagates radially outwards with an increasing velocity. On the other hand, the velocity corresponding to $\mathbf{a} = 0.5$ (figure 4.20(a)), continues to decrease, and the plot suggests that C_t may eventually pass through zero and into the negative half of the plane. Thus, the trailing edge may eventually propagate radially inwards.

Figure 4.21(a) and 4.21(b) display time histories for the above disturbances, at the radial locations $r = 912$ for $\mathbf{a} = 0.5$, and $r = 310$ for $\mathbf{a} = -0.5$. The radial locations are found at the respective boundaries of the region of absolute instability. For the rotating-disk with $\mathbf{a} = -0.5$, there is a period of rapid temporal growth followed by a strong decay. While for $\mathbf{a} = 0.5$, there is a period of rapid temporal growth followed by a relatively weak period of decay. Whether this disturbance will eventually asymptote towards a constant or grow and display a region of temporal growth, or dissipate and decay indefinitely, is unclear from the figure. However, it is clear that there is a marked difference between the behaviour of the two types of flow, even for disturbances located within the theoretical convectively unstable parameter space.

The case $\mathbf{a} = 1$

The final uniform normal flow considered is that where $\mathbf{a} = 1$. Of all the mean flows considered, this is by far the most stable, at least, when the parallel flow approximation is applied. Lingwood (1997a) found the critical Reynolds number for absolute instability for this flow to be approximately $Re = 1861$. This is almost four times

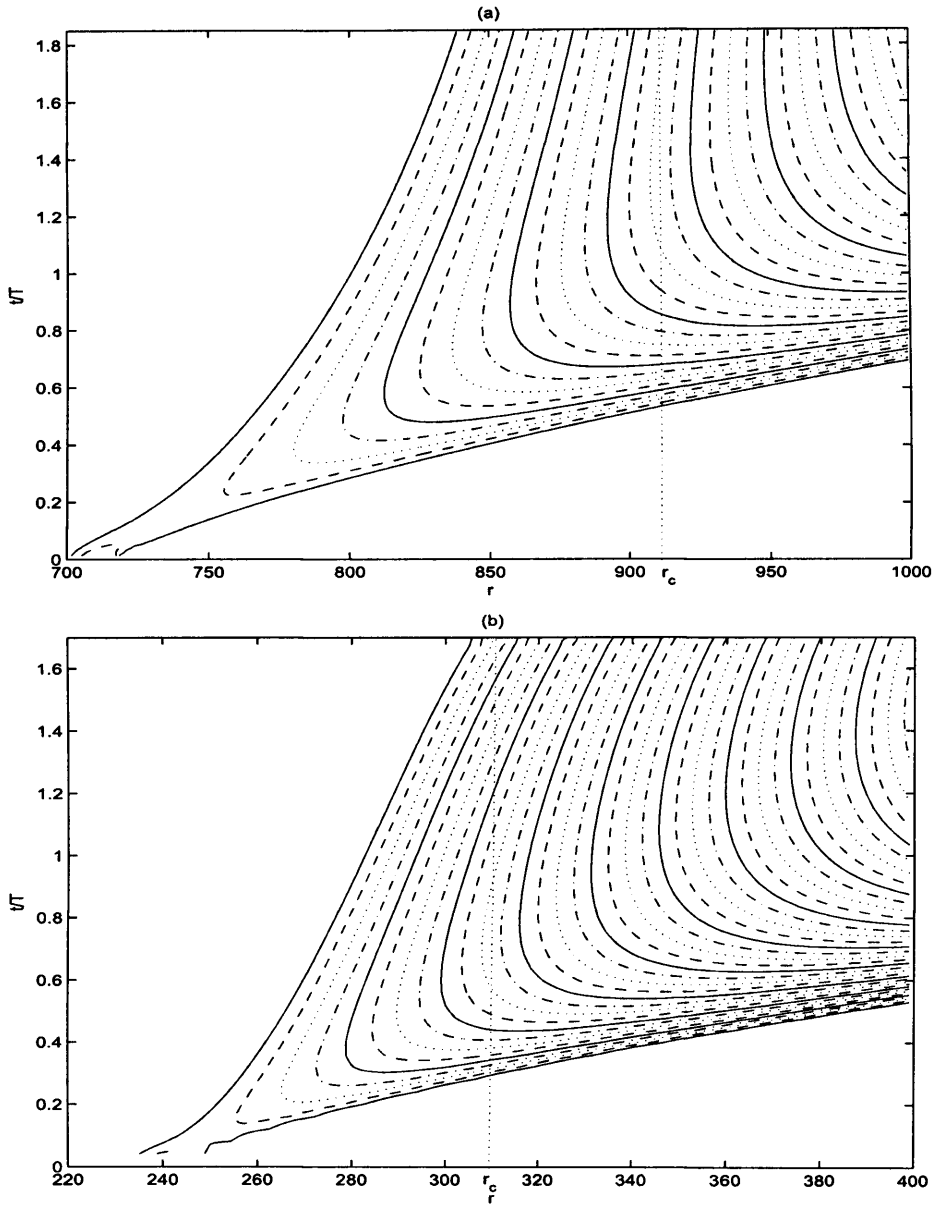

Figure 4.19: *Spatio-temporal development of* $|\omega_{\theta,w}|$ *for an impulsively excited disturbance in a non-parallel flow with: (a):* $\mathbf{a} = 0.5$ *for an azimuthal mode number* $n = 113$ *excited at* $r_e = 712$*; (b):* $\mathbf{a} = -0.5$ *for an azimuthal mode number* $n = 43$ *excited at* $r_e = 240$*. Here* r_c *indicates the onset of absolute instability, as predicted by Lingwood (1997a).*

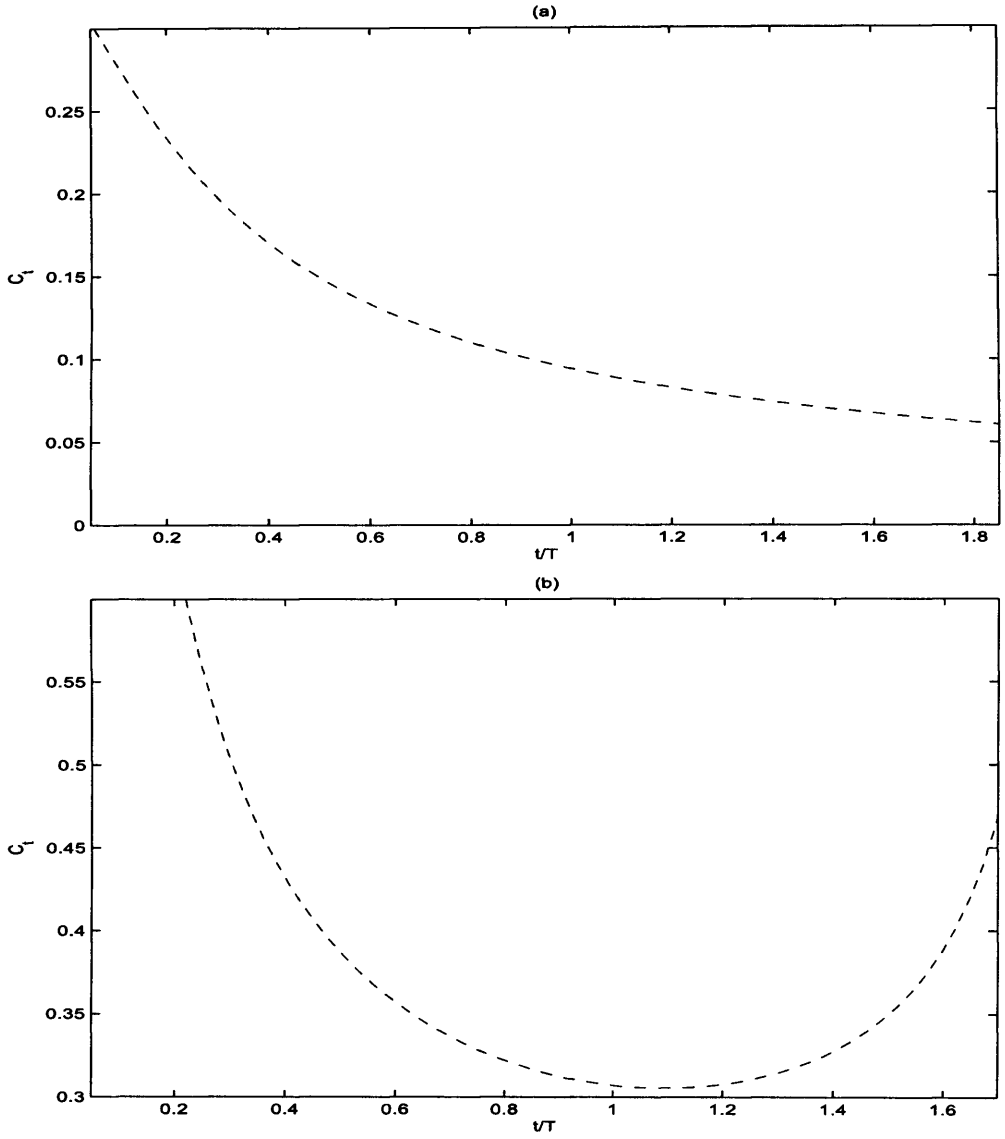

Figure 4.20: *Velocity profiles of the trailing edge as a function of time. (a):* $\mathbf{a} = 0.5$ *for an azimuthal mode number* $n = 113$ *excited at* $r_e = 712$*; (b):* $\mathbf{a} = -0.5$ *for an azimuthal mode number* $n = 43$ *excited at* $r_e = 240$.

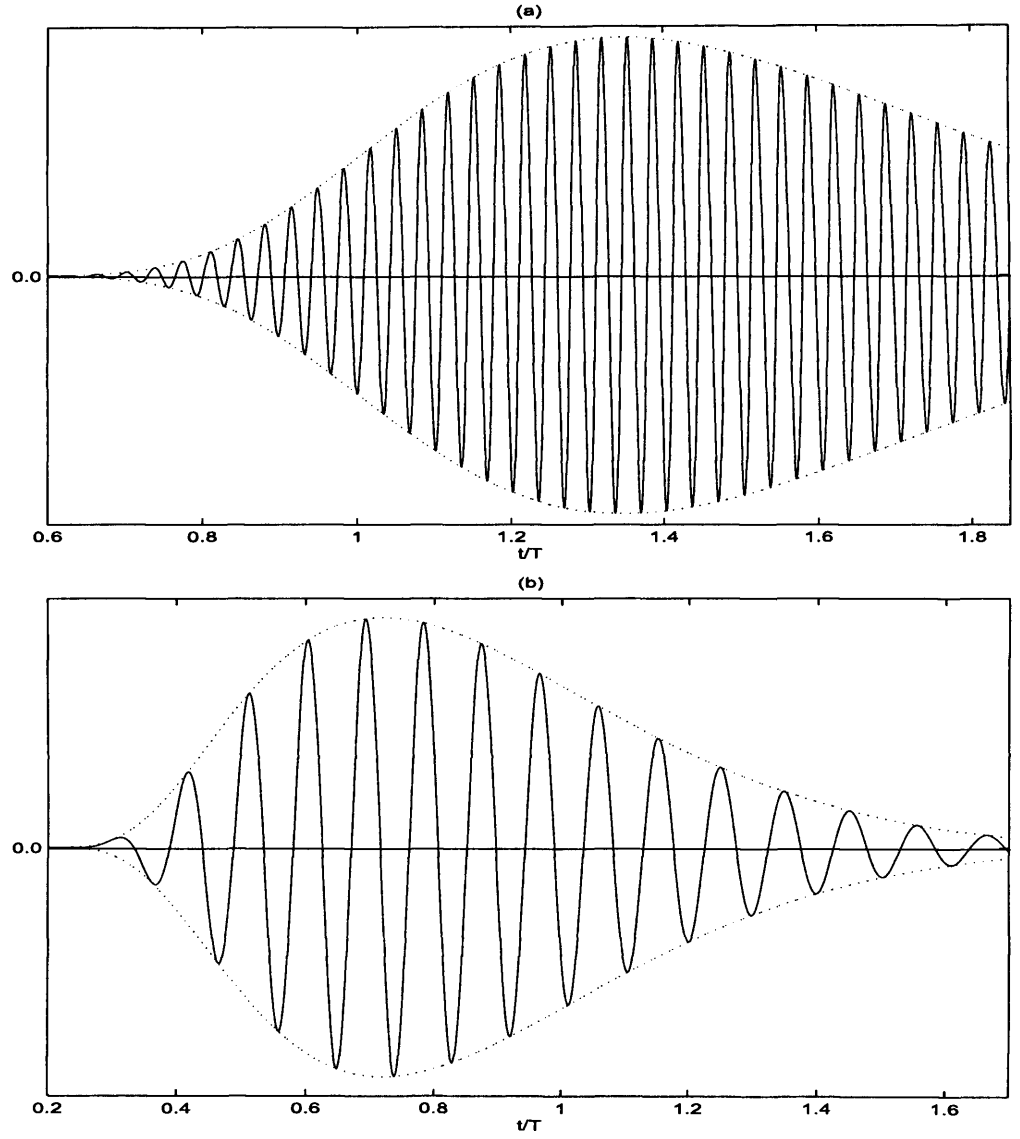

Figure 4.21: *Time history for $\omega_{\theta,w}$ (solid line) with corresponding envelope $\pm|\omega_{\theta,w}|$ (dotted line), for an impulsively excited disturbance in a non-parallel flow with: (a) :* **a** *= 0.5 for an azimuthal mode number n = 113 excited at r_e = 712. The temporal development is plotted for r = 912. (b) :* **a** *= -0.5 for an azimuthal mode number n = 43 excited at r_e = 240. The temporal development is plotted for r = 310.*

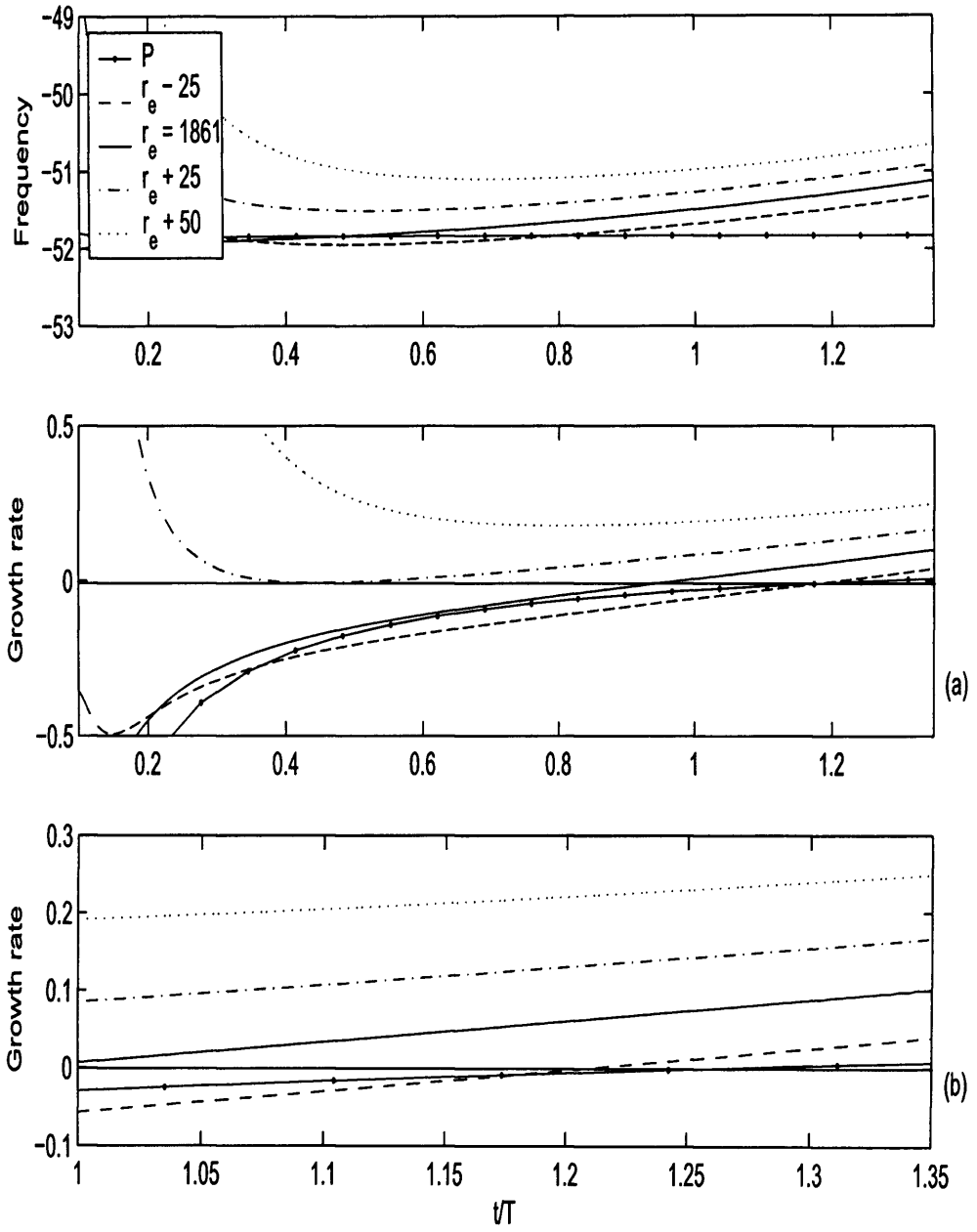

Figure 4.22: *Local temporal frequencies $\omega_r Re$ and temporal growth rates $\omega_i Re$ for a disturbance with $n = 194$ developing in a non-parallel flow with suction* $\mathbf{a} = 1$, *centred at $r_e = 1861$. The temporal development is plotted for four different radial positions, r_e - 25, r_e, r_e + 25 and r_e + 50. The solid lines labeled with a P show the development in a parallel flow with Re = 1861. The temporal growth rates are displayed over a full time range (a), and for a reduced time range, (b).*

that of the zero normal flow case, namely the von Kármán flow.

A disturbance was impulsively excited at the radial position $r_e = 1861$ with an azimuthal normal mode number $n = 194$. These are the critical parameters for absolute instability. The temporal frequencies and growth rates for this disturbance are plotted in figure 4.22. The solid lines labelled P refer to the corresponding parallel disturbance, where the Reynolds number $Re = 1861$. The frequency for the parallel flow is consistent with that found by Lingwood (1997a). As expected, the non-parallel frequencies display behaviour that is qualitatively similar to that found in the previous rotating-disk flows; the magnitude decreases with increasing time.

For all selected radial locations the growth rate increases at a steady rate. There is no indication that the temporal growth rates will reverse or even asymptote to a constant value. This suggests that the growth rate will increase at all radial positions. It may also be noted that the temporal growth found here is stronger than that experienced at the critical point of absolute instability for $\mathbf{a} = 0.5$. (Compare figure 4.22 with figure 4.16).

In another simulation, a disturbance was excited at $r_e = 1911$ with $n = 194$. This is well within the region of the absolutely unstable parameter space. Figure 4.23 compares the time histories of the disturbance in the non-parallel flow (dotted line) and corresponding parallel flow (solid line), where $Re = 1911$. Initially the two plots are almost identical. However, for a larger time interval the amplitude of the non-parallel disturbance is clearly larger than the parallel disturbance. Thus, the non-parallel flow effects can be seen to be destabilizing.

The destabilization is clearly evident in the growth rates, plotted in figure 4.24. The growth rates can be seen to increase steadily with time and so temporal growth is clearly evident for all the selected radial positions. For the radial position $r = r_e - 50$, corresponding to the location of critical absolute instability $r_c = 1861$, a temporally growing disturbance is visible after $t/T > 0.4$. Several other simulations

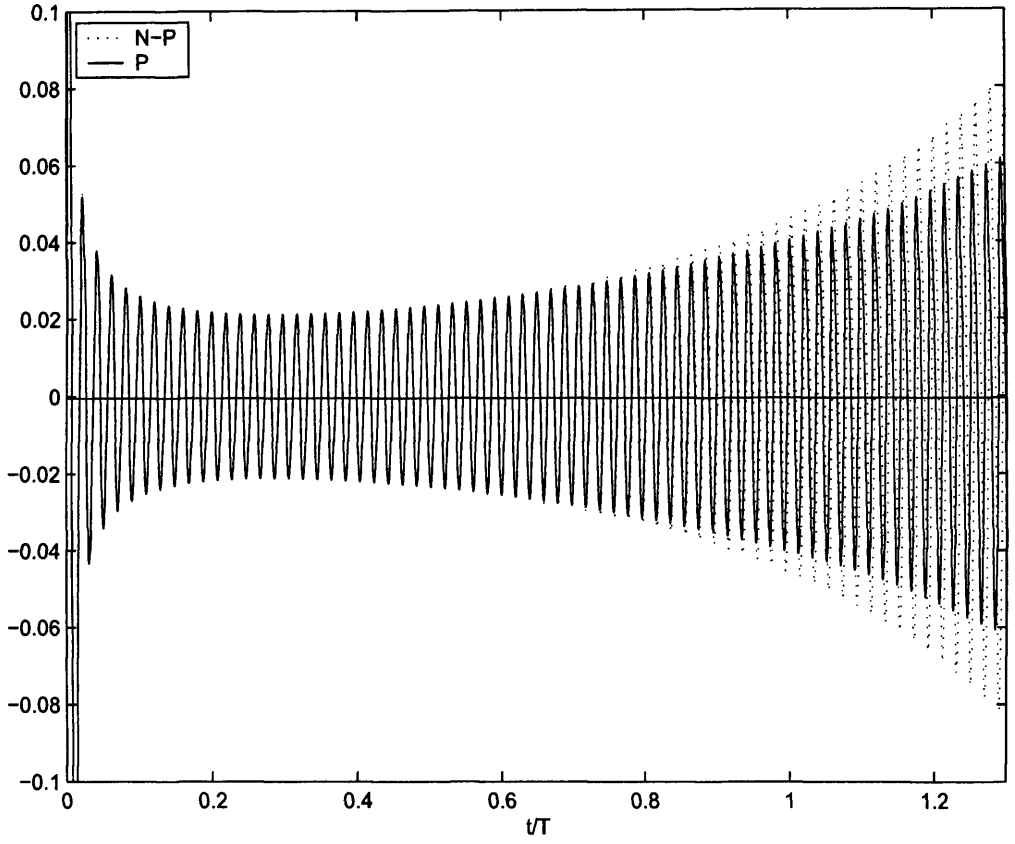

Figure 4.23: *Comparison of the variation of* $|\omega_{\theta,w}|$ *for a disturbance with* $n = 194$ *evolving in a non-parallel and parallel flow with* $\boldsymbol{a} = 1$. *The temporal development is shown for the radius* $r_e = 1911$ *where the impulsive excitation was centred. Dotted line: The non-parallel flow labeled N-P; solid line: parallel flow labeled P with* $Re = 1911$.

were conducted by exciting disturbances further into the absolutely unstable region and the growth rates were found to increase every time.

In another simulation, which mimics an experimentally feasible set-up, a disturbance was excited radially inward of the absolutely unstable boundary. The location

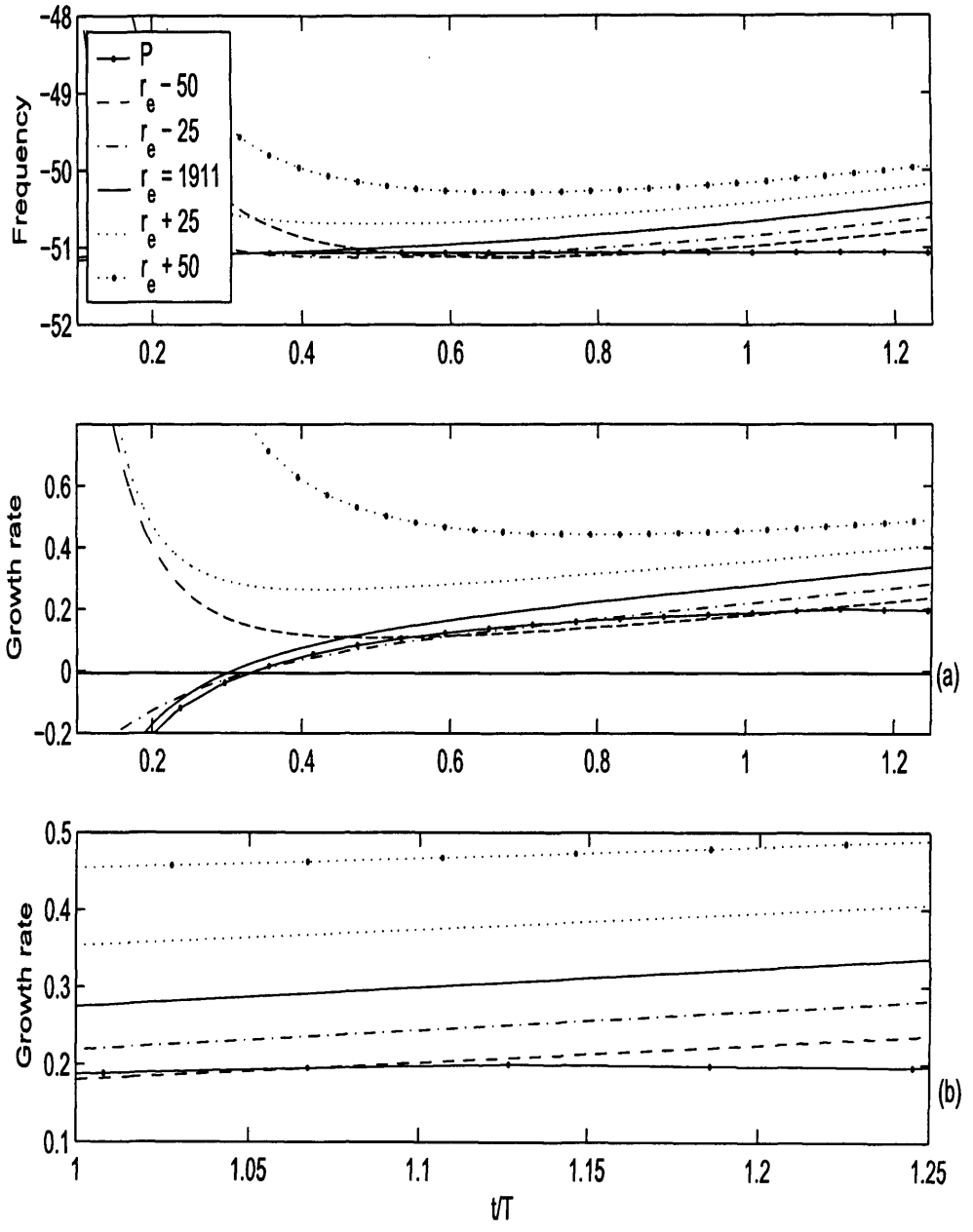

Figure 4.24: *Local temporal frequencies $\omega_r Re$ and temporal growth rates $\omega_i Re$ for a disturbance with $n = 194$ developing in a non-parallel flow with suction* $\mathbf{a} = 1$, *centred at $r_e = 1911$. The temporal development is plotted for five different radial positions, $r_e - 50 = r_c$, r_e - 25, r_e, $r_e + 25$ and $r_e + 50$. The solid lines labeled with a P show the development in a parallel flow with $Re = 1911$. The temporal growth rates are displayed over a full time range (a), and for a reduced time range, (b).*

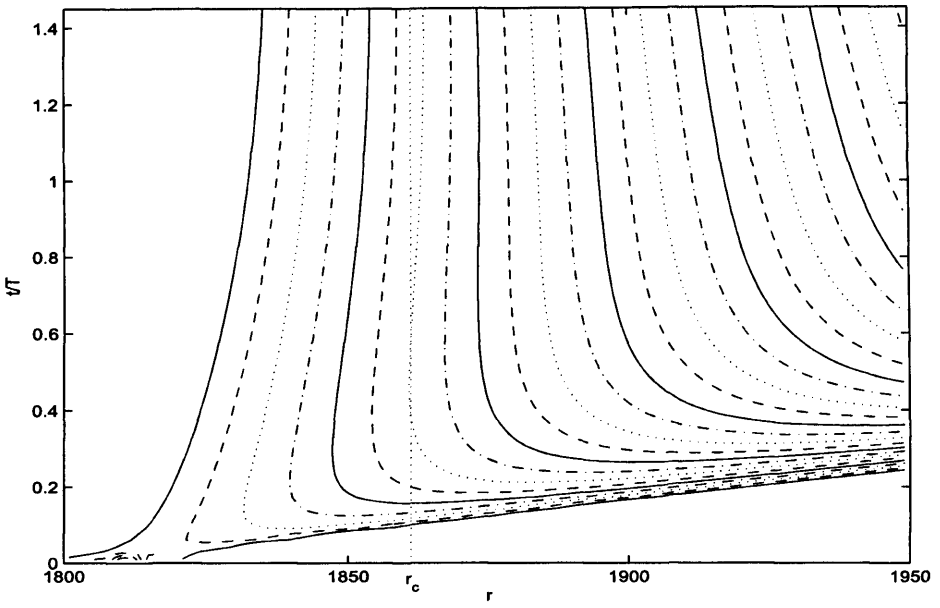

Figure 4.25: *Spatio-temporal development of* $|\omega_{\theta,w}|$ *for an impulsively excited disturbance in a non-parallel flow with suction* $\mathbf{a} = 1$. *The azimuthal mode number is* $n = 194$ *and the disturbance was excited at* $r_e = 1811$.

of the disturbance was at $r_e = 1811$ with an azimuthal mode number $n = 194$. Figure 4.25 displays the spatio-temporal development for the above disturbance. Initially the trailing edge of the wavepacket disturbance propagates radially outwards, but as soon as it reaches the absolutely unstable region, the trailing edge slows down and appears to be tending towards a vertical line, radially inward of the critical point of absolute instability, $r_c = 1861$. Figure 4.26 displays the temporal frequencies and growth rates at the radial locations $r_e = 1811$, $r_e + 25$, $r_e + 50$ and $r_e + 100$ for the above disturbance. The frequency and growth rate for the parallel flow with $Re = 1811$ are also included in the plot (labeled P). The growth rates at all radial locations are initially decreasing and for $r \leq r_e + 50$ there is a period of temporal decay. However, this does not persist for long and the growth rates eventually reverse direction

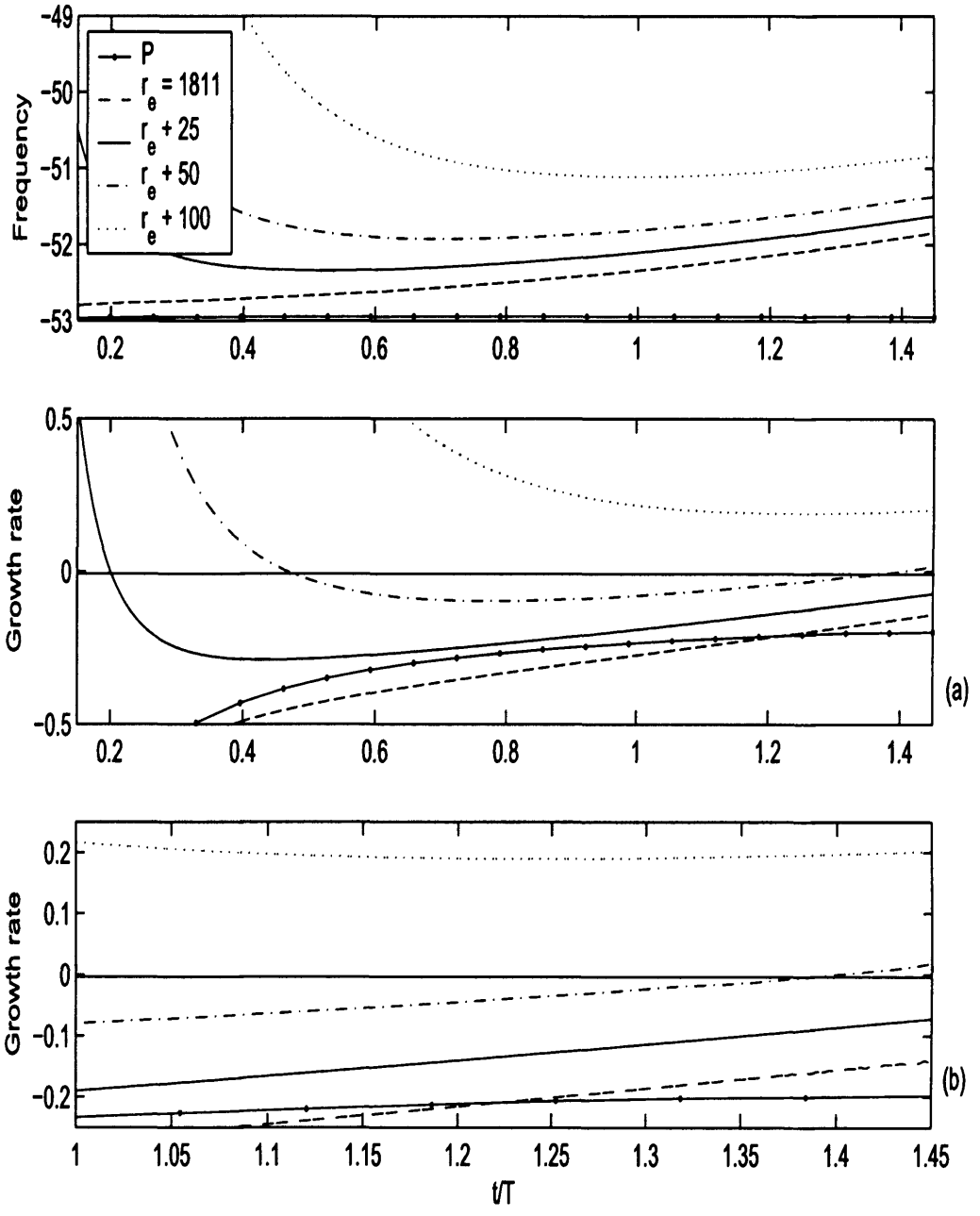

Figure 4.26: *Local temporal frequencies $\omega_r Re$ and growth rates $\omega_i Re$ for a disturbance with $n = 194$ developing in a non-parallel flow with suction* $\mathbf{a} = 1$, *centred at $r_e = 1811$. The temporal development is plotted for four different radial positions, r_e, $r_e + 25$, $r_e + 50$ and $r_e + 75$. The solid lines labeled with a P show the development in a parallel flow with $Re = 1811$. The temporal growth rates are displayed over a full time range, (a), and for a reduced time range, (b).*

and increase. The radial position $r_c = 1861 = r_e + 50$ exhibits temporal growth after $t/T = 1.4$. Bearing in mind the gradient of the growth rate at this point, it is plausible to suggest that temporal growth will continue to be displayed for all time $t/T > 1.4$. Similar behaviour was found for all radial locations $r > 1861$, where the growth was more pronounced for increasing radial positions. An increasing temporal growth rate is clearly visible for the radial position $r = 1911 = r_e + 100$. Although none of the growth rates for $r_e < 1861$ quite reached the positive domain, it did appear that they would eventually become positive given sufficient time. Thus, such locations will display temporal growth. As already mentioned, convergence problems with the iteration scheme were met which prevented longer simulations from being carried out. Refer back to sections 4.2.3 and 4.3.2 for further details of problems met during the investigation (e.g. effects due to the finite computational radial domain and the convergence of the iteration scheme used in the discretization).

A second disturbance was impulsively excited at the radial location $r_e = 1661$, for an azimuthal mode number $n = 194$. This problem corresponds to a radial position further inboard than any other example, so far investigated. Figure 4.27 displays the non-parallel temporal growth rates for the above disturbance, at the radial locations r_e, $r_e + 100$, $r_e + 150$, $r_e + 200$ and $r_e + 240$. For the radial position r_e, the growth rate increases at what appears to be a steady, linear rate in the negative half of the plane. The growth rates at all other selected radial locations, initially, decreases at a rapid rate. However, after this initial period, the decrease in growth deteriorates, and can be seen to reverse direction and increase at the radial locations $r_e + 100$ and $r_e + 150$. The growth rates at the radial locations $r_e + 200$ and $r_e + 240$, has not yet reversed direction. However, given sufficient time, it seems plausible that the growth rates at the two locations $r_e + 200$ and $r_e + 240$, will eventually undergo this process, i.e. reverse direction and increase. If the growth continues to increase at the rate shown, temporal growth may eventually be found at all points. Therefore, behaviour

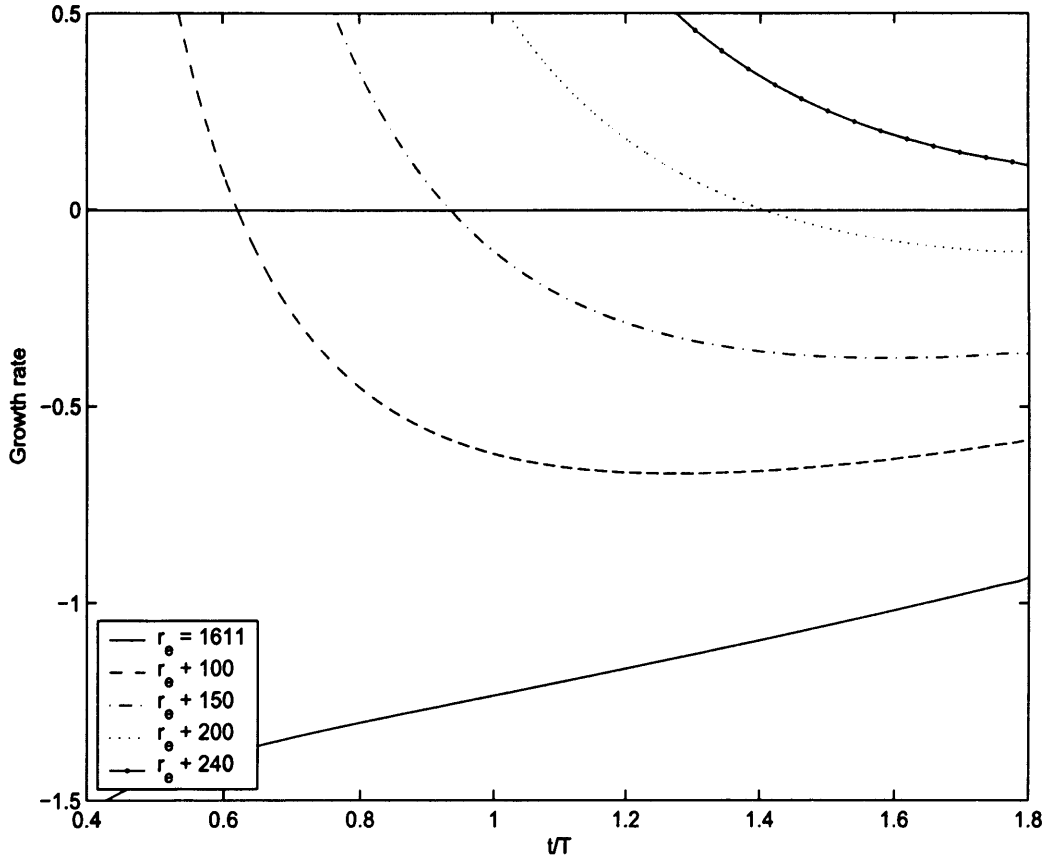

Figure 4.27: *Local temporal growth rates $\omega_i Re$ for a disturbance with $n = 194$ developing in a non-parallel flow with suction* $\mathbf{a} = 1$, *centred at $r_e = 1661$. The temporal development is plotted for four different radial positions, r_e, $r_e + 100$, $r_e + 150$, $r_e + 200$ and $r_e + 240$.*

compatible with global instability could be displayed.

4.4 Comparing growth rates

A number of uniform normal flows have been investigated and there were found to be distinct differences between the injection and suction flows. Figure 4.28 compares

the growth rates at the critical point of absolute instability for all of the previous flows. The solid line represents the $\mathbf{a}$ = -1 case, where $r_e = 202$, $n = 29$; the dashed line represents the $\mathbf{a}$ = -0.5 case, where $r_e = 310$, n =43; the dashed-dotted line represents the $\mathbf{a} = 0$ case, where $r_e = 508$, $n = 68$; the dotted line represents the $\mathbf{a}$ = 0.5 case, where $r_e = 912$, $n = 113$; and the solid-dotted line represents the $\mathbf{a} = 1$ case, where $r_e = 1861$, $n = 194$. The growth rates have been plotted using the global non-dimensionalization that has been used throughout the thesis. (Further details of the global non-dimensionalization are given in chapter 7 and Davies, Thomas & Carpenter (2007)). Interestingly the growth rates of all five flows are of comparable magnitude. Initially all five plots behave in an analogous manner; the growth rates originate from the negative half of the plane and increase rapidly. (In chapter 8 we will see that the initial behaviour can be traced to a $1/t^2$ term in the Green's solutions). However, after only $t/T = 0.4$, differences in the growth rates are observed. The growth rates corresponding to those flows with $\mathbf{a} \leq 0$ begin to reverse direction and decrease. The growth rate for the case $\mathbf{a}$ = -1 decreases far more strongly than the $\mathbf{a}$ = -0.5 and $\mathbf{a}$ = 0, problems. On the other hand the flows corresponding to normal suction continue to increase, although this increase is far weaker than the initial growth. It can be seen that the increase in growth is stronger for the $\mathbf{a} = 1$ case than the $\mathbf{a}$ = 0.5 case. For both suction cases there is no indication that the growth will begin to decrease.

Figure 4.29 displays the gradients of the growth rates in figure 4.28. The data lines are as before. For $\mathbf{a} \leq 0$ the gradients decrease and are eventually negative, which corresponds to the growth rates decreasing. For $\mathbf{a}$ = 0.5 the gradient remains positive for the time period displayed. However, the gradient continues to decrease, suggesting that the corresponding growth rate may eventually decrease and display temporal decay. The gradient for $\mathbf{a} = 1$ initially decreases, but as time increases, it appears to asymptote towards a positive constant. This would suggest that temporal growth and an increasing growth rate would be observed for this problem.

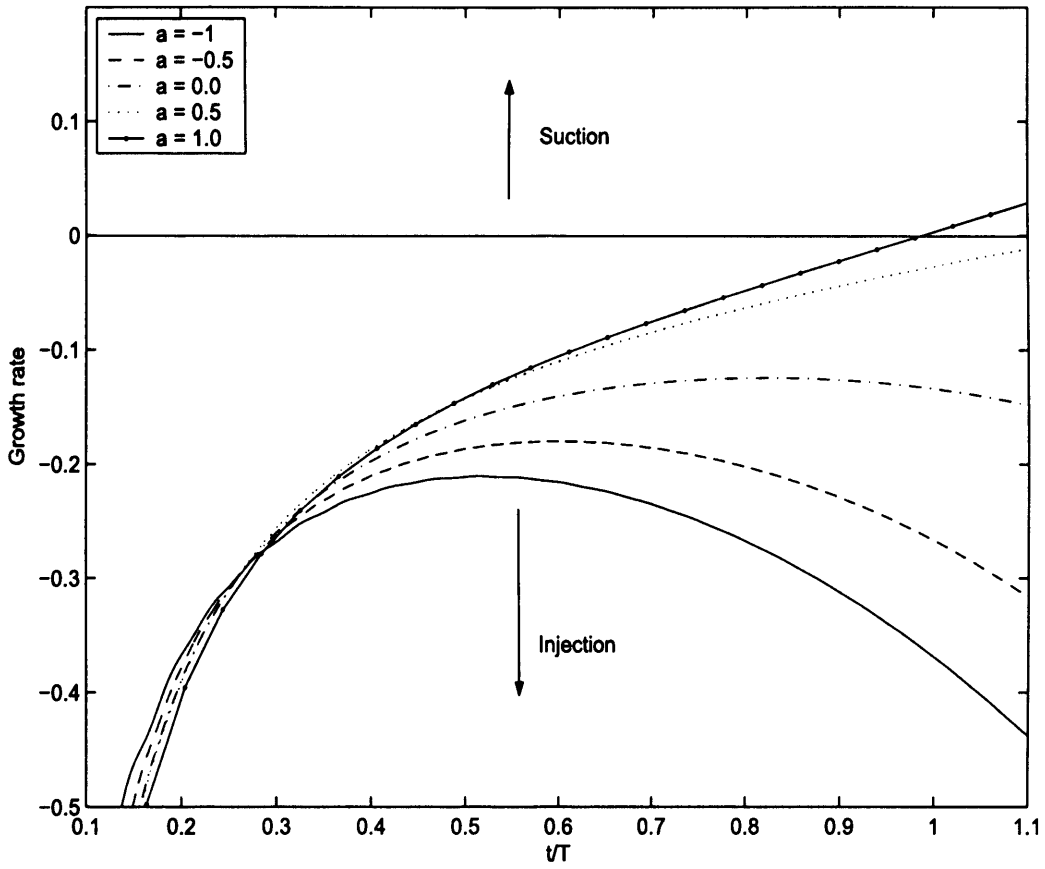

Figure 4.28: *Comparing growth rates at the critical point of absolute instability for the various normal flows. Solid line:* $\mathbf{a}$ *= -1 where* r_e *= 202,* n *= 29; dashed line:* $\mathbf{a}$ *= -0.5 where* r_e *= 310,* n *= 43; dashed-dotted line:* $\mathbf{a}$ *= 0.0 where* r_e *= 508,* n *= 67; dotted line:* $\mathbf{a}$ *= 0.5 where* r_e *= 912,* n *= 113; solid-dotted line:* $\mathbf{a}$ *= 1 where* r_e *= 1861,* n *= 194.*

It is quite apparent that the growth rates increase for increasing $\mathbf{a}$. Thus, we may predict that normal flows with $\mathbf{a} > 1$ may display growth rates that are larger than those displayed in figure 4.28. Nonetheless, further investigation is required to prove this theory. However, at present there are no eigenvalues available (in the research literature) for $\mathbf{a} > 1$, which prevents further investigation. Figure 4.28 also suggests

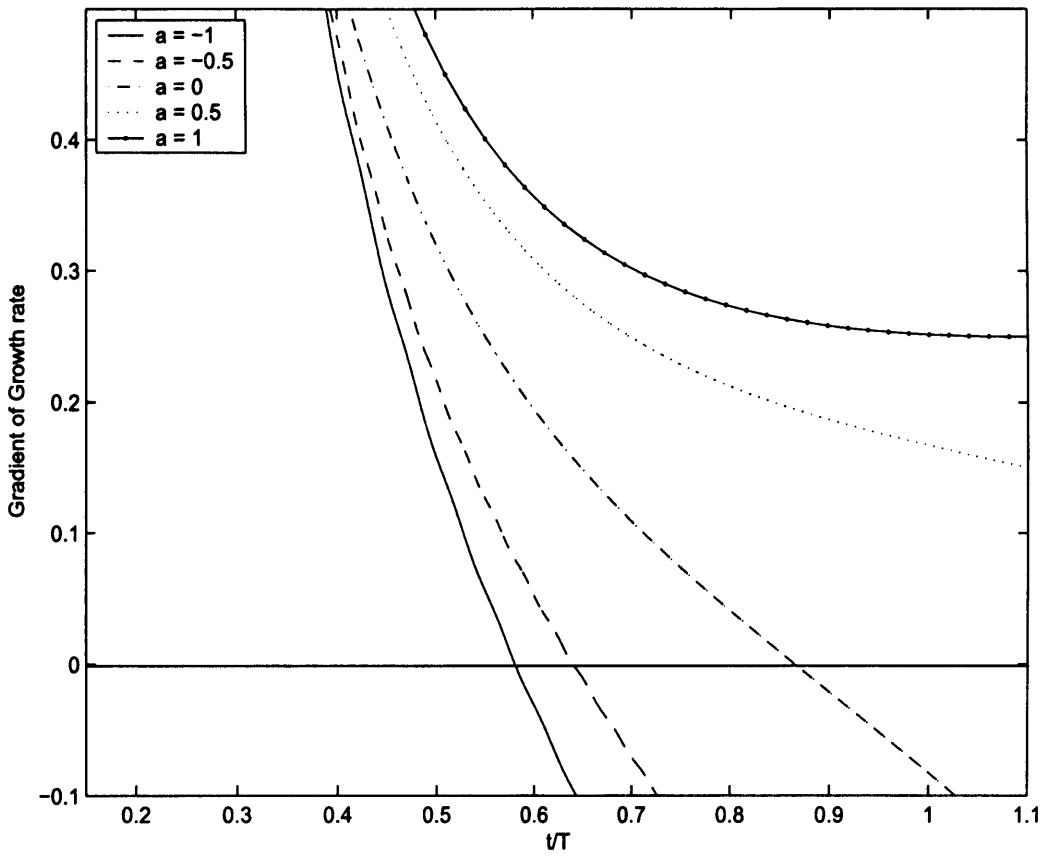

Figure 4.29: *Comparing the gradients of the growth rates in figure 4.28. Data lines are the same as those in figure 4.28.*

that there may exist a critical value $\mathbf{a_c}$, such that the growth rate does not increase or decrease, but instead tends towards a constant. The plot suggests that there may be a critical value within the region $0.0 < \mathbf{a_c} < 1$.

4.5 Discussion and conclusions

A study has been carried out on the effects of injection and suction on the global behaviour corresponding to the absolute instability of the rotating-disk boundary-layer. Four cases with normal flow are investigated; $\mathbf{a} = \pm\ 0.5$ and $\pm\ 1$, where the parameter $\mathbf{a}$ is negative for mean flows with uniform normal injection and positive for mean flows with uniform normal suction. The investigation was undertaken using the novel velocity-vorticity method described by Davies & Carpenter (2001). The system of equations used in this method are equivalent to the complete linearized Navier-Stokes equations. Since the equations are linear, they are separable with respect to the azimuthal coordinate θ. Thus, allowing simulations with a single azimuthal mode number. Impulse like excitation was used for all simulations. This produces a disturbance wavepacket that initially contains a wide range of frequencies. When disturbances are simulated using the so-called parallel flow approximation (spatially homogeneous flow), the results are fully in accordance with the theoretical results of Lingwood (1997a). If the flow parameters lie within the theoretical absolutely unstable parameter space, the simulations produce identical behaviour. The same is true for disturbances excited within the convectively unstable region. For disturbances excited at the critical point of absolute instability, the calculated frequencies and wavenumbers are in excellent agreement with those given in Lingwood (1997a); refer to table 4.2. The temporal frequencies ω_c were found to be identical to within three decimal places in all cases considered, while the radial wavenumbers α_c, were the same to within two decimal places, in most cases.

For the non-parallel flow simulations (spatially inhomogeneous), the injection and suction flows produce quite different behaviour. The investigated uniform normal injection flows produce behaviour that is similar to that observed by Davies & Carpenter (2003) for the von Kármán flow, $\mathbf{a} = 0$. Initially, disturbances within the absolutely

unstable region exhibit temporal growth and inward propagation. However, this does not last and the study suggests that convective behaviour will eventually dominate, for all Reynolds numbers investigated. This behaviour was not only identified near the known boundary of absolute instability, but for radial locations far further outboard. For the injection case $\mathbf{a}$ = -1, what appeared to be convective behaviour was found at approximately one and half times that of the critical Reynolds number for absolute instability. Thus, in a similar manner to Davies & Carpenter (2003) and their study on the global behaviour corresponding to the absolute instability of the von Kármán flow, the simulation results for the injection mean flows suggest that the absolute instability does not produce a linear amplified global mode, but is instead consistent with convective behaviour.

Therefore, we may describe the results from the study using the schematic drawings of Davies & Carpenter (2003), figures 4(a, b). (Plotted here in figure 2.4). The two figures depict wavepacket evolutions for the rotating-disk boundary-layer with $\mathbf{a}$ = 0, -0.5 and -1. Figure 2.4(a) depicts the case where the point of forcing arises within the convective region of the stability plane. Here r_e is the point of impulsive forcing and r_c is the critical value for absolute instability. The suggestion is that the disturbance continues to propagate radially outwards, even when it passes into the theoretical region of absolute instability. Figure 2.4(b) displays a wavepacket for a disturbance excited within the absolutely unstable region, $r_e > r_c$. Initially the disturbance wavepacket behaves in a manner consistent with absolute instability and large temporal growth. However, the trailing edge of the disturbance wavepacket eventually reverses direction and propagates radially outwards. Thus, for larger times the wavepacket behaves convectively.

On the other hand the flows with positive suction are found to be destabilized by non-parallel effects. For the time period, for which the linearized simulation results could be relied upon, disturbances excited within the absolutely unstable region

exhibit an increasing temporal growth and a radial inward propagation. The study suggests that the absolutely unstable behaviour dominates for all Reynolds numbers, even those found corresponding to radial positions in board of the boundary of absolute instability. Therefore, the disturbance will eventually contaminate the entire spatial region. Disturbances excited in the convective region of instability were found to propagate downstream towards the region of absolute instability (as we would expect). However, on reaching this region, the disturbance displays absolutely unstable characteristics, since the trailing edge of the wavepacket disturbance appears to either asymptote towards a vertical line or reverse direction and propagate radially inwards with a weak velocity.

On comparing the growth rates for the separate cases of uniform injection/suction, there is a distinct increase in growth for an increase in the parameter **a**. Thus, suggesting that mean flows with $\mathbf{a} > 1$ may display stronger growth than those studied previously. Similarly, mean flows with $\mathbf{a} < -1$ may display stronger decay than those seen previously. A future study will be carried out to verify the behaviour of the problems with $|\mathbf{a}| > 1$. Figure 4.28 also indicates that there may exist a value $\mathbf{a}_c$ such that the growth rate tends towards a constant for large time.

The investigated mean flows with uniform suction may be described using the schematic plots, figure 4.30. Again r_c is the critical value for absolute instability and r_e is the location of the impulsive excitation. The first plot depicts a disturbance excited within the region of convective instability. The disturbance propagates radially outwards until it reaches the absolutely unstable domain. On reaching the absolutely unstable region, the trailing edge of the disturbance either propagates towards a vertical line near r_c or reverses direction and begins to propagate radially inward. It is hypothesized that the inward propagation will become more pronounced for larger values of the injection/suction parameter **a**. The second plot displays a wavepacket

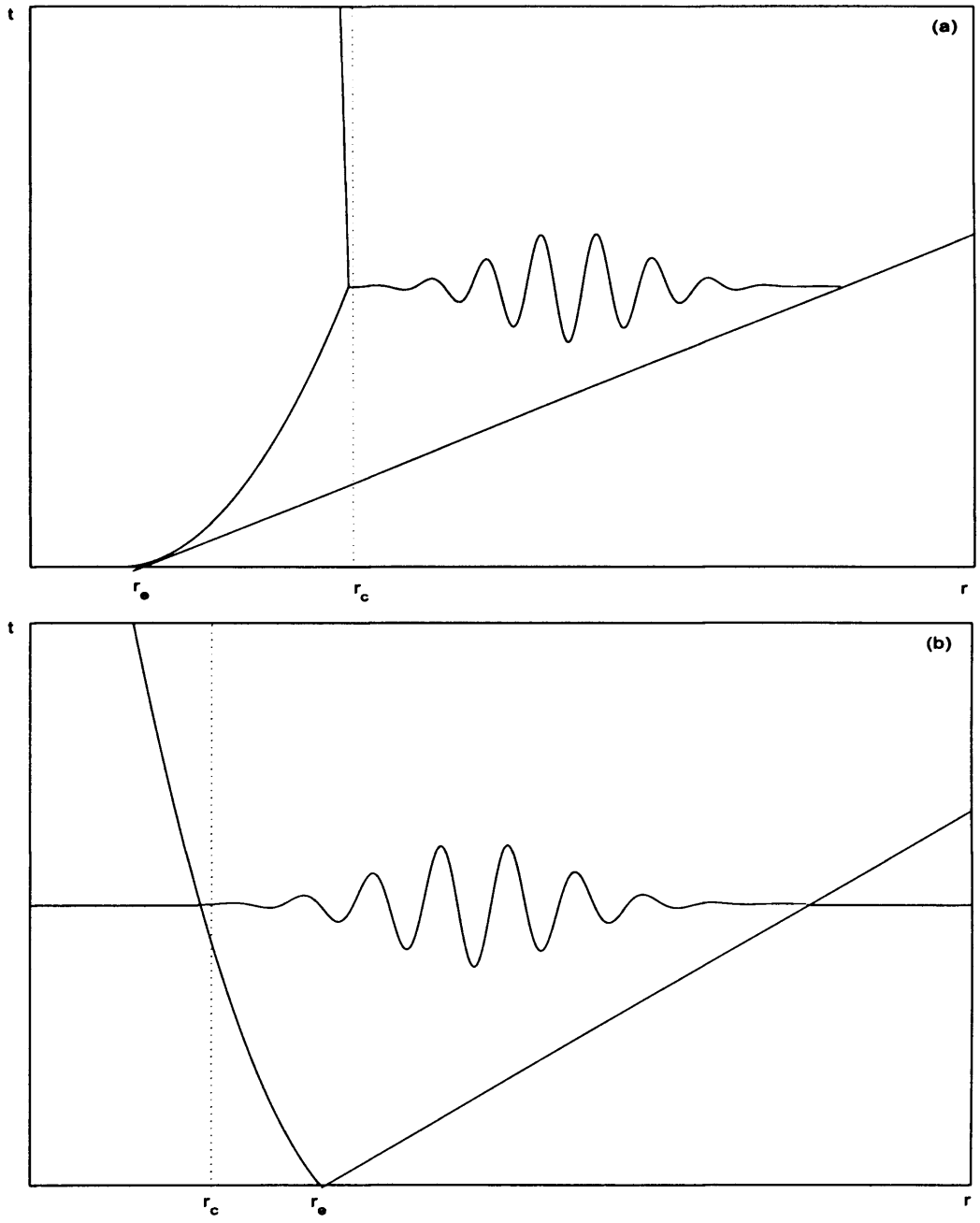

Figure 4.30: *Sketch of a typical wavepacket evolution for the rotating-disk boundary-layer as revealed by the results on rotating-disk flows with normal suction. (a): impulse excitation for* $r_e < r_c$*, (b): Impulse excitation for* $r_e > r_c$.

disturbance centered within the theoretical absolutely unstable region. The study suggests that the trailing edge propagates upstream with an increasing velocity. Thus, exhibiting temporal growth and behaviour consistent with global instability.

The results of the above investigation have come as quite a surprise. Suction is known to be stabilizing, while injection is destabilizing. However, when non-parallel effects are included, flows with suction are found to be destabilized in the region of the theoretical absolute instability. Whether or not disturbances within the rotating-disk boundary-layer with uniform suction produce global instability or eventually dissipate and dampen cannot be determined unequivocally from the time duration limited simulations. Our numerical simulation results strongly suggest the former, albeit without any selection of a dominant frequency, as would be more usual for an unstable global mode. However, it could be that flows with suction initially exhibit regions of temporal growth, and that after a period of time decrease and display temporal decay in a similar style to the flows with injection.

Healey (2005, personal communication) points out that since the Reynolds number and azimuthal mode number are a good deal greater for the flows with suction (than the injection flows), the non-parallel effects are small and insignificant. Therefore the problem is essentially parallel. In the study by Davies & Carpenter (2003) on the rotating-disk with zero mass transfer, convective type behaviour was found for a disturbance excited at $r_e = 750$, which is approximately one and half times the critical Reynolds number for the onset of absolute instability in the von Kármán flow. Such a radial location is of similar size to the problems investigated, with uniform suction $\mathbf{a} = 0.5$; centre of forcing $r_e = 712, 912, 962$. For $\mathbf{a} = 0.5$ the growth rates were found to eventually increase at all radial locations considered. Hence, the reasoning for the difference in behaviour between injection and suction flows, appears to be unaffected by the radial location of impulsive forcing. Evidently longer simulations are required to prove whether temporal growth is intrinsic to rotating-disk flows with

suction. However, at present the numerical iteration scheme restricts the time length of numerical simulations, as has been discussed earlier in the chapter.

As we will see in a later chapter (chapter 7: The global stability of the rotating disk), the global stability can be understood by considering the results at various radii. By considering the parallel flow approximation, the results from the numerical simulations can be plotted using a global non-dimensionalization. The global non-dimensionalization has been used throughout the present study, and was recently described by Davies, Thomas & Carpenter (2007) and further details of the non-dimensionalization are given in chapter 7. The parallel flow results suggest that the global frequency increases linearly with the Reynolds number. Thus, for the genuine non-parallel flow, where the Reynolds number is replaced by the non-dimensional radius, it might be expected that the disturbance frequency would increase linearly with the radius. The stability characteristics of the present chapter can also be understood by making comparisons with the Green's solutions to the Ginzburg-Landau equation (refer to chapter 8).

The results from the present chapter could give a possible reasoning for why previous experimental investigators (Gregory & Walker, 1960) were unable to use suction to extend the laminar flow region to radii corresponding to that given by linear theory. The numerical simulations suggest that suction promotes globally unstable behaviour. Thus, the location for the onset of instability (predicted by stability studies that make use of the parallel flow approximation) may be lowered, causing transition to turbulence to be triggered at radii, which may be smaller than the location of critical absolute instability (predicted by Lingwood, 1997a).

As outlined by Davies & Carpenter (2003) and earlier in the chapter there are many problems that arise for numerical simulations (i.e. convergence problems) and of course the reader may have some critical views of such a study. However, the author took great care when simulating the earlier results and the same behaviour

was found in all cases for various radial lengths, iteration numbers, radial increments Δr, time increments Δt, etc. In order to ensure that the above understanding of the global behaviour is correct, it would be necessary to increase the time period for each simulation. However, due to the constraints of time and convergence problems, this was not feasible.

It should be noted that the results do not invalidate the theory of Lingwood (1997a), or imply that absolute instability does not play a role in the laminar-turbulent transition process. In the cases of uniform injection, local temporal growth in the region of the absolute instability, may be enough to cause the already large convective disturbances to grow at a rapid rate. Thus, triggering the onset of non-linear effects and transition to turbulence. While in the cases of uniform suction, the increasing temporal growth in the region of the absolute instability, may lower the radial location for the onset of non-linear effects and turbulence.

Professor Thomas Corke and Mr Cory McElrath of Notre Dame University in the USA are planning to conduct several experiments on the rotating-disk with uniform suction, to check the disturbance behaviour. This extends the boundary-layer study by Othman & Corke (2006) who investigated the problem with zero suction.

Chapter 5

The rotating-disk boundary-layer with a magnetic field

5.1 Introduction

The flow of an electrically conducting rotating fluid in the presence of a magnetic field has many important engineering applications. It exhibits interesting differences from the more usual non-conducting problem. Magnetic fields are used in the driving and stirring of flows. Magnetohydrodynamic (MHD) systems are also useful in reducing instabilities and suppressing the onset of turbulence. There are a number of applications found in industry, such as the stirring and casting of metals, and in the growth of crystals (Hicks & Riley, 1989; Organ & Riley, 1987).

One of the fundamental aspects of a MHD system, is the formation of a Hartmann layer, which arises due to a balance between the Lorentz[1] and viscous forces. The Hartmann layer forms along the boundary in any electrically conducting fluid. It was first described by Hartmann & Lazarus (1937), and the non-dimensional Hartmann parameter is given as

$$H = \left(\frac{\sigma}{\rho\nu}\right)^{\frac{1}{2}} BL, \tag{5.1}$$

where B is the magnetic field intensity, L is the typical length of the flow, ρ is the

[1]The Lorentz force is the force exerted on a charged particle in an electromagnetic field.

fluid density, ν is the kinematic viscosity and σ is the electrical conductivity of the fluid. A stability analysis of the Hartmann boundary-layer was first carried out by Lock (1955), who neglected the Lorentz force term and found the critical Reynolds number for instability to be $Re_c \approx 50000$. Lingwood & Alboussiere (1999) conducted a stability study on the full equations that include the Lorentz force effects and found $Re_c \approx 48250$. Further theoretical and experimental studies on the Hartmann layer are available by Alboussiere & Lingwood (2000), Moresco & Alboussiere (2003, 2004a,b), and Krasnov, Zienicke, Zikanov, Boeck & Thess (2004).

The flow of an electrically conducting fluid due to a rotating-disk with a uniform normal magnetic field was first investigated (to the authors knowledge) by Sparrow & Cess (1962). In their study they considered the effects of a normal magnetic field on the flow and heat transfer. They found that the presence of a magnetic field decreases the flow velocities. Thus, the magnetic field has a stabilizing effect on the flow. It was also shown that the heat transfer at the disk surface decreased with increasing magnetic field.

Suryaprakasarao & Gupta (1966) have also investigated the rotating-disk flow with a uniform normal magnetic field. The torque experienced by the disk was found to increase with an increase in the magnetic field. The qualitative behaviour of the mean flow was found to resemble that given by the rotating-disk mean flows with uniform normal suction. That is to say that the magnitude of the undisturbed flow over the disk decreases.

The rotating-disk flow with a circular magnetic field has been investigated by Pao (1968). The circular magnetic field was found to increase the boundary-layer thickness. Thus, such magnetic fields are considered to be destabilizing. Above some critical value of the magnetic field, Pao found that the boundary-layer separated from the disk surface.

Further studies on MHD flows have been carried out by Stephenson (1969), Kumar, Thacker & Watson (1987) and Thacker, Watson & Kumar (1990). Stephenson (1969) conducted a theoretical and experimental study on the MHD flow between two rotating coaxial disks with a uniform axial magnetic field. While Kumar *et al.* (1987) and Thacker *et al.* (1990) looked at the effects of a circular magnetic field and a normal magnetic field, respectively.

Aboul-Hassan & Attia (1997), Attia & Aboul-Hassan (2001, 2004) have studied the MHD mean flow due to a rotating-disk with Hall effect. The Hall effect is caused by the current flow (which is made up of many small charged electrons) in a conductor. The magnetic field exerts a force (Lorentz force) on the electrons, which tends to push them towards one side of the conductor. This phenomenon was first discovered and later named after, by *Sir Edwin Hall* in 1879. It is worth noting that the Hall effect only needs to be considered if the conductor is large.

In the studies by Aboul-Hassan & Attia, the MHD mean flow over a rotating-disk is considered with a uniform axial magnetic field. They solved the resulting system of ordinary differential equations using finite difference approximations. For large positive values of the Hall parameter, the magnetic field enlarges the velocity profiles in the radial and normal directions. More interestingly, for some values of the Hall term, the radial and normal velocity components reverse direction. This is due to the magnetic force exceeding the centrifugal force (Aboul-Hassan & Attia, 1997; Attia & Aboul-Hassan, 2004).

5.1.1 Absolute instability

Jasmine (2003), Jasmine & Gajjar (2005a) conducted a stability analysis on the rotating-disk flow with a uniform normal magnetic field. In their study they neglected the Hall effect. The mean flow profiles were solved using a finite-difference scheme and were found to agree with that found by previous authors.

For a magnetic field strength parameter m (defined in the subsequent section), it was found that increasing m is generally stabilizing. For $m = 0$ (i.e. zero magnetic field), the critical Reynolds numbers for the stationary convective instabilities were given as $Re_1 = 285.9$ and $Re_2 = 451.4$, respectively. While for $m = 1$, the respective critical Reynolds numbers were given as $Re_1 = 1278.4$ and $Re_2 = 2214.1$. The travelling modes were also stabilized by increasing m. For a frequency $\omega = 7.9$ and $m = 0$, $Re_1 = 316.51$ and $Re_2 = 64.45$, while for $m = 1$, $Re_1 = 1317.8$ and $Re_2 = 1061.1$. Here the subscripts 1 and 2 refer to the Type-1 and Type-2 modes, described in chapters 2 and 4.

Using similar methods as Lingwood (1995), Jasmine (2003), Jasmine & Gajjar (2005a) were able to show that there also exists regions of absolute instability in the flows with a uniform normal magnetic field. The onset of absolute instability is suppressed by the introduction of a magnetic field. For $m = 0$ the critical Reynolds number for absolute instability is $Re_c = 507.06$, while for $m = 0.5$, $Re_c = 1091.9$.

It is worth noting that throughout the investigation by Jasmine (2003), Jasmine & Gajjar (2005a), the parallel flow approximation was employed; the radial dependence of the mean flow is ignored.

In the present chapter, the problem considered is similar to that given by Jasmine (2003), Jasmine & Gajjar (2005a). It is assumed that the effects due to the electric field are negligible and that the fluid motion has no affect on the magnetic field. The only additional term to be considered in the governing equations is due to the Lorentz force. By considering the above assumptions, the magnetic Reynolds number (to be defined later) is assumed to be small $Re_m << 1$.

By extending the velocity-vorticity formulation of Davies & Carpenter (2001) to include flows with a normal magnetic field, we are able to study flows with and without the parallel flow approximation. The parallel flow simulations produce behaviour that is equivalent to the theory of Jasmine (2003), Jasmine & Gajjar (2005a). If the

flow parameters lie within the theoretical absolutely unstable region, the simulations always exhibit equivalent behaviour. Likewise for convective instability. However, the non-parallel simulations produce quite different behaviour. The results are similar to those given in the previous chapter for the mean flows with uniform suction. There appears to be a tendency for disturbances to exhibit an increasing temporal growth rate. The study suggests that for cases with a sufficiently strong magnetic field, temporal growth will eventually dominate the flow. On comparing the temporal growth rates for each flow, the study also suggests that the growth rates increase with increasing magnetic field. (An abstract of the present investigations was recently discussed by Davies & Thomas (2006)).

The remainder of this chapter is outlined as follows; in section 5.2 the mean flow equations and the extended velocity-vorticity formulation by Davies & Carpenter (2001) are discussed. Section 5.3 contains results for several cases of the uniform magnetic field parameter m, and their growth rates are compared. The cases investigated are for $m = 0.0, 0.1, 0.2, 0.5, 0.4$ and 0.5. Finally conclusions are given in section 5.5.

5.2 Rotating-disk theory

5.2.1 The mean flow

The three-dimensional boundary-layer is the same as that outlined in chapter 4. The only difference is that the fluid is now electrically conducting and a uniform magnetic field $\mathbf{B} = B_0\mathbf{k}$ is applied to the system, where $\mathbf{k}$ is a unit vector parallel to the normal direction. The magnetic field strength B_0 is measured in units of Tesla. The effects of the electric field are assumed to be negligible and the magnetic field is unaffected by the fluid motion. There is only one additional force term to be included in the momentum equations, the Lorentz force, which is given as $(\mathbf{J} \wedge \mathbf{B})$. Here $\mathbf{J}$ is the

current density, defined as

$$\mathbf{J} = \sigma^*(\mathbf{E} + \mathbf{U}^* \wedge \mathbf{B} - \beta^*(\mathbf{J} \wedge \mathbf{B})), \tag{5.2}$$

for an electric field $\mathbf{E}$ and velocity $\mathbf{U}^* = (U_r^*, U_\theta^*, U_z^*)$. Here σ^* is the electrical conductivity of the fluid and the last term in equation (5.2) describes the Hall effect, where $\beta^* = 1/n^*q^*$ is the Hall factor, for n^* the electron concentration per unit volume and $-q^*$ the charge of the electron.

The momentum and continuity equations in cylindrical polar coordinates are now given as

$$\begin{aligned}\frac{\partial U_r^*}{\partial t^*} + (\mathbf{U}^*.\nabla)U_r^* - \frac{U_\theta^{*2}}{r} - 2\Lambda^* U_\theta^* &= -\frac{1}{\rho^*}\frac{\partial P^*}{\partial r^*} + \nu^*\left(\nabla^2 U_r^* - \frac{U_r^*}{r^{2*}} - \frac{2}{r^{2*}}\frac{\partial U_\theta^*}{\partial \theta^*}\right) \\ &\quad - \frac{\sigma^* B_0^2}{\rho^*(1+H_a^2)}(U_r^* - H_a U_\theta^*),\end{aligned} \tag{5.3}$$

$$\begin{aligned}\frac{\partial U_\theta^*}{\partial t^*} + (\mathbf{U}^*.\nabla)U_\theta^* + \frac{U_\theta^* U_r^*}{r} + 2\Lambda^* U_r^* &= -\frac{1}{r^*\rho^*}\frac{\partial P^*}{\partial \theta^*} + \nu^*\left(\nabla^2 U_\theta^* - \frac{U_\theta^*}{r^{2*}} + \frac{2}{r^{2*}}\frac{\partial U_r^*}{\partial \theta^*}\right) \\ &\quad - \frac{\sigma^* B_0^2}{\rho^*(1+H_a^2)}(U_\theta^* + H_a U_r^*),\end{aligned} \tag{5.4}$$

$$\frac{\partial U_z^*}{\partial t^*} + (\mathbf{U}^*.\nabla)U_z^* = -\frac{1}{\rho^*}\frac{\partial P^*}{\partial z^*} + \nu^*\nabla^2 U_z^*, \tag{5.5}$$

$$\frac{1}{r^*}\frac{\partial (r^* U_r^*)}{\partial r^*} + \frac{1}{r^*}\frac{\partial U_\theta^*}{\partial \theta^*} + \frac{\partial U_z^*}{\partial z^*} = 0, \tag{5.6}$$

where P^* denotes the mean pressure, Λ^* the constant angular velocity, ν^* the kinematic viscosity and ρ^* the fluid density. (Where $*$ denotes dimensional quantities). Here $H_a = \sigma^*\beta^* B_0$ is the Hall parameter. However, for the present study, the Hall effects are neglected, i.e. $H_a = 0$.

The above momentum and continuity equations are coupled with

$$\frac{\partial \mathbf{B}}{\partial t} = \nabla \wedge (\mathbf{U} \wedge \mathbf{B}) + \frac{1}{Re_m}\nabla^2 \mathbf{B}, \tag{5.7}$$

which is known as the induction equation[1] and

$$\nabla.\mathbf{J} = 0, \qquad \nabla \wedge \mathbf{E} = -\frac{\partial \mathbf{B}}{\partial t}, \qquad \nabla.\mathbf{B} = 0, \tag{5.8}$$

to form the full system of governing equations for the present MHD problem. The first expression in (5.8) is the continuity equation[2], the second expression is Faraday's law of magnetic induction[3] and the final equation is the solenoidal condition for the magnetic induction[4]. Here $Re_m = \sigma^* \mu_0^* \Lambda^* \delta^{*2}$ is the magnetic Reynolds number, where μ_0^* is the magnetic permeability of free space and $\delta^* = (\nu^*/\Lambda^*)^{\frac{1}{2}}$ is the boundary-layer displacement thickness. For many liquid metals the magnetic Reynolds number is usually a great deal smaller than the Reynolds number of the fluid. In Jasmine & Gajjar (2005a) an example is given for mercury at a temperature of 30^o. The corresponding magnetic Reynolds number is found to be of the order 10^{-7} times smaller than the Reynolds number of the fluid. For such problems, we may neglect the effect of the fluid motion on the magnetic field.

On substituting the von Kármán similarity variables (4.5) into the momentum equations (5.3) - (5.5) and continuity equation (5.6), we obtain the following non-dimensional mean flow equations

$$F^2 + F'H - (G+1)^2 + mF = F'', \tag{5.9}$$

$$2F(G+1) + G'H + m(G+1) = G'', \tag{5.10}$$

$$P' + H'H = H'', \tag{5.11}$$

$$2F + H' = 0, \tag{5.12}$$

[1]The induction equation: a local change in the magnetic field is due to both convection and diffusion effects

[2]The divergence of the current density is equal to the rate of change in charge density, which is zero here.

[3]A spatially varying electric field can induce a magnetic field

[4]There are no sources or sinks for the magnetic field lines.

where the prime denotes differentiation with respect to the normal component z. Equations (5.9)-(5.12) are solved subject to the boundary conditions

$$F(0) = G(0) = H(0) = P(0) = 0, \tag{5.13}$$

$$F(z \to \infty) = 0, \qquad G(z \to \infty) = -1, \tag{5.14}$$

where $m = \frac{\sigma^* B_0^2}{\rho^* \Lambda^*}$ is the magnetic interaction parameter. The non-dimensional undisturbed flow, Reynolds number and non-dimensional rotation rate are again given by (4.12) - (4.14).

The above system of ordinary differential equations may be solved using an adapted version of the Matlab code, given for the suction/injection problem; refer to the appendices.

m	$F'(0)$	$G'(0)$	$H(\infty)$
0.0	0.51023262	-0.61592206	-0.88447339
0.0	*0.511*	*-0.616*	*-0.885*
0.0	**0.5102**	**-0.6159**	**-0.88447**
0.2	0.45314093	-0.70879532	-0.68347665
0.5	0.38513261	-0.84872383	-0.45888038
0.5	*0.385*	*-0.849*	*-0.459*
0.5	**0.3851**	**-0.8487**	**-0.45887**
1.0	0.30925802	-1.06905332	-0.25331430
1.0	*0.310*	*-1.069*	*-0.253*
1.0	**0.3092**	**-1.0690**	**-0.25331**
2.0	0.23055923	-1.44209393	-0.10858375
2.0	*0.231*	*-1.442*	*-0.109*
2.0	**0.2305**	**-1.4420**	**-0.10858**
5.0	0.14851930	-2.24345218	-0.02940157

Table 5.1: *Values of F', G' at $z = 0$ and H at infinity for various values of m. Results: roman - current thesis; italics - Sparrow & Cess (1962); bold - Jasmine (2003).*

Figure 5.1 displays the radial, azimuthal and normal mean velocity profiles for the rotating-disk flow, with m = 0.0, 0.5, 1, 2 and 5. The maximum magnitude

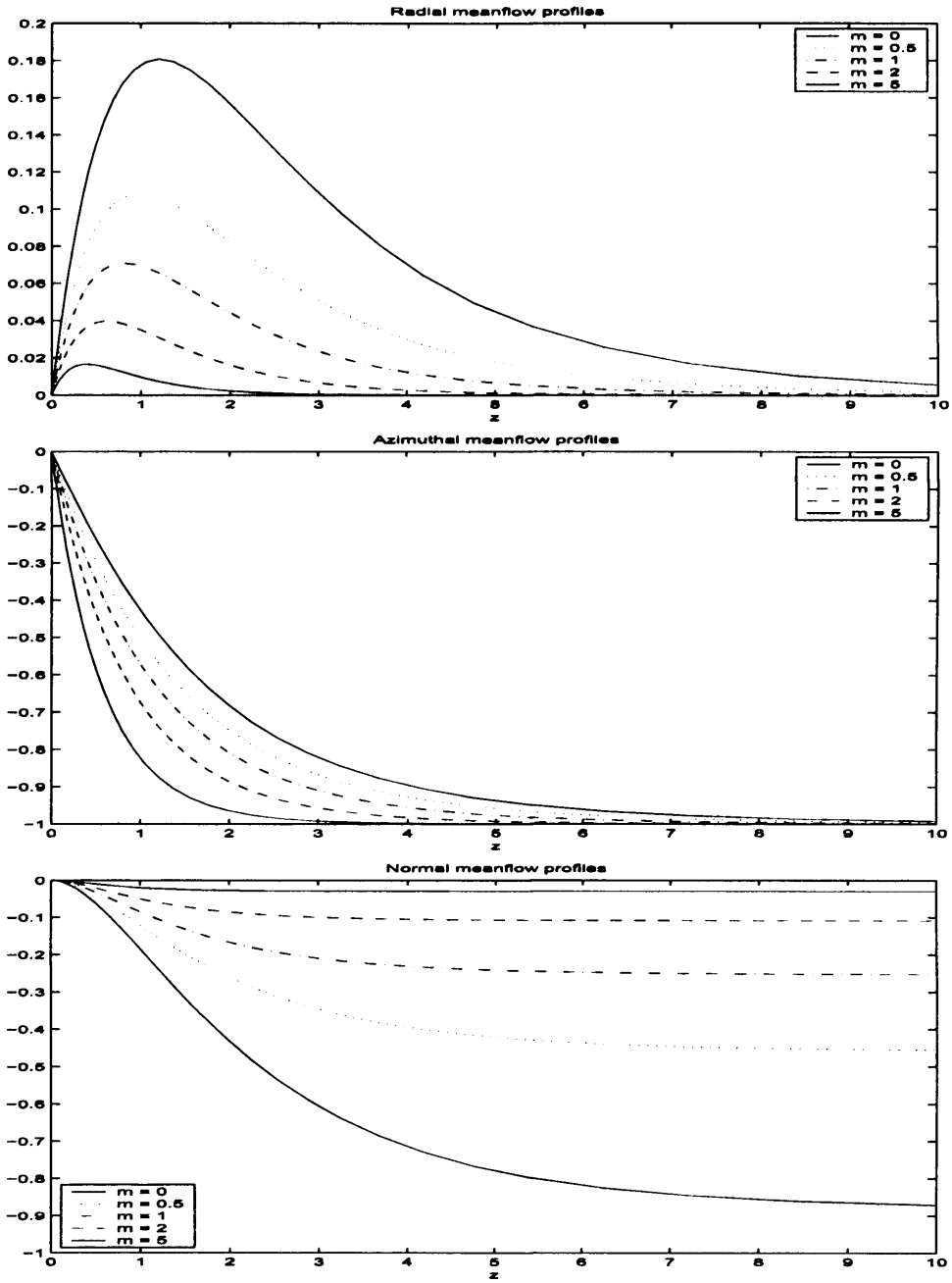

Figure 5.1: *The mean flow velocity profiles for the radial (F), azimuthal (G) and normal (H) components for different values of m.*

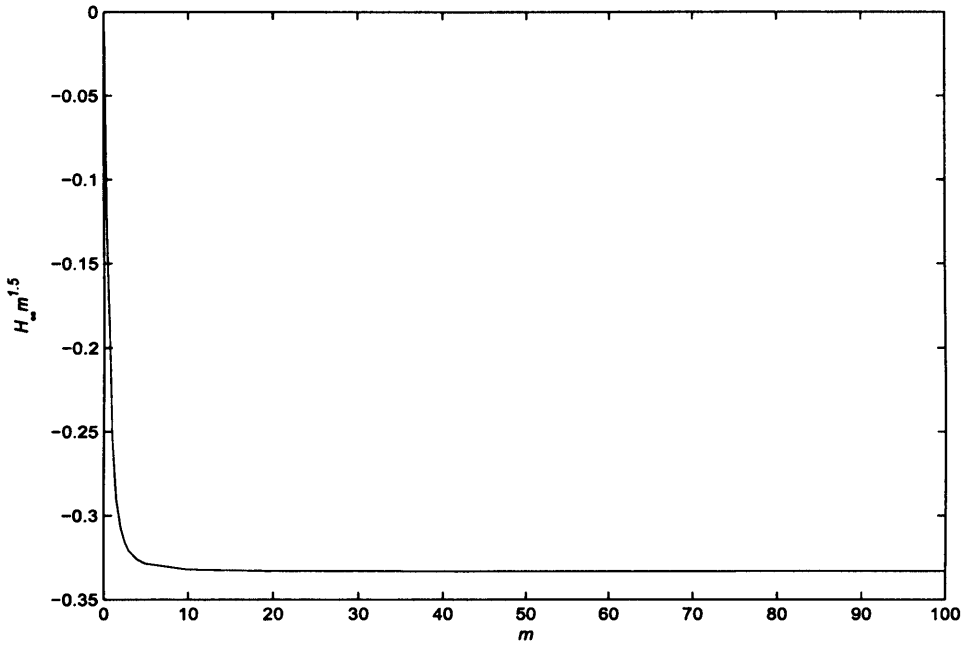

Figure 5.2: *Plot of the magnetic field parameter m against $H_\infty m^{1.5}$.*

corresponding to the radial velocity component, decreases with increasing m. The same is true of the magnitude of the normal component at infinity. Table 5.1 gives (to eight decimal places) F', G' at $z = 0$, and H as $z \to \infty$ for various values of m, which agree with the earlier tabulated results of Sparrow & Cess (1962) (italics) and Jasmine (2003) (bold). It was shown by Sparrow & Cess (1962) that as m increases, the mean velocity terms $F'(0)$, $G'(0)$ and $H(\infty)$ behave as follows,

$$G'(0) = -\sqrt{m}, \quad F'(0) = \frac{1}{3\sqrt{m}}, \quad H(\infty) = -\frac{1}{3m^{\frac{3}{2}}}. \tag{5.15}$$

The approximate solutions and tabulated results are plotted in figure 5.3. While figure 5.2 displays a plot of $H_\infty m^{1.5}$ against m, where $H_\infty = H(\infty)$. As m increases, $H_\infty m^{1.5}$ can be seen to asymptote to approximately $-1/3$.

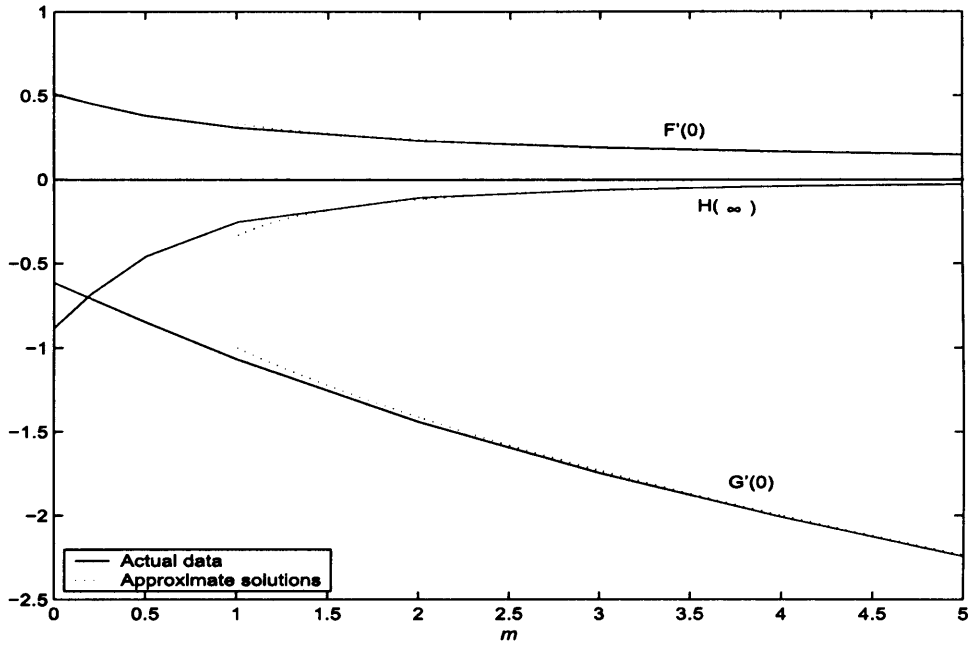

Figure 5.3: *Variations in $F'(0)$, $G'(0)$ and $H(\infty)$, for various values of m, with approximate solutions (5.15).*

5.2.2 Velocity-vorticity formulation

For velocity $\underline{u} = \{u_r, u_\theta, u_z\}$ and vorticity $\underline{\omega} = \{\omega_r, \omega_\theta, \omega_z\}$ perturbation fields, the velocity-vorticity formulation of chapter 4, is now given by

$$\frac{\partial \omega_r}{\partial t} + \frac{1}{r}\frac{\partial N_z}{\partial \theta} - \frac{\partial N_\theta}{\partial z} - 2\Lambda\left\{\omega_\theta + \frac{\partial u_z}{\partial r} - \frac{m}{2}\left(\omega_r - \frac{1}{r}\frac{\partial u_z}{\partial \theta}\right)\right\} = \frac{1}{Re}\left(\left(\nabla^2 - \frac{1}{r^2}\right)\omega_r - \frac{2}{r^2}\frac{\partial \omega_\theta}{\partial \theta}\right), \tag{5.16}$$

$$\frac{\partial \omega_\theta}{\partial t} + \frac{\partial N_r}{\partial z} - \frac{\partial N_z}{\partial r} + 2\Lambda\left\{\omega_r - \frac{1}{r}\frac{\partial u_z}{\partial \theta} + \frac{m}{2}\left(\omega_\theta + \frac{\partial u_z}{\partial r}\right)\right\} = \frac{1}{Re}\left(\left(\nabla^2 - \frac{1}{r^2}\right)\omega_\theta + \frac{2}{r^2}\frac{\partial \omega_r}{\partial \theta}\right), \tag{5.17}$$

$$\nabla^2 u_z = \frac{1}{r}\left(\frac{\partial \omega_r}{\partial \theta} - \frac{\partial (r\omega_\theta)}{\partial r}\right), \tag{5.18}$$

where the convection term $\mathbf{N}$ is defined by equations (4.22) - (4.25) and $\{\omega_r, \omega_\theta, u_z\}$ are taken to be the primary variables. The remaining secondary variables $\{u_r, u_\theta, \omega_z\}$

are again defined by (4.27) - (4.29).

Also, the system has been linearized, which allows modes to be separable with respect to the azimuthal direction (4.30). Finally, equations (4.34) - (4.36) are again taken to provide integral constraints on the primary variables.

Introducing the Lorentz force to the velocity-vorticity equations

The non-dimensional Lorentz force terms in the Navier-Stokes equations (5.3) - (5.4) are given by

$$\text{L.F.} = \{m\Lambda u_r, m\Lambda u_\theta, 0\}. \tag{5.19}$$

where L.F. denotes the Lorentz force, m is the magnetic field parameter and Λ is the angular velocity of the rotating-disk. (Note: we have moved the Lorentz force terms to the left-hand-side of equations (5.3) - (5.4), to remove the negative signs). On taking the curl of (5.19), we obtain

$$\text{L.F.} = \left\{ -m\Lambda\frac{\partial u_\theta}{\partial z}, m\Lambda\frac{\partial u_r}{\partial z}, \frac{m\Lambda}{r}\left(\frac{\partial (ru_\theta)}{\partial r} - \frac{\partial u_r}{\partial \theta}\right)\right\}. \tag{5.20}$$

Then by taking z-derivatives of the secondary variable definitions (4.27) and (4.28), we obtain

$$\frac{\partial u_r}{\partial z} = \omega_\theta + \frac{\partial u_z}{\partial r}, \tag{5.21}$$

$$\frac{\partial u_\theta}{\partial z} = \frac{1}{r}\frac{\partial u_z}{\partial \theta} - \omega_r, \tag{5.22}$$

which on substituting into equation (5.20), gives the Lorentz force terms appearing in the governing equations (5.16) - (5.17).

5.3 Results

Disturbances were impulsively excited using a wall motion, defined in equations (4.37) and (4.38). Table 5.2 displays the critical values for the onset of absolute instability,

for various values of m that were obtained using the parallel flow approximation. Re_c is the Reynolds number, β_c is the azimuthal wavenumber, $n_c = \beta_c Re_c$ is the integer valued azimuthal mode number (for Jasmine's results, n_c has been rounded to the nearest integer), α_c is the radial wavenumber and ω_c and $\omega_c Re_c$ are the non-dimensional temporal frequencies. The results in italic are those found (using the parallel flow approximation) by Jasmine (2003), Jasmine & Gajjar (2005a), while the data in bold refers to the results of the numerical simulations, found here. For the numerical simulations, the Reynolds number and azimuthal mode number have been rounded to integer values. This was done, to avoid excessive parametric studies.

m	Re_c	β_c	n_c	ω_c	α_c	$\omega_c\ Re_c$
0.0	*507.30*	*0.1348*	*68*	*-0.03485*	*0.2173 - i0.1216*	*-17.679*
0.0	**508**		**68**	**-0.03435**	**0.2192 - i0.1153**	**-17.451**
0.1	*594.32*	*0.128*	*76*	*-0.03402*	*0.2235 - i0.1177*	*-20.22*
0.1	**595**		**76**	**-0.03358**	**0.2233 - i0.1096**	**-19.98**
0.2	*695.97*	*0.124*	*86*	*-0.03338*	*0.2314 - i0.1147*	*-23.23*
0.2	**696**		**86**	**-0.03334**	**0.2314 - i0.1078**	**-23.21**
0.3	*812.88*	*0.118*	*96*	*-0.03208*	*0.2399 - i0.1130*	*-26.08*
0.3	**813**		**96**	**-0.03205**	**0.2396 - i0.1050**	**-26.06**
0.4	*945.36*	*0.113*	*107*	*-0.03105*	*0.2498 - i0.1116*	*-29.35*
0.4	**946**		**107**	**-0.03100**	**0.2492 - i0.1043**	**-29.33**
0.5	*1091.90*	*0.109*	*119*	*-0.03027*	*0.2609 - i0.1106*	*-33.05*
0.5	**1092**		**119**	**-0.03023**	**0.2600 - i0.1012**	**-33.02**

Table 5.2: *Critical values for the onset of absolute instability as found by Jasmine (2003), Jasmine and Gajjar (2005a). The values in bold correspond to the values found here.*

The results obtained from the numerical simulations are almost identical to those obtained by Jasmine's linear stability theory. The complex temporal frequencies ω_c are (to three decimal places) the same as those given by Jasmine (2003). The frequencies (given in bold in figure 5.2) were calculated at the radial point of excitation

$r = r_e$. The frequency at r_e was constant for all time, after the initial transient phase. While the temporal frequency at all other radial positions was found to asymptote towards the same constant ω_c. The temporal growth rates were also all found to converge towards the same constant value. For the cases here, the constant was approximately zero, since the disturbances are excited at the point of critical absolute instability.

The radial wavenumbers α_c (in bold) are also consistent (to two decimal places in most cases) with the results of Jasmine (2003).

As mentioned previously, if the circumferential periodicity of the problem is to be satisfied, the azimuthal mode number $n = \beta Re$ can only take on integer values. Therefore, to ensure that n remains constant for all simulations, the azimuthal wavenumber β must be varied accordingly.

Further validation checks on the stationary convective modes are given in the appendices. We will now investigate the rotating-disk boundary-layer with an axial magnetic field, where the magnetic field parameter $m = 0.2$, 0.4 and 0.5.

5.3.1 $m = 0.2$

For the magnetic field parameter $m = 0.2$, Jasmine (2003) found absolute instability to first arise for a Reynolds number $Re = 696$ and an azimuthal mode number $n = 86$.

A disturbance was impulsively excited at the boundary of absolute instability; $r_e = 696$ and $n = 86$. The corresponding non-parallel wavepacket is plotted in figure 5.4. The leading and trailing edges of the disturbance wavepacket are easily identified. The leading edge propagates radially outwards with what appears to be a constant velocity, while the trailing edge appears to be propagating with a diminishing velocity. Thus, it appears that we may eventually obtain behaviour comparable with critical absolute instability.

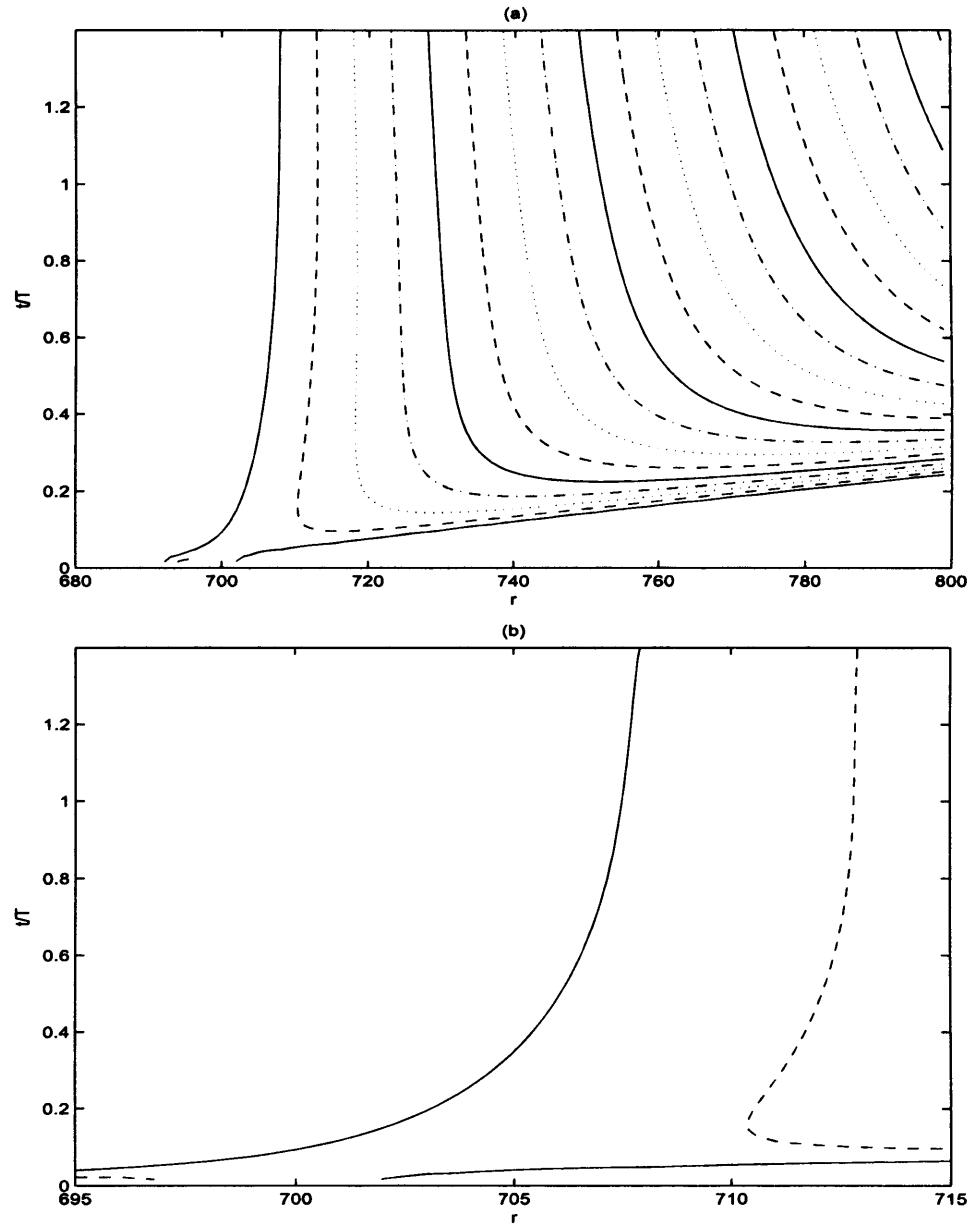

Figure 5.4: *Spatio-temporal development of* $|\omega_{\theta,w}|$ *for an impulsively excited disturbance in a non-parallel flow with a magnetic interaction parameter* $m = 0.2$. *The azimuthal mode number is* $n = 86$ *and the disturbance was excited at* $r_e = 696$. *(a) - full radial range, (b) - reduced radial range.*

The temporal frequencies and growth rates for the above disturbance are plotted in figure 5.5, which are calculated by the complex-valued quantity (4.39). The lines labeled P refer to the data obtained from the parallel flow numerical simulations. The frequency is comparable with that given by Jasmine (2003) (refer to table 5.2), and the growth rate is found to tend towards zero, which would indicate critical absolute instability. For the non-parallel simulation, the frequencies and growth rates are plotted for four equally spaced radial locations; r_e - 25, $r_e = 696$, $r_e + 25$ and $r_e + 50$. The frequencies increase at all locations with increasing time. This is analogous behaviour to that found in the previous chapter, for a rotating-disk with uniform mass transfer. The corresponding growth rates appear to be asymptoting towards a constant. Such behaviour is not too dissimilar to that observed in the flows with uniform suction, where temporal growth was observed.

A second disturbance was excited for $r_e = 796$ and $n = 86$. Figure 5.6 displays the corresponding frequencies and growth rates. Again the frequencies are increasing, but now the growth rates are decreasing, suggesting that given sufficient time we may observe temporal decay.

For the earlier disturbance $r_e = 696$, the growth rates (figure 5.5) appear to be approaching a constant, but it could be that they do indeed decrease and display temporal decay at larger locations in time.

Figure 5.7 displays the spatio-temporal development for a non-parallel disturbance excited at $r_e = 596$. This is located radially inwards of the critical radius for absolute instability. The disturbance can be seen to initially convect radially outwards. However, the trailing edge can be seen to slow down as it nears the region of absolute instability. Nonetheless, it is not possible to discern the long term behaviour of the disturbance, as the trailing edge may continue to propagate radially outwards in a convective manner or it may eventually reverse direction and display globally unstable characteristics.

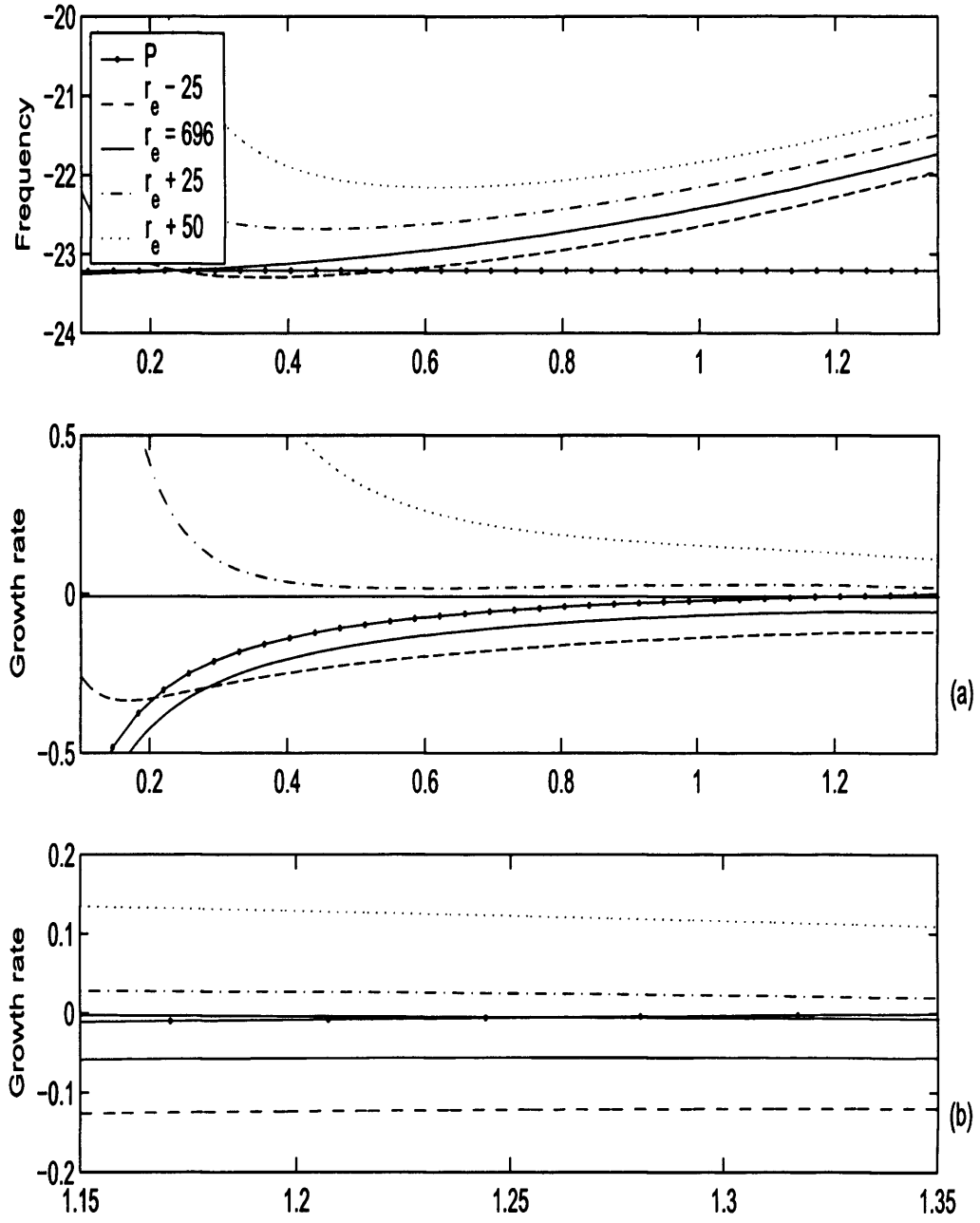

Figure 5.5: *Local temporal frequencies $\omega_r Re$ and temporal growth rates $\omega_i Re$ for a disturbance with $n = 86$ developing in a non-parallel flow with a magnetic interaction parameter $m = 0.2$, centred at $r_e = 696$. The temporal development is plotted for four different radial positions, r_e - 25, r_e, r_e + 25 and r_e + 50. The solid lines labeled with a P show the development in a parallel flow with $Re = 696$. The temporal growth rates are displayed over a full time range, (a), and for a reduced time range, (b).*

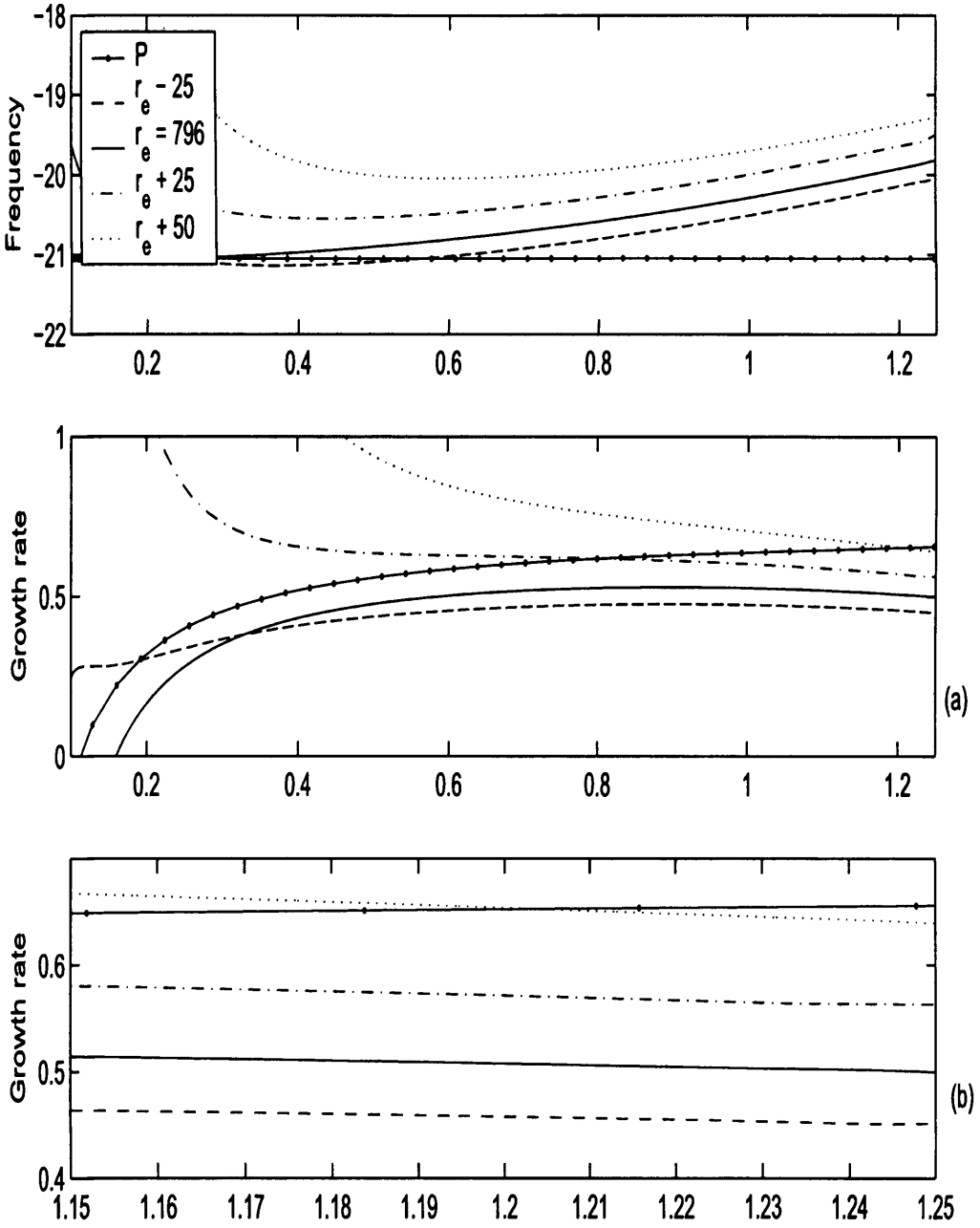

Figure 5.6: *Local temporal frequencies $\omega_r Re$ and temporal growth rates $\omega_i Re$ for a disturbance with $n = 96$ developing in a non-parallel flow with a magnetic interaction parameter $m = 0.2$, centred at $r_e = 796$. The temporal development is plotted for four different radial positions, r_e - 25, r_e, r_e + 25 and r_e + 50. The solid lines labeled with a P show the development in a parallel flow with $Re = 796$. The temporal growth rates are displayed over a full time range, (a), and for a reduced time range, (b).*

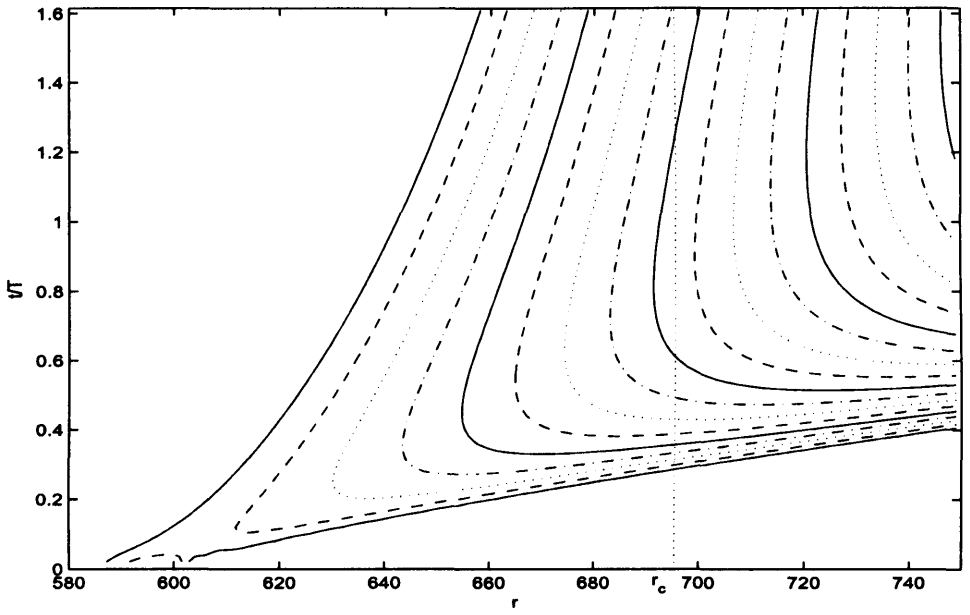

Figure 5.7: *Spatio-temporal development of* $|\omega_{\theta,w}|$ *for an impulsively excited disturbance in a non-parallel flow with a magnetic interaction parameter* $m = 0.2$. *The azimuthal mode number is* $n = 86$ *and the disturbance was excited at* $r_e = 596$.

A greater understanding of the long term features of the disturbance can be obtained by looking at the temporal growth rates at various radial locations. Figure 5.8 displays the growth rates at $r_e = 596$, r_e+25, r_e+50, $r_e + 100$ and $r_e + 150$. There is a small increase in growth for the radial positions $r \leq r_e + 50$, while there is a steady decrease in growth for all greater radial locations. Indeed for $r = 696 = r_e + 100$ (which corresponds to the radial location for the onset of absolute instability) temporal decay is found. Thus, it seems likely that the disturbance will continue to convect radially outwards, even when the disturbance has arrived at the region of absolute instability.

For $m = 0.2$ it is possible that convective behaviour will eventually dominate the disturbance response. However, the convective behaviour is not as obvious as it was

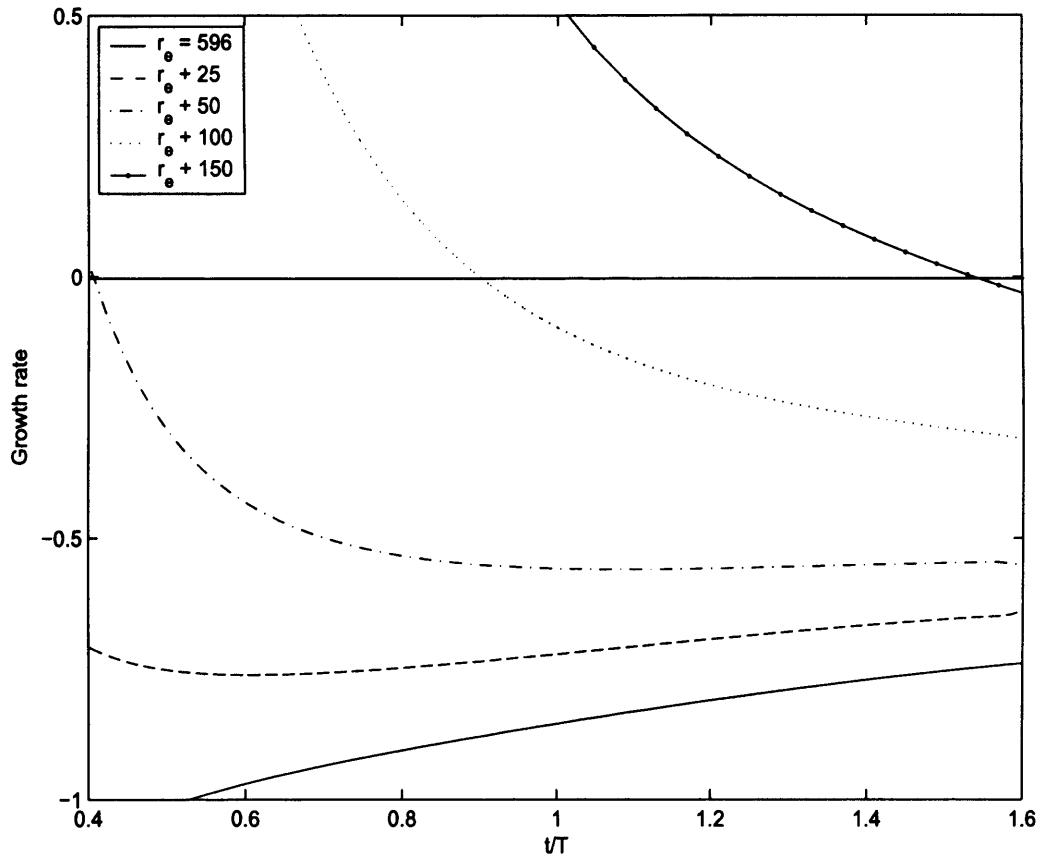

Figure 5.8: *Local temporal growth rates $\omega_i Re$ for a disturbance with $n = 86$ developing in a non-parallel flow with a magnetic interaction parameter $m = 0.2$, centred at $r_e = 596$. The temporal development is plotted for five different radial positions, r_e, $re + 25$, $r_e + 50$, $r_e + 100$ and $r_e + 150$.*

in the rotating-disk boundary-layer; Davies & Carpenter (2003).

As mentioned in the previous chapter, simulations for large time, which would show the long term response of the disturbance, were difficult to obtain. This was due to convergence problems with the iteration scheme. However, on comparing the present problem with that investigated by Davies & Carpenter (2003) (rotating-disk

with $m = 0$), we can say that the convective dominance is reduced and that temporal growth plays some small role in the disturbance development.

5.3.2 $m = 0.4$

For $m = 0.4$ the critical Reynolds number for absolute instability is given as $Re_c = 946$ for an azimuthal mode number $n = 107$; Jasmine (2003). We excited a disturbance at the radial location $r_e = 946$. Figure 5.9 displays the corresponding frequencies and growth rates. The lines labeled P refer to the frequencies and growth rates, obtained for the simulations, where the parallel flow approximation has been used. For the non-parallel flow, the frequencies increase at all selected radial locations. The corresponding growth rates are found to increase at a steady rate at all locations, and temporal growth is found for all radial locations $r \geq r_e = 946$. Thus, the behaviour is similar to that observed in the earlier simulations with uniform suction.

Figure 5.10 displays the frequencies/growth rates for a disturbance excited further into the region of absolute instability; $r_e = 996$ and $n = 107$. The growth rates are again found to increase at a steady rate, and for the given radial locations, temporal growth is observed.

The spatio-temporal development of a disturbance excited radially inwards of the boundary of absolute instability is plotted in figure 5.11. The radial location of excitation is $r_e = 896$ and the azimuthal mode number $n = 107$. The trailing edge of the wavepacket can be seen to initially propagate radially outwards, but as it nears the region of absolute instability, it appears to asymptote towards a line, parallel to the vertical direction.

The growth rates for this disturbance are displayed in figure 5.12 and are plotted for the radial locations $r_e = 896$, $re+25$, r_e+50, $r_e + 100$. For $r \leq r_e+50$ the growth rates increase at all given locations. Although temporal decay is currently being observed for these locations, it appears that given sufficient time, temporal growth

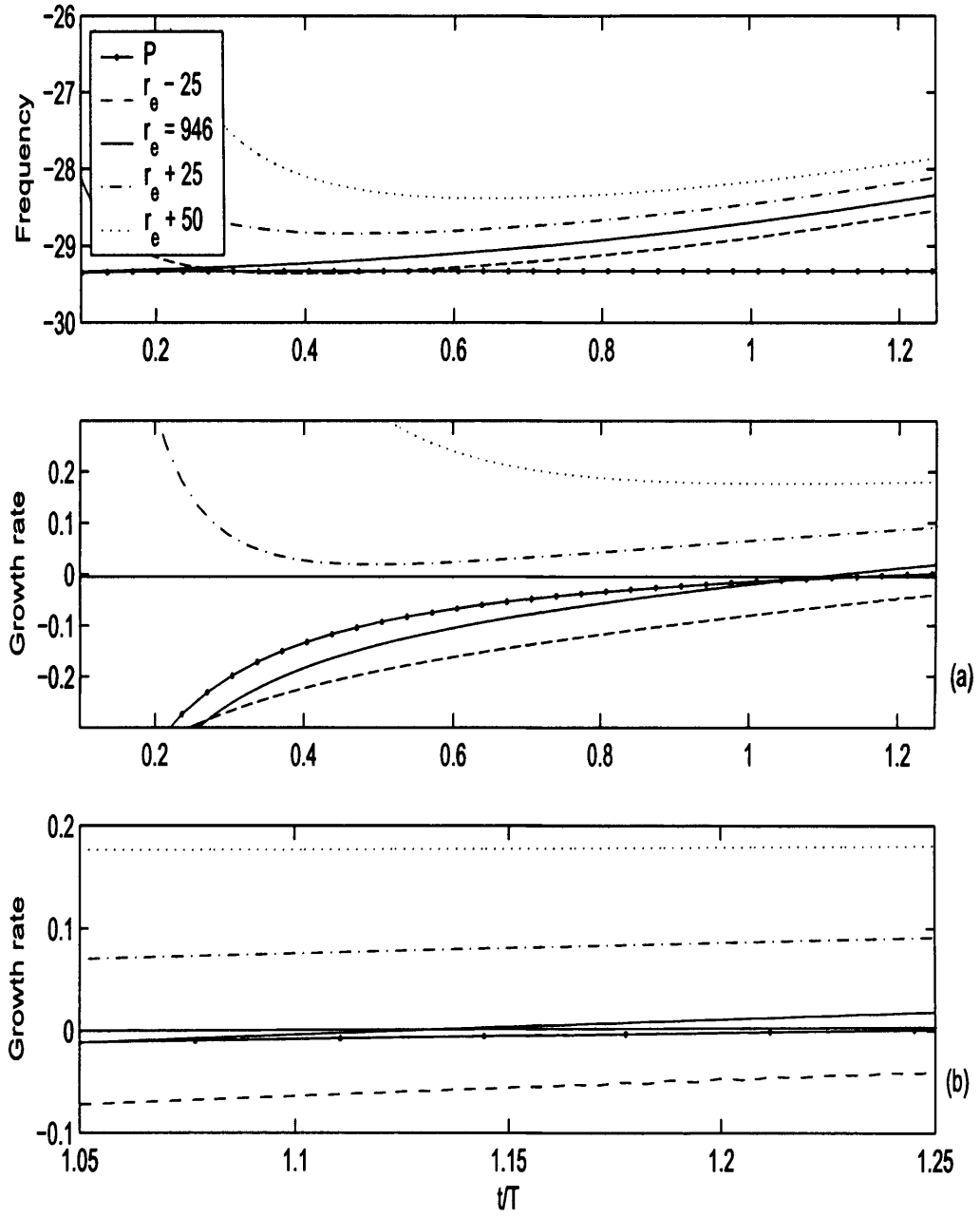

Figure 5.9: *Local temporal frequencies $\omega_r Re$ and temporal growth rates $\omega_i Re$ for a disturbance with $n = 107$ developing in a non-parallel flow with a magnetic interaction parameter $m = 0.4$, centred at $r_e = 946$. The temporal development is plotted for four different radial positions, r_e - 25, r_e, r_e + 25 and r_e + 50. The solid lines labeled with a P show the development in a parallel flow with $Re = 946$. The temporal growth rates are displayed over a full time range, (a), and for a reduced time range, (b).*

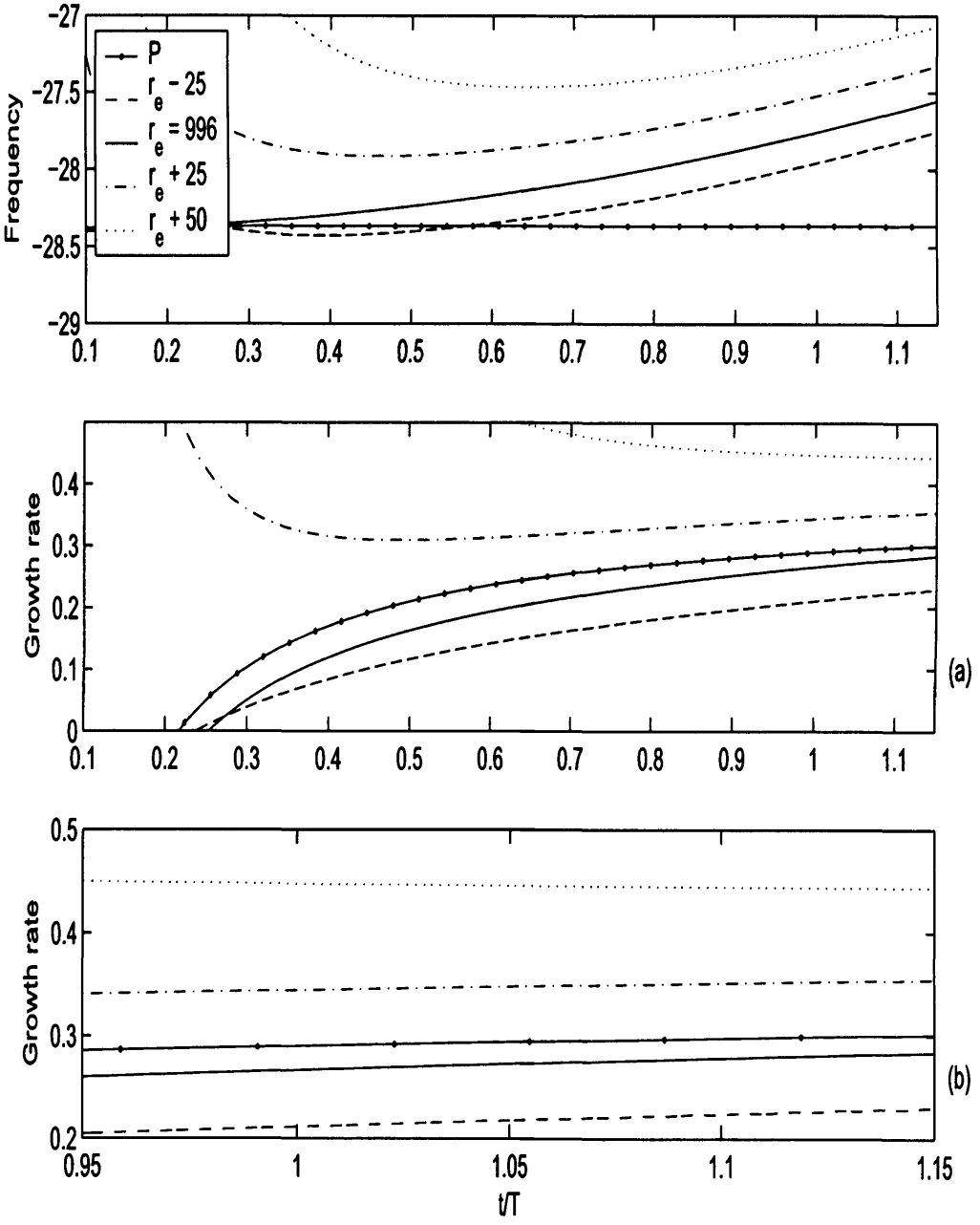

Figure 5.10: *Local temporal frequencies $\omega_r Re$ and temporal growth rates $\omega_i Re$ for a disturbance with $n = 107$ developing in a non-parallel flow with a magnetic interaction parameter $m = 0.4$, centred at $r_e = 996$. The temporal development is plotted for four different radial positions, r_e - 25, r_e, r_e + 25 and r_e + 50. The solid lines labeled with a P show the development in a parallel flow with $Re = 996$. The temporal growth rates are displayed over a full time range, (a), and for a reduced time range, (b).*

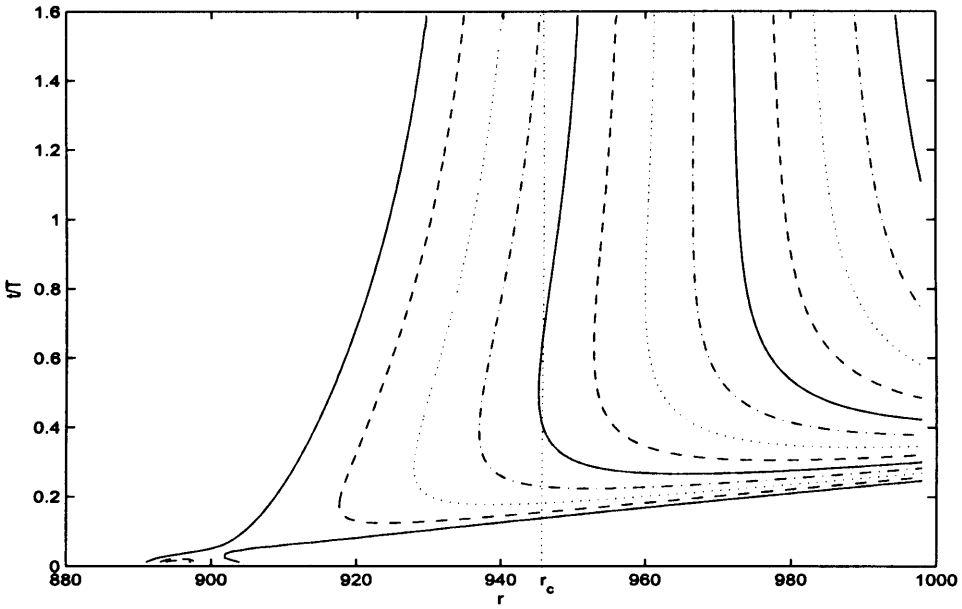

Figure 5.11: *Spatio-temporal development of* $|\omega_{\theta,w}|$ *for an impulsively excited disturbance in a non-parallel flow with a magnetic interaction parameter* $m = 0.4$. *The azimuthal mode number is* $n = 107$ *and the disturbance was excited at* $r_e = 896$.

and globally unstable behaviour may eventually be displayed. For $r = r_e + 100$, the plot of the growth rate initially decreases at a rapid rate. However, this does not persist for long and there is a suggestion that it may eventually reverse direction and increase.

On comparing the two problems, so far investigated, $m = 0.2, 0.4$, there is a strong indication that temporal growth and globally unstable behaviour is promoted by increasing the magnetic field parameter m. This would suggest that for $m = 0.5$, the growth rates would increase at a faster rate than those displayed by $m = 0.2, 0.4$.

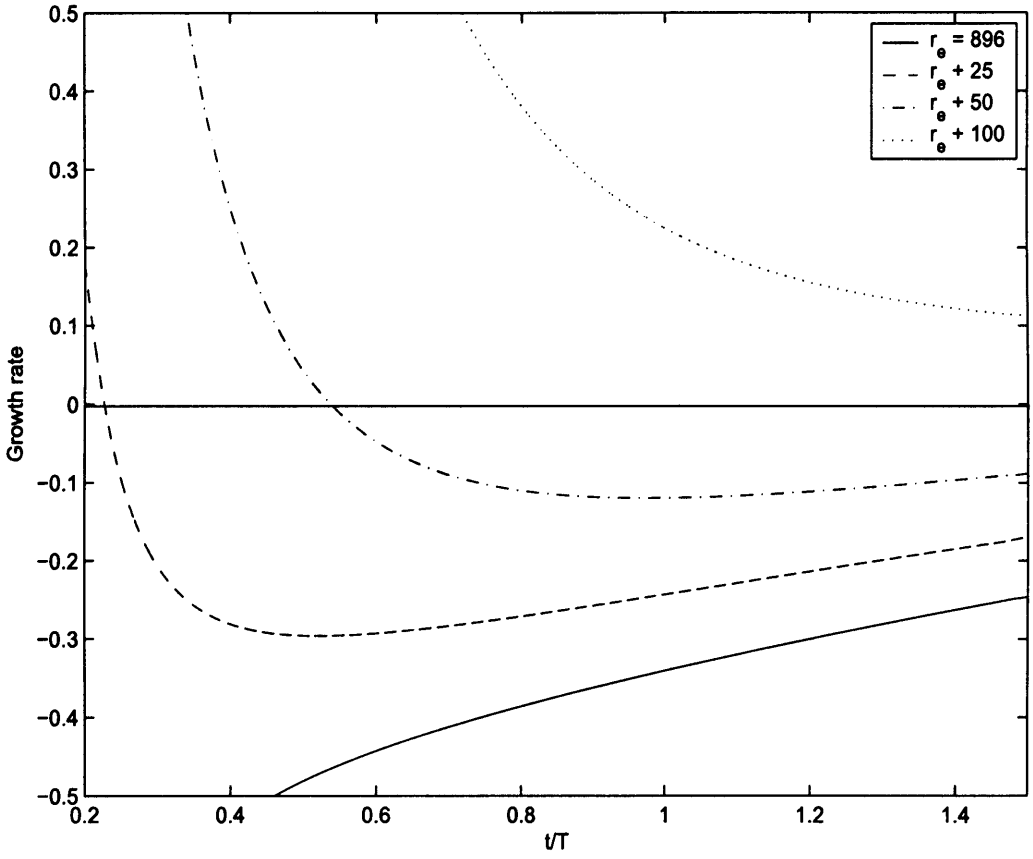

Figure 5.12: *Local temporal growth rates $\omega_i Re$ for a disturbance with $n = 107$ developing in a non-parallel flow with a magnetic interaction parameter $m = 0.4$, centred at $r_e = 896$. The temporal development is plotted for four different radial positions, r_e, $re + 25$, $r_e + 50$, $r_e + 100$.*

5.3.3 $m = 0.5$

Figure 5.13 displays the wavepacket evolution of a disturbance excited at $r_e = 1092$ for $m = 0.5$ and $n = 119$ in a non-parallel flow. These are the critical values for absolute instability as found by Jasmine (2003). From figure 5.13(a) it appears that the trailing edge is propagating with a diminishing velocity. Thus, indicating critical

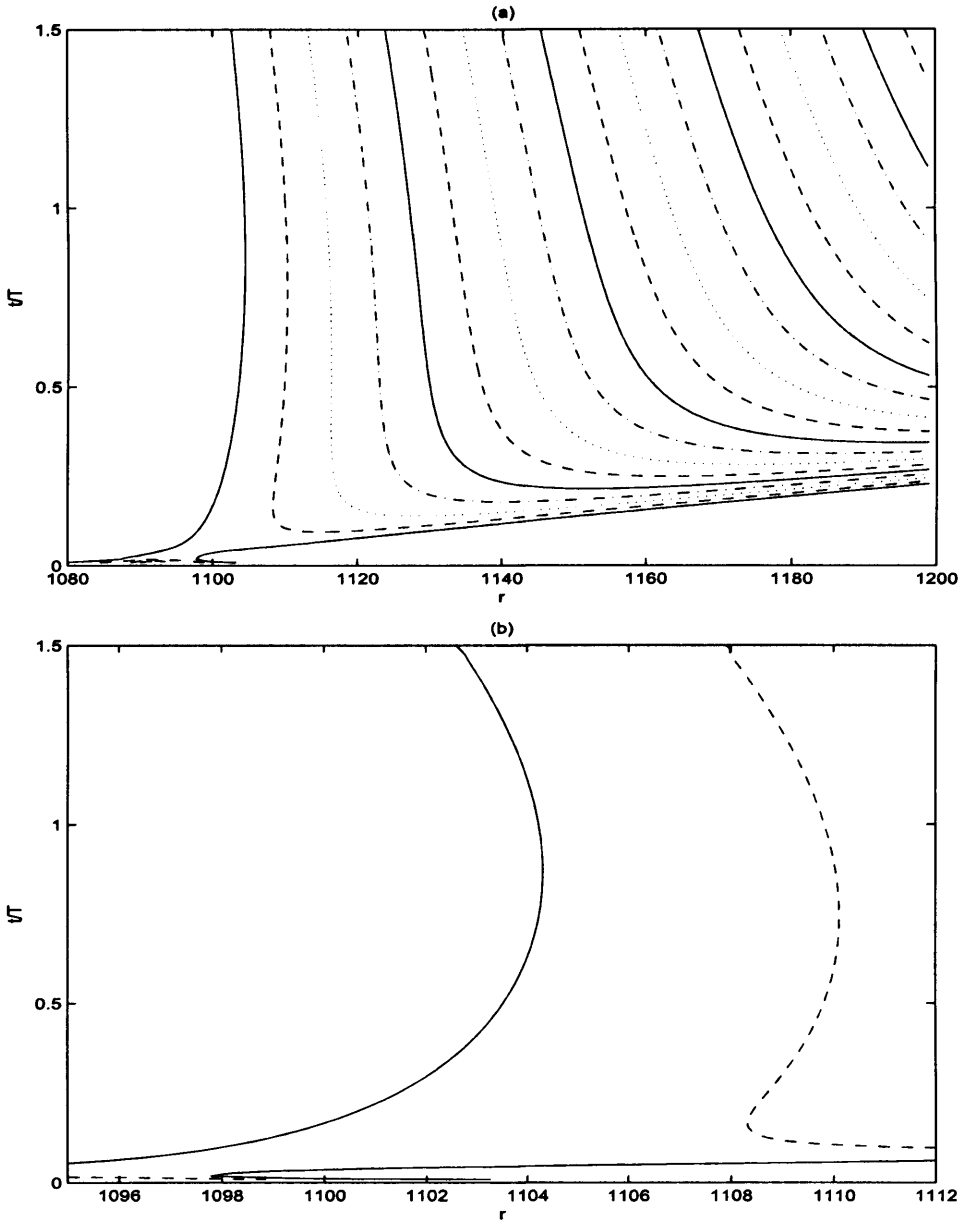

Figure 5.13: *Spatio-temporal development of* $|\omega_{\theta,w}|$ *for an impulsively excited disturbance in a non-parallel flow with a magnetic field* $m = 0.5$. *The azimuthal mode number is* $n = 119$ *and the disturbance was excited at* $r_e = 1092$. *(a) - full radial range, (b) - reduced radial range.*

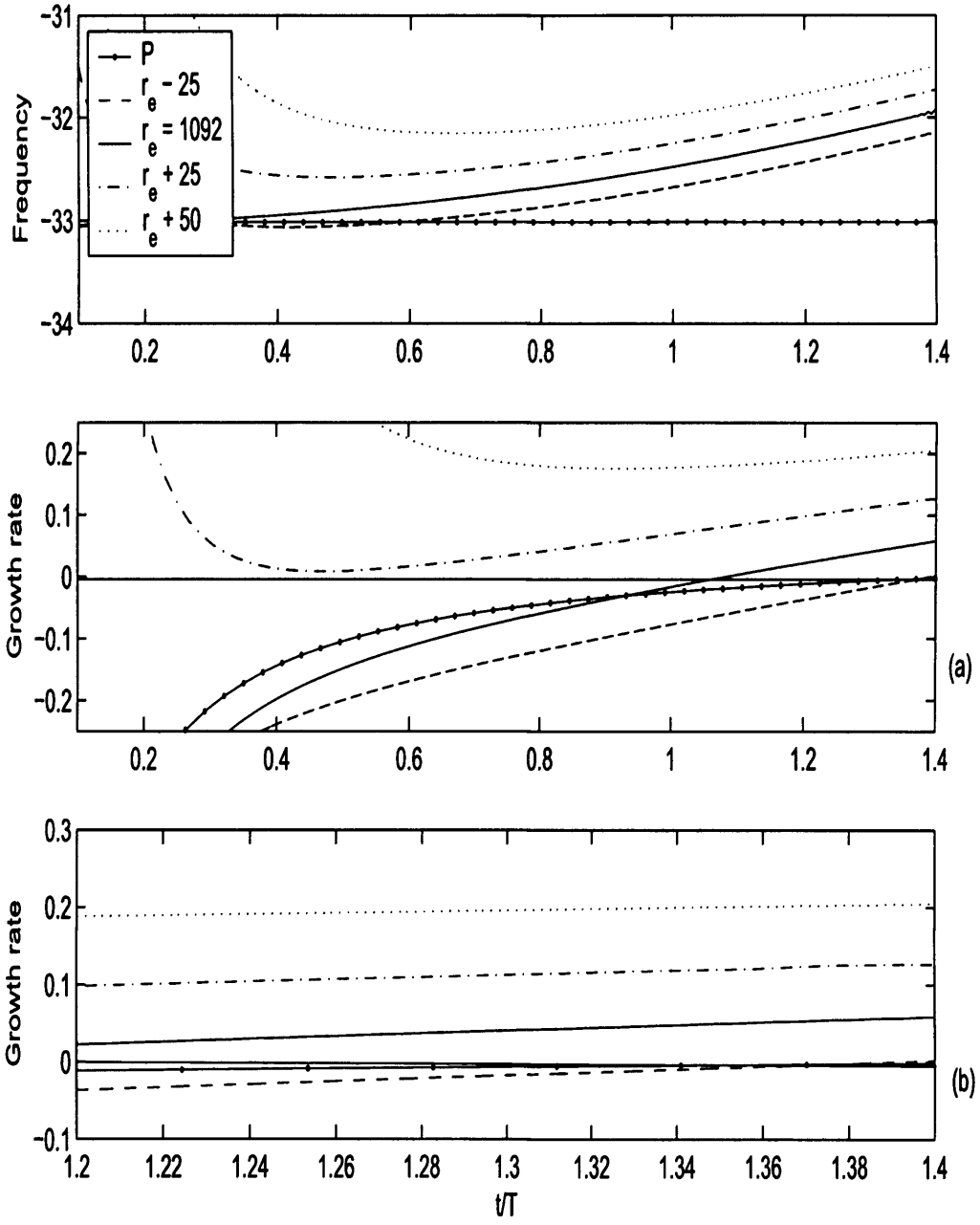

Figure 5.14: *Local temporal frequencies $\omega_r Re$ and temporal growth rates $\omega_i Re$ for a disturbance with n = 119 developing in a non-parallel flow with a magnetic interaction parameter m = 0.5, centred at r_e = 1092. The temporal development is plotted for four different radial positions, r_e - 25, r_e, r_e + 25 and r_e + 50. The solid lines labeled with a P show the development in a parallel flow with Re = 1092. The temporal growth rates are displayed over a full time range, (a), and for a reduced time range, (b).*

absolute instability. However, by taking a closer look at the trailing edge - figure 5.13(b) - it can be seen that it is propagating radially inwards with an increasing velocity. Therefore, temporal growth and globally unstable behaviour is observed.

The temporal growth is made even clearer by figure 5.14, where the growth rates are found to increase at all radial locations. For the radial location $r = r_e - 25$ (located radially inwards of the origin of the disturbance) temporal growth arises after $t/T \approx 1.4$.

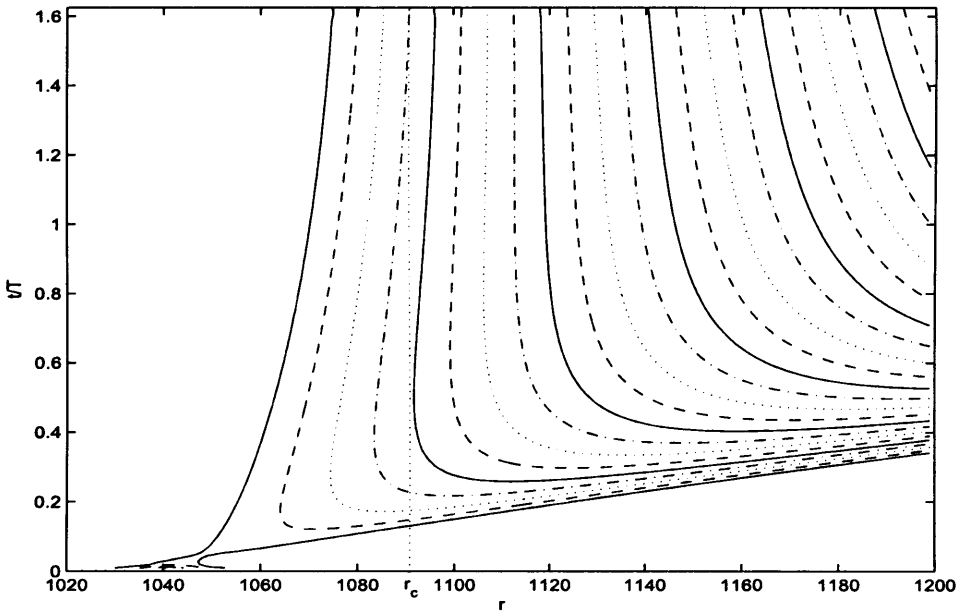

Figure 5.15: *Spatio-temporal development of* $|\omega_{\theta,w}|$ *for an impulsively excited disturbance in a non-parallel flow with a magnetic interaction parameter* $m = 0.5$. *The azimuthal mode number is* $n = 119$ *and the disturbance was excited at* $r_e = 1042$.

Figure 5.15 displays the wavepacket evolution for a disturbance impulsively excited at the radial location $r_e = 1042$. Initially the disturbance propagates radially outwards, but as it nears the absolutely unstable region, the trailing edge slows down and appears to be propagating towards a vertical line, in the vicinity of $r_c = 1092$. The

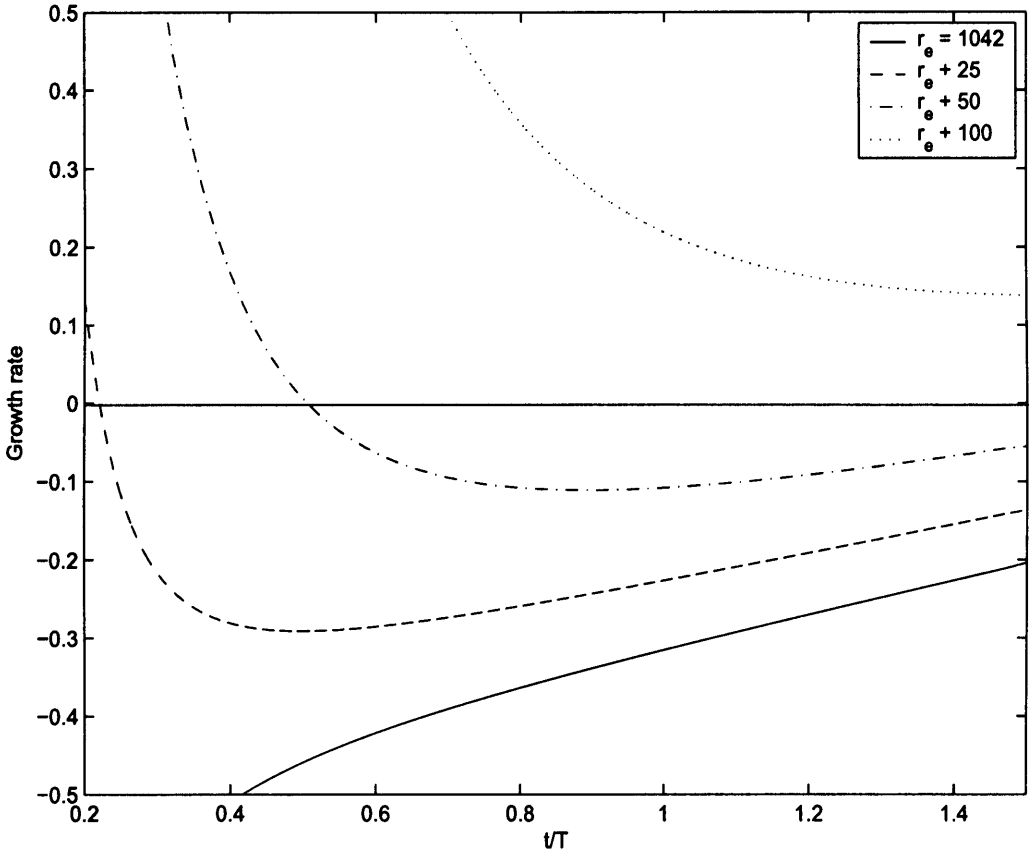

Figure 5.16: *Local temporal growth rates $\omega_i Re$ for a disturbance with $n = 119$ developing in a non-parallel flow with a magnetic interaction parameter $m = 0.5$, centred at $r_e = 1042$. The temporal development is plotted for four different radial positions, r_e, $re + 25$, $r_e + 50$, $r_e + 100$.*

growth rates for this disturbance are shown in figure 5.16. For $r \leq r_e + 50$ the growth rates increase at a steady rate, and it looks as if temporal growth will eventually be observed. For $r = r_e + 100$, the plot of the growth rate decreases with time. However, the plot suggests that it may eventually reverse direction and increase. Temporal growth is observed for the entire duration of the plot at the location $r = r_e + 100$.

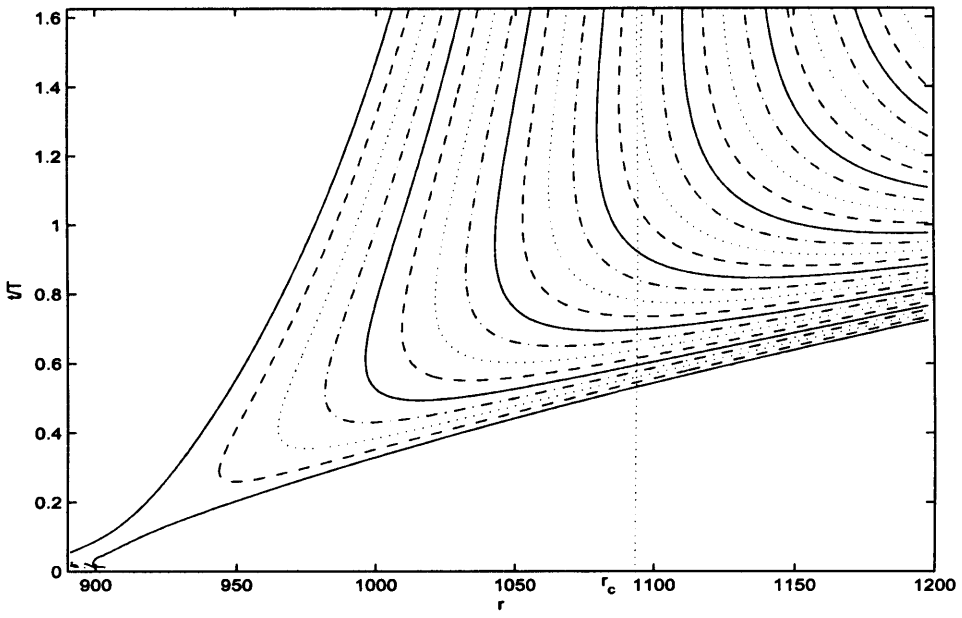

Figure 5.17: *Spatio-temporal development of* $|\omega_{\theta,w}|$ *for an impulsively excited disturbance in a non-parallel flow with a magnetic interaction parameter* $m = 0.5$. *The azimuthal mode number is* $n = 119$ *and the disturbance was excited at* $r_e = 892$.

A final disturbance is excited at the radial location $r_e = 892$ for an azimuthal mode number $n = 119$. The origin of this disturbance is located far upstream of the boundary of absolute instability. The spatio-temporal development is plotted in figure 5.17. Initially the trailing edge propagates radially outwards in a convective manner. However, as the disturbance nears the region of absolute instability, the velocity of the trailing edge can be seen to decrease.

Due to difficulties in obtaining solutions for large time, we can no longer use the leading and trailing edges to determine the long term characteristics of the disturbance. Nonetheless, we may obtain a good idea of the the prevailing behaviour, by looking at the contour lines within the wavepacket. The contour lines appear to be asymptoting towards vertical lines, in the vicinity of $r_c = 1092$, suggesting that the

trailing edge will also tend towards a vertical line. Hence, we may conjecture that temporal growth and globally unstable behaviour will eventually prevail.

5.4 Comparing growth rates

Figure 5.18 compares the growth rates at the critical radius of absolute instability r_e, for various magnetic field strengths. The solid line represents the case $m = 0.0$, where $r_e = 508$, $n = 68$; the dashed line represents the case $m = 0.1$, where $r_e = 595$, $n = 76$; the dashed-dotted line represents the case $m = 0.2$, where $r_e = 696$, $n = 86$; the dotted line represents the case $m = 0.3$, where $r_e = 813$, $n = 96$; the solid-dot line represents the case $m = 0.4$, where $r_e = 946$, $n = 107$; and the solid-star line represents the case $m = 0.5$, where $r_e = 1092$, $n = 113$. As was revealed by the earlier suction/injection problem, the growth rates of all six flows are of comparable magnitude.

Initially all six growth rates are comparable; the growth rates increase rapidly within the lower half of the plane. However, after only t/T = 0.5, there are noticeable differences in the behaviour of the growth rates. For $m = 0$ and 0.1 the growth rates reverse direction and decrease. The growth rate decreases more rapidly in the $m = 0$ problem. Conversely, the flows with $m \geq 0.2$ continue to grow, and it can be seen that the increase in growth is stronger for larger magnetic field strengths.

Figure 5.19 displays the gradients of the growth rates in figure 5.18. The data lines are as before. For $m = 0.0, 0.1$ the gradients decrease and are eventually negative, which corresponds to the growth rates decreasing. For $m = 0.2, 0.3$ the gradients remain positive for the time period displayed. However, the gradients continue to decrease, suggesting that the corresponding growth rates may eventually decrease and display temporal decay. The gradients for $m = 0.4, 0.5$ initially decrease at a rapid rate. However, at larger locations in time, the gradients decrease at a slower rate, and the plot suggests that the gradients may eventually asymptote towards positive

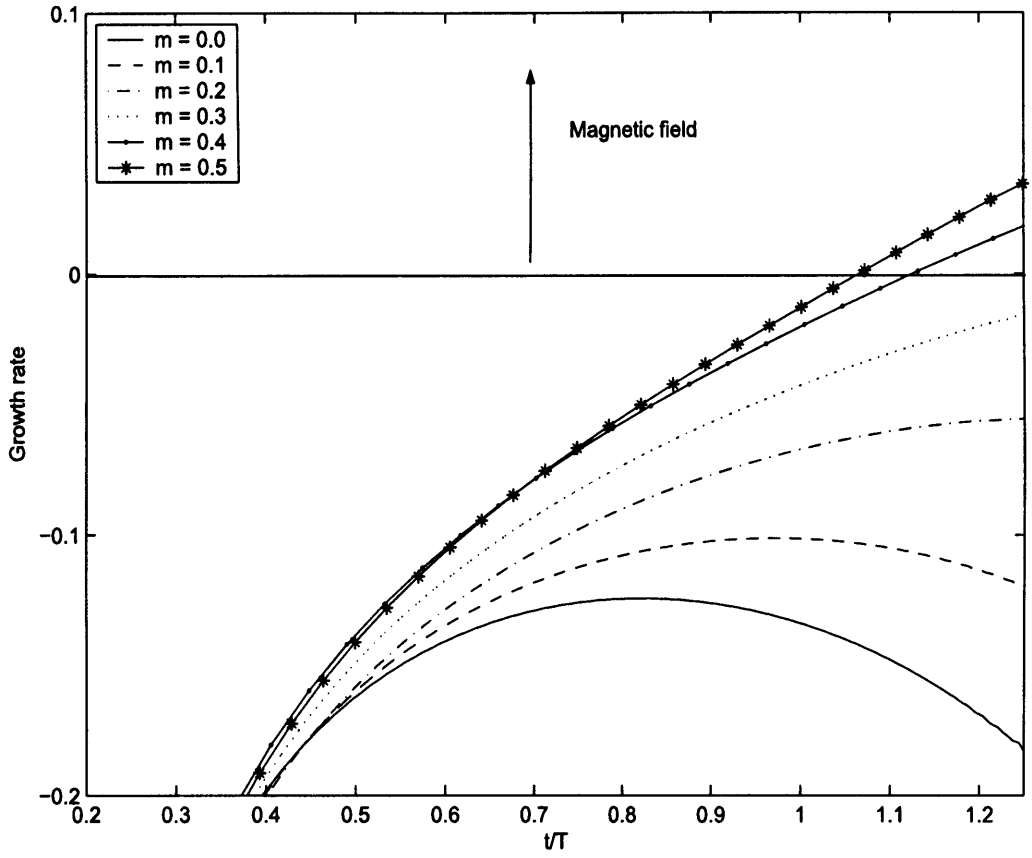

Figure 5.18: *Comparing growth rates at the critical point of absolute instability for the various normal flows. Solid line: $m = 0$ where $r_e = 508$, $n = 68$; dashed line: $m = 0.1$ where $r_e = 595$, $n = 76$; dashed-dotted line: $m = 0.2$ where $r_e = 696$, $n = 86$; dotted line: $m = 0.3$ where $r_e = 813$, $n = 96$; solid-dot line: $m = 0.4$ where $r_e = 946$, $n = 107$; solid-star line: $m = 0.5$ where $r_e = 1092$, $n = 113$.*

constants. This would suggest that temporal growth and an increasing growth rate would be observed for these problems.

The results suggest that the growth rates increase at a greater rate, as m increases. Thus, we may predict that flows with $m > 0.5$ will display growth rates that are larger than those displayed in figure 5.18. Although further investigation is required to prove

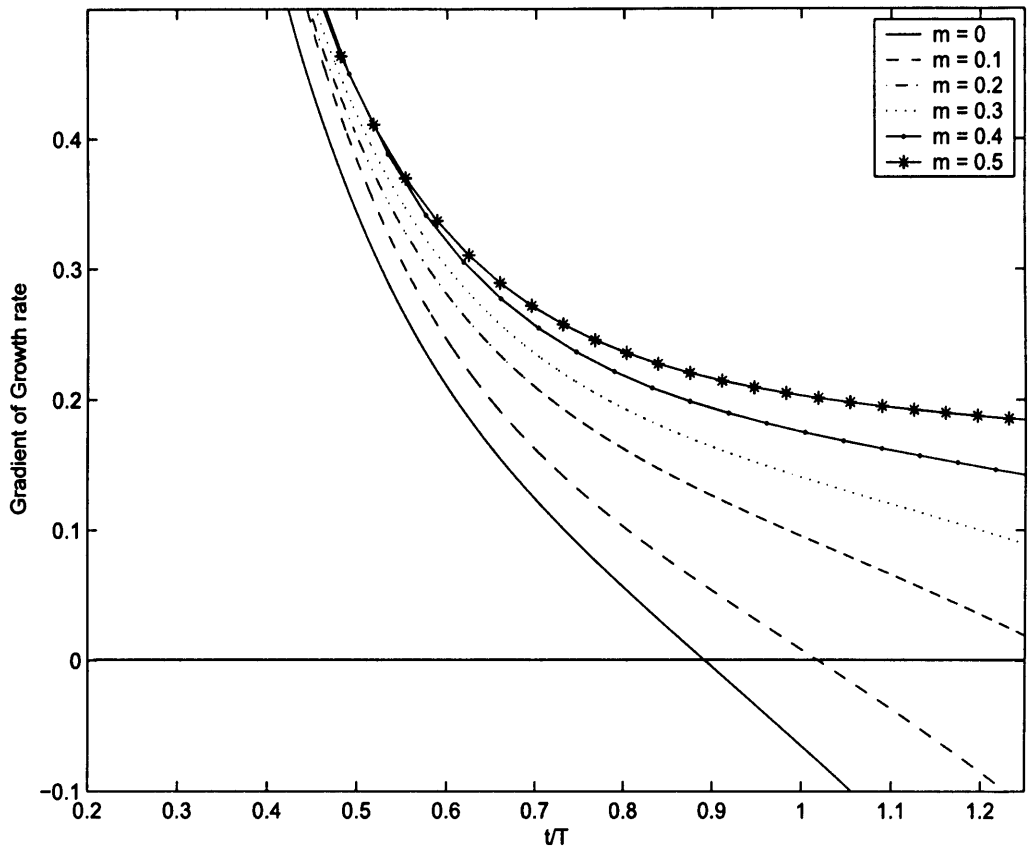

Figure 5.19: *Comparing the gradients of the growth rates in figure 5.18. Data lines are the same as those in figure 5.18.*

this theory. Figures 5.18 and 5.19 also suggest that there may exist a critical value for m, such that the growth rate does not increase or decrease, but instead tends towards a constant. The plot suggests that such a critical value (if it does indeed exist) may arise for $m > 0.2$.

5.5 Discussion and conclusions

A numerical study has been carried out on the effects of introducing a uniform magnetic field on the global behaviour corresponding to the absolute instability of the rotating-disk boundary-layer. The fluid above the disk is assumed to be electrically conducting, and the effects of the electric field are assumed to be negligible and the magnetic field is unaffected by the fluid motion. The problems that we have investigated here, are for $m = 0.0$, 0.1, 0.2, 0.3, 0.4 and 0.5, where m is the magnetic field parameter defined earlier. Since eigenvalues were unavailable for $m > 0.5$, we were unable to study the disturbance behaviour for larger values of m. The investigation was undertaken using the novel velocity-vorticity method described by Davies & Carpenter (2001). The system of equations used in this method are equivalent to the complete linearized Navier-Stokes equations. Since the equations are linear, they are separable with respect to the azimuthal coordinate θ. Thus, simulations with a single azimuthal mode number are allowed. Impulse like excitation was used for all simulations. This produces a disturbance wavepacket that initially contains a wide range of frequencies.

When disturbances are simulated using the so-called parallel flow approximation (spatially homogeneous flow), the results are fully in accordance with the theoretical results of Jasmine (2003). If the flow parameters lie within the theoretical absolutely unstable parameter space, the simulations produce identical behaviour. The same is true for disturbances excited within the convectively unstable region. For disturbances excited at the critical point of absolute instability, the temporal frequencies and radial wavenumbers are identical (to within a certain number of decimal places) with those given by Jasmine (2003); refer to table 5.2.

For the non-parallel flow simulations (spatially inhomogeneous), the behaviour is quite different. While the magnetic field parameter is small, behaviour comparable

with the results of Davies & Carpenter (2003) is found; the growth rates decrease at all locations. Thus, temporal decay is observed. The behaviour may be summarized by the schematic sketches in figure 2.4.

As the magnetic field parameter m is increased, the corresponding growth rates begin to increase. The growth rates are found to grow at a stronger rate for larger values of m. This is clearly evident in figures 5.18 and 5.19, which display the growth rates at the critical point of absolute instability for various mean flows and their corresponding gradients. This would suggest that for m sufficiently large, the behaviour may be summarized by the schematic plots in figure 4.30. Figures 5.18 and 5.19 also suggest that there may exist a critical value m_c, such that the growth rate tends towards a constant for large time. However, further investigation is required to prove this.

The results of the present study are rather surprising. The introduction of a uniform magnetic field is known to be stabilizing. However, on introducing non-parallel effects, the mean flows are destabilized in the region of the theoretical absolute instability and an increasing temporal growth rate is found. Thus, the results are similar to that observed in the earlier problems with uniform suction; globally unstable behaviour is promoted by their introduction, but there is no fixed global frequency, which would be expected for a globally unstable flow.

As mentioned in chapter 4 the behaviour observed in the numerical simulations can be understood by considering the Green's solutions to the Ginzburg-Landau equation (refer to chapter 8). Depending on the precise balance between the varying frequency and the varying growth rate, globally stable or globally unstable behaviour can be observed.

Longer simulations, which would have given a greater insight into the long term behaviour, were prevented because of convergence errors. The errors arise because of the difficulty in dealing with flow variables that vary over an $O(10^{20})$ range of

amplitudes in space and in time. Therefore, it is difficult to say whether the growth rates for $m > 0.2$ (in figure 5.18) will continue to grow indefinitely, or eventually reverse direction, decrease and display temporal decay. The above study suggests that the former statement is true. However, it is quite possible that the growth rates (for large m) do eventually decrease and display temporal decay. Further study is required to gain a greater understanding of the prevailing disturbance behaviour. Nonetheless, the results do tell us that temporal growth is promoted by the introduction of a uniform axial magnetic field, even if we cannot be sure, from the simulations, about whether it is maintained indefinitely.

Chapter 6

The BEK family

6.1 Introduction

The von Kármán (1921) rotating-disk boundary-layer is one particular example of a wider class of rotating flows. The system consists of a disk of infinite radius, rotating with a constant angular velocity Λ_d, beneath a fluid, which is infinite in extent and rotating with a constant angular velocity Λ_f. Refer to figure 6.1 for a sketch of the rotating system. Three particular examples are the Bödewadt (1940), Ekman (1905) and von Kármán (1921) boundary-layers and so the system will be known as the *BEK* family. As discussed previously, the von Kármán or rotating-disk boundary-layer arises when a disk rotates beneath a stationary fluid. The Ekman layer occurs when the disk and fluid rotate with approximately the same angular velocity and the Bödewadt layer arises when a fluid rotates above a stationary disk. Batchelor (1951) described and Rogers & Lance (1960), Faller (1991) Lingwood (1997b) obtained solutions for the *BEK* family. The mean velocity profiles become increasingly inflectional as the rotating flow changes from the von Kármán layer through to the Bödewadt layer. Thus, the flow becomes increasingly unstable.

Batchelor (1951) describes the behaviour of the *BEK* family in terms of streamlines. For rotating flows, where the fluid rotates with a greater angular velocity than

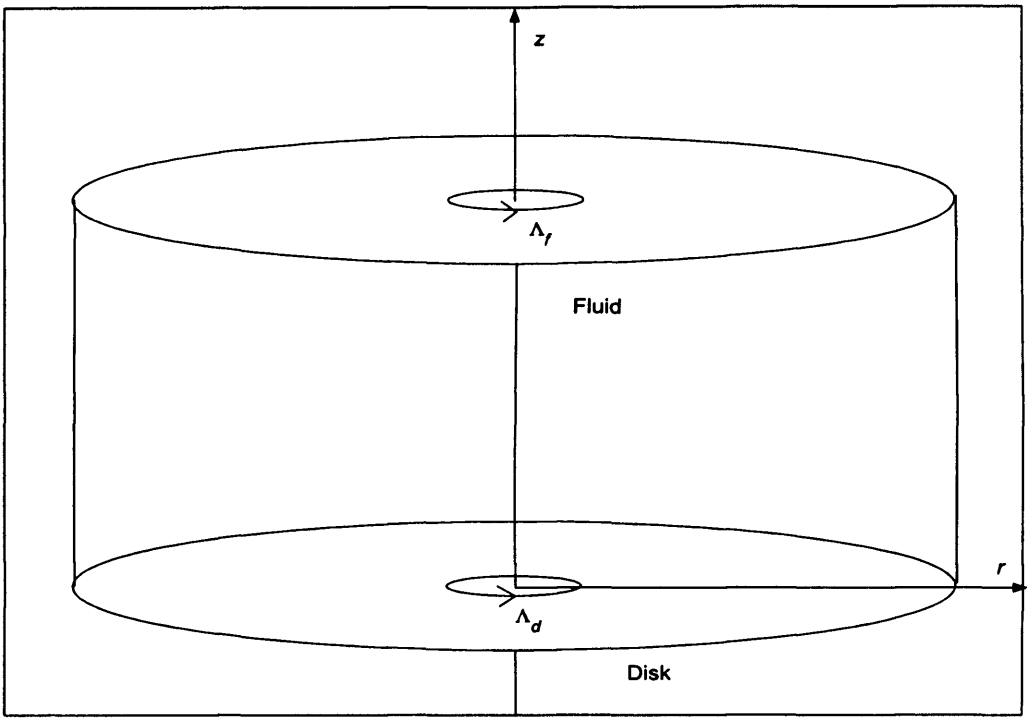

Figure 6.1: *Rotating-disk beneath a body of rotating fluid.*

the disk, it was shown that the flow will behave in the form given in figure 6.2(a). There is a radial flow directed towards the centre of the disk, while there is an axial flow directed away from the disk. The Bödewadt layer and Ekman layer (with slightly greater fluid angular velocity) belong to this type of rotating flow. Figure 6.2(b) describes a rotating flow, where the disk rotates with a greater angular velocity than the fluid. Fluid is introduced at the centre and is thrown radially outwards. The von Kármán layer and Ekman layer (with slightly greater disk angular velocity) belong to this type of rotating flow.

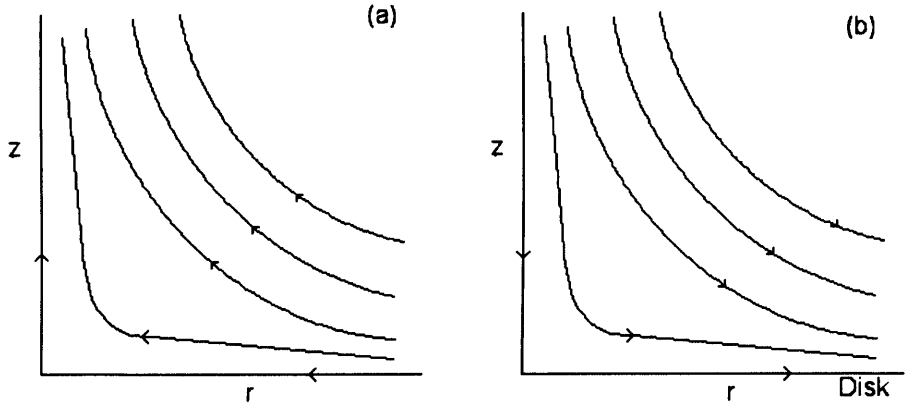

Figure 6.2: *Streamlines of the various types of rotating flow. (a) - fluid rotates with greater angular velocity than the disk; (b) - disk rotates with greater angular velocity than the fluid.*

6.1.1 The von Kármán layer

The von Kármán (1921) rotating-disk boundary-layer acts as a centrifugal fan, where the flow is introduced at the centre of the disk and is thrown radially outward. The disk is studied since the instabilities that arise are similar to those that occur on the boundary of a swept-wing. The reader is referred to chapter 2 for further background information on the subject.

6.1.2 The Ekman layer

The Ekman boundary-layer has a number of applications in meteorology and oceanography. For example, the interaction of the oceans and atmosphere, hurricanes and typhoons. Quasi-streamwise rolls have been observed in hurricanes, and such rolls are comparable with the rolls associated with instabilities inherent in the Ekman boundary-layer. The instabilities present in hurricane boundary-layers have been reviewed and studied by Nolan (2005).

Steady winds at the sea surface produce a thin boundary-layer, which is known as the Ekman layer. The boundary-layer is only a few hundred metres thick, which is thin when compared with the vast depths of the ocean. There exists a similar boundary-layer at the bottom of the ocean, known as the bottom Ekman layer. There also exists a planetary boundary-layer (*PBL*) just above the sea surface. The *PBL* occurs in the lowest part of the troposphere[1]. In the *PBL*, winds are governed by frictional forces and the boundary thickness is constantly changing, due to varying temperatures and wind speed. The *PBL* is generally found to be thicker during the day, since strong winds allow for greater convective mixing, which causes the *PBL* to expand. During the night there is a reduction of rising thermals from the earth surface. Thus, the *PBL* contracts. The *PBL* will also be thinner during the winter season, compared with the summer season. The reason being that cool air is generally denser than warm air. The *PBL* is approximately 100 - 3000 metres thick.

Within the *PBL*, wind is turbulent and surface friction due to vegetation[2] and topography[3], causes turbulent eddies and chaotic wind patterns to develop. The wind speed is far more uniform and stronger above the *PBL*, because there is a significant decrease in the frictional forces. Within the region above the *PBL*, the wind is defined as geostrophic, meaning a balance between the pressure gradient and Coriolis force. As the frictional force is more prominent within the *PBL*, the wind direction is a balance between the frictional and Coriolis forces, and the pressure gradient, and is

[1]The earth's atmosphere is made up of the troposphere and stratosphere, where the troposphere is the lower section, and is the region in which most weather phenomena occur. The Green-house effect also arises within this region. The troposphere extends from the earth surface to an altitude of approximately 16 - 18 kilometres above the equator, and to an altitude of approximately 10 kilometres above the poles. The term troposphere, stems from the Greek word tropos, meaning turning or mixing. The temperature of the troposphere varies greatly, from 17°c at the earth's surface, to approximately −52°c at the tropopause, where the tropopause marks the end of the troposphere and the beginning of the stratosphere.

[2]A general term for all the plant life in a particular region.

[3]The technique of graphically representing the exact physical features of a place; or the study and depiction of physical features, including terrain relief.

known as the gradient wind. Friction reduces the affect of the Coriolis force, causing the air to spiral into low pressure. Since frictional forces decrease with increasing height, winds are generally observed to turn or bend, as one monitors the *PBL* from the earth surface to the upper atmosphere.

Temperatures within the *PBL* are dominated more by the advection and thermal effects, than the regions above. Therefore, of all the atmospherical regions, the most dramatic temperature changes occur inside the *PBL*. This is due to significant solar heating during the day and cooling through longwave radiation at night. The temperature of the atmosphere above the *PBL* remains fairly constant during the day and night. It is very important to monitor the varying temperature changes within the *PBL* for the purpose of making weather forecasts, since an increase in temperature will cause the atmosphere to become more unstable. Thus, prompting the onset of hurricanes or typhoons, which could have devastating effects if not detected early on. For further reading on the PBL the interested reader is referred to Minto & Pleva (2002).

During an expedition to the north pole in the years 1894 - 1896 (Nansen, 1902), the vessel *Fram* was frozen into the ice. Nonetheless, the misfortune of the vessel and voyagers would soon reveal new and significant insights into the effects on the ocean, due to the wind. The oceanographer *Fridjof Nansen*, who was onboard the *Fram*, observed that the drift of the surface ice and consequently the current underneath, was directed at 20^o to 40^o to the right of the wind direction. He correctly attributed this to the Coriolis force and predicted that the current vector would spiral clockwise with increasing depth. Nansen argued that there are three forces important to the process; Wind stress $\underline{W}$, Drag $\underline{D}$ and Coriolis force $\underline{C}$. For an iceberg (or any other object), it was proposed that the frictional forces must be in the opposite direction to the resulting velocity and that the Coriolis force will be perpendicular to the resulting velocity. Finally, Nansen argued that there must be a balance between the three forces

$(\underline{W}, \underline{D}, \underline{C})$ if steady flow is to arise. See figure 6.3.

$$\underline{W} + \underline{D} + \underline{C} = 0 \tag{6.1}$$

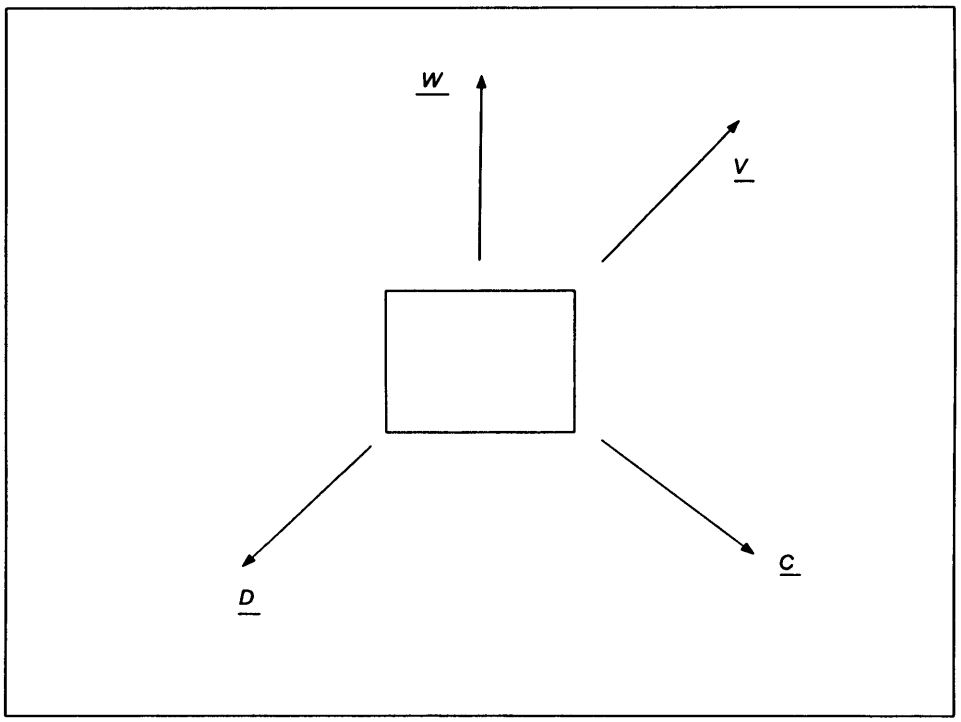

Figure 6.3: *The balance of forces acting on an iceberg in a wind on a rotating Earth.*

In order to prove such a theory, Nansen asked his colleague *Vilhelm Bjerknes* to let one of Bjerknes students to make a theoretical study on the influence of Earth's rotation on wind-driven currents. That student turned out to be *Vagn Wilfried Ekman* (1874 - 1954). Ekman was born in Stockholm, Sweden and worked out the dynamics for his doctoral thesis at Uppsala. He showed that the rotation of the Earth influenced the way that ocean currents responded to the force of the wind. He pointed out how purely viscous effects were unable to transfer horizontal momentum down into the

water column, so that it was necessary to take the turbulent downward transport of momentum into effect, by, for example, introducing a turbulent eddy viscosity coefficient V_E. Shortly after producing his thesis, Ekman produced his now famous 1905 paper, whereby his study was expanded to include the influence of continents and differences of water density. Jenkins & Bye (2004) review in detail the work and achievements of Ekman and they provide a number of applications of his theory to the oceans. Section 5.2 contains the formulation devised by Ekman, with plots of the Ekman meanflow and Ekman spiral[1].

Ekman spirals have been observed in many geophysical flows, both atmospheric and oceanic, and can be created in the laboratory for investigation. Although geophysical flows always experience turbulence due to the rough boundary-layers and possible thermal effects, the mean flow may be assumed to be steady and laminar. The Ekman layer has an exact solution to the Navier-Stokes equations and has the advantage of having a constant boundary-layer thickness and constant geostrophic velocity. Thus, making it strictly parallel.

Since the study by Ekman, a number of investigators have carried out several theoretical and experimental investigations into the Ekman boundary-layer. Faller (1963) conducted an experimental study, where the Ekman layer was produced in a large cylindrical rotating tank by withdrawing water from the centre and introducing it at the rim. This created a steady-state symmetrical vortex, in which the flow from the rim to the centre took place entirely in the shallow viscous boundary-layer at the bottom. Instability was detected for Reynolds numbers of approximately 125. This instability is known as the Type-1 mode and is very similar to the Type-1 mode present in the von Kármán layer, since both are inviscid crossflow instabilities, which are a consequence of the inflectional points in the radial mean flow velocity, (see figure

[1]Path traced out by the tip of the velocity vector in an Ekman layer, as the vertical coordinate changes.

6.6 for plots of the mean flow velocities).

Faller & Kaylor (1966) also detected the Type-1 mode in their numerical study. Instability arose for Reynolds numbers $Re \approx 118$, which is in good agreement with the earlier experimental investigation by Faller. They also detected a Type-2 mode, which again is the counterpart to the viscous Type-2 mode present in the von Kármán layer. The critical Reynolds number for the Type-2 mode was found to be $Re \approx 55$. Tatro & Mollo-Christensen (1967) verified the existence of the Type-2 mode in their experimental study. The apparatus consisted of two parallel circular rotating plates forming a spool; air was admitted through screens at the outer edge and removed through a screen cage at the hub. The travelling Type-2 mode was found to occur before the Type-1 mode, with the respective critical Reynolds numbers given as $Re \approx 56$ and $Re \approx 124.5$.

Further confirmation of the Type-1 and -2 modes are given by Lilly (1966), Melander (1983), Faller (1991) and Lingwood (1997b). Lilly and Melander found the critical Reynolds numbers for the Type-1 and -2 modes to be $Re \approx 110$, $Re \approx 55$ and $Re \approx 112.75$, $Re \approx 54.15$, respectively. While Faller found the travelling Type-2 mode to arise for $Re \approx 54$, and Lingwood found the stationary Type-1 mode to arise for $Re \approx 116.3$.

Although the Type-2 travelling mode arises for significantly lower critical Reynolds, it is the Type-1 mode that is more commonly observed in experiments. This is because there is a far more rapid growth associated with the Type-1 mode. Thus, for larger Reynolds numbers this mode will dominate.

Recently, Allen & Bridges (2003) investigated the effects of introducing a two-dimensional compliant surface into the Ekman boundary-layer. Compliance has been shown by Cooper & Carpenter (1997a,b) and Davies & Carpenter (2003) to suppress

the onset of instability and transition to turbulence in the rotating-disk boundary-layer. However, it was shown by Allen & Bridges that a compliant surface has negligible effect on the Ekman layer and the critical Reynolds number for instability. Their study leaves a number of unanswered questions: does compliance have any interesting, technological or physical application in the Ekman layer?

For further interesting investigations on the topic of the Ekman layer, the reader is referred to Stewartson (1957), Barcilon (1967), Hide (1968), Spooner & Criminale (1982) and Foster (1997). Possibly the most important study (of recent times) in the area was conducted by Lingwood (1997b). Lingwood showed that the Ekman layer and other rotating flows exhibit regions of absolute instability. It was suggested that the absolute instability mechanism may be a possible reason for transition to turbulence and nonlinear effects. This will be discussed in greater detail later in the chapter.

6.1.3 The Bödewadt layer

In similar respects to the Ekman layer, the Bödewadt flow and other rotating fluid flows are useful in studying the interaction of the atmosphere and oceans. Batchelor (1951) describes the Bödewadt layer as a radial flow directed inwards and an axial flow directed away from the disk surface. He goes onto describe such a flow; 'when a cup of tea is stirred, the sugar particles accumulate about the centre.'

Since Bödewadt (1940) discovered the solution to the mean flow, for the problem where a fluid rotates above a flat plate, there have been few experimental and theoretical studies on the subject. To the authors knowledge, the first study to be published was the experimental investigation by Savas (1987). In the experiment, circular waves were observed on the disk boundary-layer during spin-down to rest. The initial flow evolves into a steady system that exhibits the Bödewadt flow properties. The observed circular waves were found to develop in this flow. The critical

Reynolds number for instability was found to be approximately $Re = 25$. This is a great deal smaller than the critical Reynolds numbers for the von Kármán and Ekman layers. Lingwood & Alfredson (1999) also carried out an experimental study on the stability of the Bödewadt layer. The Bödewadt flow was approximated on the stator of an enclosed rotor-stator system. They found a non-axisymmetric instability for a low azimuthal wavenumber, which has an inward phase velocity that decreases in magnitude for decreasing radius and small negative wave angle. Their data suggests that the critical Reynolds number for instability lies in the range $47 < Re < 56$.

Faller (1991) conducted a stability analysis for the complete set of rotating flows. In his study he calculates the critical value for the onset of the travelling Type-2 mode. The critical Reynolds number was found to be approximately $Re = 15$ for a wavelength $L = 16.6$ at an angle $\epsilon = -33.2°$. Lingwood (1997b) also investigated the stability of the Bödewadt layer and found the critical Reynolds number for the stationary Type-1 mode to be $Re \approx 27$, which is in good agreement with the experimental investigation by Savas (1987).

A spatial linear stability analysis was conducted by Fernandez-Feria (2000). They considered the stability of axisymmetric perturbations propagating towards the axis of rotation, i.e. the azimuthal mode number $n = 0$. It was shown that the circular waves observed in previous experimental and theoretical investigations, correspond to an inertial instability. The inertial mode is present at infinite Reynolds numbers and is similar to the Type-1 mode in the rotating-disk boundary-layer. This mode is stabilized as the Reynolds number decreases below the critical value, which was found to be about $Re = 19.8$ for $n = 0$.

6.1.4 Absolute instability

Lingwood (1997b) extended her study on the absolute instability of the rotating-disk boundary-layer to the complete family of rotating flows; so called *BEK* family. The

flows were shown to be absolutely unstable in the radial direction, for a given region of the parameter space, (i.e. disturbances grow in time at every radial location within these regions). Outside such regions, the flow is either convectively unstable or stable. The convective/absolute nature was determined by examining the branch-point singularities of the dispersion relation. The Briggs (1960) criterion was invoked to establish the disturbance characteristics. (The Briggs criterion and the requirements for instability were discussed in greater detail in chapter 1). Throughout Lingwood's linear stability study, the parallel flow approximation was used, where the radial dependence of the mean flow was ignored.

The neutral-stability curves for stationary waves were presented by Lingwood (1997b) for a number of rotating flows. The critical Reynolds number for instability was found to be approximately 290, 116, and 27 for the respective von Kármán, Ekman and Bödewadt layers. The von Kármán stability curve consists of an inviscid Type-1 and a viscous Type-2 mode destabilized by Coriolis forces. The other rotating neutral stability curves consist of two similar modes. For rotating flows with a negative Rossby number Ro (corresponding to flows with a disk angular velocity greater than the fluid angular velocity), the two branches only exist for $r > r_a$, where r_a is the onset of the instability. Whereas flows with a positive Rossby number Ro (corresponding to flows with a fluid angular velocity greater than he disk angular velocity), the two branches exist for $r < r_a$. For the Ekman layer $Ro = 0^-$ (i.e. approach zero from below), the behaviour is similar to the flows with $Ro < 0$, in that disturbances propagate radially outwards, while for $Ro = 0^+$ (i.e. approach zero from below), the behaviour is like the flows with $Ro > 0$, since disturbances propagate radially inwards.

The critical Reynolds number for absolute instability was found to decrease with increasing Rossby numbers. The critical Reynolds number for absolute instability for the von Kármán, Ekman and Bödewadt layers were found to be 507.3, 198.0 and 21.6,

respectively. Stationary absolutely unstable modes first arise for $Ro \approx 0.5$. These stationary modes were found to be close to the critical point of absolute instability. Generally, for positive Ro the critical point is close to the stationary modes, while as $Ro \rightarrow -1$, the frequency at the critical point becomes increasingly negative.

For $Ro < 0$ the absolutely unstable region resides in the lower half of the real radial wavenumber plane and the modes propagate radially outwards. The opposite is true for flows with $Ro > 0$. The absolutely unstable region lies in the upper half of the real radial wavenumber plane, the modes propagate radially inwards. However, for $1 \leq Ro \leq 0.8$ there is a small region where the modes reside in the lower half plane. Thus, these flows produce similar behaviour to that described for the flows with $Ro < 0$. However, these modes only appear for Reynolds numbers that are greater than the critical Reynolds number for absolute instability. Hence, it is unlikely that this is physically relevant, since nonlinearity and transition to turbulence may have already set in.

For the rotating-disk boundary-layer, Lingwood (1995, 1996) felt that the absolutely unstable mechanism was possibly responsible for the onset of non-linear behaviour and the transition from a laminar to turbulent state. It was claimed by Lingwood that transition in the rotating-disk boundary-layer typically occurs for $Re = 513 \pm 3\%$, which is remarkably close to her critical value of $Re = 507.3$ for absolute instability. Transition in the Ekman layer was shown by Owen, Pincombe & Rogers (1985) to occur for $Re = 180$, and other investigators have found transition to arise for $180 < Re < 200$. The critical Reynolds number for absolute instability in the Ekman layer is $Re = 198$. Thus, Lingwood (1997b) felt that the absolute mechanism was again a possible reason for transition and nonlinearity. Lingwood (1997b) concluded by saying that absolute instability was a possible reason for transition and non-linearity in all rotating flows within the *BEK* family.

Lingwood understood the behaviour of the *BEK* family to be as follows; for flows

with $Ro < 0$, a laminar stable region is surrounded by a convectively unstable region, which in turn is surrounded by an absolutely unstable region. The behaviour of flows with $Ro > 0$ is similar. However, since the flow propagates radially inwards, there are some important differences. For a disturbance excited within the convectively unstable region, the disturbance propagates radially inwards towards the laminar region and if the amplitudes are sufficiently small, the disturbance will eventually decay. For a disturbance centred within the absolutely unstable region, the wavepacket envelope propagates radially inwards and outwards from the source. Lingwood suggested that the absolute instability may act as an exciter for inwardly propagating waves that pass through the three regions of the stability domain. The three regions being: stable, convectively unstable and absolutely unstable. Thus, suggesting a picture of relaminarization along the inward path.

More recently Jasmine & Gajjar (2005c) have investigated the BEK family, where the rotating fluid is between a rotating-disk and a stationary-lid. The distance between the disk and lid was allowed to vary and it was shown that instability is enhanced as the distance between the disk and lid is increased. The region of instability tends towards that given by Lingwood, for large distances.

As already discussed in previous chapters, Davies & Carpenter (2003) have studied the global behaviour of the absolute instability corresponding to the rotating-disk boundary-layer, using a velocity-vorticity formulation described in Davies & Carpenter (2001). Refer to chapters 2 and 3 for details of their study and formulation. The following study extends the investigation of Davies & Carpenter (2003) to the complete system of rotating flows; *BEK* family. The velocity-vorticity equations are adapted to include the complete family of rotating flows and an investigation is carried out on the Bödewadt, Ekman and von Kármán flows.

The remainder of the chapter is as follows; the subsequent section discusses the equations for the Ekman layer and gives plots for the mean flow and Ekman spiral.

In section 6.3, the velocity-vorticity formulation of Davies & Carpenter (2001) is extended to the complete family of rotating flows with results given in section 6.4 for various flows belonging to the *BEK* family. Finally, the results are discussed and conclusions are given in section 6.5.

6.2 The Ekman equations and spiral

The Ekman layer consists of a rotating fluid flow over a rotating flat solid surface extended infinitely in both the streamwise x and spanwise y directions. The vertical direction z above the surface, is infinite in extent and the solid surface lies on the plane $z = 0$. The fluid and plate rotate about the same vertical axis with constant angular velocity Λ. We assume that the flow $\underline{u}$ is small compared with the rotation of the system. Thus, the convective term $(\underline{u}.\nabla)\underline{u}$ in equation (2.1) is small and may be neglected in comparison with the Coriolis term $2\Lambda \wedge \underline{u}$. The Navier-Stokes equations for a weak flow $\underline{u}$ in a state of rotation with angular velocity Λ are given as

$$\text{Momentum: } \frac{\partial \underline{u}}{\partial t} + 2\Lambda \wedge \underline{u} = -\frac{1}{\rho}\nabla p + \nu \nabla^2 \underline{u},$$

$$\text{Continuity: } \nabla.\underline{u} = 0, \tag{6.2}$$

where all terms are as before and dimensional. It is assumed that variations of $\underline{u}$ with z are more rapid than those with x or y. The equations giving the mean velocity components U and V at the boundary $z = 0$ for the Ekman layer are

$$-2\Lambda V = -\frac{1}{\rho}\frac{\partial p}{\partial x} + \nu \frac{\partial^2 U}{\partial z^2}, \tag{6.3}$$

$$2\Lambda U = \nu \frac{\partial^2 V}{\partial z^2}, \tag{6.4}$$

where ρ and ν are the fluid density and kinematic viscosity, respectively. There are no-slip conditions at $z = 0$ and as $z \to \infty$, $V(z \to \infty) = V_\infty = (\partial p/\partial x)/(2\rho\Lambda)$. After some manipulation the non-dimensionalized analytic solutions (6.3) - (6.4) may be

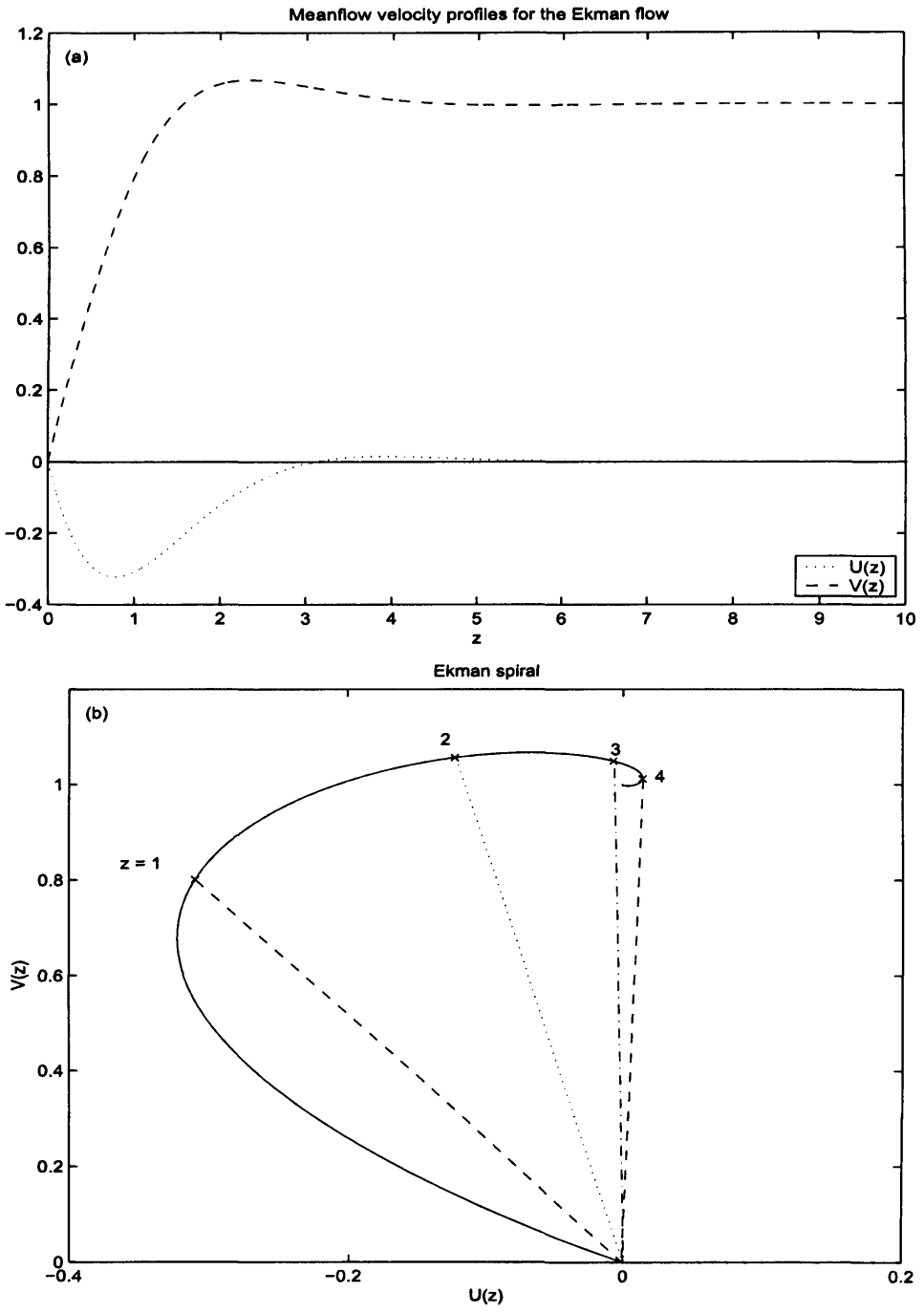

Figure 6.4: *(a): The mean flow velocity profiles for the Ekman layer. (b): The Ekman spiral.*

given as

$$U(\eta) = -e^{-\eta}\sin(\eta), \tag{6.5}$$

$$V(\eta) = 1 - e^{-\eta}\cos(\eta), \tag{6.6}$$

where $\eta = z(\Lambda/\upsilon)^{\frac{1}{2}}$ is the non-dimensional normal component.

Figure 6.4 displays the plots of the mean velocity profiles U, V against the normal direction and as an Ekman spiral.

6.3 Rotating flow theory

6.3.1 The mean flow equations

The following fluid flow model describes the family of rotating boundary-layer flows, which are induced by a rotating incompressible fluid with angular speed Λ_f^*, above a rotating disk with angular speed Λ_d^*, about the same axis of rotation. This family is commonly referred to as the *BEK* system (Lingwood, 1997b). As mentioned previously, particular cases of this system, are the Bödewadt, Ekman and von Kármán layers. The radius of the disk and the extent of the fluid above the disk are taken to be infinite. The Bödewadt layer arises when $\Lambda_d^* = 0$ and $\Lambda_f^* \neq 0$. The von Kármán layer occurs when $\Lambda_f^* = 0$ and $\Lambda_d^* \neq 0$, and for the Ekman layer $\Lambda_d^* \approx \Lambda_f^*$. In between these examples there are various flows in which both disk and fluid are rotating, but with differing angular velocities. The momentum and continuity equations in cylindrical polar coordinates r^*, θ^* and z^*, in a system rotating with angular speed Λ_d^* are given as

$$\frac{\partial U_r^*}{\partial t^*} + (\mathbf{U}^*.\nabla)U_r^* - \frac{U_\theta^{*2}}{r} - 2\Lambda_d^* U_\theta^* = -\frac{1}{\rho^*}\frac{\partial P^*}{\partial r^*} + \nu^*\left(\nabla^2 U_r^* - \frac{U_r^*}{r^{2*}} - \frac{2}{r^{2*}}\frac{\partial U_\theta^*}{\partial \theta^*}\right), \tag{6.7}$$

$$\frac{\partial U_\theta^*}{\partial t^*} + (\mathbf{U}^*.\nabla)U_\theta^* + \frac{U_\theta^* U_r^*}{r} + 2\Lambda_d^* U_r^* = -\frac{1}{r^*\rho^*}\frac{\partial P^*}{\partial \theta^*} + \nu^*\left(\nabla^2 U_\theta^* - \frac{U_\theta^*}{r^{2*}} + \frac{2}{r^{2*}}\frac{\partial U_r^*}{\partial \theta^*}\right), \tag{6.8}$$

$$\frac{\partial U_z^*}{\partial t^*} + (\mathbf{U}^*.\nabla)U_z^* = -\frac{1}{\rho^*}\frac{\partial P^*}{\partial z^*} + \nu^*\nabla^2 U_z^*, \tag{6.9}$$

$$\frac{1}{r^*}\frac{\partial(r^*U_r^*)}{\partial r^*} + \frac{1}{r^*}\frac{\partial U_\theta^*}{\partial \theta^*} + \frac{\partial U_z^*}{\partial z^*} = 0, \tag{6.10}$$

where U_r^*, U_θ^* and U_z^* are the mean radial, azimuthal and normal velocities, respectively. Here P^* denotes the mean pressure and ρ^* the fluid density. (Where $*$ denotes dimensional quantities).

The exact similarity solutions to the Navier-Stokes equations, due to von Kármán, can be generalized for the *BEK* family. Thus, we have the following dimensionless similarity variables

$$\begin{aligned}(U_r^*, U_\theta^*, U_z^*, P^*) &= (r^*\Delta\Lambda^* F(z), r^*\Delta\Lambda^* G(z), \delta^*\Delta\Lambda^* H(z), \rho^*(\delta^*\Delta\Lambda^*)^2 P(z)), \\ &= (r^*\Lambda^* RoF(z), r^*\Lambda^* RoG(z), \delta^*\Lambda^* RoH(z), \rho^*\nu^*\Lambda^* Ro^2 P(z)),\end{aligned} \tag{6.11}$$

where $\Delta\Lambda^* = \Lambda_f^* - \Lambda_d^*$, r is the dimensionless radius, and $z = z^*/\delta^*$ is the non-dimensional normal direction, where $\delta^* = (\nu^*/\Lambda^*)^{\frac{1}{2}}$ is the boundary-layer thickness, providing the non-dimensionalization of distances. Here ν^* is the kinematic viscosity, Λ^* is the system rotation rate and Ro is the Rossby number, which are defined as

$$\Lambda^* = \frac{\Lambda_f^*}{2 - Ro} + \frac{\Lambda_d^*}{2 + Ro} = \frac{\Lambda_f^* + \Lambda_d^*}{4} + \left(\left(\frac{\Lambda_f^* + \Lambda_d^*}{4}\right)^2 + \frac{(\Delta\Lambda^*)^2}{2}\right)^{\frac{1}{2}}, \tag{6.12}$$

$$Ro = \frac{\Delta\Lambda^*}{\Lambda^*}. \tag{6.13}$$

Therefore, for the von Kármán layer Ro = -1 and $\Lambda^* = \Lambda_d^*$, for the Ekman layer $Ro = 0$ and $\Lambda^* = \Lambda_d^* = \Lambda_f^*$, and for the Bödewadt layer $Ro = 1$ and $\Lambda^* = \Lambda_f^*$. On substituting equation (6.11) into the Navier-Stokes equations (6.7) - (6.10), the following non-dimensional mean flow equations are obtained

$$Ro(F^2 + HF' - (G^2 - 1)) - Co(G - 1) = F'', \tag{6.14}$$

$$Ro(2FG + HG') + CoF = G'', \tag{6.15}$$

$$Ro(HH' + P') = H'', \tag{6.16}$$

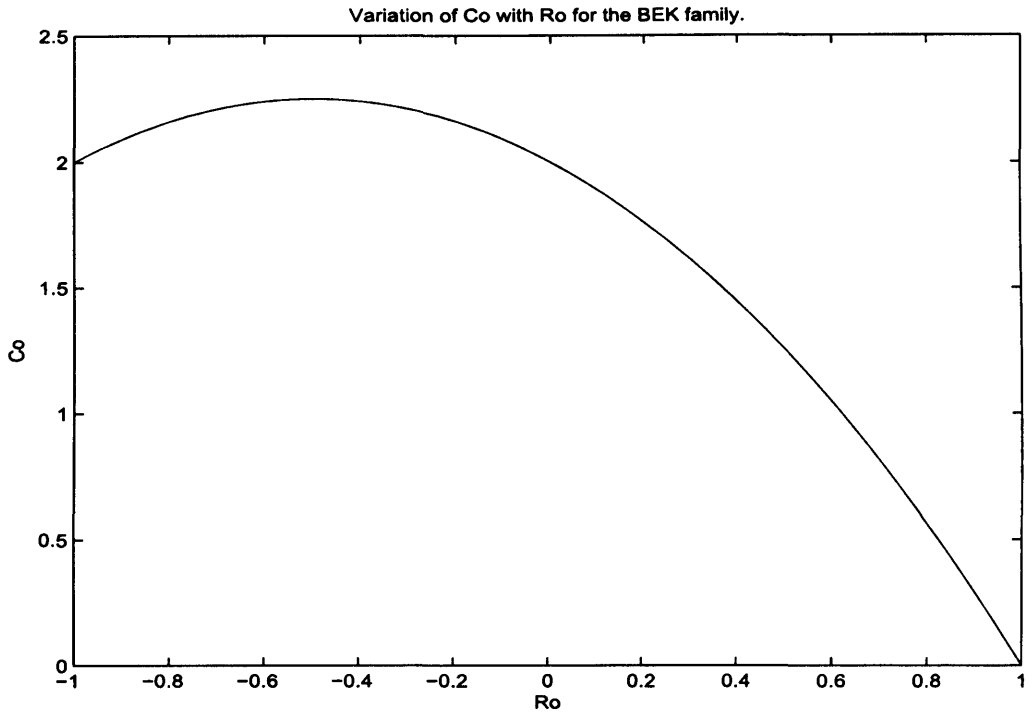

Figure 6.5: *Variation in Coriolis parameter with Rossby number.*

$$2F + H' = 0, \tag{6.17}$$

where the prime denotes differentiation with respect to the normal component z. The Coriolis parameter is defined as $Co = \frac{2\Lambda_d^*}{\Lambda^*} = 2 - Ro - Ro^2$. The variation in the Coriolis parameter with the Rossby number is plotted in figure 6.5.

For the von Kármán and Ekman flows $Co = 2$, and $Co = 0$ for the Bödewadt flow. Equations (6.14) - (6.17) are solved subject to the boundary conditions

$$F(0) = G(0) = H(0) = P(0) = 0, \tag{6.18}$$

$$F(z \to \infty) = 0, \qquad G(z \to \infty) = 1. \tag{6.19}$$

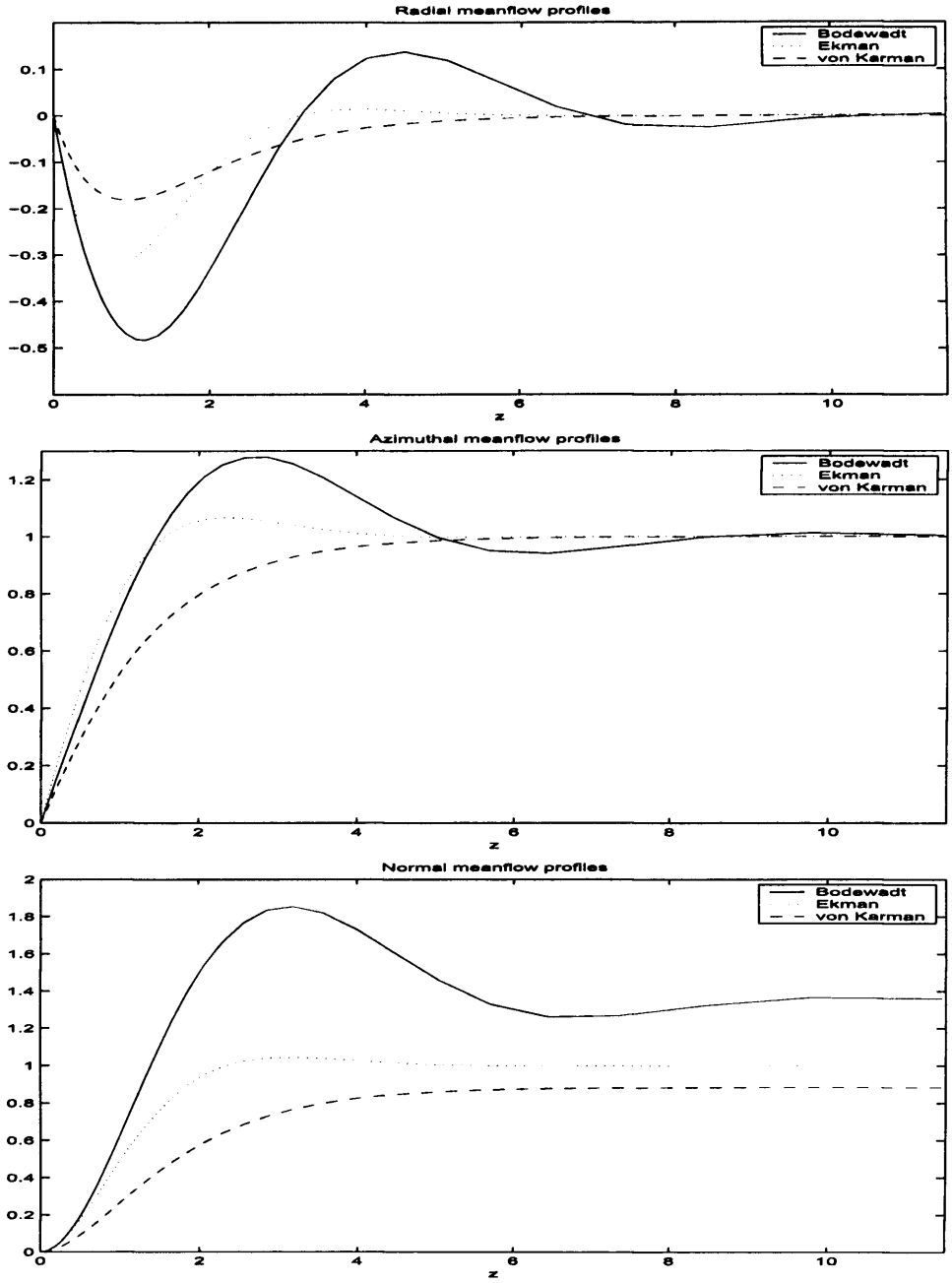

Figure 6.6: *The mean flow velocity profiles for the radial (F), azimuthal (G) and normal (H) components for the Bodewadt, Ekman and von Kármán flows.*

The non-dimensional undisturbed flow can be taken as

$$\mathbf{U}(r,z) = \left(\frac{rRo}{Re}F(z), \frac{rRo}{Re}G(z), \frac{Ro}{Re}H(z)\right), \tag{6.20}$$

where Re, the Reynolds number is defined as

$$Re = r_a^*\left(\frac{\Delta\Lambda^*\delta^*}{\nu^*}\right) = r_a Ro, \tag{6.21}$$

for some radial position r_a^*. Obviously, for Rossby numbers that are negative the Reynolds number will also be negative. However, any results that may be presented will only consider the magnitude of the Reynolds number. The non-dimensionalized velocity, pressure and time scales are $r_a^*\Lambda^* Ro$, $\rho^* r_a^{*2}\Lambda^{*2}Ro^2$ and $\delta^*/(r_a^*\Lambda^* Ro)$, respectively. Also, the non-dimensionalized rotation rate is equal to $1/Re$. Therefore, when working in a frame of reference that rotates with the disk,

$$\Lambda = \frac{1}{Re} = \frac{1}{r_a Ro}, \tag{6.22}$$

which is required for the Coriolis terms included in the velocity transport equations, which are to be discussed in the subsequent section.

The set of ordinary differential equations (6.14) - (6.19) were solved using an adaptation of the earlier program created in Matlab; refer to the appendices. The collocation points were selected as before using equations (4.15) and (4.16). Figure 6.6 displays the mean velocity profiles for the *BEK* flows; Bödewadt: solid line; Ekman: dotted line; and von Kármán: dashed line.

It can be seen for the von Kármán flow that an inflectional profile is only found for the radial velocity. However, as the Rossby number increases, the azimuthal and normal velocities also become inflectional. This can be seen in the plots for the respective Bödewadt and Ekman layers. Values for F', G' at $z = 0$ and H as $z \to \infty$ are given to eight decimal places in table 6.1 for varying Rossby numbers. On comparing with previous results, Lingwood (1997b) (italics), Jasmine & Gajjar (2005c) (bold), MacKerrell (2005) (brackets), the tabulated results agree.

Rossby number (Ro)	$F'(0)$	$G'(0)$	$H(\infty)$
1.0	-0.94197072	0.77288499	1.34925834
1.0	*-0.9420*	*0.7729*	-
1.0	**-0.941971**	**0.772885**	**1.3493**
(1.0)	(-0.9420)	(0.7729)	(1.349)
0.9	-0.95962008	0.88587380	1.28241034
0.8	-0.97833154	0.87029290	1.21892073
0.8	*-0.9783*	*0.8703*	-
0.7	-0.99494056	0.90714810	1.16502767
0.6	-1.00821710	0.93724654	1.120863233
0.6	*-1.0082*	*0.9372*	-
0.5	-1.01762653	0.96119299	1.08527848
0.4	-1.02290906	0.97942826	1.05703869
0.4	*-1.0229*	*0.9794*	-
0.3	-1.02391257	0.99226379	1.03510339
0.2	-1.02051746	0.99990618	1.01866214
0.2	*-1.0205*	*1.0000*	-
0.1	-1.01259816	1.00247277	1.00710811
0.0	-1.00000000	1.00000000	1.00000000
0.0	*-1.000*	*1.000*	-
0.0	**-1.000**	**1.000**	**0.9999**
-0.1	-0.98252154	0.99244538	0.99702417
-0.2	-0.95989730	0.97968316	0.99795520
-0.2	*-0.9599*	*0.9797*	-
-0.3	-0.93177697	0.96149252	1.00260470
-0.4	-0.89769736	0.93753544	1.01073519
-0.4	*-0.8977*	*0.9375*	-
-0.5	-0.85704142	0.90731813	1.02188487
-0.6	-0.80897549	0.87012324	1.03496431
-0.6	*-0.8090*	*0.8701*	-
-0.7	-0.75234810	0.82488398	1.04722939
-0.8	-0.68551928	0.76992535	1.05132964
-0.8	*-0.6855*	*0.7699*	-
-0.9	-0.60605895	0.70233712	1.02518373
-1.0	-0.51023262	0.61592206	0.88447339
-1.0	*-0.5102*	*0.6159*	-
-1.0	**-0.51023**	**0.61592**	**0.88447**

Table 6.1: *Values of F', G' at $z = 0$ and H at infinity for various Rossby numbers (Ro); roman - current thesis; italics - Lingwood (1997b), bold - Jasmine & Gajjar (2005a), brackets - Mackerrell (2005).*

6.3.2 Velocity-vorticity formulation

The velocity-vorticity formulation for the *BEK* family, is simply an extension of the rotating-disk formulation first described by Davies & Carpenter (2001); as discussed in chapters 2, 3, 4 and 5. For the *BEK* family, the velocity and vorticity perturbation fields may be represented as

$$\underline{u} = (u_r, u_\theta, u_z),$$

$$\underline{w} = (\omega_r, \omega_\theta, \omega_z),$$

where the subscripts r, θ and z refer to the radial, azimuthal and normal directions, respectively. Then on taking the primary variables to be the components $\{\omega_r, \omega_\theta, u_z\}$, the Navier-Stokes equations are fully equivalent to the following set of linearized governing equations

$$\frac{\partial \omega_r}{\partial t} + \frac{1}{r}\frac{\partial N_z}{\partial \theta} - \frac{\partial N_\theta}{\partial z} - Co\Lambda\left(\omega_\theta + \frac{\partial u_z}{\partial r}\right) = \frac{1}{Re}\left(\left(\nabla^2 - \frac{1}{r^2}\right)\omega_r - \frac{2}{r^2}\frac{\partial \omega_\theta}{\partial \theta}\right), \quad (6.23)$$

$$\frac{\partial \omega_\theta}{\partial t} + \frac{\partial N_r}{\partial z} - \frac{\partial N_z}{\partial r} + Co\Lambda\left(\omega_r - \frac{1}{r}\frac{\partial u_z}{\partial \theta}\right) = \frac{1}{Re}\left(\left(\nabla^2 - \frac{1}{r^2}\right)\omega_\theta + \frac{2}{r^2}\frac{\partial \omega_r}{\partial \theta}\right), \quad (6.24)$$

$$\nabla^2 u_z = \frac{1}{r}\left(\frac{\partial \omega_r}{\partial \theta} - \frac{\partial (r\omega_\theta)}{\partial r}\right), \quad (6.25)$$

where $\mathbf{N} = (N_r, N_\theta, N_z)$ is as before, equation (4.22), but its components (4.23) - (4.26), are multiplied by the Rossby term Ro. Hence,

$$N_r : \frac{Ro}{Re}(-2Gu_\theta + H\omega_\theta - rG\omega_z), \quad (6.26)$$

$$N_\theta : \frac{Ro}{Re}(rG'u_z + 2Gu_r - H\omega_r + rF\omega_z), \quad (6.27)$$

$$N_z : \frac{rRo}{Re}(-G'u_\theta - F'u_r + G\omega_r - F\omega_\theta), \quad (6.28)$$

$$\frac{\partial N_z}{\partial r} : \frac{Ro}{Re}(-G'u_\theta - rG'\frac{\partial u_\theta}{\partial r} - rF''u_z + F'inu_\theta + G\omega_r + rG\frac{\partial \omega_r}{\partial r} - F\omega_\theta - rF\frac{\partial \omega_\theta}{\partial r}). \quad (6.29)$$

Here we have assumed that modes have an $\exp\{in\theta\}$ dependence. The convective quantity $\mathbf{N}$, can only be evaluated if the remaining components $\{u_r, u_\theta, \omega_z\}$ are known. These so called secondary variables are again defined by equations (4.27) - (4.29).

6.3.3 Linearization and integral constraints

As stated above the governing equations are linearized, which allows the problem to become separable with respect to the azimuthal direction. Therefore, we can consider modes

$$\underline{u} = (u_r, u_\theta, u_z)e^{in\theta}, \qquad \underline{\omega} = (\omega_r, \omega_\theta, \omega_z)e^{in\theta}, \tag{6.30}$$

where $n = \beta\frac{Re}{Ro}$ is the integer-valued, azimuthal mode number and β is the azimuthal wavenumber.

The linearization also permits the no-slip conditions and the wall-normal zero-displacement conditions to become

$$u_r = -\frac{rRo}{Re}F'(0)\eta, \tag{6.31}$$

$$u_\theta = -\frac{rRo}{Re}G'(0)\eta, \tag{6.32}$$

$$u_z = \frac{\partial \eta}{\partial t}, \tag{6.33}$$

at $z = 0$. Where η is the non-dimensional vertical wall displacement. On substituting equations (6.31) - (6.32) into the definitions (4.27) and (4.28) for the secondary variables u_r, u_θ, the following integral constraints on the primary variables are obtained, which replace the no-slip conditions (6.31), (6.32)

$$\int_0^\infty \omega_\theta dz = \frac{rRo}{Re}F'(0)\eta - \int_0^\infty \frac{\partial u_z}{\partial r}dz, \tag{6.34}$$

$$\int_0^\infty \omega_r dz = -\frac{rRo}{Re}G'(0)\eta + \int_0^\infty \frac{inu_z}{r}dz. \tag{6.35}$$

Equation (6.33) does not change as a boundary condition and acts as the third constraint on the primary variables. Also the assumed azimuthal mode structure has been used to replace partial derivatives with respect to θ by the factor in, where n is as before.

6.4 Results

Much like chapter 4, disturbances were impulsively excited using a wall motion, defined in equations (4.37) - (4.38). Numerical simulations were carried out for the particular cases; von Kármán, Ekman and Bödewadt boundary-layers. A study was also conducted for various intermediate rotating mean flows, which can be found for $-1 < Ro < 0$ and $0 > Ro > 1$. For these examples, Lingwood's (1997b) critical values for absolute instability were used to validate the results of the parallel numerical simulations. The results are displayed in table 6.2, where Re_c is the Reynolds number, β_c is the azimuthal wavenumber, $\hat{n}_c = n_c Ro = \beta_c Re_c$ is the modified integer valued azimuthal mode number (where n_c is the azimuthal mode number), α_c is the radial wavenumber and ω_c and $\omega_c Re_c$ are the temporal frequencies for critical absolute instability. The results in roman-type are those given by Lingwood (1997b), while the data in italics refers to the results obtained by Jasmine (2003), Jasmine & Gajjar (2005c), and the data in bold refers to the results of the numerical simulations (where the parallel flow approximation has been employed). For the numerical simulations, we only checked the stability characteristics for integer values of the Reynolds number. This was to avoid excessive parametric studies. However, the results obtained from the numerical simulations are consistent with those obtained by earlier studies.

The non-dimensional frequencies ω_c are found to be exact to within three decimal places (in most cases), while the radial wavenumber α_c are the same to within two decimal places (in most cases). The temporal growth rates were found to be approximately zero (in all cases), which is consistent with critical absolute instability. Also, the modified azimuthal mode number $\hat{n}_c$ has been rounded to the nearest integer, so as to satisfy the circumferential periodicity of the problem.

Results for the mean flows with $Ro > 0.6$ are not given, since the numerical simulations did not produce very meaningful results at small Reynolds numbers. Several

Ro	Re_c	β_c	$\hat{n}_c$	ω_c	α_c	$\omega_c Re_c$
-1.0	507.3	0.1350	68	-0.0349	0.217 - i0.122	-17.705
-1.0	*507.06*	*0.1340*	*68*	*-0.0345*	*0.217 - i0.121*	*-17.49*
-1.0	**508**		**68**	**-0.03435**	**0.2192 - i0.1153**	**-17.451**
-0.8	434.8	0.155	67	-0.0393	-0.252 - i0.142	-17.088
-0.8	**435**		**67**	**-0.03924**	**0.2526 - i0.1369**	**-17.070**
-0.6	345.4	0.1690	58	-0.0418	-0.294 - i0.164	-14.438
-0.6	**346**		**58**	**-0.0416**	**0.2946 - i0.1528**	**-14.409**
-0.4	284.7	0.178	51	-0.0425	-0.329 - i0.180	-12.100
-0.4	**285**		**51**	**-0.0418**	**0.3289 - i0.1741**	**-11.920**
-0.2	238.5	0.182	43	-0.0413	-0.357 - i0.191	-9.850
-0.2	**239**		**43**	**-0.04057**	**0.3542 - i0.1878**	**-9.6952**
0.0	198.0	0.1840	36	± 0.0397	0.379 ± i0.195	± 7.861
0.0	*198.81*	*0.181*	*36*	*± 0.0378*	*0.377 ± i0.196*	*± 7.53*
0.0	**198**		**36**	**± 0.03964**	**0.3780 ± i0.1857**	**± 7.849**
0.2	161.5	0.173	28	0.0314	0.393 + i0.197	5.071
0.2	**162**		**28**	**0.03080**	**0.3917 + i0.1910**	**4.9893**
0.4	124.5	0.157	20	0.0199	0.403 + i0.191	2.478
0.4	**125**		**20**	**0.01970**	**0.4026 + i0.1802**	**2.4629**
0.6	87.3	0.1250	11	-0.00252	0.410 + i0.176	-2.200
0.6	**88**		**11**	**-0.00261**	**0.4027 + i0.1617**	**-2.3000**
0.8	51.4	0.0495	3	-0.0616	0.406 + i0.141	-3.166
0.8	-		-	-	-	-
1.0	21.6	-0.1174	-3	-0.218	0.340 + i0.0776	-4.709
1.0	*21.66*	*-0.1174*	*-3*	*-0.217*	*0.341 + 0.0803*	*-4.71*
1.0	-		-	-	-	-

Table 6.2: *Critical values for the onset of absolute instability as found by Lingwood (1997a). (Table corresponds to a small section of table III in Lingwood (1997a).) The values in italics refer to those found by Jasmine (2003). The values in bold correspond to those found from the numerical simulation results.*

problems, such as, numerical instabilities and problems with the inflow/outflow conditions, arose, which prevented satisfactory results. Thus, we were unable to obtain results for the Bödewadt flow, for either the parallel method or non-parallel method. However, as we will see shortly, the disturbance characteristics of the Bödewadt flow,

can to some extent be predicted by extrapolating the stability behaviour of other rotating boundary-layers.

The onset of absolute instability for the various mean flows is summarized in figure 6.7, (figure 10 of Lingwood, 1997b). The solid line gives the critical Reynolds number for the onset of absolute instability, as a function of the Rossby number Ro, while the dashed line gives the critical radii for the onset of absolute instability, as a function of Ro. Above these lines, exists the absolutely unstable region, while convective instability and stability are observed at smaller radii and Reynolds numbers. A singularity arises for $Ro = 0$ (Ekman layer) within the Rossby number - radius plot ($r = Re/Ro \rightarrow \infty$ as $Ro \rightarrow 0$). Hence, all radial positions are equivalent. Thus, the Ekman layer is strictly parallel.

6.4.1 The von Kármán layer

The first problem considered is the von Kármán layer or rotating-disk boundary-layer. Here the Rossby number $Ro = -1$. The critical Reynolds number for absolute instability is $Re_c = 507.3$ for an azimuthal mode number $\hat{n} = 68$, Lingwood (1995, 1996, 1997a,b), where $\hat{n} = nRo = \beta Re$. (Note that for negative Ro, the Reynolds number and modified azimuthal mode number $\hat{n}$ are negative. This is due to negative and positive Rossby-number flows being considered in the same model. However, for the subsequent study, we will only state the magnitude of Re and $\hat{n}$).

Although Davies & Carpenter (2003) have already discussed (in depth) the effects of non-parallelism within the rotating-disk boundary-layer (refer to chapter 2), we have included some further simulation results, for slightly different parameter values, with the aim of illustrating the behaviour discovered by Davies & Carpenter (2003).

A disturbance was impulsively excited, for a parallel flow, for a Reynolds number $Re = 508$ and azimuthal mode number $\hat{n} = 68$. The disturbance is located at the

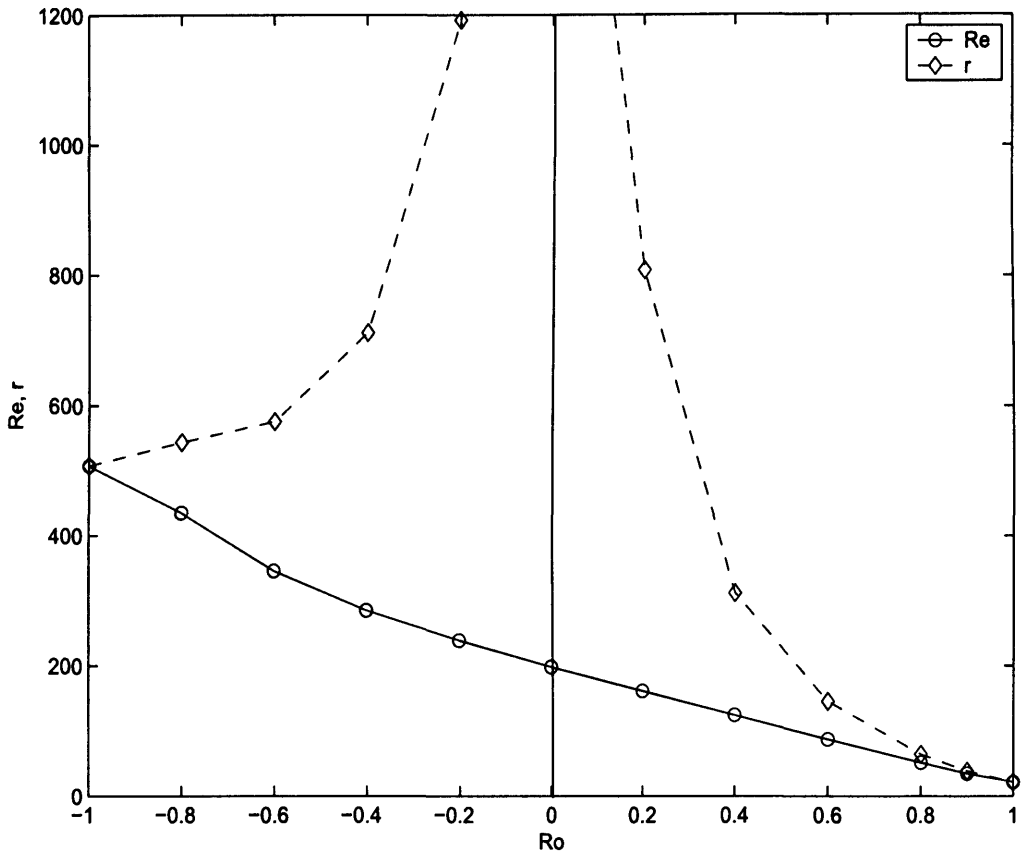

Figure 6.7: *Critical Reynolds number (solid line) and radii (dashed line) for the onset of absolute instability for the BEK family. The circles (○) and diamonds (◇) mark the calculated data points from Lingwood (1997b), and the areas above the lines correspond to the regions of absolute instability.*

boundary of absolute instability. Figure 6.8(a) displays the spatio-temporal development plot for the above disturbance. The development is plotted using contours $|\omega_{\theta,w}|$. The leading-edge propagates radially outwards with a non-zero velocity, while the trailing-edge propagates with a diminishing velocity. Hence, critical absolute instability is observed.

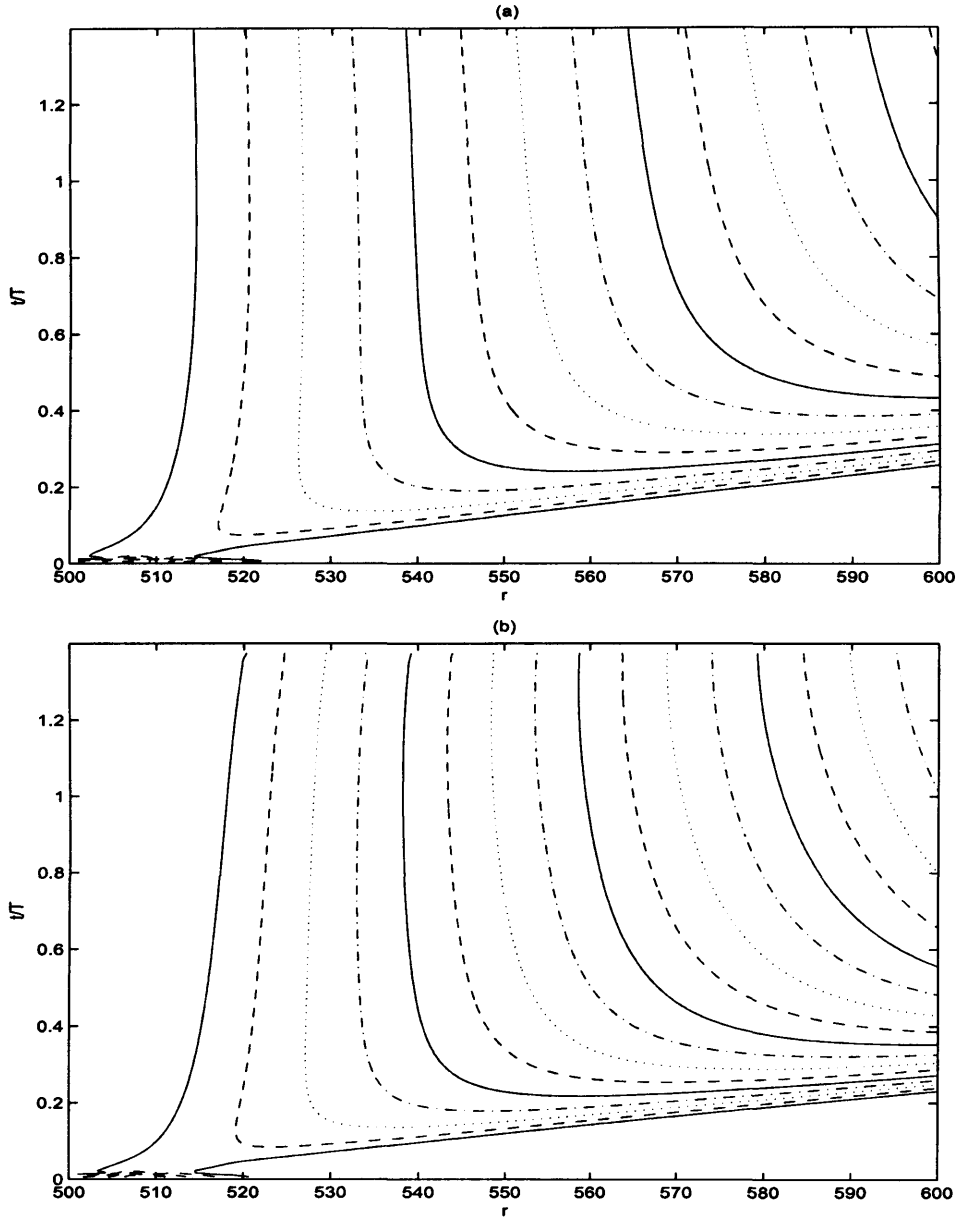

Figure 6.8: *Spatio-temporal development of* $|\omega_{\theta w}|$ *for an impulsively excited disturbance with an azimuthal mode number* $\hat{n} = 68$. *The disturbance was excited at* $r_e = 508$. *(a) - parallel flow with Re = 508, (b) - non-parallel flow. (Contours are drawn using a logarithmic scale, with levels separated by factors of two).*

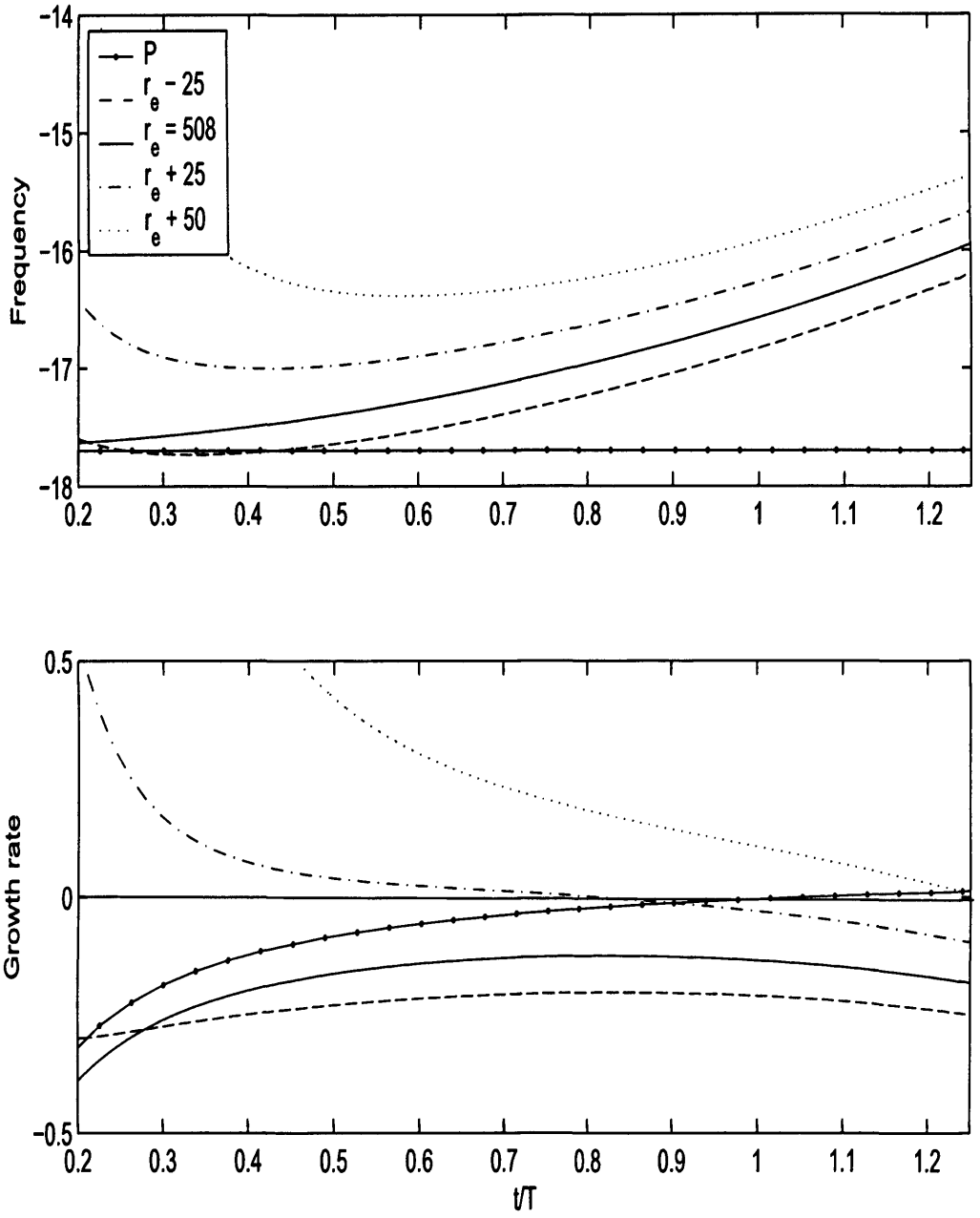

Figure 6.9: *Local temporal frequencies $\omega_r Re$ and temporal growth rates $\omega_i Re$ for a disturbance with $\hat{n}$ = 68 developing in a non-parallel flow. The impulsive excitation was centred at r_e = 508. The temporal development is plotted for four different radial positions, r_e - 25, r_e, r_e + 25 and r_e + 50. The solid lines labeled with a P show the development in a parallel flow with Re = 508.*

The corresponding non-parallel disturbance was impulsively excited at the radial location $r_e = 508$ and the disturbance wavepacket is plotted in figure 6.8(b). The leading edge propagates radially outwards with a non-zero velocity, while the trailing-edge propagates radially outward with (what appears to be) an increasing velocity. Hence, convective behaviour is observed. Therefore, the disturbance behaviour is consistent with the study by Davies & Carpenter (2003); as required.

Figure 6.9 displays the non-parallel frequencies and growth rates for the radial locations r_e - 25, $r_e = 508$, r_e + 25 and r_e + 50. The solid lines labeled with a P, show the development at the point of impulsive excitation, for the disturbance in a parallel flow, with $Re = 508$. The parallel frequency is comparable with that given by Lingwood (1997b). On the other hand the non-parallel frequencies increase in the manner observed by Davies & Carpenter (2003). The non-parallel growth rates are also consistent with the behaviour found in Davies & Carpenter (2003), since they decrease with increasing time.

6.4.2 Results for $-1 < Ro < 0$

***Ro* = -0.8**

The results for the non-parallel flow are comparable with the results of the von Kármán boundary-layer. Figure 6.10 displays the wavepacket development, frequencies and growth rates for a disturbance impulsively excited at the critical radius for absolute instability $r_e = Re/Ro = 544$. The corresponding critical Reynolds number $Re = 435$, and azimuthal mode number $\hat{n} = 67$ or $n = 84$, where $\hat{n} = nRo = \beta Re$. The trailing edge of the disturbance wavepacket can be seen to propagate radially outwards with what appears to be an increasing velocity. Thus, convective type behaviour is found. For all selected radial locations, the non-parallel frequencies and growth rates increase and decrease, respectively, in a similar manner to that found for the von Kármán boundary-layer.

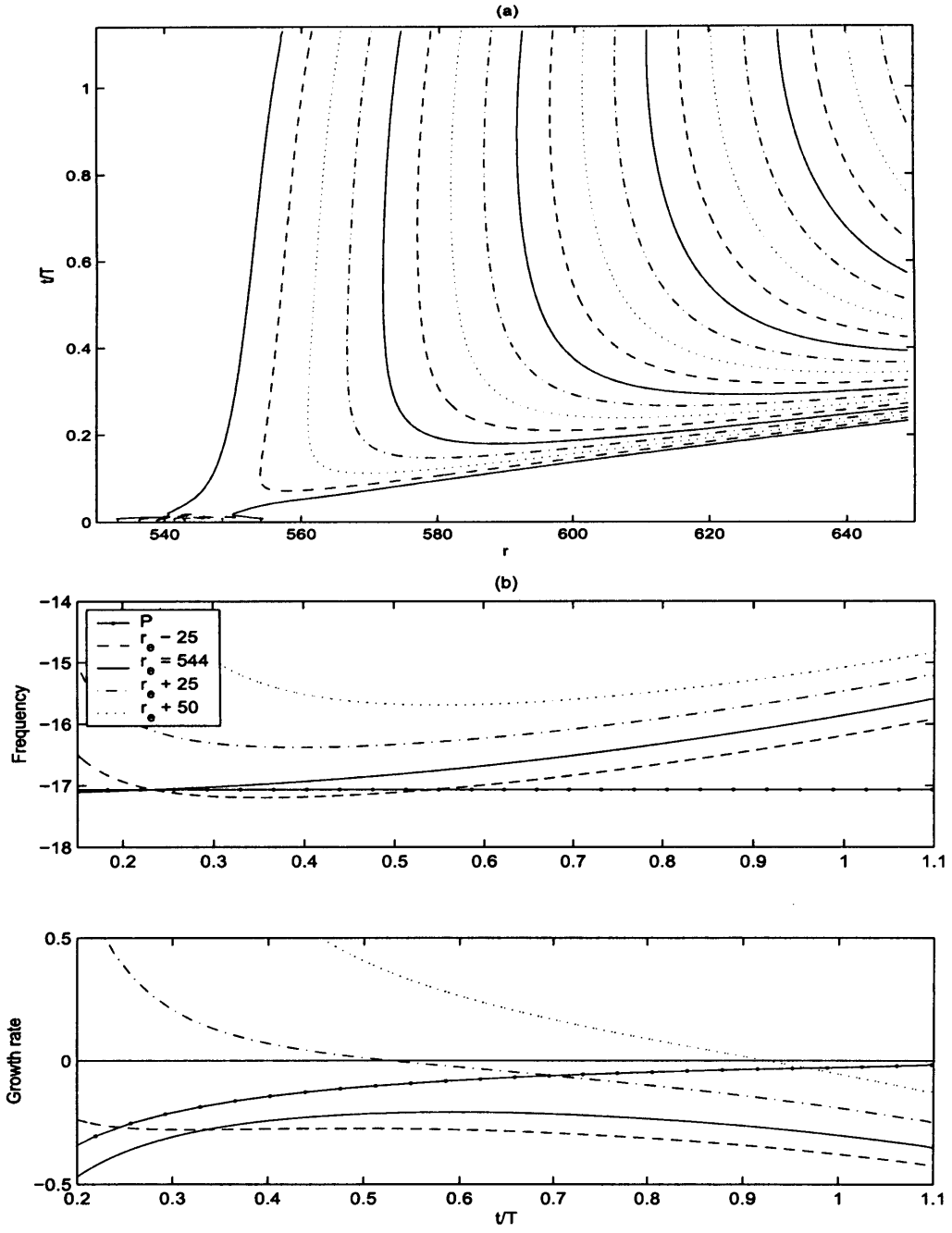

Figure 6.10: *Spatio-temporal development of* $|\omega_{\theta w}|$ *and local temporal frequencies* $\omega_r Re$ *and temporal growth rates* $\omega_i Re$ *for an impulsively excited disturbance with* $\hat{n} = nRo = \beta Re = 67$ *developing in a non-parallel flow. The disturbance was excited at* $r_e = Re/Ro = 544$. *The temporal development is plotted for four different radial positions,* r_e - 25, r_e, r_e + 25 *and* r_e + 50. *The solid lines labeled with a P show the development in a parallel flow with Re = 435 and Ro = -0.8.*

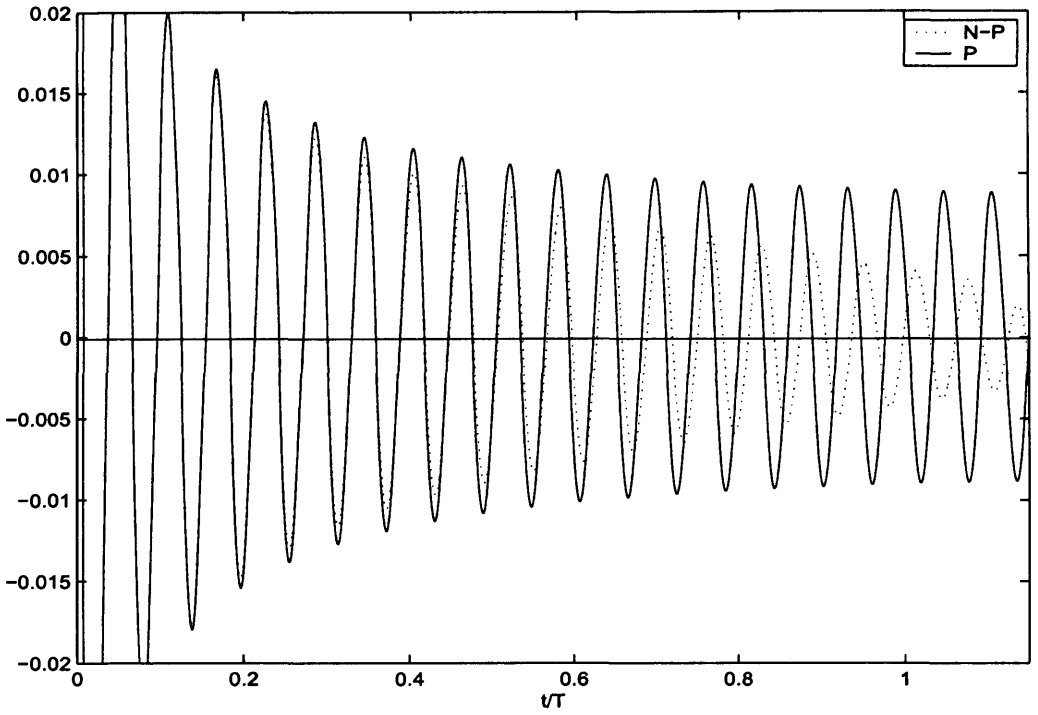

Figure 6.11: *Comparison of the variation of* $|\omega_{\theta,w}|$ *for a disturbance with* $\hat{n} = nRo = \beta Re = 67$ *evolving in non-parallel and parallel flow with Rossby number* $Ro = -0.8$. *The temporal development is shown for the radius* $r_e = Re/Ro = 544$ *where the impulsive excitation was centred. Dashed line: The non-parallel flow labeled N-P; solid line: parallel flow labeled P with* $Re = 435$.

Figure 6.11 displays the temporal evolution for the above parallel and non-parallel disturbance at the point of impulsive excitation $r_e = 544$. Initially, the two plots are quite close together. However, over a longer time period, there is a stronger decay and a clear increase in temporal frequency associated with the non-parallel case. Hence, the non-parallel effects are stabilizing.

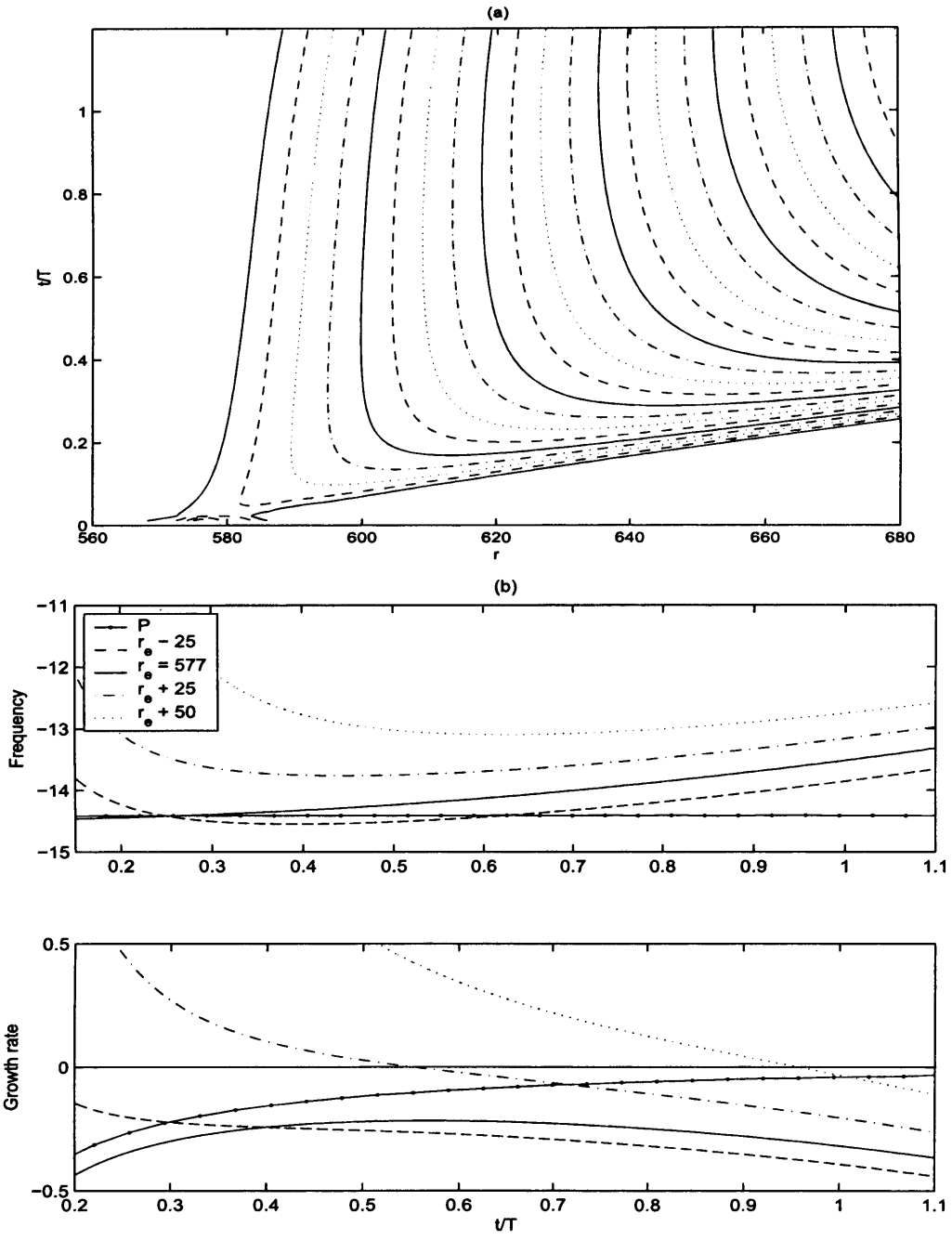

Figure 6.12: *Spatio-temporal development of* $|\omega_{\theta w}|$ *and local temporal frequencies* $\omega_r Re$ *and temporal growth rates* $\omega_i Re$ *for an impulsively excited disturbance with* $\hat{n} = 58$ *developing in a non-parallel flow. The disturbance was excited at* $r_e = Re/Ro = 577$. *The temporal development is plotted for four different radial positions,* r_e - 25, r_e, r_e + 25 *and* r_e + 50. *The solid lines labeled with a P show the development in a parallel flow with Re = 346 and Ro = -0.6.*

Ro = -0.6

A disturbance was impulsively excited at the critical radius for absolute instability $r_e = 577$, for an azimuthal mode number $\hat{n} = 58$, for $Ro = -0.6$. Figure 6.12 displays the wavepacket evolution, frequencies and growth rates for the above disturbance. The trailing edge of the wavepacket can be seen to propagate radially outwards in the convective manner we have become accustomed too.

The non-parallel temporal frequencies and growth rates are plotted for four equally spaced radial locations. Again, the frequencies increase, while the growth rates decrease. The lines labeled P refer to the parallel flow problem, where the Reynolds number $Re = 346$. The parallel frequency is approximately the same as that found by Lingwood (1997b); refer to table 6.2.

Ro = -0.4

For the rotating mean flow $Ro = -0.4$, a disturbance was impulsively excited at $r_e = 713$ for an azimuthal mode number $\hat{n} = 51$, (which corresponds to critical absolute instability). The leading edge of the disturbance (figure 6.13(a)) is propagating radially outwards with a non-zero velocity, while the trailing edge appears to be propagating with a diminishing velocity. However, if we consider a smaller radial range about the trailing edge (figure 6.14(b)), the disturbance is found to propagate radially outwards with (what appears to be) an increasing velocity. Therefore, it appears that convective behaviour is again dominating the disturbance characteristics. However, it is not as easy to identify as it was in the earlier rotating boundary-layers.

The non-parallel temporal frequencies and growth rates are plotted in figure 6.14. The frequencies and growth rates increase and decrease, respectively. However, the rate of increase (decrease) in frequency (growth), at each radial location, is far smaller than that was observed in the earlier rotating boundary-layers. This is not surprising, because the rotating flows become increasingly parallel as $Ro \rightarrow 0$. This would suggest

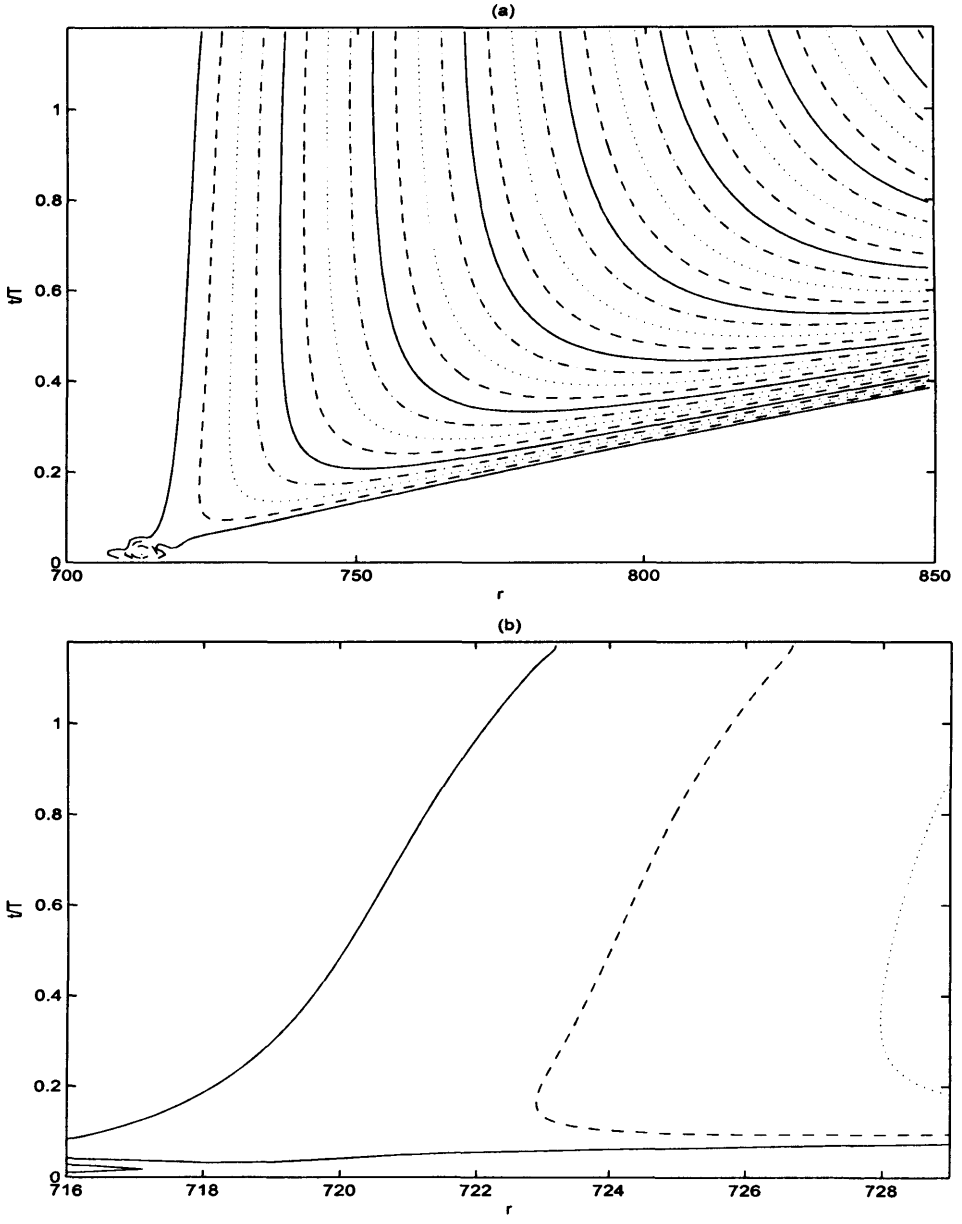

Figure 6.13: *Spatio-temporal development of* $|\omega_{\theta,w}|$ *for an impulsively excited disturbance with Rossby number Ro = -0.4, and an azimuthal mode number* $\hat{n} = 51$. *The disturbance was excited at* $r_e = Re/Ro = 713$. *(a) - full radial range, (b) - reduced radial range.*

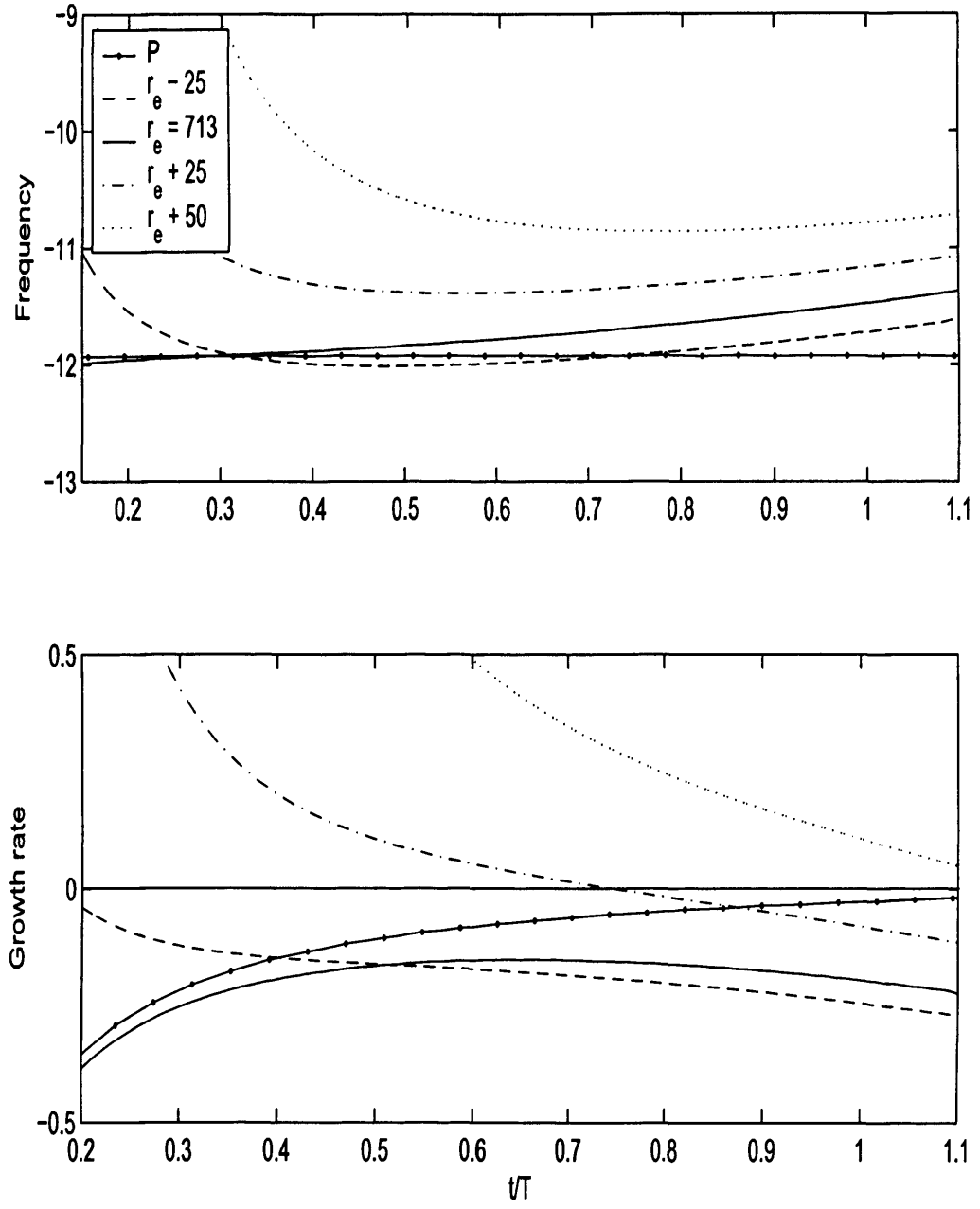

Figure 6.14: *Local temporal frequencies $\omega_r Re$ and temporal growth rates $\omega_i Re$ for a disturbance with $\hat{n}$ = 51 developing in a non-parallel flow with Rossby number Ro = -0.4. The impulsive excitation was centred at $r_e = Re/Ro$ = 713. The temporal development is plotted for four different radial positions, r_e - 25, r_e, r_e + 25 and r_e + 50. The solid lines labeled with a P show the development in a parallel flow with Re = 285.*

that for $Ro = -0.2$, the rate of change in frequency and growth at each radial location would be smaller than all previous rotating flows.

Ro = -0.2

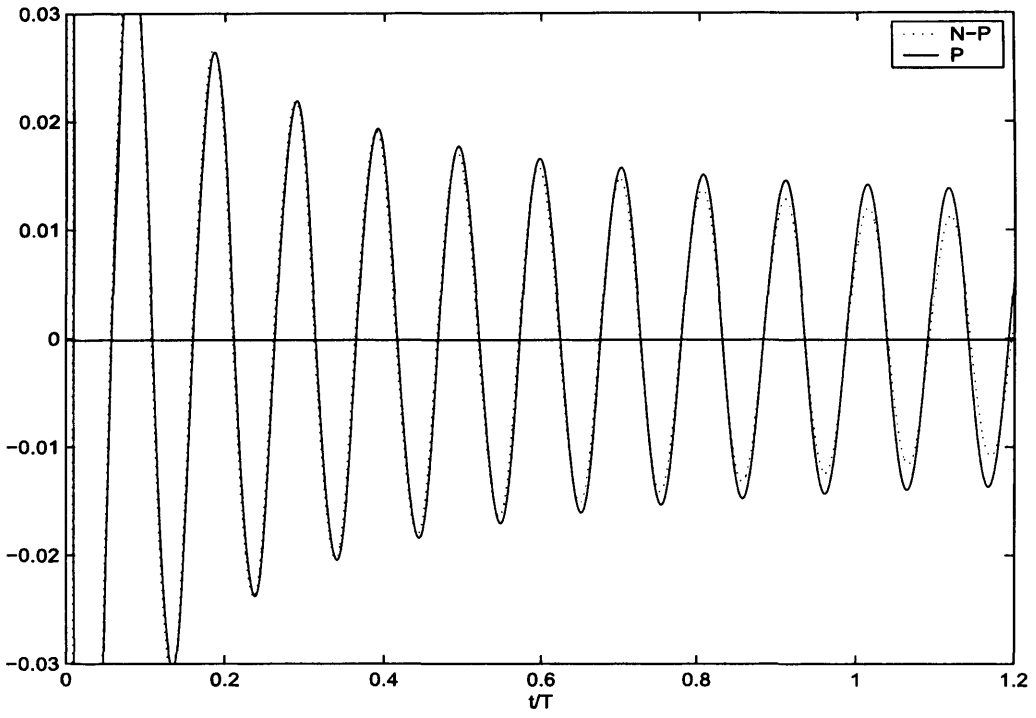

Figure 6.15: *Comparison of the variation of $|\omega_{\theta,w}|$ for a disturbance with $\hat{n} = 43$ evolving in non-parallel and parallel flow with Rossby number $Ro = -0.2$. The temporal development is shown for the radius $r_e = Re/Ro = 1195$ where the impulsive excitation was centred. Dashed line: The non-parallel flow labeled N-P; solid line: parallel flow labeled P with $Re = 239$.*

For $Ro = -0.2$ the critical Reynolds number for absolute instability is approximately $Re = 239$ for an azimuthal mode number $\hat{n} = 43$. Figure 6.15 displays the time histories for the above problem in a parallel flow (solid line) and non-parallel flow

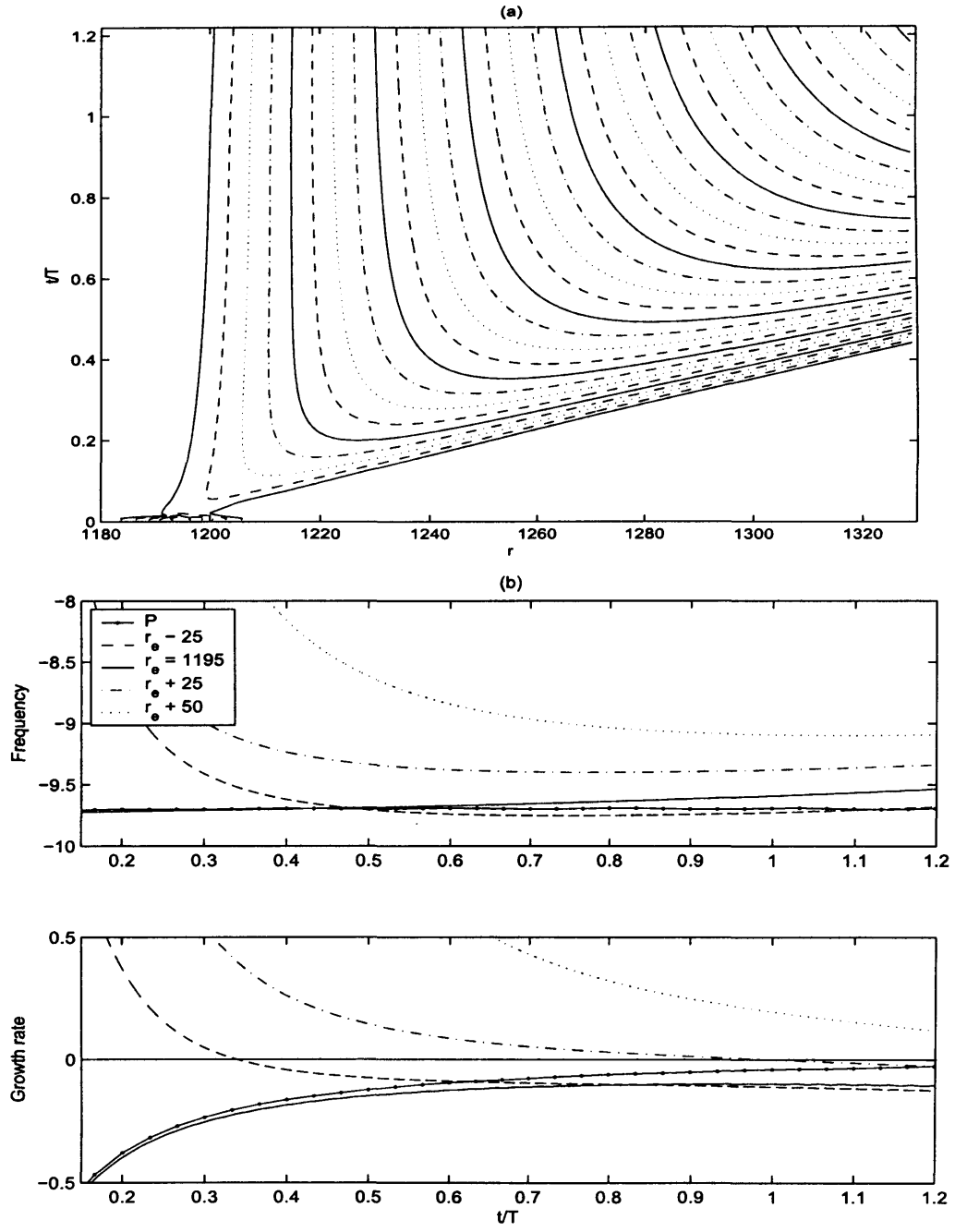

Figure 6.16: *Spatio-temporal development of* $|\omega_{\theta,w}|$ *and local temporal frequencies* $\omega_r Re$ *and temporal growth rates* $\omega_i Re$ *for an impulsively excited disturbance with* $\hat{n} = 43$ *developing in a non-parallel flow. The disturbance was excited at* $r_e = Re/Ro = 1195$. *The temporal development is plotted for four different radial positions,* r_e - 25, r_e, r_e + 25 *and* r_e + 50. *The solid lines labeled with a P show the development in a parallel flow with* $Re = 239$ *and* $Ro = -0.2$.

(dashed line), where the centre of impulsive forcing is the critical radius for absolute instability $r_e = 1195$. For the total time period considered, the two plots are almost identical. There is no visible difference in the temporal frequencies and there is only a small difference in the temporal growth.

The corresponding non-parallel disturbance wavepacket, frequencies and growth rates are plotted in figure 6.16. The trailing edge of the wavepacket appears to be propagating with a diminishing velocity. Thus, the behaviour is comparable with that given by a parallel flow disturbance at the point of critical absolute instability. However, if we were to consider a smaller radial range, about the trailing edge, the disturbance would be seen to propagate radially outwards, in the usual convective manner. Nonetheless, the convective behaviour is not as prominent as it was in previous rotating flows.

The frequency and growth rates again show tendencies to increase and decrease, respectively. However, the rate of change in frequency and growth rate, at each radial location, is very small compared with previous rotating boundary-layers (as predicted). Hence, it seems likely that temporal decay and convective behaviour will prevail, but it will be less prominent than previous rotating flows and take longer to become clearly visible.

For flows with Ro negative, the results have shown that convective behaviour once again dominates the disturbance response. However, as $Ro \rightarrow 0$, the convective behaviour becomes less obvious. This of course is to be expected, since for $Ro = 0$ the flow is strictly parallel. Hence, as $Ro \rightarrow 0$, non-parallel effects will be reduced.

6.4.3 The Ekman layer

As discussed previously, the Ekman layer is strictly parallel. Therefore, the results of a non-parallel numerical simulation will still produce parallel flow disturbance characteristics. Nonetheless, the Ekman layer problem is still helpful in validating

the equations and code. There is also the matter of what happens to the disturbance as the Rossby number Ro approaches zero, from both the negative and positive halves of the real Ro–plane, i.e. $Ro = 0^-$ and $Ro = 0^+$. Lingwood (1997b) showed that for $Ro = 0^-$, disturbances behave in a similar manner to the rotating flows with negative Rossby numbers; the disturbance propagates radially outwards. While for $Ro = 0^+$, the disturbances are comparable with the rotating mean flows with positive Rossby numbers; the disturbance propagates radially inwards.

Implementing $Ro = 0^{\pm}$

In the governing equations (6.23) - (6.25) the radius r is replaced by $\hat{r}/Ro$ where $\hat{r}$ is a dummy variable for the radius. The convective term N_r (equation (6.26)) becomes

$$\begin{aligned} N_r: &\quad \frac{1}{Re}(-2RoGu_\theta + RoH\omega_\theta - \hat{r}G\omega_z), \\ \Rightarrow N_r: &\quad -\frac{\hat{r}}{Re}G\omega_z \ \text{ for } \ Ro = 0, \end{aligned} \tag{6.36}$$

while similar results are obtained for the remaining convective terms. For

$$\begin{aligned} Ro &= 0^-, \qquad \hat{r} = -Re, \\ Ro &= 0^+, \qquad \hat{r} = Re. \end{aligned} \tag{6.37}$$

Implementing the above method, makes it possible to study the Ekman layer, for $Ro = 0^{\pm}$.

$Ro = 0^-$

The critical Reynolds number for the Ekman layer was given by Lingwood (1997b) to be $Re = 198$ for an azimuthal mode number $\hat{n} = 36$. Since the radius $r = Re/Ro$ and $Ro = 0$ for the Ekman layer, all radial points are equivalent. To overcome this, the disturbance behaviour is plotted about a modified radial forcing point $\hat{r_e} = Re$.

For $Ro = 0^-$, a disturbance is impulsively excited at the critical point of absolute instability, for a non-parallel flow (which as we will soon discover, will give results that

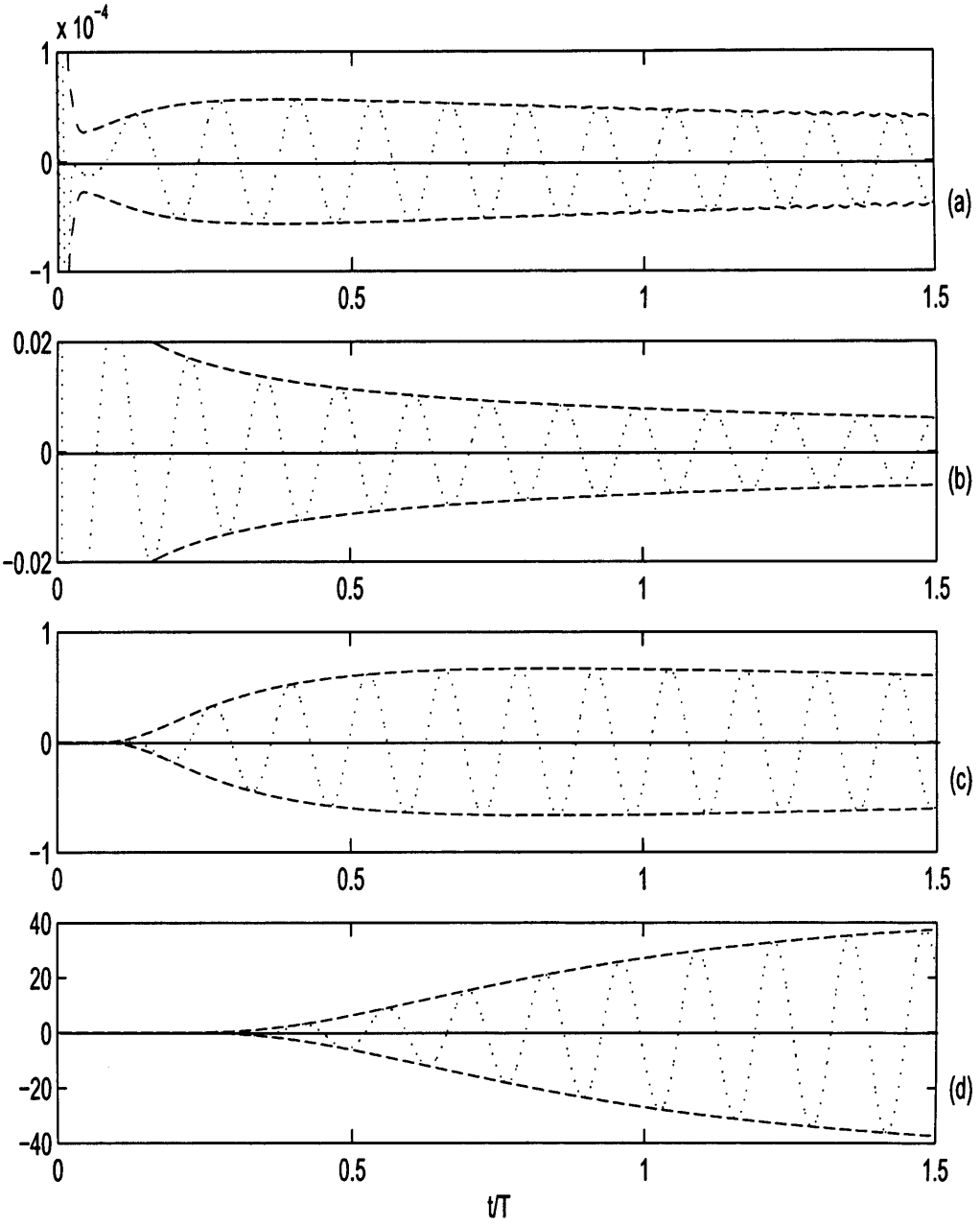

Figure 6.17: *Time histories for $\omega_{\theta,w}$ (solid lines) with corresponding envelopes $\pm|\omega_{\theta,w}|$ (dotted lines), for an impulsively excited disturbance in a parallel (non-parallel) flow with Rossby number $Ro = 0.0^-$, where $Re = 198$, for an azimuthal mode number $\hat{n} = 36$. The temporal development is plotted for four different radial positions, (a): $\hat{r}_e$-25, (b): $\hat{r}_e$, (c): $\hat{r}_e$+25, (d): $\hat{r}_e$+50.*

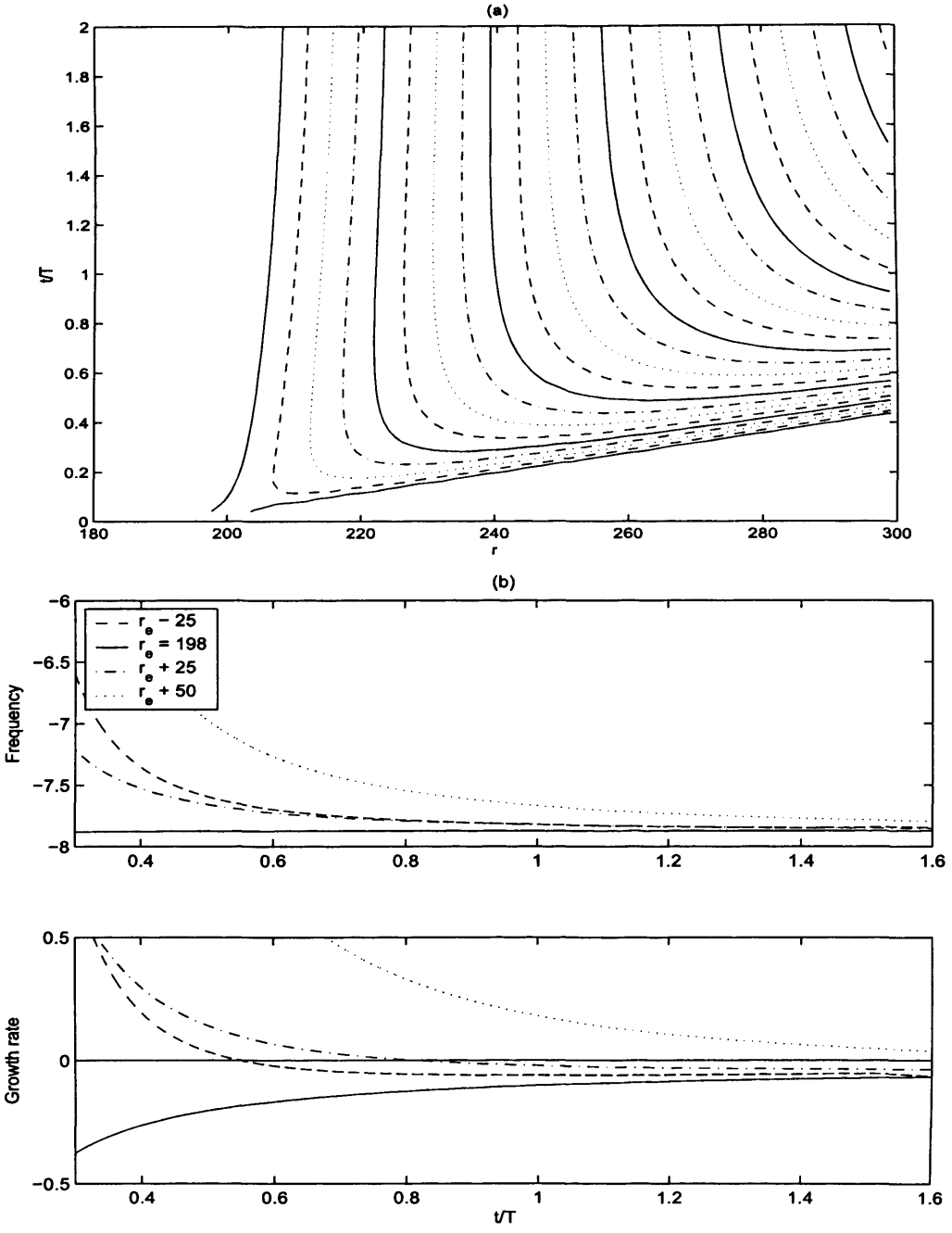

Figure 6.18: *Spatio-temporal development of* $|\omega_{\theta,w}|$ *and local temporal frequencies* $\omega_r Re$ *and temporal growth rates* $\omega_i Re$ *for an impulsively excited disturbance with* $\hat{n}$ = *36 developing in a parallel (non-parallel) flow with Rossby number* $Ro = 0.0^-$ *The temporal development is plotted for four different radial positions,* $\hat{r_e}$ - *25,* $\hat{r_e}$, $\hat{r_e}$ + *25 and* $\hat{r_e}$ + *50.*

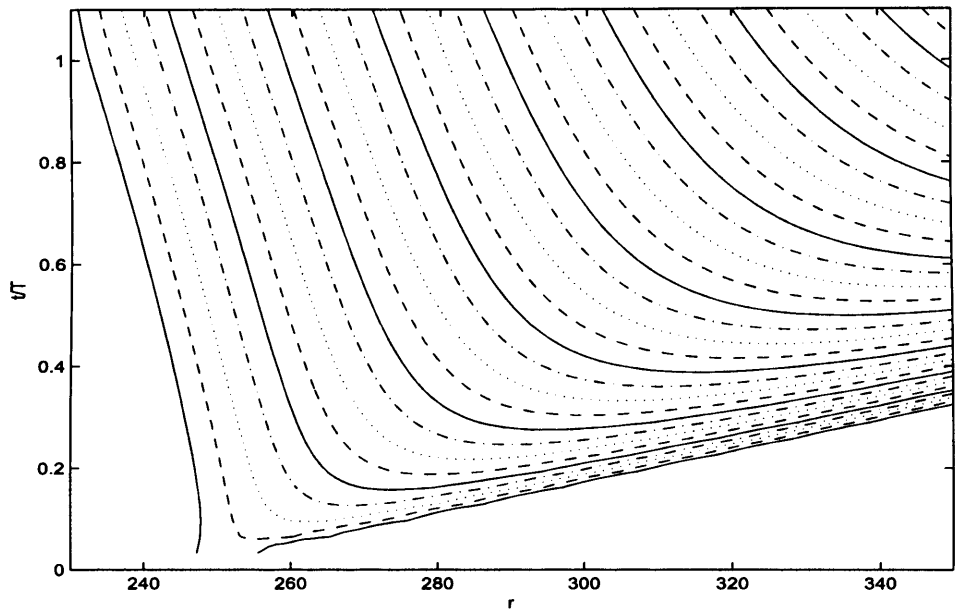

Figure 6.19: *Spatio-temporal development of* $|\omega_{\theta,w}|$ *for an impulsively excited disturbance in a parallel (non-parallel) flow with Rossby number* $Ro = 0.0^{-}$*, with an azimuthal mode number* $\hat{n} = 36$ *and* $Re = 248$*. (Contours are drawn using a logarithmic scale, with levels separated by factors of two).*

could be obtained from the parallel flow numerical simulations). Figure 6.17 displays time histories for four successive radial locations; (a): $\hat{r_e}$-25, (b): $\hat{r_e} = 198$, (c): $\hat{r_e}$+25, (d): $\hat{r_e}$+50. The azimuthal component of the vorticity $\omega_{\theta,w}$ at the wall is plotted for a fixed value of θ, along with the corresponding envelopes $\pm|\omega_{\theta,w}|$ obtained from the complex-valued amplitude. For the time history at $r = \hat{r_e}$-25 the disturbance decays, while the disturbance amplitude appears to be approaching a constant magnitude for $r = \hat{r_e}$ and $r = \hat{r_e}$+25. For the radial location $\hat{r_e}$+50, the disturbance exhibits a continuous increase in amplitude. It is evident that the flow is strongly unstable when account is taken of the different scales used for the axis.

Figure 6.18 displays the disturbance wavepacket, temporal frequencies and growth

rates, for the above problem. The trailing edge of the wavepacket is propagating with a diminishing velocity. Thus, behaviour comparable with critical absolute instability is present. The frequencies and growth rates are plotted for four equally spaced radial locations. For all positions, the frequency asymptotes to the same constant, which is comparable with that given by Lingwood (1997b). The growth rates also approach a constant, which is approximately zero. Hence, the results are comparable with critical absolute instability.

A second disturbance is impulsively excited at $\hat{r_e} = 248$, for a Reynolds number $Re = 248$ and azimuthal mode number $\hat{n} = 36$. Such a disturbance is located well within the theoretical region of absolute instability. Figure 6.19 displays the spatio-temporal development for the above disturbance. Both edges propagate in opposite directions with constant velocities. Hence, we observe absolute instability.

$\boldsymbol{Ro} = 0^+$

For $Ro = 0^+$ a disturbance is impulsively excited at $\hat{r_e} = 198$ for $Re = 198$ and $\hat{n} = 36$. Figure 6.20 displays the corresponding disturbance wavepacket, frequencies and growth rates. The wavepacket shows a disturbance propagating radially inwards that is critically absolutely unstable. The frequencies and growth rates again asymptote towards constant values. The growth rates tend towards zero, which is to be expected for critical absolute instability. While the constant frequency is the same as that found for the earlier $Ro = 0^-$ case, but of opposite sign.

Hence, for $Ro = 0^-$ disturbances propagate radially outwards, while for $Ro = 0^+$, disturbances propagate radially inwards. This would suggest that there is a singularity found for $Ro = 0$, where the direction disturbances propagate, alternates. Thus, one would expect that for the remaining positive Ro, disturbances will generally propagate radially inwards.

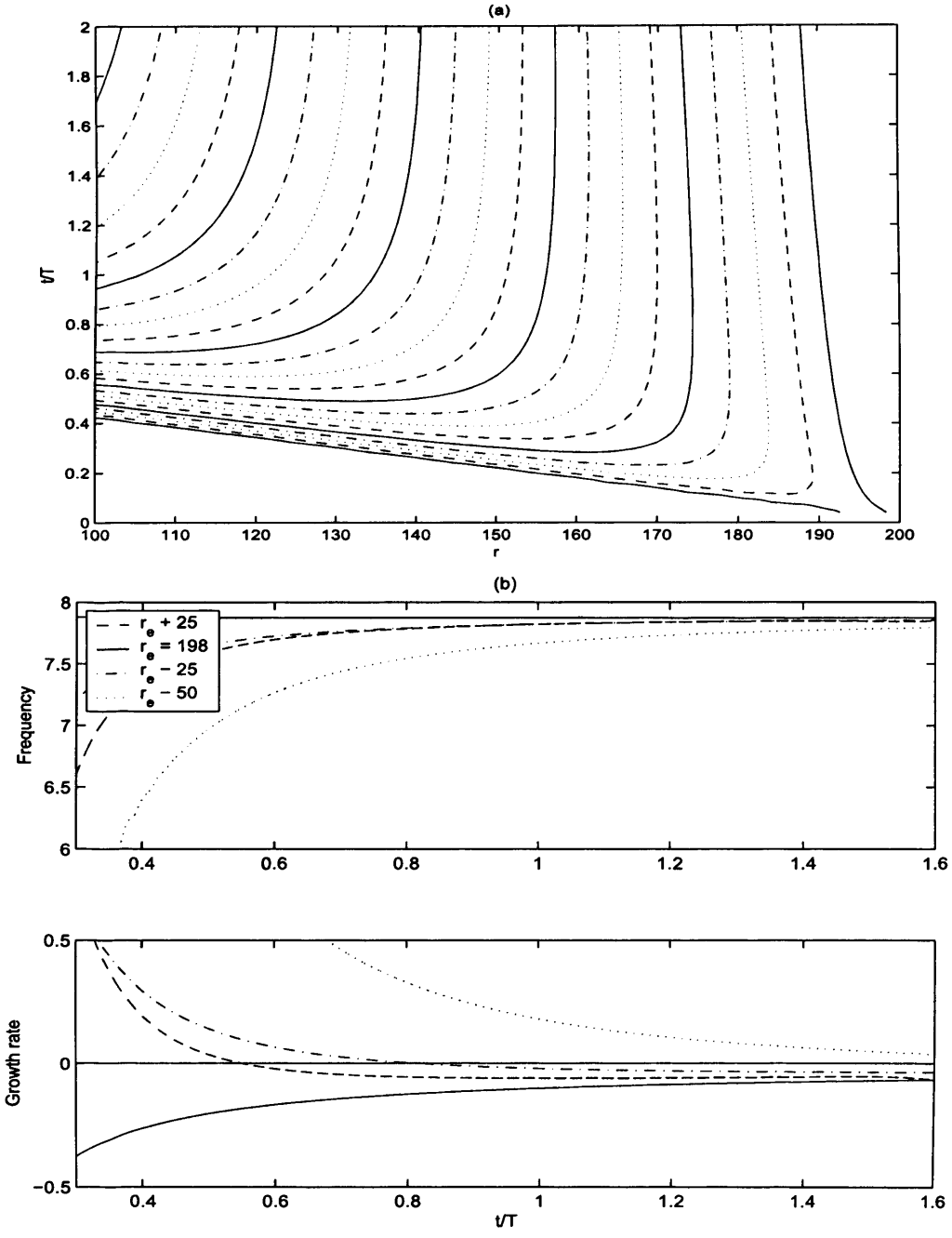

Figure 6.20: *Spatio-temporal development of* $|\omega_{\theta,w}|$ *and local temporal frequencies* $\omega_r Re$ *and temporal growth rates* $\omega_i Re$ *for an impulsively excited disturbance with* $\hat{n} = 36$ *developing in a parallel (non-parallel) flow with Rossby number* $Ro = 0.0^+$. *The temporal development is plotted for four different radial positions,* $\hat{r_e}$ - 50, $\hat{r_e}$ - 25, $\hat{r_e}$ *and* $\hat{r_e}$ + 25.

6.4.4 Results for $0 < Ro < 1$

$Ro = 0.2$

Figure 6.21 displays the spatial-temporal evolution for a disturbance centred at $r_e = 810$, with an azimuthal mode number $\hat{n} = 28$, for $Ro = 0.2$. The leading edge propagates radially inwards with a decreasing velocity, while the trailing edge is propagating with what appears to be a diminishing velocity. However, on closer inspection, the trailing edge can be seen to propagate radially inwards with an increasing velocity; refer to figure 6.21(b).

The corresponding frequencies and growth rates are plotted in figure 6.22 for four equally spaced radial locations. The growth rates are again decreasing at (what appears to be) a faster rate than the earlier negative Rossby number flows. The frequencies are also decreasing, which is the opposite of what was observed for the mean flows $Ro < 0$ (where the frequencies increased with time).

$Ro = 0.4$

Figure 6.25 displays the parallel and non-parallel wavepacket development for a disturbance excited at the critical point of absolute instability for $Ro = 0.4$. The critical Reynolds number is given as $Re_c = 125$, for a critical radii $r_e = 313$ and an azimuthal mode number $\hat{n} = 20$. The wavepacket corresponding to the parallel flow is clearly demonstrating behaviour characteristic of critical absolute instability. The leading edge is propagating radially inwards with a non-zero velocity and the trailing edge is propagating with a diminishing velocity.

For the non-parallel wavepacket disturbance, the leading edge is initially propagating inwards. However, it eventually reverses direction and it would appear that given sufficient time, the leading edge would eventually meet the inwardly propagating trailing edge. Thus, the unstable disturbance would be enclosed within this region. After this time the flow would become stable, everywhere. The corresponding

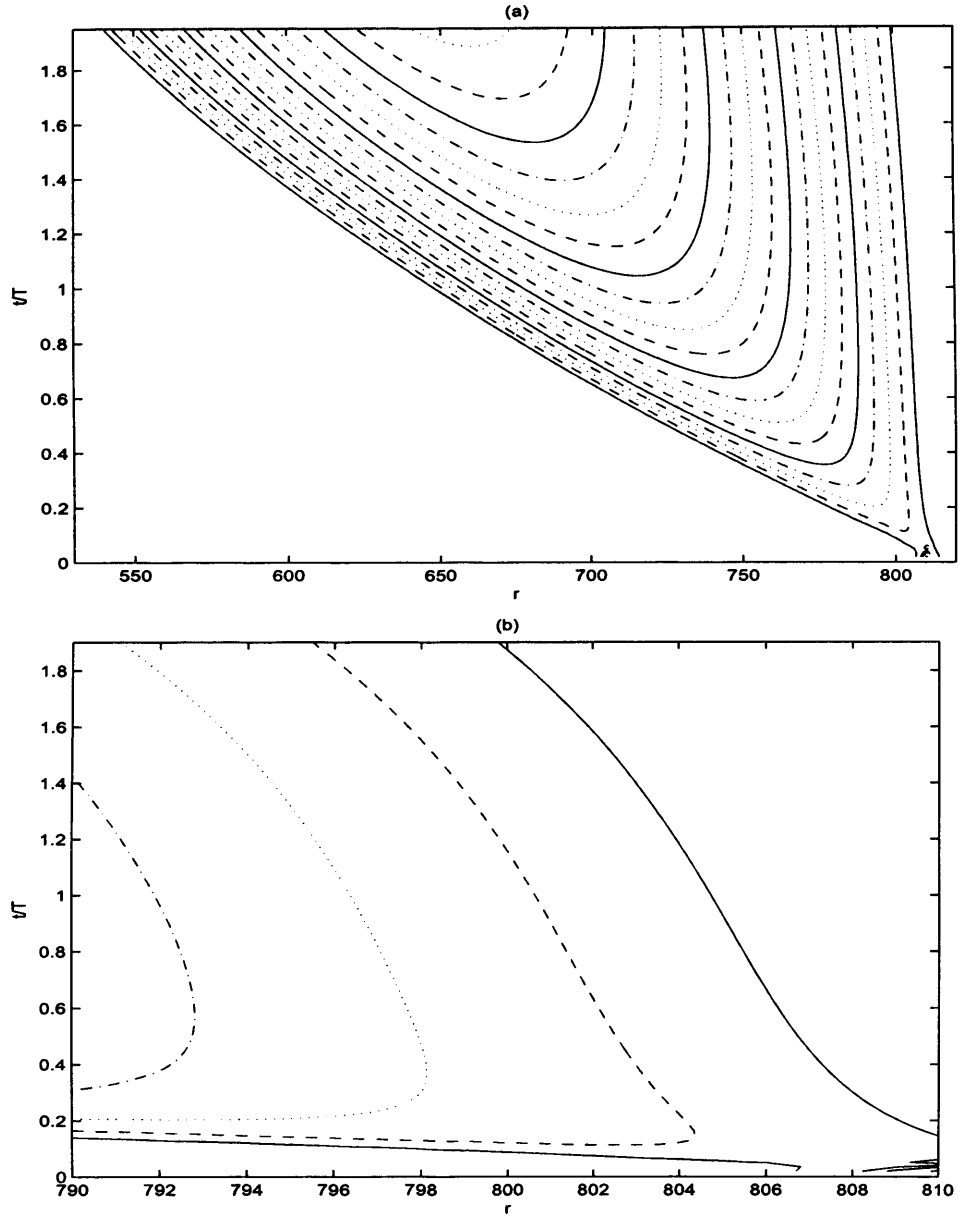

Figure 6.21: *Spatio-temporal development of* $|\omega_{\theta,w}|$ *for an impulsively excited disturbance in a non-parallel flow with Rossby number* $Ro = 0.2$*, and an azimuthal mode number* $\hat{n} = 28$*. The disturbance was excited at* $r_e = Re/Ro = 810$*. (a) - full radial range, (b) - reduced radial range. (Contours are drawn using a logarithmic scale, with levels separated by factors of two).*

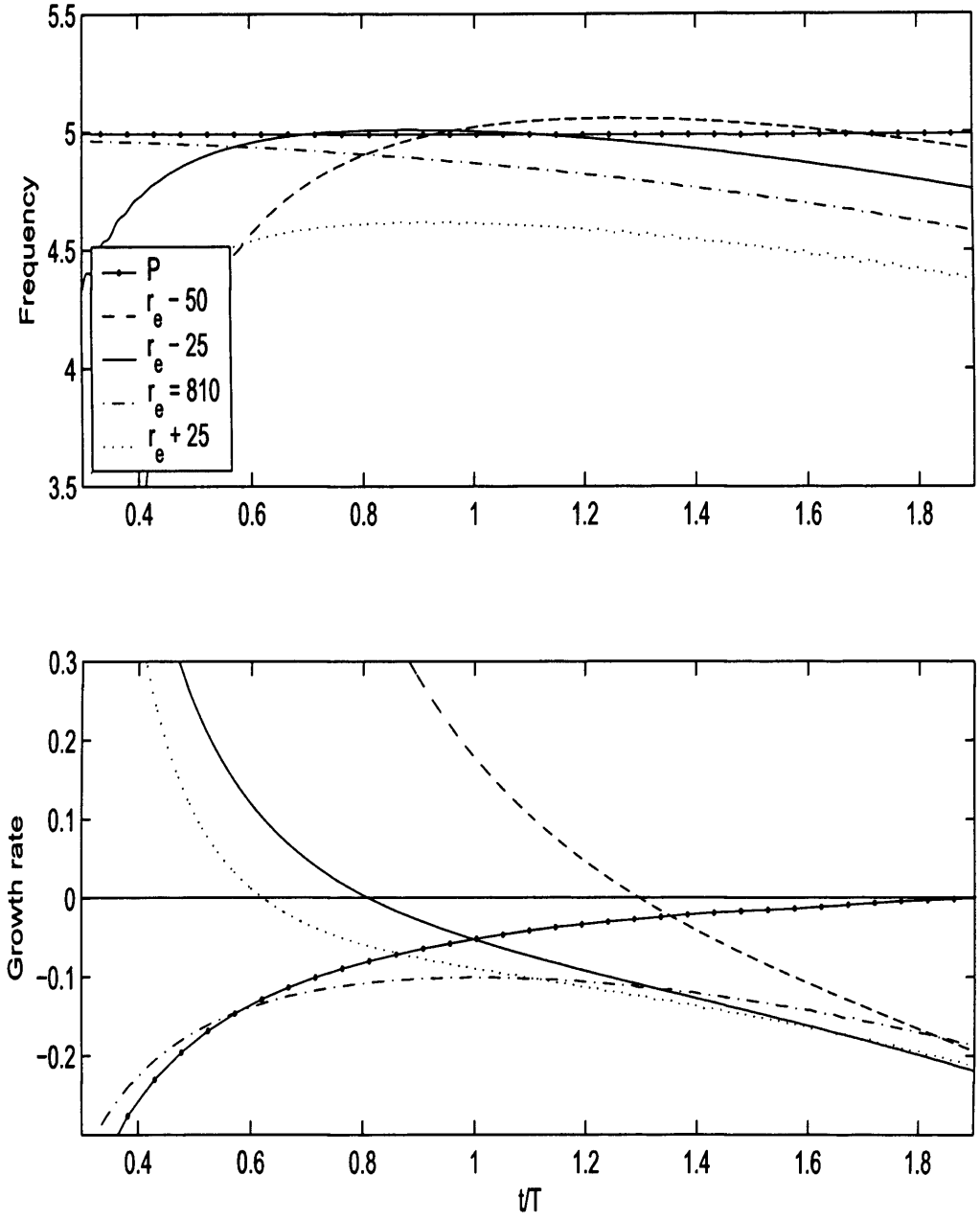

Figure 6.22: *Local temporal frequencies $\omega_r Re$ and temporal growth rates $\omega_i Re$ for a disturbance with $\hat{n}$ = 28 developing in a non-parallel flow with Rossby number Ro = 0.2. The impulsive excitation was centred at r_e = Re/Ro = 810. The temporal development is plotted for four different radial positions, r_e - 50, $r_e - 25$, r_e and r_e + 25. The solid lines labeled with a P show the development in a parallel flow with Re = 162.*

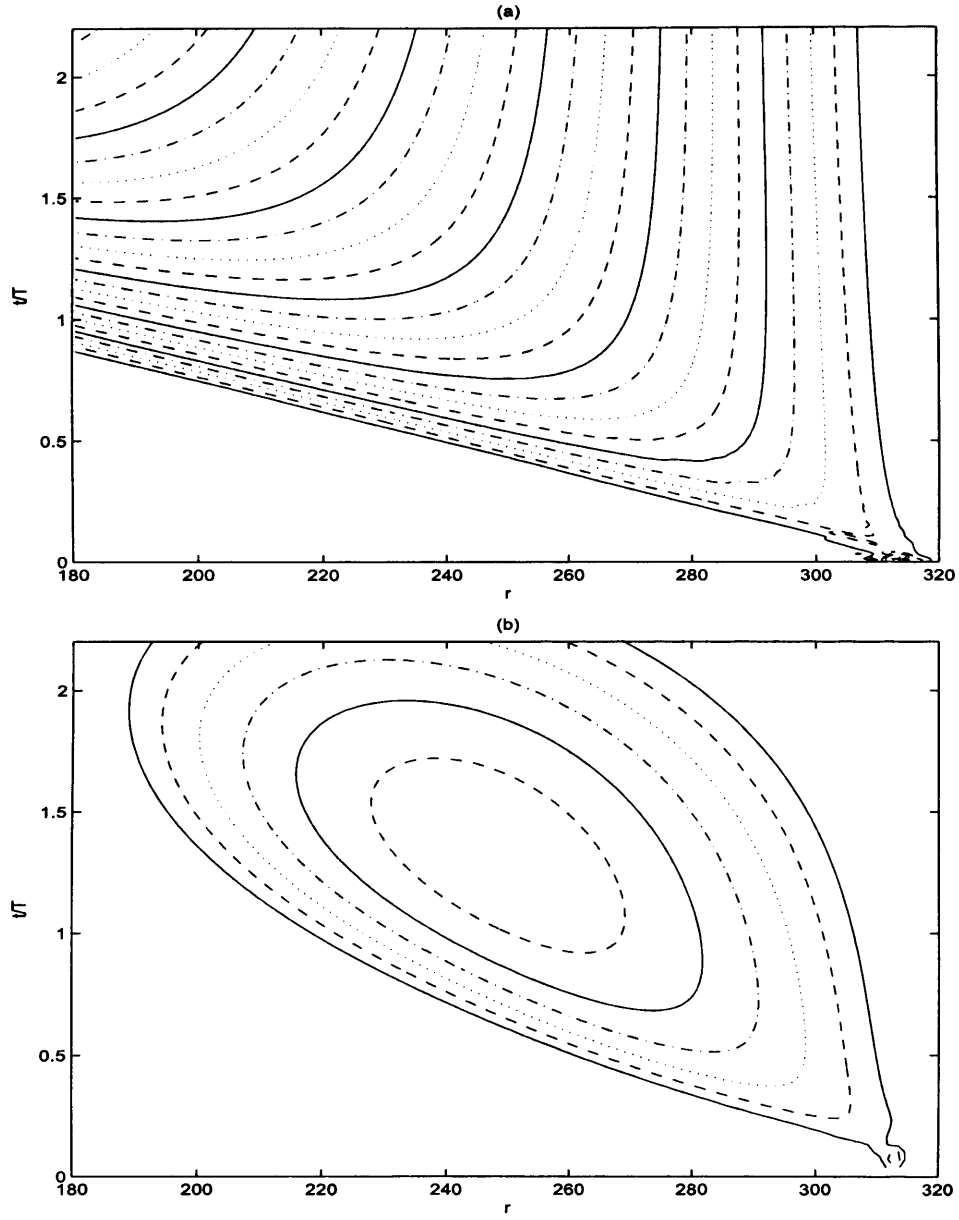

Figure 6.23: *Spatio-temporal development of* $|\omega_{\theta,w}|$ *for an impulsively excited disturbance with Rossby number* $Ro = 0.4$*, and an azimuthal mode number* $\hat{n} = 20$*. The disturbance was excited at* $r_e = Re/Ro = 313$*. (a) - parallel flow with* $Re = 125$*, (b) - non-parallel flow. (Contours are drawn using a logarithmic scale, with levels separated by factors of two).*

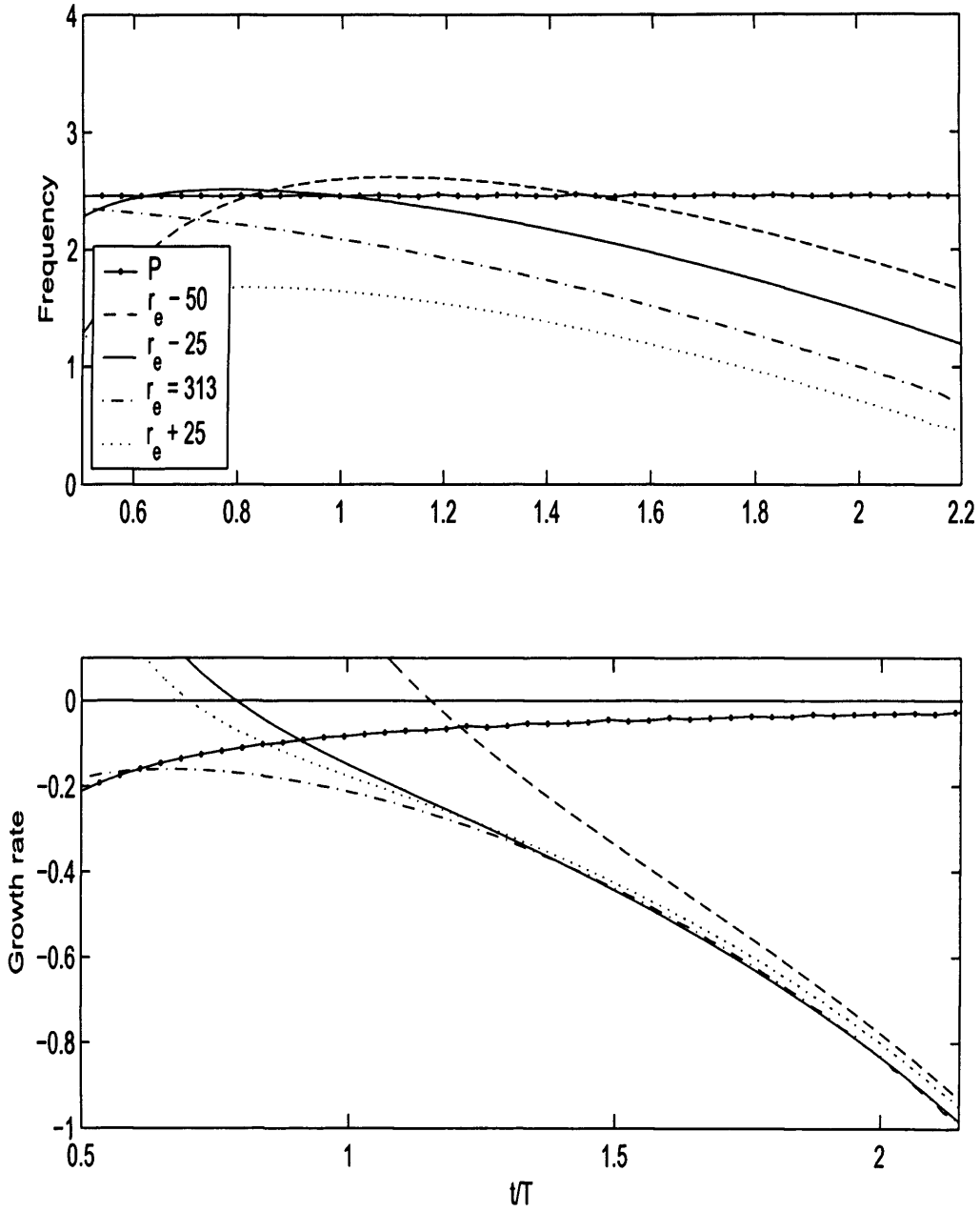

Figure 6.24: *Local temporal frequencies $\omega_r Re$ and temporal growth rates $\omega_i Re$ for a disturbance with $\hat{n}$ = 20 developing in a non-parallel flow with Rossby number Ro = 0.4. The impulsive excitation was centred at r_e = Re/Ro = 313. The temporal development is plotted for four different radial positions, r_e - 50, $r_e - 25$, r_e and r_e + 25. The solid lines labeled with a P show the development in a parallel flow with Re = 125.*

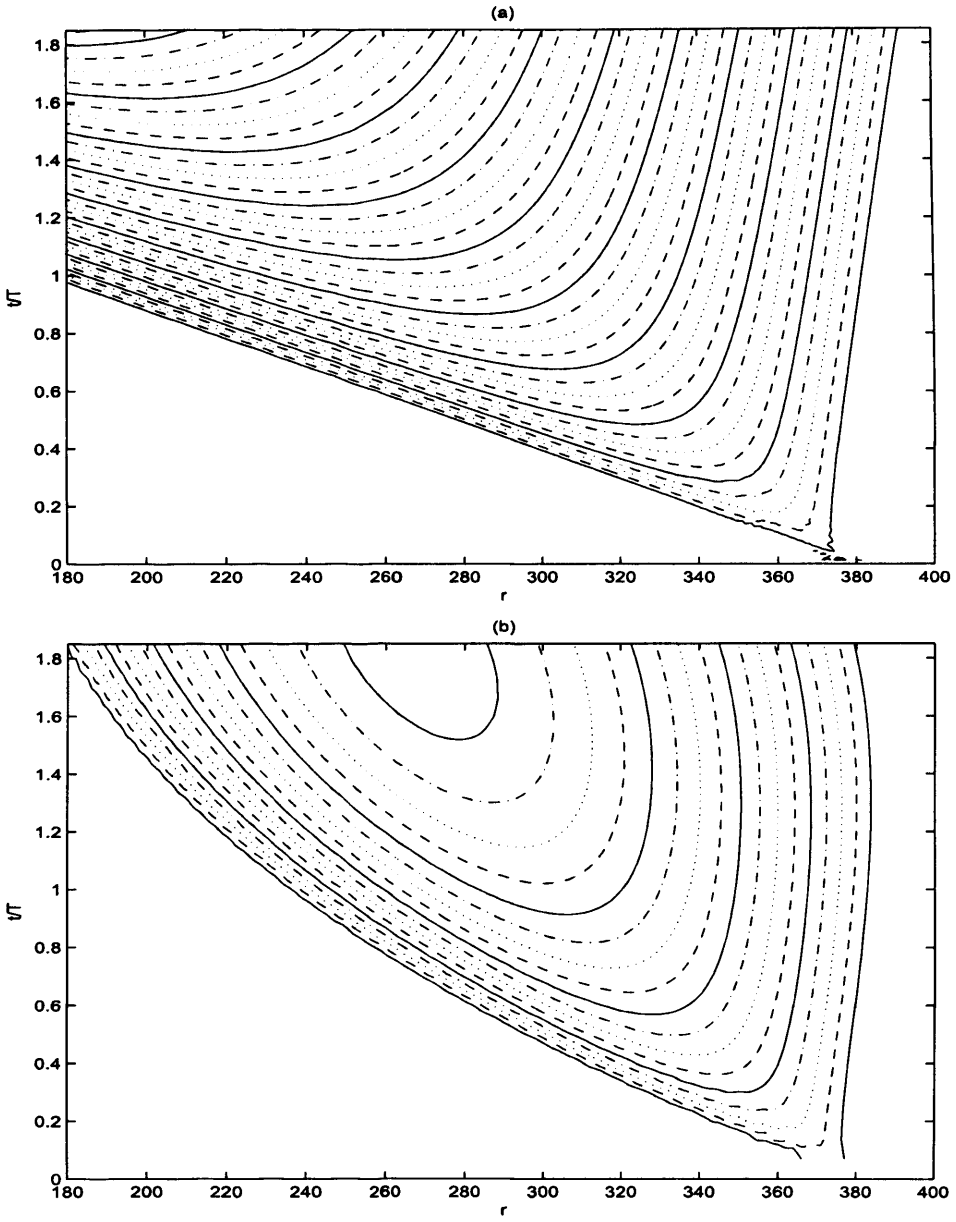

Figure 6.25: *Spatio-temporal development of* $|\omega_{\theta,w}|$ *for an impulsively excited disturbance with Rossby number* $Ro = 0.4$*, and an azimuthal mode number* $\hat{n} = 20$*. The disturbance was excited at* $r_e = Re/Ro = 375$*. (a) - parallel flow with* $Re = 150$*, (b) - non-parallel flow. (Contours are drawn using a logarithmic scale, with levels separated by factors of two).*

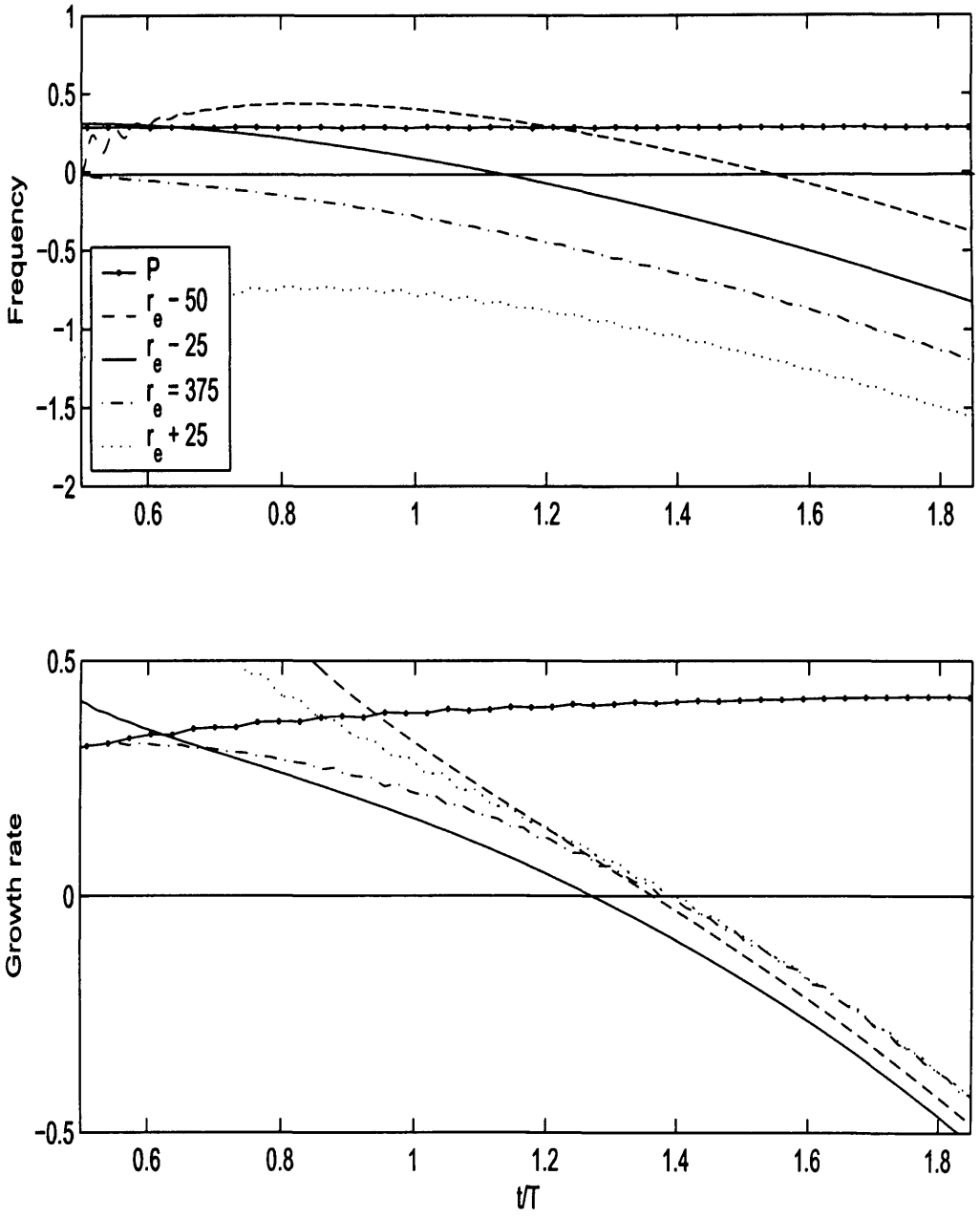

Figure 6.26: *Local temporal frequencies $\omega_r Re$ and temporal growth rates $\omega_i Re$ for a disturbance with $\hat{n}$ = 20 developing in a non-parallel flow with Rossby number Ro = 0.4. The impulsive excitation was centred at r_e = Re/Ro = 375. The temporal development is plotted for four different radial positions, r_e - 50, $r_e - 25$, r_e and r_e + 25. The solid lines labeled with a P show the development in a parallel flow with Re = 150.*

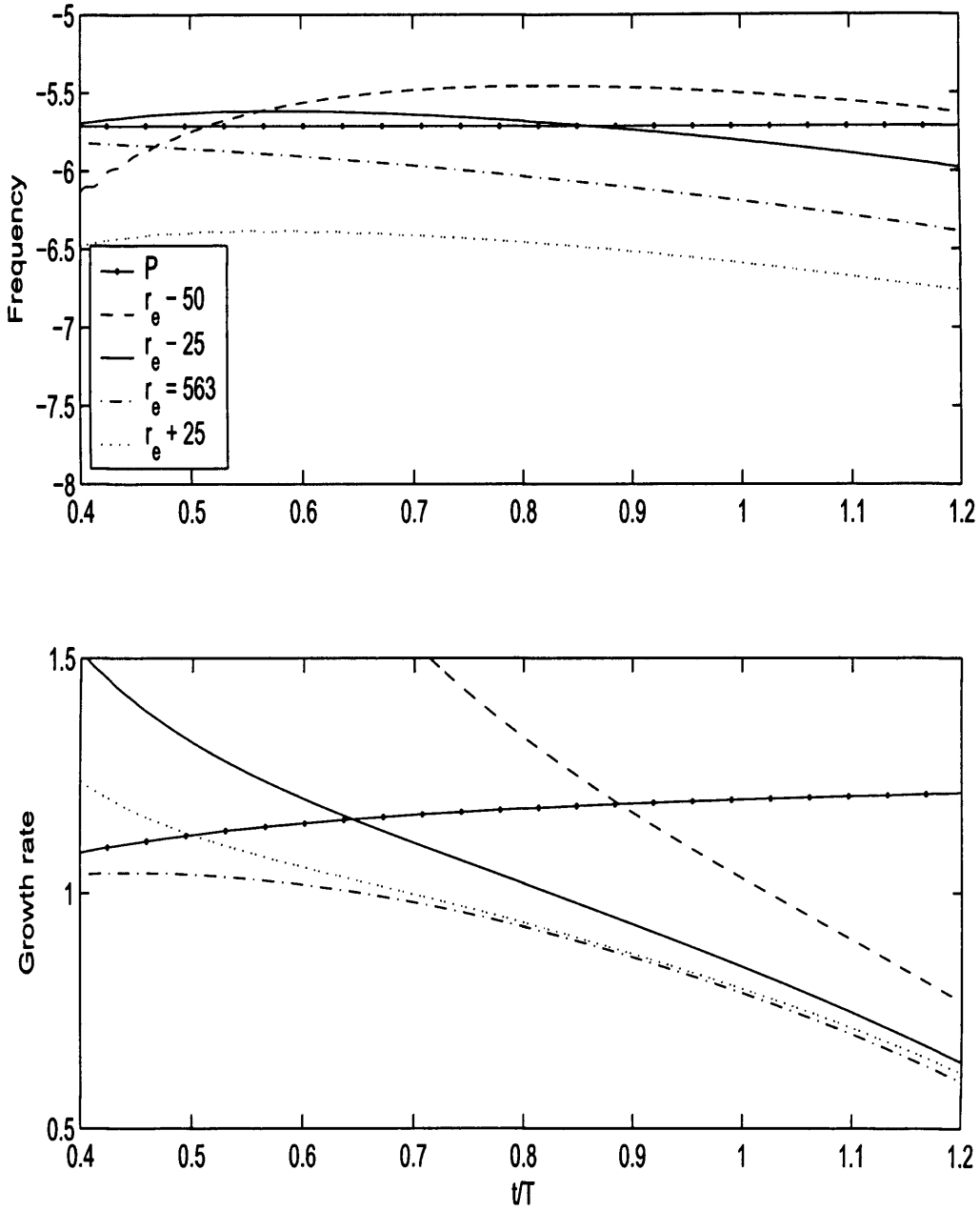

Figure 6.27: *Local temporal frequencies $\omega_r Re$ and temporal growth rates $\omega_i Re$ for a disturbance with $\hat{n}$ = 20 developing in a non-parallel flow with Rossby number Ro = 0.4. The impulsive excitation was centred at $r_e = Re/Ro$ = 563. The temporal development is plotted for four different radial positions, r_e - 50, $r_e - 25$, r_e and r_e + 25. The solid lines labeled with a P show the development in a parallel flow with Re = 225.*

frequencies and growth rates are plotted in figure 6.24. Both frequencies and growth rates decrease with time.

A second disturbance was excited for $r_e = 375$ - which corresponds to a Reynolds number $Re = 150$ - with an azimuthal mode number $\hat{n} = 20$. The parallel and non-parallel spatial-temporal evolution for the disturbance is plotted in figure 6.25. For the parallel disturbance, the leading and trailing edges are propagating in opposite directions. Thus, absolute instability is observed. However, for the non-parallel disturbance, convective behaviour appears to dominate. Initially the two edges are propagating in opposite directions. However, this does not persist for long and the trailing edge can be seen to reverse direction and propagate radially inwards. At the same time, the leading edge appears to slow down, suggesting that it too may reverse direction and eventually meet up with the inwardly propagating trailing edge. Hence, the unstable disturbance would once again be enclosed within a radial-time region, and the mean flow would remain stable for all radial locations and for all time after this point.

The temporal frequencies and growth rates for the above disturbance are plotted in figure 6.26. Again the frequencies and growth rates decrease at all selected radial positions, and temporal decay is found for all given radial locations after $t/T = 1.4$.

A third disturbance was excited at $r_e = 563$, for an azimuthal mode number $\hat{n} = 20$. This corresponds to a Reynolds number $Re = 225$, and is located well within the absolutely unstable parameter space. Figure 6.27 displays the corresponding temporal frequencies and growth rates for four equally spaced radial locations. The temporal growth rates decrease with increasing time, and although temporal decay is not observed for the time period considered, the trend of the plot suggests that this will eventually be observed.

The above disturbance behaviour suggests that the mean flow with $Ro = 0.4$, will eventually be stable everywhere, independent of the radial origin of the disturbance.

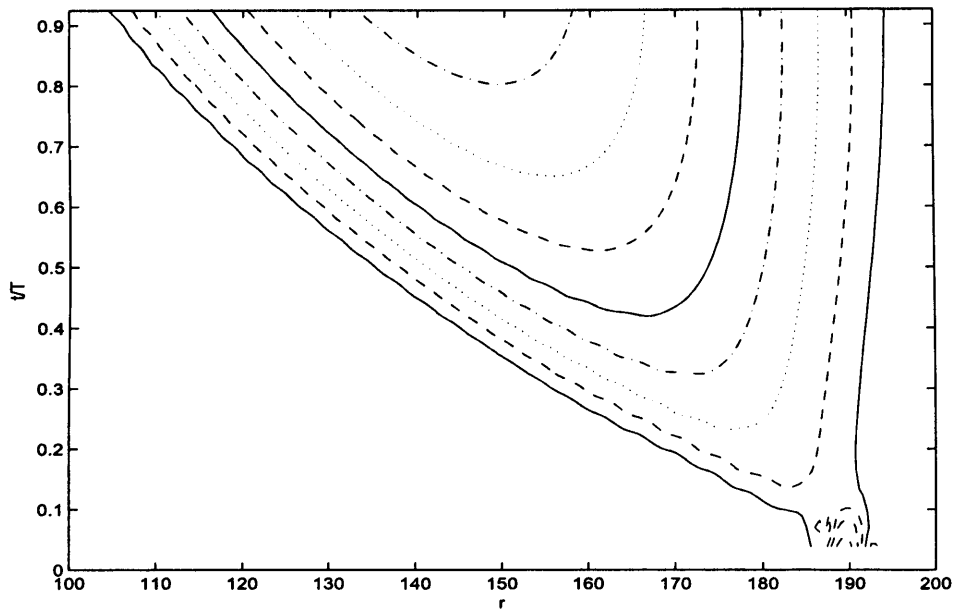

Figure 6.28: *Spatio-temporal development of* $|\omega_{\theta,w}|$ *for an impulsively excited disturbance with* $\hat{n} = 11$ *developing in a non-parallel flow with Rossby number* $Ro = 0.6$. *The disturbance was excited at* $r_e = Re/Ro = 188$.

$Ro = 0.6$

Figure 6.28 displays a disturbance excited at $r_e = 188$ for $\hat{n} = 11$, for $Ro = 0.6$. This corresponds to a radial location well inside the absolutely unstable parameter space. Initially both edges propagate in opposite directions. However, the velocities of the two edges are decreasing, suggesting that they will eventually reverse direction and adjoin, forming an enclosed region of instability.

Longer simulations (which may have verified the above ideas) were increasingly difficult to produce for the flow $Ro = 0.6$. Problems such as numerical instabilities, inflow and outflow conditions were causing several problems, which meant that reliable simulation results could not be produced for a sufficiently long time interval.

Similar problems were met for $Ro = 0.8$. Nonetheless it seems likely that the disturbance characteristics for $Ro \geq 0.6$ will be comparable with the earlier positive Rossby mean flows.

6.4.5 The Bödewadt layer

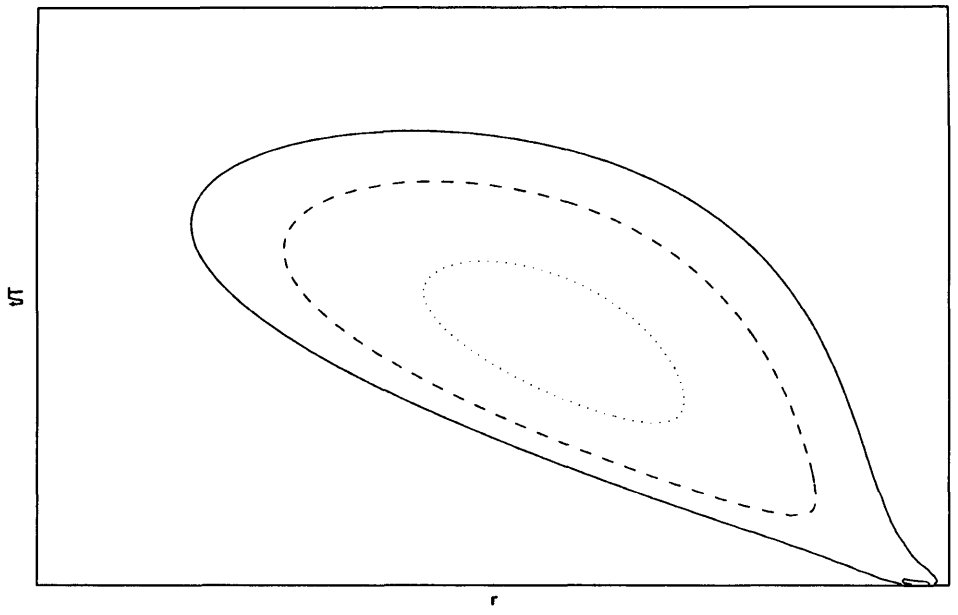

Figure 6.29: *Sketch of a typical wavepacket evolution for the Bödewadt boundary-layer for a disturbance excited within the convective region of instability,* $r < r_e = 21.6$.

The Bödewadt boundary-layer is the most unstable of all the rotating flows. The Bödewadt layer is known to be absolutely unstable for $Re_c \geq 21.6$ (Lingwood, 1997b).

Due to numerical problems (such as inflow and outflow conditions), it was very difficult to produce numerical simulations for a sufficient length of time. Nonetheless, the characteristics of the non-parallel Bödewadt flow can be anticipated from the numerical simulations that we obtained for the earlier rotating boundary-layers.

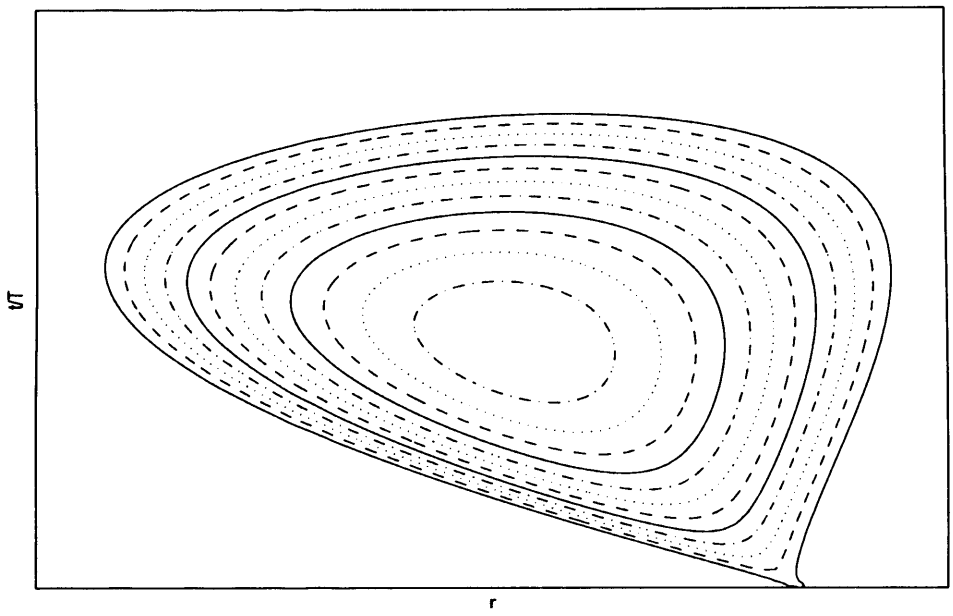

Figure 6.30: *Sketch of a typical wavepacket evolution for the Bödewadt boundary-layer for a disturbance excited within the absolutely unstable region,* $r > r_e = 21.6$.

For $Ro < 0$, disturbances propagated radially outwards in a convective manner, while the temporal frequencies increased with time at all radial locations. The opposite behaviour was found for the flows $Ro > 0$ that have been investigated. Both frequencies and growth rates decreased with time, while disturbances propagated radially inwards in a convective manner. However, the disturbance eventually stabilized, and the instability was enclosed within a radial-time region.

Figures 6.29 and 6.30 display schematic sketches describing the predicted behaviour of the Bödewadt flow. The flow is impulsively excited at a radial location less than the critical radii $r_e = 21.6$, in figure 6.30. Both edges (of the wavepacket disturbance) initially propagate radially inwards. However, the leading edge eventually

reverses direction and connects with the trailing edge. Thus, the disturbance is enclosed and the flow is stable everywhere after some time t/T. The second figure 6.30 displays a disturbance excited within the absolutely unstable region. Initially the two edges propagate in opposite directions, but eventually they reverse direction and meet. Thus, the flow is again stabilized.

6.5 Discussion and conclusions

A study has been carried out on the global behaviour corresponding to the absolute instability of the *BEK* family of rotating flows. The system includes the Bödewadt, Ekman and von Kármán flows. Numerical simulations have been conducted to investigate the behaviour of linearized disturbances for the parallel and genuine non-parallel flows. This extends the work of Davies & Carpenter (2003), which was limited to the von Kármán case. The system of equations used for the simulations is equivalent to the complete linearized Navier-Stokes equations. Since the equations are linear, they are separable with respect to the azimuthal coordinate θ. Thus, allowing simulations with a single azimuthal mode number. Impulse like excitation was used for all simulations. This produces a disturbance wavepacket that initially contains a wide range of frequencies. When disturbances are simulated using the so-called parallel flow approximation (spatially homogeneous flow), the results are fully in accordance with the theoretical results of Lingwood (1997b). If the flow parameters lie within the theoretical absolutely unstable parameter space, the simulations produce identical behaviour. The same is true for disturbances excited within the convectively unstable region. For disturbances excited at the critical point of absolute instability[1], the frequencies and wavenumbers were very close to those found by Lingwood (1997b). The temporal frequencies ω_c were identical to within three decimal places in most

[1]The Reynolds number and azimuthal mode number were rounded to the nearest integer in the numerical simulations. This was done to avoid excessive parametric studies.

cases, while the spatial wavenumbers α_c were the same to within two decimal places in almost all cases considered. (Refer to table 6.2 for further details).

The non-parallel numerical simulation results indicate that the kind of behaviour found for the von Kármán flow is carried over to other flows in the *BEK* family. For a Rossby number Ro within the range $-1 \leq Ro < 0$ (where Ro = -1 corresponds to the von Kármán flow), disturbances display a tendency to propagate outwards in a convective manner, even for those disturbances originally located within the known regions of absolute instability. The behaviour may be summarized by the schematic sketches in figure 2.4. It is also worth noting that as $Ro \rightarrow 0$ (or as we approach the Ekman layer), the convective behaviour is less marked and the non-parallel effects are reduced.

For the strictly parallel Ekman layer ($Ro = 0$), the results of the numerical simulations agree with the theory of Lingwood (1997b), as would be expected. For a disturbance excited within the theoretical absolutely unstable region, the simulations exhibit exactly the same behaviour.

If we approach $Ro = 0$ from below, we observe disturbance features inherent in mean flows with $Ro < 0$; disturbances propagate radially outward. However, if we approach $Ro = 0$ from above, the disturbance characteristics are identical to mean flows with $Ro > 0$; disturbances propagate radially inwards.

For $0 < Ro \leq 1$ ($Ro = 1$ corresponds to the Bödewadt flow), disturbances display a tendency to propagate radially inwards in a similar, though directionally opposite, convective manner to that found for the von Kármán flow. However, as the propagating disturbance approaches the centre of the disk, the wavepacket stabilizes. Figures 6.29 and 6.30 describe the typical disturbance behaviour for such flows. Although simulation results for the Bödewadt flow were unattainable, it was possible to predict the general behaviour from the trends found for other rotating flows with $Ro > 0$.

The behaviour of the rotating flows can be described as follows. For $Ro < 0$

there is a region of stability, surrounded by a region of convective instability, which in turn is surrounded by a region of absolute instability. Disturbances propagate through the convective region and into the absolutely unstable region. However, the convective behaviour continues to dominate, and so the disturbance continues to propagate radially outwards. A similar idea can be used to describe the flows with $Ro > 0$. Independent of the location of excitation (i.e. convectively unstable or absolutely unstable region), convective behaviour dominates the disturbance response, and disturbances pass through the absolutely unstable region into the convective region, and eventually into the stable region, where disturbances stabilize.

It should be noted that the results do not invalidate the theory of Lingwood (1997b), or imply that absolute instability does not play a role in the laminar-turbulent transition process. For all rotating flows $-1 \leq Ro \leq 1$, temporal growth in the region of the absolute instability, may be enough to cause the already large convective disturbances to transiently grow at a rapid rate. This may be sufficient for the disturbance to obtain an amplitude large enough to trigger the onset of non-linear effects and transition to turbulence.

Chapter 7

The global stability of the rotating-disk

7.1 Introduction

Lingwood (1995) conducted both inviscid and viscous stability studies on the absolute instability on the rotating-disk boundary-layer. Her theoretical results indicate that the growth rate associated with the absolute instability gets stronger with the increasing radius/Reynolds number. Moreover her inviscid study has shown that the absolute instability even persists at the inviscid limit. This would at first sight, appear to suggest that any stabilizing properties, attributed to the non-parallel effects, would become insignificant as the radius approaches the inviscid limit.

Nevertheless, the study by Davies & Carpenter (2003) and of earlier chapters on the rotating-disk boundary-layer, suggests that the absolute instability does not lead to any sustained unstable linear global mode. Instead the simulations of the non-parallel flow, suggest that convective behaviour dominates the disturbance. It is suggested that there is a transient temporal growth associated with the absolute instability, similar to an algebraically growing disturbance. Hence, the long-term behaviour is not consistent with a linear amplified global mode of the form

$$A \sim \exp(-i\omega_G t), \tag{7.1}$$

where ω_G is the complex global mode, i.e. $\omega_G = \omega_{G,r} + i\omega_{G,i}$.

For the present investigation we will introduce a local and global non-dimensionalization, and attempt to locate the global frequency (if indeed one exists) for the rotating-disk boundary-layer. To achieve this, we will use the global frequency selection criterion, developed by Chomaz, Huerre & Redekopp (1991) and others; refer to chapter 1 for further details.

7.1.1 The global frequency selection criterion

The local dispersion relation for the rotating-disk boundary-layer is given by

$$D(\alpha, \beta, \omega; r) = 0, \tag{7.2}$$

where α and β are the radial and azimuthal complex wavenumbers, and ω is the complex temporal frequency. Here r is a slowly varying radial parameter. The global frequency selection criterion developed by Chomaz *et al.* (1991), described in chapter 1, can be employed to determine the global stability of absolutely unstable flows. The criterion requires a double saddle point, where

$$\frac{\partial \omega}{\partial \alpha} = \frac{\partial \omega}{\partial r} = 0. \tag{7.3}$$

The first saddle point requirement is the necessary, but not sufficient condition that the group velocity disappears in order for absolute instability to arise. The second saddle point locates the position r_s of the global mode ω_G. The saddle point will generally be found off from the real $r-$axis. Therefore, the spatial parameter r must be complex. Global instability will be observed if $\omega_{G,i} > 0$, while globally stable behaviour is found if $\omega_{G,i} < 0$. (For further details of the global frequency selection criterion, the reader is referred to chapter 1, where we have briefly described the criteria developed by Chomaz *et al.* (1991) and others).

As mentioned by Davies & Carpenter (2003), it is not known whether

$$\frac{\partial \omega}{\partial r} = 0, \quad \text{for some finite real value of } r, \tag{7.4}$$

or if

$$\frac{\partial \omega}{\partial r} \to 0, \quad \text{as real } r \to \infty. \tag{7.5}$$

If the statement (7.5) is true, the saddle point r_s either

1. does not exist, or

2. it is located off the real $r-$axis, and within the complex $r-$plane.

Hence, the global frequency selection criteria developed by Chomaz *et al.* (1991), could not be applied without modification, to the rotating-disk boundary-layer. However, as mentioned by Pier (2003), for integer valued azimuthal mode numbers $n \geq 51$, the associated region of absolute instability, remains finite in extent, in the radial range. Therefore, there may exist a saddle point for some finite r.

7.1.2 Outline of chapter

For the local stability studies, the non-dimensionalization of the time variation and corresponding disturbance frequencies, are usually given by a locally defined timescale. This is obtained from the ratio of the constant boundary-layer thickness and the circumferential velocity at the surface of the rotating-disk, which varies linearly with the radius. However, there is also a globally-defined timescale, which does not depend on the radius, and is given by the inverse of the constant angular velocity of the rotating-disk. Consequently, the two types of non-dimensionalization, imply that when a locally specified frequency is constant, the corresponding globally defined frequency varies linearly with the radius.

Some of the results of the current chapter were recently discussed in Davies, Thomas & Carpenter (2007). The local and global non-dimensionalization was described and applied to the rotating-disk boundary-layer with constant azimuthal wavenumber β and constant azimuthal mode number n. It is intended that the current chapter will give a detailed account of the ideas and results that they obtained.

We will also apply the local and global non-dimensionalization to the rotating-disk boundary-layer with mass transfer, where the suction/injection parameter $\mathbf{a} = \pm 1$. (Here $\mathbf{a}$ is negative for injection and positive for suction). Davies, Thomas & Carpenter (2007) also briefly describe a simple method for calculating the global mode ω_G and corresponding saddle point location r_s. This simple method (that incorporates the behaviour observed for the results of the rotating-disk boundary-layer) will be described in full in section 7.4, and will be applied to the rotating-disk boundary-layer with mass transfer $\mathbf{a} = 0, \pm 1$. (Note: $\mathbf{a} = 0$ for the rotating-disk without mass transfer). In section 7.5 a polynomial-fit method is used to calculate the saddle points and complex global modes, and finally the results are discussed in section 7.6.

7.2 Local and global non-dimensionalization

As before, for the rotating-disk boundary-layer, cylindrical polar co-ordinates are employed, where r^*, θ^*, z^* are the dimensional radius, azimuthal angle and normal direction. The dimensional undisturbed mean flow is given by

$$\mathbf{U}^*(r^*, z^*) = (U_r^*, U_\theta^*, U_z^*) = (r^*\Lambda^* F(z), r^*\Lambda^* G(z), \delta^*\Lambda^* H(z)), \tag{7.6}$$

where Λ^* is the angular velocity of the disk, $\delta^* = (\nu^*/\Lambda^*)^{\frac{1}{2}}$ is the boundary-layer thickness, ν^* is the kinematic viscosity and $z = z^*/\delta^*$ is the non-dimensional normal direction. (Again, asterisks refer to dimensional quantities). Here F, G, H denote the non-dimensional radial, azimuthal and normal velocity profiles, which are found by solving a system of ordinary differential equations; refer to equations (4.6) - (4.9), (5.9) - (5.12) and (6.14) - (6.17) of chapters 4, 5 and 6.

The boundary-layer thickness δ^* is the reference scale for the non-dimensionalization of distances. However, there are two types of non-dimensionalization for the velocity field, depending on whether the velocity is locally or globally defined. For the locally

defined velocity, the circumferential disk velocity $r_a^*\Lambda^*$ is chosen as the reference scaling, where r_a^* is some dimensional radius. This leads to the most commonly adopted form of the non-dimensional mean flow

$$U_l(r,z) = \left(\frac{r}{Re}F(z), \frac{r}{Re}G(z), \frac{1}{Re}H(z)\right), \tag{7.7}$$

where the suffix l denotes locally defined. Here the radius $r = r^*/\delta^*$ and the local Reynolds number is given as $Re = r_a^*\Lambda^*\delta^*/\nu^* = r_a^*/\delta^* = r_a$.

For the globally defined velocity, $\delta^*\Lambda^*$ is the velocity reference scale, which gives the non-dimensional mean flow

$$U_g(r,z) = \Big(rF(z), rG(z), H(z)\Big), \tag{7.8}$$

where the suffix g denotes globally defined[1]. Since there are two types of velocity scaling, there are in turn, two types of time non-dimensionalization - local and global. The local time scale is given by $\delta^*/(r_a^*\Lambda^*) = 1/(r_a\Lambda^*)$ and the global time scale by $1/\Lambda^*$. Therefore, for the local time non-dimensionalization, the period of one rotation of the disk is given by $T_l = 2\pi Re$, while for the global time non-dimensionalization, the period of one rotation is given by $T_g = 2\pi$. By letting ω_l and ω_g denote the respective local and globally defined disturbance frequencies, we have the relation

$$\omega_g = \omega_l Re. \tag{7.9}$$

7.3 Numerical simulations for the parallel flow

As in previous chapters, the complex-valued quantity

$$\widetilde{\omega}(r,t) = \frac{i}{A}\frac{\partial A}{\partial t}, \tag{7.10}$$

is used to calculate the temporal frequencies and growth rates of the disturbance, where $A(r,t)$ is taken to be the azimuthal vorticity at the disk surface $\omega_{\theta,w}$. The

[1]Note that the suffix g is different to the suffix G, which denotes global mode.

temporal frequencies and growth rates are given by the respective real and imaginary parts of $\widetilde{\omega}$.

By considering the parallel flow approximation, the numerical simulations produce the same behaviour as that observed by Lingwood (1995). By impulsively exciting disturbances for a given Reynolds number Re and azimuthal mode number n, the temporal frequencies and growth rates (at all radial locations) will eventually asymptote to that predicted by Lingwood's local stability analysis.

For the present study, the long-time asymptotic temporal frequencies and growth rates were found by estimating the limit

$$\omega = \lim_{t \to \infty} \widetilde{\omega}(r_e, t), \tag{7.11}$$

where r_e is the radial location of impulsive forcing. The real part of ω gives the limiting value of the temporal frequency, while the imaginary part of ω gives the corresponding temporal growth rate. We consider the parallel flow approximation, where it is convenient to set the non-dimensional radial location of impulsive forcing equal to the Reynolds number, i.e. $r_e = Re$.

We will first review the results given by Davies, Thomas & Carpenter (2007) for the rotating-disk boundary-layer with constant azimuthal wavenumber β and constant azimuthal mode number n. The local and global non-dimensionalization is then applied to the rotating-disk with mass transfer $\mathbf{a} = \pm 1$, where the azimuthal mode number remains constant; the first to become absolutely unstable.

7.3.1 The rotating-disk boundary-layer

Constant azimuthal wavenumber β - Lingwood's (1995) inviscid study

Figure 7.1 displays the limiting local and globally defined frequencies and growth rates, obtained from the parallel numerical simulations, for a constant azimuthal wavenumber $\beta = n/Re$, where n is again the azimuthal mode number. The azimuthal

wavenumber $\beta = 0.126$ was chosen, so that the results would correspond to the behaviour predicted by Lingwood's (1995) inviscid absolute instability study. The inviscid absolute frequency was given by Lingwood, as $\omega = -0.0262 + i0.013$.

Figures 7.1(b, d) display the temporal frequencies $\omega_{l,r}$ and growth rates $\omega_{l,i}$ that have been non-dimensionalized in the usual locally defined manner. The local temporal frequencies and growth rates appear to be approaching constant values as the Reynolds number increases.

The asymptotic value of the local frequency and growth rate can be predicted using the plots of the globally non-dimensionalized frequencies $\omega_{g,r}$ and growth rates $\omega_{g,i}$; refer to figures 7.1(a, c). The global frequencies and growth rates appear to decrease and increase linearly with the Reynolds number, and may be fitted to the straight line relationships

$$\omega_{g,r} = -0.0268Re - 2.24339, \tag{7.12}$$

$$\omega_{g,i} = 0.0099Re - 5.2104. \tag{7.13}$$

By equation (7.9), the local complex frequency at the inviscid limit, is given as $\omega_l = -0.0268 + i0.0099$, which to two decimal places is in exact agreement with Lingwood's inviscid result.

Unfortunately, it was impossible to obtain results for larger Reynolds numbers, which may have confirmed the limiting behaviour with greater confidence. This was due to convergence problems in the numerical simulations associated with the increasingly rapid growth of the disturbances. Nonetheless, the large limit behaviour does appear to be compatible with the inviscid study by Lingwood (1995).

By taking the azimuthal wavenumber β to remain fixed, the azimuthal mode number n is allowed to vary and can take on non-integer values. Such behaviour is not physically obtainable, since n is restricted to taking only integer values, due to the circumferential periodicity of the problem. Therefore, it is more appropriate to

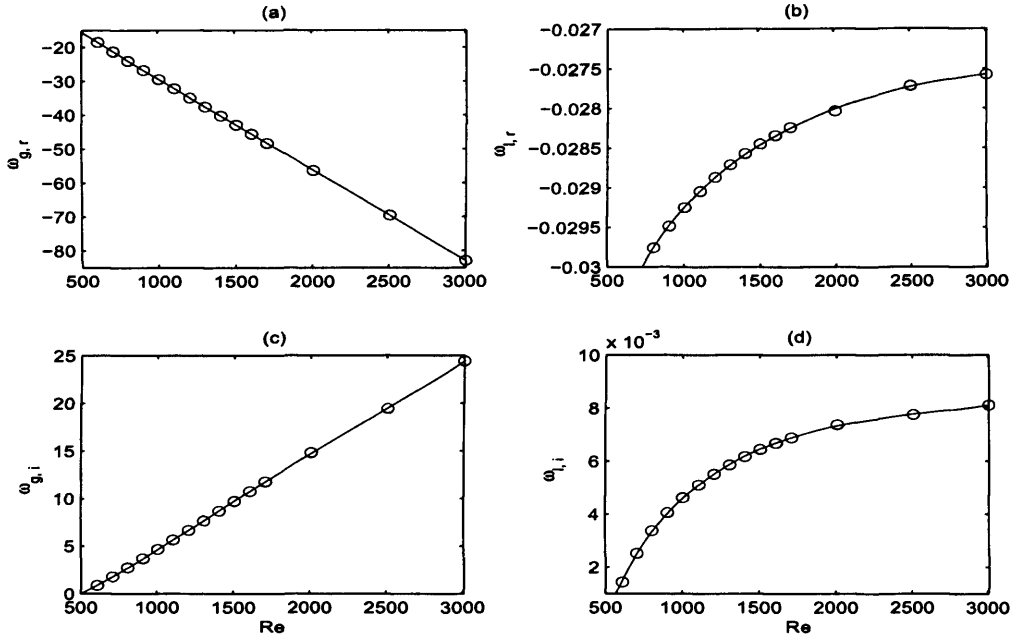

Figure 7.1: *Complex frequencies obtained in the large-time limit from simulations of impulsively excited disturbances in the parallel flow at various radii/Reynolds numbers Re. The azimuthal mode number is varied, such that* $\beta = n/Re = 0.126$. *(a)* $\omega_{g,r}$; *(b)* $\omega_{l,r}$; *(c)* $\omega_{g,i}$; *(d)* $\omega_{l,i}$. *Each data point* o *corresponds to a result obtained from a separate numerical simulation conducted at the indicated Reynolds number.*

investigate the large Reynolds number behaviour with a fixed azimuthal mode number n.

Constant azimuthal mode number n

Figure 7.2 displays the local and globally non-dimensionalized frequencies and growth rates for various radii/Reynolds numbers, corresponding to the azimuthal mode number $n = 68$, where the usual parallel flow approximation has been employed. This corresponds to the first azimuthal mode number to become absolutely unstable, as

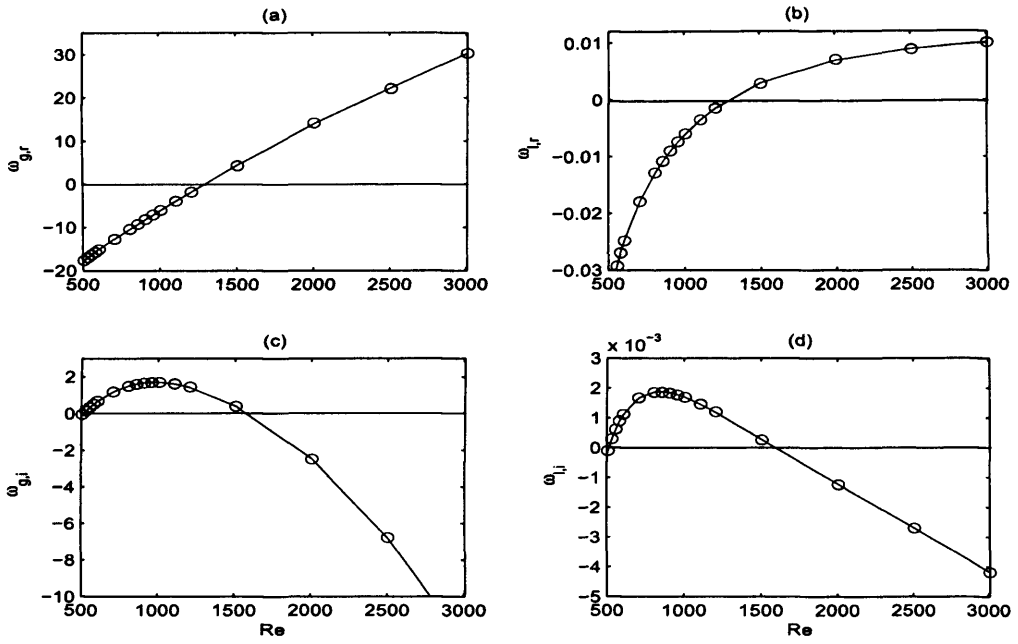

Figure 7.2: *Complex frequencies obtained in the large-time limit from simulations of impulsively excited disturbances in the parallel flow at various radii/Reynolds numbers Re. The azimuthal mode number* $n = \beta Re = 68$. *(a)* $\omega_{g,r}$; *(b)* $\omega_{l,r}$; *(c)* $\omega_{g,i}$; *(d)* $\omega_{l,i}$. *Each data point* o *corresponds to a result obtained from a separate numerical simulation conducted at the indicated Reynolds number.*

found by Lingwood (1995, 1997a,b). The range of Reynolds numbers considered extends from $Re = 500$ to $Re = 3000$. The data points o indicate the locations of the temporal frequencies and growth rates obtained from the numerical simulations. It is clear from figures 7.2(c, d) that there is a finite region of absolute instability and a stationary point. The region of absolute instability starts at approximately $Re = 507$ (corresponding to that found by Lingwood (1997a)) and extends to approximately $Re = 1650$. The global maxima occurs near $Re = 1000$. Outside the region of absolute instability, the flow is either convectively unstable or stable.

Although there is a turning point within the growth rate plot, it is essential that

there is also such a point within the frequency plot, if we are to locate the saddle point r_s along the real $r-$axis. However, the locally defined frequency appears to be asymptoting towards a constant for large Re, while the globally non-dimensional frequency appears (at least for $Re \leq 3000$) to increase linearly with the Reynolds number. Consequently, it looks as though the saddle point r_s does not exist along the real $r-$axis. Therefore, the results suggest that the saddle point (if it does exist) will be located off the real $r-$axis, and within the complex $r-$plane.

The local frequency $\omega_{l,r}$, for $n = 68$, for large Re, can be approximated by first finding a least squares-fit to the $\omega_{g,r} - Re$ plot. The global frequency $\omega_{g,r}$ can be approximated by the straight line expression

$$\omega_{g,r} \approx 0.017385Re - 24.457. \tag{7.14}$$

The gradient of the straight line will give an estimate of the local frequency $\omega_{l,r}$ as $Re \rightarrow \infty$. Thus, $\omega_{l,r} \rightarrow 0.017385$ as $Re \rightarrow \infty$.

It is also interesting to note that there is an absolutely unstable stationary mode, which appears for $Re \approx 1350$. However, such a mode would never realistically be observed in an experiment, since it is located well beyond the location of the onset of non-linear effects and transition.

7.3.2 The rotating-disk boundary-layer with injection a = -1

Figure 7.3 displays the local and globally defined frequencies and growth rates, for various radii/Reynolds numbers for the rotating-disk mean flow with injection **a** = -1. The azimuthal mode number is chosen to be $n = 29$, as this is the first to become absolutely unstable for **a** = -1. The frequencies and growth rates are plotted over the range $170 \leq Re \leq 800$, and again data points are indicated by $\circ$. The turning point within the growth rate plots is again quite evident, and the absolutely unstable region extends from $Re \approx 202$ (which corresponds to the location of critical absolute

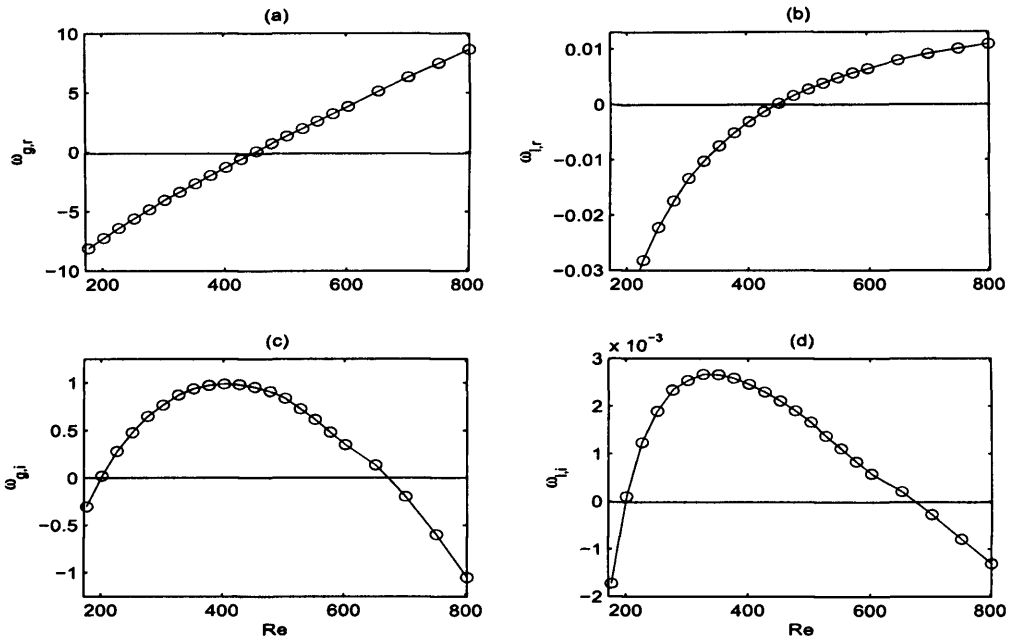

Figure 7.3: *Complex frequencies obtained in the large-time limit from simulations of impulsively excited disturbances in the parallel flow at various radii/Reynolds numbers Re, with uniform mass injection* $\boldsymbol{a}$ *= -1. The azimuthal mode number* $n = \beta Re = 29$. *(a)* $\omega_{g,r}$*; (b)* $\omega_{l,r}$*; (c)* $\omega_{g,i}$*; (d)* $\omega_{l,i}$*. Each data point* o *corresponds to a result obtained from a separate numerical simulation conducted at the indicated Reynolds number.*

instability, as found by Lingwood, 1997a) to $Re \approx 670$, with the global maximum growth rate found near $Re = 400$.

From figure 7.3(a, b), the globally defined frequency appears to vary linearly with the Reynolds number, while the locally non-dimensionalized frequency is found to asymptote towards a constant near $\omega_{l,r} = 0.0266$. The asymptotic limit of the locally defined frequency, is found by estimating the plot of the global frequencies, as a straight line. The asymptotic local frequency is given by the gradient of the expression for the straight line.

Hence, the results suggest that the saddle point r_s cannot be found along the real

$r-$axis, but instead may be located within the complex $r-$plane.

7.3.3 The rotating-disk boundary-layer with suction a = 1

For the rotating-disk flow with uniform mass suction $\mathbf{a} = 1$, the first azimuthal mode number to become absolutely unstable is $n = 194$. The corresponding frequencies and growth rates are plotted over the range $1810 \leq Re \leq 9000$, in figure 7.4, with $\circ$ indicating data points. Again there is a clear indication of a turning point in the growth rate plots. The region of absolute instability extends from $Re \approx 1860$ (which corresponds to that found by Lingwood, 1997a) to $Re \approx 5800$, and the global maximum growth rate occurs for $Re \approx 3600$.

However, there is no corresponding turning point in the $\omega_{g,r}-Re$ plot, since the globally defined frequency, appears once more to increase linearly with the Reynolds number. The local frequency $\omega_{l,r} \approx 0.013773$ at the inviscid limit. Again the limiting behaviour of $\omega_{l,r}$ is calculated by approximating $\omega_{g,r}$ as a straight line.

7.3.4 Comparing the frequency/growth rate-radius plots

Although the above study does not immediately help us to identify global modes, within the above rotating systems, there are a number of interesting features of the *frequency/growth rate* - *Re* plots, that we will now discuss.

In all cases considered, for fixed azimuthal mode number n, there was no turning point found within the frequency plots. Instead, the globally defined frequency (in all cases) was found to increase approximately linearly with the Reynolds number, yielding a locally non-dimensionalized frequency that tended towards a constant at the inviscid limit. However, a turning point was found in the growth rate plots, revealing a finite region of absolute instability. Outside the absolutely unstable parameter space the boundary-layer is either stable or convectively unstable.

For the mean flows with mass transfer, the radial extent of the region of absolute

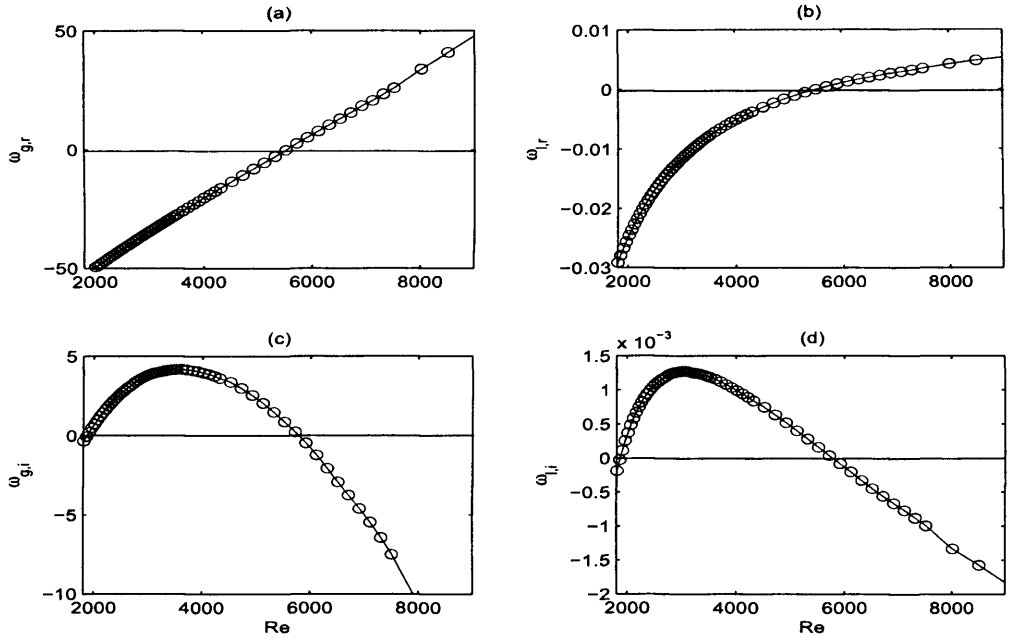

Figure 7.4: *Complex frequencies obtained in the large-time limit from simulations of impulsively excited disturbances in the parallel flow at various radii/Reynolds numbers Re, with uniform mass suction* $\boldsymbol{a} = 1$. *The azimuthal mode number* $n = \beta Re = 194$. *(a)* $\omega_{g,r}$; *(b)* $\omega_{l,r}$; *(c)* $\omega_{g,i}$; *(d)* $\omega_{l,i}$. *Each data point* o *corresponds to a result obtained from a separate numerical simulation conducted at the indicated Reynolds number.*

instability appears to decrease with injection, while it increases with suction. This may provide part of the explanation as to why the mean flows with uniform suction displayed disturbance behaviour consistent with global instability. It is possible that the region of absolute instability was of sufficient size, so as to promote globally unstable behaviour. While the region of absolute instability within the mean flows with uniform injection was too small. Table 7.1 gives a summary of the range of absolute instability for the rotating boundary-layers. (Note: the data is only given for fixed n; the first to become absolutely unstable. The regions of absolute instability will differ if we consider other values of n).

Flow	Extent of absolutely unstable region	Maximum growth $\omega_{g,i}$	Corresponding frequency $\omega_{g,r}$	Corresponding radius (Reynolds number)
von Kármán **a** = -1	202 - 670	0.99	-1.26	400
von Kármán **a** = 0	507 - 1650	1.70	-6.00	1000
von Kármán **a** = 1	1860 - 5800	4.18	-25.74	3600

Table 7.1: *Summary of range of absolute instability and maximum global growth rate for the above rotating mean flows. The azimuthal mode number n is fixed in each case.* ω_g *is the globally defined complex frequency and* ω_l *is the locally defined complex frequency, and subscripts r and i refer to frequency and growth rate.*

The maximum global growth rate attained by each flow is also given in table 7.1. The maximum globally defined growth rate appears to increase with suction, while decreasing with injection. In all cases (so far) investigated, the maximum globally defined growth rate is located well within the region of absolute instability.

Another interesting feature of the simulation results is the presence of an absolutely unstable stationary mode. Table 7.3 displays the approximate globally defined growth rate and location of the stationary modes for the given azimuthal mode number, (i.e. first to become absolutely unstable). Since the global growth rates are positive in the three cases considered, the stationary modes are absolutely unstable. In all cases considered, the stationary modes are located at Reynolds numbers/radii, well beyond the inner boundary of the absolutely unstable region. Hence, it is unlikely that these modes will ever be observed in an experiment, as non-linear effects and transition to turbulence would be expected to have set in motion at much lower

Flow	Growth ($\omega_{g,i}$) of stationary mode	Corresponding radius (Reynolds number)	Inviscid limit for $\omega_{l,r}$
von Kármán a = -1	0.9702	440	0.0266
von Kármán a = 0	0.9905	1350	0.0174
von Kármán a = 1	0.8800	5600	0.0138

Table 7.2: *Summary of stationary modes and their location for the above rotating flows. The azimuthal mode number n is fixed in each case.* ω_g *is the globally defined complex frequency and* ω_l *is the locally defined complex frequency, and subscripts r and i refer to frequency and growth rate.*

radii.

7.4 A simple method for determining the global frequency

A simple heuristic method for determining the global frequency and saddle point location was briefly described by Davies, Thomas & Carpenter (2007). The results of the previous section appear to suggest that the globally defined frequency ω_r (note that the suffix g, used to denote globally defined complex frequencies has been dropped) varies linearly with the Reynolds number/radii, while the behaviour of the global growth rate ω_i is consistent with a quadratic function, where there is a finite range of radii over which the flow is absolutely unstable. Figure 7.5 displays a plot of the approximate behaviour of the global frequency (solid line) and growth rate (dashed line), as indicated by the earlier study. The labels r_c and r_m refer to the radial locations/ Reynolds numbers for the onset of absolute instability and the maximum

growth rate. By letting $\omega_{m,r}$ and $\omega_{m,i}$ denote the globally non-dimensionalized frequency and growth rate at the radial location r_m, we have

$$\omega_r(r) = \omega_{m,r} + a(r - r_m), \tag{7.15}$$

$$\omega_i(r) = \omega_{m,i} + b(r - r_m)^2, \tag{7.16}$$

where a and b are unknown real constants. Thus, we obtain the following expression for the complex frequency

$$\omega(r) = \omega_m + a(r - r_m) + ib(r - r_m)^2, \tag{7.17}$$

for $\omega_m = \omega_{m,r} + i\omega_{m,i}$.

7.4.1 The global complex frequency

Differentiating (7.17) with respect to r gives

$$\begin{aligned} \frac{d\omega(r)}{dr} &= a + 2ib(r - r_m), \\ \Rightarrow r_s &= r_m + \frac{ia}{2b}, \end{aligned} \tag{7.18}$$

where r_s is the saddle point. Therefore, providing a is non-zero, the saddle point r_s will be located off the real $r-$axis. On substituting r_s into equation (7.17), we obtain the global complex frequency

$$\omega_G = \omega_m + \frac{ia^2}{4b}, \tag{7.19}$$

at the saddle point r_s. Hence, we obtain globally unstable behaviour, if

$$\omega_{m,i} + \frac{a^2}{4b} > 0. \tag{7.20}$$

The coefficient a is given by the radial derivative of equation (7.15)

$$a = \frac{d\omega_r}{dr}. \tag{7.21}$$

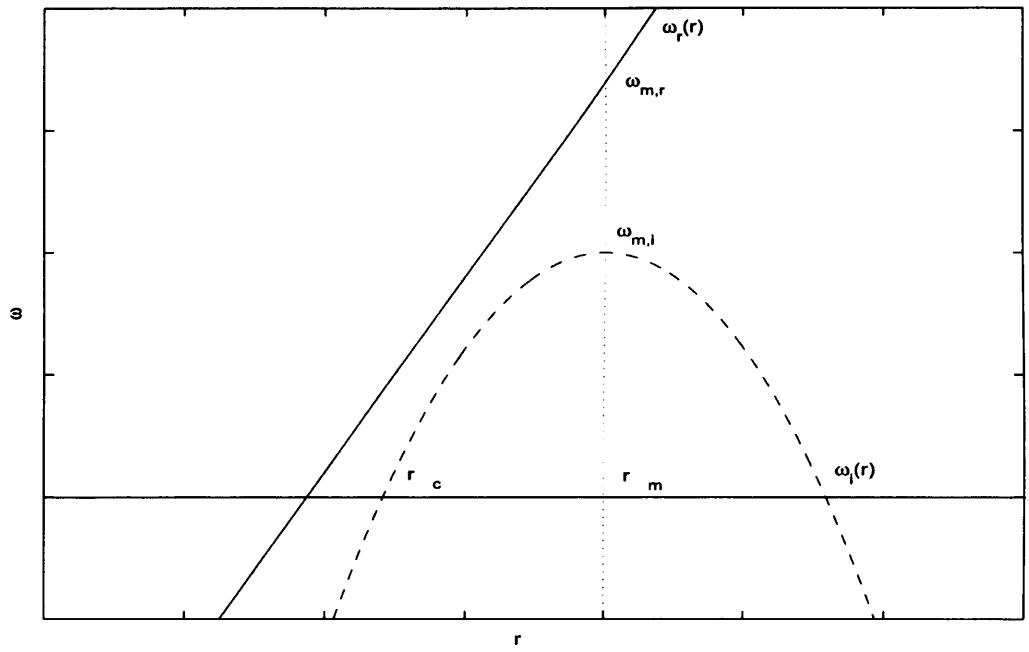

Figure 7.5: *Behaviour of the global frequencies ω_r and growth rates ω_i as ascertained by the earlier parallel simulation results. Here ω_r varies linearly, while ω_i varies quadratically with the radius.*

The second coefficient b can be derived, by analyzing the behaviour at the onset of absolute instability, which arises when $r = r_c$, or

$$\begin{aligned} \omega_i(r_c) &= 0, \\ \Rightarrow b &= -\frac{\omega_{m,i}}{(r_c - r_m)^2}, \end{aligned} \tag{7.22}$$

at which point

$$\left.\frac{d\omega_i}{dr}\right|_{r=r_c} = 2b(r_c - r_m). \tag{7.23}$$

On squaring both sides of equation (7.23) and introducing (7.22), we obtain

$$\begin{aligned} \left(\left.\frac{d\omega_i}{dr}\right|_{r=r_c}\right)^2 &= 4b^2(r_c - r_m)^2 \\ &= -4b\omega_{m,i}, \end{aligned} \tag{7.24}$$

$$\Rightarrow b = -\left(\frac{d\omega_i}{dr}\bigg|_{r=r_c}\right)^2 \Big/ (4\omega_{m,i}). \tag{7.25}$$

The complex global frequency (7.19), at the saddle point r_s, can now be given as

$$\omega_G = \omega_m - i\omega_{m,i}\left\{\frac{\frac{d\omega_r}{dr}}{\frac{d\omega_i}{dr}|_{r=r_c}}\right\}^2, \tag{7.26}$$

where the global growth rate at the saddle point is given by

$$\omega_{G,i} = \omega_{m,i}\left\{1 - \left\{\frac{\frac{d\omega_r}{dr}}{\frac{d\omega_i}{dr}|_{r=r_c}}\right\}^2\right\}. \tag{7.27}$$

Due to the restrictions of the problem (i.e. there is a definite finite region of absolute instability), the maximum growth rate $\omega_{m,i}$ is positive. Thus, we must have

$$\frac{d\omega_i}{dr}\bigg|_{r=r_c} > \frac{d\omega_r}{dr}, \tag{7.28}$$

in order to obtain a globally unstable mode. Otherwise the flow is globally stable.

7.4.2 The saddle point location

The location of the saddle point was previously given by equation (7.18), but on substituting for a and b we obtain

$$\begin{aligned} r_s &= r_m - \frac{i(r_c - r_m)^2}{2\omega_{m,i}}\frac{d\omega_r}{dr} \\ &= r_m - 2i\omega_{m,i}\left\{\frac{\frac{d\omega_r}{dr}}{(\frac{d\omega_i}{dr}|_{r=r_c})^2}\right\}. \end{aligned} \tag{7.29}$$

Hence, as noted before, the saddle point is located in the complex $r-$plane, providing that $\omega_{m,i}$ and $\frac{d\omega_r}{dr}$ are non-zero.

7.4.3 The method applied to some rotating boundary-layers

For the rotating-disk boundary-layer, the complex frequency at the location of maximum growth is approximately given by $\omega_m = -6.00 + i1.70$, for the radial location

$r_m = 1000$; Obtained using figure 7.2. The global frequency and growth rate can now be crudely approximated by the equations

$$\omega_r = 0.023(r - 1000) - 6.00, \tag{7.30}$$

$$\omega_i = 1.70 - 7.23 \times 10^{-6}(r - 1000)^2. \tag{7.31}$$

Using equation (7.29) the saddle point is given as

$$r_s \approx 1000 - i1670, \tag{7.32}$$

while the corresponding global complex frequency is given as

$$\omega_G \approx -6.00 - i17.94. \tag{7.33}$$

Hence, the global frequency at the saddle point is stable.

Table 7.3 gives the saddle point locations r_s and corresponding complex global modes ω_G, calculated using the above model, for the two other mean flows that we have considered; rotating-disk boundary-layer with mass transfer $\mathbf{a} = \pm 1$. In both cases considered, the global frequency (at the saddle point) is indicated to be stable and the saddle point is located in the lower half of the complex $r-$plane.

Problem	ω_G	r_s
$\mathbf{a} = -1$	-1.26-7.92i	400-594i
$\mathbf{a} = 1$	-25.74-36.64i	3600-5440i

Table 7.3: *The global complex frequency ω_G and saddle point r_s for the rotating-disk with mass transfer $\mathbf{a} = \pm 1$, calculated using the method developed by Davies, Thomas & Carpenter (2007).*

7.5 A polynomial fit method

The above model is rather simplistic and it is likely that the approximate global frequency (7.17) does not fully capture the characteristics of the global behaviour of

the rotating-disk boundary-layer. Instead, we will now fit the numerical simulation data of the globally defined complex frequency to a polynomial of the form

$$\omega(r) = a + br + cr^2 + dr^3 + ..., \tag{7.34}$$

where a, b, c and d are possibly complex. If the polynomial is at most a cubic, the radial derivative of the global complex frequency gives stationary points when

$$\frac{d\omega}{dr} = b + 2cr + 3dr^2 = 0, \tag{7.35}$$

which gives the saddle points

$$r = r_s = -\frac{c}{3d} \pm \sqrt{\left(\frac{c}{3d}\right)^2 - \frac{b}{3d}}. \tag{7.36}$$

7.5.1 Example

We will now apply the cubic polynomial method, equation (7.34), to the rotating-disk simulation data presented in figure 7.2(a, c). The globally non-dimensionalized frequency can be expressed as

$$\omega_r(r) = -3.03 \times 10^1 + 2.64 \times 10^{-2} r - 2.56 \times 10^{-6} r^2 + 1.86 \times 10^{-10} r^3, \tag{7.37}$$

for a globally defined growth rate

$$\omega_i(r) = -3.90 + 1.10 \times 10^{-2} r - 6.17 \times 10^{-6} r^2 + 5.32 \times 10^{-10} r^3, \tag{7.38}$$

which are valid over the real radial range $500 \leq r \leq 3000$[1]. Figure 7.6 displays a plot of the numerical simulation global frequencies/growth rates (indicated by o) and corresponding polynomial fit (dashed line). The polynomial expressions give a remarkably good fit to the simulation data.

[1]The radial range corresponds to the range of Reynolds numbers considered in figure 7.2(a, c).

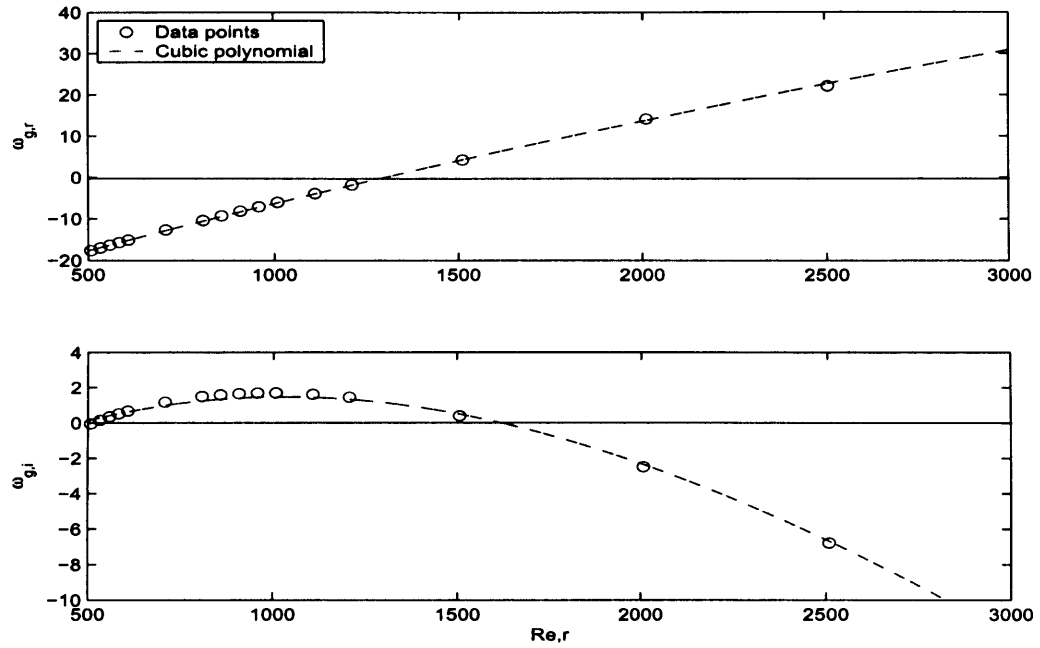

Figure 7.6: *Numerical simulation data* o *for the globally defined frequencies* ω_r *and growth rates* ω_i *for the rotating-disk boundary-layer. The dashed line refers to the cubic polynomial given by equations (7.37) and (7.37).*

On applying equation (7.36) to the polynomial expressions (7.37) and (7.38), we obtain the saddle points r_s, with corresponding global modes ω_G

$$\begin{aligned} r_s &\approx 6749 + 1697i, \quad \omega_G \approx 86.60 - 31.83i, \\ r_s &\approx 1134 - 2148i, \quad \omega_G \approx -1.76 - 22.36i. \end{aligned} \tag{7.39}$$

The first saddle point can be ignored, since the real part does not belong to the valid range of radii for the polynomial expressions (7.37) and (7.38). The second saddle point is within the valid radial range, and is globally stable.

The results obtained for the polynomial fit method are quite different to those obtained in the previous section, where $r_s \approx 1000 - i1670$ and $\omega_G \approx -6.00 - i17.94$.

This would suggest that the approximations described in section 7.4, are not good enough for accurately predicting the saddle point or global mode. Nevertheless, the simple quadratic method (described in section 7.4) does successfully predict (in this instance) that the saddle point will be located within the complex $r-$plane and that the global mode will be stable. Hence, the quadratic method is useful, since it may be used to predict the nature of the global mode.

Table 7.4 displays the saddle point locations and complex global frequencies for the rotating-disk with mass transfer $\mathbf{a} = \pm 1$, calculated using the above cubic polynomial method. In both cases, the global mode is stable.

Problem	ω_G	r_s
a = -1	-0.53 - 6.12i	389 - 470i
a = 1	-22.52 - 30.31i	3587 - 4483i

Table 7.4: *The complex global frequency and saddle point for the rotating-disk with mass transfer* $\boldsymbol{a} = \pm 1$, *calculated using the cubic polynomial method.*

The earlier study on the rotating-disk with mass transfer suggested that globally unstable behaviour was promoted by the application of uniform suction; refer to chapter 4. However, the results from the current investigation imply that the global mode ω_G is stable for the rotating-disk with mass suction $\mathbf{a} = 1$. The methods used in the current chapter are rather simplistic and may not fully describe the disturbance characteristics of the rotating-disk boundary-layer with mass suction. Thus, globally unstable behaviour may still prevail for those mean flows with mass suction.

7.6 Conclusions

The results of Lingwood (1995, 1997a,b) suggest that the growth rate associated with the absolute instability gets stronger as the radius/Reynolds number increases.

Indeed her inviscid study has shown that the absolute instability even persists at the inviscid limit, which would suggest that non-parallel effects would have no influence on the behaviour at large radii/Reynolds number. Nonetheless, Davies & Carpenter (2001) have shown (using numerical simulations) that the absolute instability does not lead to a linear unstable global mode. Instead convective behaviour appears to dominate the global response, even at radial locations well within the region of absolute instability. Such behaviour can be understood by considering two types of non-dimensionalization - local and global.

This idea was recently described by Davies, Thomas & Carpenter (2007). The locally-defined non-dimensional timescale is given as the ratio of the constant boundary-layer thickness and the radially varying angular disk velocity. While for the global study, the time non-dimensionalization is given as the inverse of the angular velocity of the disk, which does not depend on the radius. From the two types of non-dimensionalization, equation (7.9) may be derived, which relates the locally and globally defined disturbance frequencies.

The local and global non-dimensionalizations are then applied to a number of rotating-disk boundary-layers, where the numerical simulations were conducted using the parallel flow approximation. Three problems are considered; the rotating-disk boundary-layer (or von Kàrmàn flow) - this case was used as an example by Davies, Thomas & Carpenter (2007); the rotating-disk with uniform mass injection $\mathbf{a}$ = -1; and the rotating-disk with uniform suction $\mathbf{a} = 1$.

For the rotating-disk boundary-layer, the azimuthal wavenumber β is initially taken to be constant, and is chosen as $\beta = 0.126$, in order to match the results of Lingwood's (1995) inviscid study. The complex local frequency at the inviscid limit was found to be $\omega_l \approx -0.0268 + i0.009$, which to two decimal places is consistent with that found by Lingwood; $\omega = -0.0262 + i0.013$. Due to the relation (7.9), the respective globally defined frequency and growth rate, decrease and increase,

in linear proportion with the radius/Reynolds number. Hence, there is a different globally non-dimensionalized frequency at each radial location.

Similar behaviour is found for the problems with a constant integer-valued azimuthal mode number n. The azimuthal mode number can only take on integer values, due to the circumferential periodicity of the rotating-disk. In the three cases considered, n was chosen as the first azimuthal mode number to become absolutely unstable, i.e. for the rotating-disk, $n = 68$. The locally defined frequency was found to approach a constant as the radius increased, and in turn the globally defined frequency was found to increase linearly in direct proportion with the radius. Whereas the locally and globally non-dimensionalized growth rates were found to display finite radial regions of absolute instability. Outside of these regions the problem is either stable or convectively unstable. The region of absolute instability was found to increase with suction and decrease with injection. Similarly the maximum globally defined growth rate was largest for the suction problem and smallest for the injection problem. Another interesting feature of the study, was the discovery of absolutely unstable stationary modes, which were located in all cases considered, at radial locations considerably larger than the radial location for the onset of absolute instability.

The global frequency selection method devised by Chomaz *et al.* (1991) requires that there exists a double saddle point (equation (7.3)), if we are to locate global modes ω_G. The first term requires that the group velocity is zero, and the second term requires that a saddle point exists in the complex $r-$plane. If the complex part of the global frequency ω_G is negative, the flow is globally stable, otherwise, if there exists a global frequency with a positive imaginary part, global instability is observed.

The results of the parallel numerical simulations (with constant n) show that there exists a turning point within the globally defined growth rate plots, i.e. $\frac{\partial \omega_{g,i}}{\partial r} = 0$ for some radial location r_m. However, no such point exists within the globally defined frequency plots.

Nonetheless, using a simple method (that was first described by Davies, Thomas & Carpenter (2007)), we are able to estimate the location of the saddle point and corresponding global mode. By considering a linearly varying frequency and a quadratically varying growth rate, (which appears to be consistent with the results of the parallel numerical simulations), the location of the saddle point is always found off the real $r-$axis and within the complex radial plane, providing that the variations in frequency and growth rate are always non-zero. The global response is determined by the inequality (7.28). If the inequality (7.28) is satisfied, the global mode is unstable, otherwise the problem is globally stable. For the three examples considered, globally stable modes are obtained, while the saddle points are located in the lower half of the complex $r-$plane. This would suggest that for the problem with mass suction (where our earlier study suggests that globally unstable behaviour appears to be present; refer to chapter 4), globally stable behaviour eventually prevails. However, the methods used in the current chapter may not fully describe the disturbance characteristics for the rotating-disk with mass suction. Hence, globally unstable behaviour may still play an important role in the disturbance development.

A cubic polynomial-fit method is also implemented to fit the numerical simulation data of the globally defined frequency, so as to improve the accuracy of the saddle point locations and global modes.

The inequality (7.28) relates the varying frequency and the varying growth rate, and has the general form of a criterion for global in/stability given in the subsequent chapter. The criterion under consideration also relates the varying frequency and varying growth rate, and is found by considering solutions to the linearized complex Ginzburg-Landau equation (Hunt & Crighton, 1991; Hunt, 1995). We will now study these solutions and make comparisons with the rotating-disk boundary-layer.

Chapter 8

The Green's solutions to the Ginzburg-Landau equation

8.1 Introduction

The results of Davies & Carpenter (2003) and of previous chapters has indicated that the rotating-disk boundary-layer does not give rise to any fixed unstable global mode, although globally unstable behaviour does appear to be promoted in some cases, e.g. rotating-disk with uniform suction - refer to chapter 4. A greater understanding of the rotating-disk boundary-layer can be obtained by making comparisons with a much simpler system: the linearized complex Ginzburg-Landau equation. Using the results of the numerical simulations for the linearized disturbances in the rotating-disk boundary-layer, we can model and match the behaviour to solutions of the Ginzburg-Landau equation.

8.1.1 The Ginzburg-Landau equation

The linearized Ginzburg-Landau equation is a simple and convenient model for studying the linear space-time development of a disturbance amplitude $A(r,t)$. It is given as

$$\frac{\partial A}{\partial t} + U\frac{\partial A}{\partial r} = \mu(\epsilon r)A + \frac{\gamma \partial^2 A}{\partial r^2}, \tag{8.1}$$

where $\epsilon \ll 1$ incorporates slow streamwise variation effects, μ characterizes linear temporal growth and temporal frequency[1], U is the convection velocity and γ describes the diffusion and dispersion effects. Here r refers to the streamwise/radial direction and t is the time variable.

If the three terms μ, U and γ are independent of the spatial co-ordinate r, the linearized complex Ginzburg-Landau equation can be used to model the disturbance development of the numerical simulations with a parallel flow. While if any one of the three parameters μ, U and γ is allowed to vary with streamwise direction r, the Ginzburg-Landau equation may be thought of as modeling the development of a disturbance in a non-parallel flow.

The three parameters μ, U and γ can be expressed in terms of the results of the numerical simulations of the rotating-disk boundary-layer. We can derive definitions for global in/stability from the Ginzburg-Landau equation and match the results with the rotating-disk simulation data. From the ensuing results we are able to understand why the rotating-disk boundary-layer does not give any fixed globally unstable mode, and why a globally unstable flow may not give a constant global frequency.

8.1.2 Analytic Solutions to the Ginzburg-Landau equation - Hunt & Crighton (1991)

Hunt & Crighton (1991), Hunt (1995) obtained analytic solutions to the Ginzburg-Landau equation

$$\frac{\partial G}{\partial t} + U\frac{\partial G}{\partial r} = \mu(\epsilon r)G + \frac{\gamma \partial^2 G}{\partial r^2} + \delta(r)\delta(t), \tag{8.2}$$

where $G = G(r,t)$ is the Green's function representing the response to an impulsive forcing of the usual Dirac delta form $\delta(r)\delta(t)$. The Green's solutions were calculated using a computer based symbolic algebra manipulation package. The package

[1]The temporal frequency is only included if μ is taken to be complex, i.e. the real part of μ refers to the local temporal growth, while the complex part of μ is the local temporal frequency.

obtained general results for the Green's function and the time periodic response for varying forms of the stability parameter μ. Hunt & Crighton considered the cases where the stability parameter $\mu(r)$ was

1. constant, $\mu(r) = \mu_0$,
2. linearly varying, $\mu(r) = \mu_0 + \mu_1 r$, and
3. quadratically varying, $\mu(r) = \mu_0 + \mu_1 r + \frac{1}{2}\mu_2 r^2$.

They also considered the effects of a linearly varying convection velocity, $U(r) = U_0 + U_1 r$.

Throughout the investigation by Hunt & Crighton (1991) the three parameters μ, U and γ were real only. However, Hunt (1995) did consider the more general case, where μ, U and γ can be complex. Hunt (1995) gave the equations for the disturbance wavepacket edges in terms of the real parts of the complex stability, convection velocity and diffusion/dispersion parameters. This led Hunt to derive definitions for global stability and globally convective instability. The reader is referred to Hunt (1995) for further details.

8.1.3 Further studies on the Ginzburg-Landau equation

Other investigations on the global stability of the Ginzburg-Landau equation, of interest, have been carried out by Chomaz, Huerre & Redekopp (1988) and Cossu & Chomaz (1997). Chomaz *et al.* (1988) investigated the Ginzburg-Landau equation with a stabilizing cubic nonlinearity. Their stability parameter μ was allowed to vary linearly with the streamwise direction, i.e. $\mu = \mu_0 + \mu' r$, with $\mu' < 0$. For $\mu_{0,i} < 0$ and $r > 0$, μ is always negative. Therefore, any flow is both locally and globally stable. As $\mu_{0,i}$ is increased above the real zero axis a region of local convective instability develops near the origin of the source. This results in a region of local transient

growth. However, the disturbance eventually decays and the flow is globally stable. As $\mu_{0,i}$ is increased further, a region of local absolute instability develops near the origin. If the region of local absolute instability is sufficiently small the transient growth persists and the flow remains globally stable. On the other hand if $\mu_{0,i}$ is greater than some critical value, globally unstable behaviour prevails. Thus, it was concluded that although the existence of a region of local absolute instability was a necessary condition, it was not a sufficient condition for proof of an amplified global mode.

Cossu & Chomaz (1997) considered the behaviour of a flow with a quadratically varying stability parameter, i.e. $\mu = \mu_0 + \frac{1}{2}\mu_2 r^2$, where $\mu_2 < 0$. For $\mu_0 < 0$ the flow was found to be locally stable everywhere, while a finite region of local convective instability appears when μ_0 is increased above zero. In both instances the flow is globally stable. As μ_0 is increased further, a region of local absolute instability develops, but again the flow is still globally stable. It is only when the stability parameter μ_0 adopts a value that is greater then some critical constant that the flow becomes globally unstable. Cossu & Chomaz (1997) found this critical value to be $\mu_c = U^2/4|\gamma|^2 + (\sqrt{-2\mu_2\gamma}/2)\cos[\mathrm{Arg}(\gamma)/2]$.

It should also be noted that Floriani, Dudok de Wit & Le Gal (2000) conducted a study on the nonlinear interactions of the rotating-disk boundary-layer, that is described in terms of weakly interacting Fourier modes, using a Volterra series equation. Floriani *et al.* (2000) show that the Volterra model is similar to the Ginzburg-Landau equation and formulate analytical relations between the coefficients of the Ginzburg-Landau equation and the Kernels of the Volterra model. The results obtained for the Ginzburg-Landau coefficients in relation to the rotating-disk mean flow were found to be compatible with previous experimental investigations.

Gajjar (1996) and Gajjar, Arebi & Sibanda (1996) conducted a theoretical study on the non-linear stability of stationary and non-stationary instabilities developing in

three-dimensional boundary-layers. The example chosen for their investigation was the rotating-disk boundary-layer, where they studied the crossflow instability. Using a high Reynolds number asymptotic analysis, they were able to derive a novel integro-partial differential equation. By considering linearized disturbances, the amplitude equation (given in their investigations) did not retain any diffusion/dispersion terms. However, as we will see shortly, the inclusion of diffusion/dispersion effects are required, if we are to successfully model the behaviour shown in our numerical simulations of the rotating-disk boundary-layer. This is especially true for the mean flows obtained when there is uniform suction or a sufficiently large uniform axial magnetic field.

8.1.4 The remainder of the chapter

For the current study, the behaviour observed in the numerical simulations of the rotating-disk boundary-layer, is modeled using the linearized Ginzburg-Landau equation. We may derive expressions for the parameters μ, U and γ in terms of the rotating-disk simulation data. The resulting Green's solutions of the Ginzburg-Landau equation display characteristics consistent with that depicted by the numerical simulations. We may then formulate expressions for global stability, which allow us to understand the disturbance behaviour of the rotating-disk boundary-layer.

If we allow the stability term μ and dispersion/diffusion term γ to be complex, and μ is linearly varying, the global stability may be characterized by the relationship between the ratio of the linearly varying frequency and growth rate, and the ratio of the dispersion and diffusion effects. Davies, Thomas & Carpenter (2007) recently discussed the case where the stability parameter μ is linearly varying. They compared the Green's solutions of the Ginzburg-Landau equation with the non-parallel simulations of the rotating-disk boundary-layer. The example given in their recent paper (for the rotating-disk boundary-layer) is also used here to model and compare

disturbance characteristics. Further examples are given later in the chapter, where the simulation results of the rotating-disk with uniform mass transfer are used.

The remainder of this chapter is as follows; the following section describes the Green's function solutions that were obtained by Hunt & Crighton (1991), Hunt (1995). We derive expressions for global stability and present plots of frequencies, growth rates and disturbance development wavepackets for the Green's solutions that match the behaviour found in the numerical simulation results. Finally, the investigation is discussed and an explanation is given for why the non-parallel rotating-disk mean flows produce the behaviour found in Davies & Carpenter (2003) and chapters 4, 5 and 6.

8.2 Analysis of the Green's function solutions

Hunt & Crighton (1991), Hunt (1995) obtained Green's solutions to the linearized Ginzburg-Landau equation

$$\frac{\partial G_0}{\partial t} + U\frac{\partial G_0}{\partial r} = \mu(\epsilon r)G_0 + \frac{\gamma\partial^2 G_0}{\partial r^2} + \delta(r)\delta(t), \tag{8.3}$$

where $\epsilon \ll 1$[1] is a small positive parameter ($\epsilon = 1$ for the following investigation), and μ, U and γ ($\Re(\gamma) > 0$) are the stability, convection velocity and diffusion/dispersion terms, respectively. Here G_0 is the Green's function $G_0(r,t)$, where r and t denote the streamwise direction and time unit, respectively. The equation is subject to impulsive forcing $\delta(t)\delta(r)$, where δ is the usual Dirac delta function. To simplify the subsequent notation we have shifted the streamwise co-ordinate r, so that the centre of forcing is centred at $r = 0$, rather than at $r = r_e$, which was the case for the earlier numerical simulations. (Here we have, in effect, introduced a new streamwise variable $\hat{r} = r - r_e$. However, it would be rather monotonous to keep track of the difference between r

[1]Note that no assumption is required about the size of ϵ, in order for Hunt & Crighton's solutions to be valid. Here we have set $\epsilon = 1$ to simplify the problem and reduce the number of variables.

and $\hat{r}$, when we are comparing the results of the Ginzburg-Landau equation with the numerical simulation data).

8.2.1 $\mu = \mu_0$, a real constant

The exact analytic expression for the Green's function, for a stability parameter $\mu = \mu_0$, a real constant is given as

$$G_0(r,t) = \sqrt{\frac{4}{\pi\gamma t}}\exp\{\mu_0 t - (r - Ut)^2/4\gamma t\}, \tag{8.4}$$

where $U = U_0$, a constant. When μ and γ are real only (dispersion effects are ignored), the disturbance characteristics may be found by calculating the leading and trailing edges of the spatial-temporal disturbance wavepacket. (This was the method employed by Hunt & Crighton in their study). The edges of the wavepacket at any time t, are defined as the values of r, for which the real part of the argument of the exponential of (8.4) vanishes. The wavepacket will be exponentially large inside the wavepacket and exponentially small outside the wavepacket. There is of course the possibility that no real root exists for r. Thus, the wavepacket has no edges and the solution is exponentially small everywhere. This would imply stability. On the other hand if the edges exist, locally convective or absolutely unstable behaviour would be observed. Hunt & Crighton noted that the edges occur for $r = \{U \pm\sqrt{(4\mu_0\gamma)}\}t$. Therefore, stability arises for $\mu_0 < 0$, since the roots are complex. For $0 < \mu_0 < U^2/4\gamma$ the two edges are travelling in the same direction. Hence, any fixed r will eventually be within the decaying region of the wavepacket; convective instability is present. For $\mu_0 > U^2/4\gamma$ the edges travel in opposite directions - any fixed r will eventually be within the region of exponential growth; absolute instability. (Refer to figure 1.1 for schematic drawings of convectively and absolutely unstable disturbance wavepackets).

8.2.2 $\mu = \mu_0$, a complex constant

The stability parameter μ is now considered to be a complex constant, and the term γ is also complex, i.e. $\mu = \mu_{0,r} + i\mu_{0,i}$ and $\gamma = \gamma_r + i\gamma_i$. Therefore, dispersion effects are now included. The Green's function (8.4) can be re-written as

$$G_0(r,t) = \sqrt{\frac{1}{4\pi\gamma t}}\exp\left(\mu_0 t - \frac{\gamma_r(r-Ut)^2}{4|\gamma|^2 t} + \frac{i\gamma_i(r-Ut)^2}{4|\gamma|^2 t}\right), \tag{8.5}$$

where $|\gamma|^2 = \gamma_r^2 + \gamma_i^2$, and μ_0 and U are as before.

If we are to fit the numerical simulation data of the rotating-disk boundary-layer to the Green's solution of the Ginzburg-Landau equation, we must determine expressions for the unknown terms μ, U and γ. However, before we proceed to find expressions for the three unknown terms, we will consider the full disturbance structure

$$G(r,t) = G_0(r,t)\exp\{i(\alpha_s r - \omega_s t)\}, \tag{8.6}$$

where G_0 is the Green's function (8.5), and α_s and ω_s are the respective complex wavenumber and frequency, which are obtained from the numerical simulation results. Hence, we have

$$G(r,t) = \sqrt{\frac{1}{4\pi\gamma t}}\exp\left(\mu_0 t - \frac{\gamma_r(r-Ut)^2}{4|\gamma|^2 t} + \frac{i\gamma_i(r-Ut)^2}{4|\gamma|^2 t} + i\alpha_s r - i\omega_s t\right), \tag{8.7}$$

which can be rearranged, for convenience, as

$$\begin{aligned} G(r,t) &= \sqrt{\frac{1}{4\pi\gamma t}}\exp\left(\bar{\mu}_0 t - \frac{\gamma_r r^2}{4|\gamma|^2 t} + \frac{i\gamma_i r^2}{4|\gamma|^2 t} + i\hat{\alpha}_s r\right) \\ &= G_*\exp(i\hat{\alpha}_s r). \end{aligned} \tag{8.8}$$

Here $\bar{\mu}_0 = \mu_0 - i\omega_s - U^2/(4\gamma)$ and $\hat{\alpha}_s = \alpha_s - iU/(2\gamma)$, while the modified Green's function G_* satisfies the modified Ginzburg-Landau equation

$$\frac{\partial G_*}{\partial t} = \bar{\mu}(r)G_* + \frac{\gamma\partial^2 G_*}{\partial r^2} + \delta(r)\delta(t). \tag{8.9}$$

The convection velocity U has been removed from the Green's solution, by the introduction of the wavenumber $\hat{\alpha}_s$. As we are trying to model the rotating-disk simulation results, using the Ginzburg-Landau equation, we assume for convenience that $\hat{\alpha}_s$ corresponds to the radial wavenumber of the rotating-disk simulations. The radial wavenumber is calculated using equation (4.40) and the interested reader is referred to section 4.3 for further details.

Likewise we assume (in order to match the Green's solutions to the simulation data) that

$$\bar{\mu}_0 = -i\omega_s, \tag{8.10}$$

which implies that

1. $\bar{\mu}_{0,r} = \omega_{s,i}$, the temporal growth rate from the simulation results, and
2. $\bar{\mu}_{0,i} = -\omega_{s,r}$, which is the corresponding temporal frequency.

Definitions for the locally defined frequency and growth rate can be obtained by applying the complex-valued expression

$$\omega_l = \frac{i}{G}\frac{\partial G}{\partial t}, \tag{8.11}$$

where G is the Green's function (8.8) at all radial positions and points in time. If the complex quantity ω_l, does not vary too rapidly in either the radial direction or time, its real and imaginary parts may be interpreted as being, the local temporal frequency and local temporal growth rate, respectively. Here we have assumed that there is only one significant mode of disturbance, at all specified radial locations and points in time. If there were several different discrete modes, which were superimposed, it would not be possible to identify the temporal frequency and growth rate, from the real and imaginary parts of complex ω_l.

The local frequency and local growth rate for the Green's function (8.8) are given as

$$\begin{aligned} \omega_{l,r} &= -\bar{\mu}_{0,i} + \frac{\gamma_i r^2}{4|\gamma|^2 t^2} \\ &\longrightarrow -\bar{\mu}_{0,i} \text{ as } t \to \infty, \end{aligned} \tag{8.12}$$

and

$$\begin{aligned} \omega_{l,i} &= \bar{\mu}_{0,r} - \frac{1}{2t} + \frac{\gamma_r r^2}{4|\gamma|^2 t^2} \\ &\longrightarrow \bar{\mu}_{0,r} \text{ as } t \to \infty. \end{aligned} \tag{8.13}$$

As time tends towards infinity, the local complex frequency ω_l will approach the complex numerical simulation frequency ω_s. The local behaviour is specified by the long term behaviour of the local growth rate $\omega_{l,i}$. If

1. $\bar{\mu}_{0,r} < 0$, the disturbance is either stable or convectively unstable, and if
2. $\bar{\mu}_{0,r} > 0$, absolute instability is observed.

Similar expressions for the local wavenumber $\alpha_{l,r}$ and local streamwise growth rate $\alpha_{l,i}$ may be found, by using the complex-valued quantity

$$\alpha_l = -\frac{i}{G}\frac{\partial G}{\partial r}, \tag{8.14}$$

where G is the Green's function given in equation (8.8). The local wavenumber and streamwise growth rate for the Green's function are given by

$$\begin{aligned} \alpha_{l,r} &= \frac{\gamma_i r}{2|\gamma|^2 t} + \hat{\alpha}_{s,r} \\ &\longrightarrow \hat{\alpha}_{s,r} \text{ as } t \to \infty, \end{aligned} \tag{8.15}$$

and

$$\begin{aligned} \alpha_{l,i} &= \frac{\gamma_r r}{2|\gamma|^2 t} + \hat{\alpha}_{s,i} \\ &\longrightarrow \hat{\alpha}_{s,i} \text{ as } t \to \infty. \end{aligned} \tag{8.16}$$

As time tends to infinity, the complex wavenumber corresponding to the Green's function (8.8), asymptotes towards $\hat{\alpha}_s$ - the complex wavenumber obtained from the numerical simulation results.

The parameters $\bar{\mu}_0$ and $\hat{\alpha}_s$ are defined in terms of results given by the numerical simulations. Therefore, the only unknown parameter left to calculate, is complex γ.

On calculating the unknown γ

Firstly, we calculate the leading and trailing edges of the wavepacket, for any time t, for values of r, such that the real part of the argument of the exponential of (8.8) is zero. The real part of the exponential is given as

$$\bar{\mu}_{0,r} - \frac{\gamma_r c^2}{4|\gamma|^2} - \hat{\alpha}_{s,i} c = 0, \tag{8.17}$$

where $r = ct$. The two solutions for c, are the leading U_L, and trailing U_T, edges of the disturbance wavepacket. The edges U_L and U_T are calculated using the spatio-temporal simulation plots of the rotating-disk boundary-layer. The respective leading and trailing edges are given by the following expressions

$$U_L = c_1 = -2\frac{|\gamma|^2}{\gamma_r}\hat{\alpha}_{s,i} + \sqrt{4\frac{|\gamma|^2}{\gamma_r}\left(\frac{|\gamma|^2}{\gamma_r}\hat{\alpha}_{s,i}^2 + \bar{\mu}_{0,r}\right)}, \tag{8.18}$$

$$U_T = c_2 = -2\frac{|\gamma|^2}{\gamma_r}\hat{\alpha}_{s,i} - \sqrt{4\frac{|\gamma|^2}{\gamma_r}\left(\frac{|\gamma|^2}{\gamma_r}\hat{\alpha}_{s,i}^2 + \bar{\mu}_{0,r}\right)}. \tag{8.19}$$

Now

$$(8.18) + (8.19) = U_L + U_T = -4\frac{|\gamma|^2}{\gamma_r}\hat{\alpha}_{s,i}, \tag{8.20}$$

and similarly

$$(8.18) \times (8.19) = U_L U_T = -4\frac{|\gamma|^2}{\gamma_r}\bar{\mu}_{0,r}. \tag{8.21}$$

By rearranging equations (8.20) and (8.21) we obtain the following expressions

$$\frac{\gamma_r}{|\gamma|^2} = -\frac{4\alpha_{s,i}}{U_L + U_T} = -\frac{4\bar{\mu}_{0,r}}{U_L U_T}. \tag{8.22}$$

Since we have $\Re(\gamma) > 0$ (i.e. positive diffusion), $\gamma_r/|\gamma|^2$ will also be positive.

The final parameter required for solving the Green's function (8.8), is the complex part of γ; $\gamma_i/|\gamma|^2$. To find the expression for $\gamma_i/|\gamma|^2$, we first calculate the streamwise $r-$derivatives of equations (8.15) and (8.16), giving

$$\frac{\partial \alpha_{l,r}}{\partial r} = \frac{\gamma_i}{2|\gamma|^2 t}, \tag{8.23}$$

$$\frac{\partial \alpha_{l,i}}{\partial r} = \frac{\gamma_r}{2|\gamma|^2 t}. \tag{8.24}$$

Now (8.23) $\div$ (8.24) and rearranging, gives

$$\frac{\gamma_i}{\gamma_r} = \frac{\partial \alpha_{l,r}}{\partial r} \Big/ \frac{\partial \alpha_{l,i}}{\partial r}. \tag{8.25}$$

On substituting (8.22) into (8.25), we obtain

$$\frac{\gamma_i}{|\gamma|^2} = -\frac{4\alpha_{s,i}}{U_L + U_T}\left(\frac{\partial \alpha_{l,r}}{\partial r} \Big/ \frac{\partial \alpha_{l,i}}{\partial r}\right) = -\frac{4\bar{\mu}_{0,r}}{U_L U_T}\left(\frac{\partial \alpha_{l,r}}{\partial r} \Big/ \frac{\partial \alpha_{l,i}}{\partial r}\right). \tag{8.26}$$

For the rotating-disk boundary-layer, $\gamma_i/|\gamma|^2$ has always been found to be greater than zero. However, for rotating flows with a Rossby number $Ro > 0$, $\gamma_i/|\gamma|^2$ was found to be negative.

Example: Comparing the parallel numerical simulations and Green's function (8.8)

The example chosen - to model the parallel numerical simulation results using the Ginzburg-Landau equation - is the rotating-disk boundary-layer, where the Reynolds number $Re = 530$ and the azimuthal mode number $n = 68$. The simulation frequencies, growth rates and spatio-temporal disturbance wavepacket for this example are plotted in figures 8.1(a), 8.2(a) and 8.3(a).

The frequencies and growth rates are obtained by considering the complex-valued quantity (4.39), where A is taken to be a measure of the disturbance amplitude at all radial locations and points in time. The azimuthal vorticity $\omega_{\theta,w}$ was chosen for A. If

the complex quantity ω, does not vary too rapidly in either the radial direction or time, its real and imaginary parts may be interpreted as being, the local temporal frequency and local temporal growth rate, respectively. Here we have assumed that there is only one significant mode of disturbance, at all specified radial locations and points in time. If there were several different discrete modes, which were superimposed, it would not be possible to identify the temporal frequency and growth rate, from the real and imaginary parts of complex ω. The frequencies and growth rates are plotted for four equally spaced radial locations $r_e - 25$, $r_e = 530$, $r_e + 25$ and $r_e + 50$. The complex frequency eventually asymptotes towards $\omega \approx -16.4 + i0.2$, while figure 8.3(a) clearly displays absolute instability, since the edges of the disturbance wavepacket are moving in opposite directions.

Using the earlier expression (8.10) for $\bar{\mu}_0$, we can set,

$$\bar{\mu}_0 \approx 0.2 + i16.4, \tag{8.27}$$

while

$$\hat{\alpha}_s \approx 0.21 - i0.12. \tag{8.28}$$

The leading and trailing edges U_L, U_T can be estimated by calculating the gradients of the edges of the disturbance wavepacket, figure 8.3(a); $U_L \approx 400$ and $U_T \approx -8$. We also obtain (after some manipulation) $\gamma_i/\gamma_r \approx 1.2$.

We are now able to plot the frequencies, growth rates and spatial-temporal disturbance wavepacket for the Green's function (8.8); figures 8.1(b), 8.2(b) and 8.3(b). The frequencies, growth rates are again plotted for four equally spaced streamwise positions. Due to the symmetry, about $r = 0$, in equations (8.12) and (8.13) (for frequency and growth rate), the data lines $r_e - 25$ and $r_e + 25$ overlap. Nonetheless, the behaviour is still generally consistent with that given by the numerical simulation results. (Note: Asymmetric behaviour may be obtained if a smeared impulse distribution is used instead of the point forcing. Refer to the appendices for further

details).

The initial behaviour of the frequency/growth rate data lines is attributed to the $1/t^2$ terms appearing in equations (8.12) and (8.13). However, as time increases, this term diminishes, and the local complex frequency $\omega_l \rightarrow -16.4 + i0.2$ at all radial positions.

Further examples - where the numerical simulation results are modeled using the Ginzburg-Landau equation - can be found in section 8.3. The examples given are for the rotating-disk with mass transfer $\mathbf{a} = \pm 1$.

8.2.3 Linear variation of the stability parameter μ - (a)

It is the intention of the current and subsequent sections to model the non-parallel numerical simulation data by the Ginzburg-Landau equation, with a linearly varying stability parameter; $\mu(r) = \mu_0 + \mu_1 r$. We will show that it is essential that both μ and γ should be complex, if we are to obtain stability characteristics consistent with that displayed by the earlier numerical simulations results; refer to chapters 4, 5 and 6.

The present study considers four possible scenarios and the type of disturbance that prevails. The first scenario that we discuss is the problem investigated by Hunt & Crighton (1991), i.e. μ_1 and γ are real only.

Using the series solution method, Hunt & Crighton calculated the exact analytic solution to the Green's function to be

$$G_0(r,t) = \sqrt{\frac{1}{4\pi\gamma t}}\exp\left(\mu_0 t - \frac{(r-Ut)^2}{4\gamma t} + \frac{1}{2}\epsilon\mu_1 rt + \frac{1}{12}\epsilon^2\mu_1^2\gamma t^3\right), \tag{8.29}$$

where all parameters are as stated previously. (Here ϵ again incorporates slow streamwise variation effects and we assume $\epsilon = 1$ for simplicity). For γ and μ_1 real, the stability behaviour can be investigated using the same kind of approach that was adopted for the situation where μ was a real constant. By considering the argument

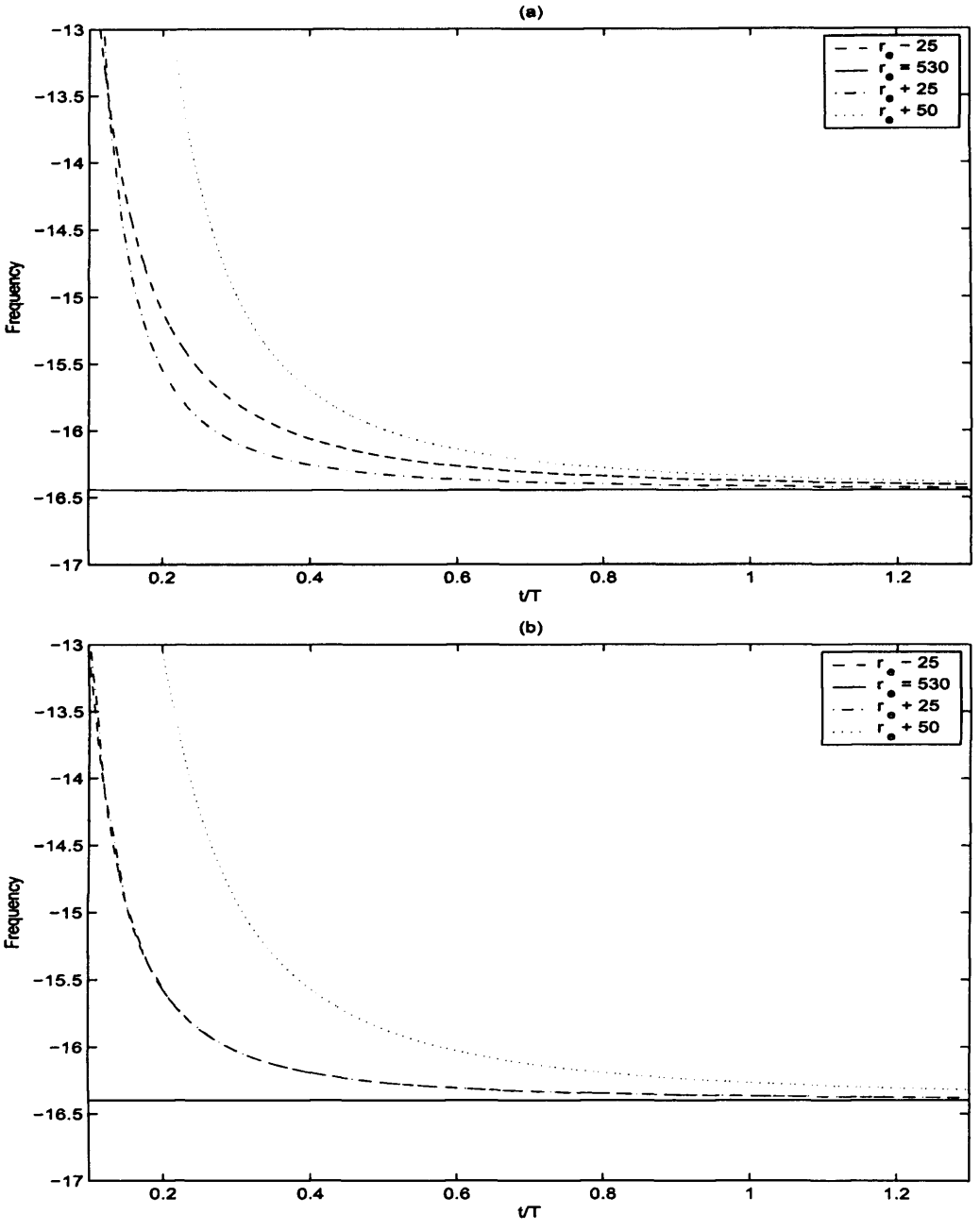

Figure 8.1: *The temporal frequencies for: (a) the parallel numerical simulation results for the rotating-disk boundary-layer, where Re = 530 and n = 68; (b) the Green's function, where the stability parameter $\mu = \mu_0$ is a constant. The frequencies are plotted for four equally spaced points. (Note: $T = 2\pi Re$).*

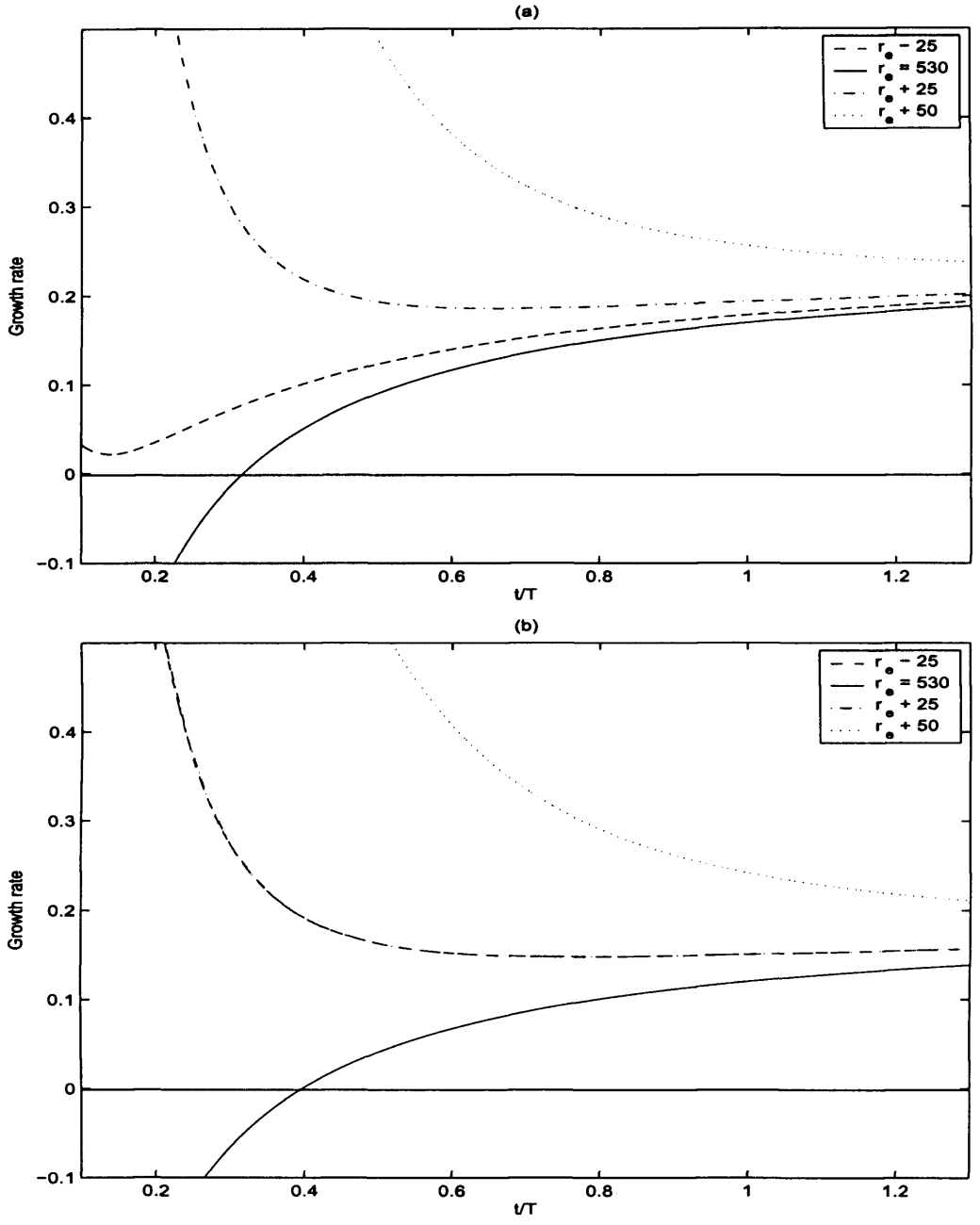

Figure 8.2: *The temporal growth rates for: (a) the parallel numerical simulation results for the rotating-disk boundary-layer, where Re = 530 and n = 68; (b) the Green's function, where the stability parameter $\mu = \mu_0$ is a constant. The growth rates are plotted for four equally spaced points. (Note: $T = 2\pi Re$).*

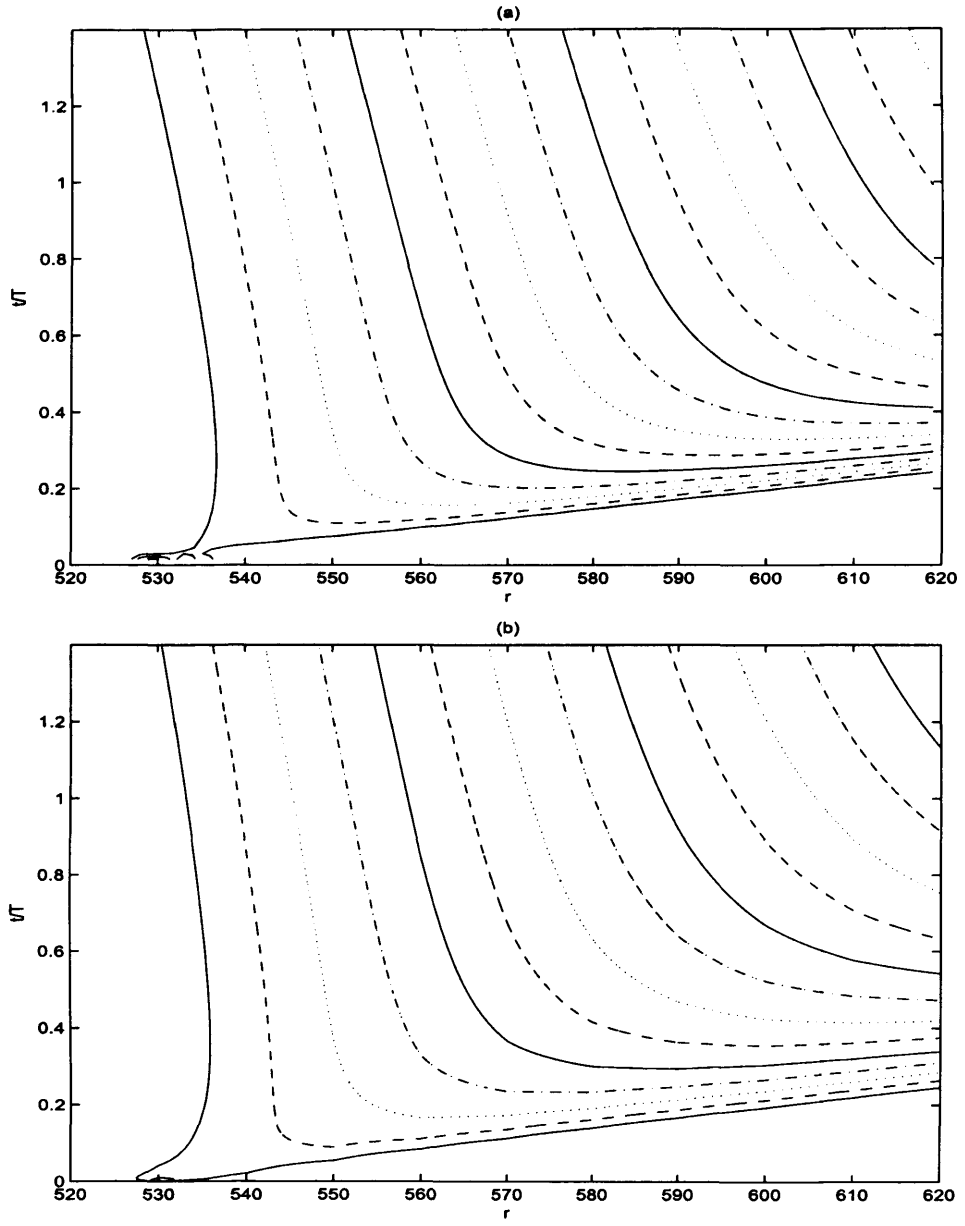

Figure 8.3: *The disturbance development wavepackets for: (a) the parallel numerical simulation results for the rotating-disk boundary-layer, where Re = 530 and n = 68; (b) and the Green's function, where the stability parameter $\mu = \mu_0$ is a constant. (Contours are drawn using a logarithmic scale, with levels separated by factors of two).*

of the exponential in the exact solution (8.29), the edges of the wavepacket occur along $r \sim (1 \pm \frac{2}{\sqrt{3}})\epsilon\mu_1\gamma t^2$ as $t \longrightarrow \infty$, (as found by Hunt & Crighton, 1991). Therefore, one edge will eventually move towards $+\infty$ and the other towards $-\infty$. Thus, any fixed r will eventually display exponential growth. Hence, for any real linear variation of the stability parameter μ, the flow will exhibit global instability. Figure 5 of Hunt & Crighton (1991) illustrates two basic possibilities for the Green's function response; initially the wavepacket is either propagating towards the region of local absolute instability (where $\mu_0 + \mu_1 r > U^2/4\gamma$) or away from it. Inevitably as time increases the leading and trailing edges of the wavepacket diverge in opposite directions towards infinity.

This scenario will not re-produce the behaviour found in the non-parallel simulation results, since the rotating-disk boundary-layer has been shown by Davies & Carpenter (2003) to exhibit decreasing growth rates and convective behaviour.

8.2.4 Linear variation of the stability parameter μ - (b)

The second scenario considered is where the stability parameter μ_1 remains real, but the diffusion/dispersion parameter γ is complex. In keeping with the earlier approach, we now consider the full disturbance Green's function (8.6), where G_0 is now specified by equation (8.29) and α_s and ω_s are as before. Therefore, the Green's function is now given by

$$G(r,t) = \sqrt{\frac{1}{4\pi\gamma t}}\exp\left(\mu_0 t - \frac{(r-Ut)^2}{4\gamma t} + \frac{1}{2}\mu_1 r t + \frac{1}{12}\mu_1^2\gamma t^3 + i\alpha_s r - i\omega_s t\right), \quad (8.30)$$

which can be rearranged (for convenience) as

$$\begin{aligned} G(r,t) &= \sqrt{\frac{1}{4\pi\gamma t}}\exp\left(\bar{\mu}_0 t - \frac{\gamma_r r^2}{4|\gamma|^2 t} + \frac{i\gamma_i r^2}{4|\gamma|^2 t} + \frac{1}{2}\mu_1 r t + \frac{1}{12}\mu_1^2\gamma t^3 + i\hat{\alpha}_s x\right) \\ &= G_* \exp(i\hat{\alpha}_s r), \end{aligned} \quad (8.31)$$

where $\bar{\mu}_0$ and γ are again given as (8.10), (8.22), (8.25) and (8.26) and $\hat{\alpha}_s = \alpha_s - iU/2\gamma$. The function G_* satisfies the modified Ginzburg-Landau equation (8.9). The

convection velocity U has again been removed by re-defining the complex wavenumber $\hat{\alpha}_s$. The local frequency and growth rate for the Green's function (8.31), are calculated by applying the complex-valued expression (8.11). The local frequency and growth rate are given as

$$\omega_{l,r} = -\bar{\mu}_{0,i} + \frac{\gamma_i r^2}{4|\gamma|t^2} - \gamma_i \mu_1^2 \frac{t^2}{4}, \tag{8.32}$$

and

$$\omega_{l,i} = \bar{\mu}_{0,i} - \frac{1}{2t} + \frac{\gamma_r r^2}{4|\gamma|t^2} + \frac{\mu_1 r}{2} + \gamma_r \mu_1^2 \frac{t^2}{4}, \tag{8.33}$$

where all coefficients are as before.

The local frequency (8.32) will depend on the term $-\gamma_i \mu_1^2 t^2/4$ for large time. If the term is positive the frequencies will increase with time (in a manner consistent with the rotating-disk boundary-layer), and if the term is negative, frequencies will decrease with time (similar to the rotating flows with a positive Rossby number). It is the sign of γ_i which will ultimately decide the long term behaviour of the frequencies. For the rotating-disk, γ_i has always been found to be greater than zero. Hence, the frequencies (8.32) will decrease for large time. Therefore, the local frequencies for the Green's function do not match those given by the numerical simulation results for the rotating-disk boundary-layer, where all frequencies show a tendency to increase with time; refer to chapters 4, 5, 6 or Davies & Carpenter (2003).

The local growth rate (8.33) depends on the term $\gamma_r \mu_1^2 t^2/4$ for large time. The term γ_r is always found to be positive, when modeling the rotating-disk simulation data. Therefore, the local growth rate will increase with time and globally unstable behaviour will eventually be displayed. Therefore, if μ_1 is taken to be real, the stability characteristics for the Green's function (8.31) are not consistent with the non-parallel rotating-disk boundary-layer or mean flows with injection, where all growth rates have shown a tendency to decrease with time; refer to chapter 4.

8.2.5 Linear variation of the stability parameter μ - (c)

We now consider μ_1 to be complex, but γ is now real; we ignore dispersion effects. We again consider the full disturbance structure (8.6), where G_0 is equation (8.29). On rearranging, the Green's function is again of the form (8.31), where $\gamma_i = 0$. Using the complex-valued expression (8.11), the local frequency and growth rate are now given as

$$\omega_{l,r} = -\bar{\mu}_{0,i} - \frac{1}{2}\mu_{1,i}r - 2\gamma_r\mu_{1,r}\mu_{1,i}\frac{t^2}{4}, \tag{8.34}$$

and

$$\omega_{l,i} = \bar{\mu}_{0,r} - \frac{1}{2t} + \frac{\gamma_r r^2}{4|\gamma|^2 t^2} + \frac{\mu_{1,r}r}{2} + \gamma_r(\mu_{1,r}^2 - \mu_{1,i}^2)\frac{t^2}{4}. \tag{8.35}$$

Hence, the long term characteristics of the disturbance are entirely dependent on the relation between the real and complex parts of the stability coefficient μ_1.

Before we continue to analyze the long-term behaviour of the frequencies and growth rates, it is important to describe how the unknown complex variable μ_1 can be expressed in terms of the numerical simulation data. This is important since we are attempting to model the non-parallel rotating-disk results using the Ginzburg-Landau equation. The two coefficients can be found by taking streamwise $r-$derivatives of equations (8.34) and (8.35) and rearranging. Thus, giving

$$\mu_{1,r} = 2\frac{d\omega_{l,i}}{dr}, \tag{8.36}$$

$$\mu_{1,i} = -2\frac{d\omega_{l,r}}{dr}, \tag{8.37}$$

where $\frac{d\omega_{l,r}}{dr}$ and $\frac{d\omega_{l,i}}{dr}$ are the variations in the frequency and growth rate, which are obtained from the numerical simulation results. (Note: $\frac{d\omega_{l,r}}{dr}$ and $\frac{d\omega_{l,i}}{dr}$ have (so far) always been found to be positive for the rotating-disk boundary-layer. Also, $|\frac{d\omega_{l,r}}{dr}| > |\frac{d\omega_{l,i}}{dr}|$ has always (so far) been found to be true).

From the expression (8.34), if $\mu_{1,r} \times \mu_{1,i}$ is found to be positive, the local frequencies will decrease at all locations for large time. On the other hand, if $\mu_{1,r} \times \mu_{1,i}$ is

negative, the local frequencies will increase at all locations for large time. Bearing in mind the expressions (8.36) and (8.37), the coefficients $\mu_{1,r}$ and $\mu_{1,i}$ will be positive and negative, respectively. Therefore, the frequency will increase as time tends to infinity, and as a result will exhibit features that are consistent with the rotating-disk boundary-layer.

The local growth rate (8.35), is dependent on the sign of $\mu_{1,r}^2 - \mu_{1,i}^2$, as time tends to infinity. If $|\mu_{1,r}| > |\mu_{1,i}|$ the disturbance will exhibit temporal growth and global instability, and if $|\mu_{1,r}| < |\mu_{1,i}|$ the disturbance will display a decreasing growth rate, and globally stable behaviour will prevail. For this second case, there may be local regions of convective instability or absolute instability. It is this second case that is similar to the simulation plots for the rotating-disk boundary-layer (and injection flows), where the growth rates are found to decrease with increasing time, Davies & Carpenter (2003).

By making use of equations (8.36) and (8.37), we obtain $\mu_{1,r}^2 - \mu_{1,i}^2 = 4(\frac{d\omega_{l,i}}{dr}^2 - \frac{d\omega_{l,r}}{dr}^2)$. As stated previously, $|\frac{d\omega_{l,r}}{dx}| > |\frac{d\omega_{l,i}}{dx}|$, is always found to be true for the numerical simulation results, even those rotating-disk flows with uniform suction. Hence, the growth rate (8.35) (corresponding to the Green's function (8.31)) will always display a decreasing growth rate.

Therefore, it is feasible that the solutions to the Ginzburg-Landau equation, with a linearly varying, complex stability parameter μ and real diffusion term γ, can be used to successfully model the rotating-disk boundary-layer (with/without mass injection) simulation results. The solutions show that depending on the precise balance between the varying growth rates and corresponding shifts in frequency, it is possible for an absolutely unstable disturbance to remain globally stable.

Similar behaviour has been observed in the field of astrophysical fluids, Soward (1977, 1992) and Harris, Bassom & Soward (2000). By considering a problem where there is marginal absolute instability, at all spatial locations, sufficiently large local

variations in frequency, can have stabilizing effects. This phenomenon is known in the astrophysical fluids community as phase-mixing. In Harris *et al.* (2000), a non-linear equation is derived which governs the amplitude modulation of Taylor vortices, between two rotating spheres. Vortices off the equator are observed to oscillate and phase-mixing is introduced. For problems without phase-mixing, the amplitudes of the vortices grow, indefinitely. While for problems with phase-mixing, the vortex amplitudes are bounded.

Although the above behaviour is acceptable for modeling the rotating-disk mean flow and those mean flows with uniform injection, it is not consistent with the characteristics shown by the flows with uniform suction, where increasing growth rates and globally unstable behaviour was observed. This suggests that it is not sufficient to consider γ real and μ complex, if we are to successfully model all rotating boundary-layers by the Ginzburg-Landau equation.

8.2.6 Linear variation of the stability parameter μ - (d)

When the diffusion term γ and linear stability parameter μ are both considered to be complex, the behaviour can differ profoundly from the above scenarios; as we will see shortly. Using the complex-valued expression (8.11), the local frequency and growth rate are given as

$$\omega_{l,r} = -\bar{\mu}_{0,i} + \frac{\gamma_i r^2}{4|\gamma|^2 t^2} - \frac{\mu_{1,i} r}{2} - \left(2\gamma_r \mu_{1,r}\mu_{1,i} + \gamma_i(\mu_{1,r}^2 - \mu_{1,i}^2)\right)\frac{t^2}{4}, \tag{8.38}$$

and

$$\omega_{l,i} = \bar{\mu}_{0,r} - \frac{1}{2t} + \frac{\gamma_r r^2}{4|\gamma|^2 t^2} + \frac{\mu_{1,r} r}{2} + \left(\gamma_r(\mu_{1,r}^2 - \mu_{1,i}^2) - 2\gamma_i \mu_{1,r}\mu_{1,i}\right)\frac{t^2}{4}, \tag{8.39}$$

where $\mu_{1,r}$ and $\mu_{1,i}$ are again the respective real and imaginary parts of the linear stability coefficient μ_1.

The complex coefficient μ_1 may be calculated by the same method applied in section 8.2.5. The two coefficients can be found by taking streamwise $r-$derivatives

of equations (8.38) and (8.39) and rearranging. The resulting expressions for $\mu_{1,r}$ and $\mu_{1,i}$ are the same as before, i.e. equations (8.36) and (8.37).

As time increases, the local frequency is governed by the t^2 term. Whether the frequency increases or decreases, is entirely dependent on the sign of the quantity $B = 2\gamma_r\mu_{1,r}\mu_{1,i} + \gamma_i(\mu_{1,r}^2 - \mu_{1,i}^2)$. If $B > 0$ the frequency decreases and if $B < 0$ the frequency increases. For small time t, the $1/t^2$ term will dominate, which is consistent with the behaviour that is seen in the early stages of the plots given in figure 8.4. However, as time increases this term will diminish indefinitely and eventually the quantity B will dominate the frequency.

Turning now to the growth rates, it may be observed that initially equation (8.39) depends on a $1/t^2$ term, which can be observed in figure 8.5. However, for larger times, the sign of the quantity $C = \gamma_r(\mu_{1,r}^2 - \mu_{1,i}^2) - 2\gamma_i\mu_{1,r}\mu_{1,i}$ will govern the behaviour of the disturbance. If $C > 0$ the disturbance exhibits temporal growth and global instability, otherwise the disturbance exhibits global stability with at most a local region of convective or absolute instability.

The long-term nature of the frequency and growth rate

We are now going to derive conditions for the behaviour of the complex frequencies. If we are to match the Green's solution frequencies to the non-parallel numerical simulation results, where increasing frequencies were observed, it is essential that $B < 0$. Therefore,

$$\begin{aligned} B = 2\gamma_r\mu_{1,r}\mu_{1,i} + \gamma_i(\mu_{1,r}^2 - \mu_{1,i}^2) &< 0, \\ \Rightarrow \left(\lambda + \frac{1}{\Gamma}\right)^2 - \left(1 + \frac{1}{\Gamma^2}\right) &< 0, \end{aligned} \tag{8.40}$$

where $\Gamma = \gamma_i/\gamma_r$ and $\lambda = \mu_{1,r}/\mu_{1,i}$. Hence, we are left with an equality relating the real and complex parts of the stability coefficient μ_1, and the real and complex parts of γ.

There are two possible solutions to (8.40), either

1. $\lambda < -\frac{1}{\Gamma} + \sqrt{1 + \frac{1}{\Gamma^2}}$, or
2. $\lambda > -\frac{1}{\Gamma} - \sqrt{1 + \frac{1}{\Gamma^2}}$.

Thus, if the local frequencies are going to increase with increasing time, it is essential that the parameter λ, lies within the region

$$-\frac{1}{\Gamma} - \sqrt{1 + \frac{1}{\Gamma^2}} < \lambda < -\frac{1}{\Gamma} + \sqrt{1 + \frac{1}{\Gamma^2}}. \tag{8.41}$$

If this does not arise, the local frequencies will decrease.

By a similar approach we can obtain an inequality, which determines whether a system is globally stable or unstable. If we consider the case of temporal growth and global instability, we obtain

$$\begin{aligned} C = \gamma_r(\mu_{1,r}^2 - \mu_{1,i}^2) - 2\gamma_i\mu_{1,r}\mu_{1,i} &> 0, \\ \Rightarrow (\lambda - \Gamma)^2 - (1 + \Gamma^2) &> 0. \end{aligned} \tag{8.42}$$

There are two possible solutions to (8.42) for global instability, either

1. $\lambda < \Gamma - \sqrt{1 + \Gamma^2}$, or
2. $\lambda > \Gamma + \sqrt{1 + \Gamma^2}$.

Hence, if globally stable behaviour is to prevail, λ must satisfy the following inequality

$$\Gamma + \sqrt{1 + \Gamma^2} > \lambda > \Gamma - \sqrt{1 + \Gamma^2}. \tag{8.43}$$

If λ does not satisfy (8.43), the local growth rates will increase at all streamwise locations and globally unstable behaviour will eventually be displayed. Therefore, the global response of a system is determined by the ratio of the varying frequency and varying growth rate, and the ratio of the diffusion/dispersion effects.

If γ is real only, equation (8.43) becomes

$$1 > \lambda > -1, \tag{8.44}$$

or

$$\left|\frac{\mu_{1,r}}{\mu_{1,i}}\right| < 1, \tag{8.45}$$

which on substituting for $\mu_{1,r}$ and $\mu_{1,i}$ (equations (8.36) and (8.37)) gives a similar expression to that given in chapter 7; equation (7.28), which relates the varying frequency and the varying growth rate.

Example: Comparing the non-parallel numerical simulations and the Green's function (8.29)

The example considered - that matches the Green's function to the non-parallel simulation results for the rotating-disk - is that where the point of forcing $r_e = 530$ and azimuthal mode number $n = 68$. The simulation frequencies, growth rates and spatial-temporal disturbance wavepacket for this problem are plotted in figures 8.4(a), 8.5(a) and 8.6(a). The frequencies/growth rates are again plotted for four equally spaced radial locations.

We assume for convenience that

$$\bar{\mu}_0 \approx 0.2 + i16.4, \tag{8.46}$$

while

$$\hat{\alpha}_s \approx 0.21 - i0.12, \tag{8.47}$$

where γ is again defined by equations (8.22), (8.25) and (8.26), where $U_L \approx 400$, $U_T \approx -8$ and $\gamma_i/\gamma_r \approx 1.2$. The variations $\frac{d\omega_{l,r}}{dr}$ and $\frac{d\omega_{l,i}}{dr}$ are approximately given as 0.012 and 0.003, respectively.

We are now able to plot the frequencies, growth rates and disturbance wavepacket for the Green's function (8.29); figures 8.4(b), 8.5(b) and 8.6(b). The frequencies

and growth rates are consistent with the results of the numerical simulations; they increase and decrease, respectively. The spatial-temporal disturbance wavepackets are also similar, since (in both cases) the trailing edge initially propagates inwards, but as time increases, it reverses direction and propagates outwards.

Further examples comparing the simulation results with the Green's solutions, can be found in the subsequent section.

8.3 Further comparisons between the numerical simulations and Green's function solutions

Two more examples are discussed, where the numerical simulation results of the rotating-disk boundary-layer, have been matched to the Green's solutions of the Ginzburg-Landau equation. The problems considered are for the rotating-disk with mass transfer $\mathbf{a} = \pm 1$; **a** is negative for injection and positive for suction.

8.3.1 Example: a = -1, $Re = 252$, $n = 29$

μ - Constant

Figures 8.7(a), 8.8(a) and 8.9(a) display the parallel frequencies, growth rates and disturbance wavepacket for the simulation results for the rotating-disk boundary-layer with mass injection **a** = -1, where the Reynolds number $Re = 252$ and azimuthal mode number $n = 29$. The complex frequency $\omega_s \approx -5.5 + i0.5$ and the complex wavenumber $\hat{\alpha}_s \approx 0.18 - i0.11$. The wavepacket edges are estimated as $U_L = 250$ and $U_T = -20$, while $\gamma_i/\gamma_r \approx 0.8$.

Using the above data, the frequencies, growth rates and disturbance wavepacket for the Green's function (8.8) can be plotted; figures 8.7(b), 8.8(b) and 8.9(b). The data lines $r_e - 25$ and $r_e + 25$ again lie on top of each other, due to the symmetry about $r = 0$; equations (8.12) and (8.13). The Green's solution plots are consistent

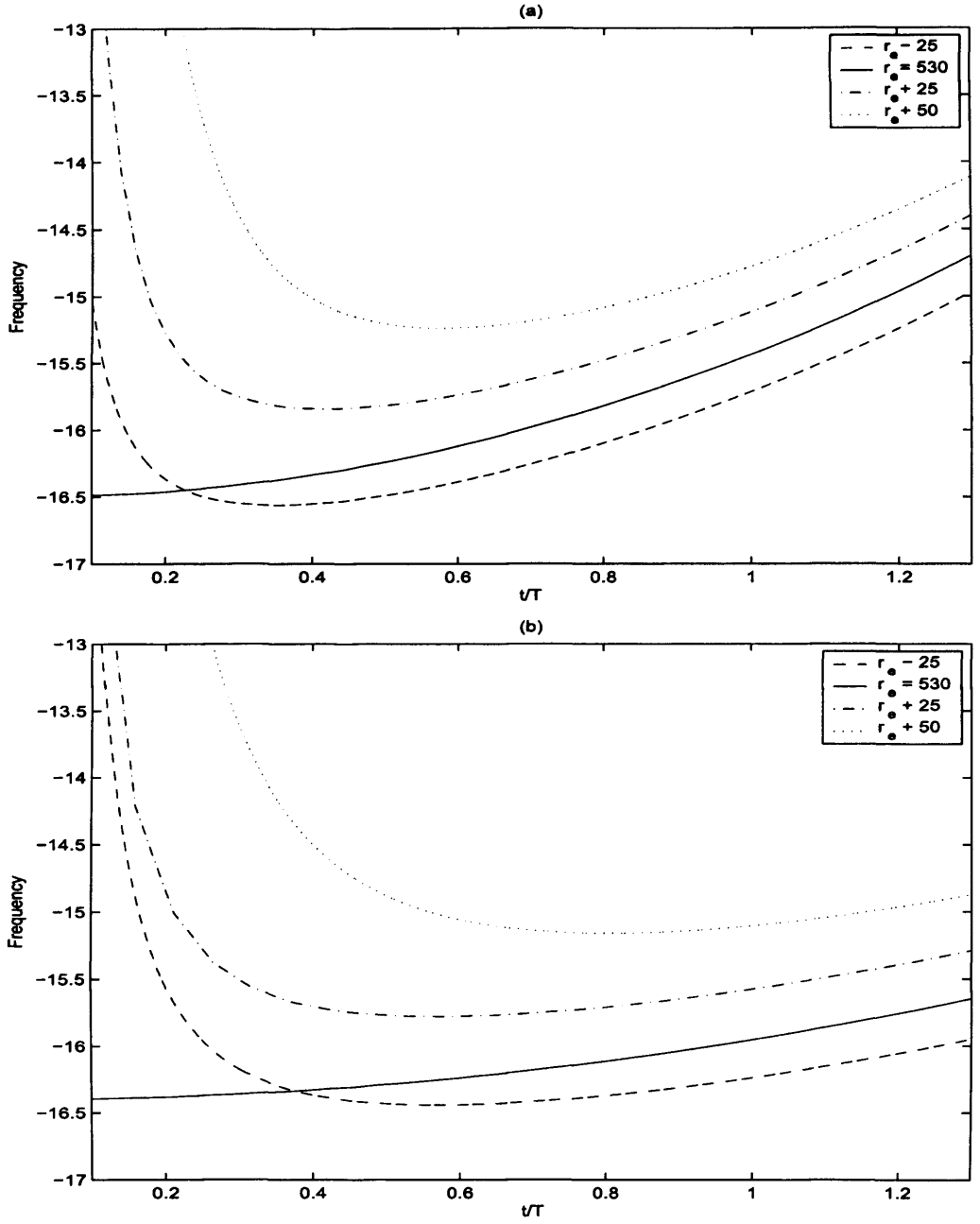

Figure 8.4: *The temporal frequencies for: (a) the non-parallel numerical simulation results for the rotating-disk boundary-layer, where $r_e = 530$ and $n = 68$; (b) the Green's function, where the stability parameter $\mu = \mu_0 + \mu_1 r$. The frequencies are plotted for four equally spaced points. (Note: $T = 2\pi r_a$ where r_a is the inner radius).*

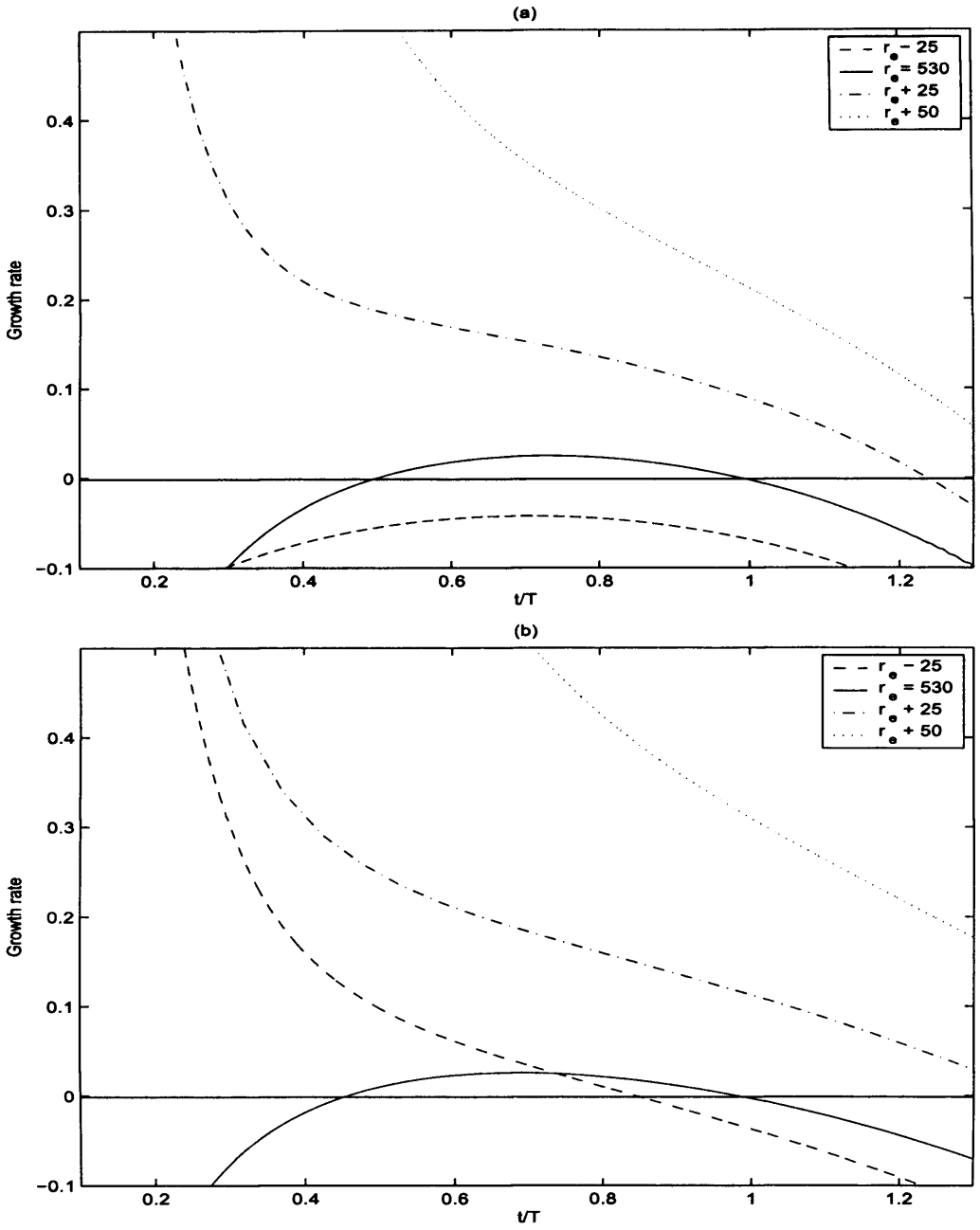

Figure 8.5: *The temporal growth rates for: (a) the non-parallel numerical simulation results for the rotating-disk boundary-layer, where r_e = 530 and n = 68; (b) the Green's function, where the stability parameter $\mu = \mu_0 + \mu_1 r$. The growth rates are plotted for four equally spaced points. (Note: $T = 2\pi r_a$ where r_a is the inner radius).*

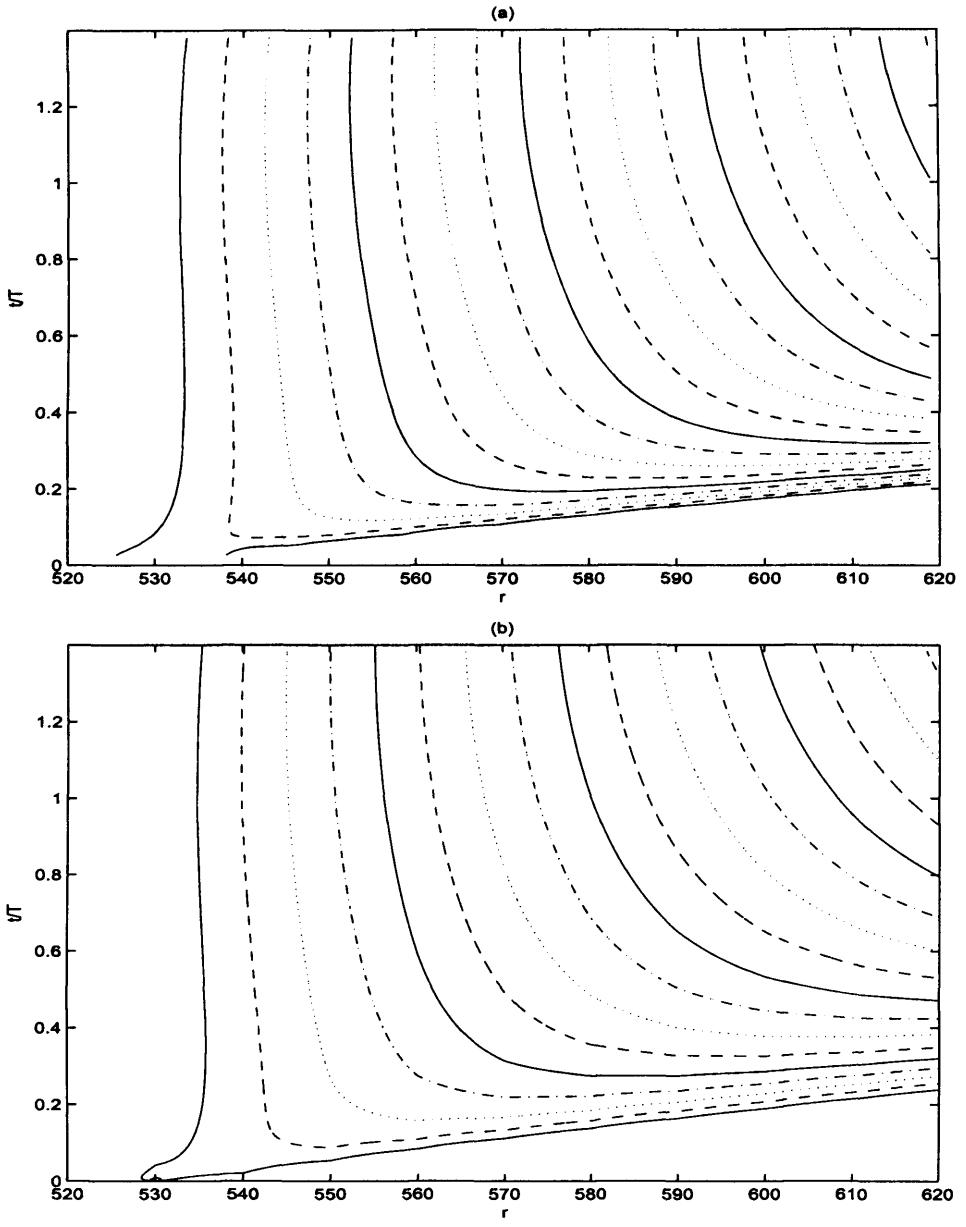

Figure 8.6: *The disturbance development wavepackets for: (a) the non-parallel numerical simulation results for the rotating-disk boundary-layer, where $r_e = 530$ and $n = 68$; (b) and the Green's function, where the stability parameter $\mu = \mu_0 + \mu_1 r$. (Contours are drawn using a logarithmic scale, with levels separated by factors of two).*

with the simulations, since $\omega_l \rightarrow \omega_s$ for all radial positions, and absolute instability is displayed.

μ - Linearly Varying

Figures 8.10(a), 8.11(a) and 8.12(a) display the frequencies, growth rates and disturbance wavepackets for the non-parallel simulation results and the Green's function with a linearly varying stability parameter; equation (8.31). The parameters $\bar{\mu}_0$, $\hat{\alpha}_s$, γ are as before, while the variations $\frac{d\omega_{l,r}}{dr}$ and $\frac{d\omega_{l,i}}{dr}$ are approximately given as 0.014 and 0.0035, respectively. The frequencies increase at all locations considered, for both problems, while the growth rates decrease at all locations. The wavepackets are also similar, since the trailing edge of both wavepackets, initially propagates inwards. However, this does not persist for long, as the trailing edge can be seen to reverse direction and propagate radially outwards.

8.3.2 Example: a = 1, Re = 1911

μ - Constant

Figures 8.13(a), 8.14(a) and8.15(a) display the frequencies, growth rates and disturbance wavepackets for the parallel numerical simulation results for the rotating-disk boundary-layer with mass suction **a** = 1, where the Reynolds number $Re = 1911$ and azimuthal mode number $n = 194$. The complex frequency $\omega_s \approx -51.2 + i0.2$ and the complex wavenumber $\hat{\alpha}_s \approx 0.34 - i0.12$. The wavepacket edges are estimated as $U_L = 450$ and $U_T = -7$, while $\gamma_i/\gamma_r \approx 1.6$.

Using the above data, the frequencies, growth rates and disturbance wavepacket for the Green's function (8.8) can be plotted; figures 8.13(b), 8.14(b) and 8.15(b). The data lines $r_e - 25$ and $r_e + 25$ again lie on top of each other, due to the symmetry about $r = 0$; equations (8.12) and (8.13). The Green's solution plots are consistent with the simulations, since $\omega_l \rightarrow \omega_s$ for all radial positions, and absolute instability

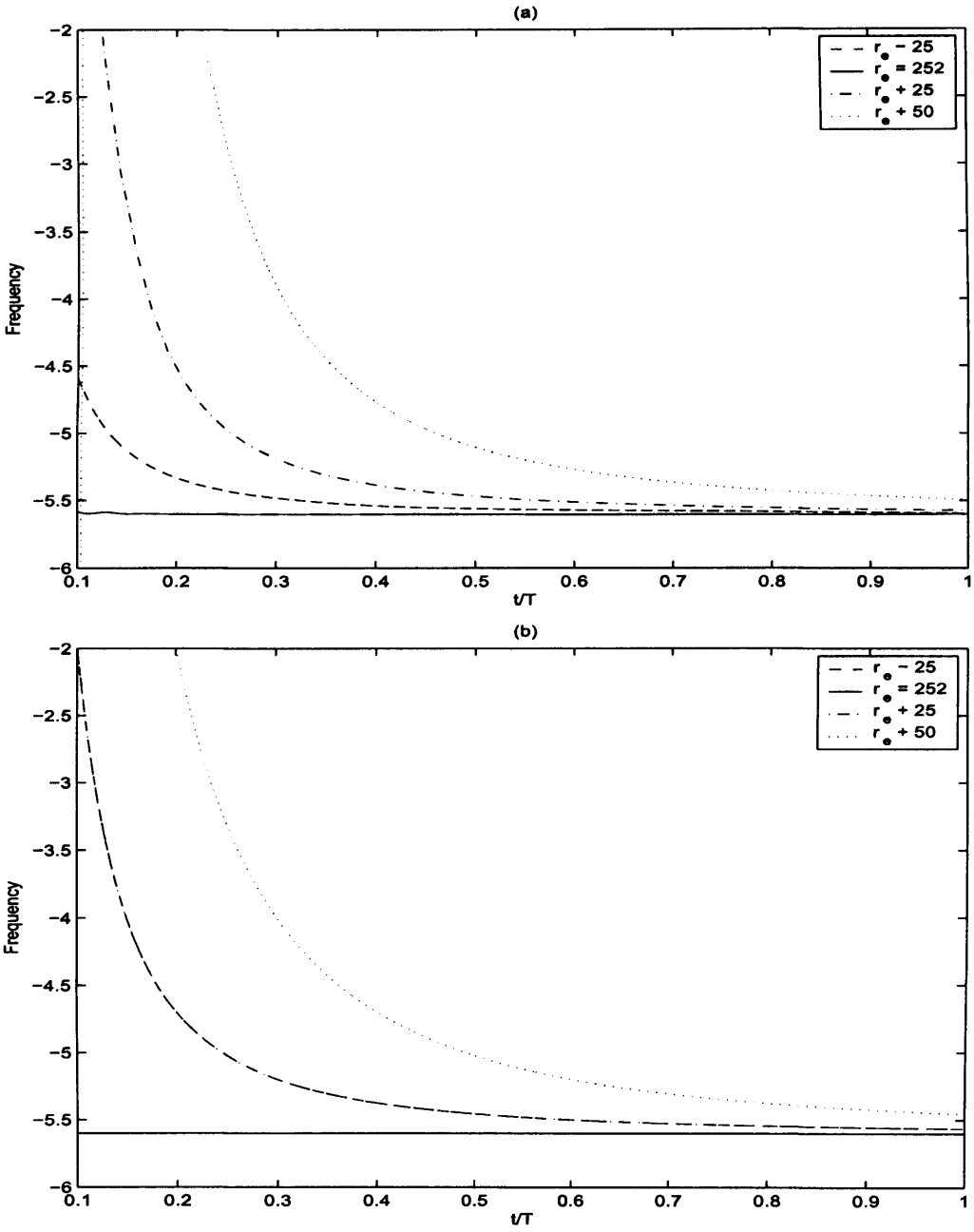

Figure 8.7: *The temporal frequencies for: (a) the parallel numerical simulation results for the rotating-disk boundary-layer with* $\boldsymbol{a}$ *= -1, where Re = 252 and n = 29; (b) the Green's function, where the stability parameter* $\mu = \mu_0$ *is a constant. The frequencies are plotted for four equally spaced points. (Note:* $T = 2\pi Re$*).*

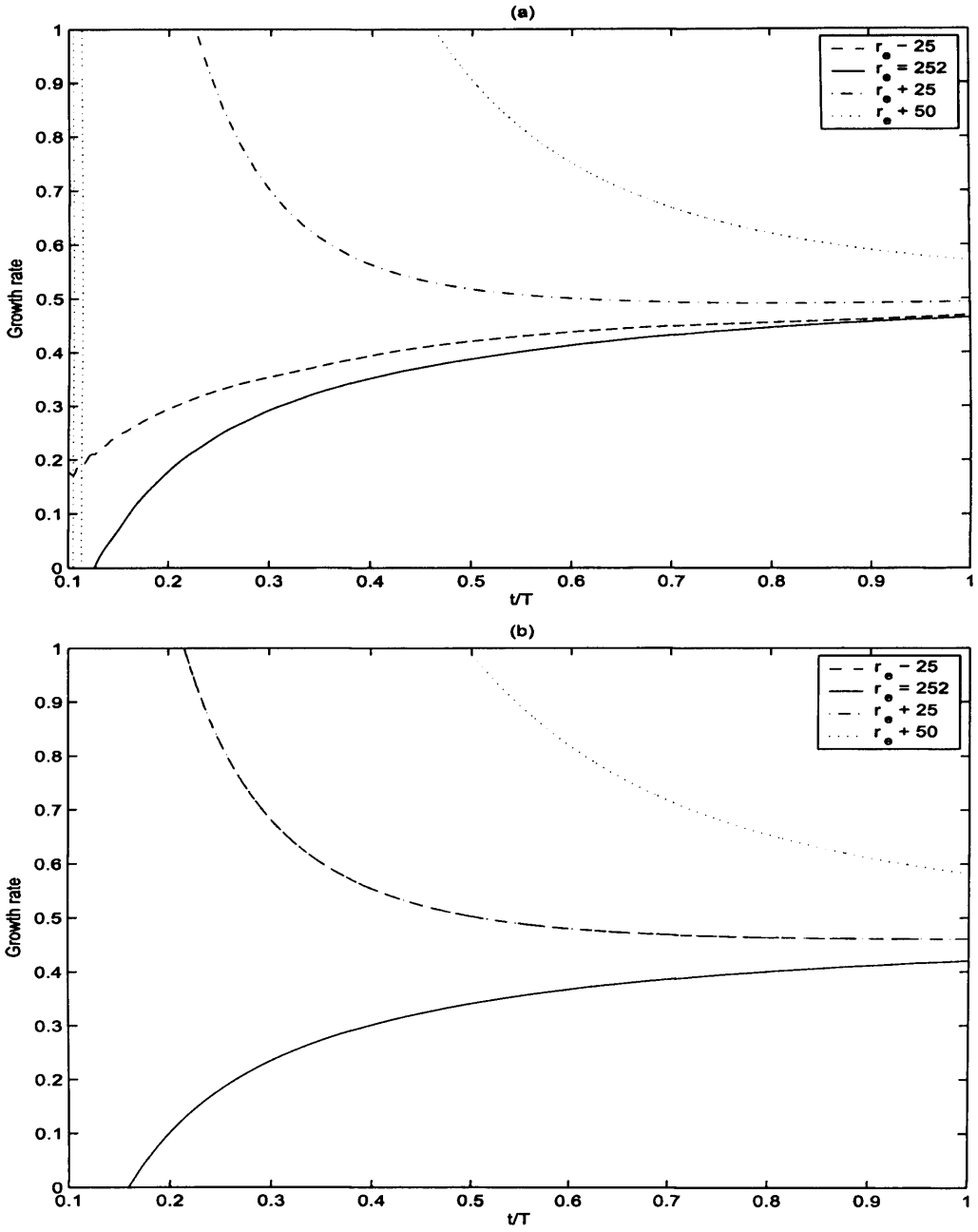

Figure 8.8: *The temporal growth rates for: (a) the parallel numerical simulation results for the rotating-disk boundary-layer with* $\boldsymbol{a}$ *= -1, where Re = 252 and n = 29; (b) the Green's function, where the stability parameter* $\mu = \mu_0$ *is a constant. The growth rates are plotted for four equally spaced points. (Note: T =*$2\pi Re$*).*

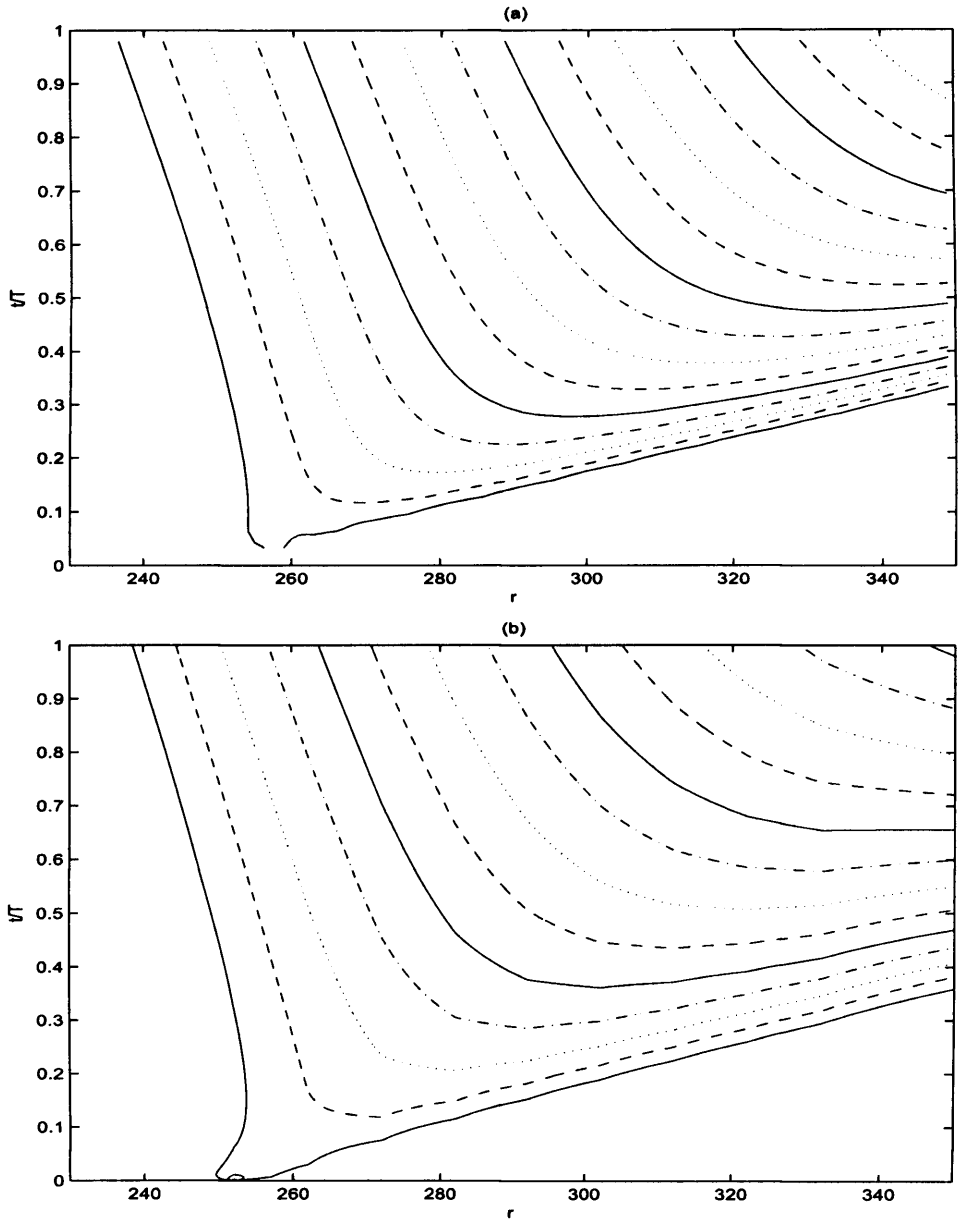

Figure 8.9: *The disturbance development wavepackets for: (a) the parallel numerical simulation results for the rotating-disk boundary-layer with* $\boldsymbol{a}$ *= -1, where Re = 252 and n = 29; (b) and the Green's function, where the stability parameter* $\mu = \mu_0$ *is a constant. (Contours are drawn using a logarithmic scale, with levels separated by factors of two).*

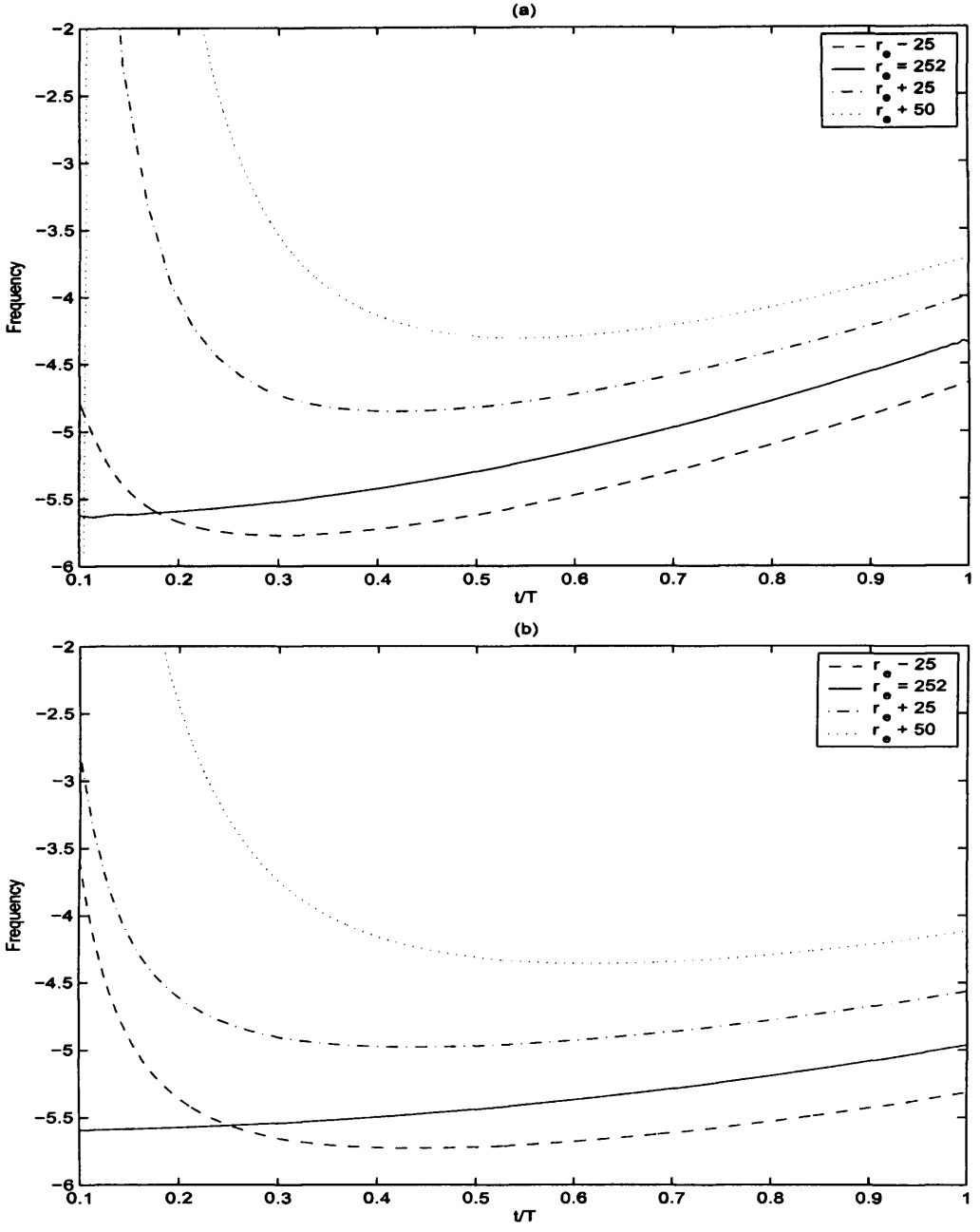

Figure 8.10: *The temporal frequencies for: (a) the non-parallel numerical simulation results for the rotating-disk boundary-layer with* $\boldsymbol{a}$ *= -1, where* r_e *= 252 and n = 29; (b) the Green's function, where the stability parameter* $\mu = \mu_0 + \mu_1 r$ *. The frequencies are plotted for four equally spaced points. (Note:* $T = 2\pi r_a$ *where* r_a *is the inner radius).*

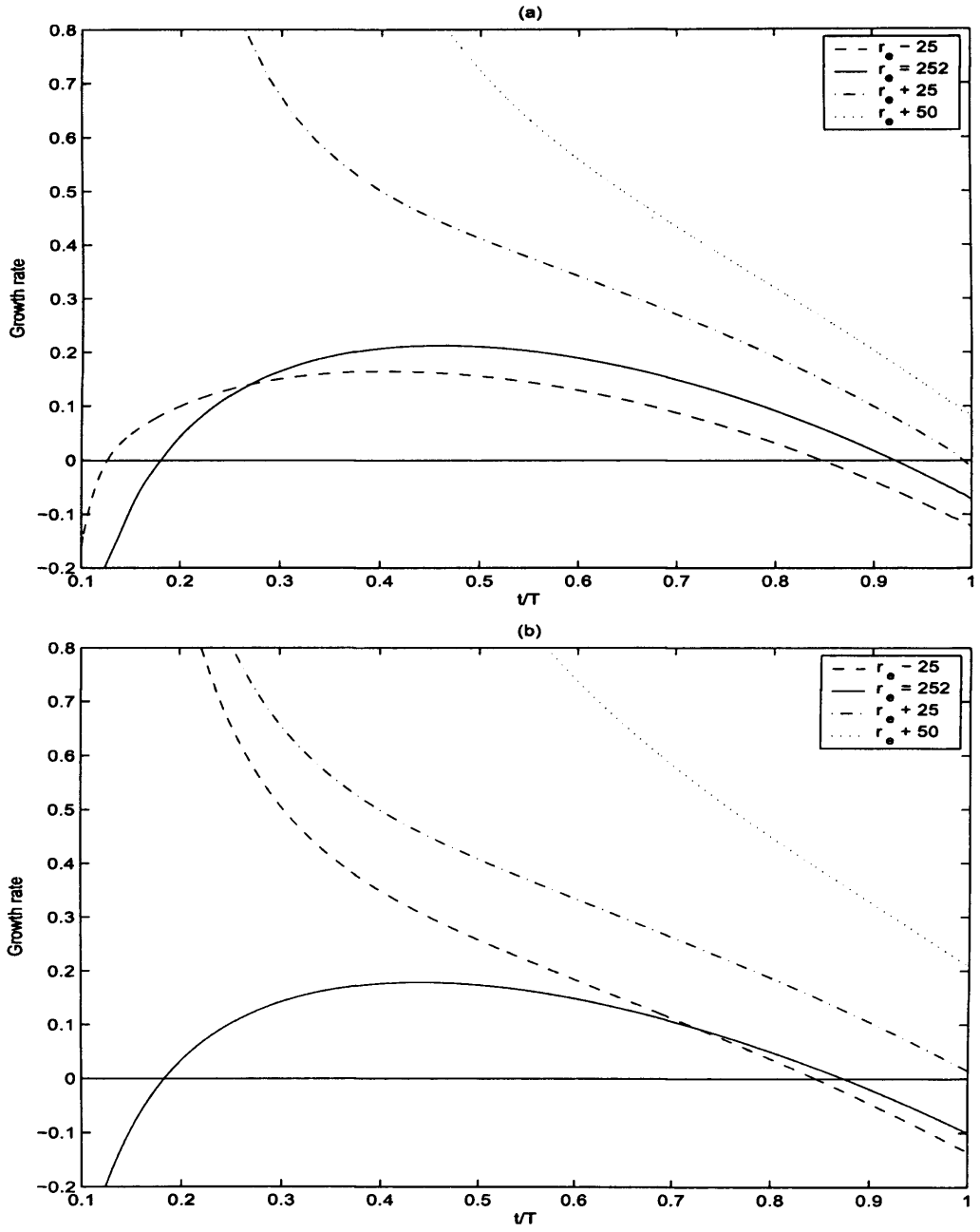

Figure 8.11: *The temporal growth rates for: (a) the non-parallel numerical simulation results for the rotating-disk boundary-layer with* $\boldsymbol{a}$ *= -1, where* r_e *= 252 and n = 29; (b) the Green's function, where the stability parameter* $\mu = \mu_0 + \mu_1 r$ *. The growth rates are plotted for four equally spaced points. (Note:* $T = 2\pi r_a$ *where* r_a *is the inner radius).*

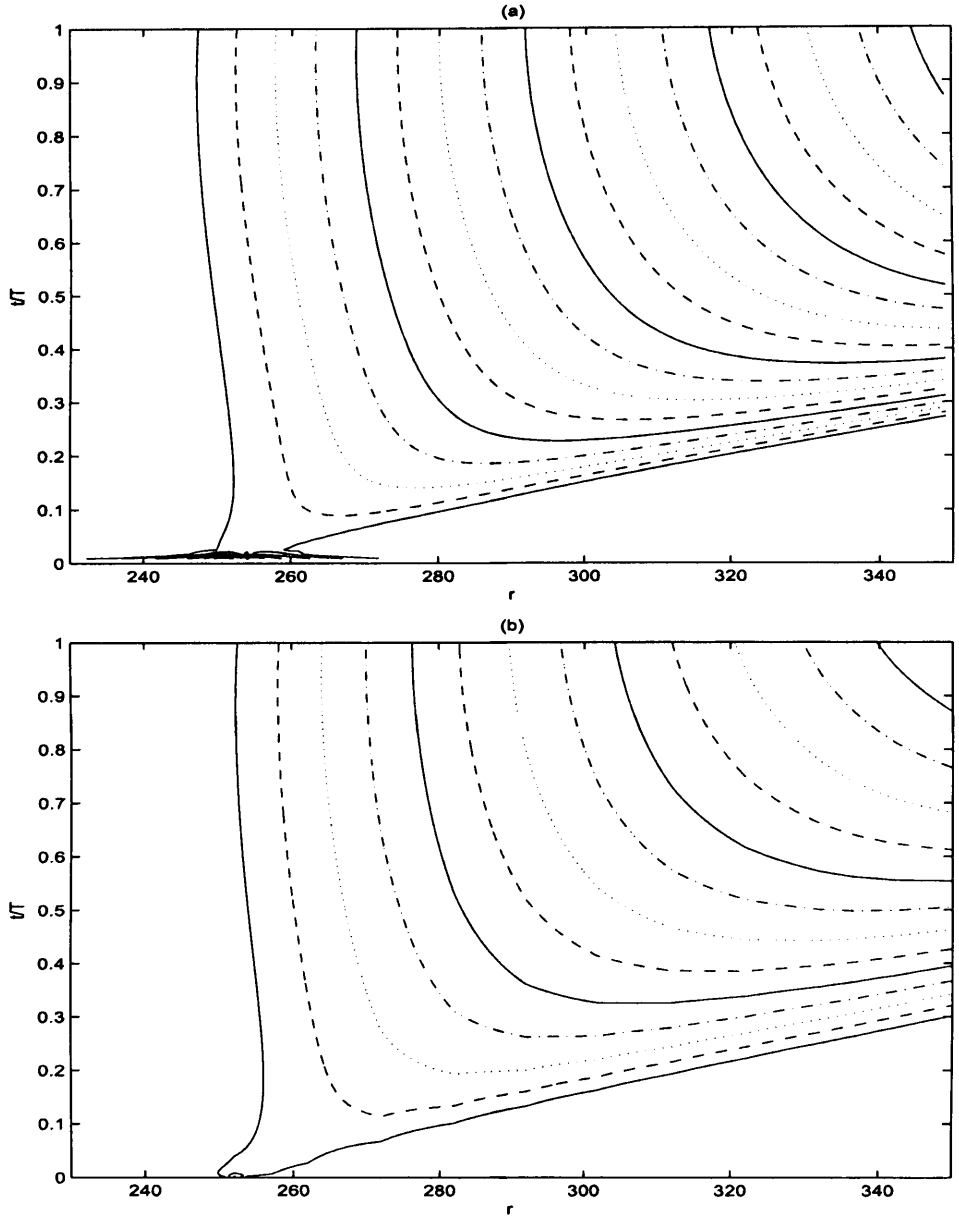

Figure 8.12: *The disturbance development wavepackets for: (a) the non-parallel numerical simulation results for the rotating-disk boundary-layer with* a = -1, *where* r_e = 252 *and* n = 29; *(b) and the Green's function, where the stability parameter* $\mu = \mu_0 + \mu_1 r$. *(Contours are drawn using a logarithmic scale, with levels separated by factors of two).*

is displayed.

μ - Linearly Varying

Figures 8.16, 8.17 and 8.18 display the frequencies, growth rates and disturbance wavepackets for the non-parallel numerical simulation results and Green's function with a linearly varying stability parameter; equation (8.31). The disturbance in the simulation results is excited for $r_e = 1911$, for an azimuthal mode number $n = 194$. The parameters $\bar{\mu}_0$, $\hat{\alpha}_s$, γ are as before, while the variations $\frac{d\omega_{l,r}}{dr}$ and $\frac{d\omega_{l,i}}{dr}$ are approximately given as 0.011 and 0.003, respectively. For the two problems, the frequencies and growth rates increase in an analogous manner. The disturbance wavepackets are also comparable, since the two trailing edges propagate in opposite directions.

8.4 Discussion and conclusions

The results of the numerical simulations for the rotating-disk boundary-layer have been modeled using the Green's solutions to the Ginzburg-Landau equation, obtained by Hunt & Crighton (1991), Hunt (1995). The parameters μ, U and γ that represent stability, convection and diffusion/dispersion effects, can be defined in terms of quantities that can be determined from the numerical simulation results; refer to equations (8.10), (8.22), (8.25), (8.26), (8.36) and (8.37). In the study by Hunt & Crighton (1991) all parameters were real only and they considered a stability parameter μ that could be a constant, vary linearly or vary quadratically with the streamwise direction[1]. However, by letting the terms μ, U and γ be complex, we have shown that the Green's solutions can display behaviour consistent with that observed for the rotating-disk boundary-layer.

[1]In the previous study, we considered the cases where the stability parameter μ was a constant and linearly varying. The problem where μ is quadratically varying is discussed in the appendix.

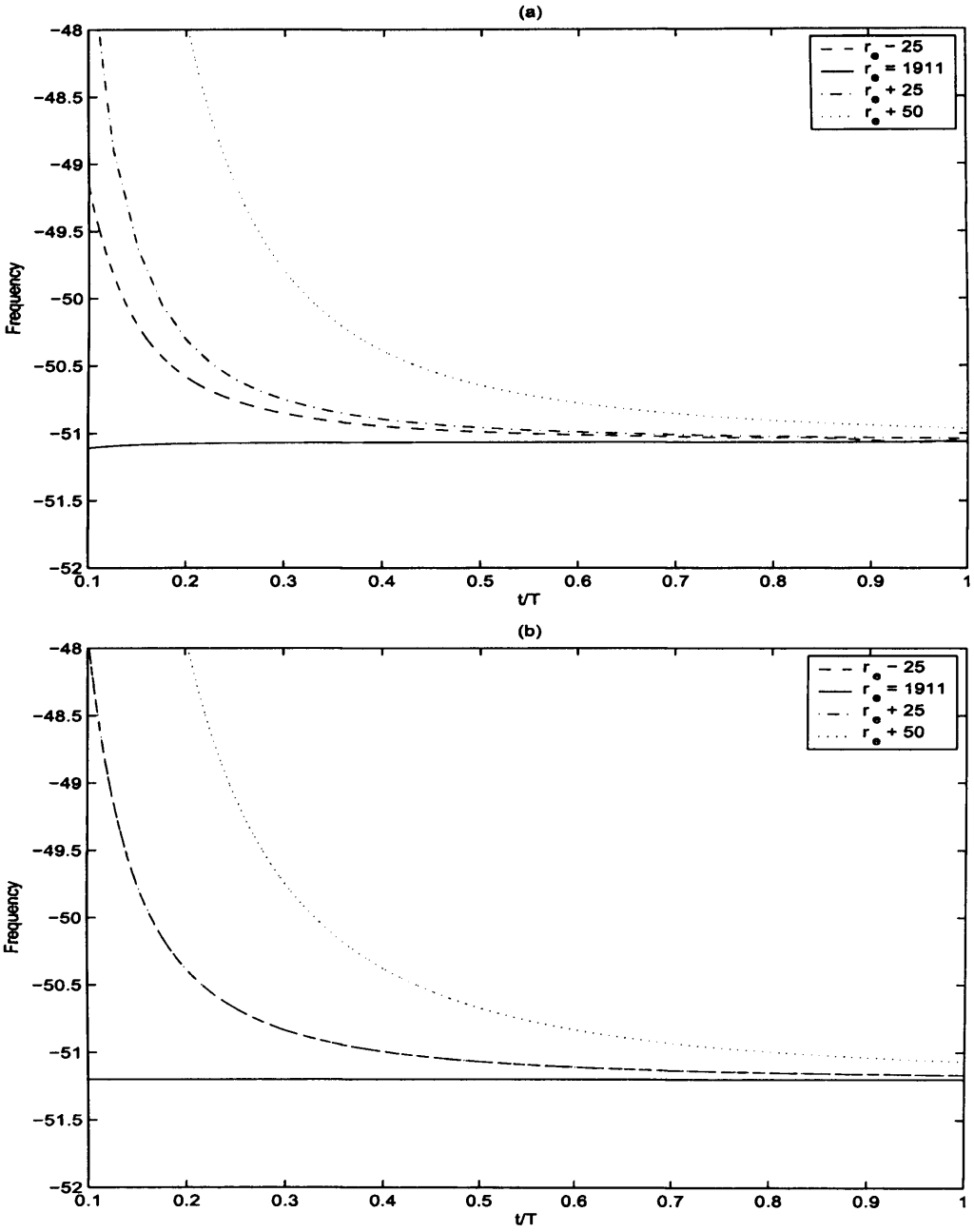

Figure 8.13: *The temporal frequencies for: (a) the parallel numerical simulation results for the rotating-disk boundary-layer with* $\boldsymbol{a} = 1$, *where* $Re = 1911$ *and* $n = 194$; *(b) the Green's function, where the stability parameter* $\mu = \mu_0$ *is a constant. The frequencies are plotted for four equally spaced points. (Note:* $T = 2\pi Re$*).*

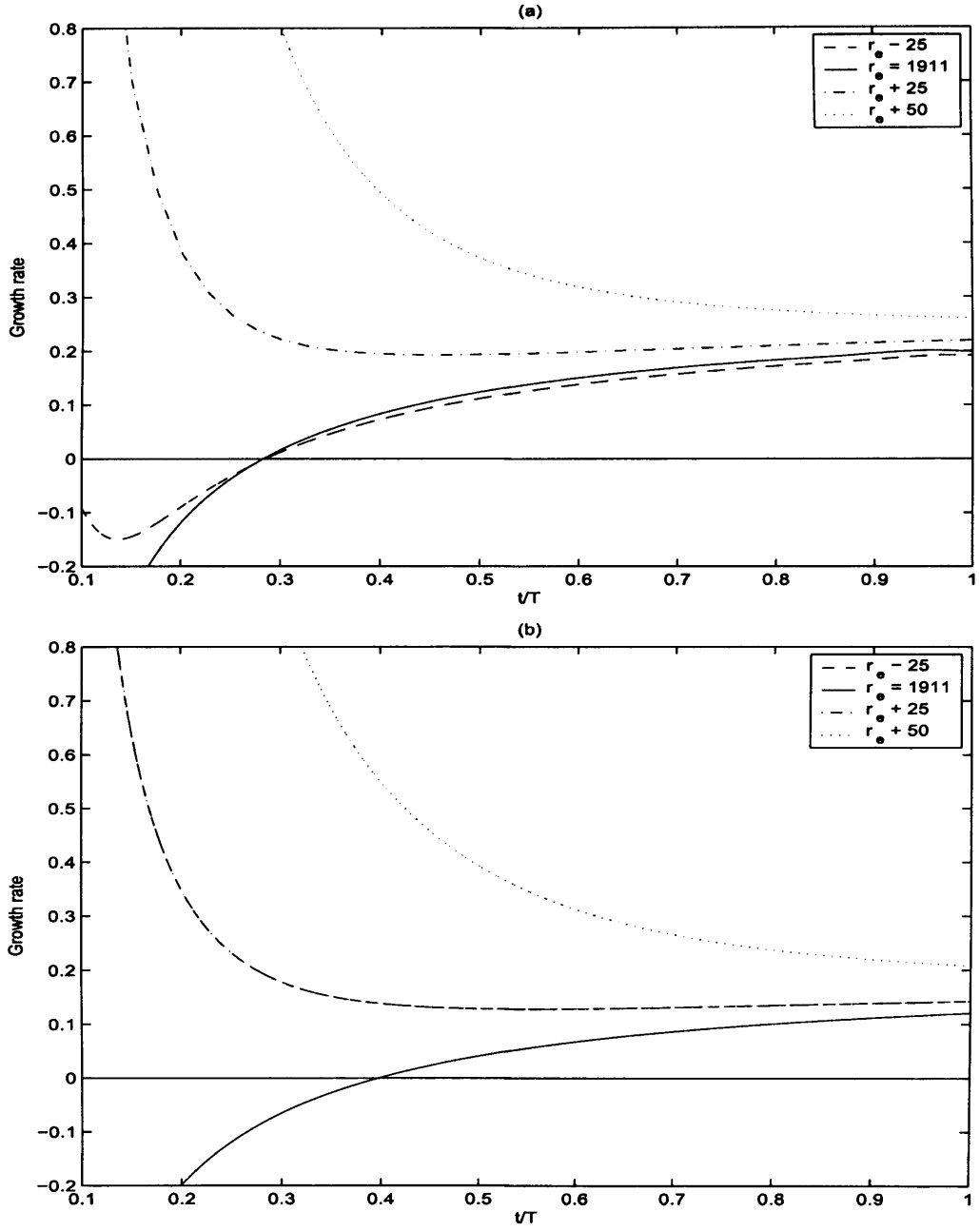

Figure 8.14: *The temporal growth rates for: (a) the parallel numerical simulation results for the rotating-disk boundary-layer with* $\boldsymbol{a} = 1$, *where* $Re = 1911$ *and* $n = 194$; *(b) the Green's function, where the stability parameter* $\mu = \mu_0$ *is a constant. The growth rates are plotted for four equally spaced points. (Note:* $T = 2\pi Re$*).*

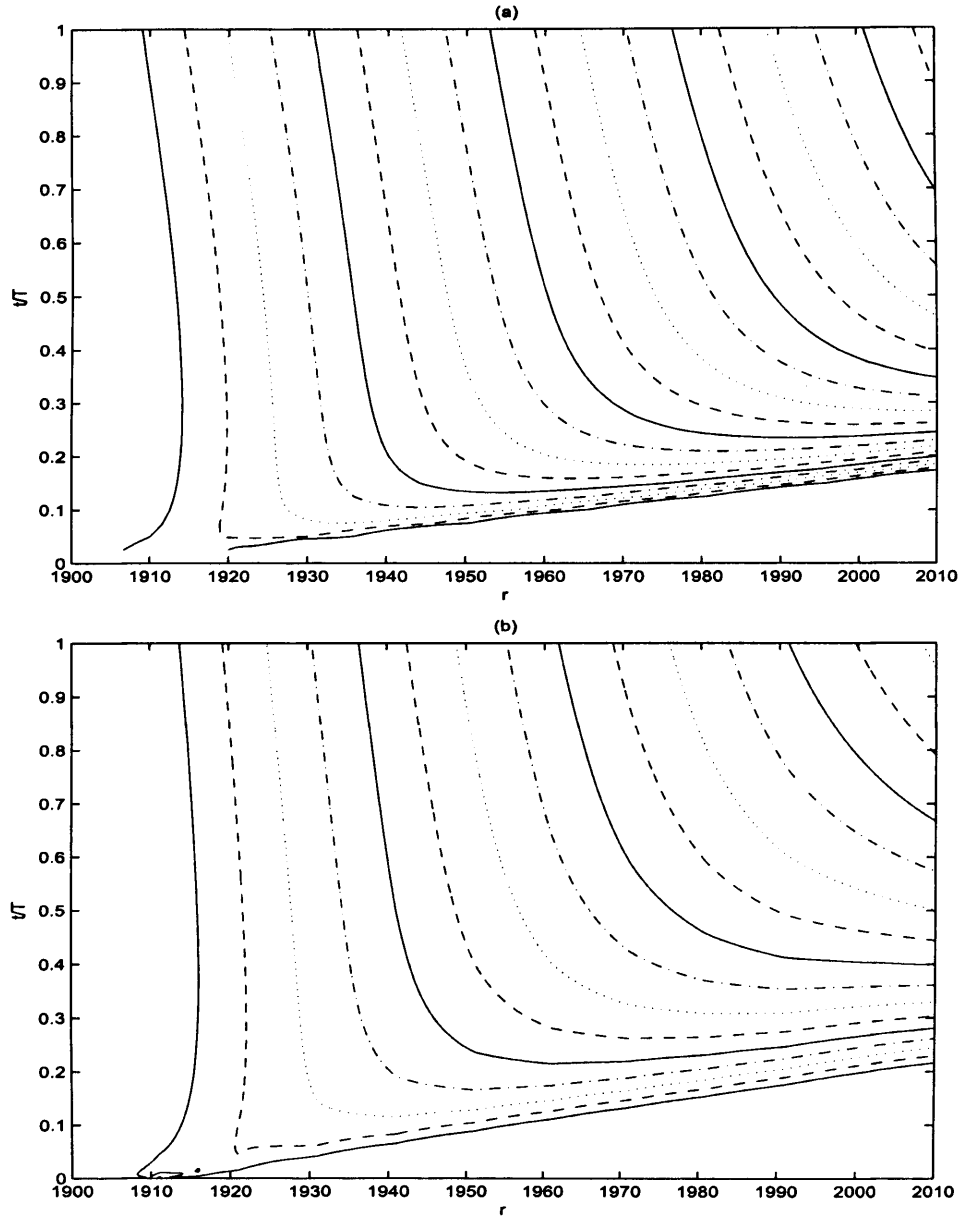

Figure 8.15: *The disturbance development wavepackets for: (a) the parallel numerical simulation results for the rotating-disk boundary-layer with* $\boldsymbol{a}$ *= -1, where Re = 252 and n = 29; (b) and the Green's function, where the stability parameter* $\mu = \mu_0$ *is a constant. (Contours are drawn using a logarithmic scale, with levels separated by factors of two).*

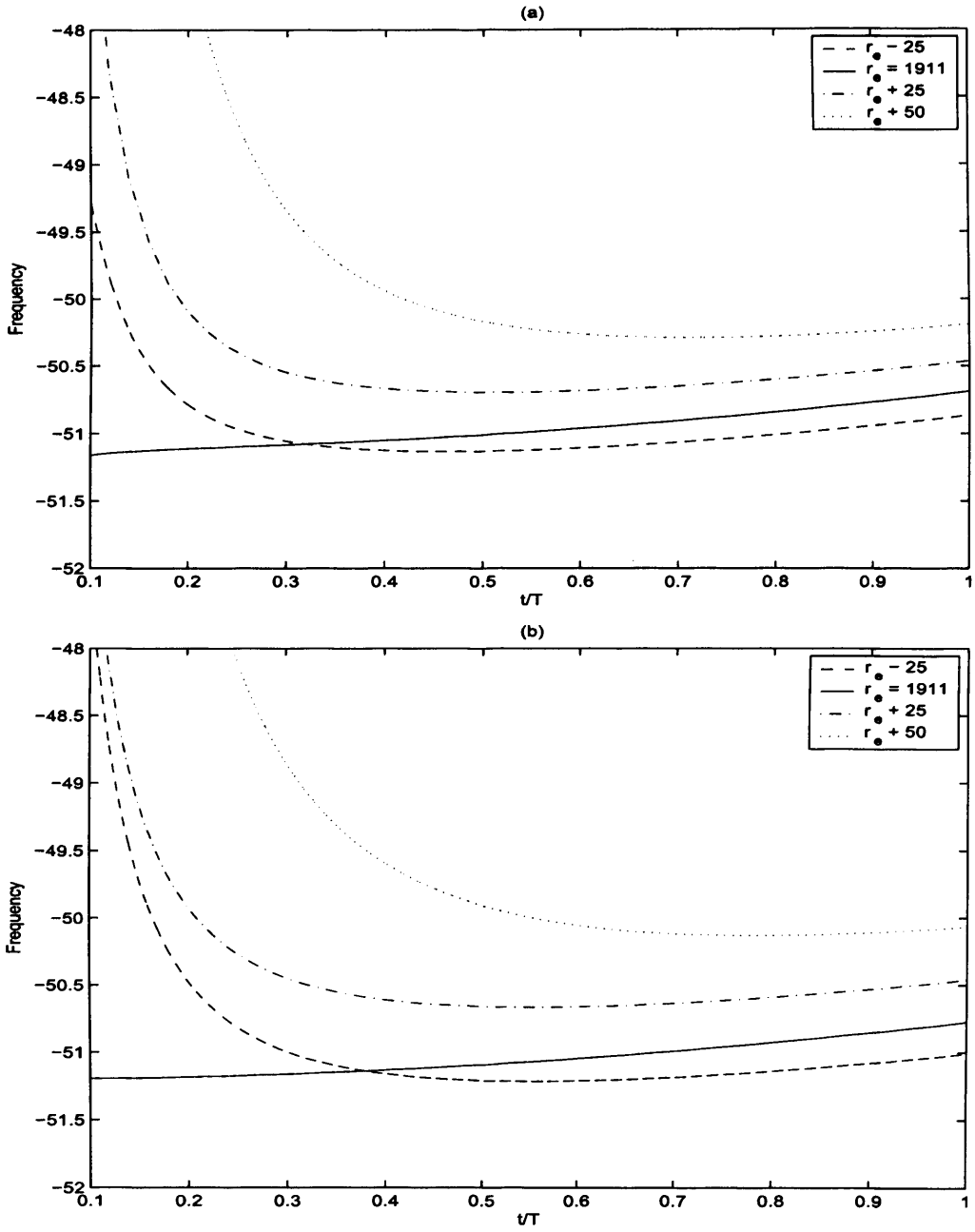

Figure 8.16: *The temporal frequencies for: (a) the non-parallel numerical simulation results for the rotating-disk boundary-layer with* $\boldsymbol{a} = 1$, *where* $r_e = 1911$ *and* $n = 194$; *(b) the Green's function, where the stability parameter* $\mu = \mu_0 + \mu_1 r$. *The frequencies are plotted for four equally spaced points. (Note:* $T = 2\pi r_a$ *where* r_a *is the inner radius).*

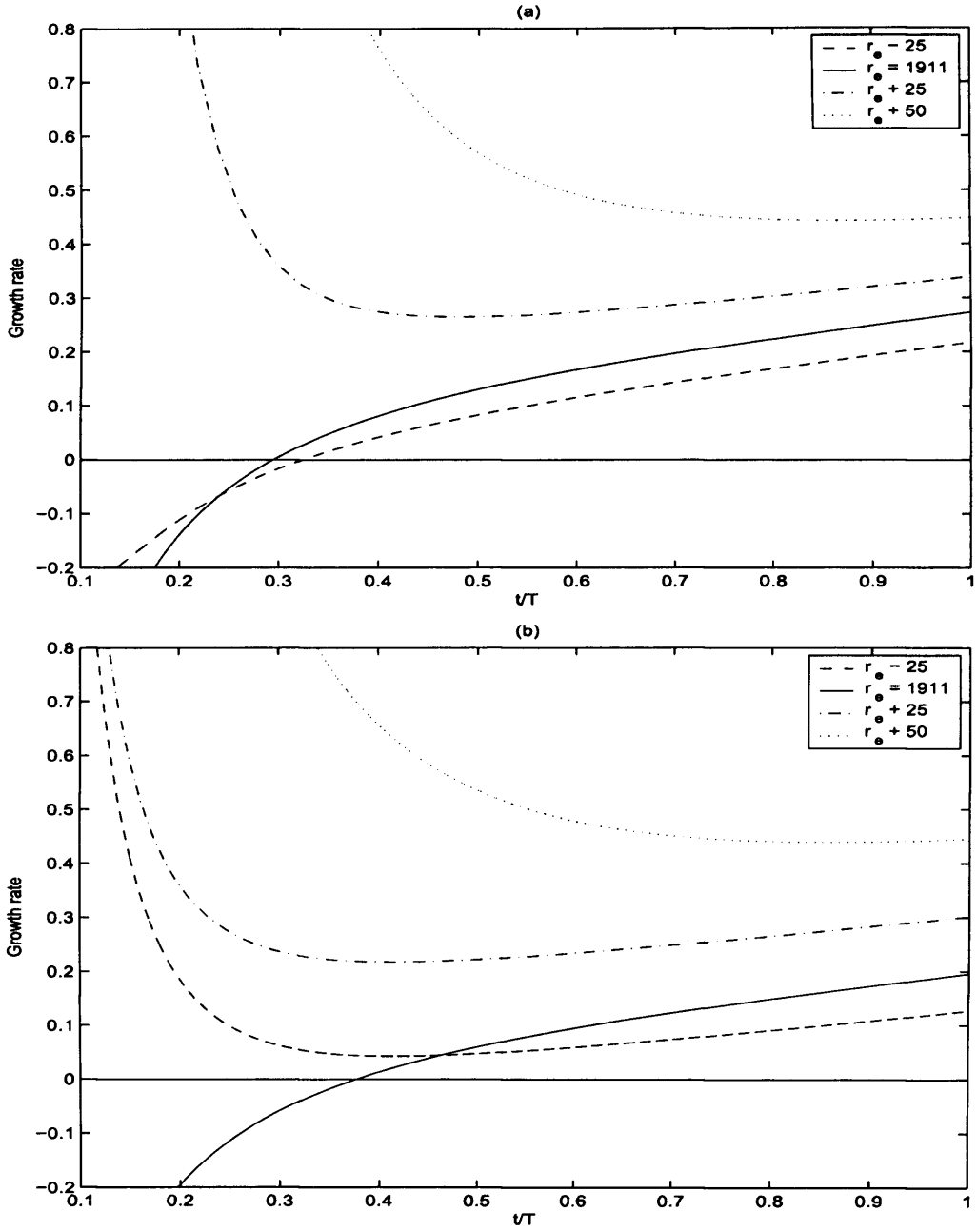

Figure 8.17: *The temporal growth rates for: (a) the non-parallel numerical simulation results for the rotating-disk boundary-layer with* $\boldsymbol{a} = 1$, *where* $r_e = 1911$ *and* $n = 194$; *(b) the Green's function, where the stability parameter* $\mu = \mu_0 + \mu_1 r$. *The growth rates are plotted for four equally spaced points. (Note:* $T = 2\pi r_a$ *where* r_a *is the inner radius).*

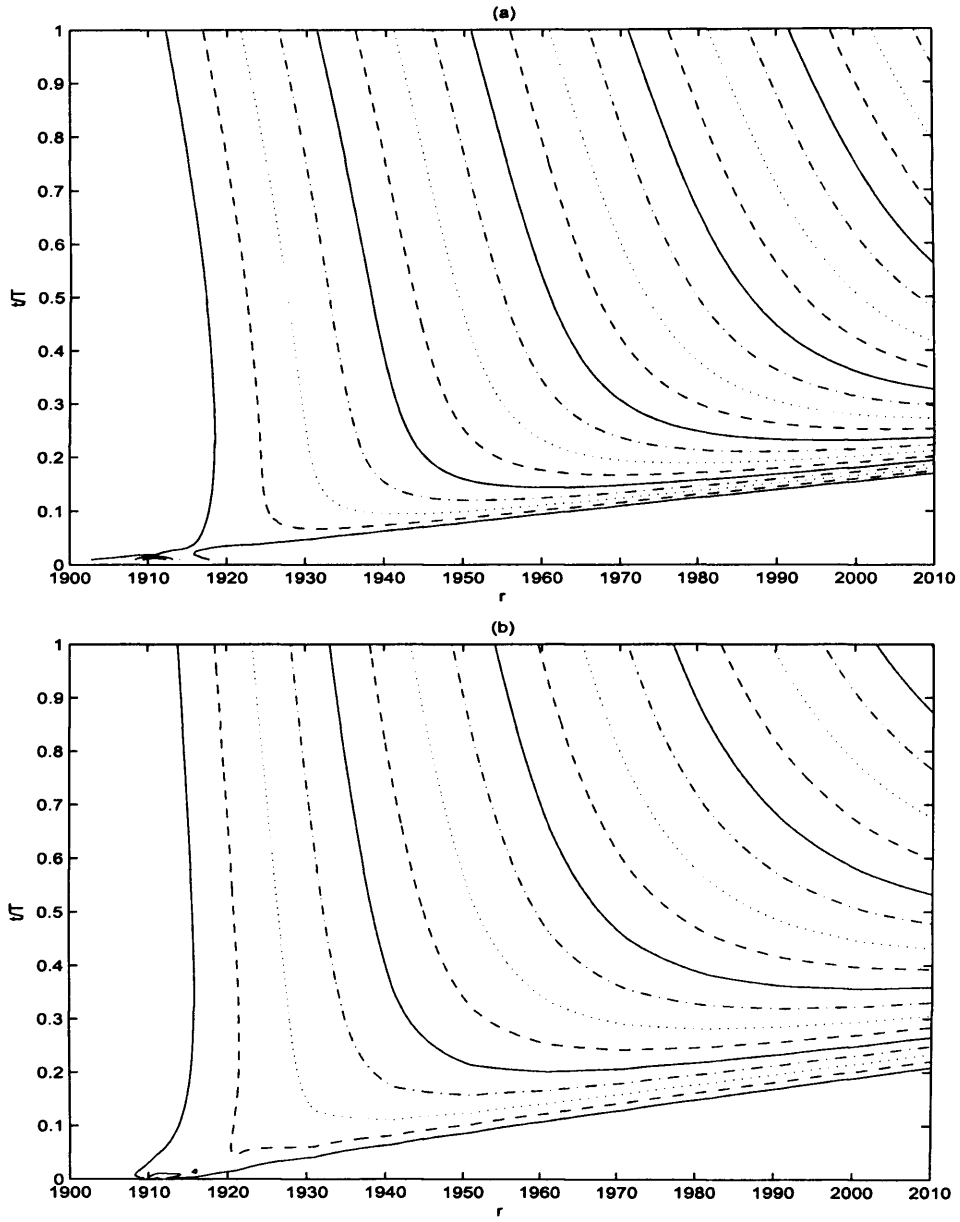

Figure 8.18: *The disturbance development wavepackets for: (a) the non-parallel numerical simulation results for the rotating-disk boundary-layer with* $a = 1$, *where* $r_e = 1911$ *and* $n = 194$; *(b) and the Green's function, where the stability parameter* $\mu = \mu_0 + \mu_1 r$. *(Contours are drawn using a logarithmic scale, with levels separated by factors of two).*

If the parameters μ, U and γ are independent of the streamwise direction r, the Green solutions may be matched to the parallel flow simulations. The temporal evolution for the frequencies, growth rates and disturbance wavepacket for the Green's solution is consistent with that displayed by the numerical simulations of the rotating-disk. Whereas if one of the terms μ, U and γ is dependent on r, the Green's solutions may be used to model the non-parallel flow simulations.

In the above study, the stability parameter μ was allowed to vary linearly with the streamwise direction r; $\mu = \mu_0 + \mu_1 r$, for μ_1 possibly complex. The real part of μ_1 characterizes variations in growth, while the complex part of μ_1 includes variations in the frequency.

In section 8.2.5 - where μ was complex and γ was real only - it was shown that the Green's solutions to the Ginzburg-Landau equation, could successfully model the simulation results for the rotating-disk boundary-layer and mean flows with mass injection. The solutions suggest that the varying frequency may be enough to globally stabilize disturbances. Depending on the precise balance between the radial increase in growth and the corresponding shifts in frequency, it is possible for an absolutely unstable flow to remain globally stable.

However, due to the definitions for the real and imaginary parts of μ_1 (equations (8.36) and (8.37)), it was not possible to match the solutions of the Ginzburg-Landau equation, with the simulation results of the rotating-disk boundary-layer with mass suction. The solutions of the Ginzburg-Landau equation always gave globally stable behaviour, while the simulation results suggest that global instability is promoted by mass suction; refer to chapter 4. Hence, it was not sufficient to consider μ complex and γ real only, when attempting to model all the rotating-disk mean flows.

When μ and γ are both complex (refer to section 8.2.6), the global behaviour could be determined by the inequality (8.43), which relates the variations in frequency and growth rate, and the diffusion and dispersion effects. If this inequality is satisfied,

decreasing growth rates will be observed and globally stable behaviour prevails. However, if it is not satisfied, increasing growth rates and globally unstable behaviour will persist indefinitely.

When the Green's solution was matched to the rotating-disk boundary-layer and those mean flows with mass injection, equation (8.43) was satisfied, and globally stable behaviour was observed. However, for the mean flows with uniform suction, the inequality (8.43) was not satisfied, and global instability was displayed.

Therefore, when attempting to model the non-parallel rotating-disk simulation results with the Green's solutions to the Ginzburg-Landau equation, it is essential that the linearly varying stability parameter μ and diffusion/dispersion term γ are complex. The global disturbance characteristics can then be determined by the precise balance between the variation in frequency, variation in growth rate and diffusion/dispersion effects.

Chapter 9

Conclusions and future studies

In this final chapter, the main results and conclusions of this thesis will be outlined in section 9.1 On going experimental investigations and future studies will be discussed in section 9.2.

9.1 Conclusions

The main results and conclusions are as follows:

1. The velocity-vorticity formulation, developed by Davies & Carpenter (2001) has been successfully applied to the rotating-disk boundary-layer, with mass transfer and an axial magnetic field, and the so-called BEK family; Bödewadt, Ekman von Kármán mean flows. This extends the work of Davies & Carpenter (2003), who studied the more usual rotating-disk problem, in the absence of any mass transfer or magnetic field. Refer to chapters 4, 5 and 6.

2. When disturbances are simulated using the so-called parallel flow approximation, the results are consistent with the theoretical results of Lingwood (1995, 1997a,b), Jasmine (2003) and Jasmine & Gajjar (2005a). In particular within the theoretical absolutely unstable parameter space, the simulations produce the expected behaviour. Refer to chapters 4, 5 and 6.

3. For the non-parallel flow simulations, the mean flows with mass injection produce similar behaviour as that seen by Davies & Carpenter (2003) for the rotating-disk boundary-layer. Initially disturbances within the absolutely unstable region exhibit temporal growth and upstream propagation. However, this does not persist indefinitely and the study suggests that convective behaviour will eventually dominate at all Reynolds numbers considered. However, the mean flows with mass suction are found to be destabilized by the non-parallel effects. Disturbances excited within the absolutely unstable region appear to exhibit an increasing temporal growth and radial inward propagation. The study suggests that for cases with sufficiently strong suction, temporal growth will eventually dominate the flow, albeit without any selection of a dominant frequency, as would be more usual for an unstable global mode. Refer to chapter 4.

4. The simulation results suggest that globally unstable behaviour can be promoted when a uniform axial magnetic field is applied to the rotating-disk boundary-layer. Impulsively excited disturbances were found to display an increasingly rapid growth at the radial position of the impulse, albeit without any selection of a dominant frequency. Refer to chapter 5.

5. The simulation results indicate that the kind of behaviour found for the von Kármán flow is carried over to other flows in the *BEK* family. For a Rossby number Ro within the range $-1 \leq Ro < 0$ (where Ro = -1 corresponds to the von Kármán flow), disturbances display a tendency to propagate outwards in a convective manner, even for those disturbances originally located within the known regions of absolute instability. While for $0 < Ro \leq 1$ ($Ro = 1$ corresponds to the Bödewadt flow), disturbances display a tendency to propagate radially inwards in a similar, though directionally opposite, convective manner

to that found for the von Kármán flow. However, as the propagating disturbance approaches the centre of the disk, the wavepacket stabilizes. Refer to chapter 6.

6. A local and globally defined non-dimensionalization is applied to the parallel flow simulations of the rotating-disk boundary-layer. For a fixed azimuthal mode number (first to become absolutely unstable), the globally defined frequency is found to increase in linear proportion with the Reynolds number/radius, while the globally defined growth rate displays a finite region of absolute instability. The Chomaz *et al.* (1991) global frequency selection criterion may be applied to the rotating-disk, if, we consider a simple model, that crudely matches the behaviour of the globally defined complex frequency. The corresponding saddle points are always located in the complex $r-$plane. Refer to chapter 7.

7. The numerical simulation results of the rotating-disk boundary-layer can be modeled using a much simpler system - the linearized complex Ginzburg-Landau equation. The Ginzburg-Landau equation can be used to model the disturbance development in a parallel flow, if the parameters μ, U, γ (stability, convection, diffusion/dispersion), are independent of the streamwise direction. However, if one of the terms μ, U, γ, depends on the streamwise coordinate, the Ginzburg-Landau equation can be used to match the disturbance development of a non-parallel flow. The parameters μ, U, γ, may be expressed in terms of the results of the numerical simulations of the rotating-disk boundary-layer. Conditions for global in/stability may be derived. The solutions to the Ginzburg-Landau equation show that behaviour consistent with the non-parallel simulation results can be obtained if μ is complex and linearly varying, and γ is complex. The results suggest that the behaviour depends on the precise balance of the varying frequency, varying growth rate, and diffusion/dispersion effects. Refer

to chapter 8.

9.2 Future studies

The current investigation has produced several interesting results. Nonetheless, there are a number of items that need to be addressed for future studies.

9.2.1 Extending the current study

Mass transfer and a magnetic field

The results of chapters 4 and 5 suggest that uniform suction and an axial magnetic field promote behaviour consistent with global instability. However, to ensure that this understanding is correct, a study should be conducted for $\mathbf{a} > 1$ and $m > 0.5$, where $\mathbf{a}$ and m are the suction and magnetic field parameters, respectively.

Before numerical simulations are conducted for $\mathbf{a} > 1$ and $m > 0.5$, a linear stability study is required to obtain eigenvalues (for comparison with the numerical simulations) for each particular problem. At present there are no eigenvalues available (in the research literature) for $\mathbf{a} > 1$ and $m > 0.5$.

It would also be advantageous to extend the current study (for $-1 \leq \mathbf{a} \leq 1$, $0 \leq m \leq 0.5$), for longer simulation time lengths.

The Bödewadt flow

Unfortunately we were unable to obtain any results for the Bödewadt flow. Numerical instabilities, (which possibly arose due to the small Reynolds numbers considered for the Bödewadt boundary-layer), made it impossible to observe sufficiently long and valid simulations for the Bödewadt flow. However, we were able to predict the disturbance behaviour from other rotating boundary-layers. Nonetheless, it would be good to confirm these predictions by obtaining numerical simulation results for the Bödewadt boundary-layer.

9.2.2 On-going experimental studies

The results obtained on uniform suction and the rotating-disk boundary-layer, has prompted Professor Tom Corke and Mr Cory McElrath of the University of Notre Dame, in the USA, to conduct an experimental investigation on the rotating-disk boundary-layer with uniform suction. For their problem the suction parameter $\mathbf{a} = 0.4$. This extends the experimental study by Othman & Corke (2006), who studied the rotating-disk boundary-layer without uniform suction. It is hoped that their study will produce results that support the theoretical findings of the current thesis.

9.2.3 Further studies

Below we have listed several ideas for future investigation:

1. The effect of mass transfer on the Ekman and Bödewadt boundary layers.
2. The effect of an axial magnetic field on the Ekman and Bödewadt boundary layers.
3. The effect due to to the Hall factor (refer to chapter 5).
4. The rotating-disk beneath a stationary-disk or lid.
5. The rotating-disk with a temperature dependent viscosity.
6. The rotating-disk in a compressible boundary-layer.
7. The rotating-sphere boundary-layer.
8. The rotating-cone boundary-layer.
9. A non-linear study on rotating boundary-layers.

Appendix A

A velocity-vorticity eigen-solver for the Orr-Sommerfeld equation

We are concerned with calculating eigenvalue solutions to a given system of ordinary differential equations

$$\sum_{k=0}^{m} \alpha^{m-k} A_k \phi = 0, \tag{A.1}$$

where ϕ is a set of complex variables, A_k are linear differential operators and α is an eigenvalue. Such problems arise in many areas in fluid dynamics. The Orr-Sommerfeld equation can be written in the form (A.1). Thus, the corresponding eigenvalues to a flow can be calculated. Bridges & Morris (1984) considered the Orr-Sommerfeld equation and the case of a plane Poiseuille flow. They rearranged the system of equations into companion matrix form and found approximations to the eigenvalues. The approximate solutions were then refined using a cubically convergent iteration scheme that was derived by Lancaster (1964). We will now discuss and apply the companion matrix method and iteration scheme to a velocity-vorticity version of the Orr-Sommerfeld equation.

A.1 Method

The solution to a given problem (i.e. Orr-sommerfeld equation), involves the expansion of a complex variable - say the vorticity ω - in terms of a finite Chebyshev series and representing the given equations as an $N \times N$ matrix system. Using a mathematical programming language (namely Matlab) and a cubic iteration scheme, eigenvalues can be first approximated and then correctly calculated.

A.1.1 The linear companion matrix method

In the analysis of linear stability, an investigator generally decides to choose, either spatial or temporal theories. For the spatial theory, one assumes that disturbances evolve in space from an initial temporal distribution. Thus, the method assumes that the frequency is real, while the wavenumber is complex. The opposite is true for temporal theory, as the frequency is complex and the wavenumber is real. This implies that disturbances grow or decay with time from an initial spatial distribution. It is also possible to consider a complex frequency and wavenumber, when absolute instability is suspected.

Independent of the theory utilized, one is able to call upon a simple but effective method for calculating the eigenvalues of a given problem, that being the linear companion matrix method.

The linear companion matrix method involves rearranging the given problem into the form

$$\mathbf{A}\underline{v} = \lambda \mathbf{B}\underline{v}, \tag{A.2}$$

where $\mathbf{A}$ and $\mathbf{B}$ are square matrices (possibly complex), λ is an eigenvalue with a corresponding eigenvector $\underline{v}$. Once in this form the eigenvalues can be determined by a mathematical programming language - Matlab.

A.1.2 Local iteration scheme

Once a satisfactory approximation is available for a single eigenvalue, it is possible to calculate the root by a locally convergent algorithm. The method employed throughout this chapter, is the cubically convergent method, derived by Lancaster (1964). The iterative formula may be written as

$$\alpha_{k+1} = \alpha_k - \frac{2f(\alpha_k)}{|f(\alpha_k)|^2 - f^{(1)}(\alpha_k)}, \qquad k = 0, 1, 2, ..., \tag{A.3}$$

where

$$f(\alpha_k) = Tr\{\mathbf{D}^{-1}(\alpha_k)\mathbf{D}^{(1)}(\alpha_k)\}, \tag{A.4}$$

and

$$f^{(1)}(\alpha_k) = Tr\{\mathbf{D}^{-1}(\alpha_k)\mathbf{D}^{(2)}(\alpha_k) - |\mathbf{D}^{-1}(\alpha_k)\mathbf{D}^{(1)}(\alpha_k)|^2\}. \tag{A.5}$$

Here $\mathbf{D}$ is the lambda equation (where the lambda equation is $\mathbf{D}(\alpha) = C_0 + \alpha C_1 + \alpha^2 C_2 + ...$ in its most general form; C_i are matrices and α is the eigenvalue), $Tr\{A\}$ is the trace of A, $\mathbf{D}^{-1}$ is the inverse of $\mathbf{D}$ and $\mathbf{D}^{(1)}$ and $\mathbf{D}^{(2)}$ are the respective first and second derivatives of $\mathbf{D}$ with respect to α.

The above cubic iteration scheme is called upon for the following Orr-Sommerfeld problem. The code for the iteration scheme may be found in appendix B.

A.2 Orr-Sommerfeld equation - velocity-vorticity formulation

The governing equations for the two-dimensional Orr-Sommerfeld equation are given as

$$\frac{\partial \omega}{\partial t} + U\frac{\partial \omega}{\partial x} + U''v = \frac{1}{Re}\nabla^2\omega, \tag{A.6}$$

$$\nabla^2 v = -\frac{\partial \omega}{\partial x}, \tag{A.7}$$

where v denotes the wall-normal velocity component and ω is the associated vorticity perturbation. While $U = U(y)$ is the parallel flow, x is the streamwise direction, y is the wall-normal direction and Re is the Reynolds number.

We may now introduce a stream function ϕ such that

$$v = -\frac{\partial \phi}{\partial x}, \tag{A.8}$$

so that the governing equations may be re-written as

$$\frac{\partial \omega}{\partial t} + U\frac{\partial \omega}{\partial x} - U''\frac{\partial \phi}{\partial x} = \frac{1}{Re}\nabla^2\omega, \tag{A.9}$$

$$\nabla^2\phi = \omega. \tag{A.10}$$

As the problem is linear, the vorticity and stream function may assume the form

$$\begin{aligned} \omega(x,y,t) &= \omega(y)\exp[i(\alpha x - \gamma t)], \\ \phi(x,y,t) &= \phi(y)\exp[i(\alpha x - \gamma t)], \end{aligned} \tag{A.11}$$

where α is the wavenumber and γ is the frequency. Thus, by making the substitutions $\partial/\partial t \rightarrow -i\gamma$ and $\partial/\partial x \rightarrow i\alpha$, equations (A.9) and (A.10) may be re-written as

$$-i\gamma\omega + i\alpha U\omega - i\alpha U''\phi = \frac{1}{Re}(D^2 - \alpha^2)\omega, \tag{A.12}$$

$$(D^2 - \alpha^2)\phi = \omega, \tag{A.13}$$

where $D^2 = d^2/dy^2$.

Equations (A.12) and (A.13) are now integrated twice with respect to the mapped variable ξ (equation (3.27)), giving

$$-i\gamma\mathbf{I}\omega + i\alpha\mathbf{I}U\omega - i\alpha\mathbf{I}U''\phi = \frac{1}{Re}\mathbf{K}\omega - \frac{\alpha^2}{Re}\mathbf{I}\omega, \tag{A.14}$$

$$\mathbf{K}\phi - \alpha^2\mathbf{I}\phi = \mathbf{I}\omega, \tag{A.15}$$

where **I** and **K** are defined in equations (3.54) and (3.56). The variables ω and ϕ are approximated by the finite, odd Chebyshev series (3.26). While the basic flow is given by the even Chebyshev series

$$U(y) = \sum_{k=1}^{\infty} a_k T_{2(k-1)}(\xi). \tag{A.16}$$

Boundary conditions

The boundary conditions for the Orr-sommerfeld equation are

$$\int_0^{\infty} \omega + \frac{\partial v}{\partial x} dy = 0, \tag{A.17}$$

$$v = 0. \tag{A.18}$$

On substituting equation (A.8) for the stream function, into equations (A.17) and (A.18), and by assuming linear modes (A.11), we obtain

$$\int_0^{\infty} \omega + \alpha^2 \phi dy = 0, \tag{A.19}$$

$$\phi = 0. \tag{A.20}$$

Equations (A.19) and (A.20) are of the type (3.41) and (3.52), respectively. Thus, the methods discussed previously can be used to discretize the boundary conditions (A.19) and (A.20), to give

$$\sum_{k=1}^{N} p_k \omega_k + \alpha^2 \sum_{k=1}^{N} p_k \phi_k = 0, \tag{A.21}$$

$$\sum_{k=1}^{N} \phi_k = 0. \tag{A.22}$$

As suggested earlier, we can now consider either a temporal or spatial theory to determine the eigenvalues of the Orr-Sommerfeld equations.

A.2.1 Temporal solver

By considering a temporal theory, the wavenumber is assumed to be real, while the frequency is complex. The maximum power corresponding to the frequency is of order one, (for the Orr-Sommerfeld problem). Hence, the Orr-Sommerfeld problem may be rearranged into the companion matrix form

$$\Big(A_0 - \gamma A_1\Big)(\omega, \phi)^T = 0, \tag{A.23}$$

where ω^T is the transpose of ω. The matrices A_0 and A_1 are

$$A_0 = \begin{pmatrix} \sum_{k=1}^{N} p_k & \alpha^2 \sum_{k=1}^{N} p_k \\ \frac{1}{Re}\mathbf{K} - \frac{\alpha^2}{Re}\mathbf{I} - i\alpha\mathbf{I}U & i\alpha\mathbf{I}U'' \\ \underline{0} & \underline{1} \\ \mathbf{I} & -\mathbf{K} + \alpha^2\mathbf{I} \end{pmatrix}, \tag{A.24}$$

and

$$A_1 = \begin{pmatrix} \underline{0} & \underline{0} \\ -i\mathbf{I} & 0_{N-1,N} \\ \underline{0} & \underline{0} \\ 0_{N-1,N} & 0_{N-1,N} \end{pmatrix}. \tag{A.25}$$

The terms $\underline{0}$ and $0_{N-1,N}$ refer to a $1 \times N$ vector of zeros and a $(N-1) \times N$ matrix of zeros, respectively. While $\underline{1}$ refers to a $1 \times N$ vector of ones. All other terms are as before. The first and third rows of each matrix are of size $1 \times 2N$ and make up the boundary conditions (A.21) and (A.22). The second and fourth rows of each matrix are of size $(N-1) \times 2N$ and make up the Orr-Sommerfeld equations (A.14) and (A.15). Hence, each matrix is square and of size $2N \times 2N$.

Since (A.23) is of the general form (A.2), we are able to calculate the temporal eigenvalues of the problem.

A.2.2 Spatial solver

For spatial theory, the frequency is assumed to be real, while the wavenumber is complex. For the Orr-Sommerfeld equation, the maximum power corresponding to the wavenumber α is of order two. Hence, the problem can be written as a lambda matrix of degree two

$$\Big(B_0 + \alpha B_1 + \alpha^2 B_2\Big)(\omega, \phi)^T = 0. \tag{A.26}$$

The matrices B_0, B_1 and B_2 are given as

$$B_0 = \begin{pmatrix} \sum_{k=1}^{N} p_k & \underline{0} \\ -i\gamma\mathbf{I} - \frac{1}{Re}\mathbf{K} & 0_{N-1,N} \\ \underline{0} & \underline{1} \\ \mathbf{I} & -\mathbf{K} \end{pmatrix}, \tag{A.27}$$

$$B_1 = \begin{pmatrix} \underline{0} & \underline{0} \\ i\mathbf{I}U & -i\mathbf{I}U'' \\ \underline{0} & \underline{0} \\ 0_{N-1,N} & 0_{N-1,N} \end{pmatrix}, \tag{A.28}$$

and

$$B_2 = \begin{pmatrix} \underline{0} & \sum_{k=1}^{N} p_k \\ \frac{1}{Re}\mathbf{I} & 0_{N-1,N} \\ \underline{0} & \underline{0} \\ 0_{N-1,N} & \mathbf{I} \end{pmatrix}. \tag{A.29}$$

$\mathbf{I}$, $\mathbf{K}$, $\underline{0}$, $0_{N-1,N}$ and $\underline{1}$ are as before and the matrices B_0, B_1 and B_2 are square and of size $2N \times 2N$.

In order to calculate the spatial eigenvalues of the Orr-Sommerfeld problem, the lambda matrix (A.26) has to be transformed, such that it is of the general companion matrix form (A.2). This may be achieved by making the substitution

$$\mathbf{x} = (\omega, \phi)^T, \qquad \mathbf{x}_1 = \alpha\mathbf{x}, \tag{A.30}$$

and by constructing the matrix

$$\left\{\begin{pmatrix} -B_1 & -B_2 \\ I & \mathbf{0} \end{pmatrix} - \alpha \begin{pmatrix} B_0 & \mathbf{0} \\ \mathbf{0} & I \end{pmatrix}\right\} \begin{bmatrix} \mathbf{x}_1 \\ \mathbf{x} \end{bmatrix} = 0. \tag{A.31}$$

The terms $\mathbf{0}$ and I represent a $(2N \times 2N)$ zero matrix and a $2N \times 2N$ identity matrix. Therefore, equation (A.31) is of size $4N \times 4N$ and of the general companion matrix form (A.2). Thus, the spatial eigenvalues corresponding to the Orr-Sommerfeld equation may now be evaluated.

A.2.3 Falkner-Skan boundary-layers

Mean velocity profile

The mean velocity profile of a flow over a flat plate is influenced by pressure gradients, as they can accelerate or decelerate the freestream velocity. Such flows are known as Falkner-Skan boundary-layers. The flow can be represented in the streamwise coordinate direction U^*_∞, by

$$U^*_\infty(x) = C^*(x^*)^m, \tag{A.32}$$

where $*$ denotes dimensional quantities. Here x^* is the coordinate in the streamwise direction and C^* is a constant. Equation (A.32) is associated with a freestream mean pressure gradient, given as

$$\frac{dP^*_\infty}{dx^*} = -U^*_\infty \frac{dU^*_\infty}{dx^*}. \tag{A.33}$$

On introducing a wall-normal similarity variable

$$\eta = \sqrt{\frac{m+1}{2} \frac{Re^2_{\delta^*} \upsilon^*}{U^*_\infty (x^*)^{m-1}}} y, \tag{A.34}$$

and a stream function

$$\Psi = \sqrt{\frac{2U^*_\infty \upsilon^* x^*}{m+1}} f(\eta), \tag{A.35}$$

where υ^* is the kinematic viscosity, and

$$u = \frac{\partial \Psi}{\partial y}, \qquad v = -\frac{\partial \Psi}{\partial x}, \tag{A.36}$$

one can obtain (after some manipulation) the ordinary differential equation for f

$$f''' + ff'' + \beta_H(1 - f'^2) = 0. \tag{A.37}$$

This is solved subject to the boundary conditions

$$f(0) = f'(0) = 0, \qquad f'(\infty) = 1. \tag{A.38}$$

The parameter β_H is the two-dimensional pressure-gradient parameter, known as the Hartree parameter and is related to m by

$$\beta_H = \frac{2m}{m+1}, \qquad m = \frac{\beta_H}{2 - \beta_H}. \tag{A.39}$$

The Hartree parameter is a measure of the acceleration or deceleration of the freestream.

The Blasius boundary-layer

The Blasius boundary-layer arises for a flow with zero pressure gradient, i.e. $\beta_H = m = 0$. The non-dimensional streamwise velocity component is given as

$$U(\eta) = f'(\eta), \tag{A.40}$$

and the streamwise velocity second derivative, is given as

$$U''(\eta) = \delta^2 f'''(\eta). \tag{A.41}$$

The Blasius mean velocity profiles for U and U'' are plotted against η/δ in figure A.1, where δ takes the familiar value 1.2167.

A.2.4 Results

The critical parameters for the Blasius boundary-layer were found to be $Re_c = 519.2$, $\alpha_c = 0.303$ and $\omega_c = 0.1201$, which are almost identical to those given by Schmid & Henningson (2001); refer to table A.1. (Here Re_c is the Reynolds number, α_c is the

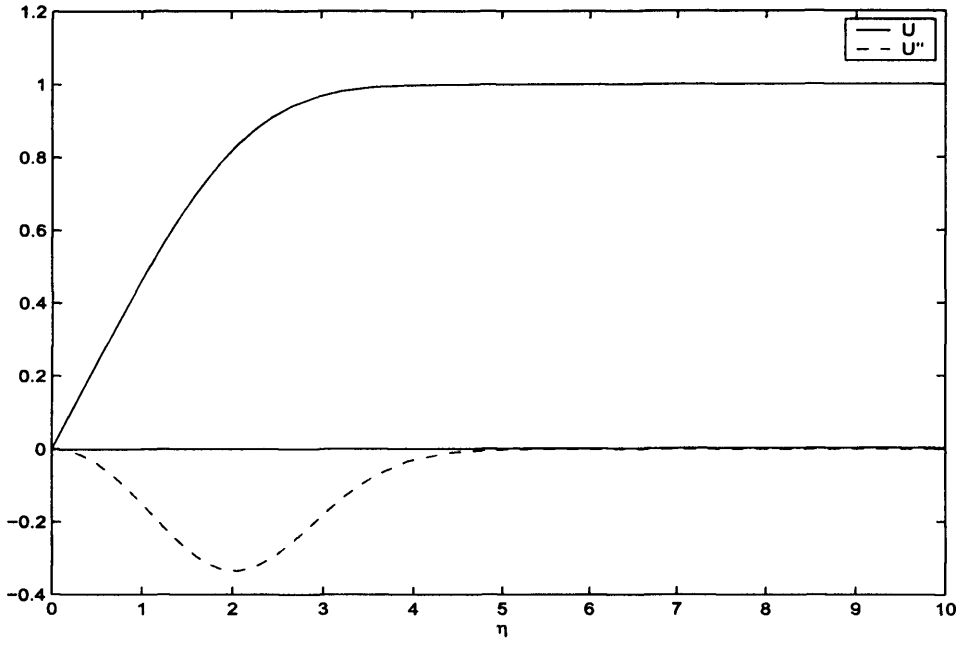

Figure A.1: *The profiles for the velocity (U) and second derivative (U'') for the Blasius flow.*

wavenumber and ω_c is the frequency). Several other eigenvalue comparisons are given in table A.1, which were used in order to validate the numerical solvers.

The eigenvalues of the Orr-Sommerfeld equation (A.9) and (A.10) for the Blasius flow are shown in figure A.2. The Reynolds number was taken to be the critically unstable value, as given above. Figure A.2(a) displays a set of the discrete and continuous spectra ω_n for $\alpha = 0.303$. The eigenvalues are located along two well-defined branches. The first set of eigenvalues are found along the branch $\omega_r \rightarrow \alpha_r$ (i.e. $\omega \rightarrow 0.303$), while the second set of eigenvalues are located along the branch $\omega_n \rightarrow 0$, where the maximum occurs at $\omega = 0.1201$. This mode is unstable and is known as a Tollmien-Schlichting (TS) wave (Tollmien (1936), Schlichting (1933)), after the researchers who first showed that the Orr-Sommerfeld equation has unstable

Author	Reynolds number	Frequency	Wavenumber
Schmid & Henningson (2001)	519.4	0.1201	0.303
Present Thesis	519.2	0.1201	0.303
Schmid & Henningson (2001)	800	0.2944 - i0.0824 0.4641 - i0.1698 0.5834 - i0.2136 0.2375 - 0.2144	1.000
Present Thesis	800	0.2944 - i0.0824 0.4641 - i0.1697 0.5798 - i0.2079 0.2375 - i0.2144	1.000
Grosch & Orszag (1977)	580	0.0652	0.179
Present Thesis	580	0.0625	0.179

Table A.1: *Eigenvalues for the Blasius boundary-layer compared with those found by previous authors.*

disturbances for mean flows without inflection points. The TS wave is always located along the branch $\omega_n \rightarrow 0$.

Figure A.2(b) displays the wavenumber eigenvalues for the parameters $Re = 520$ and $\omega = 0.1201$. Again there is a set of discrete eigenvalues found along the branch $\alpha \rightarrow \omega$, and there is also an eigenvalue located at $\alpha = 0.303$, as expected.

The neutral curve

The neutral curve of a given problem is defined as the boundary between areas of exponential growth and decay. The region within the neutral curve is unstable, while the region outside the neutral curve is stable. Figure A.3 displays the neutral curve for the Blasius boundary-layer.

For any given horizontal line, which is allowed to pass through the region of instability, there are two points of intersection with the neutral curve. This will in turn divide the neutral curve into two parts: an upper branch and a lower branch.

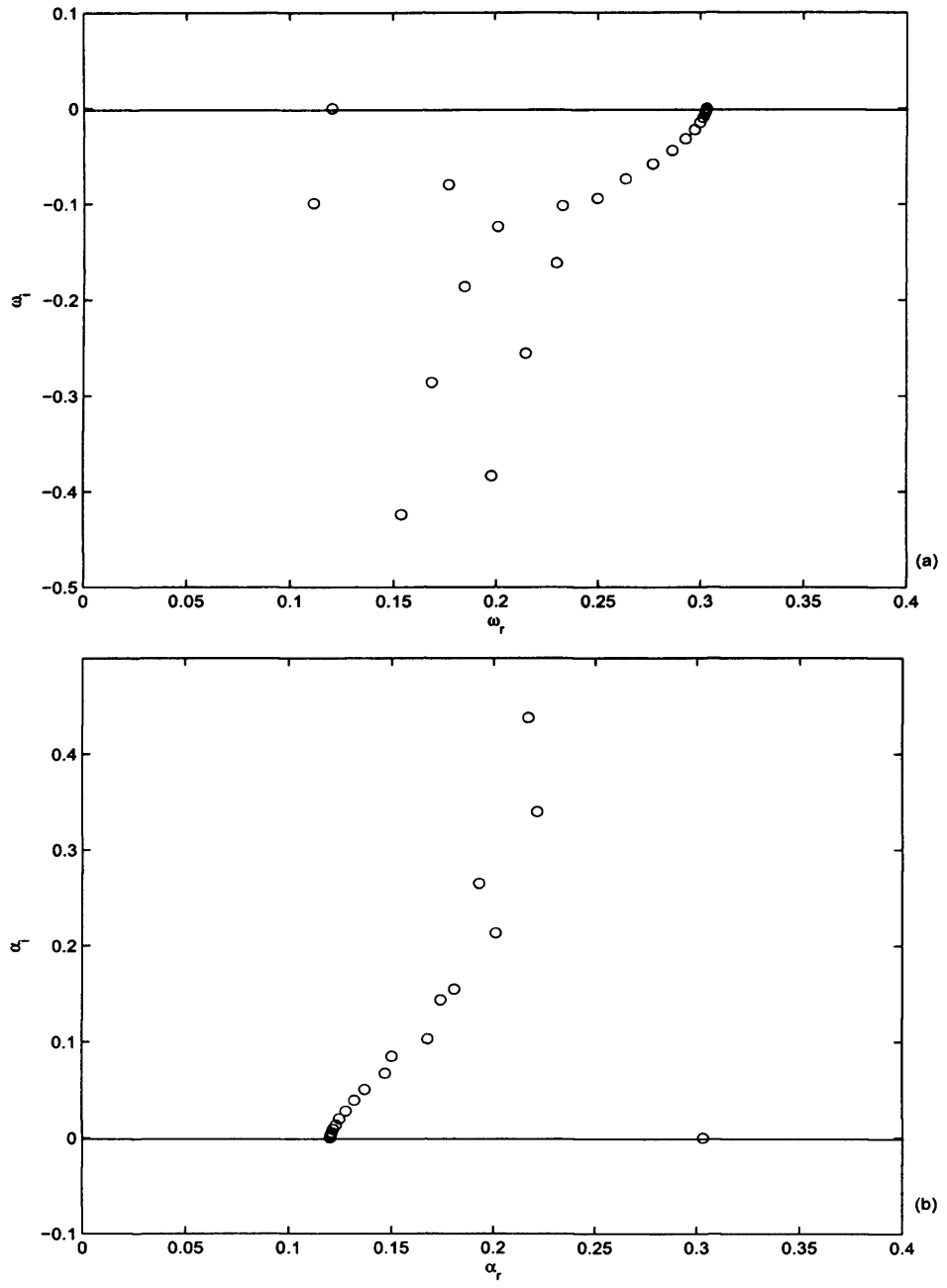

Figure A.2: *Spectrum for Blasius boundary-layer at critical Reynolds number Re = 519: (a) - frequency spectra for wavenumber $\alpha = 0.303$; (b) - wavenumber spectra for frequency $\omega = 0.1201$.*

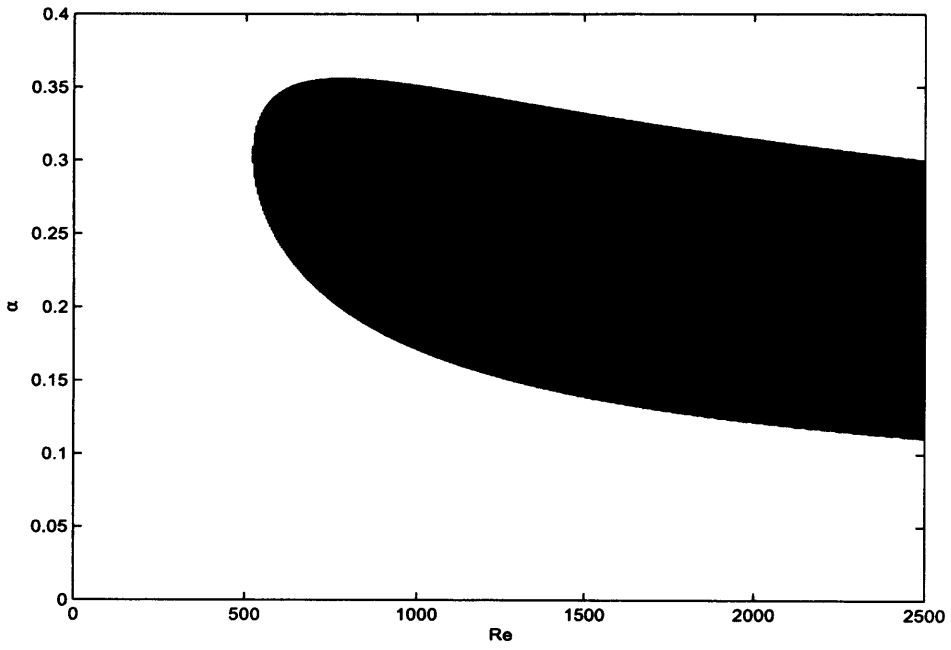

Figure A.3: *Neutral curve: area of instability is shaded.*

Appendix B

Code for the Orr-Sommerfeld eigen-solver

B.1 Solvers

B.1.1 Spatial solver

```
% Function to calculate eigenvalues of the Orr-Sommerfeld equation.
% Input data required to solve problem: Number of Chebyshevs, Reynolds number
% and frequency
    N = 64;
    Re = input(' Reynolds number: Re = ? ');
    wr = input(' Frequency: wr = : ');
    wi = input(' Growth: wi = : ');
% Complex constant
    i = sqrt(-1);
% Frequency
    w = wr+i*wi;
% Mapping parameter
    L = 1.64368166657907;
    M = 1/(L*L);
```

```
% Call integral boundary coefficients
   [FINT] = Boundaryconditioncoef(N);
% Call integral operator I
   [IA] = IntegralA(N);
% Call integral operator K
   [IB] = IntegralB(N);
% Call meanflow chebyshev matrices U and D2U
   [U, D2U] = Meanflowsolver(N);
% Identity matrix
   I = eye(N);
% Set up matrices in form
% [a^2 C0 + a^2 C1 + a^0 C0][w phi]' = 0
% where C0, C1, C2 are 2N x 2N matrices.
% Firstly introduce boundary conditions
   C2 = [zeros(1,N), FINT; zeros(N-1,2*(N)); zeros(N,2*(N))];
   C1 = [zeros(2*(N))];
   C0 = [FINT, zeros(1,N); zeros(N-1,2*(N)); zeros(1,N), ones(1,N); zeros(N-1,2*(N))];
% Now include main equations
   C2 = C2 + [(1/Re)*IA, zeros(N); zeros(N) IA];
   C1 = C1 + [i*IA*U, -i*IA*D2U; zeros(N,2*(N))];
   C0 = C0 + [-i*w*IA - (M/Re)*IB, zeros(N); IA, -M*IB];
% Can now rearrange into form
% [a^1 D0 + a^0 D1][ax x]' = 0, where x = [w, phi]'.
   B0 = [-C1, -C2; eye(2*(N)) zeros(2*(N))];
   B1 = [C0, zeros(2*(N)); zeros(2*(N)), eye(2*(N))];
% Can either calculate eigenvalues of companion matrix or lambda matrix
   e = polyeig(C0, C1, C2);
```

```
% Determine the wavenumbers with maximum real and imaginary parts
   [m,l] = max(real(e));
   disp('Eigenvalue with largest real part = ')
   disp(e(l))
   [m,l] = max(imag(e));
   disp('Eigenvalue with largest imaginary part = ')
   disp(e(l))
% Iteration solver
% Set approximate eigenvalue to b
   b = e(l);
% Number of iterations Q = 10;
% Loop to solve eigenvalue b
   for K = 1:Q
         D = C0 + b(K)*C1 + b(K)*b(K)*C2;
         D1 = C1 + 2*b(K)*C2;
         D2 = 2*C2;
         Dinv = inv(D);
         f = trace(Dinv*D1);
         f1 = trace(Dinv*D2 - [Dinv*D1]*[Dinv*D1]);
         b(K+1) = b(K) - 2*f/(f*f - f1);
   end
% plot eigenvalues
   plot(real(e), imag(e),'ro');axis([-1 1 -1 1]);
```

B.1.2 Temporal solver

```
% Function to calculate eigenvalues of the Orr-sommerfeld equation
% Input data required to solve problem: Reynolds number, wavenumber.
```

```
N=64;
Re = input(' Reynolds number: Re = ? ');
ar = input(' Wavenumber: ar = : ');
ai = input(' Growth: ai = : ');
% Complex constant
i = sqrt(-1);
% Wavenumber
a = ar+i*ai;
% Mapping parameter
L = 1.64368166657907;
M = 1/(L*L);
% Call Chebyshev integrals, boundary coefficients, meanflow
[IA] = IntegralA(N);
[IB] = IntegralB(N);
[FINT] = Boundaryconditioncoef(N);
[U, D2U] = Meanflowsolver(N);
% Need to sort out boundary conditions
A11 = [FINT; zeros(N-1,N)];
A12 = [(a*a)*FINT; zeros(N-1,N)];
A21 = [zeros(N)];
A22 = [ones(1,N); zeros(N-1,N)];
% Now include equations
A11 = A11 + (M/Re)*IB - ((a*a)/Re)*IA - i*a*IA*U;
A12 = A12 + i*a*IA*D2U;
A21 = A21 + IA;
A22 = A22 - M*IB + (a*a)*IA;
A = [A11 A12; A21 A22];
```

```
% Sort out right-hand-side of problem
   B1 = -i*IA;
   B2 = 0*IA;
   B = [B1 B2; B2 B2];
% Calculate eigenvalues of problem
   e = eig(A,B);
% Determine the eigenvalues with largest real and imaginary parts
   [m,l] = max(real(e));
   disp('Eigenvalue with largest real part = ')
   disp(e(l))
   [m,l] = max(imag(e));
   disp('Eigenvalue with largest imaginary part = ')
   disp(e(l))
% Iteration solver
% Set approximate eigenvalue to b
   b = e(l);
% Number of iterations
   Q = 10;
% Loop to resolve eigenvalue b
   for K = 1:Q
         D = A - b(K)*B;
         D1 = -B;
         D2 = zeros(2*(N));
         Dinv = inv(D);
         f = trace(Dinv*D1);
         f1 = trace(Dinv*D2 - [Dinv*D1]*[Dinv*D1]);
         b(K+1) = b(K) - 2*f/(f*f - f1);
```

```
    end
%plot eigenvalues
    plot(real(e), imag(e),'ro');axis([0 1 -1 0]);
```

B.2 Boundary coefficients and integrals

B.2.1 Boundary coefficients

```
function [FINT] = Boundaryconditioncoef(N);
    A = 1;
    B = 2;
    C = 1;
    L = 1.64368166657907;
    for K = 2:N-1
            F(1)=1;
            F(K)=(1/K)*(mod(K,2));
    end
    for K = N-2:-1:1
            BET(N-1) = B;
            GAM(N-1) = F(N-1);
            CBET(K) = C/(BET(K+1));
            BET(K) = B - CBET(K)*A;
            GAM(K) = F(K) - CBET(K)*GAM(K+1);
    end
    for K = 2:N-1
            W(1) = GAM(1)/BET(1);
            W(K) = (GAM(K) - A*W(K-1))/BET(K);
    end
```

```
for K = 2:N-1
        FINT(1) = L*2*W(1);
        FINT(K) = L*2*(W(K) - W(K-1));
        FINT(N) = -L*2*W(N-1);
end
```

B.2.2 Chebyshev integrals

Integral I

```
function [IA] = IntegralA(N);
% Function to calculate the integral operator I which acts on odd chebyshev
% polynomials and is written in a tridiagonal manner.
% Calculates the coefficients f(K-1), f(K), f(K+1).
   for K = 2:N+1
        a(K) = 1/(8*(2*K-1)*(K-1));
        b(K) = -1/(8*K*(K-1))
        c(K) = 1/(8*K*(2*K-1));
   end
% Creates the tridiagonal matrix.
   IA = diag(b(1:N),0) + diag(a(2:N),-1) + diag(c(1:N-1),1);
```

Integral K

```
function [IB] = IntegralB(N);
% Function to calculate the integral operator K which acts on odd chebyshev
% polynomials and is written in a pentadiagonal manner.
% Calculates the coefficients f(K-2), f(K-1), f(K), f(K+1), f(K+2).
   for K = 2:N+2
        a1(K) = 1/16;
```

```
        b1(K) = 1/4;
        c1(K) = 3/8;
        d1(K) = 1/4;
        e1(K) = 1/16;
        a2(K) = 1/(16*(2*K-1));
        b2(K) = 1/(8*(2*K-1));
        c2(K) = 0;
        d2(K) = -1/(8*(2*K-1));
        e2(K) = -1/(16*(2*K-1));
        a3(K) = 1/(32*(K-1)*(2*K-1));
        b3(K) = 1/(32*K*(K-1)*(2*K-1));
        c3(K) = -1/(32*(K-1)*K);
        d3(K) = -1/(32*K*(K-1)*(2*K-1));
        e3(K) = 1/(32*K*(2*K-1));
        a(K) = (a1(K) - 6*a2(K) + 6*a3(K));
        b(K) = (b1(K) - 6*b2(K) + 6*b3(K));
        c(K) = (c1(K) - 6*c2(K) + 6*c3(K));
        d(K) = (d1(K) - 6*d2(K) + 6*d3(K));
        e(K) = (e1(K) - 6*e2(K) + 6*e3(K));
        b(2) = (b1(2)+a1(2) - 6*(b2(2)+a2(2)) + 6*(b3(2)+a3(2)));
    end
    IB = diag(c(1:N),0) + diag(b(2:N),-1) + diag(d(1:N-1),1);
    IB = IB + diag(a(3:N),-2) + diag(e(1:N-2),2);
```

B.3 Mean flow solver

```
function [U, D2U] = Meanflowsolver(N);
% Function to transform the mean velocity profiles from collocation space to
```

```
% Chebyshev space.
% Collocation values for U and U''
M1 = [0.000000000000000000; 0.000282959826495337; 0.001132694492131107;
0.002551775533010251; 0.004544508840776532; 0.007116964915322029;
0.010277021734211642; 0.014034420765414753; 0.018400836816274111;
0.023389962590386885; 0.029017609018465982; 0.035301822642907835;
0.042263021572698345; 0.049924151789873243; 0.058310865885997161;
0.067451726642569251; 0.077378438249061141; 0.088126108383279611;
0.099733544868301743; 0.112243586658369160; 0.125703085474088840;
0.140162787563543330; 0.155678082277931010; 0.172309413067983810;
0.190122654620963450; 0.209189502609298690; 0.229587783399974150;
0.251399474889032580; 0.274709727098769120; 0.299608078640860360;
0.326187775921186310; 0.354544401601672220; 0.384768565221385310;
0.416939393914891540; 0.451122324763552300; 0.487359576818445720;
0.525650219929556740; 0.565933832462586440; 0.608064048047086140;
0.651784704086493690; 0.696656823122624450; 0.742076148885554730;
0.787257935681726860; 0.831050446620130940; 0.872095613969664060;
0.908916569889709480; 0.940062426410669840; 0.964415132962072820;
0.981551413490585610; 0.992017489365257470; 0.997294784907640230;
0.999344391475489920; 0.999900693387071770; 0.999992311429745320;
0.999999792658503250; 0.999999998217581790; 1.000000000025288400;
0.999999999993113620; 0.999999999999882540; 1.000000000000046000;
1.000000000000001100; 1.000000000000000000; 1.000000000000000000;
1.000000000000000000];
M2 = [0.000000000000000000 -0.000000059285521856 -0.000000949996403597
-0.000004821441696169 -0.000015291846444472 -0.000037503201616729
-0.000078199640696901 -0.000145830968394501 -0.000250683486000673
```

```
-0.000405040816390607 -0.000623378035768106 -0.000922593072477855
-0.001322280034500118 -0.001845049868001658 -0.002516904508894791
-0.003367671428042255 -0.004431506119054188 -0.005747470519947258
-0.007360195409595532 -0.009320637882472041 -0.011686949375501972
-0.014525221797035895 -0.017910587265962605 -0.021928356593549674
-0.026675161512582653 -0.032260074630909921 -0.038805644088130142
-0.046448035538733744 -0.055336399385716273 -0.065632659410805858
-0.077508913993729250 -0.091141995976364895 -0.106702613879449790
-0.124339165575672870 -0.144155443544363600 -0.166172178862819070
-0.190273572482252460 -0.216133702460587970 -0.243112462357646470
-0.270148350500162890 -0.295577792014319110 -0.317074012165833090
-0.331629895227252390 -0.335578815616557000 -0.325204101062522450
-0.297785052677842050 -0.253037686836590450 -0.194735124500390100
-0.131333192176974560 -0.074194340142948109 -0.032961888571106240
-0.010523218383097537 -0.002114337177937716 -0.000219088960191523
-0.000008140072457660 -0.000000095887770295 0.000000000944915165
-0.000000001030438495 -0.000000000043537120 0.000000000010812587
0.000000000000473505 0.000000000000014067 -0.000000000000000137
0.000000000000000000];
% Use cosine transform to get Chebyshev values
    M1 = [M1; 1];
    M2 = [M2; 0];
    J = [2:N];
    K = [1:N+1];
    M = sqrt(2/N)*[0.5*ones(N+1,1), cos((J-1)'*(K-1)*pi/(N))', 0.5*(-1).^(K-1)'];
    U1 = sqrt(2/N)*M*M1;
    U2 = sqrt(2/N)*M*M2;
```

```
% Matrix multiplier for U and U''
    for K = 1:N
        for J = 1:N
            J1 = abs(K-J)+1;
            J2 = K+J;
            U(K,J) = 0.5*U1(J1);
            if (J2 <= N)
                U(K,J) = U(K,J) + 0.5*U1(J2);
            end
        end
    end
    for K = 1:N
        for J = 1:N
            J1 = abs(K-J)+1;
            J2 = K+J;
            D2U(K,J) = 0.5*U2(J1);
            if (J2 <= N)
                D2U(K,J) = D2U(K,J) + 0.5*U2(J2);
            end
        end
    end
```

Appendix C

Mean flow solver

```
% The following code was used to calculate the mean flow velocity profiles for all
% rotating flows with suction/injection.
% The code was adapted to include the effects of a uniform magnetic field, and
% also to study the BEK family.
% The code can also be used to calculate the meanflow profiles for a
% rotating-disk with temperature-dependent viscosity or
% BEK family with mass transfer/magnetic field.

function Suction-Injection
% The following code solves the above problem.
    infinity = 10;
    maxinfinity = 120;
    solinit = bvpinit(linspace(0,infinity, 120), [0 0 1 0 0]);
    options = bvpset('AbsTol', 1e-40, 'RelTol', 1e-20);
    sol = bvp4c(@fsode,@fsbc, solinit, options);
    z = sol.x;
    f =sol.y;
% Plot the graph of f, g and h
```

```
figure
plot(z,f(1,:),'-b',z,f(3,:),'-.r',z,f(5,:),'-g');
axis([0 maxinfinity -1.6 1.6]);
title('Solution to the von Karman flow over a rotating disk for a = ');
xlabel('z');
h = legend('f','g','h',2);
drawnow
shg
% Extending solution to maxinfinity
for j = infinity + 1:maxinfinity
        solinit = bvpinit(sol, [0 j]);
        options = bvpset('AbsTol', 1e-40, 'RelTol', 1e-20);
        sol = bvp4c(@fsode, @fsbc, solinit, options);
        z = sol.x;
        f = sol.y;
        plot(z,f(1,:),'-b',z,f(3,:),'-.r',z,f(5,:),'-g');
        axis([0 maxinfinity -1.6 1.6]);
        title('Solution to the von Karman flow over a rotating disk for a = ?');
        xlabel('z');
        h = legend('f','g','h',2);
end
hold off
% Output solution at 48 points
n = 48;
for k = 1:n
        u(k) = cos((k-1)*pi/(2*n));
        y(k) = 4*((1/u(k))- 1);
```

```
        f = deval(sol,y);
        fprintf('12.18f',u,f);
    end
% The differential equations
    function dfdz = fsode(z,f)
    dfdz = [f(2)
        f(5) * f(2) + f(1)^2 - (f(3) + 1)^2
        f(4)
        f(5) * f(4) + 2 * f(1) * (f(3) + 1)
        -2 * f(1) ];
% The boundary conditions
    function res = fsbc(f0, finf) a = 1;
    res = [f0(1)
        f0(3)
        f0(5) + a
        finf(1)
        finf(3) + 1];
```

The mean velocity profiles for the *BEK* family and the rotating-disk with a uniform magnetic field can be found by altering *The differential equations function* and *The boundary conditions function.*

C.1 Mean velocity profiles for a temperature-dependent viscosity

For a rotating-disk with temperature-dependent viscosity, the system of ordinary differential equations is given as

$$(1+\epsilon S)^2(F^2+F'H-(G+1)^2)+\epsilon S'F'=(1+\epsilon S)F'', \tag{C.1}$$

$$(1+\epsilon S)^2(2F(G+1)+G'H)+\epsilon S'G'=(1+\epsilon S)G'', \tag{C.2}$$

$$2F+H'=0, \tag{C.3}$$

$$S''-P_rS'H=0, \tag{C.4}$$

where F, G, H and S refer to the radial, azimuthal, normal directions and temperature. Primes refer to derivatives with respect to z, ϵ is a parameter controlling the temperature dependence of viscosity and P_r is the Prandtl number, which is taken to be equal to 0.72, in order to be consistent with the study by Jasmine (2003) and Jasmine & Gajjar (2005b). The system of ordinary differential equations is solved subject to the boundary conditions

$$F(0)=G(0)=H(0)=0, \qquad S(0)=1 \tag{C.5}$$

and

$$F(z\rightarrow\infty)=S(z\rightarrow\infty)=0, \qquad G(z\rightarrow\infty)=-1. \tag{C.6}$$

Figure C.1 and table C.1 displays the profiles of F, G, H and S, and the values of $F'(0), G'(0), S'(0)$ and $H(\infty)$. The tabulated results agree with those given by Jasmine (2003) and Jasmine & Gajjar (2005b) (italics).

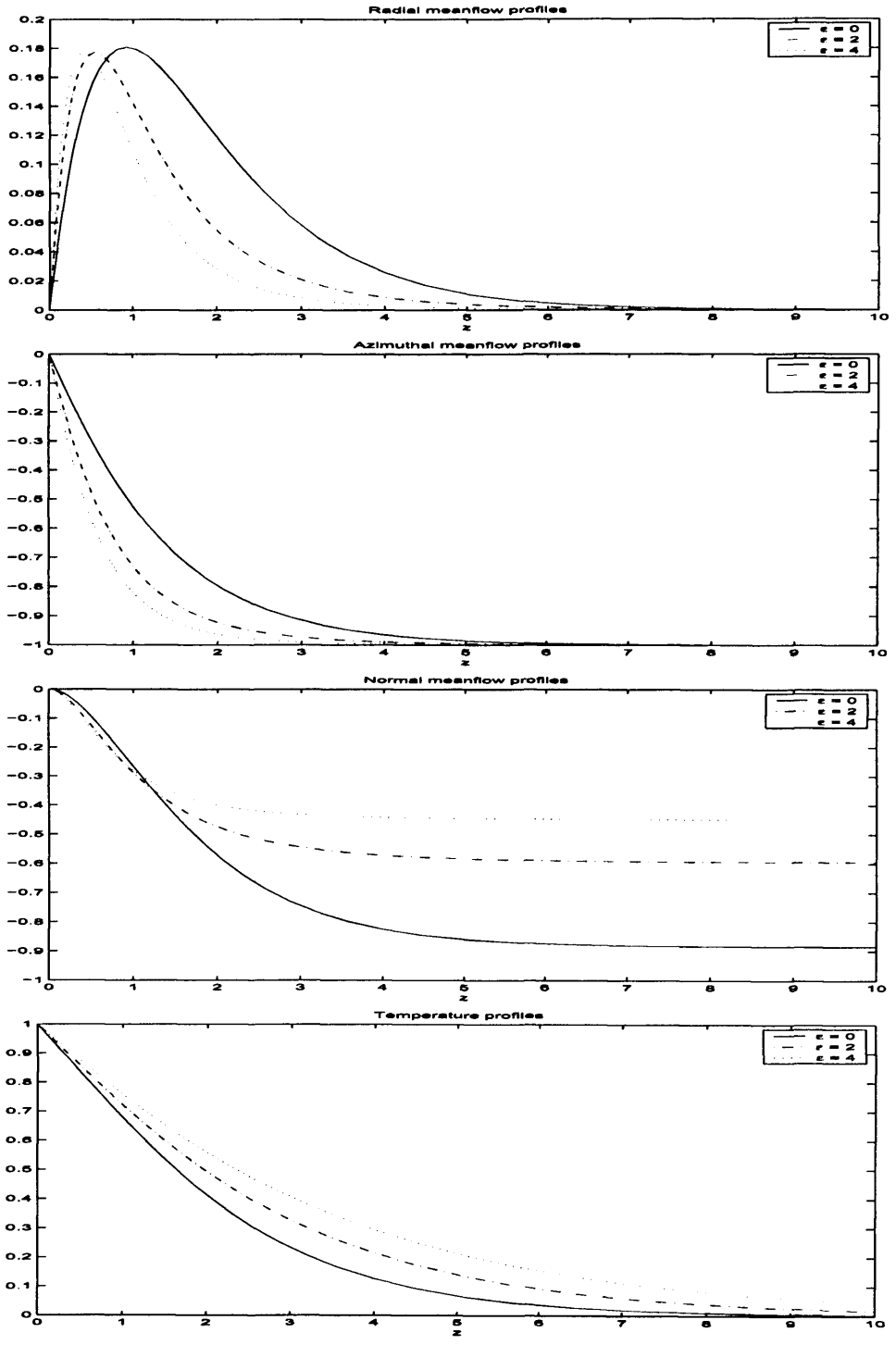

Figure C.1: *Profiles for the radial F, azimuthal G and normal H velocities and temperature profile S, for different values of* ϵ.

ϵ	$F'(0)$	$G'(0)$	$H(\infty)$	$S'(0)$
0	0.51023262	-0.61592206	-0.88447339	-0.32857284
0	*0.5102*	*-0.6159*	*-0.88447*	*-0.3285*
1	0.72166155	-0.90531614	-0.71418364	-0.30806332
2	0.88338965	-1.10969670	-0.59502185	-0.28658208
2	*0.8833*	*-1.1097*	*-0.59503*	*-0.2866*
3	1.02916791	-1.27641962	-0.51017318	-0.26669842
4	1.14081101	-1.42125005	-0.44882179	-0.24909599

Table C.1: *Values of $F', G'.S'$ at $z = 0$ and H at infinity for various values of ϵ.*

Appendix D

An eigen-solver for the rotating-disk boundary-layer

D.1 Method

The following method was developed using a technique described by Professor Neil Sandham of the University of Southampton, at a lecture course in Keele, in September 2006.

The sixth-order system (2.12) - (2.13) is solved using a Chebyshev-collocation method. Variables are expanded in terms of Chebyshev polynomials

$$u(\xi) = \sum_{k=0}^{N} \hat{u} T_k(\xi), \tag{D.1}$$

where T_k is the kth Chebyshev polynomial of the first kind and $\xi \epsilon [-1, 1]$ is the mapped wall normal coordinate, defined as

$$\xi = \frac{z - L}{z + L}, \tag{D.2}$$

where $L = 5$ for the subsequent problems and $z \epsilon [0, \infty]$ is the physical wall normal coordinate .

The derivative of the variable (D.1) is given as

$$u'_j = \sum_{j=0}^{N} D_{jk} u_k, \tag{D.3}$$

where the elements of the differentiation operator D are given as

$$\begin{aligned} D_{jk} &= \frac{c_j(-1)^{j+k}}{c_k(\xi_j - \xi_k)} \qquad j \neq k, \\ &= \frac{-\xi_j}{2(1-\xi_j^2)} \qquad j = k, j \neq 0, N, \\ &= \frac{2N^2+1}{6} \qquad j = k = 0, \\ &= \frac{-(2N^2+1)}{6} \qquad j = k = N, \end{aligned} \tag{D.4}$$

where

$$\begin{aligned} c_j &= 2 \qquad j = 0, N, \\ &= 1 \qquad 0 < j < N, \end{aligned} \tag{D.5}$$

and

$$\xi_j = -cos\left(\frac{\pi j}{N}\right) \qquad 0 \leq j \leq N. \tag{D.6}$$

Since we are considering a grid mapping (D.2), derivatives with respect to the physical component z are re-written as

$$\frac{du}{dz} = \frac{du}{d\xi}\frac{d\xi}{dz}, \tag{D.7}$$

$$\frac{d^2u}{dz^2} = \frac{d^2u}{d\xi^2}\left(\frac{d\xi}{dz}\right)^2 + \frac{du}{d\xi}\frac{d\xi^2}{dz^2}, \tag{D.8}$$

$$\frac{d^3u}{dz^3} = \frac{d^3u}{d\xi^3}\left(\frac{d\xi}{dz}\right)^3 + 3\frac{d^2u}{d\xi^2}\frac{d\xi}{dz}\frac{d\xi^2}{dz^2} + \frac{du}{d\xi}\frac{d\xi^3}{dz^3}, \tag{D.9}$$

$$\frac{d^4u}{dz^4} = \frac{d^4u}{d\xi^4}\left(\frac{d\xi}{dz}\right)^4 + 6\frac{d^3u}{d\xi^3}\left(\frac{d\xi}{dz}\right)^2\frac{d\xi^2}{dz^2} + 3\frac{d^2u}{d\xi^2}\left(\frac{d^2\xi}{dz^2}\right)^2 + 4\frac{d^2u}{d\xi^2}\frac{d\xi}{dz}\frac{d\xi^3}{dz^3} + \frac{du}{d\xi}\frac{d\xi^4}{dz^4}. \tag{D.10}$$

D.2 The temporal solver

The sixth-order system (2.12) - (2.13) is now rearranged into the companion matrix form

$$\Big(A_0 - \omega A_1\Big)(h,\eta)^T = 0, \tag{D.11}$$

where ω is the temporal frequency, h and η are variables defined earlier, and A_0 and A_1 are $2N \times 2N$ matrices. The elements of A_0 and A_1 can be easily identified by rearranging equations (2.12) - (2.13).

The corresponding spatial solver can be defined and evaluated using a similar method as was defined in appendix A.

D.3 Results

D.3.1 Convective instabilities

Stationary waves

Figure D.1 displays the neutral curves for the stationary convective instability for the rotating-disk boundary-layer with mass transfer. Here the dashed-dotted line refers to the case **a** = -0.5; solid line refers to the case **a** = 0; and the dashed line refers to the case **a** = 0.5, where **a** is negative for injection and positive for suction.

Figure D.2 displays the radial wavenumber spectra for the rotating-disk boundary-layer, where $Re = 286$, $\beta = 0.077$ and $\omega = 0$. The critical radial wavenumber for stationary waves is given as $\alpha = 0.38089$. There are also two continuous branches $\alpha \rightarrow \pm\beta$.

D.3.2 Absolute instability

Figure D.3 displays the frequency spectra for a Reynolds number $Re = 507.3$, radial wavenumber $\alpha = 0.2173 - 0.1216i$ and azimuthal wavenumber $\beta = 0.1348$. These are the critical values for absolute instability as found by Lingwood (1997). There

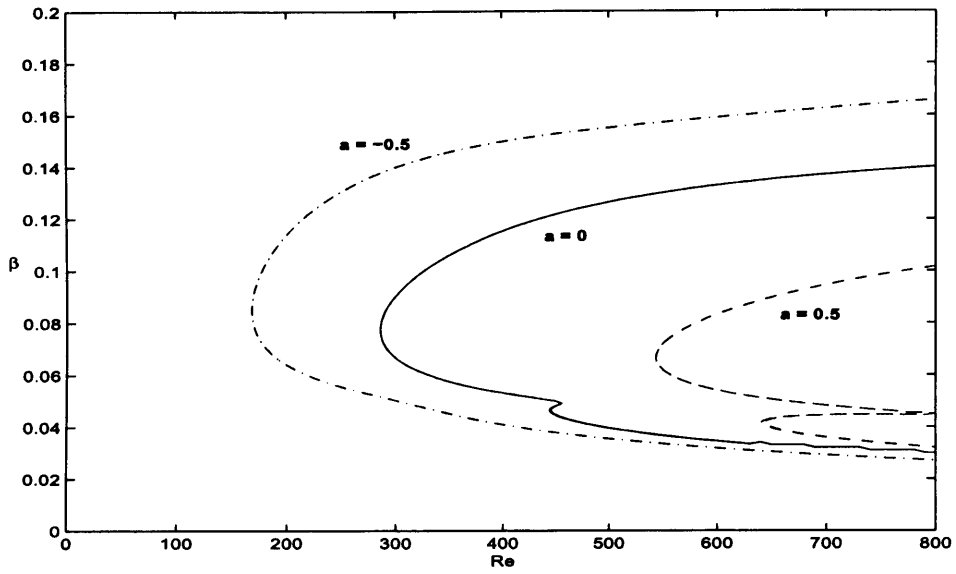

Figure D.1: *Neutral curves for the stationary convective instability for the rotating-disk boundary-layer with mass transfer.*

are two branches found asymptoting towards $\omega = 0$ and $\omega = -\beta$, while the critical frequency for absolute instability is given as $\omega = -0.03488$, where the imaginary part (which determines whether disturbances grow or decay in time) is zero (to five decimal places). This is (to four decimal places) comparable with that observed by Lingwood (1997); $\omega = -0.03485$ is the critical frequency in her study. Table D.1 displays several other comparisons between Lingwood (1997) and the above eigensolver method.

The sixth-order system (2.12) - (2.13) may also be extended to include

1. the family of rotating flows, BEK family,

2. a uniform magnetic field,

3. Hall effects, *etc.*

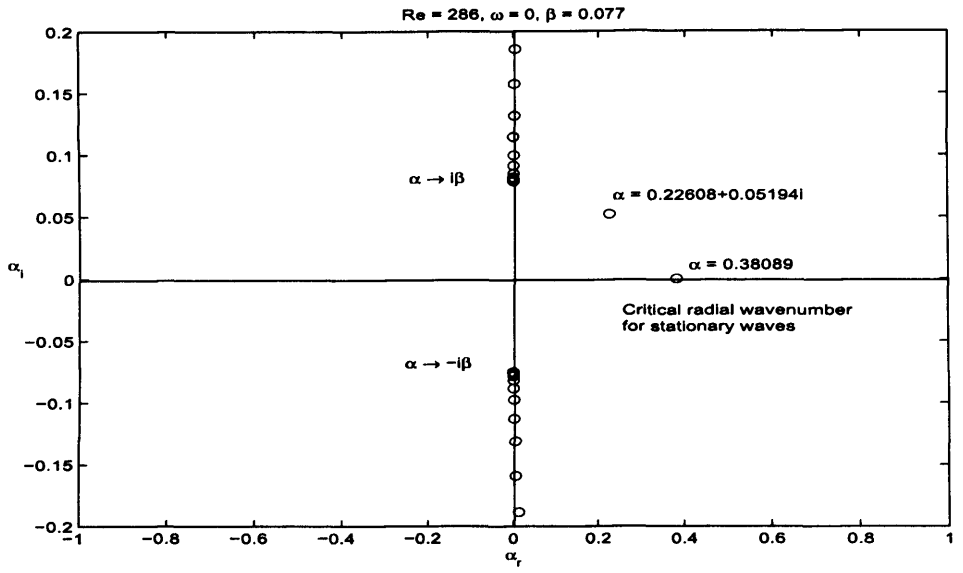

Figure D.2: *Radial wavenumber spectra for stationary waves* $\omega = 0$, *for azimuthal wavenumber* $\beta = 0.077$ *and Reynolds number* $Re = 286$.

a	Re_c	β_c	ω_c	α_c
-1.0	*201.54*	*0.1424*	*-0.03622*	*0.1735 - i0.1166*
-1.0			**-0.03626**	
-0.5	*309.71*	*0.1398*	*-0.03550*	*0.1903 - i0.1197*
-0.5			**-0.03552**	
0.0	*507.30*	*0.1348*	*-0.03485*	*0.2173 - i0.1216*
0.0			**-0.03488**	
0.5	*911.54*	*0.1235*	*-0.03261*	*0.2637 - i0.1228*
0.5			**-0.03265**	
1.0	*1860.82*	*0.1044*	*-0.02796*	*0.3420 - i0.1300*
1.0			**-0.02800**	

Table D.1: *Critical values for the onset of absolute instability as found by Lingwood (1997) - italics. (Table corresponds to table III in Lingwood (1997)). The values in bold correspond to the values found here.*

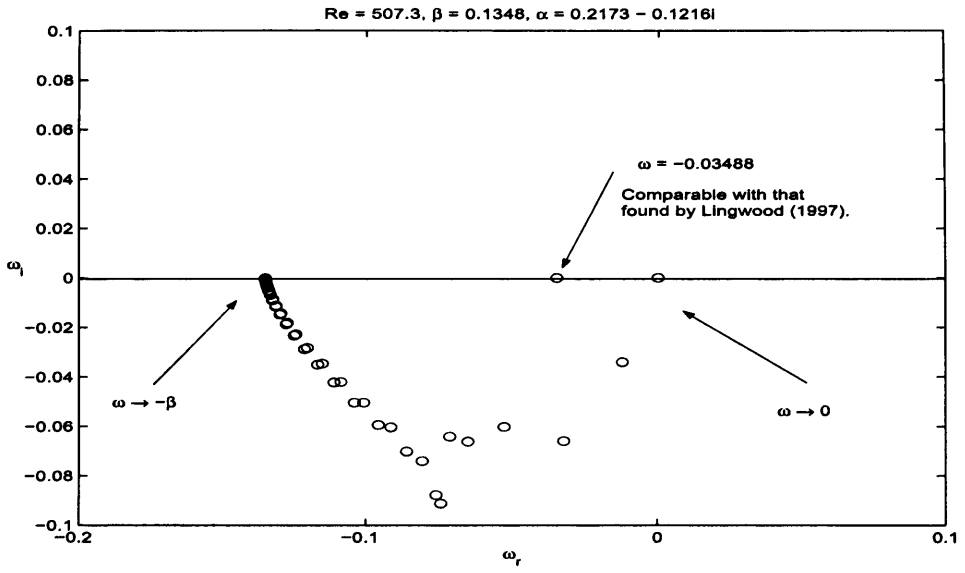

Figure D.3: *Frequency spectra for spatial wavenumber* $\alpha = 0.2173 - 0.1216i$, *azimuthal wavenumber* $\beta = 0.1348$ *and Reynolds number* $Re = 507.3$

Appendix E

Eigenvalue checks for the numerical simulations - part 1

Tables E.1, E.2 and E.3 display the eigenvalues found using the numerical simulation results for the rotating-disk with mass transfer, the rotating-disk with a magnetic field and the Ekman flow. The eigenvalues correspond to the stationary and travelling Type-1 and -2 modes. Subscripts s refer to stationary and subscripts t refer to travelling. Also included are the corresponding eigenvalues, given by previous authors. (Note: BM refers to Balakumar & Malik).

a	reference	Mode type	Re_c	β_c	ω_c	α_c
-0.5	Lingwood (1997)	2_t	62.9	-0.102	0.1253	0.264
-0.5	Current Thesis	2_t	63	-0.102	0.1253	0.2455
0.0	Malik (1986)	1_s	285.36	0.07759	-	0.38402
0.0	BM (1990)	1_s	286.1	0.07781	-	0.38643
0.0	Lingwood (1997a)	1_s	290.1	0.077	-	0.381
0.0	Current Thesis	1_s	290	0.077	-	0.3779
0.0	Malik (1986)	2_s	440.88	0.04672	-	0.13228
0.0	BM (1990)	2_s	451.4	0.04641	-	0.13109
0.0	Current Thesis	2_s	451	0.04641	-	0.1336
0.0	BM (1990)	1_t	283.36	0.09379	-0.01023	0.36661
0.0	Current Thesis	1_t	284	0.09379	-0.01023	0.36064
0.0	BM (1990)	2_t	64.46	-0.10594	0.12237	0.28027
0.0	Lingwood (1997)	2_t	64.4	-0.106	0.1225	0.276
0.0	Current Thesis	2_t	65	-0.106	0.1225	0.2661
0.5	Dhanak (1992)	1_s	552.776	0.06690	-	0.45876
0.5	Current Thesis	1_s	553	0.06690	-	0.44431
0.5	Dhanak (1992)	2_s	698.937	0.04113	-	0.15941
0.5	Current Thesis	2_s	699	0.04113	-	0.15905
0.5	Lingwood (1997)	2_t	87.9	-0.0775	0.0897	0.265
0.5	Current Thesis	2_t	88	-0.0775	0.0897	0.2601

Table E.1: *Critical points for the von Kármán layer and flows with injection/suction obtained for the stationary/travelling type 1 and 2 modes together with previous results from the literature.*

m	reference	Mode type	Re_c	β_c	ω_c	α_c
0.2	Jasmine (2003)	1_s	405.6	0.06584	-	0.4019
	Current Thesis	1_s	406	0.06584	-	0.3905
0.2	Jasmine (2003)	2_s	674.1	0.03826	-	0.1339
	Current Thesis	2_s	674	0.03826	-	0.1429
0.4	Jasmine (2003)	1_s	565.4	0.05726	-	0.4279
	Current Thesis	1_s	566	0.05726	-	0.4144
0.6	Jasmine (2003)	1_s	765.4	0.05087	-	0.4589
	Current Thesis	1_s	766	0.05087	-	0.4498
0.8	Jasmine (2003)	1_s	1004.1	0.04577	-	0.4900
	Current Thesis	1_s	1004	0.04577	-	0.4804
1.0	Jasmine (2003)	1_s	1278.4	0.04193	-	0.5140
	Current Thesis	1_s	1279	0.04193	-	0.5109

Table E.2: *Critical data for the rotating-disk boundary-layer with a uniform normal magnetic field, obtained for the stationary/travelling type 1 and 2 modes together with previous results from the literature.*

Reference	Mode type	Re_c	β_c	ω_c	α_c
Lingwood (1997a)	1_s	116.3	0.137	-	0.528
Current Thesis	1_s	116	0.137	-	0.5299
Lilly (1966)	1_t	110	0.0695	0.050	0.5280
Faller & Kaylor (1966)	1_t	118	0.1110	-	0.5712
Melander (1983)	1_t	112.75	0.0697	0.0518	0.5513
Faller (1991)	1_t	113.1	0.0663	-	0.548
Current Thesis	1_t	113	0.0663	0.0416	0.527
Lilly (1966)	2_t	55	-0.1089	0.187	0.2992
Faller + Kaylor (1966)	2_t	55	-0.0701	-	0.2618
Melander (1983)	2_t	54.155	-0.1364	0.1949	0.3162
Faller (1991)	2_t	54.3	-0.1331	-	0.312
Current Thesis	2_t	55	-0.1331	-	0.3142

Table E.3: *Critical points for the Ekman layer obtained for the stationary/travelling type 1 and 2 modes together with previous results from the literature.*

Appendix F

Eigenvalue checks for the numerical simulations - part 2

When validating the parallel numerical simulation results with those obtained by previous authors, the Reynolds number Re and azimuthal mode number n were always rounded to integer values; refer to tables 4.2, 5.2 and 6.2 of chapters 4, 5 and 6. This was done to avoid excessive parametric studies about the critical location for absolute instability. However, the temporal frequencies and radial wavenumbers obtained from the numerical simulations were always comparable (to a few decimal places) with those obtained by Lingwood (1995, 1997a,b) and Jasmine (2003). Nevertheless the reader may still have some doubts to the accuracy of the results.

Table F.1 and F.2 display temporal frequencies and radial wavenumbers for the rotating-disk boundary-layer, obtained using the parallel flow numerical simulation results. In table F.1 the azimuthal mode number $n = 68$, and the Reynolds number $Re = 507$, 508 and 509. While table F.2 displays the results for a Reynolds number $Re = 508$, and azimuthal mode numbers $n = 67$, 68 and 69. In each case, the temporal frequencies and radial wavenumbers are the same to two or three decimal places. Hence, the frequencies and radial wavenumbers do not vary much over small increments in the Reynolds number or azimuthal mode number. Therefore, the results given in tables 4.2, 5.2 and 6.2 of chapters 4, 5 and 6, (where the Reynolds number

and azimuthal mode number are rounded to integer values for the numerical simulations), are sufficient for comparing with those given by Lingwood (1995, 1997a,b) and Jasmine (2003).

Re_c	n_c	ω_c	α_c
507	68	-0.03447	0.2193 - i0.1153
508	68	-0.03435	0.2192 - i0.1153
509	68	-0.03423	0.2191 - i0.1152

Table F.1: *Eigenvalues for the rotating-disk boundary-layer, obtained using the numerical simulation results. The azimuthal mode number n = 68, while the Reynolds number Re = 507, 508 and 509.*

Re_c	n_c	ω_c	α_c
508	67	-0.03351	0.2184 - i0.1159
508	68	-0.03435	0.2192 - i0.1153
508	69	-0.03519	0.2199 - i0.1148

Table F.2: *Eigenvalues for the rotating-disk boundary-layer, obtained using the numerical simulation results. The azimuthal mode number n = 67, 68 and 69 while the Reynolds number Re = 508.*

Appendix G

Checks on the influence of the outflow boundary condition

As mentioned in earlier chapters, several checks were performed to ensure that the disturbance evolution was not contaminated by any spurious effects caused by the radial outflow boundary. Simulations were checked for a number of radial lengths, and in all cases considered, the disturbance behaviour displayed no significant differences. To illustrate this, we will look at the disturbance with an azimuthal mode number $n = 194$, which is impulsively excited at $r_e = 1861$. The suction/injection parameter $\mathbf{a} = 1$. Thus, the mean flow is subject to uniform suction.

Figure G.1 displays the time evolution of the disturbance at three equally spaced radial locations; $r = r_e$, $r = r_e + 25$ and $r = r_e + 50$. Data is presented from two different numerical simulations. For the data represented by dots, the radial outflow is located at $r_o = 2361$, while for the data represented by dashed lines, the outflow is at $r_o = 3001$. For the three radial locations there is no visible differences in the disturbance behaviour, over all time considered. For the radial location r_e, the disturbance initially decays, but eventually appears to asymptote towards a constant amplitude, while at the two other positions, temporal growth is visible for all time considered. This is equivalent behaviour to that observed earlier in the thesis.

Figure G.2 displays the radial variation of the disturbance wavepacket for three

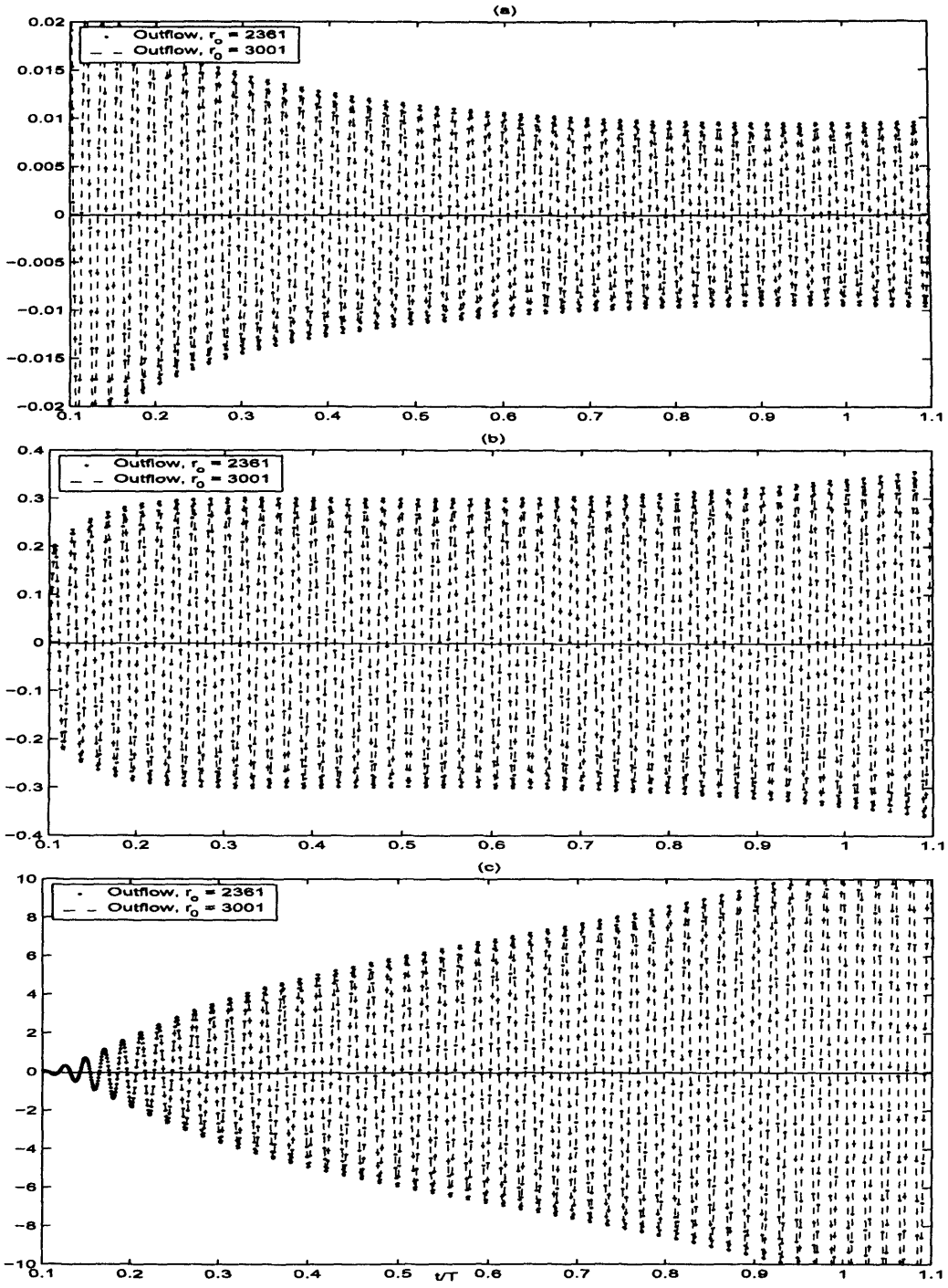

Figure G.1: *Instantaneous radial variation of* $\omega_{\theta,w}$ *for an impulsively excited disturbance with* $n = 194$, $r_e = 1861$ *and* $\boldsymbol{a} = 1$. *(a):* $r = r_e$; *(b):* $r = r_e + 25$; *(c):* $r = r_e + 50$. *The computational outflows are located at* $r_o = 2361$ *(dots);* $r_o = 3001$ *(dashed lines).*

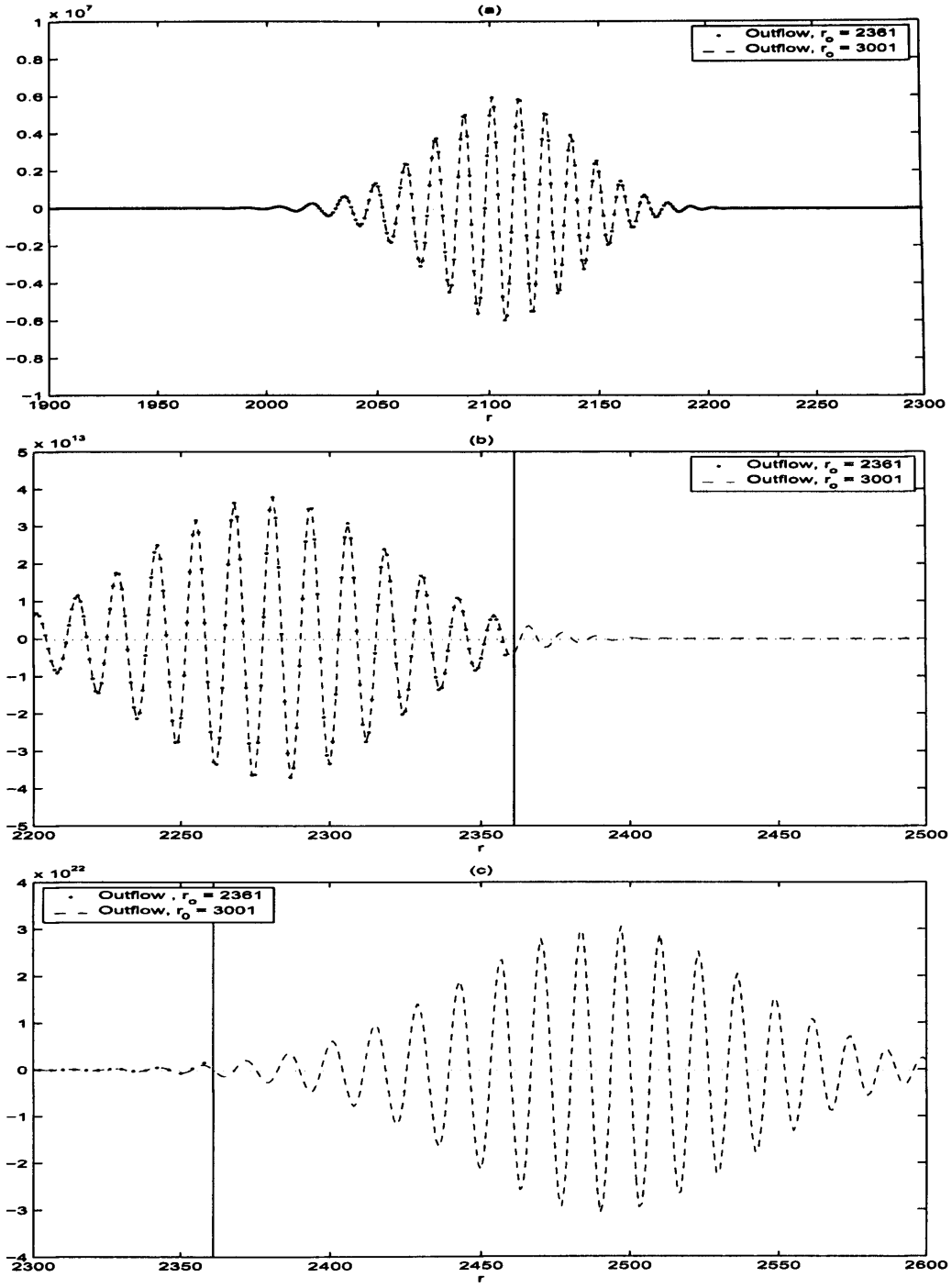

Figure G.2: *Instantaneous radial variation of* $\omega_{\theta,w}$ *for an impulsively excited disturbance with* $n = 194$, $r_e = 1861$ *and* $a = 1$. *(a):* $t/T = 0.612$; *(b):* $t/T = 0.948$; *(c):* $t/T = 1.305$. *The computational outflows are located at* $r_o = 2361$ *(dots) (indicated in (b) by a vertical line);* $r_o = 3001$ *(dashed lines).*

points in time; $t/T = 0.612$, $t/T = 0.948$ and $t/T = 1.305$. Again data is plotted for two simulations; dots correspond to outflow radius $r_o = 2361$ and dashed lines refer to $r_o = 3001$. For the first time instant, the maximum wavepacket amplitude is located well before the outflow boundary used in both simulations. For the second time instant, the disturbance amplitude at the outflow boundary, corresponding to the shorter radial length, is a significant fraction of the maximum wavepacket amplitude. This is not the case for the data obtained using the larger radial domain. The amplitude of the disturbance at the outflow is very small compared to the maximum amplitude. Nonetheless, there is no noticeable differences between the two simulations. For the third selected time, the maximum amplitude occurs after the outflow boundary of the simulation with the shorter radial length. However, there are again no discernible differences between the two simulations, and the shorter radial domain does not appear to have produced any spurious effects.

Appendix H

Frequency and growth rate solver

Consider the complex-valued quantity defined by

$$\omega = \frac{i}{A}\frac{\partial A}{\partial t}, \tag{H.1}$$

where A is taken to be the azimuthal vorticity $\omega_{\theta w}$. Once ω has been found, its real and imaginary parts may be interpreted as being the local temporal frequencies and local temporal growth rates, respectively. A central difference scheme was used to solve equation (H.1), where $A = A_n = a_n + ib_n$ and $\frac{\partial A_n}{\partial t} = \frac{A_{n+1} - A_{n-1}}{2\Delta t}$. The following code was then used to calculate the frequency and growth rate for some given disturbance.

```
function omega = frequency(A);
% Ensure A is of the form A = a + ib,
% where a and b are the real and imaginary parts of A, i is complex.
% Boundary conditions
    u0 = f(1);
    u1 = f(2);
    f(l+1) = 0;
```

```
    l = length(f);
% For loop
    for n = 2:l
            omega(n) = Re*i*(f(n+1) - f(n-1))/(f(n)*2*Δt);
    end

% Where Re is the Reynolds number and Δt is the time step. The real and imaginary
& parts of 'omega' then give the temporal frequency and growth rate.
& A similar method can be used to calculate the spatial wavenumber
& and growth rate.
```

Appendix I

Green's function solver

The following code was used to calculate the Green's function for constant stability. A similar approach could be used for the linearly varying and quadratically varying stability problems.

```
% Reynolds number/inner radius
    R = ;
% Time period
    T = 2*pi*R;
% Leading-edge
    UL = ;
    UL = UL/T;
% Trailing-edge
    UT =;
    UT = UT/T;
% Local growth rate
    mu0 = ;
    mu0 = mu0/R;
% Local frequency
```

```
    w0 =
% Imaginary part of wavenumber
    ai = ;
% Real part of wavenumber
    ar = ;
    a = ar+i*ai;
% Real part of diffusion/dispersion parameter
    gamr = -(UL+UT)/(4*ai);
% Imaginary part of diffusion/dispersion parameter
    gami = gamr*(∂α_{l,r}/∂r ÷ ∂α_{l,i}/∂r);
% Fixed constant M
    M = 1700;
% Calculate Green's function for fixed x
    for t = 1:1:M
            x = ;
            Ga(t) = sqrt((gamr-i*gami)/(4*pi*t));
            Ga(t) = Ga(t)*exp(mu0*t-(x*x)*gamr/(4*t));
            Ga(t) = Ga(t)*exp(i*(x*x)*gami/(4*t) + i*ar*x - ai*x);
    end
% Calculate complex frequency
    for n = 3:M-1
            w1(n) = i*(Ga(n+1) - Ga(n-1))/(Ga(n)*2);
    end
% Frequency
    b11=w0+real(R*w1);
% Growth rate
    c11=imag(R*w1);
```

Appendix J

The Ginzburg-Landau equation with a smeared impulse

In section 8.2, the parallel rotating-disk numerical simulations were modeled using the Ginzburg-Landau equation (8.3) with constant stability $\mu = \mu_0$. However, when attempting to plot the frequencies and growth rates for the Green's solution (8.8) to the Ginzburg-Landau equation, the data lines $r_e - 25$ and $r_e + 25$ were found to overlap. This was due to the symmetry about $r = r_e = 0$ (the point of forcing).

To overcome this problem, we will consider a smeared impulsive distribution, instead of a point forcing. Figure J.1 displays a smeared impulsive distribution (solid line) and a point forcing (dotted line). Here k is a small displacement about the radial position r.

We assume that the Green's function (8.8) can be approximately given as

$$G(r,t) \sim G(r+k,t) + G(r-k,t), \tag{J.1}$$

for the smeared impulsive distribution. The complex-valued expression (8.11) may once again be called upon to calculate the local frequencies and growth rates, where G is the Green's function (J.1) at all spatial positions and points in time. The real and imaginary parts may be interpreted as being, the local temporal frequency and

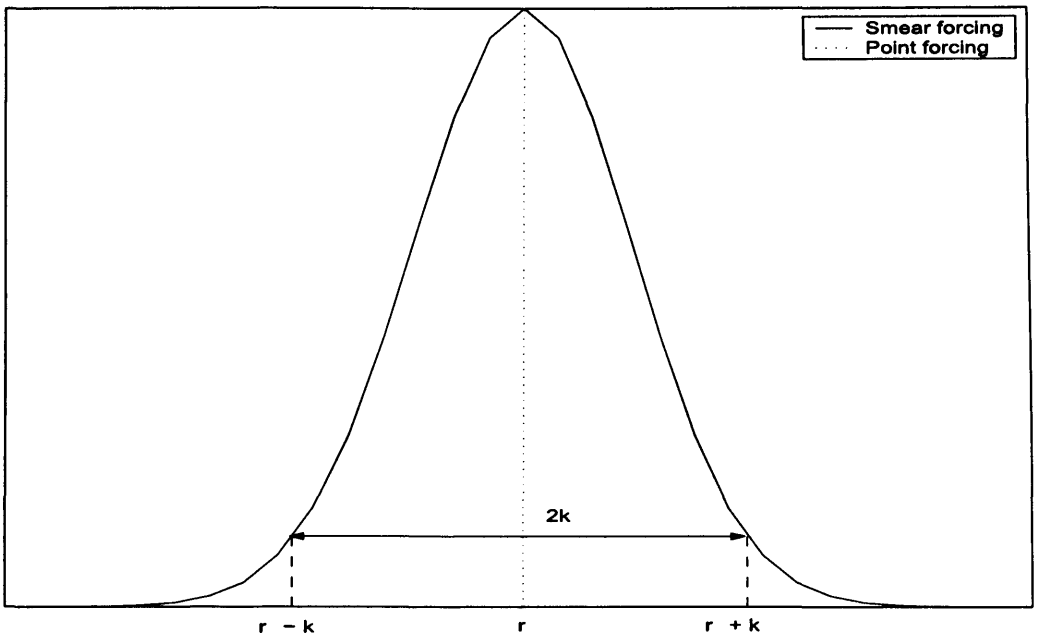

Figure J.1: *Plot depicting a smeared impulsive distribution (solid line) and a point forcing (dotted line).*

local temporal growth rate, respectively. The complex frequency is given as

$$\omega_l = -\mu_{0,i} + \frac{\gamma_i(r^2+k^2)}{4|\gamma|^2t^2} + \frac{\gamma_i kr}{2|\gamma|^2t^2}H + i\left\{\bar{\mu}_{0,r} - \frac{1}{2t} + \frac{\gamma_r(r^2+k^2)}{4|\gamma|^2t^2} + \frac{\gamma_r kr}{2|\gamma|^2t^2}H\right\}, \quad \text{(J.2)}$$

where

$$\begin{aligned} H &= \frac{G(r+k)-G(r-k)}{G(r+k)+G(r-k)}, \\ &= \frac{i\{\sin(\alpha k)+\sin(\frac{\gamma_i kr}{2|\gamma|^2t})\}-\sinh(\frac{\gamma_r kr}{2|\gamma|^2t})}{\cos(\alpha k)+\cos(\frac{\gamma_i kr}{2|\gamma|^2t})+\cosh(\frac{\gamma_r kr}{2|\gamma|^2t})}. \end{aligned} \quad \text{(J.3)}$$

Hence, the local frequency and growth rate are given as

$$\omega_{l,r} = -\mu_{0,i} + \frac{\gamma_i(r^2+k^2)}{4|\gamma|^2t^2} - \frac{kr}{2|\gamma|^2t^2}\left\{\frac{\gamma_r\{\sin(\alpha k)+\sin(\frac{\gamma_i kr}{2|\gamma|^2t})\}+\gamma_i\sinh(\frac{\gamma_r kr}{2|\gamma|^2t})}{\cos(\alpha k)+\cos(\frac{\gamma_i kr}{2|\gamma|^2t})+\cosh(\frac{\gamma_r kr}{2|\gamma|^2t})}\right\}, \quad \text{(J.4)}$$

$$\omega_{l,i} = \mu_{0,r} - \frac{1}{2t} + \frac{\gamma_r(r^2+k^2)}{4|\gamma|^2t^2} + \frac{kr}{2|\gamma|^2t^2}\left\{\frac{\gamma_i\{\sin(\alpha k)+\sin(\frac{\gamma_i kr}{2|\gamma|^2t})\} - \gamma_r\sinh(\frac{\gamma_r kr}{2|\gamma|^2t})}{\cos(\alpha k)+\cos(\frac{\gamma_i kr}{2|\gamma|^2t})+\cosh(\frac{\gamma_r kr}{2|\gamma|^2t})}\right\}. \tag{J.5}$$

We may now use the above expressions (J.4) and (J.5), to show that the local frequencies and growth rates, at the positions $r_e - 25$ and $r_e + 25$, are different. (Note: $r_e = 0$). The absolute differences in the local frequencies and growth rates may be given (after some manipulation) as

$$|\omega_{l,r}(r_e+25) - \omega_{l,r}(r_e-25)| = \frac{25\gamma_r k}{|\gamma|^2t^2}\left\{\frac{\sin(\alpha k)}{\cos(\alpha k)+\cos(\frac{25\gamma_i k}{2|\gamma|^2t})+\cosh(\frac{25\gamma_r k}{2|\gamma|^2t})}\right\}, \tag{J.6}$$

$$|\omega_{l,i}(r_e+25) - \omega_{l,i}(r_e-25)| = \frac{25\gamma_i k}{|\gamma|^2t^2}\left\{\frac{\sin(\alpha k)}{\cos(\alpha k)+\cos(\frac{25\gamma_i k}{2|\gamma|^2t})+\cosh(\frac{25\gamma_r k}{2|\gamma|^2t})}\right\}. \tag{J.7}$$

Since $k > 0$, the data lines $r_e - 25$ and $r_e + 25$ will follow different paths towards the constant frequency and growth rate, found at large time t/T.

J.1 Example

In keeping with the earlier study on the Green's solution to the Ginzburg-Landau equation (refer to chapter 8), the example chosen, is the rotating-disk boundary-layer, where the Reynolds number $Re = 530$ and the azimuthal mode number $n = 68$. For a smeared impulsive distribution, the Green's solution (8.8) is estimated as

$$G(r,t) = 0.1\{G(r+5,t)+G(r-5,t)\}+0.4\{G(r+2.5)+G(r-2.5)\}+0.6G(r,t). \tag{J.8}$$

Using the expressions and parameter constants given in section 8.2.2, we are able to calculate the local frequencies and growth rates for the Green's function (J.8). Figure J.2 displays the corresponding local frequencies and growth rates at the radial positions $r = r_e - 25$ and $r = r_e + 25$. The data lines follow different paths towards the complex frequency ($\omega_l \approx -16.4 + i0.2$) found for large time t/T.

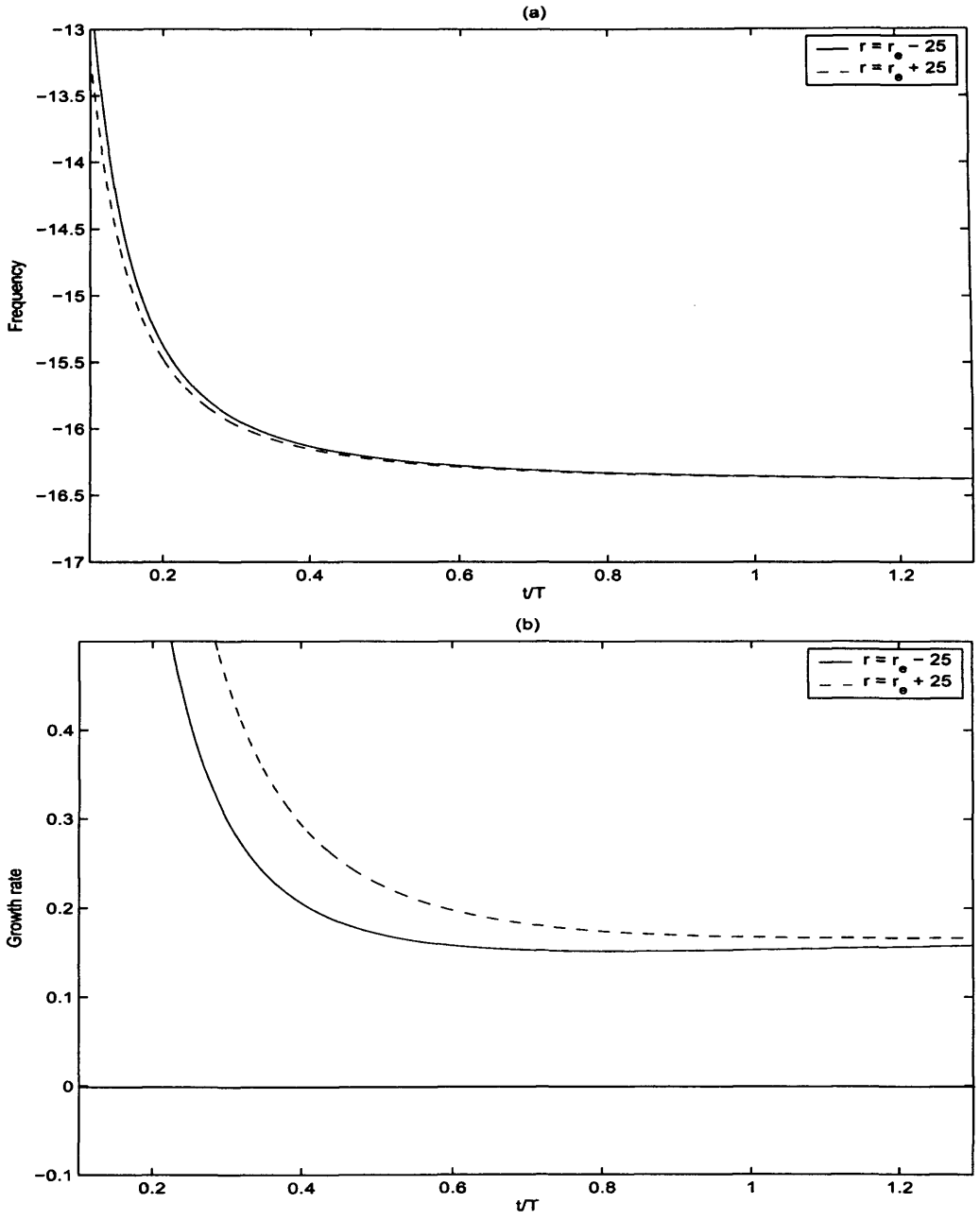

Figure J.2: *The temporal frequencies (a) and growth rates (b), at the positions* $r = r_e - 25$ *and* $r = r_e + 25$, *for the Green's function (J.8). The plots are matched to the rotating-disk boundary-layer, where* $Re = 530$, $n = 68$ *and* $r_e = 530$.

Appendix K

The Ginzburg-Landau equation - quadratically varying stability

In chapter 8, the numerical simulations for the rotating-disk were modeled using the Green's solutions to the Ginzburg-Landau model. The stability parameter μ that appeared in the Green's solutions, was a constant when we wanted to match the parallel numerical simulation results, and was linearly varying when we attempted to match the non-parallel numerical simulations.

We will now consider the Ginzburg-Landau equation with a quadratically varying stability term; $\mu(r) = \mu_0 + \mu_1 r + \frac{1}{2}\mu_2 r^2$. Here μ_2 is assumed to be a real negative.

K.1 Quadratic variation of the stability parameter μ - (a)

For the case where γ and μ are real only, Hunt & Crighton obtained the following exact expression for the Green's function to the Ginzburg-Landau equation (8.3)

$$
\begin{aligned}
G_0(r,t) &= \exp\left[\left(\mu_0 - \frac{\mu_1^2}{2\mu_2} - \frac{U^2}{4\gamma}\right)t + \frac{Ur}{2\gamma} + \frac{\mu_1}{\sqrt{(-2\mu_2\gamma)}}\right. \\
&\times \left.\left(r + \frac{\mu_1}{\epsilon\mu_2}\right)\tanh\left(\frac{1}{2}\sqrt{(-2\mu_2\gamma)}\epsilon t\right) - \epsilon r^2 \frac{\sqrt{(-2\mu_2\gamma)}}{4\gamma}\coth(\sqrt{(-2\mu_2\gamma)}\epsilon t)\right] \\
&\times \left(\frac{\epsilon\sqrt{(-2\mu_2\gamma)}}{4\pi\gamma\sinh(\sqrt{(-2\mu_2\gamma)}\epsilon t)}\right)^{\frac{1}{2}}, \qquad \text{(K.1)}
\end{aligned}
$$

where we let $\epsilon = 1$ and all other terms are as given in chapter 8.

The edges of the wavepacket occur along $r^2 \sim (\sqrt{(-8\gamma/\mu_2)}(\mu_{max} - U^2/4\gamma) - 2\gamma)t$ as time tends to infinity. Here μ_{max} is the maximum value that $\mu(x)$ takes, i.e. $\mu_{max} = \mu_0 - \mu_1^2/(2\mu_2)$. The flow is globally stable, if the equation for the wavepacket edges has no real solution. This arises if either

$$\mu_{max} - U^2/4\gamma < 0, \qquad \text{(K.2)}$$

or

$$(\mu_{max} - U^2/4\gamma)^2 < -\frac{1}{2}\mu_2\gamma. \qquad \text{(K.3)}$$

(See equations (42) and (43) of Hunt & Crighton (1991)). If (K.2) is satisfied, the flow is either: locally stable everywhere, providing $\mu_0 < 0$, or there exists a region of local convective instability, if $0 < \mu_0 < U^2/4\gamma$. In this last instance the disturbance is convected through the region of instability into the region of stability, where it is eventually damped. The second condition (K.3), implies that a small region of local absolute instability exists, but on the whole the flow is globally stable. If neither condition holds, the flow is globally unstable.

K.2 Quadratic variation of the stability parameter μ - (b)

The diffusion/dispersion term γ and stability parameter μ are now allowed to be complex. By considering the full disturbance structure $G(x,t) = G_0\exp\{i(\alpha_s x - \omega_s t)\}$,

we obtain the Green's function

$$\begin{aligned} G(r,t) &= \exp\left[\left(\bar{\mu}_0 + \frac{(\gamma_r + i\gamma_i)\mu_1^2}{\eta^2}\right)t + \frac{\mu_1}{\eta}\left(r - \frac{2(\gamma_r + i\gamma_i)\mu_1}{\eta}\right)\tanh(\frac{1}{2}\eta t)\right. \\ &\quad \left. -r^2\frac{(\gamma_r - i\gamma_i)\eta}{4|\gamma|^2}\coth(\eta t) + i\hat{\alpha}_s r\right]\left(\frac{(\gamma_r - i\gamma_i)\eta}{4\pi|\gamma|^2\sinh(\eta t)}\right)^{\frac{1}{2}}, \\ &= G_* \exp(i\hat{\alpha}_s r), \end{aligned} \tag{K.4}$$

where G_0 is equation (K.1). Here $\hat{\alpha}_s$ is the complex wavenumber, obtained from the numerical simulation results; $\bar{\mu}_0 = -i\omega_s$ (where ω_s is the numerical simulation complex frequency), and μ_1 and γ are again given by equations (8.22), (8.25), (8.26), (8.36) and (8.37). The stability parameter μ_2 has been replaced by η, where

$$\eta^2 = -2\mu_2\gamma. \tag{K.5}$$

Since γ is allowed to complex, η will also be complex. However, we will only consider real η for the subsequent discussion, so as to simplify the problem.

The local frequency and growth rate for equation (K.4) are obtained by applying the complex-valued expression (8.11). The full and limiting behaviour solutions, are given as

$$\begin{aligned} \omega_{l,r} &= -\bar{\mu}_{0,i} + \frac{\gamma_i\eta^2 r^2}{4|\gamma|^2}\mathrm{cosech}^2(\eta t) - \frac{\mu_{1,i}r}{2}\mathrm{sech}^2\left(\frac{1}{2}\eta t\right) \\ &\quad -\frac{\tanh^2(\frac{1}{2}\eta t)}{\eta^2}\left(2\gamma_r\mu_{1,r}\mu_{1,i} + \gamma_i(\mu_{1,r}^2 - \mu_{1,i}^2)\right), \end{aligned} \tag{K.6}$$

$$\rightarrow -\bar{\mu}_{0,i} - \frac{1}{\eta^2}\left(2\gamma_r\mu_{1,r}\mu_{1,i} + \gamma_i(\mu_{1,r}^2 - \mu_{1,i}^2)\right) \text{ as } t \rightarrow \infty, \tag{K.7}$$

and

$$\begin{aligned} \omega_{l,i} &= \bar{\mu}_{0,r} + \frac{\gamma_r\eta^2 r^2}{4|\gamma|^2}\mathrm{cosech}^2(\eta t) + \frac{\mu_{1,r}r}{2}\mathrm{sech}^2\left(\frac{1}{2}\eta t\right) - \frac{\eta}{2}\coth(\eta t) \\ &\quad +\frac{\tanh^2(\frac{1}{2}\eta t)}{\eta^2}\left(\gamma_r(\mu_{1,r}^2 - \mu_{1,i}^2) - 2\gamma_i\mu_{1,r}\mu_{1,i}\right), \end{aligned} \tag{K.8}$$

$$\rightarrow \bar{\mu}_{0,r} + \frac{1}{\eta^2}\left(\gamma_r(\mu_{1,r}^2 - \mu_{1,i}^2) - 2\gamma_i\mu_{1,r}\mu_{1,i}\right) \text{ as } t \rightarrow \infty. \tag{K.9}$$

Equations (K.7) and (K.9) arise, since $\tanh(\frac{1}{2}\eta t) \to 1$, $\coth(\eta t) \to 1$, $\mathrm{sech}(\frac{1}{2}\eta t) \to 0$ and $\mathrm{cosech}(\eta t) \to 0$ as $t \to \infty$. Hence, for large time t, the frequency and growth rate asymptote towards constant values. The long term behaviour of the frequency and growth rate will be discussed later in the section.

The local frequency (K.6) and growth rate (K.8) are to first order, in η, given as

$$\omega_{l,r} = \text{Equation (8.38)} + \Delta(\eta^2), \tag{K.10}$$

$$\omega_{l,i} = \text{Equation (8.39)} + \Delta(\eta^2), \tag{K.11}$$

which are obtained by approximating the hyperbolic functions to first order, i.e. $\cosh(\eta t) = 1$ and $\sinh(\eta t) = \eta t$. Thus, to first order, the local frequency and growth rate are identical to the results obtained for a linearly varying stability parameter μ; refer to section 7.2.6. It is quite obvious that for the first order equations (K.10) and (K.11), the earlier constraints (8.41) and (8.43), also hold. Hence, to at least first order (in η) the disturbance behaviour is dependent on the parameters γ and μ_1.

Expressions for the complex wavenumber are obtained by applying equation (8.14) (where G is taken to be the Green's function (K.4)). The full and limiting behaviour solutions to the wavenumber and spatial growth rate are given as

$$\alpha_{l,r} = \hat{\alpha}_{s,r} + \frac{\gamma_i \eta r}{2|\gamma|^2}\coth(\eta t) + \frac{\mu_{1,i}}{\eta}\tanh(\frac{1}{2}\eta t), \tag{K.12}$$

$$\to \hat{\alpha}_{s,r} + \frac{\gamma_i \eta r}{2|\gamma|^2} + \frac{\mu_{1,i}}{\eta} \quad \text{as } t \to \infty, \tag{K.13}$$

and

$$\alpha_{l,i} = \hat{\alpha}_{s,i} + \frac{\gamma_r \eta r}{2|\gamma|^2}\coth(\eta t) - \frac{\mu_{1,r}}{\eta}\tanh(\frac{1}{2}\eta t), \tag{K.14}$$

$$\to \hat{\alpha}_{s,i} + \frac{\gamma_r \eta r}{2|\gamma|^2} - \frac{\mu_{1,r}}{\eta} \quad \text{as } t \to \infty, \tag{K.15}$$

where we have used the fact that $\tanh(\frac{1}{2}\eta t) \to 1$ and $\coth(\eta t) \to 1$ as $t \to \infty$.

We assume for convenience that $\bar{\mu}_0$, γ and μ_1 are as defined in chapter 8. (Refer to equations (8.10), (8.22), (8.25), (8.26), (8.36) and (8.37)). The only term left to define

(if we are to model the numerical simulation results using the Green's function (K.4)) is the parameter η. This can be derived by calculating the streamwise $r-$derivatives of the solutions (K.13) and (K.15). On rearranging, η may be given as

$$\eta = 2\frac{|\gamma|^2}{\gamma_i}\frac{\partial \alpha_{l,r}}{\partial r}, \tag{K.16}$$

or

$$\eta = 2\frac{|\gamma|^2}{\gamma_r}\frac{\partial \alpha_{l,i}}{\partial r}. \tag{K.17}$$

(It is worth noting that $(K.16) \div (K.17)$ and rearranging, gives the expression (8.26)). The derivatives $\frac{\partial \alpha_{l,r}}{\partial r}$ and $\frac{\partial \alpha_{l,i}}{\partial r}$ are calculated using the numerical simulation results of the rotating-disk boundary-layer.

K.2.1 Comparing the Green's functions with linearly and quadratically varying stability μ

Figures K.1(a, b) and K.2 display the local frequency, growth rate and the disturbance development wavepacket, for the Green's function with a linearly varying stability parameter μ (labeled L and dotted lines in figure K.2), and the Green's function with a quadratically varying stability parameter μ (labeled Q and solid lines in figure K.2). The plots are modeled to match the non-parallel numerical simulation results for the rotating-disk boundary-layer, where the point of forcing $r_e = 530$ and azimuthal mode number $n = 68$. The frequencies and growth rates are plotted for four equally spaced locations, r_e - 25, r_e = 530, r_e + 25 and r_e + 50. All variables are as stated in the examples given in chapter 8; i.e. $\bar{\mu}_0 \approx 0.2 + i16.4$, $\hat{\alpha}_s \approx 0.21 - i0.12$, $U_L \approx 400$, $U_T \approx -8$, $\gamma_i/\gamma_r \approx 1.2$, $\frac{d\omega_{l,r}}{dr} \approx 0.012$ and $\frac{d\omega_{l,i}}{dr} \approx 0.003$. The parameter η was calculated using (K.16), where it was found that $\frac{\partial \alpha_{l,r}}{\partial r}$ could be given as approximately 10^{-4}.

For the time period considered, the frequencies, growth rates (for both L and Q problems) increase and decrease, respectively. The spatio-temporal disturbance wavepackets are also similar, since the trailing edges initially propagate inwards, but eventually reverse direction and propagate downstream.

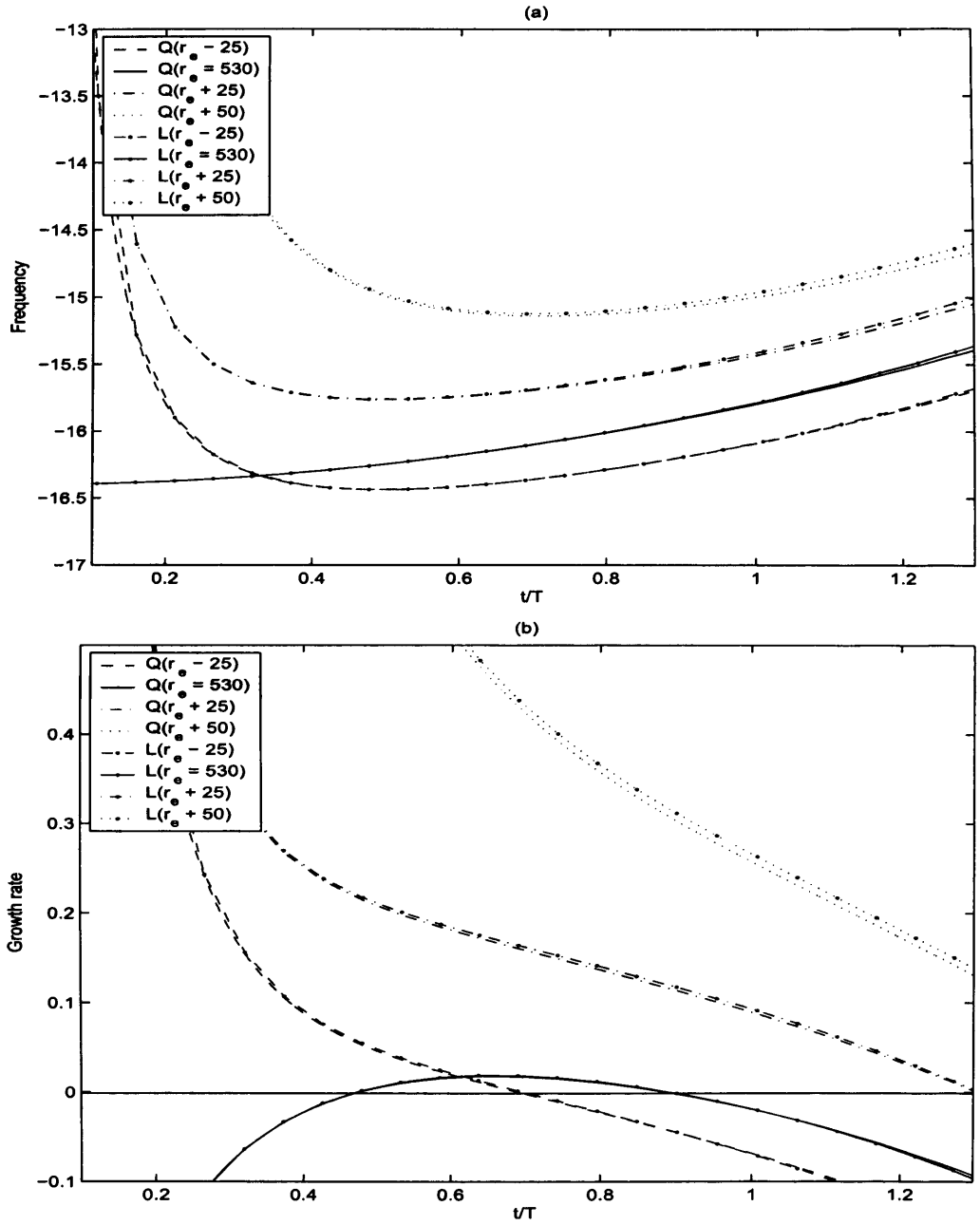

Figure K.1: *The frequencies (a) and growth rates (b), for the Green's function with a linearly varying stability μ; (labeled L) and quadratically varying stability μ; (labeled Q). The frequencies and growth rates are plotted for four equally spaced streamwise points. The case corresponds to the rotating-disk boundary-layer, with point of forcing $r_e = 530$ and $n = 68$.*

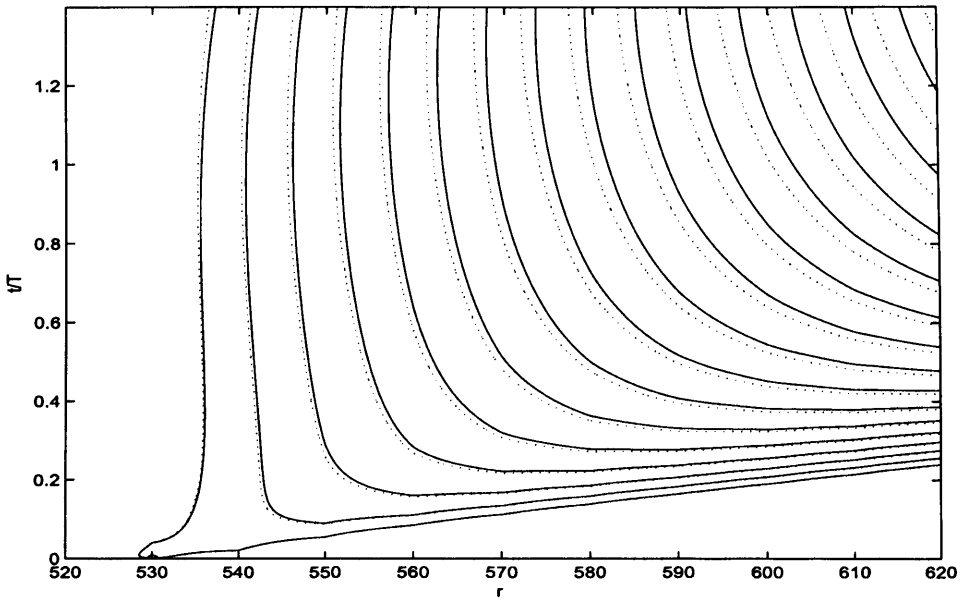

Figure K.2: *The wavepacket for the Green's function with a linearly varying stability μ; (dotted lines) and quadratically varying stability μ; (solid lines). The case corresponds to the rotating-disk boundary-layer, with point of forcing $r_e = 530$ and $n = 68$. (Contours are drawn using a logarithmic scale, with levels separated by factors of two).*

K.2.2 The long-term behaviour

The long-term behaviour of the frequencies and growth rates can be identified by equations (K.7) and (K.9), respectively. Both the frequency and growth rate asymptote towards constants, as time tends to infinity. Hence, the global response to the disturbance will be governed by the value given by equation (K.9). If this value is positive, global instability occurs, but if the value is negative, global stability prevails.

Figures K.3 and K.4 display the long-term behaviour of the frequencies, growth rates and disturbance wavepacket for the Green's function with a linearly varying stability parameter μ (labeled L and dotted lines in figure K.2), and the Green's

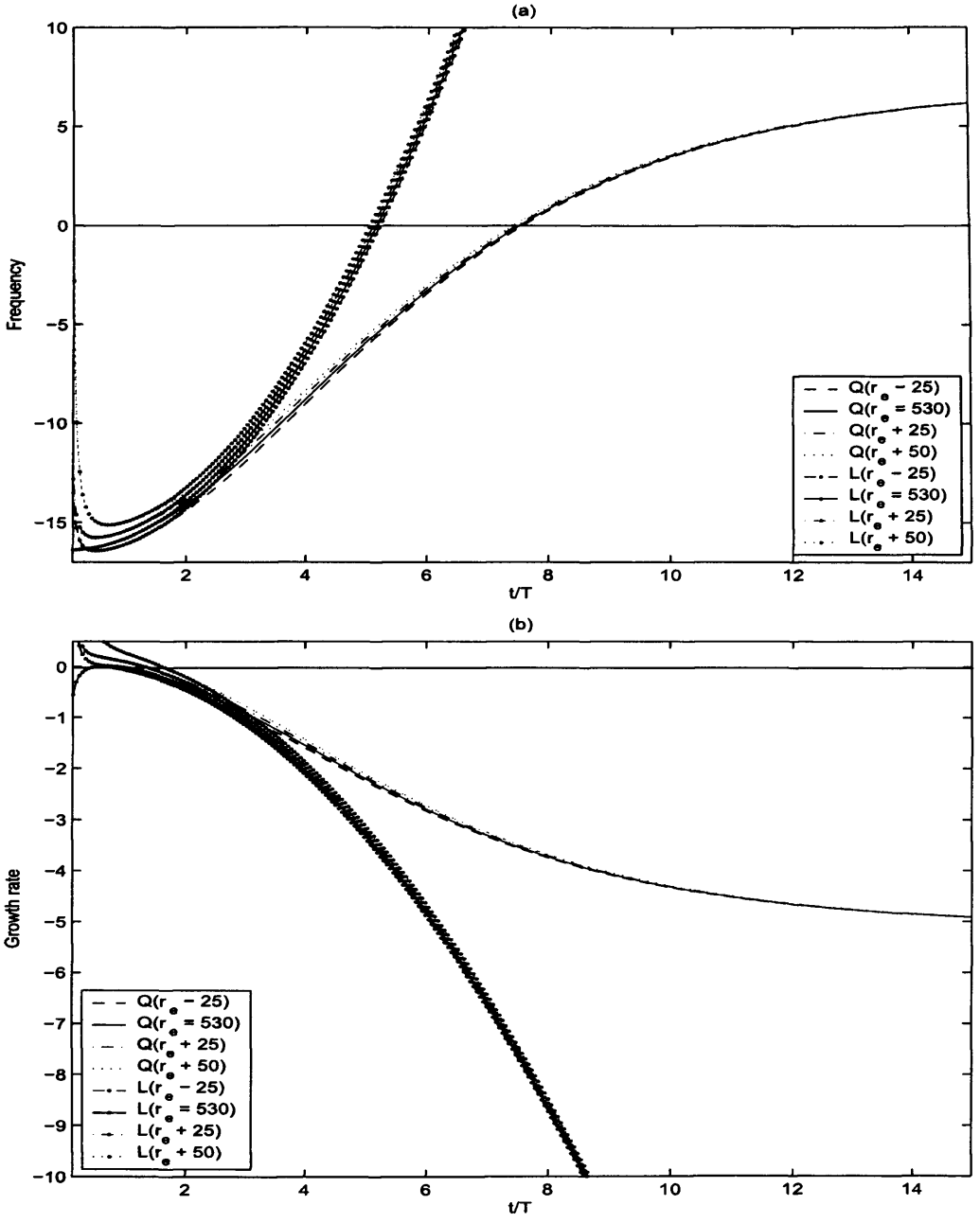

Figure K.3: *he frequencies (a) and growth rates (b), for the Green's function with a linearly varying stability μ; (labeled L) and quadratically varying stability μ; (labeled Q). The frequencies and growth rates are plotted for four equally spaced streamwise points. The case corresponds to the rotating-disk boundary-layer, with point of forcing $r_e = 530$ and $n = 68$.*

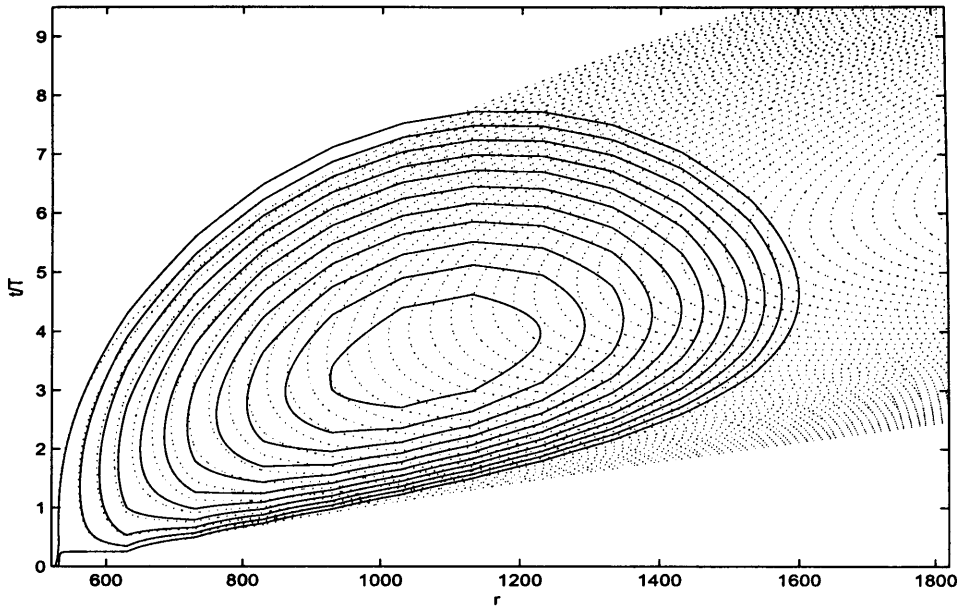

Figure K.4: *The wavepacket for the Green's function with a linearly varying stability μ; (dotted lines) and quadratically varying stability μ; (solid lines). The case corresponds to the rotating-disk boundary-layer, with point of forcing r_e = 530 and n = 68. (Contours are drawn using a logarithmic scale, with levels separated by factors of two).*

function with a quadratically varying stability parameter μ (labeled Q and solid lines in figure K.2). The plots are modeled to match the non-parallel numerical simulation results for the rotating-disk boundary-layer, where the point of forcing $r_e = 530$ and azimuthal mode number $n = 68$. The frequencies and growth rates have been plotted for t=*15T*, and the wavepackets have been plotted for t=*9.5T*, where $T = 2\pi r_a$ is the period of one rotation of the disk and r_a is the inner radius.

The frequency at all selected streamwise locations, is found to tend towards a constant in the region $\omega_r r_a = 7$, while the growth rate at all selected points is found to asymptote towards a constant near $\omega_i r_a$ = -5. This would imply global stability.

The disturbance wavepacket for the quadratically varying stability problem (illustrated in figure K.4, solid lines), displays a disturbance, convected outwards. The leading edge propagates with a diminishing velocity, which eventually reverses direction and propagates inwards, while the trailing edge propagates with an increasing velocity. The edges of the disturbance wavepacket eventually meet, and the unstable disturbance is enclosed within this region. Hence, global stability prevails.

Appendix L

Publications

L.1 Paper 1

Christopher Davies & Christian Thomas - Global stability of the rotating disk boundary layer and the effects of suction and injection, Bulletin of the American Physical Society, 58th Annual Meeting of the Division of Fluid Dynamics, Chicago, Illinois, 50(9):266, 2005.

The von Kármán boundary layer over a rotating disk is known to be absolutely unstable (Lingwood 1995). However, numerical simulations indicate that this absolute instability does not give rise to an unstable linear global mode, when account is taken of the radial dependence of the basic flow (Davies & Carpenter 2003). Analogous behaviour can be found in solutions of the linearized complex Ginzburg-Landau equation, similar to those derived by Hunt & Crighton (1991). These solutions show that detuning, arising from the radial variation of the local temporal frequency, may be enough to globally stabilize disturbances, even when local temporal growth rates increase with radius. Depending on the precise balance between the radial increase in growth rates and the corresponding shifts in frequency, it is possible for an absolutely unstable flow to remain globally stable. For the von Kármán rotating disk boundary layer, the earlier numerical simulation results suggest that the balance in this case

does in fact give rise to global stability. Similar behaviour has been identified in more recent numerical simulations that we have conducted, where mass injection was introduced at the disk surface. The modified flow still appears to be globally stable, despite the fact that injection is known to be locally destabilizing. More interestingly, it was also found that globally unstable behaviour was promoted when suction was applied.

L.2 Paper 2

Christopher Davies & Christian Thomas - The effects of a uniform axial magnetic field on the global stability of the rotating-disk boundary-layer, Bulletin of the American Physical Society, 59th Annual Meeting of the Division of Fluid Dynamics, Tampa Bay, Florida, 51(9):74, 2006.

Following on from the earlier discovery by Lingwood (1995) that the rotating-disk boundary-layer is absolutely unstable, Jasmine & Gajjar (2005) have shown that the application of a uniform axial magnetic field can raise the critical Reynolds number for the onset of absolute instability. As with Lingwood's analysis, a 'parallel-flow' type of approximation is needed to derive this locally-based stability result. The approximation amounts to a 'freezing out' of the underlying radial variation of the mean flow. Numerical simulations have been conducted to investigate the behaviour of linearized disturbances in the genuine rotating-disk boundary-layer, where the radial dependence of the mean flow is fully accounted for. This extends the work of Davies & Carpenter (2003), who studied the more usual rotating-disk problem, in the absence of any magnetic field. The simulation results suggest that globally unstable behaviour can be promoted when a uniform axial magnetic field is applied. Impulsively excited disturbances were found to display an increasingly rapid growth at the radial position of the impulse, albeit without any selection of a dominant frequency, as would be more usual for an unstable global mode. This is very similar to the behaviour to that was observed in a recent investigation by Davies & Thomas (2005) on the effects of mass transfer,

where suction was found to promote global instability.

L.3 Paper 3

Christopher Davies, Christian Thomas & Peter W. Carpenter - Global stability of the rotating disc boundary layer, *Journal of Engineering Mechanics*, **57(3)**, *219-236*, 2007

The global stability of the von Kármán boundary layer on the rotating disk is reviewed. For the genuine, radially homogeneous base flow, linearized numerical simulations indicate that convectively propagating forms of disturbances are predominant at all radii. The presence of absolute instability does not lead to the formation of any unstable global mode, even though the temporal growth rate of the absolute instability increases along the radial direction. Analogous behaviour can be found in the impulse solutions of a model amplitude equation, namely the linearized complex Ginzburg-Landau equation. These solutions show that, depending on the precise balance between spatial variations in the temporal growth rate and the corresponding shifts in the temporal frequency, globally stable behaviour can be obtained even in the presence of a strengthening absolute instability. The radial dependency of the absolute temporal frequency is sufficient to detune the disturbance oscillations at different radial positions, thus overcoming the radially increasing absolute growth, thereby giving rise to a stable global response. The origin of this form of behaviour can be traced to the fact that the cylindrical geometry of the rotating-disk flow dictates a choice of a globally valid time non-dimensionalization that, when properly employed, leads to a significant radial variation in the frequency for the absolute instability.

Bibliography

ABOUL-HASSAN, A. L. & ATTIA, H. A. 1997 Flow due to a rotating disk with Hall effect. *Physics Letters A* **228**, 286–290.

ALBOUSSIERE, T. & LINGWOOD, R. J. 2000 A model for the turbulent Hartmann layer. *Physics of Fluids* **1535-1543**, 12.

ALLEN, L. & BRIDGES, T. J. 2003 Hydrodynamic stability of the Ekman layer including interaction with a compliant surface: a numerical framework. *European Journal of Mechanics B/Fluids* **22**, 239–258.

ATTIA, H. A. & ABOUL-HASSAN, A. L. 2001 Effect of Hall current on the unsteady MHD flow due to a rotating disk with uniform suction or injection. *Applied Mathematical Modelling* **25**, 1089–1098.

ATTIA, H. A. & ABOUL-HASSAN, A. L. 2004 On hydromagnetic flow due to a rotating disk. *Applied Mathematical Modelling* **28**, 1007–1014.

BALAKUMAR, P. & MALIK, M. R. 1990 Travelling disturbances in rotating-disk flow. *Theoretical and Computational Fluid Dynamics* **2**, 125–137.

BANKS, W. H. H. 1965 The boundary layer on a rotating sphere. *Quarterly Journal of Mechanics and Applied Mathematics* **18**, 443–454.

BANKS, W. H. H. 1976 The laminar boundary layer on a rotating sphere. *Acta Mechanica* **24**, 273–287.

BARCILON, V. 1967 On the motion due to sources and sinks distributed along the vertical boundary of a rotating fluid. *Journal of Fluid Mechanics* **27**, 551–560.

BASSOM, A. P. & GAJJAR, J. S. B. 1988 Non-stationary crossflow vortices in 3-dimensional boundary-layer flows. *Proceedings of the Royal Society of London Series A - Mathematical Physical and Engineering Sciences* **417**, 179–212.

BASSOM, A. P. & SEDDOUGUI, S. O. 1992 The effects of suction on the nonlinear stability of the three-dimensional boundary layer above a rotating disc. *Proceedings of the Royal Society of London. Series A* **436**, 405–415.

BATCHELOR, G. K. 1951 Note on a class of solutions of the Navier-Stokes equations representing steady rotationally-symmetric flow. *Quarterly Journal of Mechanics and Applied Mathematics* **4**, 29–41.

BERS, A. 1975 Linear waves and instabilities. *Physique des Plasmas (ed. C. DeWitt & J. Peyraud)* pp. 117–215.

BÖDEWADT, U. T. 1940 Die Drehstromung uber festem Grund. *Z. Angew. Mathematical Mechanics* **20**, 241–253.

BRIDGES, T. J. & MORRIS, P. J. 1984 Differential eigenvalue problems in which the parameter appears nonlinearly. *Journal of Computational Physics* **55**, 437–460.

BRIGGS, R. J. 1964 *Electron-Stream Interactions in Plasmas (M.I.T. Press, Cambridge, MA)* .

CHOMAZ, J. 2004 Transition to turbulence in open flows: What linear and fully nonlinear local and global theories tell us. *European Journal of Mechanics B/Fluids* **23**, 385–399.

CHOMAZ, J. M., HUERRE, P. & REDEKOPP, L. G. 1988 Bifurcations to local and global modes in spatially developing flows. *Physical Review Letters* **60**, 25–28.

CHOMAZ, J.-M., HUERRE, P. & REDEKOPP, L. G. 1991 A frequency selection criterion in spatially developing flows. *Studies in Applied Mathematics* **84**, 119–144.

COCHRAN, W. G. 1934 The flow due to a rotating disk. *Proceedings of the Cambridge Philosophical Society* **30**, 365–375.

COOPER, A. J. & CARPENTER, P. W. 1997a The stability of rotating-disc boundary-layer flow over a compliant wall. 1. Type I and II instabilities. *Journal of Fluid Mechanics* **350**, 231–259.

COOPER, A. J. & CARPENTER, P. W. 1997b The stability of rotating-disc boundary-layer flow over a compliant wall. 2. Absolute instability. *Journal of Fluid Mechanics* **350**, 261–270.

COSSU, C. & CHOMAZ, J. M. 1997 Global measures of local convective instabilities. *Physical Review Letters* **78**, 4387–4390.

DAVIES, C. & CARPENTER, P. W. 1997a Numerical simulation of the evolution of Tollmien-Schlichting waves over finite compliant panels. *Journal of Fluid Mechanics* **335**, 361–392.

DAVIES, C. & CARPENTER, P. W. 1997b Instabilities in a plane channel flow between compliant walls. *Journal of Fluid Mechanics* **352**, 205–243.

DAVIES, C. & CARPENTER, P. W. 2001 A novel velocity-vorticity formulation of the Navier-Stokes equations with applications to boundary layer disturbance evolution. *Journal of Computational Physics* **172**, 119–165.

DAVIES, C. & CARPENTER, P. W. 2003 Global behaviour corresponding to the absolute instability of the rotating-disc boundary layer. *Journal of Fluid Mechanics* **486**, 287–329.

DAVIES, C. & THOMAS, C. 2005 Global stability of the rotating disk boundary layer and the effects of suction and injection. *Bulletin of the American Physical Society* **50(9)**, 266.

DAVIES, C. & THOMAS, C. 2006 The effects of a uniform axial magnetic field on the global stability of the rotating-disk boundary-layer. *Bulletin of the American Physical Society* **51(9)**, 74.

DAVIES, C., THOMAS, C. & CARPENTER, P. W. 2007 Global stability of the rotating disc boundary layer. *Journal of Engineering Mathematics* **57(3)**, 219–236.

DHANAK, M. R. 1992 Effects on uniform suction on the stability of flow on a rotating disc. *Proceedings of the Royal Society of London A* **439**, 431–440.

EKMAN, V. W. 1905 On the influence of the Earth's rotation on ocean currents. *Ark. Mat. Astr. Fys.* **2**.

FALLER, A. 1963 An experimental study of the instability of the laminar Ekman boundary layer **15**, 560–576.

FALLER, A. 1991 Instability and transition of disturbed flow over a rotating disk. *Journal of Fluid Mechanics* **230**, 245–269.

FALLER, A. & KAYLOR, R. 1966 A numerical study of the instability of the laminar Ekman boundary-layer. *Journal of Atmospheric Science* **23**, 466–480.

FASEL, H. 1980 In the numerical solution of the Navier-Stokes equations and hydrodynamic stability problems. *Computational Fluid Dynamics* pp. 168–279.

FEDOROV, B. I., PLAVNIK, G. Z., PROKHOROV, I. V. & ZHUKHOVITSKII, L. G. 1976 Transitional flow conditions on a rotating disk. *Journal of Engineering Physics* **31**, 1448–1453.

FERNANDEZ-FERIA, R. 2000 Axisymmetric instabilities of Bödewadt flow. *Physics of Fluids* **12**, 1730–1739.

FLORIANI, E., DUDOK DE WIT, T. & LE GAL, P. 2000 Nonlinear interactions in a rotating disk flow: from a Volterra model to the Ginzburg-Landau equation. *Chaos* **10**, 834–847.

FOSTER, R. C. 1997 Structure and energetics of optimal Ekman layer perturbations. *Journal of Fluid Mechanics* **333**, 97–123.

GAJJAR, J. S. B. 1996 On the nonlinear evolution of a stationary cross-flow vortex in a fully three-dimensional boundary layer flow. *P. W. Duck and P. Hall (Eds.) Nonlinear Instability and Transition in Three-Dimensional Boundary Layers, IUTAM Symposium, Manchester, UK, 1995, Kluwer* pp. 317–327.

GAJJAR, J. S. B., AREBI, M. A. & SIBANDA, P. 1996 Nonlinear development of cross-flow instabilities in compressible and incompressible boundary layer flows. *AIAA Paper No. 96-2159* .

GARRETT, S. & PEAKE, N. 2002 The stability and transition of the boundary layer on a rotating sphere. *Journal of Fluid Mechanics* **456**, 199–218.

GARRETT, S. & PEAKE, N. 2004 The stability of the boundary layer on a sphere rotating in a uniform axial flow. *European Journal of Mechanics B/Fluids* **23**, 241–253.

GARRETT, S. J. & PEAKE, N. 2007 The absolute instability of the boundary layer on a rotating cone. *European Journal of Mechanics B/Fluids* **26**, 344–353.

GATSKI, T. B. 1991 Review of incompressible fluid flow computations using the vorticity-velocity formulation. *Applied Numerical Methods* **7**, 227.

GRAY, W. E. 1952 The nature of the boundary layer at the nose of a swept back wing. *Unpublished, Min. Aviation, London* .

GREGORY, N., STUART, J. T. & WALKER, W. S. 1955 On the stability of three-dimensional boundary-layers with application to the flow due to a rotating disk. *Philosophical transactions of the Royal Society of London* **248**, 155–199.

GREGORY, N. & WALKER, W. S. 1960 Experiments on the effect of suction on the flow due to a rotating disk. *Journal of Fluid Mechanics* **9**, 225–234.

GROSCH, C. E. & ORSZAG, S. A. 1977 Numerical solution of problems in unbounded regions: coordinate transforms. *Journal of Computational Physics* **25**, 273–295.

HALL, P. 1986 An asymptotic investigation of the stationary modes of instability of the boundary layer on a rotating disc. *Proceedings of the Royal Society of London. Series A* **406**, 93–106.

HALL, P., BALALUMAR, P. & PAPAGEURGIU, D. 1992 On a class of unsteady three-dimensional Navier-Stokes solutions relevant to rotating disc flows: threshold amplitudes and finite-time singularities. *Journal of Fluid Mechanics* **238**, 297–323.

HALL, P., MALIK, M. R. & POLL, D. I. A. 1984 On the stability of an infinite attachment line boundary layer. *Proceedings of the Royal Society of London. Series A* **395**, 229–245.

HAMMOND, D. A. & REDEKOPP, L. G. 1997 Global dynamics of symmetric and asymmetric wakes. *Journal of Fluid Mechanics* **331**, 231–260.

HARRIS, D., BASSOM, A. P. & SOWARD, A. M. 2000 An inhomogeneous Landau equation with application to spherical Couette flow in the narrow gap limit. *Physica D* **137**, 260–276.

HARTMANN, J. & LAZARUS, F. 1937 Experimental investigations on the flow of mercury in a homogeneous magnetic field. *K. Dan. Vidensk. Selsk. Mat. Fys. Medd.* **15**, 1–45.

HEALEY, J. J. 2004 On the relation between the viscous and inviscid absolute instabilities of the rotating-disk boundary layer. *Journal of Fluid Mechanics* **511**, 179–199.

HEALEY, J. J. 2005 Long-wave theory for a new convective instability with exponential growth normal to the wall. *Philosophical Transactions of the Royal Society A* **363**, 1119–1130.

HEALEY, J. J. 2006a A new convective instability of the rotating-disk boundary layer with growth normal to the disk. *Journal of Fluid Mechanics* **560**, 279–310.

HEALEY, J. J. 2006b Inviscid long-wave theory for the absolute instability of the rotating-disk boundary layer. *Proceedings of the Royal Society A - Mathematical Physical and Engineering Sciences* **462**, 1467–1492.

HICKS, T. W. & RILEY, N. 1989 Boundary layers in magnetic Czochralski crystal growth. *Journal of Crystal Growth* **96**, 957–968.

HIDE, R. 1968 On source-sink flows in a rotating fluid. *Journal of Fluid Mechanics* **32**, 737–764.

HOWARTH, L. 1951 Note on the boundary layer on a rotating sphere. *Philosophical Magazine* **42**, 1308–1315.

HUERRE, P. 2000 Open shear flow instabilities pp. 159–229.

HUERRE, P. & MONKEWITZ, P. A. 1990 Local and global instabilities in spatially developing flows. *Annual Review of Fluid Mechanics* **22**, 473–537.

HUERRE, P. & ROSSI, M. 1998 *Hydrodynamic instabilities in open flows.*. Hydrodynamics and Nonlinear Instabilities, (ed. C. Godreche & P. Manneville) Cambridge University Press.

HUNT, R. E. 1995 *Spatially developing flows with localized forcing*. Ph.D. Thesis, Trinity College, Cambridge.

HUNT, R. E. & CRIGHTON, D. G. 1991 Instability of flows in spatially developing media. *Proceedings of the Royal Society of London. Series A* **435**, 109–128.

JASMINE, H. A. 2003 *Absolute and convective instabilities in some rotating flows*. Ph.D. Thesis, University of Manchester.

JASMINE, H. A. & GAJJAR, J. S. B. 2005a Convective and absolute instability in the incompressible boundary layer on a rotating disk in the presence of a uniform magnetic field. *Journal of Engineering Mathematics* **52**, 337–353.

JASMINE, H. A. & GAJJAR, J. S. B. 2005b Absolute and convective instabilities in the incompressible boundary layer on a rotating disk with temperature-dependent viscosity. *International Journal of Heat and Mass Transfer* **48**, 1022–1037.

JASMINE, H. A. & GAJJAR, J. S. B. 2005c Absolute instability of the von Kármán, Bödewadt and Ekman flows between a rotating disc and a stationary lid. *Philosophical Transactions of the Royal Society A* **1555**.

JENKINS, A. D. & BYE, J. A. J. 2004 The rotation of the Earth and processes near the air-sea interface: some aspects of the work of V. W. Ekman and its consequences. *Proceedings, Conference 'Climate Change in High Latitudes'* .

KOBAYASHI, R. 1981 Linear stability theory of boundary layer along a cone rotating in axial flow. *Bulletin of the Japan Society of Mechanical Engineers* **24**, 934–940.

KOBAYASHI, R. 1994 Review: Laminar-to-turbulent transition of three-dimensional boundary layers on rotating bodies. *Journal of Fluids Engineering* **116**, 200–209.

KOBAYASHI, R. & IZUMI, H. 1983 Boundary-layer transition on a rotating cone in still fluid. *Journal of Fluid Mechanics* **127**, 353–364.

KOBAYASHI, R., KOHAMA, Y. & KUROSAWA, M. 1983 Boundary-layer transition on a rotating cone in axial fluid. *Journal of Fluid Mechanics* **127**, 341–352.

KOBAYASHI, R., KOHAMA, Y. & TAKAMADATE, C. 1980 Spiral vortices in boundary layer transition regime on a rotating disk. *Acta Mechanica* **35**, 71–82.

KOCH, W. 1985 Local instability characteristics and frequency determination of self excited wake flows. *Journal of Sound and Vibration* **99**, 53–83.

KOHAMA, Y. 1984 Study on boundary layer transition of a rotating disk. *Acta Mechanica* **50**, 193–199.

KOHAMA, Y. & KOBAYASHI, R. 1983 Boundary-layer transition and the behaviour of spiral vortices on rotating spheres. *Journal of Fluid Mechanics* **137**, 153–164.

KOHAMA, Y. P. 2000 Three-dimensional boundary layer transition study. *Current Science* **79**, 800–807.

KRASNOV, D. D., ZIENICKE, E., ZIKANOV, O., BOECK, T. & THESS, A. 2004 Numerical study of the instability of the Hartmann layer. *Journal of Fluid Mechanics* **504**, 182–211.

KUIKEN, H. K. 1971 The effect of normal blowing on the flow near a rotating disk of infinite extent. *Journal of Fluid Mechanics* **47**, 789–798.

KUMAR, S. K., THACKER, W. I. & WATSON, L. T. 1987 Magnetohydrodynamic flow past a porous rotating disk in a circular magnetic field. In *International Journal for Numerical Methods in Fluids*, , vol. 8, pp. 659–669.

LANCASTER, P. 1964 Algorithms for Lambda matrices. *Numerische Mathematik* **6**, 388–394.

LE DIZES, S., HUERRE, P., CHOMAZ, J.-M. & MONKEWITZ, P. A. 1996 Linear global modes in spatially developing media. *Philosophical Transactions of the Royal Society of London. A* **354**, 169–212.

LILLY, D. K. 1966 On the instability of Ekman boundary flow. *Journal of Atmospheric Sciences* **23**, 481–494.

LINGWOOD, R. & ALFREDSON, P. 1999 Experimental study of the stability of the Bödewadt layer. *Laminar-Turbulent Transition* **Springer**, 553–558.

LINGWOOD, R. J. 1995 Absolute instability of the boundary-layer on a rotating-disk. *Journal of Fluid Mechanics* **299**, 17–33.

LINGWOOD, R. J. 1996 An experimental study of absolute instability of the rotating-disk boundary-layer flow. *Journal of Fluid Mechanics* **314**, 373–405.

LINGWOOD, R. J. 1997a On the effects of suction and injection on the absolute instability of the rotating-disk boundary layers. *Physics of Fluids* **9**, 1317–1328.

LINGWOOD, R. J. 1997b Absolute instability of the Ekman layer and related rotating flows. *Journal of Fluid Mechanics* **331**, 405–428.

LINGWOOD, R. J. 1997c On the impulse response for swept boundary-layer flows. *Journal of Fluid Mechanics* **344**, 317–334.

LINGWOOD, R. J. & ALBOUSSIERE, T. 1999 On the stability of the Hartmann layer. *Physics of Fluids* **11**, 2058–2068.

LOCK, R. C. 1955 The stability of the flow of an electrically conducting fluid between parallel planes under a transverse magnetic field. *Proceedings of the Royal Society of London A* **233**, 105–125.

MACK, L. M. 1985 The wave pattern produced by point source on a rotating disk. *AIAA Paper 85-0490* .

MACKERRELL, S. O. 2005 Stability of Bödewadt flow. *Philosophical Transactions of the Royal Society A* **1559**.

MALIK, M. R. 1986 The neutral curve for stationary disturbances in rotating-disk flow. *Journal of Fluid Mechanics* **164**, 275–287.

MALIK, M. R. & BALAKUMAR, P. 1992 Nonparallel stability of rotating disk flow using PSE. *Instability, Transition and Turbulence* pp. 168–180.

MALIK, M. R., WILKINSON, S. P. & ORSZAG, S. A. 1981 Instability and transition in rotating disk flow. *AIAA* **19**, 1131–1138.

MANOHAR, R. 1967 The boundary layer on a rotating sphere. *Zeitschrift fur angewandte Mathematik und Physik* **18**, 320–330.

MELANDER, M. V. 1983 An algorithmic approach to the linear stability of the Ekman layer. *Journal of Fluid Mechanics* **132**, 283–293.

MINTO, S. L. & PLEVA, E. 2002 Website:www.met.tamu.edu/class/metr452/ models/2001/PBLproject.html.

MONKEWITZ, P. A. 1990 The role of absolute and convective instability in predicting the behaviour of fluid systems. *European Journal of Mechanics, B/Fluids* **9**, 395–413.

MONKEWITZ, P. A., HUERRE, P. & CHOMAZ, J. 1993 Global linear stability analysis of weakly non-parallel shear flows. *Journal of Fluid Mechanics* **251**, 1–20.

MORESCO, P. & ALBOUSSIERE, T. 2003 Weakly nonlinear stability of Hartmann boundary layers. *European Journal of Mechanics, B-Fluids* **22**, 245–253.

MORESCO, P. & ALBOUSSIERE, T. 2004a Stability of Bödewadt-Hartmann layers. *European Journal of Mechanics, B-Fluids* **23**, 851–859.

MORESCO, P. & ALBOUSSIERE, T. 2004b Experimental study of the instability of the Hartmann layer. *Journal of Fluid Mechanics* **504**, 167–181.

NANSEN, F. 1902 Oceanography of the north polar basin: The Norwegian north polar expedition 1893 - 1896. *Scientific Results* **Vol III**.

NOLAN, D. S. 2005 Instabilities in hurricane-like boundary-layers. *Dynamics of Atmospheres and Oceans* **40**, 209–236.

OCKENDON, H. 1972 An asymptotic solution for steady flow above an infinite rotating disc with suction. *Quarterly Journal of Mechanics and Applied Mathematics* **25**, 291–301.

OKAMOTO, T., YAGITA, M. & KAMIJIMA, Y. 1976 Experimental investigation on the boundary-layer flow over a rotating cone-cylinder body in a uniform stream. *Bulletin of the Japan Society of Mechanical Engineers* **19**, 930–937.

ORGAN, A. E. & RILEY, N. 1987 Oxygen transport in magnetic Czochralski growth of Silicon. *Journal of Crystal Growth* **82**, 465–476.

OTHMAN, H. & CORKE, T. 2006 Experimental investigation of absolute instability of a rotating-disk boundary-layer. *Journal of Fluid Mechanics* **565**, 63–94.

OWEN, J. M., PINCOMBE, J. R. & ROGERS, R. H. 1985 Source-sink flow inside a rotating cylindrical cavity. *Journal of Fluid Mechanics* **155**, 233–265.

PAO, H. P. 1968 Magnetohydrodynamic flows over a rotating disk. *AIAA Journal* **6**, 1285–1291.

PIER, B. 2003 Finite-amplitude crossflow vortices, secondary instability and transition in the rotating-disk boundary layer. *Journal of Fluid Mechanics* **487**, 315 – 343.

PIERREHUMBERT, R. T. 1984 Local and global baroclinic instability of zonally varying flow. *Journal of Atmospheric Sciences* **41**, 2141–2162.

REED, H. L. & SARIC, W. S. 1989 Stability of three-dimensional boundary-layers. *Annual Review of Fluid Mechanics* **21**, 235–284.

ROGERS, M. H. & LANCE, G. N. 1960 The rotationally symmetric flow of a viscous fluid in the presence of an infinite rotating disk. *Journal of Fluid mechanics* **7**, 617–631.

SAVAS, O. 1987 Stability of Bödewadt flow. *Journal of Fluid Mechanics* **183**, 77–94.

SCHLICHTING, H. 1933 Berechnung der Anfachung kleiner störungen bei der Plattenströmung. *ZAMM* **13**, 171–174.

SCHMID, P. J. & HENNINGSON, D. S. 2001 Stability and transition in shear flows. *Applied Mathematical Sciences, Springer* **142**.

SOWARD, A. M. 1977 On the finite amplitude thermal instability of a rapidly rotating sphere. *Geophysical and Astrophysical Fluid Dynamics* **9**, 19–74.

SOWARD, A. M. 1992 Thin disc kinematics $\alpha\omega$-dynamo models ii. Short length scale modes. *Geophysical and Astrophysical Fluid Dynamics* **64**, 201–225.

SPALART, P. R. 1991 On the cross-flow instability near a rotating disk. *Boeing Commercial Airplane Group* .

SPARROW, E. M. & CESS, R. D. 1962 Magnetohydrodynamic and heat transfer about a rotating disk. *ASME Journal of Applied Mechanics* **29**, 181–187.

SPARROW, E. M. & GREGG, J. L. 1960 Mass transfer, flow, and heat transfer about a rotating disk. *Journal of Heat Transfer* **82**, 294–302.

SPEZIALE, C. G. 1987 On the advantages of the vorticity-velocity formulation of the equations of fluid dynamics. *Journal of Computational Physics* **73**, 476–480.

SPOONER, G. F. & CRIMINALE, W. O. 1982 The evolution of disturbances in an Ekman boundary layer. *Journal of Fluid Mechanics* **115**, 327–346.

STEPHENSON, C. J. 1969 Magnetohydrodynamic flow between rotating coaxial disks. *Journal of Fluid Mechanics* **38**, 335–352.

STEWARTSON, K. 1957 On almost rigid rotations. *Journal of Fluid Mechanics* **3**, 17–26.

STUART, J. T. 1954 On the effects of uniform suction on the steady flow due to a rotating disk. *Quarterly Journal of Mechanics and Applied Mathematics* **7**, 446–457.

SURYAPRAKASARAO, U. & GUPTA, A. S. 1966 Hydromagnetic flow due to a rotating disc subjected to large suction. *Journal of the Physical Society of Japan* **21**, 2390–2400.

TANIGUCHI, H., KOBAYASHI, R. & FUKUNISHI, Y. 1998 Stability of the boundary layer on a sphere rotating in still fluid. *Acta Mechanica* **129**, 243–253.

TATRO, P. R. & MOLLO-CHRISTENSEN, E. L. 1967 Experiments on Ekman layer instability. *Journal of Fluid Mechanics* **28**, 531–543.

THACKER, W. I., WATSON, L. T. & KUMAR, S. K. 1990 Magnetohydrodynamic free convection from a disc rotating in a vertical plane. *Applied Mathematical Modelling* **14**, 527–535.

TIEN, C. L. & CAMPBELL, D. T. 1963 Heat and mass transfer from rotating cones. *Journal of Fluid Mechanics* **17**, 105–112.

TOLLMIEN, W. 1936 General instability criterion of laminar velocity distributions. *Tech. Memor. Nat. Adv. Comm. Aero. Wash* **1**, 79–114.

TURKYILMAZOGLU, M. & GAJJAR, J. S. B. 1997 Absolute/convective instabilities and direct spatial resonance in fully 3-D boundary layer flows.

VON KÁRMÁN, T. 1921 Über laminare und turbulente Reibung. *Z. Angew. Math. Mech.* **1**, 233–252.

WILKINSON, S. P. & MALIK, M. R. 1983 Stability experiments in the flow over a rotating disk. *AIAA* **23**, 588–595.

WILSON, L. O. & SCHRYER, N. L. 1978 Flow between a stationary and a rotating disk with suction. *Journal of Fluid Mechanics* **85**, 479–496.